frontiers | Research Topics

Understanding the causes of asymmetries in earth's magnetosphere-ionosphere system

Edited by
Denny Oliveira, Daniel Welling, Hyomin Kim, Christine Gabrielse, Jone Peter Reistad and Karl Laundal

Published in
Frontiers in Astronomy and Space Sciences

ISSN 1664-8714
ISBN 978-2-83252-147-2
DOI 10.3389/978-2-83252-147-2

About Frontiers

Frontiers is more than just an open access publisher of scholarly articles: it is a pioneering approach to the world of academia, radically improving the way scholarly research is managed. The grand vision of Frontiers is a world where all people have an equal opportunity to seek, share and generate knowledge. Frontiers provides immediate and permanent online open access to all its publications, but this alone is not enough to realize our grand goals.

Frontiers journal series

The Frontiers journal series is a multi-tier and interdisciplinary set of open-access, online journals, promising a paradigm shift from the current review, selection and dissemination processes in academic publishing. All Frontiers journals are driven by researchers for researchers; therefore, they constitute a service to the scholarly community. At the same time, the *Frontiers journal series* operates on a revolutionary invention, the tiered publishing system, initially addressing specific communities of scholars, and gradually climbing up to broader public understanding, thus serving the interests of the lay society, too.

Dedication to quality

Each Frontiers article is a landmark of the highest quality, thanks to genuinely collaborative interactions between authors and review editors, who include some of the world's best academicians. Research must be certified by peers before entering a stream of knowledge that may eventually reach the public - and shape society; therefore, Frontiers only applies the most rigorous and unbiased reviews. Frontiers revolutionizes research publishing by freely delivering the most outstanding research, evaluated with no bias from both the academic and social point of view. By applying the most advanced information technologies, Frontiers is catapulting scholarly publishing into a new generation.

What are Frontiers Research Topics?

Frontiers Research Topics are very popular trademarks of the *Frontiers journals series*: they are collections of at least ten articles, all centered on a particular subject. With their unique mix of varied contributions from Original Research to Review Articles, Frontiers Research Topics unify the most influential researchers, the latest key findings and historical advances in a hot research area.

Find out more on how to host your own Frontiers Research Topic or contribute to one as an author by contacting the Frontiers editorial office: frontiersin.org/about/contact

Understanding the causes of asymmetries in earth's magnetosphere-ionosphere system

Topic editors

Denny Oliveira — University of Maryland, Baltimore County, United States
Daniel Welling — University of Texas at Arlington, United States
Hyomin Kim — New Jersey Institute of Technology, United States
Christine Gabrielse — The Aerospace Corporation, El Segund, United States
Jone Peter Reistad — University of Bergen, Norway
Karl Laundal — University of Bergen, Norway

Citation

Oliveira, D., Welling, D., Kim, H., Gabrielse, C., Reistad, J. P., Laundal, K., eds. (2023). *Understanding the causes of asymmetries in earth's magnetosphere-ionosphere system*. Lausanne: Frontiers Media SA. doi: 10.3389/978-2-83252-147-2

Table of contents

frontiers | Frontiers in Astronomy and Space Sciences

TYPE Editorial
PUBLISHED 28 March 2023
DOI 10.3389/fspas.2023.1173630

OPEN ACCESS

EDITED AND REVIEWED BY
Joseph E. Borovsky,
Space Science Institute, United States

*CORRESPONDENCE
Denny M. Oliveira,
denny.m.deoliveira@nasa.gov

SPECIALTY SECTION
This article was submitted to Space Physics, a section of the journal Frontiers in Astronomy and Space Sciences

RECEIVED 24 February 2023
ACCEPTED 07 March 2023
PUBLISHED 28 March 2023

CITATION
Oliveira DM, Welling DT, Kim H, Gabrielse CE, Reistad JP and Laundal K (2023), Editorial: Understanding the causes of asymmetries in Earth's magnetosphere-ionosphere system. *Front. Astron. Space Sci.* 10:1173630. doi: 10.3389/fspas.2023.1173630

Editorial: Understanding the causes of asymmetries in Earth's magnetosphere-ionosphere system

Denny M. Oliveira[1,2]*, Daniel T. Welling[3], Hyomin Kim[4], Christine E. Gabrielse[5], Jone Peter Reistad[6] and Karl Laundal[6]

[1]Goddard Planetary Heliophysics Institute, University of Maryland, Baltimore County, Baltimore, MD, United States, [2]NASA Goddard Space Flight Center, Greenbelt, MD, United States, [3]Birkeland Centre for Space Science, Department of Physics and Technology, University of Bergen, Bergen, Norway, [4]New Jersey Institute of Technology, Newark, NJ, United States, [5]The Aerospace Coorporation, El Segundo, CA, United States, [6]Climate and Space Sciences and Engineering Department, University of Michigan, Ann Arbor, MI, United States

KEYWORDS

magnetosphere-ionophere coupling, IMF B_y effects, season effects, data analisys, numerical modeling

Editorial on the Research Topic
Understanding the causes of asymmetries in Earth's magnetosphere-ionosphere system

Geomagnetic activity observed in geospace, the upper atmosphere, and on the ground results from solar-terrestrial interactions. Such interactions correspond to the coupling between the solar wind, magnetosphere, and the thermosphere-ionosphere (MIT) system (Khazanov, 2016). However, given the complexity of the whole system and its large spatial scale and long-term solar variability, effects resulting from this coupling can be asymmetric. For example, inter-hemispherical asymmetric responses can arise when a hemisphere receives more energy than the other (e.g., Knipp et al., 2021; Pakhotin et al., 2021), local time effects can take place due to the occurrence of intense dawn-dusk interplanetary electric fields (e.g., Haaland et al., 2017), and asymmetric geomagnetic field and mapping are caused by the Earth's dipole offset and tilt (e.g., Laundal et al., 2017).

The drivers that generate asymmetric MIT coupling response are generally recognized as long term: solar activity (Zhang et al., 2022) and dipole offset and tilt (Laundal et al., 2017); middle term: seasons (Lu et al., 2010); and short term: the y and z components of the interplanetary magnetic field (IMF) (Cowley, 1981; Li et al., 2011; Knipp et al., 2021). Thermospheric neutral mass density can present local time asymmetries associated with IMF B_y (Forster et al., 2017), and inter-hemispheric asymmetries can be generated by cross-hemispheric propagation of large-scale gravity waves (Bruinsma and Forbes, 2007). In addition, forcing from the mesosphere and lower thermosphere can generate inter-hemispheric neutral wind asymmetric patterns that can in turn asymmetrically impact neutral density in different hemispheres (Stober et al., 2021).

This Research Topic received 10 articles dealing with asymmetric responses of the MIT system to different types of solar wind forcing. Most articles focused on effects caused by the IMF B_y component, but there are contributions with focus on seasonal effects as well as effects on the ionosphere and upper thermosphere caused by large-scale gravity waves coming from the lower thermosphere. The articles focus on a variety of data analysis techniques, including machine learning and data assimilation, as well as numerical simulations. Data analyses include solar wind and IMF data, magnetic field in geosynchronous orbit, low-Earth orbit thermospheric neutral mass density data, ionospheric current data, and ground magnetometer data. Physics-based models and empirical models are used in the simulations.

We start with the contribution provided by Ohma et al., who performed a statistical and superposed epoch analysis study of the magnetic field in nightside geosynchronous orbit to investigate how substorms evolve in association with B_y. The authors found that $|B_y|$ in the magnetotail increases during the loading phase of substorms, i.e., prior to substorm onset. Then, $|B_y|$ reaches maximum values during the expansion phase and is significantly reduced during the remaining unloading phase. Eggington et al. conducted magnetohydrodynamic simulations of a geomagnetic storm to study the timescales over which asymmetries in the magnetotail appeared in response to variations in the IMF By component. They concluded that during strong solar wind driving, asymmetries in the magnetotail caused by IMF B_y appear after convection has communicated the information. However, during weaker driving, induced B_y effects can drive asymmetries in the 15–40 Earth radii region on shorter timescales.

Laundal et al. introduced the concept of a displacement field, a two-dimensional vector defined on a spherical shell that explains how magnetic field line footprints between both northern and southern hemispheres are displaced to one another as a result from perturbations in the geomagnetic field in the magnetosphere. By using an empirical model to account for ionospheric convection (Weimer, 2005), Laundal et al. (2018) found that inter-hemispheric asymmetries generated by the displacement field associated with the dipole tilt can sometimes surpass the asymmetric effects generated by the IMF B_y. By using an empirical model based on magnetic field measurements in low-Earth orbit, Hatch et al. found that Birkland current densities are mirrored from the northern to the southern hemispheres when the signs of IMF B_y and of the dipole tilt angle are reversed.

The effects of sudden changes in solar wind ram pressure caused by interplanetary discontinuities were investigated by Madelaire et al. The authors used 2.5 decades of ground magnetometer data to discover two interesting local time asymmetries: 1) a dawn-dusk asymmetry when IMF $B_z > 0$ in the first 30 min with stronger perturbations on the dawn side, and 2) a noon-midnight asymmetry when IMF $B_z < 0$ with stronger perturbations on the nightside. Madelaire et al. attributed the first effect to the amplification of the partial ring current, and the second effect to significant contributions by dipolarization of the near-tail geomagnetic field. Madelaire et al. used the same event list provided by Madelaire et al. to investigate the effects of dynamic pressure on the high-latitude transient geomagnetic field response. The authors found a pre-noon current vortex that moves westward, and a post-noon current vortex that does not move toward the nightside as suggested by previous numerical and experimental works.

Weygand et al. studied inter-hemispheric variations of the horizontal ground geomagnetic field recorded by southern hemisphere stations in Antarctica and the corresponding conjugate northern hemisphere stations in Canada and Iceland. The authors showed differences of onset times of the field variations associated with moderate IMF B_y (0.5–2.5 nT) occurring during summer and winter seasons.

An integrated study of inter-hemispheric asymmetries in the ionosphere-thermosphere system using experimental analysis and numerical simulations was performed by Hong et al. The authors used field-aligned currents observed by the Active Magnetosphere and Planetary Electrodynamics Response Experiment to specify the high-latitude electric potential in the Global Ionosphere and Thermosphere Model during a magnetic storm. Results show that inter-hemispheric asymmetries are highly dependent on IMF B_y, with intense asymmetries occurring around the equinox with more Joule heating associated with high-latitude electric potential in the southern hemisphere. Zhu et al. found with numerical simulations that large-scale gravity waves launched in different hemispheres with different phase speeds during an intense magnetic storm can generate asymmetric negative storm phases at the equatorial ionization anomaly peak region located in the afternoon sector of the ionosphere. Maute et al. studied the effects caused by lower atmospheric forcing on the magnetosphere-ionosphere system and the subsequent thermospheric neutral mass density during a moderate magnetic storm. Using more realistic lower boundary conditions in Whole Atmosphere Community Climate Model extended simulations, the authors showed that the northern hemisphere neutral density can be improved by up to 15% against climatological lower boundary conditions.

In summary, this Research Topic provides a good overview of asymmetric effects in the MIT system caused by several drivers, in particular the IMF B_y. These contributions result from ongoing efforts and include future perspectives, new methodologies, and new aspects concerning the combination of data analyses and numerical simulations.

Author contributions

All authors listed have made a substantial, direct, and intellectual contribution to the work and approved it for publication.

Funding

DO acknowledges funding provided by the NASA HGIO program through grant 80NSSC22K0756. CG was funded by NASA grant 80NSSC20K0606, the CUSIA DRIVE Center. JR was funded by the Norwegian Research Council (NRC) through grant 300844/F50.

Conflict of interest

Author CG was employed by the company The Aerospace Coorporation.

The remaining authors declare that the research was conducted in the absence of any commercial or financial relationships that could be construed as a potential conflict of interest.

Publisher's note

References

Bruinsma, S. L., and Forbes, J. M. (2007). Global observation of traveling atmospheric disturbances (TADs) in the thermosphere. *Geophys. Res. Lett.* 34, L14103. doi:10.1029/2007GL030243

Cowley, S. W. H. (1981). Magnetospheric asymmetries associated with the y-component of the IMF. *Planet. Space Sci.* 29, 79–96. doi:10.1016/0032-0633(81)90141-0

Forster, M., Doornbos, E., and Haaland, S. E. (2017). "The role of the upper atmosphere for dawn-dusk differences in the coupled magnetosphere-ionosphere-thermosphere system," in *Dawn-dusk asymmetries in planetary plasma environments*. Editors S. Haaland, A. Runov, and C. Forsyth (Hoboken, NJ: Wiley), 125–141. doi:10.1002/9781119216346.ch10

Haaland S., Runov A., and Forsyth C. (Editors) (2017). "Dawn-dusk asymmetries in planetary plasma environments," *Geophysical monograph series* (Washington, D.C.: American Geophysical Union), 230. doi:10.1002/9781119216346

Khazanov, G. V. (2016). *Space weather fundamentals*. Boca Raton, FL: CRC Press.

Knipp, D., Kilcommons, L., Hairston, M., and Coley, W. R. (2021). Hemispheric asymmetries in poynting flux derived from DMSP spacecraft. *Geophys. Res. Lett.* 48, e2021GL094781. doi:10.1029/2021GL094781

Laundal, K. M., Cnossen, I., Milan, S. E., Haaland, S. E., Coxon, J., Pedatella, N. M., et al. (2017). North-South asymmetries in Earth's magnetic field. *Space Sci. Rev.* 206, 225–257. doi:10.1007/s11214-016-0273-0

Laundal, K. M., Finlay, C. C., Olsen, N., and Reistad, J. P. (2018). Solar wind and seasonal influence on ionospheric currents from swarm and CHAMP measurements. *J. Geophys. Res. Space Phys.* 123, 4402–4429. doi:10.1029/2018JA025387

Li, W., Knipp, D., Lei, J., and Raeder, J. (2011). The relation between dayside local Poynting flux enhancement and cusp reconnection. *J. Geophys. Res.* 116, 1–16. doi:10.1029/2011JA016566

Lu, G., Mlynczak, M. G., Hunt, L. A., Woods, T. N., and Roble, R. G. (2010). On the relationship of joule heating and nitric oxide radiative cooling in the thermosphere. *J. Geophys. Res.* 115. doi:10.1029/2009JA014662

Pakhotin, I. P., Mann, I. R., Xie, K., Burchill, J. K., and Knudsen, D. J. (2021). Northern preference for terrestrial electromagnetic energy input from space weather. *Nat. Commun.* 21, 199. doi:10.1038/s41467-020-20450-3

Stober, G., Kuchar, A., Pokhotelov, D., Liu, H., Liu, H.-L., Schmidt, H., et al. (2021). Interhemispheric differences of mesosphere-lower thermosphere winds and tides investigated from three whole-atmosphere models and meteor radar observations. *Ann. Geophys.* 21, 13855–13902. doi:10.5194/acp-21-13855-2021

Weimer, D. R. (2005). Improved ionospheric electrodynamic models and application to calculating Joule heating rates. *J. Geophys. Res.* 110, A05306–A05321. doi:10.1029/2004JA010884

Zhang, X. J., Deng, L. H., Fei, Y., Li, C., Tian, X. A., and Wan, Z. J. (2022). Hemispheric asymmetry of long-term sunspot activity: Sunspot relative numbers for 1939-2019. *Mon. Notices R. Astronomical Soc.* 514, 1140–1147. doi:10.1093/mnras/stac1231

frontiers | Frontiers in Astronomy and Space Sciences

ORIGINAL RESEARCH
published: 05 May 2022
doi: 10.3389/fspas.2022.904620

Geomagnetic Response to Rapid Increases in Solar Wind Dynamic Pressure: Event Detection and Large Scale Response

Michael Madelaire[1], Karl M. Laundal[1], Jone P. Reistad[1], Spencer M. Hatch[1], Anders Ohma[1] and Stein Haaland[1,2]*

[1]Birkeland Centre for Space Science, Bergen, Norway, [2]Max Planck Institute for Solar System Research, Göttingen, Germany

Discontinuities in the solar wind trigger a variety of processes in the magnetosphere-ionosphere system. A rapid increase in solar wind dynamic pressure causes compression of the magnetosphere. This manifests itself as a positive perturbation of the horizontal ground magnetic field at low/mid latitudes. In this study we present a method for detecting these discontinuities *in situ* solar wind data by using the random forest machine learning algorithm. Each detected event is propagated to Earth and its arrival time is aligned with a corresponding response in the low latitude ground magnetic field. A list of 3,867 events, detected between 1994 and 2019, is presented. We use the list in a superposed epoch analysis of the low/mid latitude response in the ground magnetic field at different local times, and of the high latitude response using the Polar Cap index. A dawn-dusk asymmetry is found at low/mid latitudes with weaker positive perturbations at dawn compared to any other local time sector. This suggests a stronger ring current contribution at dawn assuming the magnetopause contribution to be uniform. During northward IMF the initial response is asymmetric, but returns to symmetry after 30 min. During southward IMF the low/mid latitude response decays rapidly in all local sectors except dawn. After around 30 min the asymmetry has flipped such that the strongest positive perturbation is at dawn. This suggests an amplification of the partial ring current. In addition, a noon-midnight asymmetry is observed during southward IMF with the strongest positive perturbation on the night side suggesting a significant contribution from dipolarization of the geomagnetic field in the near tail. The complex geomagnetic response to rapid increases in solar wind dynamic pressure demonstrates a need for further statistical analyses. Event lists, such as the one presented here, are critical components in such studies.

Keywords: solar wind dynamic pressure, rapid pressure increase, magnetospheric compression, sudden commencement, machine learning, superposed epoch analysis, ring current asymmetry

OPEN ACCESS

Edited by:
Olga V. Khabarova, Institute of Terrestrial Magnetism Ionosphere and Radio Wave Propagation (RAS), Russia

Reviewed by:
Zdenek Nemecek, Charles University, Czechia
Vladimir Parkhomov, Baikal State University, Russia

****Correspondence:***
Michael Madelaire
michael.madelaire@uib.no

Specialty section:
This article was submitted to Space Physics, a section of the journal Frontiers in Astronomy and Space Sciences

Received: *25 March 2022*
Accepted: *08 April 2022*
Published: *05 May 2022*

Citation:
Madelaire M, Laundal KM, Reistad JP, Hatch SM, Ohma A and Haaland S (2022) Geomagnetic Response to Rapid Increases in Solar Wind Dynamic Pressure: Event Detection and Large Scale Response. Front. Astron. Space Sci. 9:904620. doi: 10.3389/fspas.2022.904620

1 INTRODUCTION

The solar wind flows radially outward from the Sun, populating the interplanetary space and carrying with it the Sun's magnetic field referred to as the Interplanetary Magnetic Field (IMF). The magnetosphere-ionosphere-thermosphere system is heavily dependent on conditions in the solar

wind and IMF. Understanding this complex system is a difficult task. Natural phenomena in the solar wind can perturb the entire system. Studying their characteristics in combination with those of the perturbed system may result in a deeper understanding of the dynamic system and its dependencies.

In this study we focus on rapid increases in solar wind dynamic pressure P_d. This type of event can have various origins. The best known of these are coronal mass ejections, a large and sudden release of plasma from the Sun. The ejecta is referred to as interplanetary coronal mass ejection when propagating through interplanetary space and can form an interplanetary shock (IS). Another well known origin is a stream interaction region which occurs in the rarefaction zone of two solar wind streams. However, ISs (of the forward type) rarely evolve in these rarefaction zones before they have passed Earth and are therefore seldom observed at Earth (Smith and Wolfe, 1976). A detailed description of ISs is given by Oliveira and Samsonov (2018).

Rapid changes in P_d can occur without the formation of a shock. In their examination of such solar wind structures Dalin et al. (2002a) found that the majority of cases occurred due to increases in solar wind number density and not solar wind speed. Additionally, they found that their occurrence rate was independent of solar cycle, unlike ISs (Oliveira and Samsonov, 2018).

Rapid increases in P_d are linked to Sudden Commencements (SC). The term SC comes from storm sudden commencement which is a pressure-induced magnetic perturbation on ground that precedes a geomagnetic storm. However, it was suspected that the phenomena could occur without being followed by a storm and thus SC was termed. In addition, the term sudden impulse was coined after the discovery of a characteristic perturbation in the H-component later shown to be caused by the same mechanism as the SC. We will use the term SC as a general expression for both storm sudden commencement and sudden impulse as suggested by Curto et al. (2007).

Following Araki (1994), we divide the ground response D_{sc} into a low-latitude (DL) and high-latitude (DP) response:

$$\begin{aligned} D_{sc} &= DL + DP \\ DP &= DP_{PI} + DP_{MI} \end{aligned} \tag{1}$$

DL is thought to be a direct effect of magnetospheric compression which increases the magnetic flux density resulting in a positive perturbation of the horizontal magnetic field. DP is connected to vortices in the high latitude ionosphere. The vortices occur in two pairs; the first is the preliminary impulse PI and the second is the main impulse MI.

Describing these contributions and the parameters they depend on requires a large set of events to facilitate analysis of multiple sub-sets with a statistically meaningful size. This study will focus on finding suitable events and on analysis of the magnetospheric contribution. The ionospheric contribution will be addressed in a later study.

Several statistical studies of the geospace response to ISs have been made (Russell et al., 1994a,b; Russell and Ginskey, 1995). It was found that an increase in the horizontal magnetic field due to compression of the magnetosphere, at 20° latitude, is expected to be around 18.4 $nT/nPa^{\frac{1}{2}}$ during northward IMF (Russell et al., 1994a) and 13.8 $nT/nPa^{\frac{1}{2}}$ (i.e., 25% lower) during southward IMF (Russell et al., 1994b). It was also found that the magnetic field perturbation is dependent on local time, being largest on the dayside and smallest at night. In their examination of the response at subauroral latitudes, Russell and Ginskey (1995) found that the PI lasted for ~1 min, and was followed by a steady increase over a 5-min period as a result of magnetospheric compression and the main impulse.

Our goal is to isolate the influence of dipole tilt and IMF orientation on SC development. None of the lists of events described in existing statistical studies of SCs are appropriate for our purposes, since to our knowledge these studies are tailored to ISs and/or the lists contain too few events to separate events into bins based on more than one environmental parameter without compromising the ability to yield statistically meaningful conclusions.

Before the use of *in situ* observations of solar wind plasma, lists of SC were made by inspection of observations from ground magnetometer stations. A historical overview of the study of SCs is given in Curto et al. (2007). Various lists from the early to mid-19th century are mentioned, one of which is still maintained and can be accessed at http://www.obsebre.es/en/rapid.

During the late 20th century *in situ* solar wind data became more common and the connection between SC and changes in P_d was made (Friis-Christensen et al., 1988). At the same time lists of various solar wind events were made, typically either through cumbersome manual inspection or through manual verification after applying an algorithm to the raw data. Two classic lists of interplanetary coronal mass ejections and stream interaction regions using the manual approach were presented by Richardson and Cane (1995) and Jian et al. (2006), respectively. A list of ISs was presented by Oliveira and Raeder (2015), containing 461 events spanning 1995–2013. The list is a compilation of four other lists combined with the authors own manually verified events detected by an algorithm. In addition, Boudouridis and Zesta (2021) recently presented an algorithm for automated detection of rapid pressure increases by fitting a logistic function to *in situ* solar wind data.

These lists are all based on measurements from the solar wind, and only a few provide the arrival time at Earth. We know only one analysis where the arrival time was determined based on ground magnetometers: Huang and Yumoto (2006) presented 160 instances of P_d enhancements between 1998 and 2005, and arrival times were determined based on a corresponding ground response. We use this concept when addressing arrival time in **Section 3.2**.

In **Section 2**, we describe the solar wind and magnetometer measurements that we use to derive our list. In **Section 3**, we describe our methodology for automated identification of rapid P_d increase via the random forest machine learning algorithm and the estimated arrival time at Earth. In **Section 4**, we discuss the resulting list of 3,867 events, which covers a 26-year period, and perform a superposed epoch analysis using various subsets of the event list to isolate the influence of controlling parameters. In **Sections 5** we discuss the implications of the event detection method, a seasonal dependence of the occurrence rate, and the

interpretation of a possible dawn-dusk ring current asymmetry. **Section 6** concludes the paper.

2 DATA

The aim of this study is two-fold; to create a list of rapid P_d increases leading to measurable magnetic ground perturbation, and to perform a statistical analysis of these magnetic ground perturbations. In order to achieve this, both *in situ* solar wind measurements and ground-based magnetic field measurements are required.

2.1 *In Situ* Solar Wind

In situ observations of the solar wind spanning 1994–2019 was provided by the Advanced Composition Explorer (ACE) and Wind missions. The two spacecraft measure solar wind plasma characteristics using the Solar Wind Experiment (SWE) (Ogilvie et al., 1995) and the Solar Wind Electron, Proton and Alpha Monitor (SWEPAM) (McComas et al., 1998). The IMF is measured using the Magnetic Fields Investigation (MFI) (Lepping et al., 1995) and magnetometer (MAG) (Smith et al., 1998) instruments. Plasma data with a temporal resolution of 3- and 64-s and IMF data with a temporal resolution of 3- and 16-s for ACE and Wind, respectively, was downloaded from the Coordinated Data Analysis Web (CDAWeb) at https://cdaweb.gsfc.nasa.gov/index.html/. All solar wind observations were up- or down-sampled to 1-min resolution after interpolating data gaps smaller than 4 min.

Measurements from Wind were provided in the GSE reference frame. A rotation into GSM was therefore carried out using the method described in Hapgood (1992). The GSM reference frame is preferred as it better describes coupling between the IMF and Earth's magnetic field.

2.2 Indices

The SYM-H index (Iyemori et al., 2010) at 1-min resolution was used for arrival time estimates of events. The SYM-H index is closely related to the ground magnetic perturbation due to the ring current and is strongly correlated with P_d enhancements (Burton et al., 1975). This index is accessible at https://omniweb.gsfc.nasa.gov.

For the superposed epoch analysis another ring current index was used: SMR (Newell and Gjerloev, 2012) is a ring current index provided by the SuperMAG web service (https://supermag.jhuapl.edu/), based on a much larger number of magnetometers than SYM-H. This is important for the study of asymmetry as it allows for a local time dependent index SMR LT which is provided in four 6-h wide sectors centered at midnight/dawn/noon/dusk (00/06/12/18). The high latitude response was investigated using the polar cap index PC for the northern hemisphere PCN. This index is based on the Thule magnetometer station on Greenland (Willer, 2021). It is accessible at https://omniweb.gsfc.nasa.gov. Both indices are provided in a 1-min resolution.

3 METHODS

In this section we introduce the method with which the list of rapid P_d increases is generated. The process is separated into two main steps. First an algorithm processes the *in situ* solar wind data to find events. Then the event is aligned with a corresponding response on ground. In this study an event refers to a step-like increase in P_d that provokes a measurable geomagnetic response on ground.

Section 3.1 focuses on detection of events, while **Section 3.2** describes how we match the detected events with a response measured by magnetometers on ground.

3.1 Event Detection

Detection of events is done using 120 min segments of *in situ* solar wind measurements of P_d as input into a machine learning algorithm. The algorithm is designed to classify whether or not a rapid pressure increase (an event) is present in these segments. The algorithm is based on a set of features determined from each segment.

The training data is described in **Section 3.1.1**, the features are explained in detail in **Section 3.1.2**, and an introduction to the random forest machine learning algorithm is given in **Section 3.1.3**.

3.1.1 Training Data

In this study we work with two classes: *events* and *non-events*. Our training data must contain examples of each of these classes.

The training data were compiled in two ways. The *events* were taken from a list of ISs provided by Oliveira and Raeder (2015). Initially, it consisted of 461 ISs. After removing events with data gaps 383 remained. In a second post-processing step the time of detection was corrected, typically not by more than a couple of minutes, to match the observed onset of the pressure jump.

The list of *non-events* is significantly longer with ~1700 entries. The first 700 were determined by randomly selecting a point on the P_d time series from either ACE or Wind. This point is referred to as an Evaluation Point (EP). We determined if the EP was located at the onset of a rapid P_d increase or not by visual inspection. Segments with large data gaps were discarded. It was also enforced that the EPs should be uniformly distributed in seven groups according to background levels: 0–2, 2–3, 3–4, 4–5, 5–6, 6–7 and above 7 nPa. This was done to include information about the spread in *non-events*. The last 1,000 entries were determined by manually inspecting a ±60 min window around randomly chosen EPs where the subsequent data-point experienced an increase of 0.4 nPa or more (resolution between each data-point is 1-min). This group represents situations with larger P_d variance around the EP than the first group.

3.1.2 Features

The algorithm is designed to predict if an EP is the onset of a rapid P_d increase. This is done by evaluating a set of features chosen to best describe the step-like behavior that we search for. We have chosen a total of five features. All features are determined on a

relative scale such that events can be compared independent of the background level and size of the jump. The features are:

3.1.2.1 Slope

The gradient in the pressure jump. This is estimated by the slope of a linear regression fit based on the EP and the following two data-points. To facilitate intercomparison of events the resulting slope was divided by the largest of the three data-points. This feature is highly sensitive to data gaps and so if any of these three data-points were missing the EP was discarded.

3.1.2.2 Maximum Prior Difference

The difference between the minimum and maximum value in the 60-min interval prior to the EP. This was calculated using normalized data with mean and standard deviation determined from a ±60 min window around the EP.

3.1.2.3 Relative Increase

The relative increase from before to after the EP. This is a percentage increase between the maximum 60 min prior to and the median between 3 and 8 min after the EP.

3.1.2.4 PCA_5 and PCA_{20}

The last two features are based on a principal component analysis of the P_d measurements in the *events* from the training data. The first principal component shows a very clear step-like behavior (see **Figure 1**). The features, PCA_5 and PCA_{20}, are defined as the dot product between a candidate event and the first principal component, using time windows that are ±5 and ±20 min, respectively. When calculating the dot product, we fill in data gaps by interpolation and extrapolation.

The features are conceptually illustrated in **Figure 1**. In the top row the three first principal components in the *events* training dataset are shown. The first component has a step-like increase between epoch 0 and 2 and explains 88.57% of the variance. The second and third principal components also experience rapid increases at epoch 0 followed by a decay. These two components explain only 4.93 and 1.8% of the variance and could be related to pressure increases that last for only a short duration. The bottom row of **Figure 1** shows an example event observed by ACE. Superimposed are the features when the EP is located at the onset of the jump. The calculated linear fit from which the slope is determined is illustrated in orange. The minimum and maximum prior to the EP is indicated by the blue lines, over the range from which they were determined. The median after the EP, used to calculate the percentage increase, is shown as a red line.

An active check for data gaps is only carried out during calculation of the slope. For the rest of the features, EPs were only discarded if the entire time series used for calculating a metric was missing.

The 5D space spanned by the features, commonly referred to as feature space, is illustrated for the training data in **Figure 2**. *Events* are shown in blue while the first part of *non-events* are

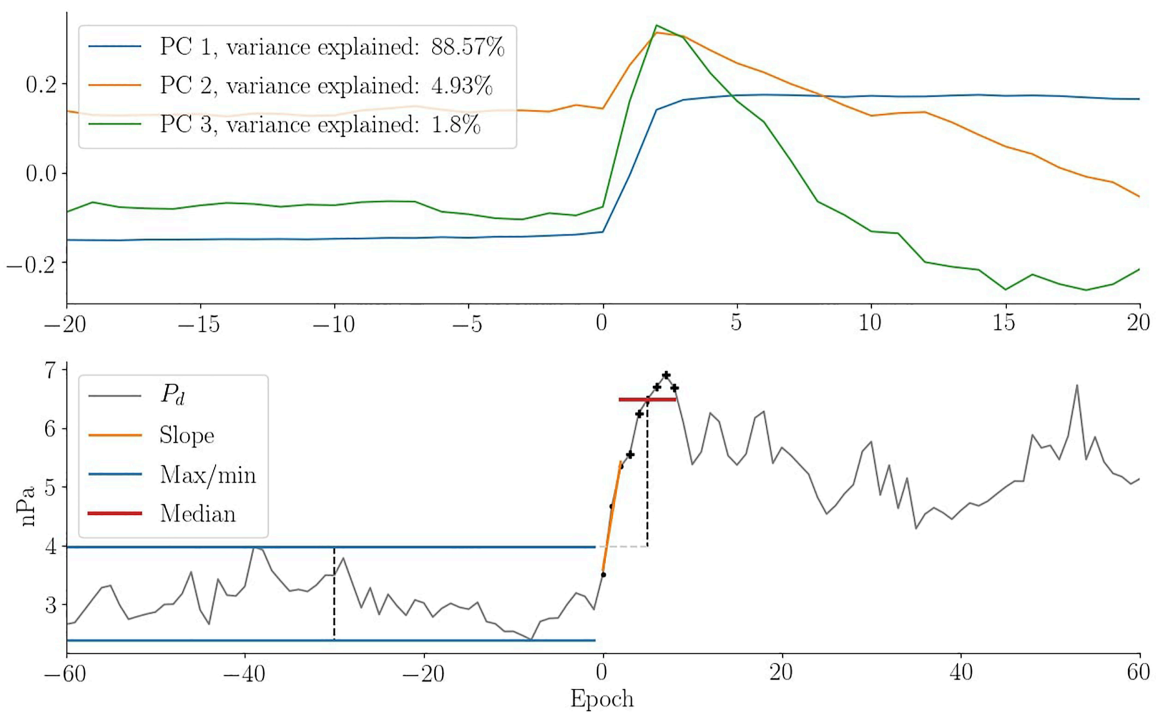

FIGURE 1 | Illustration of the features used in the random forest algorithm. The top panel shows the first three principal components as a result of a PCA analysis of the data used in *events*. The bottom panel shows the slope in orange, the minimum and maximum before onset in blue and the median after onset in red. The P_d time series itself is an event observed May 8, 1998 at 09:20 by ACE.

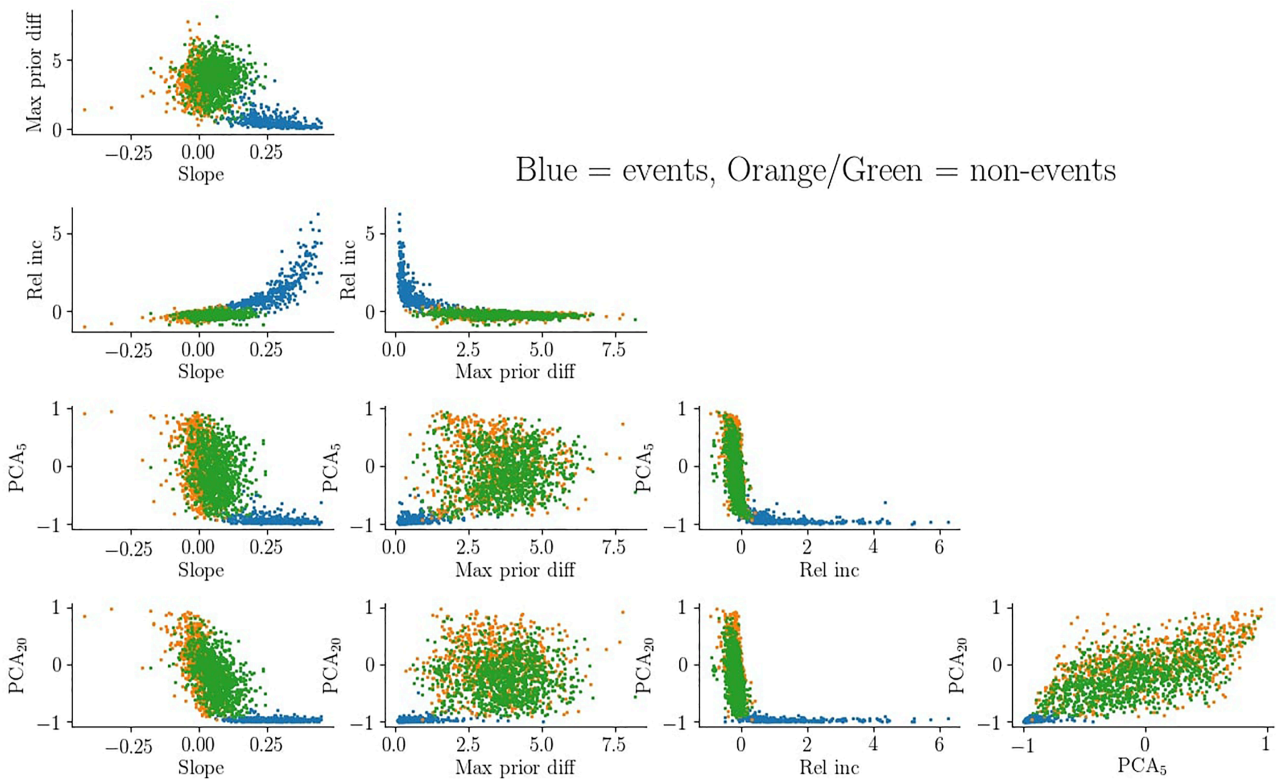

FIGURE 2 | Distribution of *events* and *non-events* with respect to the features described in **Section 3.1.2**. The blue dots illustrate *events* while the orange and green dots are *non-events*. Data in *non-events* associated with more quiet conditions are orange while the ones associated with more active conditions are green.

shown in orange and the last part in green. It is evident that the features provide a clear distinction between the two classes which is crucial for the success of the algorithm.

3.1.3 Random Forest

To separate between events and non-events we employ the random forest machine learning algorithm, a variation of the well-known supervised algorithm called decision tree. Training data are used to set up a series of binary questions (yes/no) with the purpose of separating data belonging to different classes. These binary questions are the basis for classifying events after training. If a decision tree is used in a bootstrapping format it is referred to as a random forest (Ho, 1995).

The random forest algorithm works by training a series of decision trees on individual data sets sampled from the training data. Each decision tree can then provide a classification when asked to predict the class of a potential event. In this way numerous decision trees can be used to calculate the probability that a given EP belongs to a particular class. Potential events are commonly assigned to whichever class has the highest probability. We used a stricter criteria by enforcing that 90% of all decision trees have to agree before a potential event can be classified as an *event*.

In practice the Python implementation by scikit-learn was used. In most practical implementations certain parameter choices have to be made (e.g., the number of decision trees, the maximum depth etc.). A complete description of the method used for selecting these parameters as well as illustrative plots is given in appendix.

3.1.4 Event Merging

Multiple EPs close to a P_d increase can be classified as *events*. In this scenario the EP with the highest classification probability was kept. During highly disturbed times multiple discontinuous P_d structures may appear resulting in events being very close in time. A minimum spacing of 1 h between events was enforced with the first come first serve principle. Events were detected with both ACE and Wind. When two events with similar arrival time estimates (discussed in the following section) arose ACE was prioritized and the Wind event discarded.

3.2 Arrival Time

Our definition of arrival is when information about magnetospheric compression has propagated to Earth and is observed in SYM-H. Estimation of arrival time at Earth is done in three main steps.

Initially, arrival time at Earth was crudely estimated by propagating the events to the magnetopause, assumed to be located at 10 R_E along the Sun-Earth line, using the spacecraft's x coordinate and the measured solar wind velocity. The distribution of the normalized SYM-H responses is shown in **Figure 5A** for this step. Each response is normalized for better comparison as

background level and jump size can vary. It is clear that the alignment is quite poor resulting in a gradual increase starting several minutes prior to epoch zero. This is because we do not take into account the location of the magnetopause given the preexisting solar wind conditions or the orientation of the solar wind structure (Weimer et al., 2003; Mailyan et al., 2008). In addition, the delay between impact with the magnetopause and observing a response on ground is not trivial, resulting in additional uncertainty.

A comprehensive correction of the initial arrival time estimate was done using a correlation analysis between P_d and SYM-H. **Figure 3** showcases an example of the analysis. In the first row we show a ±10 min window of P_d (blue line) around the time of detection along with a ±40 min window of SYM-H (red line) around the crudely estimated arrival time. The second row shows the correlation resulting from sliding P_d over SYM-H. In the third row the slope from a fit between $\sqrt{P_d}$ and SYM-H is illustrated by a thin grey line while the product between the slope and correlation is shown in black. The blue dot indicates the maximum of the curve while ensuring that the correlation (second row) is above 0.6 and the slope (grey line in third row) is above 6 nT/nPa$^{\frac{1}{2}}$. If no lag fulfills these two criteria the event is discarded. These two thresholds were set low to accommodate differences in rise time between SYM-H and P_d. The fourth panel shows the result of using the blue dot from the third panel as the new arrival time. The improvement to the superposed SYM-H response after applying this correction is clearly seen in **Figure 5B**.

Figure 3 suggests that the arrival time for all events can be shifted ±30 min. However, a custom threshold is determined for each event as a combination of uncertainty in the propagation ε_1 and the magnetospheric-ionospheric coupling ε_2. Ridley (2000) investigated the uncertainty in using various propagation techniques and found propagation along the Sun-Earth line had an average uncertainty of $\varepsilon_{\text{mean}} = 0.219D_{YZ} + 1.63$ min when the spacecraft's euclidean distance D_{YZ} to the Sun-Earth line is given in Earth radii. We used a slightly more conservative estimate to allow for scenarios outside the norm by defining $\varepsilon_1 = 2\varepsilon_{\text{mean}}$. An additional delay due to propagation through the magnetosphere and rise time of the response was accounted for by setting $\varepsilon_2 = 10$ min. The maximum allowed correction of any event is thus $[-\varepsilon_1, \varepsilon_1 + \varepsilon_2]$ which is a function of the spacecraft position. ACE and Wind have a maximum D_{YZ} around 50 and 100 Earth radii leading to an ε_1 of around 20–45 min, respectively.

The step-like increase in P_d is often more rapid than the SYM-H response. It is therefore clear that their correlation can exhibit a maximum somewhere between the SYM-H onset and the following plateau. In order to ensure the best possible alignment we perform a minor correction to the result of the correlation analysis using an algorithm to estimate the onset and plateau of the SYM-H response and then change the arrival time estimate to match that of the estimated onset.

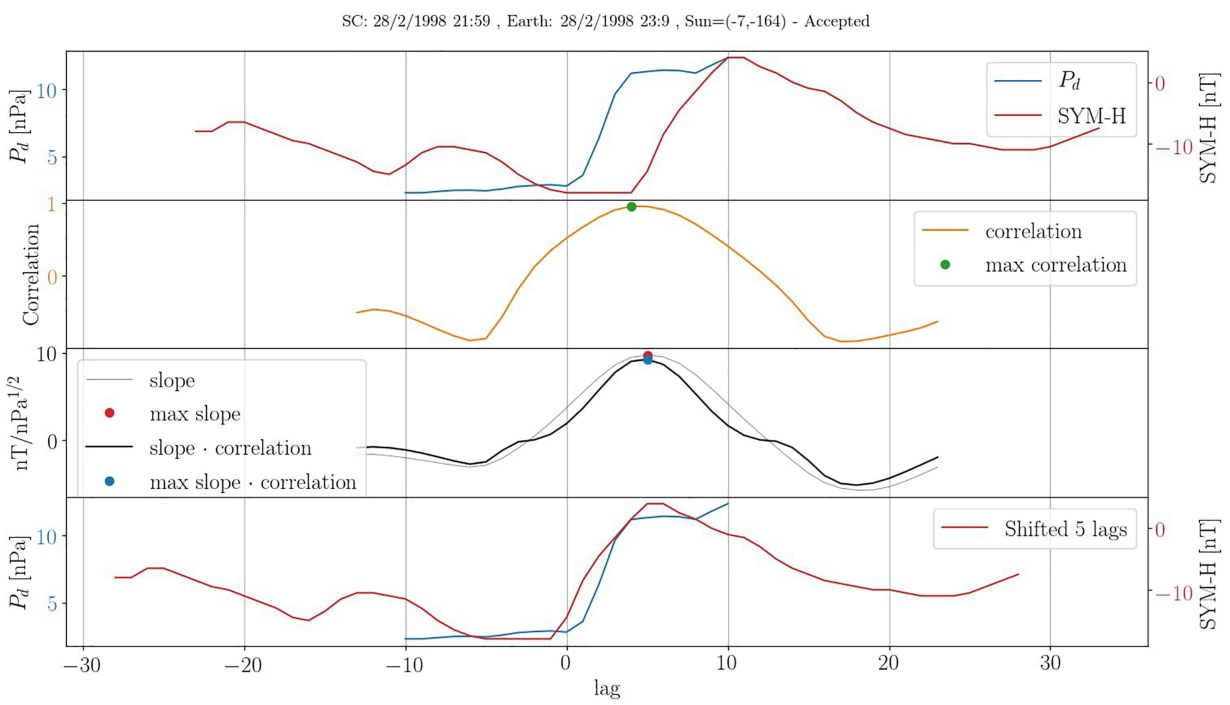

FIGURE 3 | Example of the correlation analysis on event detected by ACE at 22 UT the February 28, 1998. The first panel shows P_d increase as observed by ACE along with SYM-H after around the event's initial arrival time estimate. The second panel shows the correlation when sliding P_d over SYM-H in the first panel. The third panel shows the slope from a linear fit between SYM-H and $\sqrt{P_d}$ and the product of the slope and correlation. The fourth panel repeats the first panel when correcting the arrival time using the lag indicated by the blue dot in the third panel.

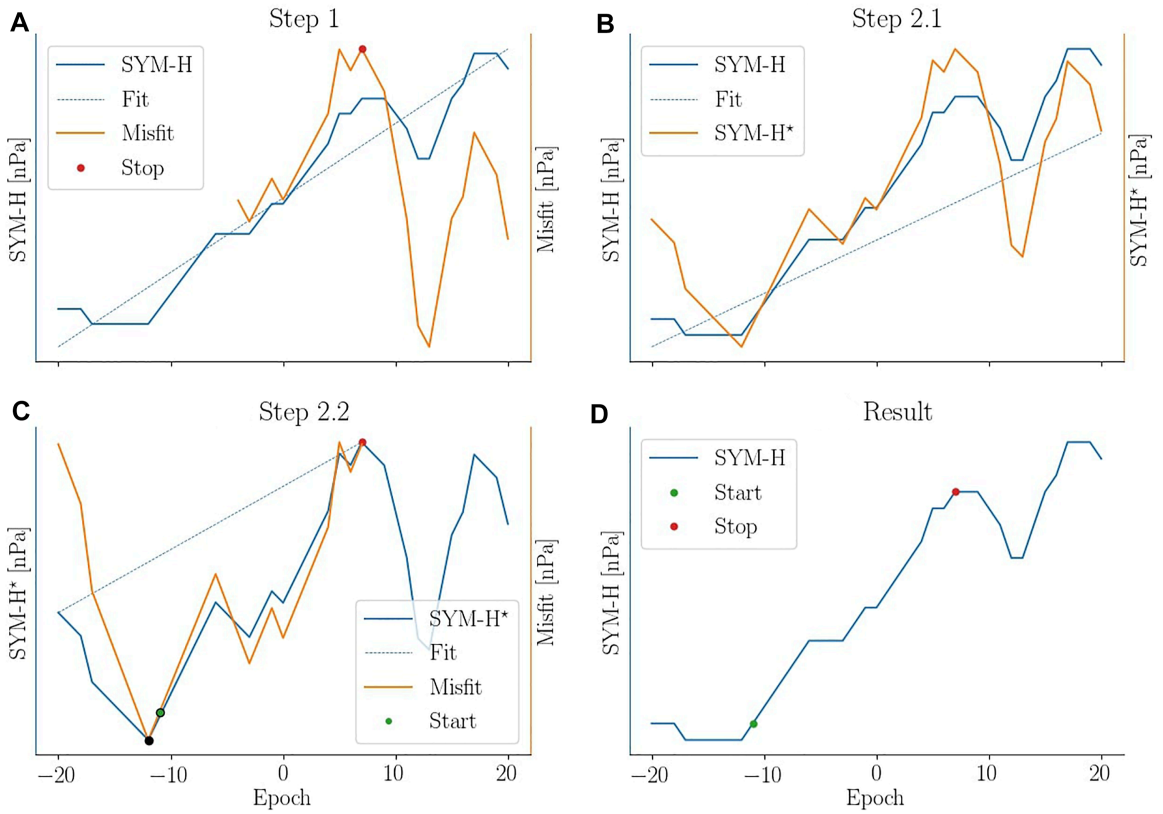

FIGURE 4 | Example of algorithm used to find the onset of the response in SYM-H. In **(A)** the peak of the response is found. In **(B)** the SYM-H response is detrended. In **(C)** the onset if located. **(D)** shows the estimated onset and peak of the SYM-H response.

The algorithm for finding the onset is divided into two steps as illustrated in **Figure 4**. The first step, **Figures 4A**, is to determine when the increase begins to plateau. First a linear fit (dashed blue) to the SYM-H (blue) is made. Then the misfit (orange) between the two is determined. The end of the rise time (red dot) is then determined as the maximum misfit after epoch −5.

The second step is separated into two sub-steps for illustration. First, **Figure 4B**, the SYM-H time series is detrended (indicated by the asterisk) by subtracting a linear fit (dashed blue) to the first 15 min from the entire time series. The next part, **Figures 4C**, is done on the detrended time series (blue). Epoch −20 and the red dot from 4a are connected by a straight line (dashed blue). From this the misfit (orange) between the detrended SYM-H and the linear fit is determined. The onset of the SYM-H response is then determined as the first misfit value, going from right to left, that falls below the 5% quantile of the misfit. Here two point fulfill the requirement, but the rightmost (green) is chosen. It is easy to tell from **Figure 4D** that the onset is not aligned with epoch 0. Using the newly determined onset the estimated arrival time is shifted accordingly.

The effect of this last response correction is evident when comparing **Figures 5B,C**. The onset is no longer observed as a gradual increase prior to epoch 0. The 90% confidence interval after onset has however become broader which makes sense given the varying rise time between events.

4 RESULTS

This section presents the results of the study. The first part will focus on the list of events while the second part will showcase a superposed epoch analysis of the low and high latitude geomagnetic response to rapid increases in P_d as observed in various indices.

4.1 Event List

The event detection algorithm described in **Section 3** was applied to the *Pd* series in a sliding window fashion evaluating all data points as potential events. The resulting event list contains 3,867 rapid increases in P_d between the year 1994 and 2019. A detailed description of the method used to make the list is given in **Section 3**. It is important to reiterate that the focus of this study is rapid increases in P_d regardless of origin.

Classifications by the event detection algorithm are made entirely based on P_d measurements. It is therefore interesting to see how the events in the list are characterized with respect to other solar wind parameters and thus how they distinguish themselves from other space weather phenomena. A summary of various solar wind parameters, before and after onset, is given in **Figure 6**. The statistics in **Figures 6B–F** were calculated from two 12-min windows offset 3 min to either side of the P_d onset. The median is shown for most variables. The exceptions are

downstream P_d, the solar wind velocity and number density, for which the maximum is shown.

The number of detected events per year is shown in **Figure 6A** along with the monthly sunspot number downloaded from SILSO World Data center at http://www.sidc.be/silso/. The ratio between events detected at solar max (cycle 23) and solar min (between cycle 23 and 24) for our list is ~2.2 while it is ~5.5 for the IS list in Oliveira and Raeder (2015). Our events are determined solely on P_d and don't necessarily uphold the Rankine-Hugoniot jump conditions. Dalin et al. (2002a) found the occurrence rate of pressure increases that are not shocks to be independent of the solar cycle. The difference in solar cycle dependence between the two lists is therefore consistent with our list containing non-shock events.

Figure 6B shows the IMF clock angle given as

$$\theta_c = \arctan2\,(B_Y, B_Z) \tag{2}$$

where B_Y and B_Z are the IMF components in the Y and Z (GSM) direction. The angle is thus 0° for purely northward IMF

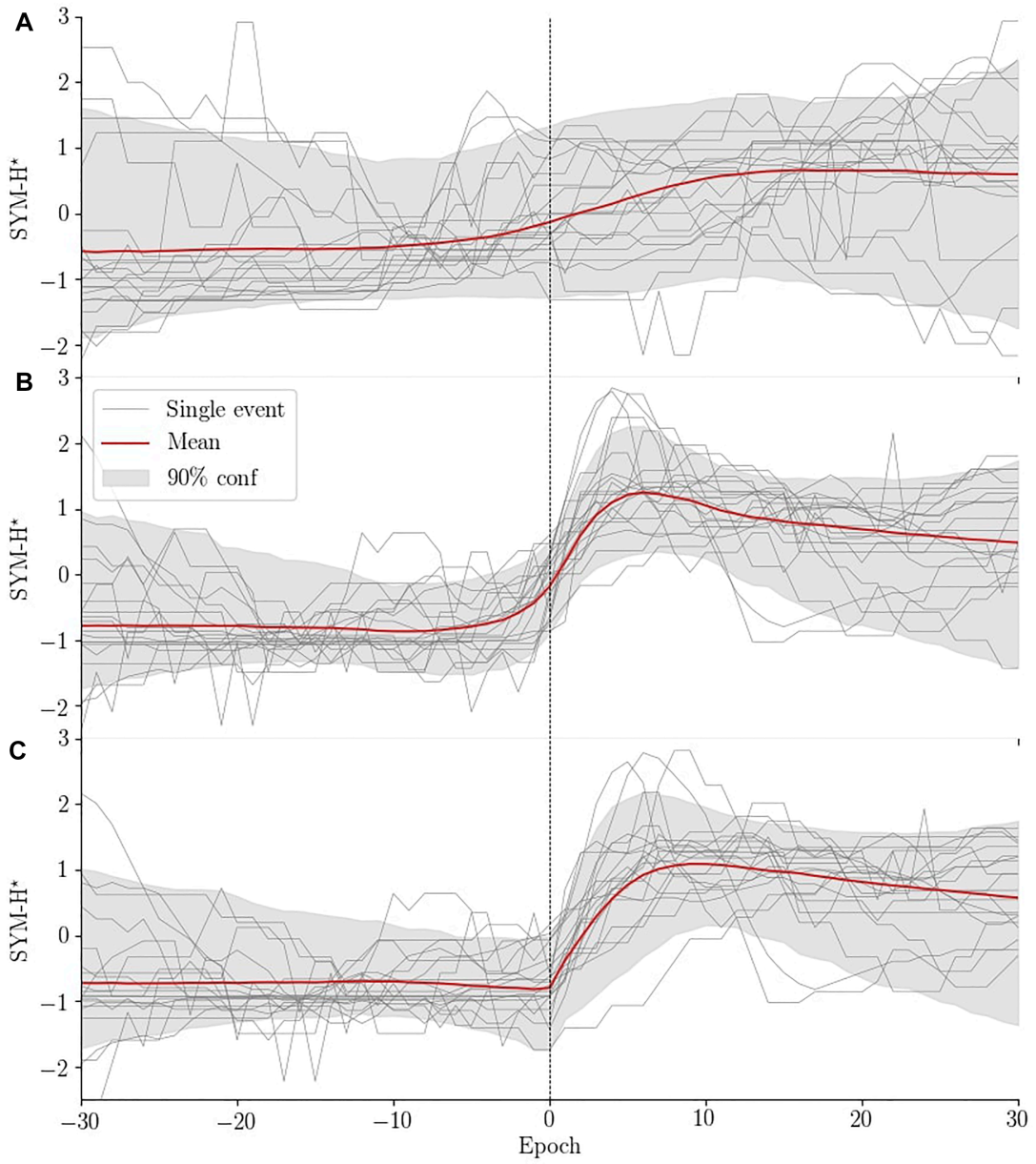

FIGURE 5 | Comparison of normalized superposed SYM-H before any arrival time correction **(A)**, after correlation analysis **(B)** and after aligning the onset of the SYM-H response **(C)**. The shaded area illustrates the 90% confidence interval, the grey lines are 20 randomly selected events and the red lines are the mean of the distribution. Each event has been normalized, indicated by the asterisk in the axis label, in order to improve comparison between events.

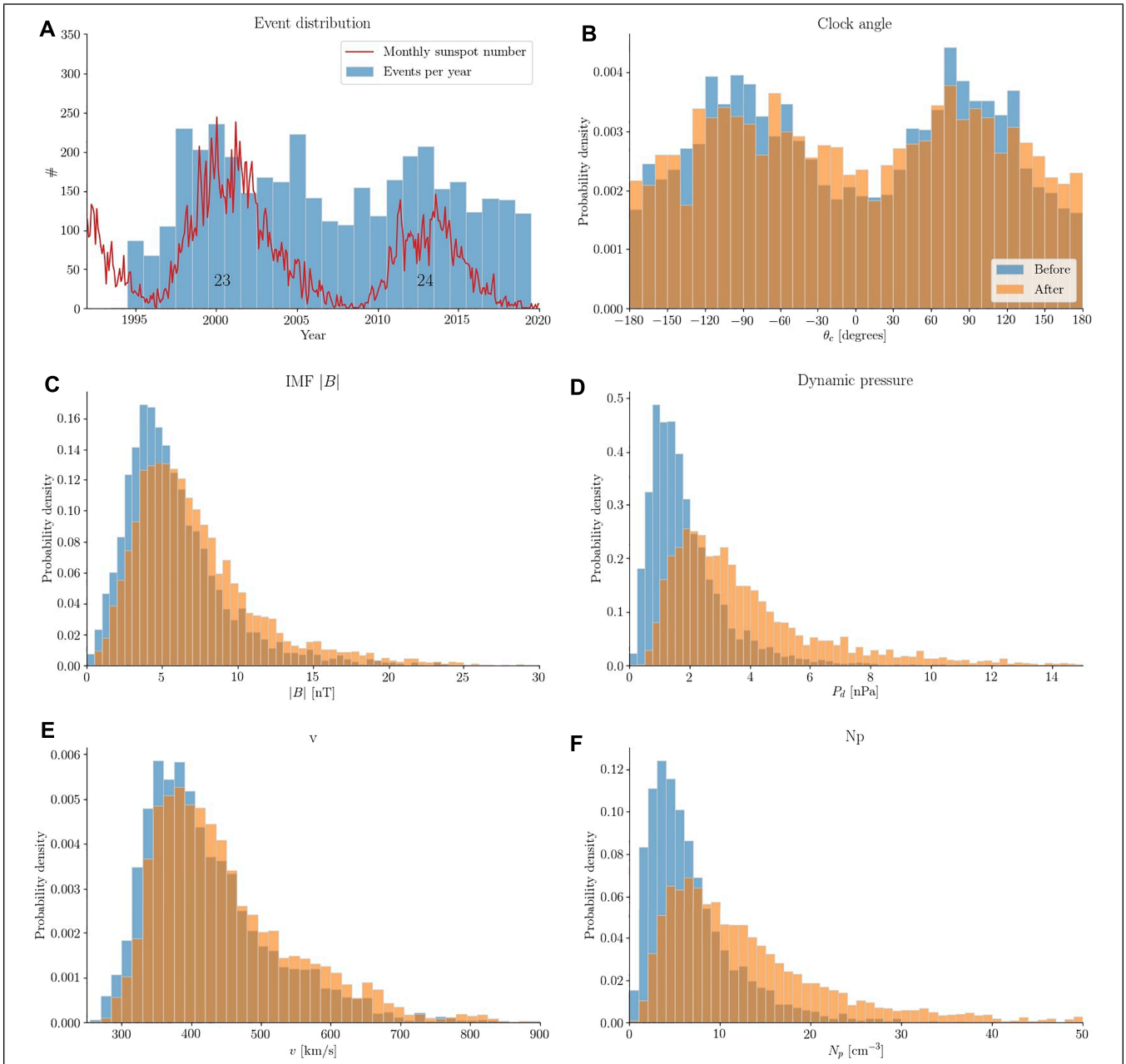

FIGURE 6 | Summary of statistics related to the event list. **(A)** shows the number of events detected for individual years along with the monthly sunspot number. **(B–F)** show statistics of the upstream (orange) and downstream (blue) IMF clock angle, IMF magnitude, solar wind dynamic pressure, solar wind bulk velocity and ion number density.

and ±180° for purely southward IMF. The distribution is bimodal illustrating a statistically dominant B_Y component. The distribution after onset has slightly broadened. It is tempting to suggest from this figure that θ_c for individual events is similar before and after onset, but that is far from the case. Only 40% (61%) of events stay within ±22.5 (±45) degrees of the pre-onset clock angle.

The IMF magnitude, **Figure 6C**, has a mode around 4nT prior to onset which increases to 5 nT afterwards. Similarly, the mode of the P_d distribution, **Figure 6D**, changes from 1.1 to 2 nPa while the spread also is significantly increased as shown by the heavy tail. Note that the distribution shown in the figure is truncated at 15 nPa leaving 98 events outside. **Figures 6E,F** are distributions of solar wind bulk velocity and ion number density. Their modes are 365 km/s and 3.5 cm^{-3} before onset, and 380 kms/s and 6 cm^{-3} after. It is evident that the P_d increases are generally caused by rapid changes in solar wind ion number density consistent with Dalin et al. (2002a) who found their events to

be either slow shocks or rotational discontinuities. Khabarova and Zastenker (2011) confirms that rapid increases in P_d are often caused by abrupt changes in ion number density. They likewise found that these types of event are not associated with coronal mass ejections, stream interaction regions and ISs, but are highly correlated with crossings of the heliospheric current sheet. It has later been shown that bends and kinks in the heliospheric current sheet can result in small magnetic islands that are related to ULF-variations in ion number density and IMF (Khabarova et al., 2021).

There are differences between our list and previously published IS lists. Oliveira and Samsonov (2018) have reviewed ISs and their characteristics (e.g., orientation, shock speed). Studies of ISs often investigate the importance of orientation as frontal impacts tend to be more geoeffective than those with a high inclination (Takeuchi et al., 2002; Oliveira et al., 2015; Oliveira and Raeder, 2015; Selvakumaran et al., 2016). The angle between the shock normal and Sun-Earth line can be determined as

$$\theta_{X_n} = cos^{-1}(n_x) \tag{3}$$

where n_x is the component along the Sun-Earth line of the shock normal. Here $\theta_{X_n} = 180$ and 90 is parallel and perpendicular to the Sun-Earth line, respectively. Calculating θ_{X_n} requires an estimate of the shock normal which can be determined as described by Schwartz (1998) if the assumption of coplanarity holds. This is based on the Rankine-Hugoniot jump conditions and assumes that the normal to the shock plane and magnetic field on either side of the shock lie in the same plane. The convention is to point the shock normal into the unshocked medium, commonly making n_x negative. **Figure 7** compares the distributions of estimates of θ_{X_n} between our event list (blue) and that of Oliveira and Raeder (2015) (orange). The orange distribution has a mean of ~145 and is skewed towards more frontal angles. The blue distribution illustrates the result when the assumption of coplanarity does not hold for a majority of the events and should not be considered credible. The shock normal often has its dominating component in the Y or Z direction (GSM) leading to an estimated orientation parallel to the Sun-Earth line. Estimates of orientation for rapid P_d increases that are not IS are best achieved using timing analysis with multiple spacecrafts. Such analyses were carried out by Richardson and Paularena (1998); Dalin et al. (2002b); Riazantseva et al. (2003). They found that solar wind plasma structures tend to be oriented with an angle between frontal and the Parker spiral and are thus slightly skewed towards dusk.

Figure 7 underlines that the majority of events in our list are not IS and thus comparisons to IS studies should be done with caution. We do not attempt to distinguish between events that are IS and events that are not, although a comparison of the effectiveness between shocks and non-shocks would be interesting.

4.2 Superposed Epoch Analysis

Our motivation for creating the event list is to provide the necessary data for a statistical analysis of the geospace response to rapid increases in P_d. In the following we showcase how the event list can be used in a superposed epoch analysis of the response for different angles of IMF clock angle and dipole tilt. Dipole tilt, θ_d, will also be referred to as season and is positive when the dipole axis points towards the Sun in the northern hemisphere.

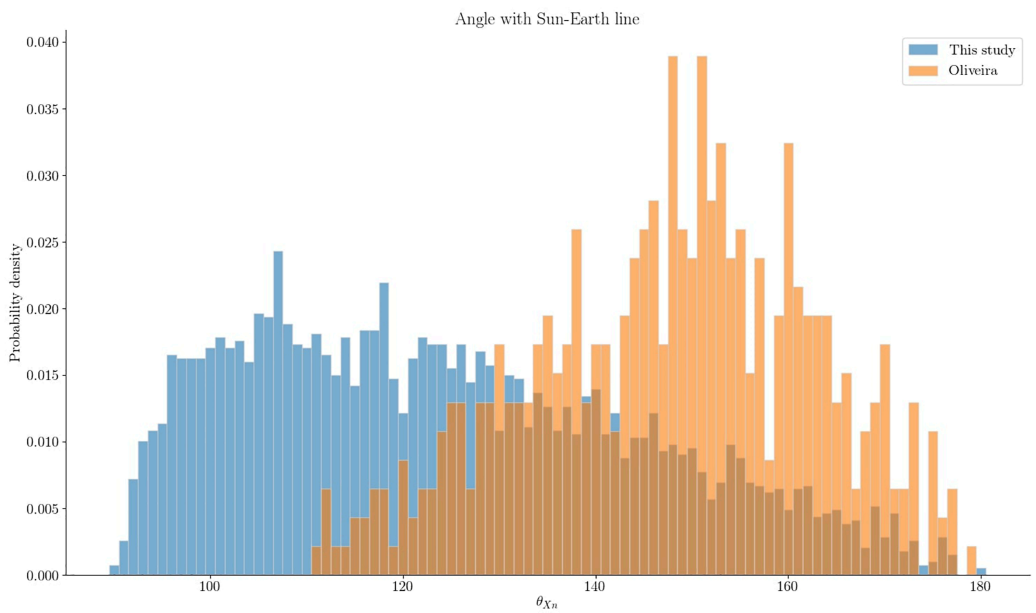

FIGURE 7 | Comparison of θ_{X_n} estimates between the events found in this study (blue) and those presented in Oliveira and Raeder (2015) (orange) under the assumption of coplanarity (Schwartz, 1998). A shock is aligned with the Sun-Earth line if $\theta_{X_n} = 180°$ and perpendicular when $\theta_{X_n} = 90°$. The assumption of coplanarity does not hold for a majority of the events in this study and the estimates (blue) should not be considered credible.

4.2.1 Event Groups

The effect of θ_c and θ_d can be studied by separating the event list into groups. From **Figure 6B** it is evident that the IMF is more prone to be oriented east/west than north/south and we therefore use slightly uneven angular ranges to achieve an approximately equal amount of events in each group. Additionally, the clock angle can change drastically from before ($\theta_{c,b}$) to after ($\theta_{c,a}$) onset. This can make the interpretation of the effect of the rapid pressure increase difficult as it has to be separated from the effect of changing IMF orientation. For this reason we impose constraints on either side of the onset.

All 3,867 events can be represented in a 3D space, **Q**, spanned by θ_d, $\theta_{c,b}$ and $\theta_{c,a}$. The following criteria were imposed to group the events by dipole tilt and IMF orientation:

$$\begin{aligned}
&\text{Summer} : \mathbf{Q} \cap (\ 13° < \theta_d\ )\\
&\text{Equinox} : \mathbf{Q} \cap (\ -13° < \theta_d < 13°\ )\\
&\text{Winter} \ : \mathbf{Q} \cap (\ \theta_d < -13°\ )\\
&B_Z+ \ : \mathbf{Q} \cap (\ -55° < \theta_{c,a} < 55°\ ) \cap (\ -55° < \theta_{c,b} < 55°\ )\\
&B_Y+ \ : \mathbf{Q} \cap (\ 55° < \theta_{c,a} < 125°\ ) \cap (\ 55° < \theta_{c,b} < 125°\ )\\
&B_Z- \ : \mathbf{Q} \cap (\ 125° < \theta_{c,a} < -125°\ ) \cap (\ 125° < \theta_{c,b} < -125°\ )\\
&B_Y- \ : \mathbf{Q} \cap (\ -125° < \theta_{c,a} < -55°\ ) \cap (\ -125° < \theta_{c,b} < -55°\ )
\end{aligned} \tag{4}$$

Table 1 summarizes the number of events in the different groups. Only 2058 events were used in the analysis due to the criterion on both $\theta_{c,a}$ and $\theta_{c,b}$, **Eq. 4**.

The clock angle distributions of these 2058 events are shown in **Figure 8**. Here the grey and colored bars illustrate the distributions prior to and after onset, respectively, and each grey circle signifies 10 events. Comparing the occurrence rate of $B_Y\pm$ events show a higher rate of B_Y+ events during summer than during winter.

4.2.2 Low Latitude Geomagnetic Response

The general expectation of the low/mid latitude geomagnetic response to a rapid increase in P_d is a positive step-like perturbation of the horizontal magnetic field. To the first order this can be thought of as uniform and caused by compression of the magnetosphere. Magnetic indices such as SYM-H describe this well. However, the response is a superposition of multiple magnetospheric sources where the primary contributors are the magnetopause and ring current. The ring current is known to be asymmetric (Walsh et al., 2014; Ganushkina et al., 2015; Lühr et al., 2017) and responds near instantaneously to rapid increases in P_d (Shi et al., 2005). It is therefore no surprise that the low latitude magnetic perturbation would be local time dependent.

TABLE 1 | Summary of the amount of event in each group after imposing the criteria in **Eq. 4**.

	Summer	Equinox	Winter	Sum
B_Z+	175	251	125	551
B_Y+	181	209	114	504
B_Z-	181	207	125	513
B_Y-	145	229	116	490
Sum	682	896	480	2058

Using numerous magnetometer stations between ±50° latitude (Newell and Gjerloev, 2012) produced a local time ring current index called SMR that is provided for midnight, dawn, noon and dusk. **Figure 9** summarizes the results of a superposed epoch analysis of SMR with respect to the groups defined in **Section 4.2.1**. The results are generated by scaling the SMR time series for each event by $\Delta\sqrt{P_d}$ and subtracting a baseline value before onset. The ensemble of these time series constitutes a distribution at all epochs from which the mean is determined. The blue/orange/green/red lines are the mean for the SMR index at midnight/dawn/noon/dusk. The black line is the mean of the global SMR index while the dashed black lines are its 25% and 75% percentiles, respectively.

4.2.2.1 Dawn-Dusk Asymmetries

It is clear that the response depends on local time. The initial peak at dawn is consistently lower than in any other sector. Two of the main contributors to ring current indices are the magnetopause and ring current (Haaland and Gjerloev, 2013) and according to Araki (1977) the main contribution to DL is the magnetopause current. The magnetopause current generates a positive perturbation while the ring current generates a negative. Assuming the magnetopause current's contribution to be symmetric with respect to local time, the asymmetry originates from the ring current. Under this assumption the dawnside ring current must generate a stronger magnetic perturbation compared to any other sector.

Several studies report that the ring current is strongest at dusk (Newell and Gjerloev, 2012; Walsh et al., 2014; Ganushkina et al., 2015; Lühr et al., 2017). Studies on ring current asymmetry tend to investigate the effect during the main/recovery phase of geomagnetic storms. In that scenario the asymmetric ring current is caused by an intensification of the partial ring current. However what we are interested in is the initial response, the sudden commencement, which occurs before the main phase of the geomagnetic storm and evolves on a timescale of minutes while the storm evolves on a timescale of hours and days.

Ring current asymmetry is highly dependent on the geomagnetic disturbance level (Le et al., 2004). The majority of events used in this study (81%) experience SYM-H above −30 nT before onset, which is considered quiet. It is therefore interesting that Zhang et al. (2011) found higher current density on the dawn side when investigating the local time distribution of the ring current using Cluster.

Following the argumentation presented by Shi et al. (2005) an azimuthal electric field is induced (Faraday's law) as a result of magnetospheric compression when the solar wind pressure enhancement impinges on the magnetosphere. This causes a near instantaneous adiabatic energization of ring current particles. Under the assumption that the ring current is strongest at dawn during geomagnetic quiet times, a rapid increase in P_d results in a larger negative perturbation at dawn and therefore accounts for the consistently weaker response observed in **Figure 9**. However, one must keep in mind that there are other sources of perturbation. A more thorough analysis that includes contributions from field aligned currents has to be made.

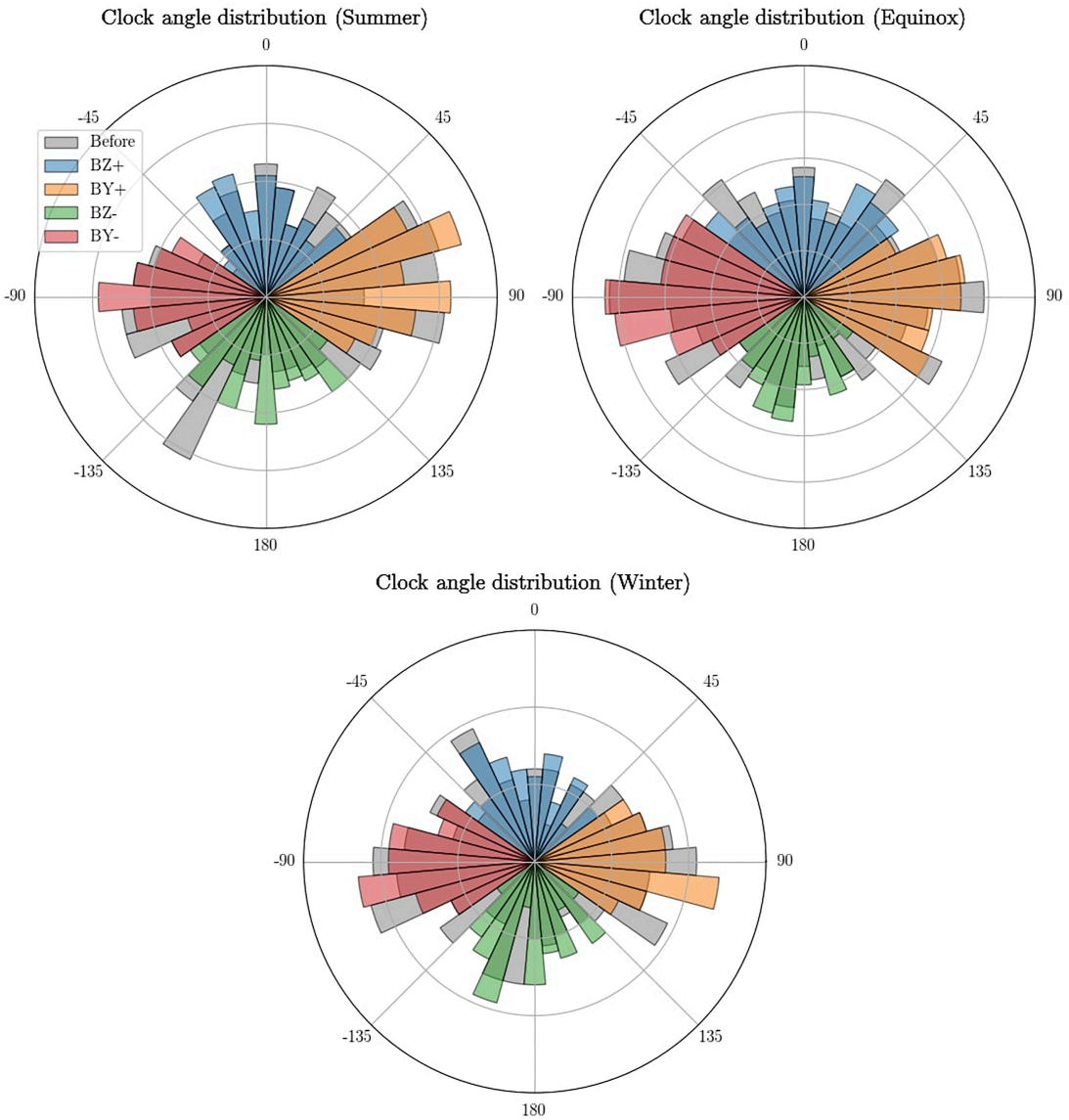

FIGURE 8 | Polar histograms of the IMF clock angle distribution in each of the 12 groups. The grey bars indicate the distribution before the increase in P_d while the colored bars indicate the distribution after. Each circle represents 10 events.

4.2.2.2 Decay

The trend following the initial step-like increase exhibits different behavior with respect to local time and clock angle. In all scenarios the trend at dawn is slightly positive or constant while the opposite is true for all local time sectors. During northward IMF all local time sectors appear to converge towards symmetry. However, during southward IMF the decay at noon/dusk/midnight is much more rapid resulting in the perturbation to reduce below the baseline prior to onset. This is in agreement with the higher probability of geomagnetic storms occurring during southward IMF. The ring current asymmetry remains strong, but has changed from being dominating at dawn to dominating at dusk.

4.2.2.3 Noon-Midnight Differences

We see a noon-midnight asymmetry during southward IMF as the response in SMR-00 tends to be stronger than SMR-12 (and the other sectors). A similar result was found in case studies by Lee and Lyons (2004). They observed dipolarization of the geomagnetic field at geosynchronous orbit consistent with a reduction of the cross-tail current which will result in a positive perturbation of the horizontal magnetic field. This effect was not found for events during northward IMF. It is likely a result of acceleration of already Earthward moving plasma in the tail as part of the Dungey cycle. Boudouridis et al. (2004) found that compression of the magnetosphere enhances reconnection in the tail and increases magnetospheric convection.

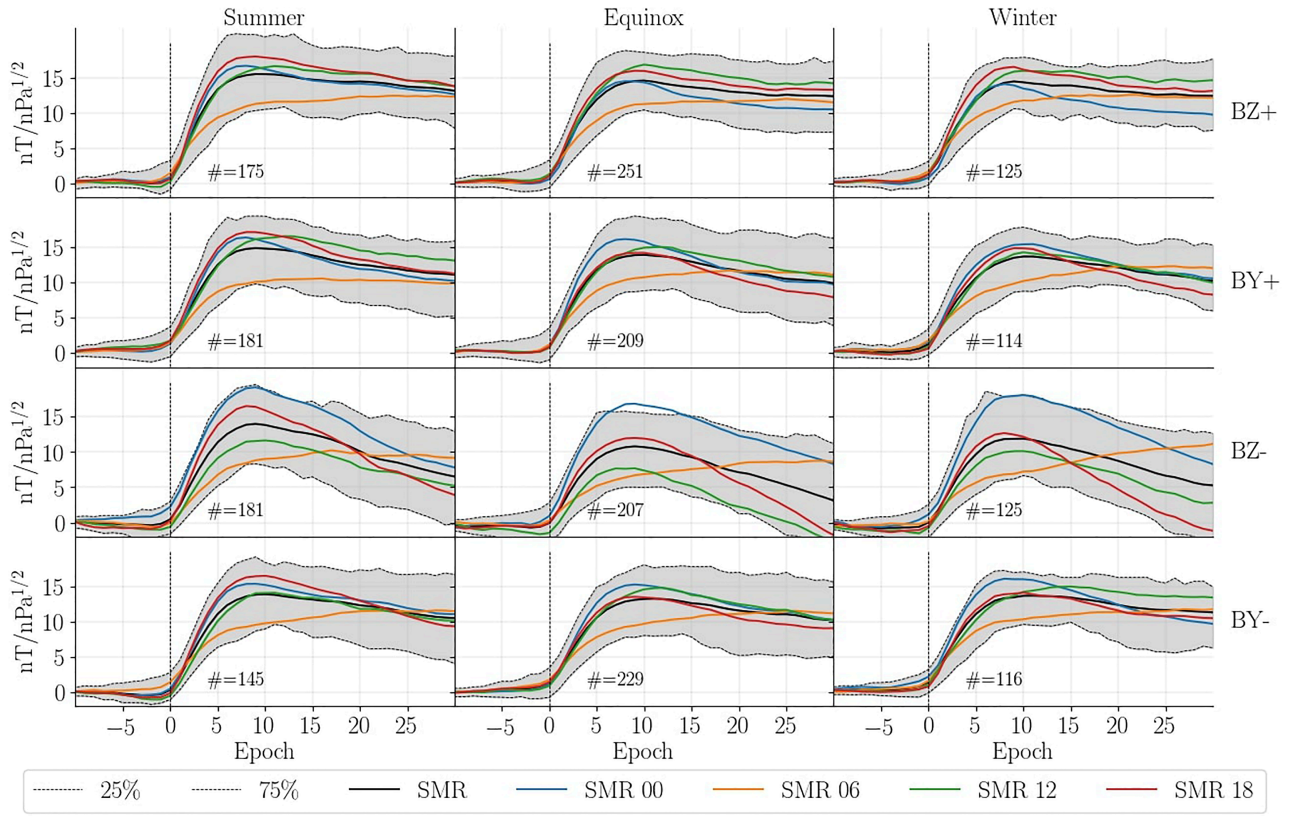

FIGURE 9 | Superposed epoch analysis of the low/mid latitude response to rapid increases in P_d using the SMR index. The solid lines indicate the mean of SMR and its local time components. The dashed grey lines indicate the 25 and 75% percentile. The SMR time series for each event has been scaled with respect to the increase in $\sqrt{P_d}$ and a baseline prior to onset subtracted. The number in each window indicates the number of events in each group.

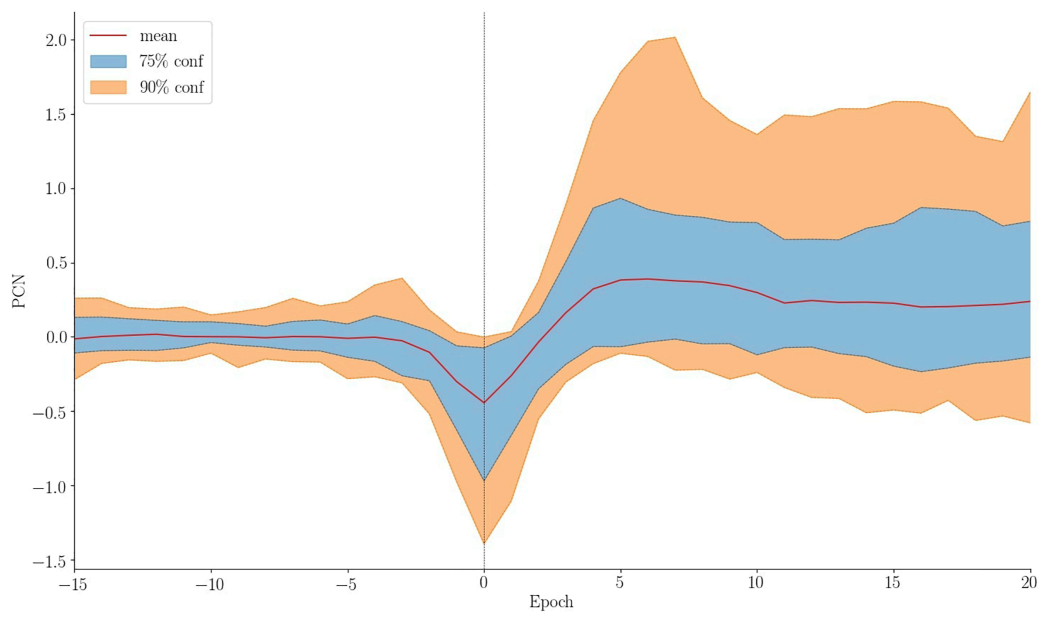

FIGURE 10 | Superposed epoch analysis of the high latitude response to rapid increases in P_d during Northward IMF and negative dipole tilt using the PCN index. The analysis is based on 90 events each of which were aligned with respect to the peak of the PI and shifted to a common baseline to improve comparison. The red line shows the mean and the blue and orange shade indicates the 75 and 90% confidence interval.

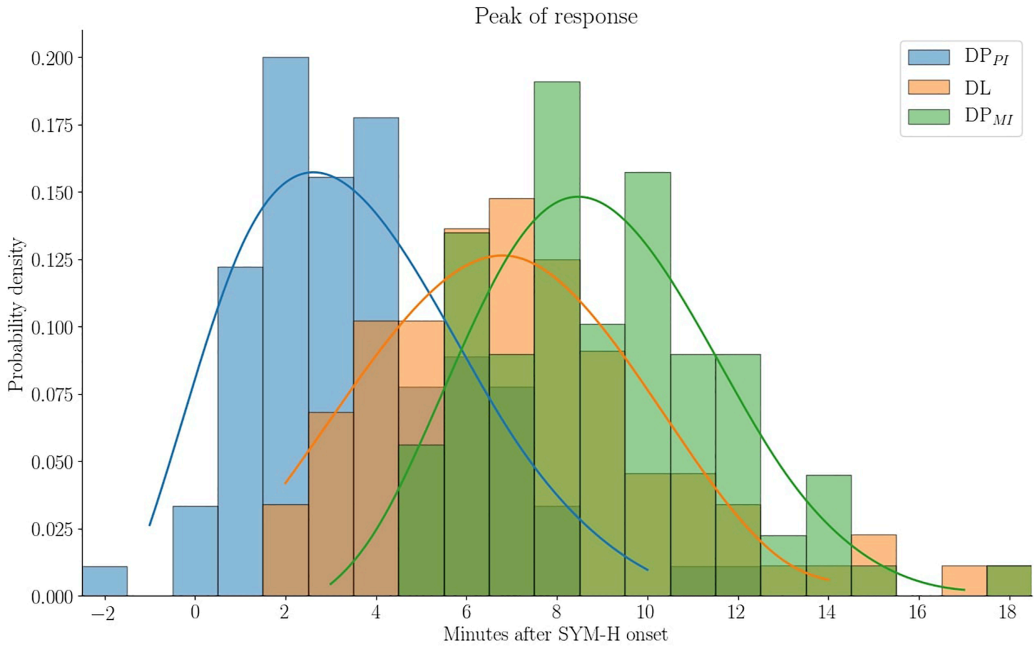

FIGURE 11 | Distribution of when the peak in DL (low latitude), DP_{PI} (high latitude preliminary impulse) and DP_{MI} (high latitude main impulse) occur relative to onset in SYM-H (epoch 0) for northward IMF during negative dipole tilt. Cubic splines are fitted and superposed to help distinguish the distributions in areas of overlap.

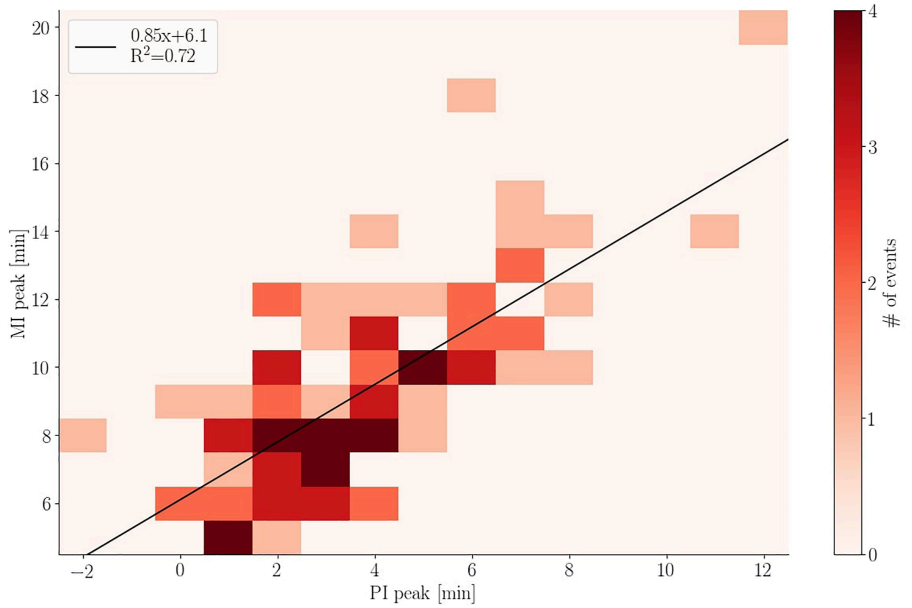

FIGURE 12 | Regression analysis of the DP_{PI} and DP_{MI} distribution in **Figure 11**.

4.2.3 High Latitude Response

The high latitude transient response following a rapid increase in P_d, earlier mentioned as DP, is caused by two sets of anti-sunward moving convection vortices, referred to as PI and MI (Araki, 1994). In previous studies a connection between PI/MI and the PC index were made (Lukianova, 2003; Huang, 2005; Stauning and Troshichev, 2008). PC indicates the antisunward convection in the polar cap by trying to quantify transpolar currents. All studies found that the PI and MI resulted in a negative and positive excursion of the PC index, respectively. Huang (2005) also found the magnitude of variation in PC caused by changes in IMF and substorms to be much greater

than that of the pressure enhancement. For this reason we limit ourselves to the group for northward IMF during winter, which is when the background convection is weakest. We manually determine the peak of PI and MI by inspecting the PCN time series for each event. Events with noisy time series or that were otherwise difficult to interpret were discarded, leaving 90 events.

Figure 10 is a superposed epoch analysis of the PCN when realigning the time series with the PI peak. For better comparison a baseline value prior to epoch 0 has been removed. We find that the average PI amplitude is 0.44 mV/m. If alignment is done with the MI peak its average is found to be 0.50 mV/m. This is lower than results from Huang (2005), but in agreement with results by Stauning and Troshichev (2008). The average value of the MI peak cannot be read directly from **Figure 10** as the PI alignment does not ensure alignment of MI.

Figure 11 shows the time of the peak of each response relative to the onset in SYM-H. The superposed lines are spline fits to help visualize the overlapping distributions. We find that the PI peaks around 2–3 min after onset while the low latitude response takes 6–7 min and the MI peak occur around 8–10 min after onset.

A regression analysis is performed between each of the distributions in **Figure 11**. The analysis between PI and MI, **Figure 12**, shows a strong relationship (R^2 = 0.72) between when the two responses peak. From the intercept we see that the average time between the PI and MI peak is ~6 min. The analysis between DL and PI/MI indicates a low level of correlation between low and high latitude response with R^2 = 0.29 and 0.32.

5 DISCUSSION

Event detection is highly relevant in space weather research. Certain events (e.g., coronal mass ejection, solar flare, stream interaction region etc.) can have a large impact on satellites and the electrical infrastructure on ground. Event detection and forecasting is the first step in handling a potential problem such that precautionary measures can be taken. Machine learning is used frequently as a means to find connections not immediately obvious as well as to remove human bias. A review of its role in space weather was given by Camporeale (2019).

The event detection approach used in this paper was designed to be as objective as possible. Nevertheless, we used a supervised algorithm meaning it is "taught" what is and is not an event. These definitions are based on the training data which is to some extent subjective. One could take an unsupervised approach in which the training data does not include a list of the varies classes and the algorithm will have to define them itself. However, this is far more complex: More data would be required as the algorithm needs to discover classes autonomously. Including variables other than P_d would introduce more difficulty as rapid pressure increases might be split into multiple sub-classes. Borovsky et al. (2019) used the unsupervised algorithm self organizing maps to analyze 10 years of ACE data leading to four classes of solar wind instead of the general two; slow and fast solar wind. One of these classes was ejecta which is related to coronal mass ejections and thereby rapid P_d increases. In the future the majority of classification might be done in a similar fashion, but for the task at hand it is a much too complex tool and the supervised approach seems to be a fair middle ground.

The *non-event* class contain everything that are not pressure increases. It is therefore likely that the 1700 entries do not account for all scenarios the algorithm will encounter and the outcome will therefore be unpredictable. This is one of the drawbacks when having to create training data. We tried to combat this potential problem by only accepting classifications of type *event* if 90% of the decision trees agreed.

Features in the training data were selected based on a comparison of numerous potential features and boiled down to the five presented here. The optimal features should be robust such that they do not depend heavily on single data-points or one risks discarding events unnecessarily. Our first feature, the slope, depends on 3 data-points and carries a lot of weight. An alternative to this could be to fit a logistic function as done by Boudouridis and Zesta (2021). The slope could be extracted from the fit and would therefore depend on a larger range of data and making it more robust when facing missing data.

The correlation analysis is a crucial part of creating the list of events as it ensures a measurable response on ground. However, when comparing two (or more) events it is important that they are aligned correctly in time; otherwise the statistics extracted when superposing multiple events will exhibit higher variance than necessary. The question is, what is the reference point that should be used for alignment? The rise time of the SYM-H response is around 2–10 min (Takeuchi et al., 2002). The exact number depends on the solar wind velocity since it dictates how much time is required for the discontinuity to pass Earth relative to the time of impact. The orientation of the discontinuity is another large factor in the variation of rise time. One extreme case with a 30 min rise time is analyzed in Takeuchi et al. (2002). We decided on using the onset of the SYM-H response as reference. Unfortunately, the precision of the correlation analysis also suffers from the variation in SYM-H rise times.

In the initial step of the superposed epoch analysis 12, groups were created based on dipole tilt and IMF clock angle, see **Section 4.2.1**. Unsurprisingly, there are more events around equinox than summer/winter as the dipole tilt range is larger. It is however curious that the occurrence rate is larger during summer compared to winter. The average ratio between summer and winter is ~1.4.

The reason for this asymmetry is still not clear, but we have ruled out two possible mechanisms: 1) Huang and Yumoto (2006) studied hemispheric asymmetry during rapid P_d increases and found a significant variation between hemispheres when comparing magnetic perturbation at low latitudes. They concluded that the perturbation is stronger in the summer hemisphere than in the winter hemisphere. Coincidentally, SYM-H is based on six stations where the majority are located in the northern hemisphere. However, the higher occurrence rate during positive dipole tilt is present prior to the correlation

analysis. It is also present when evaluating ACE and Wind data separately. When evaluating the individual years the ratio between summer and winter sometimes go below 1, but on average is ~1.3. We therefore find it unlikely that it is caused by data gaps. 2) Due to the eccentricity of Earth's orbit there will be a few percent more data with positive dipole tilt. Calculating the occurrence probability by normalizing the occurrence rate with the amount of data available does change the seasonal difference slightly, but not enough to be eliminated. One might suspect that it is related to solar cycles, but it is present when evaluating data from solar cycle 23 and 24 individually. We suspected it might be related to heliographic latitude. When repeating the analysis using latitude (heliographic inertial coordinates) we found a smaller difference between seasons. It was no surprise as the min/max in the latitude of Earth's orbit does not overlap with the extremes in dipole tilt (summer/winter). The cause of this seasonal difference is still not clear, but we are satisfied that it is unrelated to the method with which the events were detected and propagated to Earth.

In the superposed epoch analysis we observed a dawn-dusk asymmetry in the low latitude response. Contrary to our expectation the weakest positive perturbation was observed at dawn. Under the assumption of a uniform positive perturbation from the magnetopause current the asymmetry was caused by currents in the inner magnetosphere. Plasma in the ring current is energized instantaneously by magnetospheric compression (Shi et al., 2005). In this scenario the dawn-dusk asymmetry could be caused by a pre-existing asymmetry in the ring current plasma population. Using Cluster measurement between 4–4.5 Earth radii, Zhang et al. (2011) found significantly stronger current densities on the dawn side during quiet conditions (Dst>-30 nT) which corresponds to the pre-onset conditions for 81% of our events. It is important to keep in mind that the result came from using the SMR index. It is therefore relevant to discuss the different sources that contribute to the index. The ground magnetometers used span ±50° latitude. According to Haaland and Gjerloev (2013) the ring, magnetopause, and tail currents all contribute to the SMR index. However, Kikuchi et al. (2001) found contributions by field aligned currents and ionospheric currents at low/mid latitudes with a local time dependence. Reality is rarely as simple as the assumption we make, and a more thorough analysis of the constituents of the SMR index is therefore needed such that we can understand the origin of the observed dawn-dusk asymmetry.

6 CONCLUSION

Rapid increases in solar wind dynamic pressure result in the transient magnetospheric-ionosperic phenomena called sudden commencement, which is sometimes followed by a geomagnetic storm. In this study we develop a new method for automatic detection of these events in solar wind data. The events are propagated to Earth and paired with a corresponding response in ground magnetometers. We also use the list to conduct a superposed epoch analysis of the geomagnetic response to solar wind pressure increases. The main results are:

1. A list of 3,867 rapid pressure increases detected by ACE and Wind, between 1994–2019, including estimates of their arrival at Earth. The event list can be accessed at doi.org/10.5281/zenodo.6243103.
2. There is a clear dawn-dusk asymmetry in SMR following a compression of the magnetosphere for all seasons and IMF orientations. We suggest that an asymmetric ring current (stronger at dawn) results in weaker positive magnetic perturbation at dawn. This asymmetry is very short lived. Little asymmetry is observed after 30 min during northward IMF. During southward IMF the asymmetry changes from dawn to dusk within 30 min of the initial response in SYM-H.
3. A noon-midnight asymmetry is observed in the low latitude response for southward IMF. We believe it to be caused by dipolarization of the geomagnetic field as observed at geosynchonous orbit by Lee and Lyons (2004).
4. The geomagnetic response does not appear to have any significant dependence on IMF B_Y and dipole tilt and thus the main dependency is on IMF BZ.
5. The superposed epoch analysis of the PCN index for northward IMF during winter shows the average preliminary impulse (PI) causes a negative excursion of 0.44 mV/m from the baseline while the average main impulse (MI) causes a positive excursion of 0.50 mV/m from the baseline. The rise time of the low latitude response is approximately 7 min while the average PI (MI) peak occurs around 2 (8) min after the onset at low latitude. A regression analysis of the PI and MI response showed that their rise times are highly correlated, and that they differ by on average 6 min. A very low correlation between the low latitude response and PI/MI was found.

The purpose of creating this list was to provide the information for a statistical analysis. In the future we intend to conduct a more thorough analysis of the response by utilizing spherical harmonic modelling of the ground magnetic field perturbations. This would greatly increase the information extracted from the high latitude response compared to the PCN index analysis presented in this paper.

DATA AVAILABILITY STATEMENT

The datasets presented in this study can be found in online repositories. The names of the repository/repositories and accession number(s) can be found in the article/**Supplementary Material**.

AUTHOR CONTRIBUTIONS

MM is the primary author and developed the event detection algorithm and carried out the superposed epoch analysis. KML and JPR helped set up the overall structure of the manuscript. All co-authors contributed to the discussions and provided editorial

comment thus contributing to the article and approved the submitted version.

FUNDING

This work was funded by the Research Council of Norway (RCN) under contract 300844/F50. KML and JPR were also funded by the RCN under contract 223252/F50. KML and SMH were also funded by the Trond Mohn Foundation.

SUPPLEMENTARY MATERIAL

The Supplementary Material for this article can be found online at: https://www.frontiersin.org/articles/10.3389/fspas.2022.904620/full#supplementary-material

REFERENCES

Araki, T. (1994). A Physical Model of the Geomagnetic Sudden Commencement. *Geophys. Monogr. Ser.* 81, 183–200. doi:10.1029/GM081p0183

Araki, T. (1977). Global Structure of Geomagnetic Sudden Commencements. *Planet. Space Sci.* 25, 373–384. doi:10.1016/0032-0633(77)90053-8

Borovsky, J. E., Denton, M. H., and Smith, C. W. (2019). Some properties of the solar wind turbulence at 1 au statistically examined in the different types of solar wind plasma. *J. Geophys. Res. Space Phys.* 124, 2406–2424. doi:10.1029/2019JA026580

Boudouridis, A., and Zesta, E. (2021). Automated Technique for the Detection of Step-like Solar Wind Dynamic Pressure Changes: Application to the Response of the Transpolar Potential to Solar Wind Dynamic Pressure Fronts. *J. Geophys. Res. Space Phys.* 126, e2021JA029198. doi:10.1029/2021JA029198

Boudouridis, A., Zesta, E., Lyons, L. R., Anderson, P. C., and Lummerzheim, D. (2004). Magnetospheric Reconnection Driven by Solar Wind Pressure Fronts. *Ann. Geophys.* 22, 1367–1378. doi:10.5194/angeo-22-1367-2004

Burton, R. K., McPherron, R. L., and Russell, C. T. (1975). An Empirical Relationship between Interplanetary Conditions andDst. *J. Geophys. Res.* 80, 4204–4214. doi:10.1029/JA080i031p04204

Camporeale, E. (2019). The challenge of Machine Learning in Space Weather: Nowcasting and Forecasting. *Space Weather* 17, 1166–1207. doi:10.1029/2018SW002061

Curto, J. J., Araki, T., and Alberca, L. F. (2007). Evolution of the Concept of Sudden Storm Commencements and Their Operative Identification. *Earth Planet. Sp* 59, i–xii. doi:10.1186/BF03352059

Dalin, P. A., Zastenker, G. N., Paularena, K. I., and Richardson, J. D. (2002a). A Survey of Large, Rapid Solar Wind Dynamic Pressure Changes Observed by Interball-1 and Imp 8. *Ann. Geophys.* 20, 293–299. doi:10.5194/angeo-20-293-2002

Dalin, P. A., Zastenker, G. N., and Richardson, J. D. (2002b). Orientation of Middle-Scale Structures in the Solar Wind Plasma. *Cosmic Res.* 40, 319–323. doi:10.1023/a:1019838226629

Friis-Christensen, E., McHenry, M. A., Clauer, C. R., and Vennerstrøm, S. (1988). Ionospheric Traveling Convection Vortices Observed Near the Polar Cleft: A Triggered Response to Sudden Changes in the Solar Wind. *Geophys. Res. Lett.* 15, 253–256. doi:10.1029/GL015i003p00253

Ganushkina, N. Y., Liemohn, M. W., Dubyagin, S., Daglis, I. A., Dandouras, I., De Zeeuw, D. L., et al. (2015). Defining and Resolving Current Systems in Geospace. *Ann. Geophys.* 33, 1369–1402. doi:10.5194/angeo-33-1369-2015

Haaland, S., and Gjerloev, J. (2013). On the Relation between Asymmetries in the Ring Current and Magnetopause Current. *J. Geophys. Res. Space Phys.* 118, 7593–7604. doi:10.1002/2013JA019345

Hapgood, M. A. (1992). Space Physics Coordinate Transformations: A User Guide. *Planet. Space Sci.* 40, 711–717. doi:10.1016/0032-0633(92)90012-D

Huang, C.-S. (2005). Variations of Polar Cap index in Response to Solar Wind Changes and Magnetospheric Substorms. *J. Geophys. Res.* 110, 10616. doi:10.1029/2004JA010616

Huang, C.-S., and Yumoto, K. (2006). Quantification and Hemispheric Asymmetry of Low-Latitude Geomagnetic Disturbances Caused by Solar Wind Pressure Enhancements. *J. Geophys. Res.* 111, 11831. doi:10.1029/2006JA011831

Iyemori, T., Takeda, M., Nose, M., and Toh, H. (2010). "Mid-latitude Geomagnetic Indices Asy and Sym for 2009 (Provisional)," in *Internal Report of Data Analysis Center for Geomagnetism and Space Magnetism* (Japan: Kyoto University).

Jian, L., Russell, C. T., Luhmann, J. G., and Skoug, R. M. (2006). Properties of Stream Interactions at One AU during 1995 - 2004. *Sol. Phys.* 239, 337–392. doi:10.1007/s11207-006-0132-3

Khabarova, O., Malandraki, O., Malova, H., Kislov, R., Greco, A., Bruno, R., et al. (2021). Current Sheets, Plasmoids and Flux Ropes in the Heliosphere. *Space Sci. Rev.* 217. doi:10.1007/s11214-021-00814-x

Khabarova, O., and Zastenker, G. (2011). Sharp Changes of Solar Wind Ion Flux and Density within and outside Current Sheets. *Sol. Phys.* 270, 311–329. doi:10.1007/s11207-011-9719-4

Kikuchi, T., Tsunomura, S., Hashimoto, K., and Nozaki, K. (2001). Field-aligned Current Effects on Midlatitude Geomagnetic Sudden Commencements. *J. Geophys. Res.* 106, 15555–15565. doi:10.1029/2001JA900030

Kuhn, M., and Johnson, K. (2013). Remedies for Severe Class Imbalance. *Appl. Predictive Model.* 2013, 419–443. doi:10.1007/978-1-4614-6849-3_16

Le, G., Russell, C. T., and Takahashi, K. (2004). Morphology of the Ring Current Derived from Magnetic Field Observations. *Ann. Geophys.* 22, 1267–1295. doi:10.5194/angeo-22-1267-2004

Lee, D.-Y., and Lyons, L. R. (2004). Geosynchronous Magnetic Field Response to Solar Wind Dynamic Pressure Pulse. *J. Geophys. Res.* 109, 10076. doi:10.1029/2003JA010076

Lepping, R. P., Acũna, M. H., Burlaga, L. F., Farrell, W. M., Slavin, J. A., Schatten, K. H., et al. (1995). The Wind Magnetic Field Investigation. *Space Sci. Rev.* 71, 207–229. doi:10.1007/BF00751330

Lühr, H., Xiong, C., Olsen, N., and Le, G. (2017). Near-earth Magnetic Field Effects of Large-Scale Magnetospheric Currents. *Space Sci. Rev.* 206, 521–545. doi:10.1007/s11214-016-0267-y

Lukianova, R. (2003). Magnetospheric Response to Sudden Changes in Solar Wind Dynamic Pressure Inferred from Polar Cap index. *J. Geophys. Res.* 108. doi:10.1029/2002JA009790

Mailyan, B., Munteanu, C., and Haaland, S. (2008). What Is the Best Method to Calculate the Solar Wind Propagation Delay? *Ann. Geophys.* 26, 2383–2394. doi:10.5194/angeo-26-2383-2008

McComas, D. J., Bame, S. J., Barker, P., Feldman, W. C., Phillips, J. L., Riley, P., et al. (1998). Solar Wind Electron Proton Alpha Monitor (Swepam) for the Advanced Composition Explorer. *Space Sci. Rev.* 86, 563–612. doi:10.1007/978-94-011-4762-0_20

Newell, P. T., and Gjerloev, J. W. (2012). Supermag-based Partial Ring Current Indices. *J. Geophys. Res.* 117, a–n. doi:10.1029/2012JA017586

Ogilvie, K. W., Chornay, D. J., Fritzenreiter, R. J., Hunsaker, F., Keller, J., Lobell, J., et al. (1995). Swe, a Comprehensive Plasma Instrument for the Wind Spacecraft. *Space Sci. Rev.* 71, 55–77. doi:10.1007/BF00751326

Oliveira, D. M., and Raeder, J. (2015). Impact Angle Control of Interplanetary Shock Geoeffectiveness: A Statistical Study. *J. Geophys. Res. Space Phys.* 120, 4313–4323. doi:10.1002/2015JA021147

Oliveira, D. M., Raeder, J., Tsurutani, B. T., and Gjerloev, J. W. (2015). Effects of Interplanetary Shock Inclinations on Nightside Auroral Power Intensity. *Braz. J. Phys.* 46, 97–104. doi:10.1007/s13538-015-0389-9

Oliveira, D. M., and Samsonov, A. A. (2018). Geoeffectiveness of Interplanetary Shocks Controlled by Impact Angles: A Review. *Adv. Space Res.* 61, 1–44. doi:10.1016/j.asr.2017.10.006

Riazantseva, M. O., Dalin, P. A., Zastenker, G. N., and Richardson, J. (2003). Orientation of Sharp Fronts of the Solar Wind Plasma. *Cosmic Res.* 41, 382–391. doi:10.1023/a:1025061711391

Richardson, I. G., and Cane, H. V. (1995). Regions of Abnormally Low Proton Temperature in the Solar Wind (1965-1991) and Their Association with Ejecta. *J. Geophys. Res.* 100, 23397–23412. doi:10.1029/95JA02684

Richardson, J. D., and Paularena, K. I. (1998). The Orientation of Plasma Structure in the Solar Wind. *Geophys. Res. Lett.* 25, 2097–2100. doi:10.1029/98GL01520

Ridley, A. J. (2000). Estimations of the Uncertainty in Timing the Relationship between Magnetospheric and Solar Wind Processes. *J. Atmos. Solar-Terrestrial Phys.* 62, 757–771. doi:10.1016/S1364-6826(00)00057-2

Russell, C. T., Ginskey, M., and Petrinec, S. M. (1994b). Sudden Impulses at Low Latitude Stations: Steady State Response for Southward Interplanetary Magnetic Field. *J. Geophys. Res.* 99, 13403–13408. doi:10.1029/94JA00549

Russell, C. T., Ginskey, M., and Petrinec, S. M. (1994a). Sudden Impulses at Low-Latitude Stations: Steady State Response for Northward Interplanetary Magnetic Field. *J. Geophys. Res.* 99, 253–261. doi:10.1029/93JA02288

Russell, C. T., and Ginskey, M. (1995). Sudden Impulses at Subauroral Latitudes: Response for Northward Interplanetary Magnetic Field. *J. Geophys. Res.* 100, 23695–23702. doi:10.1029/95JA02495

Schwartz, E. (1998). Doriot Anthony Dwyer, Flute. *Am. Music* 16, 249–270. doi:10.2307/3052576

Selvakumaran, R., Veenadhari, B., Ebihara, Y., Kumar, S., and Prasad, D. S. V. V. D. (2017). The role of interplanetary shock orientation on sc/si rise time and geoeffectiveness. *Adv. Space Res.* 59, 1425–1434. doi:10.1016/j.asr.2016.12.010

Shi, Y., Zesta, E., Lyons, L. R., Boudouridis, A., Yumoto, K., and Kitamura, K. (2005). Effect of Solar Wind Pressure Enhancements on Storm Time Ring Current Asymmetry. *J. Geophys. Res.* 110, 11019. doi:10.1029/2005JA011019

Smith, C. W., L'Heureux, J., Ness, N. F., Acuña, M. H., Burlaga, L. F., and Scheifele, J. (1998). The Ace Magnetic fields experiment. *Space Sci. Rev.* 86, 613–632. doi:10.1023/A:1005092216668

Smith, E. J., and Wolfe, J. H. (1976). Observations of interaction regions and corotating shocks between one and five au: Pioneers 10 and 11. *Geophys. Res. Lett.* 3, 137–140. doi:10.1029/GL003i003p00137

Stauning, P., and Troshichev, O. A. (2008). Polar Cap Convection and Pc index during Sudden Changes in Solar Wind Dynamic Pressure. *J. Geophys. Res.* 113, a–n. doi:10.1029/2007JA012783

Takeuchi, T., Russell, C. T., and Araki, T. (2002). Effect of the Orientation of Interplanetary Shock on the Geomagnetic Sudden Commencement. *J. Geophys. Res.* 107, 6–1. doi:10.1029/2002JA009597

Tin Kam Ho, T. H. (1995). Random Decision Forests. *Proc. 3rd Int. Conf. Document Anal. Recognition* 1, 278–282. doi:10.1109/ICDAR.1995.598994

Walsh, A. P., Haaland, S., Forsyth, C., Keesee, A. M., Kissinger, J., Li, K., et al. (2014). Dawn-dusk Asymmetries in the Coupled Solar Wind-Magnetosphere-Ionosphere System: a Review. *Ann. Geophys.* 32, 705–737. doi:10.5194/angeo-32-705-2014

Weimer, D. R., Ober, D. M., Maynard, N. C., Collier, M. R., McComas, D. J., Ness, N. F., et al. (2003). Predicting Interplanetary Magnetic Field (Imf) Propagation Delay Times Using the Minimum Variance Technique. *J. Geophys. Res.* 108. doi:10.1029/2002JA009405

[Dataset] Willer, A. N. (2021). The Polar Cap North (PCN) index (Definitive) [Data Set]. *PCN index*. doi:10.11581/DTU:00000057

Zhang, Q.-H., Dunlop, M. W., Lockwood, M., Holme, R., Kamide, Y., Baumjohann, W., et al. (2011). The Distribution of the Ring Current: Cluster Observations. *Ann. Geophys.* 29, 1655–1662. doi:10.5194/angeo-29-1655-2011

Conflict of Interest: The authors declare that the research was conducted in the absence of any commercial or financial relationships that could be construed as a potential conflict of interest.

frontiers | Frontiers in Astronomy and Space Sciences

ORIGINAL RESEARCH
published: 31 May 2022
doi: 10.3389/fspas.2022.916739

Low- and Mid-Latitude Ionospheric Response to the 2013 St. Patrick's Day Geomagnetic Storm in the American Sector: Global Ionosphere Thermosphere Model Simulation

Qingyu Zhu[1]*, *Gang Lu*[1] and *Yue Deng*[2]

[1]High Altitude Observatory, National Center for Atmospheric Research, Boulder, CO, United States, [2]Department of Physics, University of Texas at Arlington, Arlington, TX, United States

OPEN ACCESS

Edited by:
Denny Oliveira,
University of Maryland, Baltimore County, United States

Reviewed by:
Dogacan Ozturk,
University of Alaska System, United States
Ram Singh,
Chungnam National University, South Korea
Bapan Paul,
Bhavan's Tripura College of Science and Technology, India

***Correspondence:**
Qingyu Zhu
qingyu@ucar.edu

Specialty section:
This article was submitted to Space Physics, a section of the journal Frontiers in Astronomy and Space Sciences

Received: 09 April 2022
Accepted: 04 May 2022
Published: 31 May 2022

Citation:
Zhu Q, Lu G and Deng Y (2022) Low- and Mid-Latitude Ionospheric Response to the 2013 St. Patrick's Day Geomagnetic Storm in the American Sector: Global Ionosphere Thermosphere Model Simulation. Front. Astron. Space Sci. 9:916739. doi: 10.3389/fspas.2022.916739

In this study, the low-and mid-latitude ionospheric response to the main phase of the 2013 St. Patrick's Day geomagnetic storm in the American sector on the dayside has been investigated using the ground-based measurements and the Global Ionosphere Thermosphere Model (GITM). First, it is found that the observed ionospheric response can be well reproduced by GITM when it is driven by the electric potential and electron precipitation patterns derived from the Assimilative Mapping of Ionospheric Electrodynamics (AMIE) technique. The AMIE-driven GITM simulation also significantly improves the data-model comparison as compared with the simulation driven by the high-latitude empirical models. Second, it is found that the transport process associated with the neutral wind is largely responsible for the observed ionospheric response. Specifically, the traveling atmospheric disturbances (TADs) propagating from the opposite hemisphere play an important role in the formation of the negative storm phase at low and middle latitudes. Third, it is found that the asymmetric negative storm phases occurred at the nominal equatorial ionization anomaly (EIA) peak region in the afternoon sector are mainly attributed to the interaction of the TADs launched in different hemispheres with different phase speeds. Specifically, stronger Joule heating deposited in the northern hemisphere (NH) generates TADs with faster phase speeds than those launched in the southern hemisphere (SH). Consequently, the locations where the TADs originated from the different hemispheres interact are asymmetric about the geomagnetic equator, leading to the formation of asymmetric ionospheric negative storm phases. This study highlights the importance of accurately specifying high-latitude electrodynamic forcings in global I-T simulations and provides a new insight into the cause of the interhemispheric asymmetry phenomena during geomagnetic storms.

Keywords: geomagnetic storm, ionospheric response, GITM, AMIE, travelling atmospheric disturbance

INTRODUCTION

Earth's ionosphere and thermosphere (I-T) system can be significantly disturbed during geomagnetic storms when the high-latitude electric field and electron precipitation undergo significant modifications. The topology and intensity of the high-latitude electric field are directly influenced by the orientation of the interplanetary magnetic field (IMF) and solar wind conditions. Sudden changes in the IMF and solar wind could cause the high-latitude electric field to penetrate towards to the equatorial region. A sudden southward turning of the IMF could produce an eastward prompt penetration electric field (PPEF) on the dayside (Fejer and Scherliess, 1997) which reinforces the dayside fountain effect and can significantly contribute to the ionospheric positive storm effect (e.g., an increase of the F-region electron density) at low and middle latitudes (e.g., Tsurutani et al., 2004; Mannucci et al., 2005; Huang et al., 2005; Lei et al., 2008a; Lu et al., 2012). Meanwhile, a tremendous amount of electromagnetic energy from the magnetosphere is deposited into the ionosphere-thermosphere (I-T) system during geomagnetic storms, and the majority of this energy input is converted to Joule heating which is an important energy source of the I-T system (e.g., Lu et al., 1995; Thayer et al., 1995; Knipp et al., 2004; Deng et al., 2011; Deng et al., 2018; Knipp et al., 2021). Strong heating at high latitudes could generate equatorward-propagating disturbance neutral winds, which push the plasma upward along the magnetic field line and contribute to a positive ionospheric storm phase at low and middle latitudes (e.g., Lin et al., 2005; Lu et al., 2008). In addition, the storm-time disturbance neutral wind also generates a westward electric field on the dayside (Blanc and Richmond, 1980), which could suppress the dayside fountain effect (Scherliess and Fejer, 1997). Joule heating not only modifies the thermospheric circulation but also alters thermospheric neutral temperature, neutral density and neutral composition, and the changes in thermospheric composition can also change the ion and electron densities through chemical processes (e.g., Fuller-Rowell et al., 1994; Burns et al., 1995; Zhang et al., 2003; Cai et al., 2021). Furthermore, impulsive Joule heating could induce large-scale traveling atmospheric disturbances (TADs) and traveling ionospheric disturbances (TIDs) (Richmond and Matsushita, 1975; Bauske and Prölss, 1997; Balthazor and Moffett, 1999; Lee et al., 2004; Shiokawa et al., 2007; Lei et al., 2008b; Bruinsma and Forbes, 2009; Guo et al., 2014; Lu et al., 2016; Ren and Lei, 2017; Lyons et al., 2019; Zhang et al., 2019; Lu et al., 2020; Sheng et al., 2021; Wang et al., 2021; Pham et al., 2022).

This study focuses on the ionospheric response to the 2013 St. Patrick's Day geomagnetic storm, which is an intense storm that has drawn substantial community interests and lots of significant processes have been made (e.g., Kalita et al., 2016; Liu et al., 2016; Lyons et al., 2016; Verkhoglyadova et al., 2016; Yue et al., 2016; Dmitriev et al., 2017; Guerrero et al., 2017; Marsal et al., 2017; Xu et al., 2017; Dang et al., 2019; Ferdousi et al., 2019; Kumar and Kumar, 2019; Lin et al., 2019; Zhai et al., 2020; Amaechi et al., 2021). However, it is still challenging for the community to accurately describe and simulate the ionospheric response, including both positive and negative phases, to the geomagnetic storms. For example, the simulation work shown in Yue et al. (2016) utilized the National Center of Atmospheric Research Thermosphere-Ionosphere-Electrodynamics General Circulation model (NCAR-TIEGCM, Qian et al., 2014) to study the ionospheric response to the storm. In their study, high-latitude empirical models were used to specify the high-latitude electrodynamic forcings in the NCAR-TIEGCM. However, the complex coexistence of the ionospheric positive and negative storm phases during the main storm phase in the American sector were not well reproduced in their simulations, preventing us from a better understanding of such interesting ionospheric response at low and middle latitudes. The data-model discrepancies in their study may be attributed to the fact that high-latitude empirical models often fail to capture the dynamic spatial and temporal variations of high-latitude electrodynamic forcings (Heelis and Maute, 2020). In this work, whether and to what extent the more realistic high-latitude electrodynamic forcings could help improve the data-model comparison are assessed. Meanwhile, the physical processes contributing to the ionospheric variations during the 2013 St. Patrick's Day storm are examined.

In this study, the numerical simulations using the Global Ionosphere Thermosphere Model (GITM, Ridley et al., 2006) are performed, driven by two types of high-latitude electrodynamic forcings: the electric and electron precipitation patterns derived from the Assimilative Mapping Ionospheric Electrodynamics (AMIE) procedure (Richmond and Kamide, 1988; Richmond, 1992) and the patterns provided by a recently developed empirical model, Auroral Spectrum and High-Latitude Electric field variabilitY (ASHLEY, Zhu et al., 2021). The simulation results are compared with the ground-based measurements.

MODEL AND DATA DESCRIPTIONS

Global Ionosphere Thermosphere Model

GITM is a global model for the Earth's upper atmosphere which self-consistently solves for the density, velocity and temperature of neutrals, ions and electron. Unlike most global models used in the community, GITM relaxes the hydrostatic assumption and allows the propagation of acoustic waves (Deng et al., 2008; Deng and Ridley, 2014; Zhu et al., 2017; Deng et al., 2021). The version of GITM used in this study is the one coupled with the ionospheric electrodynamo solver developed by Maute and Richmond (2017), and the coupling has been described in Zhu et al. (2019). The spatial resolution of GITM is 5° in geographic longitude and 2.5° in geographic latitude and 1/3 scale height in altitude ranging from 100 to 900 km, and the time step is 2 s.

High-Latitude Electrodynamic Forcings in Global Ionosphere Thermosphere Model

In this study, the high-latitude electrodynamic forcings in GITM are specified in two different ways: by an empirical model and by the data assimilative patterns. The empirical model used in this

study is the Auroral Spectrum and High-Latitude Electric field variabilitY (ASHLEY) model (Zhu et al., 2021). Specifically, its electric potential (ASHLEY-E) and electron precipitation (ASHLEY-A) components are utilized, which are developed based on the *in-situ* ion drift and electron precipitation data from the Defense Meteorological Satellite Program (DMSP) satellites, respectively. Both ASHLEY-A and ASHLEY-E use interplanetary magnetic field (IMF) and solar wind data as inputs.

The AMIE ionospheric electric potential and electron precipitation patterns are also used for this study. AMIE provides an optimal estimation of high-latitude electrodynamic fields based on a variety of ground-based and space-based measurements, so it provides more realistic high-latitude electrodynamic forcing than empirical models. A more recent description of AMIE can be found in Lu (2017). The data inputs to AMIE for this event include horizontal magnetic perturbations measured by 217 ground stations (among them 173 stations were in the NH and 44 were in the SH), cross-track ion drift data measured by four DMSP satellites (F15, F16, F17, and F18), electron precipitation inferred from the Special Sensor of Ultraviolet Spectrographic Imager (SSUSI) onboard three DMSP satellites (i.e., F16, F17, and F18), line-of-sight ion drifts measured by Super Dual Auroral Radar Network high frequency radar network, and the horizontal magnetic perturbations measured by the Iridium satellite constellation and provided by the Active Magnetosphere and Planetary Electrodynamics Response Experiment (AMPERE) dataset (Anderson et al., 2014). The temporal resolution of AMIE pattern is 5 min, and the spatial resolution of AMIE pattern is 0.67 h in magnetic local time (MLT) and 1.67° in magnetic latitude (MLAT).

Ionospheric Dataset

In this study, the vertical total electron content (TEC) data estimated from the ground-based dual-frequency global navigation satellite system (GNSS) receivers are used to validate the simulation results. First, the line-of-sight TEC (i.e., line-integrated ionospheric electron density) is estimated by analyzing the processed L1 and L2 pseudorange and phase data (Rideout and Coster, 2006). After removing the ground receiver and satellite biases, the line-of-sight TEC with an elevation angle above 30° is then converted to the vertical TEC using a mapping function (Rideout and Coster, 2006; Vierinen et al., 2016). This study focuses on the vertical TEC data derived from the GNSS receivers distributed in the American Sector are used.

In addition to the TEC data, ionosonde measurements from four stations in the American sector are analyzed. The four stations are: Wallop Island (75.5°W, 37.9°N), Eglin (86.5°W, 30.5°N), Ramey (67.1°W, 18.5°N), and Jicamarca (76.8°W, 12.0°S). In particular, the F2 peak electron density (NmF2) and height (hmF2), which are determined from the measured ionograms using the SAO-Explorer software package (Huang and Reinisch, 1996), are used.

RESULTS AND DISCUSSION

Geophysical Conditions

Figure 1 summarizes the geophysical conditions during the 2013 St. Patrick's Day storm, including the variations of the IMF B_y and B_z components, the Dst and AE indices, along with the cross-polar-cap potential (CPCP) and hemispheric power (HP) in the northern hemisphere (NH). The latter four variables are from the AMIE outputs. The AMIE Dst index is similar to the SYM-H index but using the magnetometer data from 56 stations between −40° and 40° MLAT. The AE index is derived from 98 stations between |55°| and |76°| MLAT in both hemispheres. The northern hemisphere (NH) AMIE outputs are used. The 2013 St. Patrick's Day storm was triggered by an interplanetary coronal mass ejection (ICME). As illustrated in Verkhoglyadova et al. (2016), the shock of the ICME arrived at the Earth's bow shock at around 6 UT on 03/17/2013 and was followed by the ICME sheath region. A magnetic cloud arrived at around 15:30 UT and lasted for more than 24 h. During the passage of the sheath region, the IMF B_y and B_z components intensified and exhibited large oscillations. Meanwhile, the Dst index dropped to−120 nT at around 12 UT and gradually recovered until the arrival of the magnetic cloud. During the passage of the magnetic cloud, the IMF B_z turned southward and remained southward for about 6 h. The Dst index decreased again until 20:30 UT when it

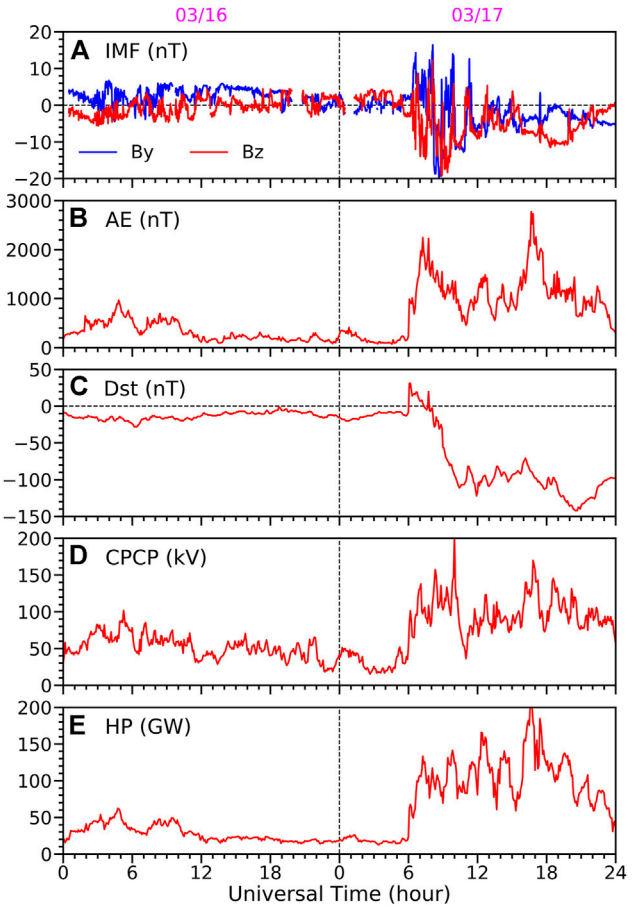

FIGURE 1 | Evolutions of **(A)** IMF (blue: B_y; red: B_z), **(B)** AE, **(C)** Dst, **(D)** CPCP and **(E)** HP during the 2013 St. Patrick's day geomagnetic storm. The IMF data is shifted by 30 min. The parameters shown in the bottom four panels are from the Northern Hemisphere AMIE output. IMF, interplanetary magnetic field; AE, auroral electrojet; CPCP, cross-polar cap potential; HP, hemispheric power; AMIE, Assimilative Mapping Ionospheric Electrodynamics.

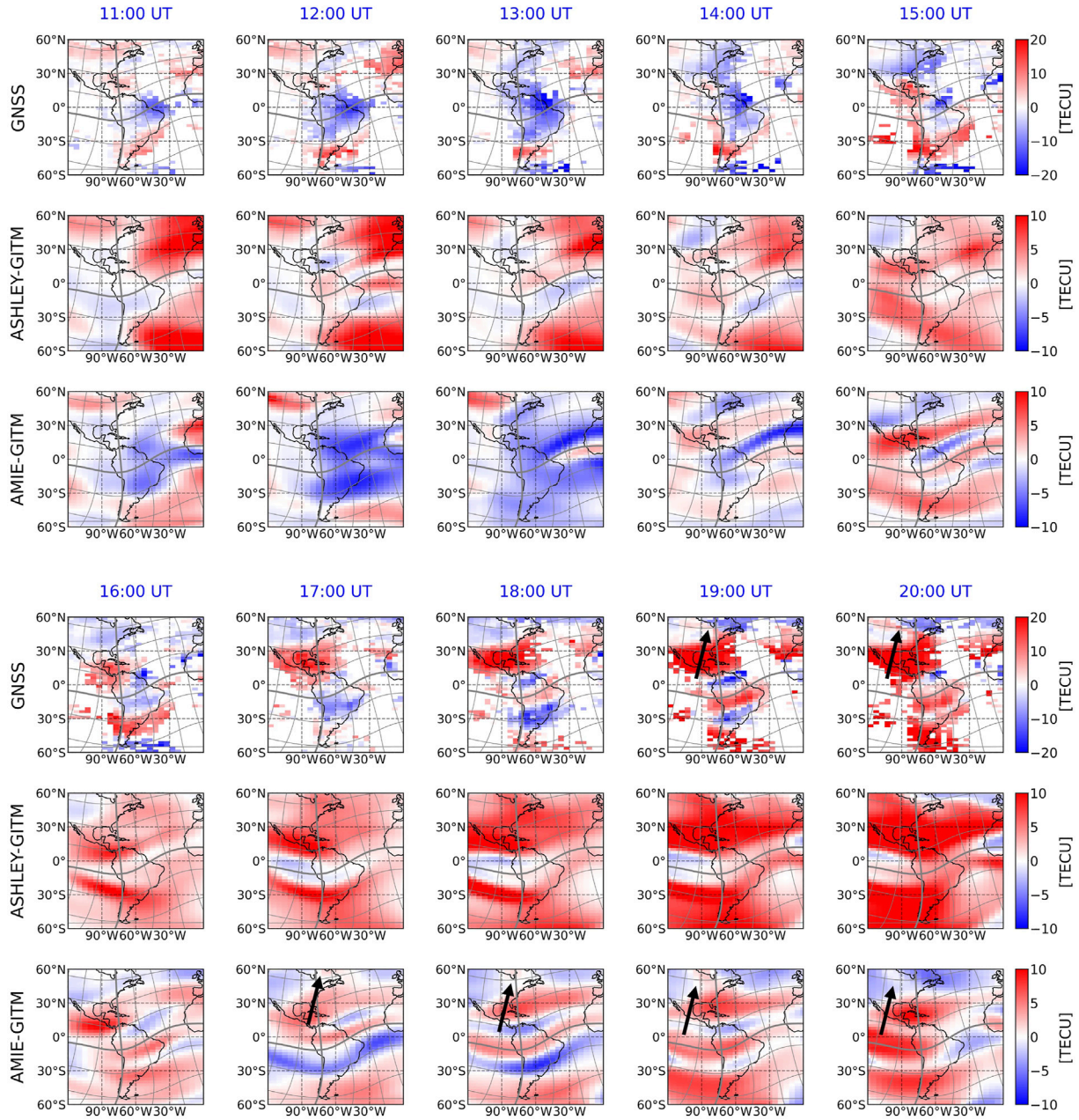

FIGURE 2 | Comparisons of the storm-quiet differential TEC in the American sector at different UTs. At each UT, from top to bottom, the results correspond to those calculated from the GNSS data, ASHLEY-driven and AMIE-driven GITM simulation outputs, respectively. Note that the color scale is smaller for the differential TEC calculated from the GITM simulation output. The grey lines indicate the Apex magnetic coordinate, with the MLON and MLAT having a 20° spacing. The 0° MLON and MLAT are marked by the thick grey lines. Black arrows indicate the SED plume. TEC, total electron content; UT, universal time; ASHLEY, Auroral Spectrum and High-Latitude Electric field variabilitY; GITM, Global Ionosphere Thermosphere Model; MLON, magnetic longitude; MLAT, magnetic latitude; GNSS, Global Navigation Satellite System; SED, storm-time enhanced density.

reached its minimum value of −140 nT. Hence, this storm displayed a two-step growth. During the main phase (6:00–20: 30 UT), the auroral electrojet showed two strong (>1,500 nT) intensifications around 7:30 and 16:30 UT as indicated by the AE index, and the maximum AE value reached ~2,800 nT. The maximum of the NH CPCP was 204 kV. The maximum of the NH HP was 205 GW.

Data-Model Comparisons in the American Sector

Figure 2 shows the comparisons of the storm-quiet differential TEC in the American sector at different UTs, with the GNSS data shown in the top row and by simulation results shown in the second and third rows. The TEC data on 03/16 is used as the quiet-time reference. We also tried several other quiet-time

references, e.g., the 5-day averaged TEC prior to 03/17, and the results do not have significant differences.

As shown in the GNSS data, a negative storm phase occurs in the equatorial region at 11 UT and extends to higher latitudes afterwards. However, a positive storm phase occurs at around −30° magnetic latitude (MLAT) and lasts for several hours. Around 15 UT, a positive storm phase starts to occur near 30° MLAT and maintains and intensifies throughout the remaining time of the main phase. However, the negative storm phase still remains around the geomagnetic equator until 17 UT when a positive storm phase appears around the geomagnetic equator. Between 17 and 19 UT, negative storm phases occur at the nominal equatorial ionization anomaly (EIA) peak region (±15° MLAT) and are asymmetric about the geomagnetic equator. More specifically, the negative storm phase in the SH is more intense and occurs in a broader region than that in the NH at 17 and 18 UT. At 70°W, the differential TECs at 3°N (~15° MLAT) are +5 TECU and −9 TECU) at 17and 18 UT, respectively, while the differential TECs at 27°S (~15° MLAT) are −5 TECU and −17 TECU at 17 and 18 UT, respectively. However, the negative storm in the NH is more intense than its SH counterpart at 19 UT. The differential TECs are −17 TECU and −10 TECU at 15° and −15° MLAT at 70°W, respectively. At 20 UT, positive storm phases cover almost the entire American sector except for the region poleward of 50° MLAT, where a strong storm-enhanced density (SED) plume cuts through a negative storm phase which has been lasted for several hours.

The second row for each UT shows the ASHLEY-driven GITM simulation results. Note that for GITM simulation results, the color scale is half of that used for the GNSS data since the GITM TEC is roughly half of the GNSS TEC during both quiet and storm times. Several reasons may be responsible for the underestimation of TEC such as no plasmasphere contribution and inaccuracy of the top boundary conditions. Improving the quantitative representation of the electron density in GITM, especially during geomagnetic storms, is an important aspect of our future model development plan. It is clear that there are large discrepancies between the observational and ASHLEY-driven simulation results, particularly the negative storm phase shown in the GNSS data is not well captured by the ASHLEY-driven GITM simulation. We have also utilized the Weimer electric potential model (Weimer, 2005) and Fuller-Rowell and Evans electron precipitation model (Fuller-Rowell and Evans, 1987), which are the default high-latitude empirical models in GITM, to specify high-latitude electrodynamic forcings in GITM. However, that GITM simulation cannot well reproduce the observed feature either. In contrast, the major storm-related features shown in the GNSS data are well captured in the AMIE-driven simulation (third row for each UT) although some discrepancies do exist. For example, the AMIE-driven GITM simulation shows that the negative storm phase occurs in a larger area than that shown in the GNSS TEC data before 14 UT (e.g., −40° ~ −20° MLAT). In addition, the AMIE-driven GITM simulation shows that the positive storm phase occurs in a larger area than that exhibited in the GNSS TEC data between 15 and 17 UT (e.g., around the geomagnetic equator). Interestingly, the SED plume which cuts through the negative storm phase occurred in the region poleward of 50° MLAT (marked by the black arrow) is roughly reproduced in the AMIE-driven simulation at 19 and 20 UT. However, the SED plume in GITM also occurs at 17 and 18 UT

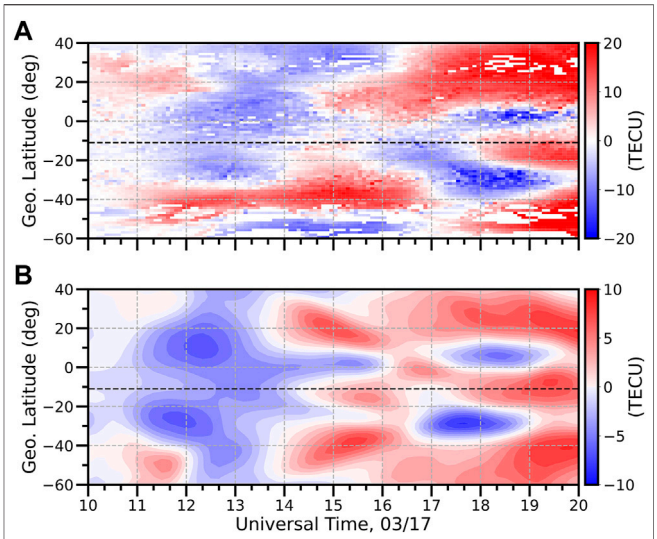

FIGURE 3 | Comparison of the storm-quiet differential TEC at 70°W as a function of UT and geographic latitude. The black dashed line in each panel corresponds to the geomagnetic equator at 70°W. **(A)** GNSS differential TEC. **(B)** GITM differential TEC.

which is not seen in the data. Meanwhile, the simulated SED plume at 19 and 20 UT is not as narrow and strong as the observed one, which may be attributed to the fact that the subauroral plasma stream (SAPS) electric field is not well specified in AMIE (Lu et al., 2020) and also to the fact that the GITM grid resolution used in this study is quite coarse. Improving the representation of the SAPS electric field in AMIE would be an interesting future work. The data-model comparisons shown in **Figure 2** demonstrate the value of using more realistic high-latitude electrodynamic forcings to investigate the storm-time ionospheric response. In the remaining part of this paper, we will focus on the comparisons of the observations with the AMIE-driven GITM simulation results.

Figure 3 shows detailed data-model comparisons at 70°W (LT~UT−5 h, LT = local time), with the GNSS differential TEC shown in the top panel and the GITM differential TEC shown in the bottom panel. The latitudinal range we focused on here is 60°S–40°N in terms of the geographic latitude (GLAT), which roughly corresponds to −50°~50° MLAT. As shown in **Figure 3A**, before 14 UT (~9 LT), a negative storm phase occurs at almost all latitudes except for the region around 40°S and 20°N, where a positive storm phase occurs. The negative storm phase is pretty well captured by GITM while the positive storm phase occurred around 20°N before 12 UT (~7 LT) and around 40°S between 12 and 14 UT (~7–9 LT) are not well captured in the GITM simulation (**Figure 3B**). Between 14 and 16 UT (~9–11 LT), the GNSS data indicates that a positive storm phase occurs from 20°S to 45°S and from 10°N to 20°N, while a weak positive storm phase occurs near the geomagnetic equator. These positive storms are reasonably well captured by GITM except that the positive storm phase at middle latitudes extends to higher latitudes in the NH in GITM simulation than that shown in the GNSS data. After 16 UT

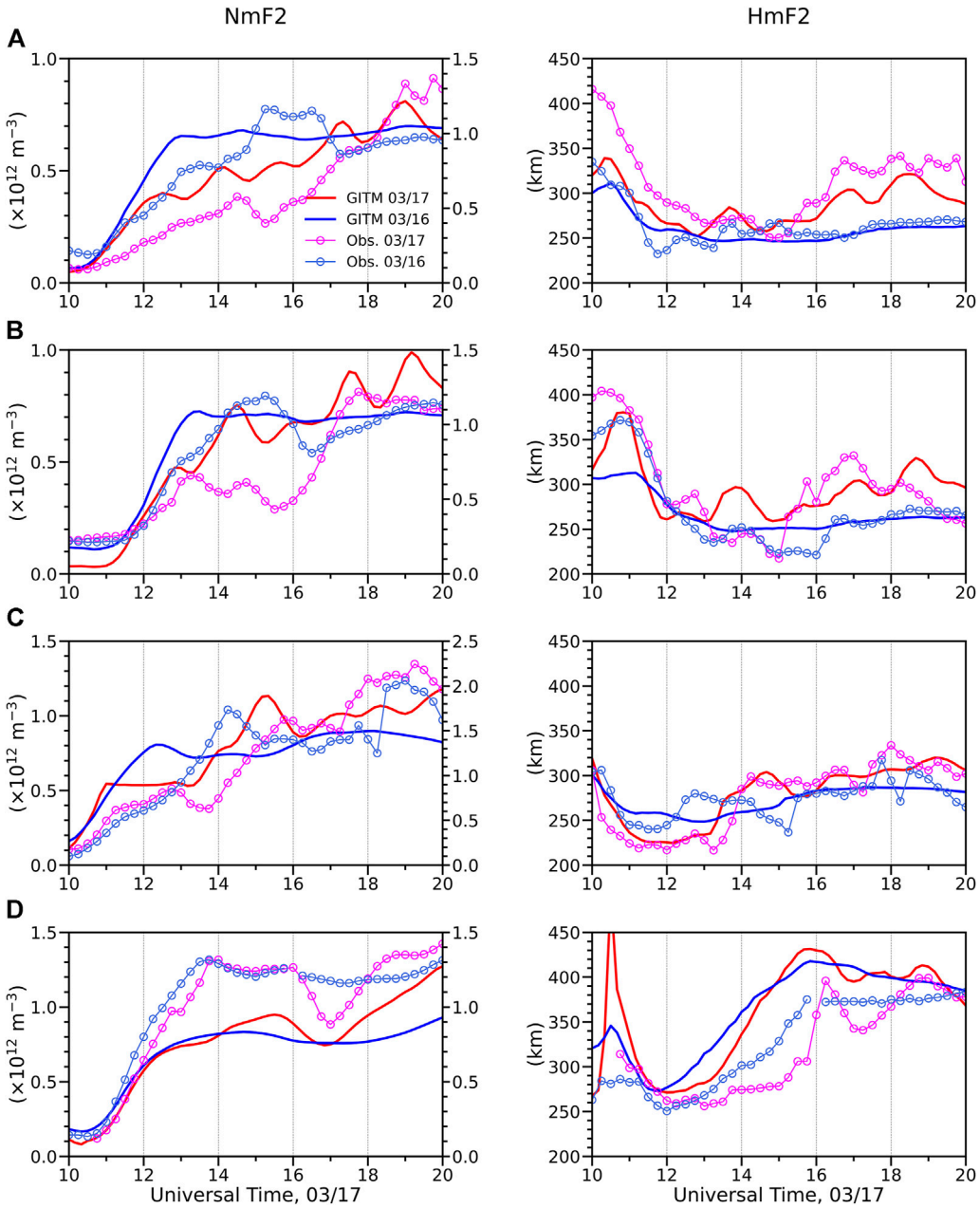

FIGURE 4 | Comparisons of the NmF2 and HmF2 between the measurements and AMIE-driven GITM simulation results at four stations at around 70°W. The sky blue and magenta lines with circles represent the parameters measured on 03/16 and 03/17, respectively. The blue and red lines represent the simulation results on 03/16 and 03/17, respectively. **(A)** Wallop Island (75.5°W, 37.9°N). **(B)** Eglin (86.5°W, 30.5°N). **(C)** Ramey (67.1°W, 18.5°N). **(D)** Jicamarca (76.8°W, 12.0°S).

(~11 LT), the GNSS data shows that positive storm phases occur poleward of the 10°N and 40°S, respectively. In addition, a positive storm phase also occurs around the geomagnetic equator (11°S) after 17:30 UT, which is preceded by a negative storm phase between ~16:00 and 17:30 UT. Moreover, sizable negative storm phases can be seen around 5°N as well as around 30°S after 17 UT following the positive storm phase, with the one occurred around 30°S having larger latitudinal extension and stronger magnitude in general. Again, GITM simulation captures the main TEC variations shown in the observation.

Figure 4 shows the data-model comparisons of the NmF2 and HmF2 at four stations located around 70°W. The red and blue lines represent the parameters on 03/17 and 03/16, respectively. The solid lines represent the parameters from the GITM simulation and the lines with circles represent the measured parameters. In general, GITM qualitatively captures the variations of NmF2 and HmF2 shown in the observation, but there are some quantitative discrepancies between the observation and simulation, which may result from the inaccurate specifications of the O^+ flux at the top boundary of

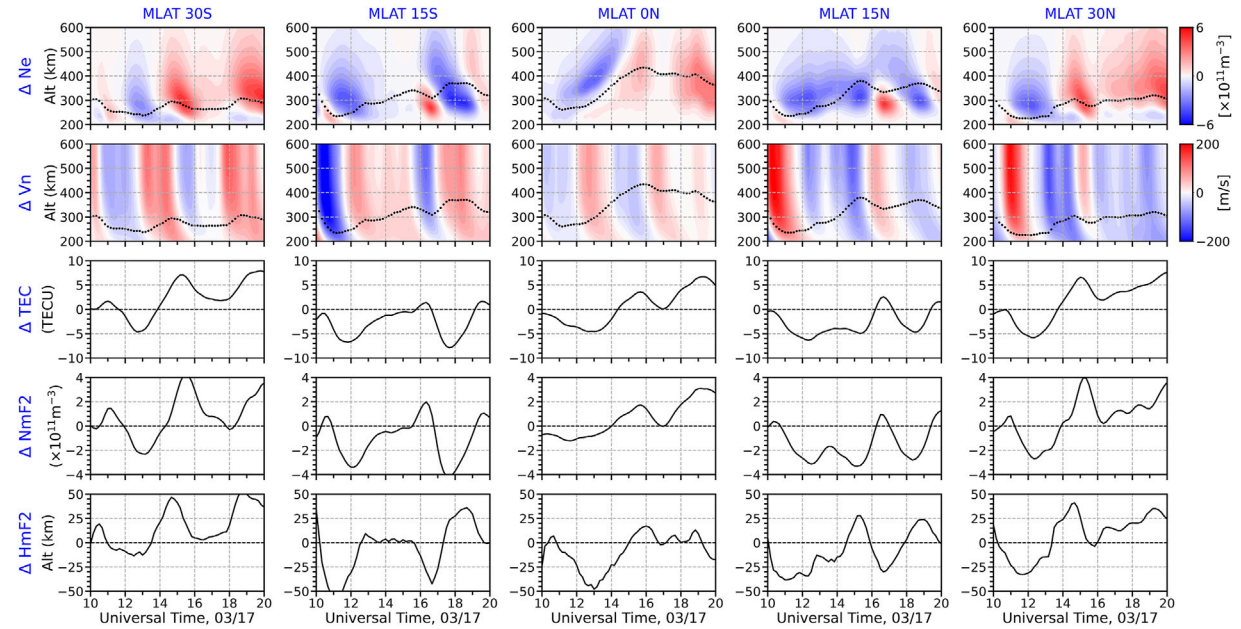

FIGURE 5 | (From top to bottom) Storm-quiet differences of the electron density, meridional wind, TEC, NmF2 and HmF2 at five locations at 70°W calculated from the GITM outputs. The electron density and meridional wind are plotted as a function of UT and altitude while other parameters are shown as a function of UT. For the meridional wind, positive values indicate northward winds (poleward in the NH and equatorward in the SH). NH, northern hemisphere; SH, southern hemisphere.

the model (Lu et al., 2001). Improving the top boundary condition of GITM is an important aspect of our future model development plan as discussed earlier.

Physical Processes Responsible for the Electron Density Variations

As illustrated in the above subsection, the AMIE-driven GITM simulation reproduces the observed ionospheric response to the 2013 St. Patrick's Day geomagnetic storm reasonably well, providing us an opportunity to explore the physical processes responsible for the ionospheric response during this storm.

Figure 5 shows the storm-quiet difference of the electron density, the meridional neutral wind, TEC, NmF2, and HmF2 at five selected latitudes along 70°W. One of them is located at the geomagnetic equator and the other four are located at ±15° MLAT and ±30° MLAT, respectively. The differences of the electron density and meridional neutral wind are shown as a function of UT and altitude while the other three parameters are show as a function of UT. In addition to the storm-time equatorward disturbance neutral winds (negative in NH and positive in SH), there are also poleward disturbance neutral winds at ±15° MLAT and ±30° MLAT, indicating the existence of the TADs. The TEC and ionospheric peak parameters also display quasi-periodic oscillations, which may be associated with the TADs. In particular, the variations of TEC and NmF2 are similar in general, while the correlation between the NmF2 and HmF2 oscillations is quite complicated. The oscillations of NmF2 and HmF2 are generally anti-correlated at ±15° MLAT but they are roughly positively correlated with some phase delay at other latitudes. As discussed in Lu et al. (2001), the correlation between the NmF2 and HmF2 depends on the relative importance of the vertical shear of the meridional neutral wind and the change of recombination near the F2 peak. The negative and positive correlations occur when the former and latter processes dominate, respectively.

Figure 5 also shows that the reduction of the electron density roughly follows the poleward disturbance wind at low and middle latitudes, indicating a significant contribution of the meridional wind to the formation of the negative storm phase. Then a question arises: how does the neutral wind contribute to the ionospheric response? To address this question, it is necessary to investigate the evolution of the neutral wind at 70°W. **Figure 6** shows the storm-quiet differences of height-integrated Joule heating, meridional neutral wind along with the vertical ion drifts associated with the neutral wind and electric field. From the meridional neutral wind and the vertical drift associated with the neutral wind (**Figures 6B,C**), it is clear that several TADs are launched during this geomagnetic storm. Of particular interest are three pairs of TADs highlighted by the thick black dashed lines. The TADs launched in the NH and SH are labeled by the numbers of 1–3 and 1′–3′, respectively. The first pair of TADs (1 and 1′) launch right after the onset of the geomagnetic storm when there is a significant enhancement of Joule heating, traveling at high phase speeds (~710 m/s) and having larger magnitudes (in terms of wind perturbations) than the TADs launched afterwards. At around 10 UT, when the 70°W meridian rotates to the dawn side, they encounter each other at the geomagnetic equator. After that, they cross each other and travel to middle and high latitudes in the opposite hemisphere.

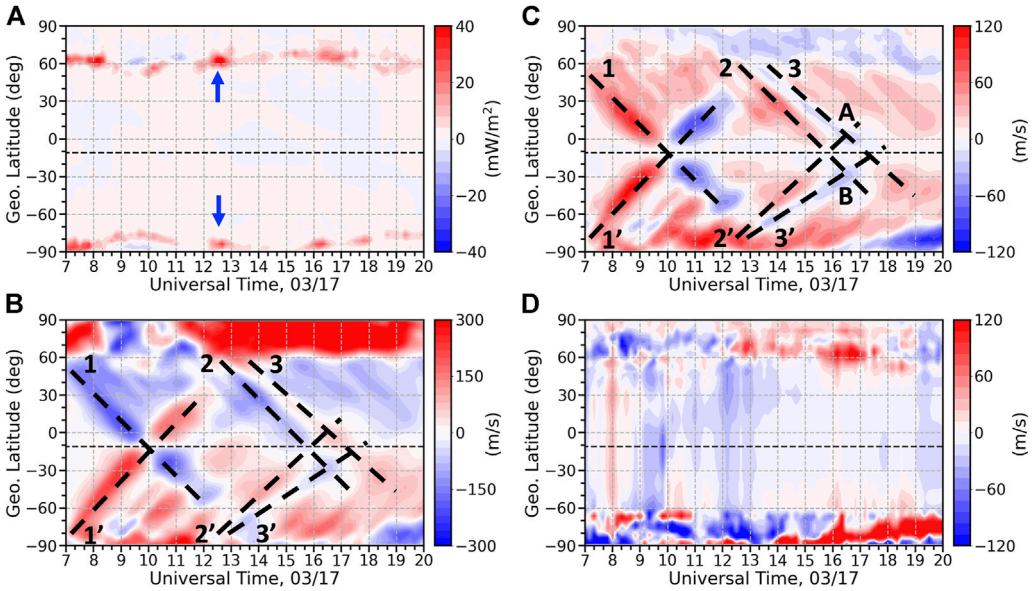

FIGURE 6 | Storm-quiet differences of **(A)** Joule heating, **(B)** meridional neutral wind, **(C)** vertical ion drift associated with the neutral wind and **(D)** vertical ion drift associated with the electric field at 300 km and at 70°W. Positive neutral wind corresponds to northward neutral wind, and positive ion drift correspond to upward ion drift. All parameters are presented as a function of universal time and geographic latitude. The thin black dashed line in each panel denotes the geomagnetic equator. The thick black dashed lines highlight the TADs. TAD, traveling atmospheric disturbance. **(A)** ΔJoule heating. **(B)** ΔVn. **(C)** ΔVi (wind, up). **(D)** ΔVi (ExB, up).

The poleward disturbance meridional winds associated with the TADs push the plasma downward along the field line (**Figure 6C**) where the recombination rate becomes large and thus cause a reduction of the electron density between 11and 14 UT at low and middle latitudes (**Figure 3**). This may also explain why the electron density reduction takes place at low latitudes at first and expands to higher latitudes as shown in **Figures 2** and **3**. The second pair of TADs (2 and 2′) launch around 12–13 UT, which are also able to travel to the opposite hemisphere before being dissipated. However, they are not as strong as the first pair in terms of wind perturbations so they cannot penetrate to latitudes as high as the first pair of TADs do. Moreover, the phase speed of TAD 2 (710 m/s) is ~40% higher than that of TAD 2′ (510 m/s). The third pair of TADs (3 and 3′) cause poleward disturbance meridional winds in the hemispheres where they are launched and are associated with the rarefaction of TADs 2 and 2′. The phase speed of TAD 3 (540 m/s) is ~13% higher than that of TAD 3′ (460 m/s). The phase speeds of those three pairs of TADs fall in the range of large-scale TADs categorized by Hunsucker (1982), and faster TAD launched in the NH has also reported in previous studies (e.g., Valladares et al., 2009; Lu et al., 2014; Pradipta et al., 2016). TAD 2 interferes with TAD 3′ at Location B (~−20° MLAT) while TAD 2′ interferes with TAD 3 at Location A (~5° MLAT) between 16 and 17 UT, causing strong poleward disturbance meridional winds at both locations. As noted above, the poleward disturbance meridional wind pushes the plasma downward along the magnetic field line, consequently reducing the plasma density later on.

Although plasma transport by the neutral wind through neutral-ion coupling can explain the observed ionospheric response, its relative importance with respect to other transport and chemical processes remains unclear. For example, **Figure 6D** shows that the vertical drift associated with the electric field may also be able to contribute to the negative storm phase occurred between 9 and 14 UT at low and middle latitudes shown in **Figure 3**. To delineate the relative contributions by the different dynamical and chemical process, following the procedures described in Lei et al. (2008a), a term analysis is applied to the ion continuity equation in GITM. Since the O^+ is the dominant ion species in the F region and is the only species advected in GITM default setup (Ridley et al., 2006), the term analysis is carried out only for the O^+. The continuity equation of O^+ is written as:

$$\frac{\partial N}{\partial t} = q - \beta N - \nabla \cdot (N\boldsymbol{V}) \tag{1}$$

here, N is the number density of O^+, q is the production, β is the loss coefficient and $\boldsymbol{V}$ is the ion drift vector. On the right-hand side, βN and $-\nabla \cdot (N\boldsymbol{V})$ represent the loss and transport processes, respectively, and the latter is a combination of transports by the E×B drift, by the neutral wind and by the ambipolar diffusion (Lei et al., 2008a; Liu et al., 2016; Lu et al., 2020). Thus, **Eq. 1** can be rewritten as:

$$\frac{\partial N}{\partial t} = (Production - Loss) + Trans_{E\times B} + Trans_{wind} + Trans_{diff} \tag{2}$$

Figure 7 shows the storm-time differences of the electron density and all the terms listed in **Eq. 2** as a function of UT and

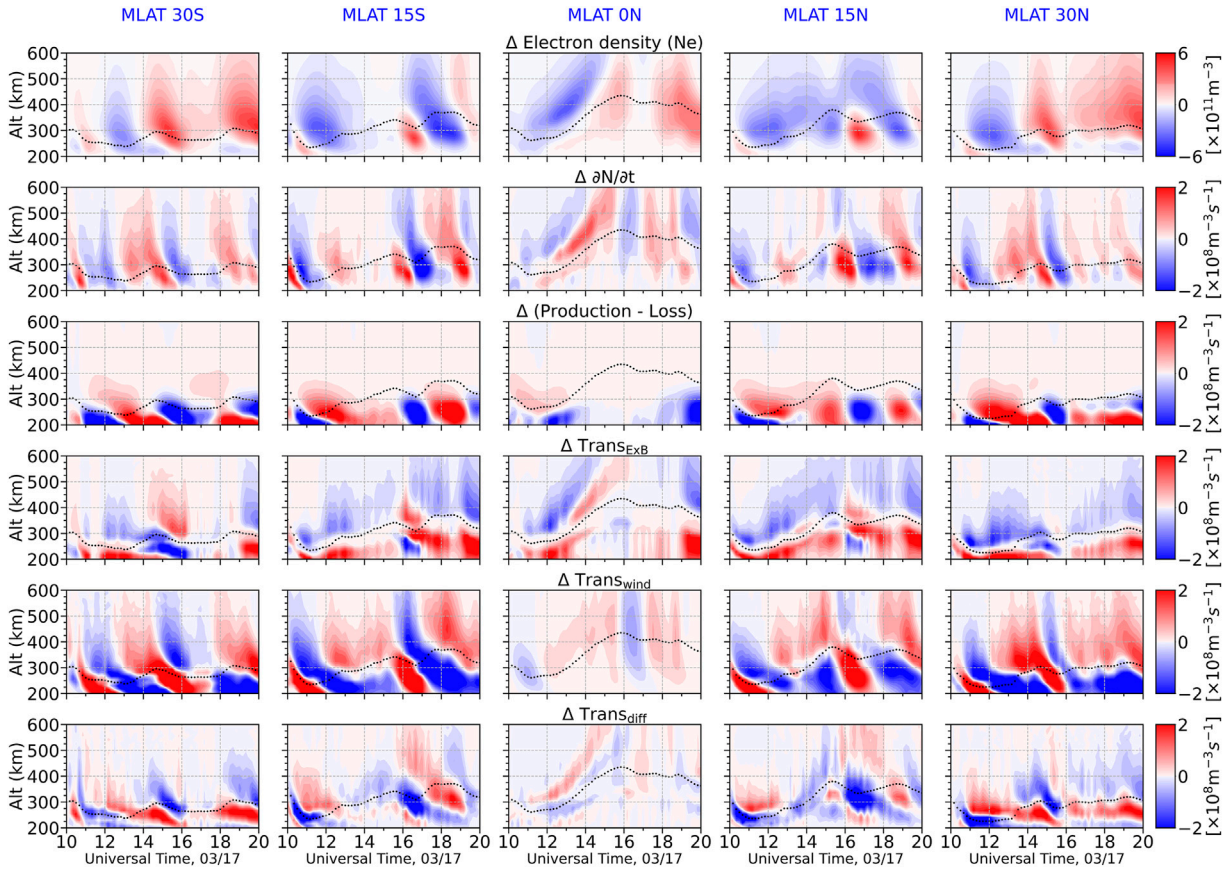

FIGURE 7 | The storm-quiet differences of the electron density (top panel) and terms in **Eq. 2** (second to last panels) at five locations at 70°W. For each plot, the parameter is shown as a function of universal time and altitude and the dotted line denotes the HmF2 on 03/17.

altitude at the five locations same as those shown in **Figure 5**. At the geomagnetic equator (middle column), when compared to the rate of O^+ density changes shown in the second row, the transport due to the E×B drift plays a more important role before 15 UT and after 19 UT. Transport due to the neutral wind is more dominant between 15 UT and 19 UT. Transport due to the neutral wind increases the electron density at first around 15 UT and reduces the electron density between 16:30 and 17:30 UT and increases the electron density afterward. Although the neutral wind cannot effectively move the plasma upward or downward near the geomagnetic equator (**Figure 6C**), the convergence and divergence of meridional neutral wind (**Figure 6B**) are mainly responsible for the enhancement and reduction of the neutral wind transport term at the geomagnetic equator shown in **Figure 7**. This is consistent with the findings by Ren and Lei (2017) who reported that both the electric field and horizontal neutral wind transport could significantly contribute to the nightside HmF2 enhancement at Sao Luis (near geomagnetic equator) during the October 2013 geomagnetic storm. At ±30° MLAT, the main electron density changes take place in the topside ionosphere, which are mainly associated with the neutral wind transport until 19 UT. At ±15° MLAT, a major electron density reduction takes place in the topside ionosphere for the negative storm phase occurred before 14 UT, which is mainly associated with the neutral wind transport. Between 16 and 19 UT, the changes of electron density occur in both topside and bottomside ionosphere. The neutral wind transport term is still the main contributor to the electron density variation in the topside ionosphere while the combination of the chemical process and neural wind transport dominates in the bottomside ionosphere. However, the variations in the chemical process are also related to the TAD (Prölss, 2011). As shown in **Figure 5**, while the topside electron density decreases between 16 and 17 UT due to the poleward disturbance neutral wind, the bottomside electron density increases significantly, leading to a net enhancement of TEC. The bottomside electron density enhancement is mainly due to the vertical shear of the meridional wind (Lu et al., 2001). After 17 UT, the bottomside electron density undergoes a reduction while the reduction of the topside electron density subsides and even the topside electron density increases. However, the TEC undergoes a reduction in general since it is a measure of the vertical column electron density. Altogether, the neutral wind transport plays an important role affecting the ionospheric electron density variations during this storm, and TADs play an important role in the formation of the negative storm phase.

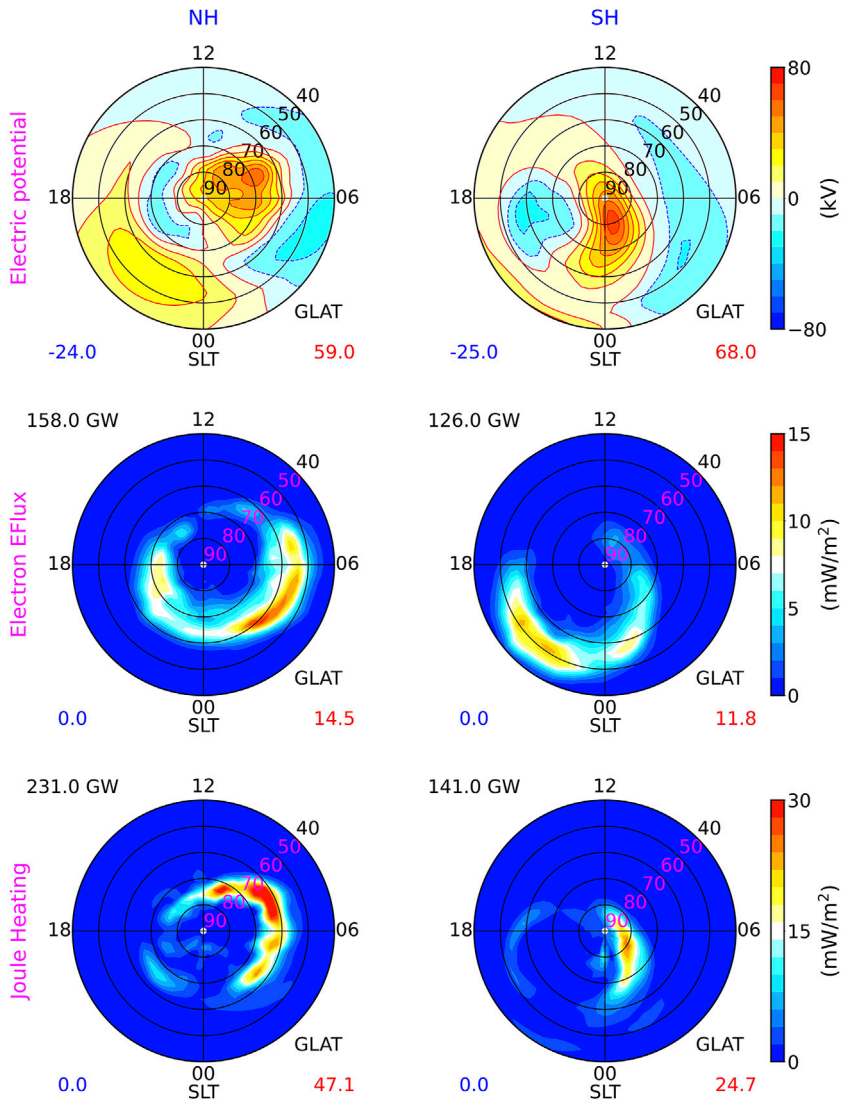

FIGURE 8 | Distributions of the (top) electric potential, (middle) total electron energy flux and (bottom) height-integrated Joule heating in the (left) NH and (right) SH at 12:30 UT on 03/17/2013. The minimum and maximum in each plot are labelled at the bottom left and right of each plot, respectively. The value at the top left of each plot in the bottom two rows represents the hemispheric integrated value. All plots are present in geographic coordinates.

One noteworthy feature shown in **Figure 3** is that the negative storm phase is stronger in the SH than the NH between 17 and 19 UT, which is caused by the stronger downward ion drift associated with the disturbance meridional wind in the SH. As shown in **Figure 6B**, the disturbance neutral winds that are responsible for the negative storm phase are quite comparable in the NH and SH between 16 and 17 UT, the difference in the vertical ion drift shown in **Figure 6C** is mainly associated with the location where the different TADs encounter. The location where TADs 3 and 2′ encounter (Location A) is closer to the geomagnetic equator than the location where TADs 2 and 3′ encounter (Location B). Since the inclination angle at the location A is smaller than that at the location B. the effect of vertical ion drift on plasma transport is more pronounced at the location B (Rishbeth and Garriott, 1969). The reason why the location B is further from the geomagnetic equator than the location A is mainly attributed to the fact that TADs 2 and 3 (launched in NH) travel faster than TADs 2′ and 3′ (launched in the SH), and the reason why TADs 2 and 3 travel faster than TADs 2′ and 3′ may lie in the fact that the Joule heating deposited in the NH and SH is asymmetric (Richmond and Matsushita, 1975). As shown in **Figure 6A**, the Joule heating deposited at 70°W in the NH is generally stronger than that deposited in the SH between 12 and 13 UT (i.e., 7–8 LT). The cause of the interhemispheric asymmetry of Joule heating between 12 and 13 UT will be discussed in detail in the next paragraph. If the phase speeds

of TADs 2 and 3 are faster or/and the phase speeds of the TADs 2′ and 3′ are slower, the negative phase occurred between 17 and 19 UT at low latitudes may be located even southward, which is the case shown in the observation (**Figure 3**). If this is the case, opposite storm phases can take place in the magnetic conjugate locations. Therefore, the northward shift of the negative storm phases in the GITM simulation may be caused by the underestimation of the phase speeds of TADs 2 and 3 or/and the overestimation of the phase speeds of TADs 2′ and 3′.

To investigate the cause of the interhemispheric asymmetry of Joule heating between 12 and 13 UT, especially on the dawn side and morning side that is responsible for the TADs shown in **Figure 6**, the distributions of high-latitude electric potential, electron precipitation and height-integrated Joule heating in the NH and SH are examined, and **Figure 8** shows an example at 12:30 UT for illustrations. Firstly, because the offset between the geomagnetic and geographic poles is different in the different hemispheres, the electric potential and electron precipitation are located more toward the dayside in the NH than in the SH. As a result, the NH receives more solar illuminations than the SH in the region where $|\mathrm{MLAT}| > 50^{\circ}$ at 12:30 UT even this storm occurs very close to the equinox. Secondly, the IMF B_y is not negligible (about −5 nT) and is comparable with the IMF B_z at 12:30 UT (**Figure 1**), which is responsible for the asymmetric distribution of the electric potential between the two hemispheres. As discussed in Hong et al. (2021), even if the auroral electron precipitation is symmetric and the geomagnetic field is a pure dipole field, the Joule heating displays a significant interhemispheric asymmetry at the equinox if the IMF B_y is not negligible. The stronger Joule heating deposited on the dawn side in the NH also results from the stronger electron precipitation in the NH, which may be associated with the IMF B_y and the substorm effects. Finally, it is worth noting that the ground-based measurements in the SH are less abundant as compared with the NH, which may partly contribute to the asymmetric distributions of high-latitude electrodynamic forcings and Joule heating in the different hemispheres shown in **Figure 8**. However, the satellite measurements in both hemispheres are comparable and abundant, so that the lack of ground-based measurements in the SH may have a smaller effect compared to the first two points on the inter-hemispheric asymmetry of the Joule heating. Altogether, the interhemispheric asymmetry of Joule heating between 12 and 13 UT may mainly result from the differences of the magnetosphere-ionosphere coupling in the different hemispheres and the geomagnetic field configuration.

SUMMARY

In this study, the dayside ionospheric response to the main phase of the 2013 St. Patrick's Day geomagnetic storm in the American sector has been studied by a combination of data analysis and numerical simulation. It is found that the GITM simulation driven by the AMIE electric potential and electron precipitation patterns is able to capture the observed ionospheric response reasonably well. In comparison, the GITM simulation driven by the electric potential and electron precipitation patterns from the empirical model ASHLEY does not reproduce the observations very well. Our efforts highlight the significance of properly specifying the high-latitude electrodynamic forcing in GCMs. The physical processes that are responsible for the observed ionospheric response have also been investigated utilizing the GITM simulation. It is found that the most observed storm-related features shown in the GNSS TEC are largely attributed to the transport process associated with the neutral winds. In particular, the negative storm phase is largely associated with the TADs launched in the opposite hemisphere. A noteworthy phenomenon is the interhemispheric asymmetric negative storm phases occurred around the nominal EIA peak latitudes in the local afternoon, with the one occurred in the SH is stronger than that in the NH. The negative storm phase is a consequence of the interference of the TADs launched in both hemispheres and their hemispheric asymmetry is caused by the different phase speeds of TADs due to the asymmetric Joule heating depositions. Particularly, stronger Joule heating deposited in the NH launches TADs with faster phase speeds than those launched in the SH. As a result, the locations where the TADs interfere in the NH is closer to the geomagnetic equator than that in the SH. Consequently, the TAD can more effectively affect the ionosphere in the SH and cause a stronger reduction of electron density in the SH than in the NH. This study also provides a new insight for how the high-latitude electrodynamic forcing can contribute to the interhemispheric asymmetry of the ionospheric response at low and middle latitudes during geomagnetic storms.

DATA AVAILABILITY STATEMENT

The IMF and solar wind data can be found at the NASA/GSFC's Space Physics Data Facility's OMNIWeb (https://omniweb.gsfc.nasa.gov). The GNSS TEC data is available at the CEDAR Madrigal database (http://cedar.openmadrigal.org/). The NmF2 and HmF2 data are available at the Global Ionospheric Radio Observatory (http://giro.uml.edu). The AMIE outputs along with the simulation outputs are stored at the NCAR GDEX repository, which can be accessed via the link: https://doi.org/10.5065/asf8-3d59.

AUTHOR CONTRIBUTIONS

QZ led the work, carried out the simulation and analyses and wrote the paper. GL created the AMIE electric potential and electron precipitation patterns. GL and YD contributed discussions. All co-authors contributed comments, edits to the manuscript.

FUNDING

QZ was supported by the National Center for Atmospheric Research Advanced Study Program Postdoctoral Fellowship. GL was supported by in part by NASA under the Living with a Star program under grant 80NSSC17K071, the Heliophysics

Supporting Research program under grant NNX17AI39G, and by AFOSR through award FA9559-17-1-0248. QZ and GL were also supported by the NASA GOLD ICON Guest Investigators Program under grant 80NSSC22K0061 through the subaward 2021GC1619. YD was supported by AFOSR through award FA9559-16-1-0364 and NASA grants 80NSSC20K0195, 80NSSC20K0606 and 80NSSC22K0061. This material is based upon work supported by the National Center for Atmospheric Research, which is a major facility sponsored by the National Science Foundation under Cooperative Agreement No. 1852977.

ACKNOWLEDGMENTS

We thank Astrid Maute for the comments and suggestions for the initial manuscript. We thank the support from the ISSI for the international team on "Multi-Scale Magnetosphere-Ionosphere-Thermosphere Interaction". We would like to acknowledge high-performance computing support from Cheyenne (doi: 10.5065/D6RX99HX) provided by National Center for Atmospheric Research's Computational and Information Systems Laboratory, sponsored by the National Science Foundation. We acknowledge use of NASA/GSFC's Space Physics Data Facility's OMNIWeb (or CDAWeb or ftp) service, and OMNI data. We acknowledge the CEDAR Madrigal database for the TEC and DMSP SSIES data. We acknowledge the Global Ionospheric Radio Observatory for the NmF2 and HmF2 data. We thank the AMPERE team and the AMPERE Science Center (http://ampere.jhuapl.edu/) for providing the Iridium-derived data products. We thank the APL SSUSI team for providing the electron precipitation data (https://ssusi.jhuapl.edu/). We acknowledge the use of SuperDARN data (http://vt.superdarn.org/tiki-index.php). SuperDARN is a collection of radars funded by national scientific funding agencies of Australia, Canada, China, France, Italy, Japan, Norway, South Africa, United Kingdom, and United States. We also wish to acknowledge the SUPERMAG database (http://supermag.jhuapl.edu) to provide a worldwide network of ground magnetometers: INTERMAGNET, Alan Thomson; CARISMA, PI Ian Mann; CANMOS, Geomagnetism Unit of the Geological Survey of Canada; The S-RAMP Database, PI K. Yumoto and Dr. K. Shiokawa; The SPIDR database; AARI, PI Oleg Troshichev; The MACCS program, PI M. Engebretson; GIMA; MEASURE, UCLA IGPP and Florida Institute of Technology; SAMBA, PI Eftyhia Zesta; 210 Chain, PI K. Yumoto; SAMNET, PI Farideh Honary; IMAGE, PI Liisa Juusola; Finnish Meteorological Institute, PI Liisa Juusola; Sodankylä Geophysical Observatory, PI Tero Raita; UiT the Arctic University of Norway, Tromsø Geophysical Observatory, PI Magnar G. Johnsen; GFZ German Research Centre For Geosciences, PI Jürgen Matzka; Institute of Geophysics, Polish Academy of Sciences, PI Anne Neska and Jan Reda; Polar Geophysical Institute, PI Alexander Yahnin and Yarolav Sakharov; Geological Survey of Sweden, PI Gerhard Schwarz; Swedish Institute of Space Physics, PI Masatoshi Yamauchi; AUTUMN, PI Martin Connors; DTU Space, Thom Edwards and PI Anna Willer; South Pole and McMurdo Magnetometer, PI's Louis J. Lanzarotti and Alan T. Weatherwax; ICESTAR; RAPIDMAG; British Artarctic Survey; McMac, PI Dr. Peter Chi; BGS, PI Dr. Susan Macmillan; Pushkov Institute of Terrestrial Magnetism, Ionosphere and Radio Wave Propagation (IZMIRAN); MFGI, PI B. Heilig; Institute of Geophysics, Polish Academy of Sciences, PI Anne Neska and Jan Reda; University of L'Aquila, PI M. Vellante; BCMT, V. Lesur and A. Chambodut; Data obtained in cooperation with Geoscience Australia, PI Andrew Lewis; AALPIP, co-PIs Bob Clauer and Michael Hartinger; MagStar, PI Jennifer Gannon; SuperMAG, PI Jesper W. Gjerloev; Data obtained in cooperation with the Australian Bureau of Meteorology, PI Richard Marshall. Additional ground magnetometer data were obtained from the THEMIS database (http://themis.ssl.berkeley.edu/gmag/), and we thank S. Mende and C. T. Russell for use of the GMAG data and NSF for support through Grant AGS-1004814; and I. R. Mann, D. K. Milling, and the rest of the CARISMA team for use of GMAG data. CARISMA is operated by the University of Alberta, funded by the Canadian Space Agency; Martin Connors and C. T. Russell and the rest of the AUTUMN/AUTUMNX team, Erik Steinmetz, Augsburg College, Peter Chi for use of the McMAC data and NSF for support through grant ATM-0245139; United States Air Force Academy (USAFA) and Peter Chi for the Falcon magnetometers; Dr. Kanji Hayashi, University of Tokyo for the STEP polar magnetometers; Tromsø Geophysical Observatory, University of Tromsø, Norway for use of the Greenland and Norway magnetometer data; the Geophysical Institute of University of Alaska for the Alaska magnetometers, Geological Survey of Sweden, and INTERMAGNET for providing the data and promoting high standards of magnetic observatory practice; the USGS Geomagnetism Program (http://geomag.usgs.gov); The Canadian Magnetic Observatory Network (CANMON), maintained and operated by the Geological Survey of Canada, provided the data used in this study (http://www.geomag.nrcan.gc.ca); University of Iceland for the use of Leirvogur data; Arctic and Antarctic Research Institute (AARI) of Department of Geophysics (http://geophys.aari.ru) for the AARI magnetometers; and Polar Experimental Network for Geospace Upper atmosphere Investigations (PENGUIn) Ground Based Observatory led by PI, Dr. C. Robert Clauer of Virginia Tech supported by the National Science Foundation through the following awards: ANT0839858, ATM922979 (Virginia Tech), and ANT0838861 (University of Michigan).

REFERENCES

Amaechi, P. O., Oyeyemi, E. O., Akala, A. O., Messanga, H. E., Panda, S. K., Seemala, G. K., et al. (2021). Ground-Based GNSS and C/NOFS Observations of Ionospheric Irregularities over Africa: A Case Study of the 2013 St. Patrick's Day Geomagnetic Storm. *Space weather.* 19 (2), e2020SW002631. doi:10.1029/2020SW002631

Anderson, B. J., Korth, H., Waters, C. L., Green, D. L., Merkin, V. G., Barnes, R. J., et al. (2014). Development of Large-Scale Birkeland Currents Determined from the Active Magnetosphere and Planetary Electrodynamics Response Experiment. *Geophys. Res. Lett.* 41 (9), 3017–3025. doi:10.1002/2014GL059941

Balthazor, R. L., and Moffett, R. J. (1999). Morphology of Large-Scale Traveling Atmospheric Disturbances in the Polar Thermosphere. *J. Geophys. Res.* 104 (A1), 15–24. doi:10.1029/1998JA900039

Bauske, R., and Prölss, G. W. (1997). Modeling the Ionospheric Response to Traveling Atmospheric Disturbances. *J. Geophys. Res.* 102 (A7), 14555–14562. doi:10.1029/97JA00941

Blanc, M., and Richmond, A. D. (1980). The Ionospheric Disturbance Dynamo. *J. Geophys. Res.* 85 (A4), 1669–1686. doi:10.1029/JA085iA04p01669

Bruinsma, S. L., and Forbes, J. M. (2009). Properties of Traveling Atmospheric Disturbances (TADs) Inferred from CHAMP Accelerometer Observations. *Adv. Space Res.* 43 (3), 369–376. doi:10.1016/j.asr.2008.10.031

Burns, A. G., Killeen, T. L., Deng, W., Carignan, G. R., and Roble, R. G. (1995). Geomagnetic Storm Effects in the Low- to Middle-Latitude Upper Thermosphere. *J. Geophys. Res.* 100 (A8), 14673–14691. doi:10.1029/94JA03232

Cai, X., Burns, A. G., Wang, W., Qian, L., Solomon, S. C., Eastes, R. W., et al. (2021). Investigation of a Neutral "Tongue" Observed by GOLD during the Geomagnetic Storm on May 11, 2019. *J. Geophys. Res. Space Phys.* 126 (6), e2020JA028817. doi:10.1029/2020JA028817

Dang, T., Lei, J., Wang, W., Wang, B., Zhang, B., Liu, J., et al. (2019). Formation of Double Tongues of Ionization during the 17 March 2013 Geomagnetic Storm. *J. Geophys. Res. Space Phys.* 124 (12), 10619–10630. doi:10.1029/2019JA027268

Deng, Y., Fuller-Rowell, T. J., Akmaev, R. A., and Ridley, A. J. (2011). Impact of the Altitudinal Joule Heating Distribution on the Thermosphere. *J. Geophys. Res.* 116 (A5), A05313. doi:10.1029/2010JA016019

Deng, Y., Lin, C., Zhu, Q., and Sheng, C. (2021). "Influence of Non-hydrostatic Processes on the Ionosphere-Thermosphere," in *Space Physics and Aeronomy Collection Volume 4: Upper Atmosphere Dynamics and Energetics, Geophys. Monogr. Ser.* Editors W. Wang, and Y. Zhang (Washington, D.C: AGU), 261. doi:10.1002/9781119507512

Deng, Y., Richmond, A. D., Ridley, A. J., and Liu, H.-L. (2008). Assessment of the Non-hydrostatic Effect on the Upper Atmosphere Using a General Circulation Model (GCM). *Geophys. Res. Lett.* 35, L01104. doi:10.1029/2007GL032182

Deng, Y., and Ridley, A. J. (2014). Simulation of Non-hydrostatic Gravity Wave Propagation in the Upper Atmosphere. *Ann. Geophys.* 32, 443–447. doi:10.5194/angeo-32-443-2014

Deng, Y., Sheng, C., Tsurutani, B. T., and Mannucci, A. J. (2018). Possible Influence of Extreme Magnetic Storms on the Thermosphere in the High Latitudes. *Space weather.* 16, 802–813. doi:10.1029/2018SW001847

Dmitriev, A. V., Suvorova, A. V., Klimenko, M. V., Klimenko, V. V., Ratovsky, K. G., Rakhmatulin, R. A., et al. (2017). Predictable and Unpredictable Ionospheric Disturbances during St. Patrick's Day Magnetic Storms of 2013 and 2015 and on 8-9 March 2008. *J. Geophys. Res. Space Phys.* 122 (2), 2398–2423. doi:10.1002/2016JA023260

Fejer, B. G., and Scherliess, L. (1997). Empirical Models of Storm Time Equatorial Zonal Electric Fields. *J. Geophys. Res.* 102 (A11), 24047–24056. doi:10.1029/97JA02164

Ferdousi, B., Nishimura, Y., Maruyama, N., and Lyons, L. R. (2019). Subauroral Neutral Wind Driving and its Feedback to SAPS during the 17 March 2013 Geomagnetic Storm. *J. Geophys. Res. Space Phys.* 124 (3), 2323–2337. doi:10.1029/2018JA026193

Fuller-Rowell, T. J., Codrescu, M. V., Moffett, R. J., and Quegan, S. (1994). Response of the Thermosphere and Ionosphere to Geomagnetic Storms. *J. Geophys. Res.* 99 (A3), 3893–3914. doi:10.1029/93JA02015

Fuller-Rowell, T. J., and Evans, D. S. (1987). Height-integrated Pedersen and Hall Conductivity Patterns Inferred from the TIROS-NOAA Satellite Data. *J. Geophys. Res.* 92 (A7), 7606–7618. doi:10.1029/JA092iA07p07606

Guerrero, A., Palacios, J., Rodríguez-Bouza, M., Rodríguez-Bilbao, I., Aran, A., Cid, C., et al. (2017). Storm and Substorm Causes and Effects at Midlatitude Location for the St. Patrick's 2013 and 2015 Events. *J. Geophys. Res. Space Phys.* 122 (10), 9994–10011. doi:10.1002/2017JA024224

Guo, J., Liu, H., Feng, X., Wan, W., Deng, Y., and Liu, C. (2014). Constructive Interference of Large-Scale Gravity Waves Excited by Interplanetary Shock on 29 October 2003: CHAMP Observation. *J. Geophys. Res. Space Phys.* 119 (8), 6846–6851. doi:10.1002/2014JA020255

Heelis, R. A., and Maute, A. (2020). Challenges to Understanding the Earth's Ionosphere and Thermosphere. *J. Geophys. Res. Space Phys.* 125 (7), e2019JA027497. doi:10.1029/2019JA027497

Hong, Y., Deng, Y., Zhu, Q., Maute, A., Sheng, C., Welling, D., et al. (2021). Impacts of Different Causes on the Inter-Hemispheric Asymmetry of Ionosphere-Thermosphere System at Mid- and High-Latitudes: GITM Simulations. *Space weather.* 19, e2021SW002856. doi:10.1029/2021SW002856

Huang, C.-S., Foster, J. C., and Kelley, M. C. (2005). Long-duration Penetration of the Interplanetary Electric Field to the Low-Latitude Ionosphere during the Main Phase of Magnetic Storms. *J. Geophys. Res.* 110 (A11). doi:10.1029/2005JA011202

Huang, X., and Reinisch, B. W. (1996). Vertical Electron Density Profiles from the Digisonde Network. *Adv. Space Res.* 18 (6), 121–129. doi:10.1016/0273-1177(95)00912-4

Hunsucker, R. D. (1982). Atmospheric Gravity Waves Generated in the High-Latitude Ionosphere: A Review. *Rev. Geophys.* 20 (2), 293–315. doi:10.1029/RG020i002p00293

Kalita, B. R., Hazarika, R., Kakoti, G., Bhuyan, P. K., Chakrabarty, D., Seemala, G. K., et al. (2016). Conjugate Hemisphere Ionospheric Response to the St. Patrick's Day Storms of 2013 and 2015 in the 100°E Longitude Sector. *J. Geophys. Res. Space Phys.* 121 (11), 11,364–11,390. doi:10.1002/2016JA023119

Knipp, D. J., Tobiska, W. K., and Emery, B. A. (2004). Direct and Indirect Thermospheric Heating Sources for Solar Cycles 21-23. *Sol. Phys.* 224, 495–505. doi:10.1007/s11207-005-6393-4

Knipp, D., Kilcommons, L., Hairston, M., and Coley, W. R. (2021). Hemispheric Asymmetries in Poynting Flux Derived from DMSP Spacecraft. *Geophys Res. Lett.* 48, e2021GL094781. doi:10.1029/2021GL094781

Kumar, S., and Kumar, V. V. (2019). Ionospheric Response to the St. Patrick's Day Space Weather Events in March 2012, 2013, and 2015 at Southern Low and Middle Latitudes. *J. Geophys. Res. Space Phys.* 124 (1), 584–602. doi:10.1029/2018JA025674

Lee, C.-C., Liu, J.-Y., Chen, M.-Q., Su, S.-Y., Yeh, H.-C., and Nozaki, K. (2004). Observation and Model Comparisons of the Traveling Atmospheric Disturbances over the Western Pacific Region during the 6-7 April 2000 Magnetic Storm. *J. Geophys. Res.* 109 (A9), A09309. doi:10.1029/2003JA010267

Lei, J., Burns, A. G., Tsugawa, T., Wang, W., Solomon, S. C., and Wiltberger, M. (2008a). Observations and Simulations of Quasiperiodic Ionospheric Oscillations and Large-Scale Traveling Ionospheric Disturbances during the December 2006 Geomagnetic Storm. *J. Geophys. Res.* 113 (A6), A06310. doi:10.1029/2008JA013090

Lei, J., Wang, W., Burns, A. G., Solomon, S. C., Richmond, A. D., Wiltberger, M., et al. (2008b). Observations and Simulations of the Ionospheric and Thermospheric Response to the December 2006 Geomagnetic Storm: Initial Phase. *J. Geophys. Res.* 113 (A1), A01314. doi:10.1029/2007JA012807

Lin, C. H., Richmond, A. D., Heelis, R. A., Bailey, G. J., Lu, G., Liu, J. Y., et al. (2005). Theoretical Study of the Low- and Midlatitude Ionospheric Electron Density Enhancement during the October 2003 Superstorm: Relative Importance of the Neutral Wind and the Electric Field. *J. Geophys. Res.* 110 (A12), A12312. doi:10.1029/2005JA011304

Lin, D., Wang, W., Scales, W. A., Pham, K., Liu, J., Zhang, B., et al. (2019). SAPS in the 17 March 2013 Storm Event: Initial Results from the Coupled Magnetosphere-Ionosphere-Thermosphere Model. *J. Geophys. Res. Space Phys.* 124 (7), 6212–6225. doi:10.1029/2019JA026698

Liu, J., Wang, W., Burns, A., Solomon, S. C., Zhang, S., Zhang, Y., et al. (2016). Relative Importance of Horizontal and Vertical Transports to the Formation of Ionospheric Storm-enhanced Density and Polar Tongue of Ionization. *J. Geophys. Res. Space Phys.* 121 (8), 8121–8133. doi:10.1002/2016JA022882

Lu, G., Goncharenko, L., Nicolls, M. J., Maute, A., Coster, A., and Paxton, L. J. (2012). Ionospheric and Thermospheric Variations Associated with Prompt Penetration Electric Fields. *J. Geophys. Res.* 117 (A8), A08312. doi:10.1029/2012JA017769

Lu, G., Goncharenko, L. P., Richmond, A. D., Roble, R. G., and Aponte, N. (2008). A Dayside Ionospheric Positive Storm Phase Driven by Neutral Winds. *J. Geophys. Res.* 113 (A8), A08304. doi:10.1029/2007JA012895

Lu, G., Hagan, M. E., Häusler, K., Doornbos, E., Bruinsma, S., Anderson, B. J., et al. (2014). Global Ionospheric and Thermospheric Response to the 5 April 2010 Geomagnetic Storm: An Integrated Data-model Investigation. *J. Geophys. Res. Space Phys.* 119 (12), 10,358–10,375. doi:10.1002/2014JA020555

Lu, G. (2017). Large Scale High-Latitude Ionospheric Electrodynamic Fields and Currents. *Space Sci. Rev.* 206 (1–4), 431–450. doi:10.1007/s11214-016-0269-9

Lu, G., Richmond, A. D., Emery, B. A., and Roble, R. G. (1995). Magnetosphere-ionosphere-thermosphere Coupling: Effect of Neutral Winds on Energy Transfer and Field-Aligned Current. *J. Geophys. Res.* 100 (A10), 19643–19659. doi:10.1029/95JA00766

Lu, G., Richmond, A. D., Lühr, H., and Paxton, L. (2016). High-latitude Energy Input and its Impact on the Thermosphere. *J. Geophys. Res. Space Phys.* 121 (7), 7108–7124. doi:10.1002/2015JA022294

Lu, G., Richmond, A. D., Roble, R. G., and Emery, B. A. (2001). Coexistence of Ionospheric Positive and Negative Storm Phases under Northern Winter Conditions: A Case Study. *J. Geophys. Res.* 106 (A11), 24493–24504. doi:10.1029/2001JA000003

Lu, G., Zakharenkova, I., Cherniak, I., and Dang, T. (2020). Large-Scale Ionospheric Disturbances during the 17 March 2015 Storm: A Model-Data Comparative Study. *J. Geophys. Res. Space Phys.* 125 (5), e2019JA027726. doi:10.1029/2019JA027726

Lyons, L. R., Gallardo-Lacourt, B., Zou, S., Weygand, J. M., Nishimura, Y., Li, W., et al. (2016). The 17 March 2013 Storm: Synergy of Observations Related to Electric Field Modes and Their Ionospheric and Magnetospheric Effects. *J. Geophys. Res. Space Phys.* 121 (11), 10,880–10,897. doi:10.1002/2016JA023237

Lyons, L. R., Nishimura, Y., Zhang, S. R., Coster, A. J., Bhatt, A., Kendall, E., et al. (2019). Identification of Auroral Zone Activity Driving Large-Scale Traveling Ionospheric Disturbances. *J. Geophys. Res. Space Phys.* 124, 700–714. doi:10.1029/2018JA025980

Mannucci, A. J., Tsurutani, B. T., Iijima, B. A., Komjathy, A., Saito, A., Gonzalez, W. D., et al. (2005). Dayside Global Ionospheric Response to the Major Interplanetary Events of October 29-30, 2003 "Halloween Storms". *Geophys. Res. Lett.* 32 (12), L12S02. doi:10.1029/2004GL021467

Marsal, S., Torta, J. M., Segarra, A., and Araki, T. (2017). Use of Spherical Elementary Currents to Map the Polar Current Systems Associated with the Geomagnetic Sudden Commencements on 2013 and 2015 St. Patrick's Day Storms. *J. Geophys. Res. Space Phys.* 122 (1), 194–211. doi:10.1002/2016JA023166

Maute, A., and Richmond, A. D. (2017). *F*-region Dynamo Simulations at Low and Mid-latitude. *Space Sci. Rev.* 206 (1–4), 471–493. doi:10.1007/s11214-016-0262-3

Pham, K. H., Zhang, B., Sorathia, K., Dang, T., Wang, W., Merkin, V., et al. (2022). Thermospheric Density Perturbations Produced by Traveling Atmospheric Disturbances during August 2005 Storm. *JGR Space Phys.* 127 (2), e2021JA030071. doi:10.1029/2021JA030071

Pradipta, R., Valladares, C. E., Carter, B. A., and Doherty, P. H. (2016). Interhemispheric Propagation and Interactions of Auroral Traveling Ionospheric Disturbances Near the Equator. *J. Geophys. Res. Space Phys.* 121 (3), 2462–2474. doi:10.1002/2015JA022043

Prölss, G. W. (2011). Density Perturbations in the Upper Atmosphere Caused by the Dissipation of Solar Wind Energy. *Surv. Geophys* 32 (2), 101–195. doi:10.1007/s10712-010-9104-0

Qian, L., Burns, A. G., Emery, B. A., Foster, B., Lu, G., Maute, A., et al. (2014). "The NCAR TIE-GCM," in *Geophysical Monograph Series*. Editors J. Huba, R. Schunk, and G. Khazanov (Chichester: John Wiley & Sons), 73–83. doi:10.1002/9781118704417.ch7

Ren, D., and Lei, J. (2017). A Simulation Study of the Equatorial Ionospheric Response to the October 2013 Geomagnetic Storm. *J. Geophys. Res. Space Phys.* 122 (9), 9696–9704. doi:10.1002/2017JA024286

Richmond, A. D. (1992). Assimilative Mapping of Ionospheric Electrodynamics. *Adv. Space Res.* 12 (6), 59–68. doi:10.1016/0273-1177(92)90040-5

Richmond, A. D., and Kamide, Y. (1988). Mapping Electrodynamic Features of the High-Latitude Ionosphere from Localized Observations: Technique. *J. Geophys. Res.* 93 (A6), 5741–5759. doi:10.1029/JA093iA06p05741

Richmond, A. D., and Matsushita, S. (1975). Thermospheric Response to a Magnetic Substorm. *J. Geophys. Res.* 80 (19), 2839–2850. doi:10.1029/JA080i019p02839

Rideout, W., and Coster, A. (2006). Automated GPS Processing for Global Total Electron Content Data. *GPS Solut.* 10 (3), 219–228. doi:10.1007/s10291-006-0029-5

Ridley, A. J., Deng, Y., and Tóth, G. (2006). The Global Ionosphere-Thermosphere Model. *J. Atmos. Solar-Terrestrial Phys.* 68 (8), 839–864. doi:10.1016/j.jastp.2006.01.008

Rishbeth, H., and Garriott, O. K. (1969). *Introduction to Ionospheric Physics*. New York, London: Academic Press.

Scherliess, L., and Fejer, B. G. (1997). Storm Time Dependence of Equatorial Disturbance Dynamo Zonal Electric Fields. *J. Geophys. Res.* 102 (A11), 24037–24046. doi:10.1029/97JA02165

Sheng, C., Deng, Y., Gabrielse, C., Lyons, L., Nishimura, Y., Heelis, R., et al. (2021). Sensitivity of Upper Atmosphere to Different Characteristics of Flow Bursts in the Auroral Zone. *J. Geophys. Res. Space Phys.* 126, e2021JA029253. doi:10.1029/2021ja029253

Shiokawa, K., Lu, G., Otsuka, Y., Ogawa, T., Yamamoto, M., Nishitani, N., et al. (2007). Ground Observation and AMIE-TIEGCM Modeling of a Storm-Time Traveling Ionospheric Disturbance. *J. Geophys. Res.* 112 (A5), A05308. doi:10.1029/2006JA011772

Thayer, J. P., Vickrey, J. F., Heelis, R. A., and Gary, J. B. (1995). Interpretation and Modeling of the High-Latitude Electromagnetic Energy Flux. *J. Geophys. Res.* 100 (A10), 19715–19728. doi:10.1029/95JA01159

Tsurutani, B., Mannucci, A., Iijima, B., Abdu, M. A., Sobral, J. H. A., Gonzalez, W., et al. (2004). Global Dayside Ionospheric Uplift and Enhancement Associated with Interplanetary Electric Fields. *J. Geophys. Res.* 109 (A8), A08302. doi:10.1029/2003JA010342

Valladares, C. E., Villalobos, J., Hei, M. A., Sheehan, R., Basu, S., MacKenzie, E., et al. (2009). Simultaneous Observation of Traveling Ionospheric Disturbances in the Northern and Southern Hemispheres. *Ann. Geophys.* 27 (4), 1501–1508. doi:10.5194/angeo-27-1501-2009

Verkhoglyadova, O. P., Tsurutani, B. T., Mannucci, A. J., Mlynczak, M. G., Hunt, L. A., Paxton, L. J., et al. (2016). Solar Wind Driving of Ionosphere-thermosphere Responses in Three Storms Near St. Patrick's Day in 2012, 2013, and 2015. *J. Geophys. Res. Space Phys.* 121 (9), 8900–8923. doi:10.1002/2016JA022883

Vierinen, J., Coster, A. J., Rideout, W. C., Erickson, P. J., and Norberg, J. (2016). Statistical Framework for Estimating GNSS Bias. *Atmos. Meas. Tech.* 9 (3), 1303–1312. doi:10.5194/amt-9-1303-2016

Wang, Z., Zou, S., Liu, L., Ren, J., and Aa, E. (2021). Hemispheric Asymmetries in the Mid-latitude Ionosphere during the September 7-8, 2017 Storm: Multi-instrument Observations. *JGR Space Phys.* 126 (4), e2020JA028829. doi:10.1029/2020JA028829

Weimer, D. R. (2005). Improved Ionospheric Electrodynamic Models and Application to Calculating Joule Heating Rates. *J. Geophys. Res.* 110 (A5), A05306. doi:10.1029/2004JA010884

Xu, Z., Hartinger, M. D., Clauer, C. R., Peek, T., and Behlke, R. (2017). A Comparison of the Ground Magnetic Responses during the 2013 and 2015 St. Patrick's Day Geomagnetic Storms. *J. Geophys. Res. Space Phys.* 122 (4), 4023–4036. doi:10.1002/2016JA023338

Yue, X., Wang, W., Lei, J., Burns, A., Zhang, Y., Wan, W., et al. (2016). Long-lasting Negative Ionospheric Storm Effects in Low and Middle Latitudes during the Recovery Phase of the 17 March 2013 Geomagnetic Storm. *J. Geophys. Res. Space Phys.* 121 (9), 9234–9249. doi:10.1002/2016JA022984

Zhai, C., Lu, G., Yao, Y., Wang, W., Zhang, S., Liu, J., et al. (2020). 3-D Tomographic Reconstruction of SED Plume during 17 March 2013 Storm. *J. Geophys. Res. Space Phys.* 125 (11), e2020JA028257. doi:10.1029/2020JA028257

Zhang, S. R., Erickson, P. J., Coster, A. J., Rideout, W., Vierinen, J., Jonah, O., et al. (2019). Subauroral and Polar Traveling Ionospheric Disturbances during the 7-9 September 2017 Storms. *Space weather.* 17 (12), 1748–1764. doi:10.1029/2019SW002325

Zhang, Y., Paxton, L. J., Kil, H., Meng, C.-I., Mende, S. B., Frey, H. U., et al. (2003). Negative Ionospheric Storms Seen by the IMAGE FUV Instrument. *J. Geophys. Res.* 108 (A9), 1343. doi:10.1029/2002JA009797

Zhu, Q., Deng, Y., Maute, A., Kilcommons, L. M., Knipp, D. J., and Hairston, M. (2021). ASHLEY: A New Empirical Model for the High-Latitude Electron Precipitation and Electric Field. *Space weather.* 19 (5), e2020SW002671. doi:10.1029/2020SW002671

Zhu, Q., Deng, Y., Maute, A., Sheng, C., Lin, C. Y., and Lin, C. (2017). Impact of the Vertical Dynamics on the Thermosphere at Low and Middle Latitudes: GITM Simulations. *J. Geophys. Res. Space Phys.* 122, 6882–6891. doi:10.1002/2017JA023939

Zhu, Q., Deng, Y., Richmond, A., McGranaghan, R. M., and Maute, A. (2019). Impacts of Multiscale FACs on the Ionosphere-Thermosphere System: GITM Simulation. *J. Geophys. Res. Space Phys.* 124 (5), 3532–3542. doi:10.1029/2018JA026082

Conflict of Interest: The authors declare that the research was conducted in the absence of any commercial or financial relationships that could be construed as a potential conflict of interest.

Publisher's Note: All claims expressed in this article are solely those of the authors and do not necessarily represent those of their affiliated organizations, or those of the publisher, the editors and the reviewers. Any product that may be evaluated in this article, or claim that may be made by its manufacturer, is not guaranteed or endorsed by the publisher.

frontiers | Frontiers in Astronomy and Space Sciences

ORIGINAL RESEARCH
published: 17 June 2022
doi: 10.3389/fspas.2022.896199

Investigation of the Differences in Onset Times for Magnetically Conjugate Magnetometers

James M. Weygand[1]*, *Eftyhia Zesta*[2], *Akira Kadokura*[3,4,5] and *Denny M. Oliveira*[6,7]

[1]Department of Earth, Planetary, and Space Sciences, University of California Los Angeles, Los Angeles, CA, United States, [2]Geospace Physics Laboratory, NASA Goddard Space Flight Center, Greenbelt, MD, United States, [3]National Institute of Polar Research, Tokyo, Japan, [4]Polar Environment Data Science Center, Joint Support-Center for Data Science Research, Research Organization of Information and Systems, Tokyo, Japan, [5]Department of Polar Science, The Graduate University for Advanced Studies, SOKENDAI, Tokyo, Japan, [6]Goddard Planetary Heliophysics Institute, University of Maryland, Baltimore, MD, United States, [7]Heliophysics Science Division, NASA Goddard Space Flight Center, Greenbelt, MD, United States

We have identified nearly 1,000 onsets using two pairs of hemispheric conjugate ground magnetometers where the onset is defined based on a sharp decline in the H component of the magnetic field at a ground magnetometer station. Specifically, we used the pair of stations at West Antarctica Ice Sheet Divide and Sanikiluaq, Canada; Syowa, Antarctica; and Tjörnes, Iceland. While the onset time in the southern hemisphere is identified by eye, the value of the differences in the onset time between the northern and southern hemispheres is determined using cross covariance. We observe differences in the onset time between the two hemispheres as large as several minutes, but 53% of the events show no difference in the onset time. Using statistics, we show that the largest differences in onset time are associated with the summer and winter seasons and when the IMF By value is limited between 0.5 and 2.5 nT, which is the IMF By range when the local time difference between the northern and southern hemisphere foot points is the smallest. The results indicate that ionospheric conductivity associated with solar illumination plays a role in the differences in onset time between the northern and southern hemisphere when only non-zero differences in onset time are considered. We validate these results with two other less robust methods. The median value of the differences in onset time indicates that the onsets occur ~23 s earlier in the winter hemisphere than that in the summer hemisphere. It has been reported that the time difference between the start of the substorm in the magnetotail and the observed auroral break up (substorm auroral onset) in the ionosphere is 30 s to 2 min in the current disruption model and the near earth neutral line model, respectively. Our results may be of interest to those two models.

Keywords: conjugacy, onset, magnetometer, auroral, ionosphere

OPEN ACCESS

Edited by:
Jone Peter Reistad,
University of Bergen, Norway

Reviewed by:
Dogacan Ozturk,
University of Alaska System, United States
Hui Li,
National Space Science Center, (CAS), China

***Correspondence:**
James M. Weygand
jweygand@igpp.ucla.edu

Specialty section:
This article was submitted to Space Physics, a section of the journal Frontiers in Astronomy and Space Sciences

Received: *14 March 2022*
Accepted: *26 April 2022*
Published: *17 June 2022*

Citation:
Weygand JM, Zesta E, Kadokura A and Oliveira DM (2022) Investigation of the Differences in Onset Times for Magnetically Conjugate Magnetometers. Front. Astron. Space Sci. 9:896199. doi: 10.3389/fspas.2022.896199

INTRODUCTION

The Time History of Events and Macroscale Interactions during Substorms (THEMIS) mission has five spacecraft dedicated to observing and understanding the onset and development of magnetospheric substorms. The mission was designed to distinguish between the two most prominent substorm models: the current disruption model (inside-out) (Lui et al., 1988; 1996)

and the near-earth neutral line model (outside-in) (Hones, 1976; Baker et al., 1996; Baumjohann et al., 1989). The inside-out and outside-in substorm models postulate specific time sequences of events (Angelopoulos et al., 2008a) that are not the same. The inside-out model states that the substorm begins with a current instability around 10 Re that launches a rarefaction wave down tail and leads to reconnection in the mid-tail. In the inside-out scenario, the auroral onset begins about 30 s after the current disruption and 30 s before reconnection starts. The outside-in model starts with reconnection in the mid-magnetotail followed by earthward flows that lead to current disruption within the inner magnetosphere. This is followed by an auroral onset in the ionosphere about 120 s after reconnection begins. This clear outline of the sequence of events for both models puts the auroral onset about 30 s to 2 min after the magnetotail onset of the substorm and high temporal resolution measurements on the order of 1–10 s on the ground and in the tail are required to address the timing. However, three different studies using conjugate auroral observations have observed differences in the auroral onset time on the order of 1–2 min (Sato et al., 1998; Frank and Sigwarth, 2003; Morioka et al., 2011). This extreme difference in onset times in the opposite hemispheres raises questions about the sequence of events in the substorm process and needs to be better explained by substorm models.

As far as we are aware, there are only the aforementioned three reports on differences in the auroral onset times in opposite hemispheres. Sato et al. (1998) observed auroral brightening on 12 September 1988 in the southern hemisphere at Syowa (SYO), Antarctica before the northern hemisphere at Husafell (HLL), Iceland by ~1 min using an all-sky imager with a temporal resolution of 1 s. However, the difference in the onset time observed in the 2 s magnetometer data from opposite hemispheres is not clear. Sato et al. (1998) suggested that the discrepancy in the auroral onset times was due to ionospheric conductivity differences, and the ionospheric conductivity differences were due to dissimilar particle precipitation. Frank and Sigwarth (2003) documented a difference in auroral onset time of about 1 min with simultaneous images of the northern and southern hemisphere with the Earth Camera for ultraviolet emissions, which had a cadence of 54 s, onboard the Polar spacecraft for a substorm on the 1 November 2001. The authors suggested that the difference in onset time is associated with ionospheric conductivity due to particle precipitation and could be explained by two facts: 1) higher electron energy in the winter hemisphere (dark hemisphere) relative to that in the summer hemisphere (sunlight hemisphere) and 2) lower electron fluxes in winter hemisphere than those in the summer hemisphere with a net effect of dimmer auroras in the summer hemisphere. These observations are inconsistent with Ohtani et al. (2009) and Newell et al. (2010). Ohtani et al. (2009) used the DMSP F7–F15 magnetic field and particle data to examine the differences in the ion and electron precipitation for the Region 1 and Region 2 current systems in the midnight sector during sunlit and dark ionosphere periods. They found the following: 1) for the Region 1 currents, the ion and electron energy flux and energy is higher in the dark ionosphere; 2) for the Region 2 currents, the ion and electron energy flux is higher in the dark ionosphere, but the electron energy is about the same in the sunlit and dark ionosphere; and 3) the occurrence rate of large height integrated Pedersen conductivity is larger in the dark ionosphere (>10 S). In addition, the occurrence rate of weak height integrated Pedersen conductivity is larger in the sunlit ionosphere (2–8 S).

Newell et al. (2010) used 10 years of DMSP particle data to examine the differences in the ion and electron precipitation in the southern and northern hemispheres. They found in the nightside of the auroral region that the ratio of the winter to summer electron energy fluxes were typically larger than 1 for diffuse electrons (~1.18) and monoenergetic electrons (1.10) during weak solar wind driving, but about 1 for broadband electron precipitation. The ratio of the winter to summer ion energy fluxes, however, was 0.89. These observed differences in particle precipitation energy flux indicate a difference in ionospheric conductivity in the opposite hemispheres.

Morioka et al. (2011) examined a number of auroral kilometric radiation events using both Cluster/WHISPER and IMAGE/RPI in 2003 and found some events where field aligned acceleration occurred in one hemisphere and not another. This observation indicated to them that the substorm current wedge does not complete its current system in both the northern and southern hemispheres. To support their statement, Morioka et al. (2011) examined conjugate all-sky camera data. One auroral onset on 19 September 2006 in their study was recorded at both SYO (Syowa, Antarctica) and HLL (Husafell, Iceland) with a difference in auroral onset time of about 2 min. However, the difference seen in the magnetometer data was of order 10 s (see their **Figure 9**), and they do not comment on the 10 s difference. Unfortunately, no IMAGE/RPI data was available for this event. Morioka et al. (2011) concluded from the spacecraft and auroral data that ionospheric conductivity controls auroral onset time difference between the hemispheres. Furthermore, they predicted that there should be seasonal and/or dipole tilt dependence in the difference in the onset time.

All three studies that observed hemispheric differences in the substorm onset time suggest that the ionospheric conductivity plays a role in the apparent onset of auroral activity. Ionospheric conductivity can be altered in two ways: particle precipitation and sunlight. Simultaneous spacecraft observations of precipitating particles differences in opposite hemispheres are difficult to obtain because two spacecraft are rarely hemispherically and magnetically conjugate. Conjugate auroral image observations from spacecraft are available, but most spacecraft auroral imagers to date have had low temporal and/or spatial resolution to be able to identify timing asymmetries less than 1–2 min and aid with the substorm onset identification. Ionospheric conductivity values can be derived from incoherent scatter radar measurements; but as far as we are aware, there are no hemispheric conjugate incoherent scatter radars to make conjugate measurements of ionospheric conductivity. Finally, using ground-based auroral images to investigate an annual variation in auroral onset time differences associated with seasonal changes of ionospheric conductivity with sunlight is impossible because the ground-based auroral imagers cannot obtain data in the sunlight. Furthermore, two of the three studies discussed before (Sato et al., 1998; Morioka et al., 2011) reported that the ground

TABLE 1 | Station location information for the southern and northern ground magnetometer data. From left to right the columns are station name, geographic latitude and longitude, corrected geomagnetic latitude and longitude, magnetic declination, and conjugate geographic latitude and longitude.

Southern stations	Geographic latitude	Geographic longitude	CGM latitude	CGM longitude	D (°)	Conjugate geographic latitude	Conjugate geographic longitude	UT of 00 MLT
SYO	−69.0	39.6	−66.4	72.5	−49.6	66.4	344.0	23.92
WSD	−79.5	−112.2	−67.0	355.7	63.1	57.2	279.8	05.13
Northern Stations								
SNKQ	56.5	280.769	66.5	356.0	−17.16	−79.1	250.3	05.26
TJO	66.19	342.07	66.64	71.73	−17.53	−69.41	40.09	23.80

magnetometer onset differences between the two hemispheres were significantly shorter than those identified by the all-sky imagers, 2 and 10 s, respectively. This magnetometer observation indicates that while there may be time differences in the substorm onset time in the two hemispheres, they are more likely on the order of few to several seconds rather than minutes.

The magnetometers function year round with time resolution in seconds or better, and onsets associated with substorms, pseudo breakups, and PBIs are clearly visible as sharp drops in the *H* component of the magnetometer data. Fortunately, there are a number of hemispheric conjugate pairs of magnetometer stations available, which provides a good tool for the study of onset timing asymmetries between hemispheres. One of the most likely causes of onset timing asymmetries between hemispheres is the orientation of the IMF. Kivelson et al. (1996) have shown that the IMF *By* may twist the magnetic field in the tail, and Østgaard et al. (2004; 2007) have demonstrated that the relative displacement of onset locations in the conjugate hemispheres is found to be controlled by IMF *By* and the IMF clock angle. Thus, if the conjugate location of the onset is further to the west in one hemisphere, say the northern hemisphere, than the other, then a substorm may appear to begin first in the southern hemisphere magnetometer and then a little later in the northern hemisphere at the near conjugate location once the westward traveling surge reaches the northern conjugate foot point. Østgaard et al. (2007) showed that the difference in magnetic local time (MLT) between the southern and northern location of the substorm onset can be as large as 1.4 h in MLT, and it has been shown that the speed of the westward traveling surge is on the order of 1 h of MLT per min (Angelopoulos et al., 2008b). Combining these facts led us to the conclusion that a maximum difference in onset time from the perspective of hemispheric conjugate ground magnetometers for a magnetic field line twisted by the IMF can be about 80 s, which is similar to the previously published observations from the all-sky imagers. Therefore, it is essential to also determine if differences in onset time are associated with IMF twisting of the Earth's magnetic field, specifically with IMF By.

In a study similar to Østgaard et al. (2007), Ganushkina et al. (2013) demonstrated the variation in the conjugacy between Syowa, Antarctica and Tjörnes, Iceland as a function of dipole tilt, IMF By, IMF Bz, and solar wind dynamic pressure. They found that the difference in latitude and longitude in the midnight sector was as large as 1° in magnetic latitude and 15° in magnetic longitude at maximum dipole tilt values. The differences were less than 0.5° in magnetic latitude and 15° in magnetic longitude for nominal solar wind dynamic pressure values < 6 nPa. For the IMF Bz between ±6 nT, the differences were less than 1° in magnetic latitude and 7° in magnetic longitude. Finally, Ganushkina et al. (2013) found that for IMF By≤|6| nT differences were less than 0.5° in magnetic latitude and 7° in magnetic longitude. Using the maximum longitudinal displacement value of 15° (associated with both the dynamic pressure and the dipole tilt) with a westward traveling surge on the order of 1 h of MLT per min, the potential differences in onset time for the displaced foot points is about 60 s. Note that this value does not take into account the latitudinal displacement.

The objective of this study is to compare differences in onset times observed by conjugate ground magnetometers and understand the cause of these differences. In the next section, we have reviewed the data we used in this study. In the third section, we have presented our results using two pairs of hemispheric conjugate ground magnetometers, and in the last section, we have discussed the importance of our results and summarized.

DATA

The data for this study come from two distinct sources: two pairs of hemispheric conjugate ground magnetometers and ACE interplanetary magnetic field (IMF) data and solar wind plasma data. The pairs of magnetometer stations used are WSD/SNKQ (West Antarctic Ice Sheet divide/Sanikiluaq, Canada) and SYO/TJO (Syowa, Antarctica/Tjörnes, Iceland). The temporal resolution of the WSD magnetometer is 10 s, and the resolution of the other three is 1 s or better. The WSD magnetometer is a part of the South American Meridional B-Field Array (SAMBA) (Boudouridis and Zesta, 2007), and the SNKQ magnetometer is part of the Canadian Magnetic Observatory System (CANMOS) magnetometer array. Data from January 2008 to June 2013 are available for this pair, but with a number of data gaps. Both SYO and TJO stations are operated by Japan's National Institute of Polar Research (http://www.nipr.ac.jp). Columns 2–8 in **Table 1** provide the geographic (GEO) and corrected geomagnetic (CGM) coordinates of the four stations, declination, and the geographic coordinates of the

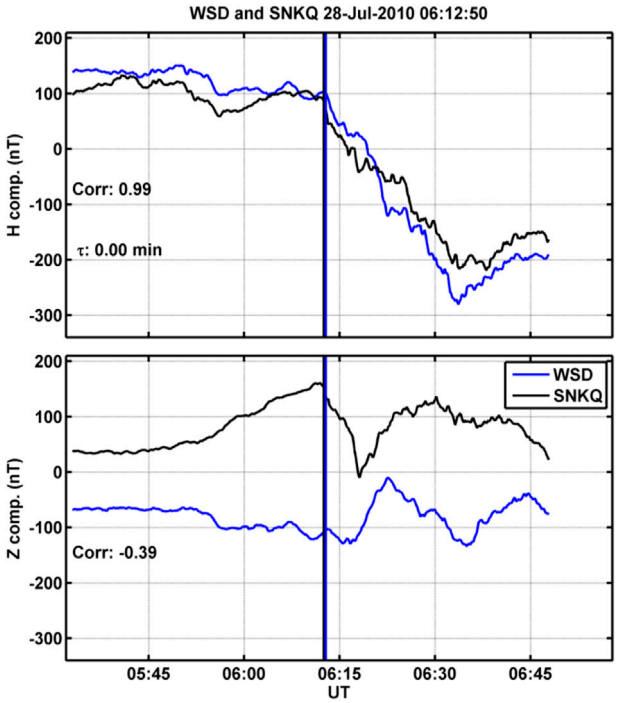

FIGURE 1 | Example of onsets that simultaneously occur in both WSD (blue curve) in the southern hemisphere and the SNKQ (black curve) in the northern hemisphere. In the top panel is the *H* component of the magnetic field data and cross correlation coefficient and the onset time difference determined from cross covariance. The southern hemisphere onset is marked with the blue vertical line, and the northern hemisphere onset is marked with the black vertical line. In the bottom panel is the Z components and the cross correlation value.

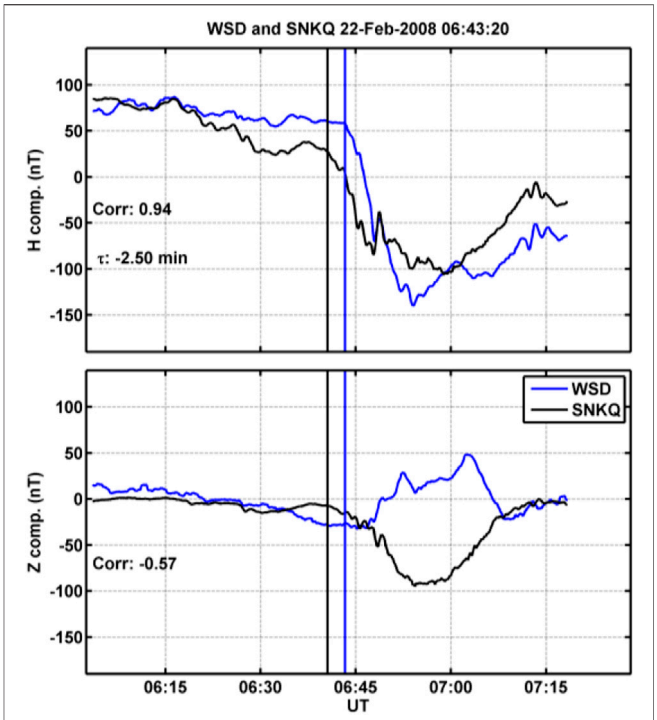

FIGURE 2 | Example of onsets that occur at different times in the southern and northern hemispheres. This figure has the same format as **Figure 1**. In the top panel, the sharp drop in the *H* component of the magnetic field begins at SNKQ about 2.5 min before the WSD station.

magnetically conjugate point of each station. We determined the magnetic conjugate location using the online International Geomagnetic Reference Field (IGRF) at (http://omniweb.gsfc.nasa.gov/vitmo/cgm_vitmo.html) with 2010 as the input year, and we remind the reader that the IGRF model is an ensemble average of different models.

ACE IMF data from the magnetic field instrument (MFI) (Smith et al., 1998) and solar wind plasma data from the Solar Wind Electron, Proton, and Alpha Monitor (SWEPAM) (McComas et al., 1998) have been propagated from their original position near the L1 point to just in front of the nose of the magnetosphere at X = 17 R_E (Weygand and McPherron, 2006a; b). This was done by using Weimer mapping technique (Weimer et al., 2003, 2004) that uses a variation of the minimum variance method to estimate the orientation of IMF structures. These data are used to investigate correlations between the differences in onset times and the IMF and solar wind plasma properties.

PROCEDURE AND OBSERVATIONS

The first step is to identify onset events. For the first part of this study, we selected events with a sharp drop in the H component of the magnetic field in just the southern hemisphere stations, but not necessarily accompanied by any of the following: sharp drop in the H component in the opposite hemisphere, sharp drop in the AL index, auroral onset, auroral expansion phase, auroral recovery phase, magnetotail dipolarizations, or particle injections. This loose definition of onset could include PBIs, substorms, and pseudo breakups. All events were identified visually using the magnetometer data from either WSD/SNKQ or SYO/TJO. The criteria to qualify as an onset included 1) sharp drop in the H component over approximately 20 min period in both hemisphere, 2) H decrease ≥ 80 nT in both hemispheres, 3) event duration of more than 30 min, 4) the *Z* component in the northern and southern hemisphere to have approximately a 180° phase shift (as expected for a current wedge), 5) ≥ 3 h between onsets, and 6) the events should occur within 3 h of local midnight. Just under 1,000 onsets were identified using about 3.5 years of conjugate WSD/SNKQ and 12 years of SYO/TJO ground magnetometer data.

We understand there are a number of automated systems for selecting onsets, specifically substorm onsets, but none of these methods obtain the same results when compared with one another. Therefore, we have selected our events by-eye because it is the difference in the onset time between the opposite hemispheres that is the focus of this study, not the specific identification of substorms.

Figure 1 and **Figure 2** show two examples of onsets that are observed at both WSD (blue curve, southern hemisphere) and SNKQ (black curve, northern hemisphere). The top panel shows the

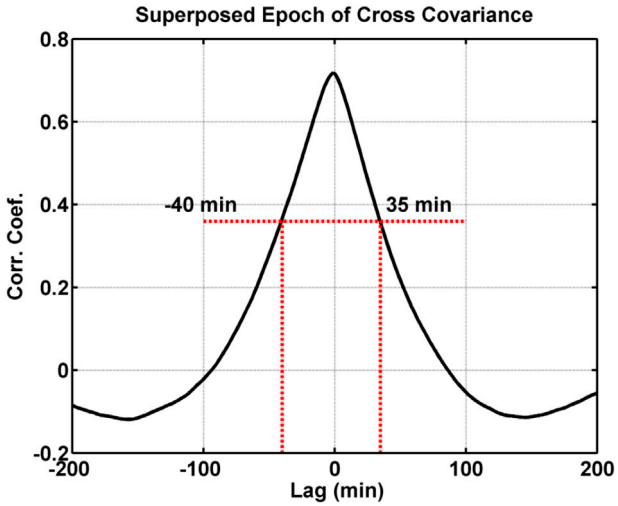

FIGURE 3 | Superposed epoch of cross covariance curves for SAL and NAL indices for over 440 onsets identified in the SAL index. Epoch time zero is the onset time in the SAL index and the red horizontal dashed line is the full width half max of the peak of the cross correlation curve.

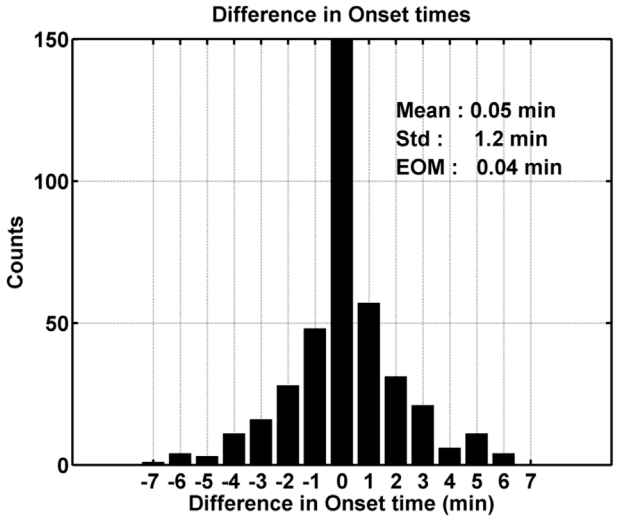

FIGURE 4 | Histogram of differences in the onset time in the *H* component. The peak of the histogram at zero is off the y-axis scale and is at ~800.

H component of the magnetic field, and the bottom panel shows the *Z* component. The black vertical line marks the visually selected onset time in the southern hemisphere, and the blue vertical line marks the visually selected onset time in the northern hemisphere, which will be discussed in the second part of this study. The cross correlation value for the *H* component and the difference in onset time determined from the cross covariance are shown in the bottom left portion of the top panel, while the bottom panel notes the cross correlation value for the Z component. **Figure 1** shows an onset that occurred on 28 July 2010 at 0612:50 UT, and there was zero onset time difference between the two hemispheres. **Figure 2** shows an onset that occurred in the southern hemisphere at 0643:20 UT on 22 February 2008 and ~2.5 min after the onset in the northern hemisphere.

While onset times were identified visually only in the southern hemisphere for the first part of this study, we performed a standard cross covariance between the north and south station of the pair to determine the lag time, for which there was a maximum correlation between the northern and southern time series. The cross covariance curve for the *H* component of the magnetometer data was determined using a data window extending 40 min before the onset and 35 min after the onset. We will explain below how this window was derived using a southern auroral electrojet index. This method provides an unbiased, clear, quantitative, and reproducible means for determining differences in onset time. The only potential weakness of this method is if the two onsets have significantly different slopes in their shape and different magnitudes of the change in the H component, then the cross correlation can underestimate the difference in onset time. This difference in the onset slope occurs in about 27% of the events.

We determined the size of the data window we used in each cross covariance of the H components of the magnetic field data by performing a superposed epoch of the cross covariance curves from over 440 onset events identified in the lower envelope of the southern auroral electrojet (SAL) index and the lower northern auroral electrojet (NAL) index developed by Weygand et al., (2008, 2014). The SAL index was developed using the same method as the standard world data center AL index from eight ground magnetometers in the auroral region in the southern hemisphere, and the NAL index is a near conjugate version of the SAL index. See Weygand et al., (2008, 2014) for more details. The SAL and NAL indices are used in the superposed epoch because they are, for the most part, an independent data set from the individual pairs of conjugate ground magnetometers. The AL index cross covariance curves were derived using 5 h of SAL and NAL index data on either side of an SAL onset time. The SAL onset time was identified visually using the criteria in Hsu and McPherron (2012), and that selection criteria included 1) sharp drop in the lower southern auroral electrojet (SAL) index over about 20 min period, 2) drop ≥100 nT, 3) ≥ 3 h between onsets, and 4) the SAL index accompanied by a decrease in the northern hemisphere NAL index.

Figure 3 shows the superposed epoch of the SAL/NAL cross covariance curves from 440 onset events. The time along the x-axis is the time lags from the cross covariance routine, and the y-axis is the cross correlation values. Epoch time zero is defined as the SAL index onset time. In **Figure 3** we have defined the range of time to include in the cross covariance of the H components of the magnetic field (35–40 min) as the full width half max of the superposed epoch of the SAL/NAL cross covariance curves. See the horizontal red dash–dot curve in **Figure 3**. This range of time of 35–40 min is then used for the cross covariance of the onsets observed in the *H* component of the pairs of hemispheric conjugate magnetometer stations.

Figure 4 is a histogram of differences in onset time between the northern and southern hemisphere determined from the cross covariance of the *H* component of the conjugate pairs of ground

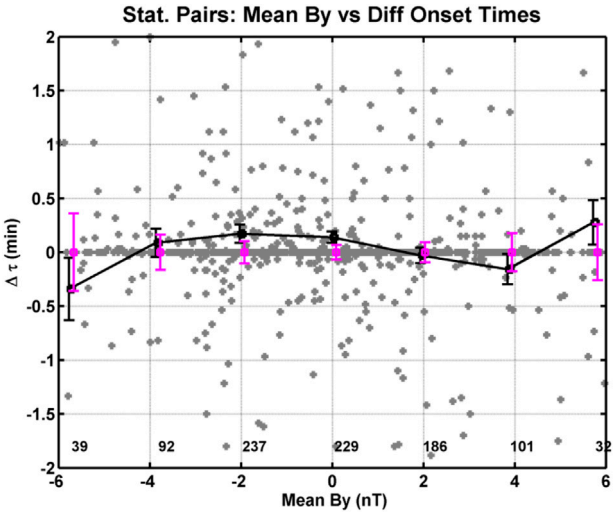

FIGURE 5 | Differences in onset time versus IMF *By*. The gray points are the individual events, the black points are means of bins 2 nT wide, and the mauve points are medians of bins 2 nT wide. The error bars are the error of the mean and median. The values at the base of the figure indicate the number points per bin.

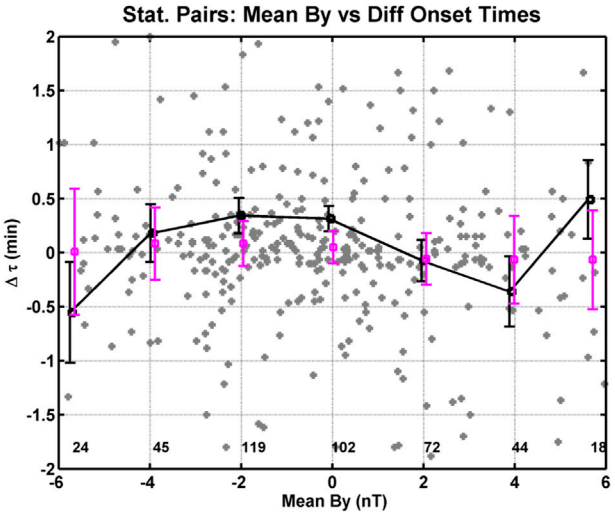

FIGURE 6 | Format of this figure is the same as **Figure 5**, except for this figure we have excluded differences in onset time equal to 0 s.

magnetometers. Along the x-axis is the difference in onset time and the bin size is 1 min, and the histogram peaks off the y-axis scale at 753. Furthermore, the difference in onset time of the 0 s bin means the absolute value of the difference is less than 0.5 min. We have limited the y-axis range to 150 to better display the wings of the distribution, which are the important features of the distribution in this study. We note here that the temporal resolution of the SNKQ magnetometer data was decimated to 10 s in order to obtain differences in the onset time from cross covariance technique. The temporal resolution of the data used for the SYO-TJO pair was 1 s. The mean, standard deviation, and error of the mean are given in the upper right corner. The histogram consists of 976 events, and we have excluded events outside of three sigma and events with a cross correlation coefficient of the northern and southern H components of less than 0.6. Of the 976 event in the histogram, 518 (53%) have a difference in onset time of zero, and the other 47% have a non-zero different in onset time. In this figure, negative values indicate that the onset occurs earlier in the northern hemisphere, and positive values indicate the onset occurs earlier in the southern hemisphere. This is a significant result indicated that approximately half of the onsets exhibit interhemispheric timing differences. In our analysis, we attempted to unravel the causes for these differences.

With all 976 hemispheric conjugate onsets, we examined any correlation that could occur between the differences in onset time and the IMF, solar wind plasma, season, UT, dipole tilt, and difference in the magnetic field line length. When we include all the hemispheric conjugate onsets, we found no strong correlation between the difference in onset time and IMF (including clock angle), solar wind speed, dynamic pressure that varied from 0.4 to 6.4 nPa, season, dipole tilt, and UT. Our results are described later in order. **Figure 5** shows the difference in onset time with respect to the IMF *By* component using all the onsets including those with zero difference in offset time. The IMF By values are 1 h averages of the IMF taken from 68 min before the onset time to 8 min before the onset time. The 8 min delay is added to account for the time the solar wind propagates from the nose of the magnetosphere about 17 Re up stream to the approximate location of reconnection point in the magnetotail. The gray points are the individual events, the black points are means of the differences in onset time for IMF *By* bins 2 nT wide, and the mauve points are medians of the differences in onset time for IMF *By* bins 2 nT wide. The black error bars are the error of the mean, and the mauve error bars are the error of the median. We noted that 35 of the individual events are outside of the range of the y-axis. A shorter y-axis has been selected to better show the means of $\Delta\tau$ near 0 s. There is a small but statistically significant difference in the means of ~+12 s for IMF *By* for the By bins at −2 and 0 nT. There is also the opposite time difference in the means of ~ −12 s for IMF By in the + 4 nT bin. We see that negative time differences, that is, onset occurring first in the Northern Hemisphere, occur for positive or duskward IMF By. The median values, on the other hand, show no statistical difference from zero.

Figure 6 shows the same time difference with respect to IMF By as in Figure 5, except only the events that had a measurable, non-zero onset difference in time between the hemispheres are included. A comparison of **Figures 5**, **6** demonstrated that systematic trends are not immediately discernible for differences in onset times. However, the calculation of binned means reveal clear trends. When we subset our data in **Figure 6** to only include differences in onset time within three standard deviations, cross correlation greater than 0.6, and include no 0 s differences in onset time, we found significant systematic trends in the differences in onset time as a function of the IMF *By* and season. In **Figure 6**, the differences in onset time in the IMF

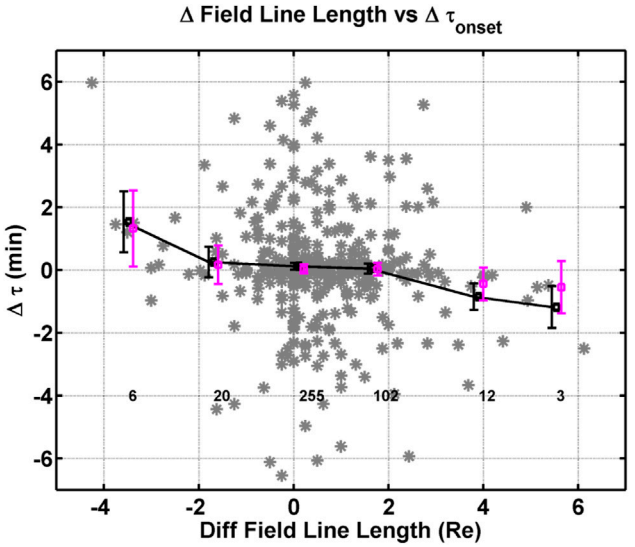

FIGURE 7 | Differences in onset time versus as a function of the difference in the magnetic field line length (from the station to the central plasma sheet). The gray points are the individual events, the black points are means of bins 2 Re wide, and the mauve points are medians of bins 2 Re wide. The error bars are the error of the mean. The values at the base of the figure indicate the number points per bin.

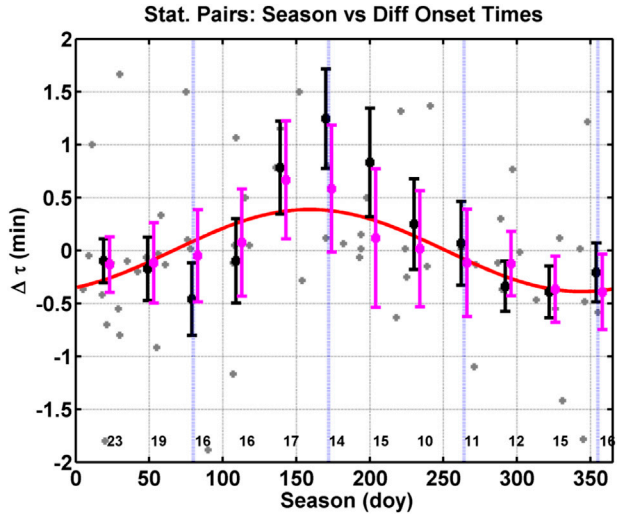

FIGURE 8 | Difference in onset time versus season (day of year). The gray points are the individual events, the black squares are means of bins 90 days wide, and the mauve squares are medians of bins 90 days wide. The number of points per bin is given at the base of the plot. The error bars are errors of the mean and medians. The blue vertical lines mark the equinoxes and the solstices. The red curve is a sine wave fit to the black squares.

By mean bins at −2 and 0 nT have grown to about 24 s, and the difference in onset time is now about −24 s for the IMF By mean bin at + 4 nT. We believe the differences in onset time between 2 and 0 nT are due to twisting of the Earth's magnetic field lines by IMF *By* that reduces the conjugacy between the station pairs. We will discuss this topic in more detail in the next section. However, the medians show no statistical difference from zero.

Another systematic trend is also present when we plot the differences in onset times versus the difference in field line length. The assumption is that reconnection in the plasma sheet in the magnetotail is start of the onset whether it is a PBI, substorm, or pseudo break up. Differences in onset time could be associated with differences in the arrival of Alfvén waves produced at the reconnection point, which potentially have to traverse different distances due to warping of the tail field lines associated with dipole tilt or some other mechanism. To determine the difference in field line length, the magnetic field was mapped using the T96 model from the location of both magnetometers to the central plasma sheet, where the magnetic field changes direction in the Bx component. **Figure 7** shows the difference in onset time as a function of the difference in the field line length between the southern and northern stations. The gray points in the figure are the individual events. We have widened the y-axis to better display the trend in the data. The black squares are means of the differences in onset time for bins 2 Re wide and the error bars are the error of the mean, and the mauve squares are medians of the differences in onset time for bins 2 Re wide and the error bars are the error of the mean and error of the median, respectively. Below each black square is the number of points in the bin. We have defined this trend as a very weak trend because the differences in onset time are only visible at the extreme differences in field line length where a small fraction of the data set is available (9 of 404 events use for the plot or ~2% of the data). We also note that the extreme differences in field line length (−3.5, 3.9, and 5.5 Re) cannot be clearly associated with a specific range of dipole tilt, season, or IMF By values. That is to say, the individual events are distributed throughout the different seasons. Nearly all median values show no statistical difference from zero except for the value at about −3.5 Re.

The only other systematic change in the differences in onset time we found are seasonal. **Figure 8** displays the difference in onset time as a function of the season (day of year). The gray points in the figure are the individual events. In addition, 10 points are off the scale, and we have shorted the y-axis to better display the trend in the data. The black squares are means of the difference in the onset time of bins 90 days wide centered on the black square, and the error bars are the error of the mean. The mauve squares are medians of the difference in the onset time of bins 90 days wide centered on the mauve square, and the error bars are the error of the median. Below each black square is the number of points in the bin. The blue vertical lines mark the spring equinox, summer solstice, autumnal equinox, and the winter solstice. The red curve is least squares fit of a sine wave to the median binned data points. The amplitude of the fit is 23.2 ± 4.4 s, the period of the sine wave is fixed to 365 days, and the phase is 65.5 ± 11.1 days. We remind the reader that the spring equinox occurs on the 79th day of the year. For **Figure 8**, we have only used IMF *By* values between 0.5 and 2.5 nT to limit the amount of twisting of the Earth's magnetic field lines by IMF By. Finally, the extreme values from **Figure 7** for differences in the field line lengths greater than 5.5 Re and less than −3.5 Re have not been included within **Figure 8**.

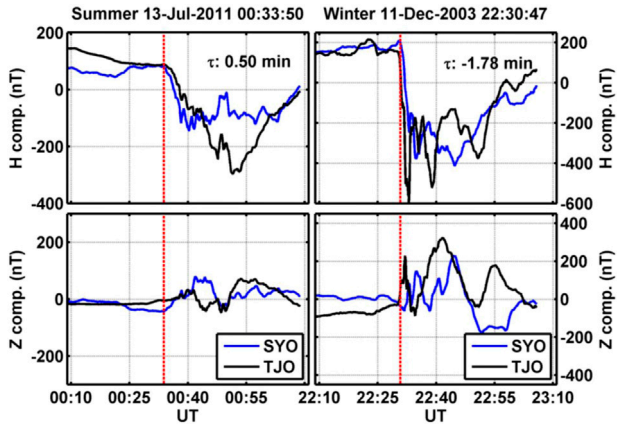

FIGURE 9 | Format of this figure is approximately the same as **Figure 2**. The left side shows a summer solstice event and the right side shows a winter solstice event. The blue curve is associated with SYO, and the black curve shows the data from TJO. The red dashed line shows the onset time at SYO.

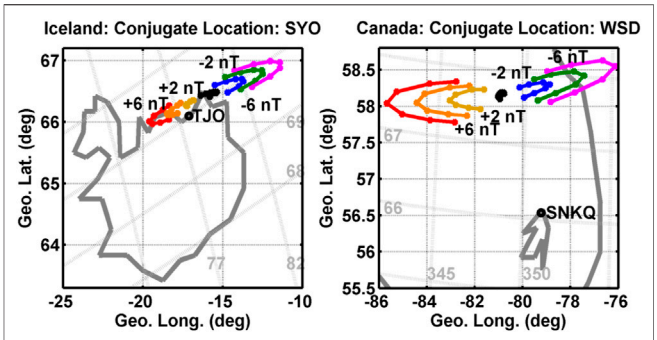

FIGURE 10 | Map of Iceland and Hudson bay Canada showing the location of the TJO and SNKQ stations, which are indicated with the circle, and the change in the location of the SYO and WSD conjugate foot point with IMF *By* from −6 nT to +6 nT and dipole tilt for 3 h around local midnight.

Figure 9 shows two examples of differences in the onset time for one summer solstice event on 17 July 201 at 0007:59 UT (left side) and one winter solstice event on 11 December 2003 at 2230: 47 UT (right side). These plots both use the SYO-TJO pair of hemispheric conjugate stations and have approximately the same format as **Figure 2**. The red dashed line marks the onset time in the southern hemisphere. The purpose of these events is to show that the differences in onset time switches between summer and winter for individual events and is not just a statistical result in **Figure 8**. In the left side, the difference in the onset time is 0.5 min and the correlation coefficient is 0.96. The top left panel shows that the H component of SYO (blue) decreases before the H component of TJO (black). In the right side, the difference in onset time is −1.78 min and the correlation coefficient is 0.87. In this event the H component of TJO decreases before the H component of SYO.

DISCUSSION AND CONCLUSION

In total, we have 976 hemispheric conjugate onsets with correlations above 0.6 and onsets in both hemispheres to investigate correlations with the IMF, solar wind plasma, and season. When we included all 976 events in our statistics, we found little to no correlation with the IMF, solar wind plasma, dipole tilt, UT, and season. However, when we subset the data to exclude differences in onset time equal to zero, then we saw a weak systematic variation associated with the IMF By, weak correlation with the difference in field line lengths, and a correlation with season. Here, we justify subsetting our data to exclude differences in onset time equal to zero. The correlation between the differences in onset time and season suggests that the ionospheric conductivity due to solar flux is responsible for the annual variation. There are a number of studies that have developed methods to determine the conductivity due to solar irradiation. Two of the more popular studies are Robinson and Vondrak (1984), which is an empirical model, and the other is the one used in the assimilative mapping of ionospheric electrodynamics (AMIE) procedure, which was develop developed by Richmond and Kamide (1988). These two studies indicate that the ionospheric conductivity for the stations with geographic latitudes similar to SYO and TJO would have a range of conductivity between 0.8 and 17 S for solar zenith angles between about 50° and 90° and f10.7 cm fluxes between 50 and 200 s. f.u. The average daily conductivity value varies systematically with season in both models such that the conductivity will be low in the midnight sector in the winter season and higher in the midnight sector in the summer season. However, it is well known that in addition to solar irradiance, particle precipitation from electron and ions determine the ionospheric conductivity. It has been shown for studies using electron precipitation from spacecraft measurements that during quiet and moderate geomagnetic conditions that the height integrated Hall conductivity, which would be most relevant to the onsets in the *H* component of the magnetic field, ranges between 0.5 and 17 S in the midnight sector (Vickrey et al., 1981; Hardy et al., 1987; Fuller-Rowel and Evans, 1987; McGranaghan et al., 2015). Moreover, during more active conditions, including substorm conditions, the height integrated Hall conductivity can be greater than 26 S (Hardy et al., 1987; Gjerloev and Hoffman, 2000), and in the study of Semeter and Doe (2002), it can be greater than 100 S in the midnight sector. If we assume that the particle precipitation is roughly equal in both hemispheres, then during some onsets the ionospheric conductivity due to particle precipitation may dominate ionospheric conductivity due to solar irradiance. Thus, ionospheric conductivity due to particle precipitation could obscure the systematic pattern associated with the differences in onset time associated with season. We used this assumption to justify removing the differences in onset that are equal to zero, which includes 518 onsets (53%). Note that the mean world data center AE index value for these 518 onsets is about 441 nT, the median is about 392 nT, and the error of the mean is 13 nT and for the not zero onset differences ,the mean is about 500 nT, the median is ~460 nT, and the error of the mean is 15 nT. This simplistic examination of the AE indices does not

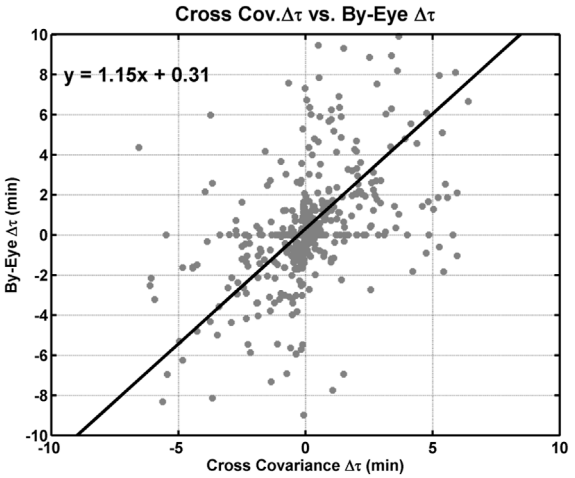

FIGURE 11 | Difference in onset time determined from the cross covariance method versus the difference in onset time determined from the by-eye method. The gray points are individual events, and the black line is a linear fit to the data. The fit to the data is given in the upper left corner.

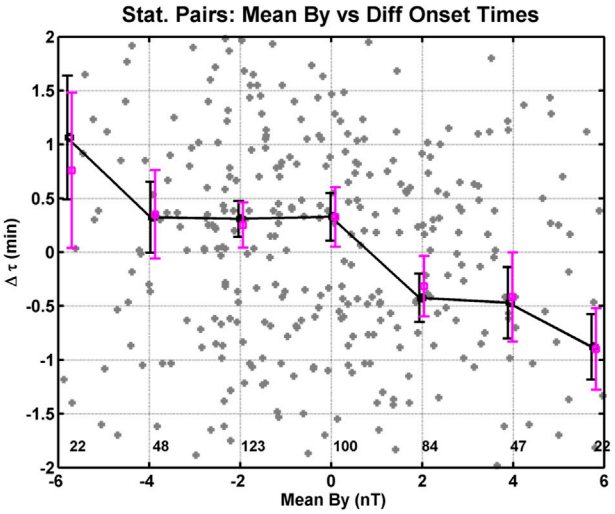

FIGURE 12 | Format of this figure is the same as **Figure 6**, except for this figure we have used the southern and northern hemisphere onsets identified by-eye to determine the difference in onset time and excluded differences in onset time equal to 0 s.

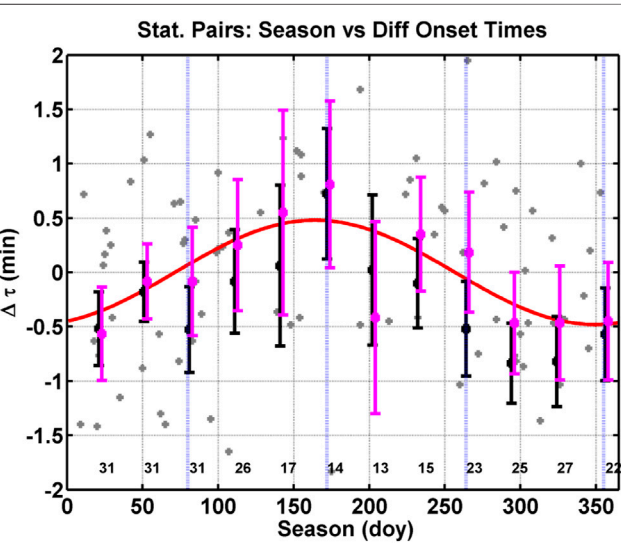

FIGURE 13 | Format of this figure is the same as **Figure 8**. In this figure, we have used the southern and northern hemisphere onsets identified by eye to determine the difference in onset time.

support our assumption. However, the only way to test our assumption would require particle precipitation at the two conjugate locations, and this test is not feasible at this time.

Figure 6 shows the weak systematic correlation between the differences in onset time and means of the IMF *By*. The differences in onset time in the median bins versus IMF *By* show that from −2 to 0 nT the differences in onset time are on the order of 24 s and from 0 to 4 nT the differences in onset time are on the order of 0 s. We believe the difference in the onset time from −4 to 0 nT is due to twisting of the magnetic field lines by the IMF in the magnetotail. We support this statement by determining the conjugate position of the SYO and WSD stations on 12 September 2010 (arbitrarily selected date) using the T01 magnetic field model (Tsyganenko, 2002a; 2002b) with the model inputs: IMF *Bz* = −1 nT, dynamic pressure of 2.1 nPa, a Dst = −10 nT, and a range of IMF *By* from −6 nT to +6 nT. **Figure 10** shows the change in position of the SYO station foot point location plotted over a map of Iceland with seven different IMF *By* values for times between 20 UT and 3 UT (left panel) and the change in position of the WSD station location plotted over a map of Falherty Island in Hudson bay with seven different IMF *By* values between 2 and 8 UT (right panel). Included on each plot are the geographic coordinates (black dashed lines) and the magnetic coordinates (gray dashed lines) some of which have been labeled. The red curve is for IMF By = + 6 nT, the orange curve for By = + 4 nT, the gold curve for By = + 2 nT, the black curve for By = 0 nT, the blue curve for By = −2 nT, the green curve for By = −4 nT, and the mauve curve for By = −6 nT. Each curve shows the change in the foot point over the 3 h on either side of local midnight for each station pair. For IMF *By* = +2 nT the TJO station and SYO foot point are approximately at the same MLT and the largest differences in magnetic longitude are about 7° for By = −6 nT, which would equate to an approximate difference in onset time of about 28 s for a westward surge of 1 MLT/min. In the right panel of **Figure 10**, the SNKQ station and WSD foot point are approximately at the same MLT for IMF *By* = 0 nT, and the largest differences in magnetic longitude are about 8° for By = +6 nT, which would equate to an approximate difference in onset time of about −32 s for a westward surge of 1 MLT/min. The difference in the IMF By aligned for the SYO/TJO and WSD/SNKQ pair of stations explains why our allowed IMF By range extends from 0.5 to 2.5 nT. We do not include 0 nT because the WSD/SNKQ pair contributes few onsets to this study and we want to limit the range of IMF By as much as possible to eliminate

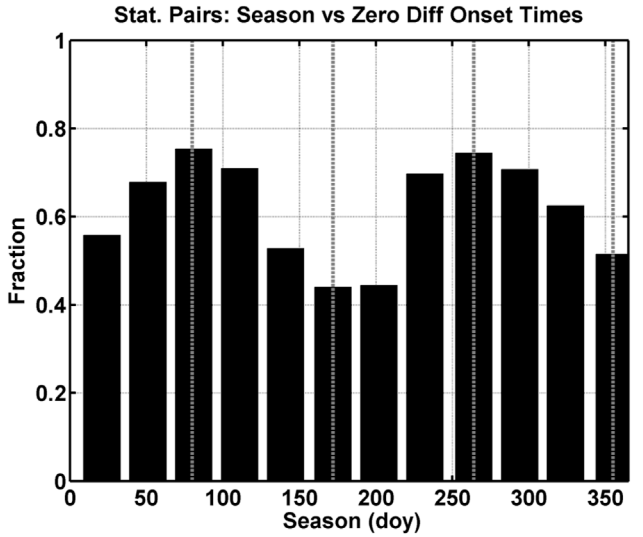

FIGURE 14 | Fraction per bin of differences in onset time with a value of zero as a function of season (doy). The black bars are counts in bins 90 days wide, and the dotted vertical lines mark the equinoxes and the solstices.

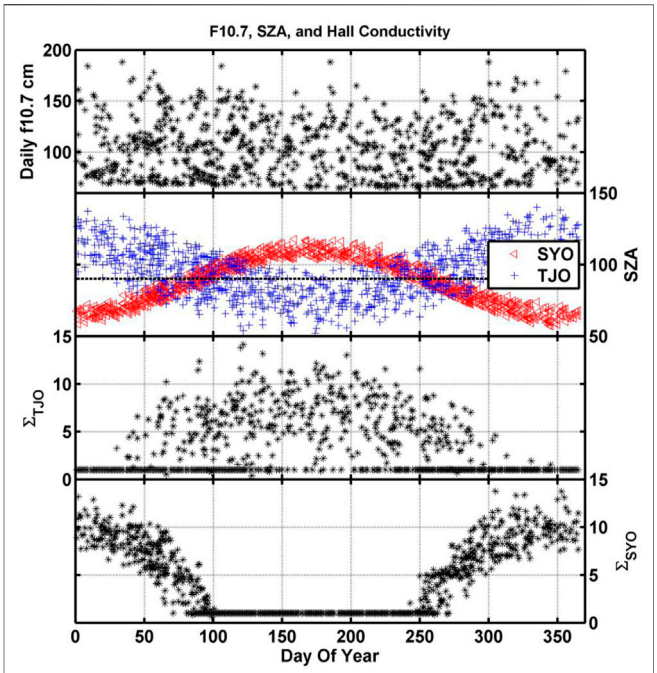

FIGURE 15 | Variation of height-integrated ionospheric conductivity due to solar illumination as a function of the day of year for all our onset events. In the top panel is the solar radio flux at 10.7 cm, and in the second panel is the solar zenith angle for TJO (blue) and SYO (red). The dashed line marked a SZA = 90°. The third panel show the TJO height-integrated ionospheric conductivity, and the forth panel show the conductivity for SYO.

contribution from westward surges. These alignments for certain IMF By values explains why the difference in onset time is approximately zero in the *By* range of 0–4 nT. For IMF By of −2 nT, the foot point of the SYO station is located further toward the dawn where the SYO station could potentially record a westward surge before the TJO station. A similar statement can be made for the WSD/SNKQ pair of stations. This shift to the east explains why the difference in onset time is positive in **Figure 6**. However, the mean difference in onset time reverses sign for IMF By = −6 and 6 nT. Why these two difference in onset time at IMF By = −6 and 6 nT do not appear to follow the same trend as the other points is not clear at this time and may be due to low counting statistics.

Østgaard et al. (2004) also demonstrated the twisting of the magenotail field with IMF *By* with simultaneous substorm auroral onsets observed in opposite hemispheres. They showed in their study that the magnetic foot point of a magnetic field line in the southern hemisphere is duskward of the foot point in the northern hemisphere for IMF By < −2 nT and the foot point in the southern hemisphere is dawnward of the foot point in the northern hemisphere for IMF By > −1 nT. From this observations, we determined that for IMF By < −2 nT if an onset that occurs on a magnetic field line with its foot point directly over a southern hemisphere magnetometer station, then the northern magnetometer stations, which is conjugate to the southern station for IMF By = 0 nT, would record the onset later once the westward surge propagates to the northern station. More specifically, Østgaard et al. (2004) showed the difference in the MLT onset location shifted 0.13 MLT per 1 nT of IMF *By*. If we make three assumptions about our data set: 1) the onset in our study are substorm onsets, 2) the MLT difference between those onsets is about 0.26 MLT for 2 nT of IMF By, and 3) the typical westward surge for these substorms is about 1 MLT per minute (Angelopoulos et al., 2008a), then the difference in onset time with the twisting of the magnetic field is on the order of 16 s. The value of 16 s is consistent with the mean value of 24 ± 10 s in our **Figure 6** at 2 nT.

If we now consider the medians, then no trend is apparent as a function of IMF By. This result does not agree with Østgaard et al. (2004). Even if we consider the results of **Figure 8**, which shows a seasonal dependence on the difference in onset time, and subset our data to the equinoxes, the median values still show no trend with IMF By. Ganushkina et al. (2013) showed a maximum displacement in the magnetic foot points on the order of 7° for an IMF By of |6| nT. For a westward surge moving with a speed of 1 MLT per min, this would amount to a potential difference in onset time of 30 s, which is smaller than the size of the error of the medians. The same can be said for smaller values of IMF By. With this data set, we cannot make definitive statements on the differences in onset time as a function of IMF By.

Figure 7 shows the difference in onset time as a function of the difference in the field line length between the southern and northern stations. The bulk of the medians are not statistically different from zero (only one data bin), and only half the means are statistically difference from zero. We questioned whether the values that are statistically different from zero have reasonable differences in onset time for the differences in field line length for typical plasma sheet Alfvén speeds. Using only the statistically significant points, we divided the difference in the field line length by the difference in onset time to determine the approximate Alfvén speed

and obtained values ranging from 240 to 500 km/s. Typical plasma sheet Alfvén speeds are on the order of 300–1400 km/s (Lui, 1987; Angelopoulos et al., 2002; 2008b; Kan et al., 2011) depending on the location within the plasma sheet. These results suggest that the difference in onset time could be due to the differences in field line length; however, these results are only meaningful at the extremes and apply to only 21 events in those three difference bins of a total of 398 events used to produce the plot. Furthermore, we have made simplistic assumptions about Alfven travel times and used a magnetic field line model that is not ideal for activity periods within the magnetotail. We note that the relationship between magnetotail reconnection and onsets within the ionosphere is complicated and future studies should be performed to more rigorously investigate these findings.

In this study, we used cross covariance in order to determine the difference in onset time between the southern and northern magnetometer data. This method was used in order to minimize potential bias and provide a clear reproducible technique. However, as a means of further validating our results, we went through our onset events a second time and identified the possible onset time by-eye in the northern hemisphere data along with the southern hemisphere observations. See the black vertical lines in **Figures 1**, **2**. **Figure 11** displays the difference in onset time determined from the cross covariance method (x-axis) versus the difference in onset time determined from the by-eye method (y-axis). The gray points are individual events, and the black line is a linear fit to the data. The fit to the data is given in the upper left corner. The slope to the fit 1.15 ± 0.11 and the intercept is 0.31 ± 0.11 min. The slope indicates that the by-eye method for the northern hemisphere appears to result in a higher difference in onset time, but in general the results are similar.

Our attempt to validate **Figures 6**–**8** using the by-eye method to determine the difference in onset time produced several results. First, the trend observed in the difference in onset time versus magnetic field line length (i.e., our reexamination of **Figure 7**) is no longer present in both the means and the medians. Figure of the difference in onset time versus magnetic field line length redone using the northern hemisphere by-eye method data is not included in this study. Second, the trend in the difference in onset time versus IMF By is more apparent. See **Figure 12**, which has the same format as **Figure 6**. In **Figure 12**, the difference in onset time is now the difference between the onset in the southern and northern onsets that were selected *by-eye*. In general, the trend in both the means (black squares) and medians (mauve squares) is same within the uncertainties, and all the values are statistically different from zero. The difference in onset time between −4 and 0 nT is ~21 s, with uncertainties around ±16 s in the median value. Furthermore, the difference in onset time become negative (about −26 s), with uncertainties on the order of ±19 s for IMF By values of 2 and 4 nT. These values are consistent with estimates, using the Ganushkina et al. (2013) results and westward surge propagation speed of 1 MLT/min.

Finally, the difference in onset time (using the results of the by-eye method) as a function of season is still present in the means even with the larger errors of the mean, but not as clear in the medians. Only the summer solstice value and the value at day of year 23 are statistically different from zero in the median because the errors on the medians have increased. See **Figure 13**, which has the same format as **Figure 8**. To be consistent with **Figure 8** we have again limited the IMF By to a range of 0.5–2.5 nT. The amplitude of the sinusoidal fit to the median values is 28.8 ± 8.5 s, the period of the sine wave is fixed to 365 days, and the phase is 70.5 ± 16.9. Thus, we have obtained roughly the same results using the by-eye method for the difference in onset time as a function of season, but not for the difference in onset time as a function of IMF By and the difference in field line length.

In order to produce the results in many of the figures (i.e., **Figures 5**–**8**, **11** and **Figure 12**), we removed the differences in onset time equal to zero. However, there is information in these events. If the differences in onset time were due to IMF or solar wind plasma, then the number of onsets with differences in onset time equal to zero should be evenly distributed throughout the year and should have no seasonal dependence. **Figure 14** is the fraction of onset times equal to zero per day of year bin as a function season for bins 90 days wide (i.e., the same size as for **Figures 8**, **13**). To be consistent with **Figure 8**, we have limited the IMF By to a range of 0.5–2.5 nT. The vertical dashed lines mark the equinoxes and solstices. The figure displays peaks at the equinoxes and minima at the solstices validating our conclusion with this semi-independent method that the differences in onset time are a function of season.

In **Figures 8**, **13**, **14**, we limited the IMF *By* affects by limiting the range of IMF By to 0.5–2.5 nT. This range was selected to include enough events for good statistics. With the remaining onsets, we showed, in **Figure 8**, that the difference in onset time is dependent on the season or more likely annual variation of ionospheric conductivity due to sunlight. In **Figure 15**, we demonstrated the annual variation in ionospheric conductivity and plotted the solar radio flux (S) f10.7 cm in the top panel, the solar zenith angle (SZA) for both TJO (blue) and SYO (red) in the second panel, and the TJO (third panel) and SYO (fourth panel) height integrated conductivity $\sum = 1.5\ (S \cos(SZA))^{0.5}$ derived in Robinson and Vondrak (1984). The first panel shows the radio flux varies between 50 and 200 s.f.u. The second panel shows the SZA varies between about 50° and 140°, and for values above 90° (marked with the dashed line) the station is in the nightside and receives no sunlight. Note that the scattering on the TJO station is larger than that on the SYO station because TJO is at a lower geographic latitude and experiences a larger range of solar zenith angles. In the third panel, the height integral solar ionospheric conductivity is largest for TJO in the northern summer season, and in the fourth panel, the conductivity for SYO is largest in the southern summer season. We noted that the height integrated conductivity is set to 1 S in Robinson and Vondrak (1984) when the ionosphere is not sunlit. The second, third, and fourth panels of **Figure 15** demonstrate the seasonal change in ionospheric conductivity due to solar illumination.

The sinusoidal variation in the differences in onset time has a significant impact on substorm models. **Figure 8** shows that onsets occur first in the unlit midnight sector by about 23 s before the sunlit hemisphere during the summer and winter solstices. To explain this difference in onset time, we can think of the ionosphere as an inductor resistor (LR) series circuit. In LR circuit the growth time of the current is $\tau = L/R$ or $\tau = L\sum$, where $\sum$ is the conductance. If we assume that the inductance is the same in both hemispheres, then when the

conductance is large, as in the sunlit ionosphere, the growth time of the ionospheric current is long and when the conductance is small, like in the unlit ionosphere, the growth time is small. Substorm onset models do not take the differences in ionospheric conductivity into account at this time; a difference of 23 s between the two hemispheres may influence the identification of an ideal substorm model. Recall that the difference between the start of the tail reconnection and the auroral onset in the outside-in model is about 120 s, where a 23 s difference in the auroral onset is about 19%. The difference between the start of current disruption and the auroral onset is 30 s for the inside-out, where a 23 s difference in the auroral onset is about 76%. Hence, our results cannot distinguish between the outside-in or inside-out models. However, we believe it is important for substorm models and future substorm studies to take into account the state of the ionosphere. Fortunately, most substorm studies identify auroral onsets with all sky images in the unlit hemisphere because they are limited to visible wavelengths; however, ultraviolet imagers onboard spacecraft are not restricted to unlit conditions. Future ultraviolet imagers with a cadence better than 23 s should be able to observe this difference in onset time as a function of season.

DATA AVAILABILITY STATEMENT

The raw data supporting the conclusions of this article will be made available by the authors, without undue reservation.

AUTHOR CONTRIBUTIONS

AK provided ground magnetometer data from Antarctica and Iceland. EZ provided ground magnetometer data from Antarctica, funding, data analysis, data interpretation, guidance, and helped with editing this manuscript. DMO provided funding and helped with editing this manuscript. JMW wrote the manuscript, performed the data analysis, performed the data interpretation, produced the figures, and helped with editing this manuscript.

FUNDING

This study was made possible by NASA THEMIS contract NAS5-02099 at UCLA; NSF Antarctic Aeronomy and Astrophysics, Office of Polar Programs grant ANT-1043621; and NSF Directorate of Atmospheric and Geosciences grant 1606014, and NASA HGI grant 80NSSC22K0756.

ACKNOWLEDGMENTS

We thank the many different groups operating magnetometer arrays for providing data for this study including: The Canadian Magnetic Observatory Network (CANMON) for data from SNKQ is maintained and operated by the Geological Survey of Canada—http://gsc.nrcan.gc.ca/geomag and National Institute of Polar Research in Japan for data from the TJO and SYO stations. We thank the CSA for logistical support in fielding and data retrieval from the GBO stations. The authors thank E. Yizengaw, M. B. Moldwin, and the rest of the SAMBA team for the WSD magnetometer data. SAMBA was also operated by UCLA and funded by NSF. We would also like to thank M.G. Kivelson, K.K. Khurana, R.L. McPherron, R.J. Strangeway, V. Angelopoulos, and R.J. Walker for their invaluable input. We acknowledge the IUGONET system for providing the data from Tjornes and Syowa Station and contribution of Dr. Yoshimasa Tanaka who is the leader of the IUGONET development team.

REFERENCES

Angelopoulos, V., Chapman, J. A., Mozer, F. S., Scudder, J. D., Russell, C. T., Tsuruda, K., et al. (2002). Plasma Sheet Electromagnetic Power Generation and its Dissipation along Auroral Field Lines. *J. Geophys. Res. Space Phys.* 107 (A8). doi:10.1029/2001ja900136

Angelopoulos, V., McFadden, J. P., Larson, D., Carlson, C. W., Mende, S. B., Frey, H., et al. (2008b). Tail Reconnection Triggering Substorm Onset. *Science* 321 (5891), 931–935. doi:10.1126/science.1160495

Angelopoulos, V., Sibeck, D., Carlson, C. W., McFadden, J. P., Larson, D., Lin, R. P., et al. (2008a). First Results from the THEMIS Mission. *Space Sci. Rev.* 141, 453–476. doi:10.1007/s11214-008-9378-4

Baker, D. N., Pulkkinen, T. I., Angelopoulos, V., Baumjohann, W., and McPherron, R. L. (1996). Neutral Line Model of Substorms: Past Results and Present View. *J. Geophys. Res.* 101 (A6), 12975–13010. doi:10.1029/95JA03753

Baumjohann, W., Paschmann, G., and Cattell, C. A. (1989). Average Plasma Properties in the Central Plasma Sheet. *J. Geophys. Res.* 94, 6597–6606. doi:10.1029/ja094ia06p06597

Boudouridis, A., and Zesta, E. (2007). Comparison of Fourier and Wavelet Techniques in the Determination of Geomagnetic Field Line Resonances. *J. Geophys. Res.* 112, a–n. doi:10.1029/2006JA011922

Frank, L. A., and Sigwarth, J. B. (2003). Simultaneous Images of the Northern and Southern Auroras from the Polar Spacecraft: An Auroral Substorm. *J. Geophys. Res.* 108 (A4), 8015. doi:10.1029/2002JA009356

Fuller-Rowell, T. J., and Evans, D. S. (1987). Height-integrated Pedersen and Hall Conductivity Patterns Inferred from the TIROS-NOAA Satellite Data. *J. Geophys. Res.* 92, 7606–7618. doi:10.1029/ja092ia07p07606

Ganushkina, N. Y., Kubyshkina, M. V., Partamies, N., and Tanskanen, E. (2013). Interhemispheric Magnetic Conjugacy. *J. Geophys. Res. Space Phys.* 118, 1049–1061. doi:10.1002/jgra.50137

Gjerløv, J. W., and Hoffman, R. A. (2000). Height-integrated Conductivity in Auroral Substorms: 1. Data. *J. Geophys. Res. Space Phys.* 105 (A1), 215–226.

Hardy, D. A., Gussenhoven, M. S., Raistrick, R., and McNeil, W. J. (1987). Statistical and Functional Representations of the Pattern of Auroral Energy Flux, Number Flux, and Conductivity. *J. Geophys. Res.* 92 (A11), 12275–12294. doi:10.1029/ja092ia11p12275

Hones, E. W., Jr. (1976), "The Magnetotail: its Generation and Dissipation," in *Physics of Solar Planetary Environments*, Editor D. J. Williams, (Washington, D.C., USA: AGU), Vol. 558.

Hsu, T.-S., and McPherron, R. L. (2012). A Statistical Analysis of Substorm Associated Tail Activity. *Adv. Space Res.* 50 (10), 1317–1343. doi:10.1016/j.asr.2012.06.034

Kan, J. R., Li, H., Wang, C., Frey, H. U., Kubyshkina, M. V., Runov, A., et al. (2011). Brightening of Onset Arc Precedes the Dipolarization Onset: THEMIS Observations of Two Events on 1 March 2008. *Ann. Geophys.* 29 (11), 2045–2059.

Kivelson, M. G., Khurana, K. K., Walker, R. J., Kepko, L., and Xu, D. (1996). Flux Ropes, Interhemispheric Conjugacy, and Magnetospheric Current Closure. *J. Geophys. Res.* 101 (27), 341350. doi:10.1029/96ja02220

Lui, A. T. (1987). *Magnetotail Physics*. Baltimore, MD: Johns Hopkins University Press.

Lui, A. T. Y. (1996). Current Disruption in the Earth's Magnetosphere: Observations and Models. *J. Geophys. Res.* 101, 13067–13088. doi:10.1029/96ja00079

Lui, A. T. Y., Lopez, R. E., Krimigis, S. M., McEntire, R. W., Zanetti, L. J., and Potemra, T. A. (1988). A Case Study of Magnetotail Current Sheet Disruption and Diversion. *Geophys. Res. Lett.* 15, 721–724. doi:10.1029/gl015i007p00721

McComas, D. J., Bame, S. J., Barker, P., Feldman, W. C., Phillips, J. L., Riley, P., et al. (1998). Solar Wind Electron Proton Alpha Monitor (SWEPAM) for the Advanced Composition Explorer. *Space Sci. Rev.* 86, 563–612. doi:10.1007/978-94-011-4762-0_20

McGranaghan, R., Knipp, D. J., Matsuo, T., Godinez, H., Redmon, R. J., Solomon, S. C., et al. (2015). Modes of High-latitude Auroral Conductance Variability Derived from DMSP Energetic Electron Precipitation Observations: Empirical Orthogonal Function Analysis. *J. Geophys. Res. Space Phys.* 120, 11,013–11,031. doi:10.1002/2015JA021828

Morioka, A., Miyoshi, Y., Tsuchiya, F., Misawa, H., Kasaba, Y., Asozu, T., et al. (2011). On the Simultaneity of Substorm Onset between Two Hemispheres. *J. Geophys. Res.* 116, a–n. doi:10.1029/2010JA016174

Newell, P. T., Sotirelis, T., and Wing, S. (2010). Seasonal Variations in Diffuse, Monoenergetic, and Broadband Aurora. *J. Geophys. Res.* 115, a–n. doi:10.1029/2009JA014805

Ohtani, S., Wing, S., Ueno, G., and Higuchi, T. (2009). Dependence of Premidnight Field-Aligned Currents and Particle Precipitation on Solar Illumination. *J. Geophys. Res.* 114, a–n. doi:10.1029/2009JA014115

Østgaard, N., Mende, S. B., Frey, H. U., Immel, T. J., Frank, L. A., Sigwarth, J. B., et al. (2004). Interplanetary Magnetic Field Control of the Location of Substorm Onset and Auroral Features in the Conjugate Hemispheres. *J. Geophys. Res.* 109, A07204. doi:10.1029/2003JA010370

Østgaard, N., Mende, S. B., Frey, H. U., Sigwarth, J. B., Åsnes, A., and Weygand, J. M. (2007). Auroral Conjugacy Studies Based on Global Imaging. *J. Atmos. Solar-Terrestrial Phys.* 69, 249–255. doi:10.1016/j.jastp.2006.05.026

Richmond, A. D., and Kamide, Y. (1988). Mapping Electrodynamic Features of the High-Latitude Ionosphere from Localized Observations: Technique. *J. Geophys. Res.* 93, 5741–5759. doi:10.1029/ja093ia06p05741

Robinson, R. M., and Vondrak, R. R. (1984). Measurements ofEregion Ionization and Conductivity Produced by Solar Illumination at High Latitudes. *J. Geophys. Res.* 89 (A6), 3951–3956. doi:10.1029/JA089iA06p03951

Sato, N., Nagaoka, T., Hashimoto, K., and Saemundsson, T. (1998). Conjugacy of Isolated Auroral Arcs and Nonconjugate Auroral Breakups. *J. Geophys. Res.* 103, 11641–11652. doi:10.1029/98JA00461

Semeter, J., and Doe, R. (2002). On the Proper Interpretation of Ionospheric Conductance Estimated through Satellite Photometry. *J. Geophys. Res.* 107 (A8), 19. doi:10.1029/2001JA009101

Smith, C. W., L'Heureux, J., Ness, N. F., Acuña, M. H., Burlaga, L. F., and Scheifele, J. (1998). The ACE Magnetic Fields Experiment. *Space Sci. Rev.* 86, 613–632. doi:10.1007/978-94-011-4762-0_21

Tsyganenko, N. A. (2002a). A Model of the Near Magnetosphere with a Dawn-Dusk Asymmetry 1. Mathematical Structure. *J. Geophys. Res.* 107 (A8), 12. doi:10.1029/2001JA000219

Tsyganenko, N. A. (2002b). A Model of the Near Magnetosphere with a Dawn-Dusk Asymmetry 2. Parameterization and Fitting to Observations. *J. Geophys. Res.* 107 (A7), 10–11. doi:10.1029/2001JA000220

Vickrey, J. F., Vondrak, R. R., and Matthews, S. J. (1981). The Diurnal and Latitudinal Variation of Auroral Zone Ionospheric Conductivity. *J. Geophys. Res.* 86 (A1), 65–75. doi:10.1029/ja086ia01p00065

Weimer, D. R. (2004). Correction to "Predicting Interplanetary Magnetic Field (IMF) Propagation Delay Times Using the Minimum Variance Technique. *J. Geophys. Res. Space Phys.* 109, A12. doi:10.1029/2004ja010691

Weimer, D. R., Ober, D. M., Maynard, N. C., Collier, M. R., McComas, D. J., Ness, N. F., et al. (2003). Predicting Interplanetary Magnetic Field (IMF) Propagation Delay Times Using the Minimum Variance Technique. *J. Geophys. Res.* 108. doi:10.1029/2002JA009405

Weygand, J. M., and McPherron, R. L. (2006b). *ACE SWEPAM Solar Wind Weimer Propagated 60 S Resolution Data in GSM Coordinates*. doi:10.21978/P8S62R

Weygand, J. M., and McPherron, R. L. (2006a). *ACE Weimer Propagated 60 S Resolution Tri-axial Fluxgate Magnetometer in GSM Coordinates*. doi:10.21978/P8933R

Weygand, J. M., and Zesta, E. (2008). Comparison of Auroral Electrojet Indices in the Northern and Southern Hemispheres. *J. Geophys. Res.* 113, a–n. doi:10.1029/2008JA013055

Weygand, J. M., Zesta, E., and Troshichev, O. (2014). Auroral Electrojet Indices in the Northern and Southern Hemispheres: A Statistical Comparison. *J. Geophys. Res. Space Phys.* 119, 4819–4840. doi:10.1002/2013JA019377

Conflict of Interest: The authors declare that the research was conducted in the absence of any commercial or financial relationships that could be construed as a potential conflict of interest.

frontiers | Frontiers in Astronomy and Space Sciences

TYPE Original Research
PUBLISHED 25 July 2022
DOI 10.3389/fspas.2022.957223

OPEN ACCESS

EDITED BY
Tuija I. Pulkkinen,
University of Michigan, United States

REVIEWED BY
Varvara Andreeva,
Saint Petersburg State University, Russia
Daniel Weimer,
Virginia Tech, United States

*CORRESPONDENCE
Karl M. Laundal,
karl.laundal@uib.no

SPECIALTY SECTION
This article was submitted to Space Physics,
a section of the journal
Frontiers in Astronomy and Space Sciences

RECEIVED 30 May 2022
ACCEPTED 07 July 2022
PUBLISHED 25 July 2022

CITATION
Laundal KM, Madelaire M, Ohma A, Reistad J and Hatch S (2022), The relationship between interhemispheric asymmetries in polar ionospheric convection and the magnetic field line footpoint displacement field.
Front. Astron. Space Sci. 9:957223.
doi: 10.3389/fspas.2022.957223

The relationship between interhemispheric asymmetries in polar ionospheric convection and the magnetic field line footpoint displacement field

Karl M. Laundal*, Michael Madelaire, Anders Ohma, Jone Reistad and Spencer Hatch

Department of Physics and Technology, University of Bergen, Bergen, Norway

Polar electrodynamics is largely controlled by solar wind and magnetospheric forcing. Different conditions can make plasma convection and magnetic field disturbances asymmetric between hemispheres. So far, these asymmetries have been studied in isolation. We present an explanation of how they are linked via displacements of magnetic field line footpoints between hemispheres, under the assumption of ideal magnetohydrodynamics. This displacement has so far been studied only on a point by point basis; here we generalize the concept to a 2D displacement vector field. We estimate displacement fields from average patterns of ionospheric convection using the Weimer et al. (J. Geophys. Res., 2005a, 110, A05306) model. These estimates confirm that the influence of the interplanetary magnetic field extends deep into the magnetosphere, as predicted by models and *in-situ* observations. Contrary to predictions, the displacement associated with dipole tilt appears uniform across the nightside, and it exceeds the effect of IMF B_y. While more research is needed to confirm these specific findings, our results demonstrate how ionospheric observations can be used to infer magnetospheric morphology, and that the displacement field is a critical component for understanding geospace as a coupled two-hemisphere system.

KEYWORDS

interhemispheric asymmetry, ionospheric convection, magnetic field line footpoints, asymmetric magnetosphere, asymmetric polar ionosphere

1 Introduction

The Earth's magnetic field can be divided in two topologically different regions: At very high latitudes, in the so-called *polar caps*, magnetic field lines are "open", connecting to the solar wind. The boundary of the polar cap approximately coincides with the poleward boundary of the aurora (e.g., Laundal et al., 2010; Longden et al., 2010). Equatorward of this, magnetic field lines are "closed", and intersect the ionosphere in two hemispheres. In the absence of parallel electric fields, plasma in the magnetosphere and

upper ionosphere does not cross magnetic field lines (e.g., Hesse et al., 1997), which means that the convection at the ionospheric intersection points of closed magnetic field lines is coupled. This coupling has long been incorporated in numerical models of low/mid latitude ionospheric dynamics (Richmond, 1995; Qian et al., 2014), but at high latitudes the implications of the coupling are still poorly understood.

Several studies of average ionospheric convection (Weimer, 2005a,Weimer, 2005b; Pettigrew et al., 2010; Thomas and Shepherd, 2018; Förster and Haaland, 2015) and electric currents (Weimer, 2001; Laundal et al., 2018) reveal how the interplanetary magnetic field (IMF) B_y component and the dipole tilt angle influence the polar ionosphere in opposite ways in the two hemispheres. The difference in convection in opposite hemispheres implies that the ionospheric footpoints of closed magnetic field lines move relative to each other. There must therefore be regions where footpoints are displaced relative to where they would be in the absence of convection, i.e., if the magnetic field was not disturbed by sources external to the Earth. Such displacements can be observed: Simultaneous observations of the aurora in the two hemispheres often show features that mirror each other—indications that they are produced by particles that precipitate from the same region in the magnetosphere. The displacement between corresponding features have shown a clear dependence on IMF B_y (Østgaard et al., 2004, Østgaard et al., 2005), consistent with an induced B_y component in the closed magnetosphere (Tenfjord et al., 2015). Observations indicate that the displacement is larger in the zonal direction than in the meridional direction. Displacements are typically 0–2 h magnetic local time (Østgaard et al., 2005), but can reach 3–4 h (Reistad et al., 2016; Østgaard et al., 2018). The magnitude of the displacement also depends on magnetospheric dynamics: Ohma et al. (2018) showed that the displacement decreases in step with nightside reconnection.

Observational estimates of displaced magnetic field lines have so far exclusively been made using simultaneous images of the aurora in the two hemispheres. Such observations are rare, and they typically only give the displacement at a single point in the nightside ionosphere. However, we expect that the displacement is different in different positions. Reistad et al. (2016) presented observations of both conjugate auroral features and ionospheric convection, showing that differences in return flow in the two hemispheres were consistent with a reduction in footpoint displacement towards the dusk flank. Simulations analyzed by Ohma et al. (2021) confirmed this non-uniformity and showed that the strongest displacements are expected at the most poleward closed field lines. Based on the studies above, it is expected that periods of low geomagnetic activity (small or northward B_z) are associated with large displacements. This is also consistent with the asymmetric azimuthal flows seen in the nighside auroral zone during northward IMF (Grocott et al., 2005, 2008), believed to be a manifestation of such large displacements.

The aims of this paper are to 1) generalize the concept of magnetic field-line footpoint displacement from single point measurements to a 2D vector field (called $\boldsymbol{\delta}$ below), 2) to lay out how the displacement field is related to ionospheric convection in the two hemispheres under the assumption of ideal magnetohydrodynamics (MHD), and 3) to use this relation to estimate the displacement field $\boldsymbol{\delta}$ from convection patterns in the two hemispheres.

In the approximation of ideal MHD

$$\mathbf{E} + \mathbf{v} \times \mathbf{B} = 0, \tag{1}$$

which means that the electric field $\mathbf{E}$ is entirely determined by the plasma velocity $\mathbf{v}$, which is frozen-in with the magnetic field $\mathbf{B}$. If, in addition, the electric field is a potential field in the ionosphere, $\mathbf{E}_{\text{ionosphere}} = -\nabla\Phi$, the electric potential Φ is the same at all points in the ionosphere that are connected by a magnetic field line. According to Hesse et al. (1997), the assumption of a potential electric field only has to hold in the ionosphere for the ionospheric potentials to map between hemispheres along magnetic field lines, but ideal MHD must hold everywhere.

Figure 1 shows an illustration of how the displacement field and the electric potential are related in a highly idealized situation: The magnetosphere (panel A) is a perfect dipole, with a purely westward perturbation magnetic field indicated by the color. The plot shows magnetic field lines traced from −60°, −65° (black), −70° (red), and −75° (green) to the northern hemisphere. Two sets of field lines are shown, separated by 90° longitude. The leftmost set of field lines would appear vertical with a dipole field, but clearly deviate from this due to the perturbation field. The displacement field, the deviation from dipole magnetic footpoint locations due to the perturbation magnetic field, is shown in panel B. The dots signify footpoints in the southern hemisphere and the pins point to the corresponding footpoint in the northern hemisphere. Panel C shows how an example electric potential in the southern hemisphere $\Phi_S(\boldsymbol{r})$ (shown in grey) changes when mapped to the northern hemisphere (black) due to the perturbation field. That is, $\Phi_N(\boldsymbol{r}) = \Phi_S(\boldsymbol{r} + \boldsymbol{\delta}(\boldsymbol{r}))$ where $\boldsymbol{\delta}(\boldsymbol{r})$ is the displacement field shown in panel B. The color in Figure 1C shows $\Delta\Phi = \Phi_N - \Phi_S$, the mismatch in potential between hemispheres at points connected by unperturbed dipole magnetic field lines. The example potential in this figure is from the Weimer (2005a),Weimer (2005b) model, with IMF B_y = 0 nT, Bz = −5 nT, solar wind velocity 400 km/s, density 8 cm^{-3}, and dipole tilt angle 0°.

Figure 1 is an example of how the displacement field can be calculated using field line tracing with perfect knowledge about the magnetic field surrounding the Earth, and how it influences the convection electric potential assuming ideal MHD. In the next section, we present a technique to estimate the displacement field $\boldsymbol{\delta}(\boldsymbol{r})$ given perfect knowledge about the electric potential in the two hemispheres, Φ_N and Φ_S. We apply this to the idealized

example in Figure 1 as an example. In Section 3 we present displacement fields implied by the Weimer (2005a),Weimer (2005b) empirical model of ionospheric convection given certain assumptions. We discuss results, limitations, and future prospects in Section 4.

2 Estimating the displacement field from convection maps

The relationship between the potentials in the two hemispheres and the footpoint displacement field $\boldsymbol{\delta}$ gives that:

$$\Phi_N(\mathbf{r}) = \Phi_S(\mathbf{r} + \boldsymbol{\delta}(\boldsymbol{r})) \approx \Phi_S(\mathbf{r}) - \mathbf{E}_S(\mathbf{r}) \cdot \boldsymbol{\delta}(\boldsymbol{r}), \tag{2}$$

where we used a first order Taylor expansion about $\mathbf{r}$, and that $\mathbf{E}_S = -\nabla\Phi_S$. Rearranging the terms, we find a relationship between $\boldsymbol{\delta}$ and the potential mismatch $\Delta\Phi = \Phi_N(\mathbf{r}) - \Phi_S(\mathbf{r})$:

$$\mathbf{E}_S(\mathbf{r}) \cdot \boldsymbol{\delta}(\boldsymbol{r}) = -\Delta\Phi. \tag{3}$$

Our aim is to find $\boldsymbol{\delta}(\boldsymbol{r})$ given Φ_N and Φ_S. To accomplish this, Eq. 3 is not sufficient, and we need additional constraints. The following discussion is an effort to include such constraints using knowledge about the magnetosphere-ionosphere system.

The displacement field $\boldsymbol{\delta}$ describes how a flux tube originating at $(\phi, -\lambda)$ in the Southern hemisphere, that nominally maps to (ϕ, λ) in the Northern hemisphere, now maps to a different location. ϕ and λ are here treated as longitude and latitude in modified Apex (MA) coordinates (Richmond, 1995). We use a MA reference radius $R = R_E + 110$ km, where R_E is the radius of the Earth. MA coordinates are defined such that ϕ and λ are constant along the magnetic field lines of a model magnetic field—usually the International Geomagnetic Reference Field (Alken et al., 2021), but in this paper a centered dipole. Assuming that the magnetospheric plasma and magnetic fields are frozen-in, the displacement $\boldsymbol{\delta}$ is a result of past differences in convection in the two hemispheres. The simplest possible differential convection field that can produce the displacement is $\mathbf{u} = \boldsymbol{\delta}/\Delta T$, a constant velocity that is present for a time interval ΔT. If we also assume that the magnetic field changes slowly, Faraday's law implies that $\mathbf{u}$, and hence also $\boldsymbol{\delta}$ relate to a potential field $-\nabla\alpha$:

$$\boldsymbol{\delta} = \frac{-\nabla\alpha \times \mathbf{B}}{B^2}. \tag{4}$$

Now we represent α in terms of a set of basis functions. We use surface spherical cap harmonics (Haines, 1985; Fiori, 2020; Torta, 2020):

$$\alpha = \sum_{k}^{25} \sum_{m}^{\max(k,3)} P^m_{n_k(m)}(\sin\lambda)\left[g^m_k \cos(m\phi) + h^m_k \sin(m\phi)\right], \tag{5}$$

where $P^m_{n_k(m)}(\sin\lambda)$ are the Legendre functions of non-integer $n_k(m)$ and integer m. Spherical cap harmonics map the global spherical harmonics to a spherical cap with a polar angle θ_0. We use $\theta_0 = 30^\circ$, which means that we do not consider displacements equatorward of 60°. The use of spherical cap harmonics has the advantage that certain boundary conditions can be applied in a straightforward way: We only use terms where $k - m$ are even, which ensures that $\partial P/\partial\lambda = 0$ for all k, m. α will therefore have zero gradient perpendicular to the equatorward boundary, and $\boldsymbol{\delta}$ can only be in the meridional direction. We truncate the sum over spherical cap harmonics at $k = 25$, $m = 3$. This truncation level, which is more or less in line with previous models of polar ionospheric electrodynamics (e.g., Weimer, 2013), is presumably not a limiting factor for the spatial resolution of our solution compared to other effects discussed below.

With the spherical cap harmonic representation for α, Eq. 5, we have discretized Eq. 3, so that $\boldsymbol{\delta}$ can be represented with 87 coefficients g^m_k and h^m_k. To use this representation, we must evaluate the gradients of α and Φ, which are perpendicular to $\mathbf{B}$ since α and Φ are magnetic field-aligned. In MA coordinates, the gradients of α and Φ have only two non-zero components. We express $\mathbf{E}$ and $\boldsymbol{\delta}$ in terms of MA basis vectors: $\mathbf{E} = E_{d_1}\mathbf{d}_1 + E_{d_2}\mathbf{d}_2$ and $\boldsymbol{\delta} = \delta_{e_1}\mathbf{e}_1 + \delta_{e_2}\mathbf{e}_2$. Equations 4.8, 4.9, 4.18, and 4.19 of Richmond (1995) give that:

$$E_{S,d_1} = \frac{-1}{R\cos\lambda}\frac{\partial\Phi_S}{\partial\phi} \tag{6}$$

$$E_{S,d_2} = \frac{1}{R\sin I}\frac{\partial\Phi_S}{\partial\lambda} \tag{7}$$

$$\delta_{e_1} = \frac{1}{B_{e_3}R\sin I}\frac{\partial\alpha}{\partial\lambda} \tag{8}$$

$$\delta_{e_2} = \frac{1}{B_{e_3}R\cos\lambda}\frac{\partial\alpha}{\partial\phi} \tag{9}$$

where

$$\sin I = 2\sin\lambda\left(4 - 3\cos^2\lambda\right)^{-1/2}. \tag{10}$$

$B_{e_3} = \mathbf{d}_3 \cdot \mathbf{B}$, where $\mathbf{d}_3$ is a magnetic field-aligned basis vector in modified apex coordinates. For a dipole field $B_{e_3} = B_0(4 - 3\cos^2\lambda)^{1/2}$, the magnetic field strength at $r = R$. B_{e_3} is constant along magnetic field lines. Here B_0 is $(R_E/R)^3$ times the reference magnetic field described by, e.g., Fraser-Smith (1987); Laundal and Richmond (2017). We use $B_0 = 28,000$ nT.

Since $\mathbf{d}_i \cdot \mathbf{e}_j = \delta_{ij}$, the dot product on the left hand side of Eq. (3) now gives:

$$\frac{1}{B_0R^2\sin(2\lambda)}\left[\frac{\partial\Phi_S}{\partial\phi}\frac{\partial\alpha}{\partial\lambda} - \frac{\partial\Phi_S}{\partial\lambda}\frac{\partial\alpha}{\partial\phi}\right] = \Delta\Phi. \tag{11}$$

where we used the expressions for B_{e_3} and $\sin I$. Eq. 11 can now be used to construct a set of linear equations that relate the spherical harmonic coefficients which define α to the electric potential in the two hemispheres.

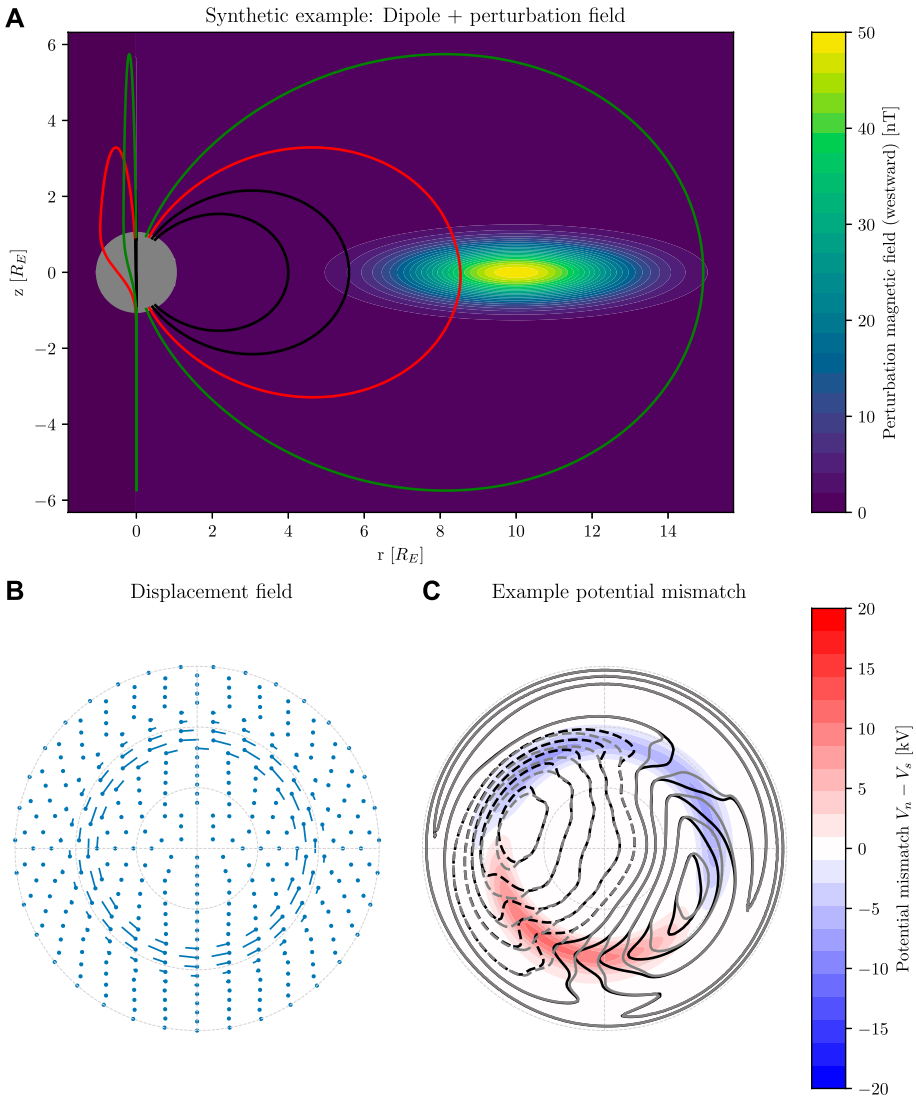

FIGURE 1
Conceptual illustration of the displacement field and its effect on ionospheric convection: **(A)** Magnetic field lines of a dipole magnetic field perturbed by a westward magnetic field indicated in color (a 2D Gaussian with peak value of 50 nT). The magnetic field lines are traced from – 60°, – 65° (black), – 70° (red), and – 75° (green) to the northern hemisphere. The dipole has a reference magnetic field (Fraser-Smith, 1987; Laundal and Richmond, 2017) of 28,000 nT. **(B)** The corresponding displacement field. The dots show footpoints in the southern hemisphere and the pins point to their conjugate point in the northern hemisphere, in a coordinate system where dipole magnetic field lines map to the same locations. In this, and in all subsequent polar plots, the view is down at the magnetic pole in the northern hemisphere, and through the Earth for the southern hemisphere, with noon on top and midnight at the bottom. The plots cover 60-90° latitude, with dashed circles every 10°. **(C)** An ionospheric convection electric potential in the southern hemisphere (grey) and the corresponding potential in the northern hemisphere (black) under the assumption that the potential maps along magnetic field lines between hemispheres. The color in the background show apparent potential misfit at coordinates that are connected by dipole magnetic field lines. The color scale used here is also used in subsequent figures.

2.1 Choosing the right reference frame

Eq. 3 involves the electric field, which is a frame-dependent quantity. As discussed by Newell et al. (2004), ionospheric convection electric fields are normally given in an Earth-fixed reference frame, which does not include the rotational motion of the Earth. The arguments above build on the premise that $\mathbf{E} + \mathbf{v} \times \mathbf{B} = 0$, which is a special case of the Generalized Ohm's law/electron momentum equation where all terms except the Lorentz force are zero. Since acceleration terms must also be zero, we believe that it is appropriate to transform $\mathbf{E}_S$ to an inertial frame by including a co-rotation electric field.

For a dipole field, the co-rotation can be expressed as

$$\mathbf{v}_c = \omega R \cos\lambda \mathbf{e}_1, \tag{12}$$

where $\omega \approx 2\pi/(24\text{ h})$ is the rotation rate of the Earth. $\omega R\cos\lambda$ is constant along magnetic field lines, and the variation in $\mathbf{v}_c$ is contained in $\mathbf{e}_1$, which is an eastward unit vector at radius R for a dipole magnetic field. This motion corresponds to a co-rotation potential via Equation (8):

$$\omega R\cos\lambda = \frac{1}{2B_0 R\sin\lambda}\frac{\partial \Phi_c}{\partial \lambda}, \tag{13}$$

where we replaced B_{e_3} with the dipole magnetic field strength at radius R, described above. Integrating this equation gives the co-rotation electric potential

$$\Phi_c = \omega B_0 R^2 \cos^2\lambda + \text{constant}. \tag{14}$$

Since Φ_c is equal on opposite ends of unperturbed magnetic field lines, it does not contribute to $\Delta\Phi$ in Eq. 3, but it does contribute to $\mathbf{E}_S$. If we did not include co-rotation, Eq. 3 would not constrain $\boldsymbol{\delta}$ in regions equatorward of the so-called Heppner-Maynard boundary (HMB) (Heppner and Maynard, 1987). Including co-rotation means that Eq. 3 helps to constrain $\boldsymbol{\delta}$ in the direction perpendicular to $\mathbf{e}_1 \times \mathbf{B}$ also equatorward of the HMB.

2.2 Inversion

If Φ_N and Φ_S (now assumed to include Φ_C) are given on a set of N points, we have N equations for as many unknowns as there are spherical harmonic coefficients, L (in our case 87). This set of equations can in principle be solved by inversion. The task is essentially to find the set of coefficients g_k^m and h_k^m that describes a displacement field $\boldsymbol{\delta}(\boldsymbol{r})$ which explains the observed potential mismatch $\Delta\Phi$. In matrix form, we write the set of equations as

$$G\mathbf{m} = \mathbf{d}, \tag{15}$$

where G is an $N \times L$ matrix, whose elements are given by Eq. 11 when (5) is used to represent α. $\mathbf{m}$ is an L-element vector composed of the spherical harmonic coefficients, and $\mathbf{d}$ is an N-element vector with the values of $\Delta\Phi$, the right-hand side of Eq. 11.

There are two major complicating factors in solving this set of equations for $\mathbf{m}$: First of all, the arguments presented above only hold for closed magnetic field lines—field lines that connect the two hemispheres. A large region surrounding the magnetic poles do not connect to the opposite hemisphere but instead connect out in the solar wind. In these regions of *open* magnetic flux (the polar caps), we expect to see mismatches in the potentials (Crooker and Rich, 1993; Reistad et al., 2019, 2021) that are unrelated to magnetic field line displacements. In regions that map to reconnection, we also expect there to be magnetic field-aligned potential differences between hemispheres (Siscoe et al., 2001). Thus, there is a region near the poles where Eq. 3 should not be applied. Because of this we do not use data points poleward of ±78°.

Since the polar caps vary in size (e.g., Milan et al., 2003; Laundal et al., 2010), such a hard limit is problematic. We therefore use an inversion scheme that allows for outliers, since there may well be points equatorward of 78° which should be allowed to have large potential misfits. This is accomplished through iteratively re-weighted least squares, with zeroth-order Tikhonov regularization. The first step in this procedure is to calculate an initial model vector $\mathbf{m}_0$, which represents the regularized least-squares solution:

$$\mathbf{m}_0 = \left(G^\top G + \kappa I\right)^{-1} G^\top \mathbf{d}, \tag{16}$$

where κ is a regularization parameter and I is the $L \times L$ identity matrix. Next, a set of weights is calculated, as

$$w_i = 1/\max\left(\epsilon, |d_{m,i} - d_i|\right), \tag{17}$$

where the index i gives the element in $\mathbf{d}$, and $d_{m,i}$ is the i'th element of the model prediction vector $G\mathbf{m}_0$. ϵ is a limit that prevents the weights from becoming extremely large. We use $\epsilon =$ 1 V, a low number considering that the potential mismatch is ~ 1 kV. After finding these weights, a second set of model parameters is calculated by calculating the weighted least-squares solution

$$\mathbf{m}_1 = \left(G^\top \text{diag}(\mathbf{w}) G + \kappa I\right)^{-1} G^\top \text{diag}(\mathbf{w})\mathbf{d}. \tag{18}$$

New weights and new model vectors are calculated until the model vector converges.

In this way, the influence of outliers is greatly reduced. In other words, model vectors that give large areas with small potential mismatch are prioritized over model vectors that accommodate a few small regions with large misfit. Except for the regularization term, the procedure outlined above effectively minimizes the L1 norm of the model data misfit $G\mathbf{m} - \mathbf{d}$ (Aster et al., 2019).

The regularization parameter κ is needed because of a second major complication: Eq. 3 only constrains $\boldsymbol{\delta}$ in the direction of $\mathbf{E}_S$, and it only constrains $\boldsymbol{\delta}$ where $\mathbf{E}_S$ is nonzero. In such regions, $\boldsymbol{\delta}$ is only constrained by the property that it can be written in terms of a potential (Eq. 4) and by the boundary condition that we apply. The magnetic field line footpoints may be displaced along equipotentials, ending up on the same electric potential and observations of $\Delta\Phi$ give no information about such displacements. We have no good fix for this problem, except to apply a conservative regularization scheme in the inversion to avoid artifacts, and to focus our analysis on regions that are well justified by coinciding electric fields.

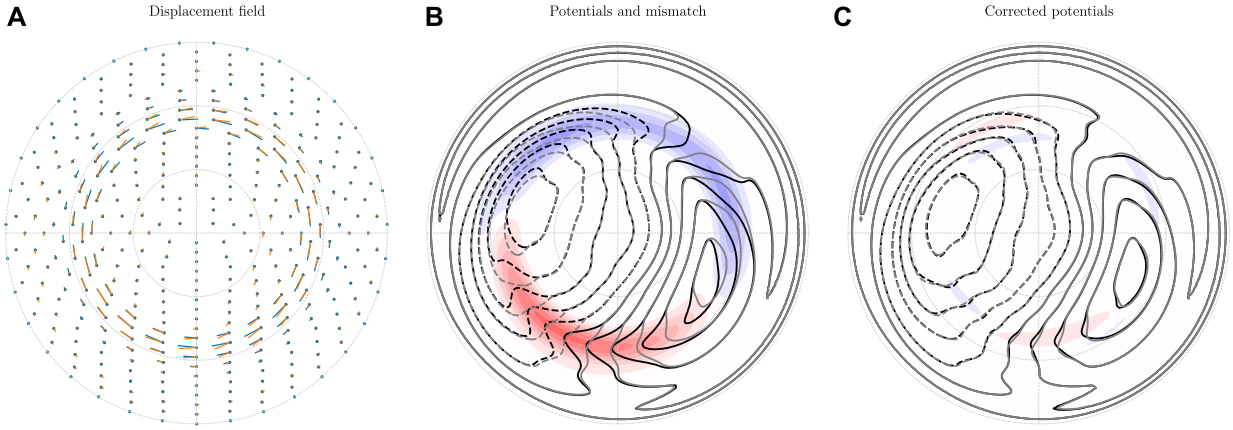

FIGURE 2
(A) The displacement field from Figure 1B, together with displacement field estimated using the technique described in Section 2 (orange pins). **(B)** The apparent potential mismatch that the displacement field is based on (a copy of Figure 1C), **(C)** The remaining potential mismatch when the estimated displacement field is taken into account in the comparison between hemispheres. The red-white-blue color scale is the same as in Figure 1.

2.3 Horizontal displacement field

The above procedure gives a set of model parameters $\mathbf{m}$, which are coefficients in the spherical cap harmonic representation of α, Eq. 5. This, in turn, relates to modified apex components of the displacement field $\boldsymbol{\delta}$ via Equations 8, 9. We have that

$$\boldsymbol{\delta} = \delta_{e_1}\mathbf{e}_1 + \delta_{e_2}\mathbf{e}_2, \tag{19}$$

where $\mathbf{e}_1$ and $\mathbf{e}_2$ are modified apex base vectors. In a dipole field at $r = R$, which we use throughout this paper, $\mathbf{e}_1$ is equal to the eastward unit vector in SM coordinates $\hat{\mathbf{e}}$. $\mathbf{e}_2$ is also a unit vector but it has both horizontal and vertical components:

$$\mathbf{e}_2 = \frac{-1}{\sqrt{4 - 3\cos^2(\lambda)}}\left(2\sin\lambda\hat{\mathbf{n}} + \cos\lambda\hat{\mathbf{r}}\right) \tag{20}$$

where $\hat{\mathbf{n}}$ and $\hat{\mathbf{r}}$ are unit vectors in the northward and radial directions in SM coordinates. In plots below, we show the horizontal SM components of $\boldsymbol{\delta}$. They can be written as

$$\boldsymbol{\delta}_h = \delta_{e_1}\hat{\mathbf{e}} - \sin I_m \delta_{e_2}\hat{\mathbf{n}}. \tag{21}$$

We note that in our implementation, we calculate the displaced coordinates at $\mathbf{r} + \boldsymbol{\delta}_h$ instead of mapping from $\mathbf{r} + \boldsymbol{\delta}$ to radius R. This simplification leads to an error which is very small since the magnetic field lines are close to vertical, and since $\boldsymbol{\delta}$ is always relatively small.

2.4 A synthetic test

Figure 2 shows the result of the technique described above applied to the synthetic example from Figure 1. In this case, the main field is a dipole, and there are no open field lines so we include $\Delta\Phi$s at high latitudes in the inversion. Apart from that, we use the regularization scheme described above. Figure 2 shows the synthetic (true) displacement field in blue (same as in Figure 1B) and the estimated $\boldsymbol{\delta}$ in orange. The estimates are based on the potentials shown in Figure 2B. Figure 2C shows the same, except that the northern hemisphere potential (black) has been "corrected" by shifting every point by a distance $-\boldsymbol{\delta}_h$. We see that our $\boldsymbol{\delta}$ removes most of the potential mismatch but not all.

In order to interpret the displacement fields that we derive in the next section, where we use statistical convection patterns from the two hemispheres, it is useful to compare the true displacement (blue) to the estimated displacement (orange) in Figure 2A. We see that they generally agree, but that there are notable deviations. For example, there are regions where $\boldsymbol{\delta}$ is too small. This is likely due to the damping that we apply in order to avoid creating artifacts. Decreasing the damping parameter reduces the potential mismatch in Figure 2C, but the estimated displacement field deviates more from the truth. Increasing the damping parameter leads to larger potential mismatches and smaller displacement fields, but with less artificial structures. We use the same damping parameter in the real (next section) and synthetic (this section) cases.

3 The displacement field implied by the Weimer 2005 convection model

The main message of the previous section is that knowledge about the electric potentials in the two hemispheres gives information about the displacement field $\boldsymbol{\delta}$ through Eq. (3). It is clear from the equation that $\boldsymbol{\delta}$

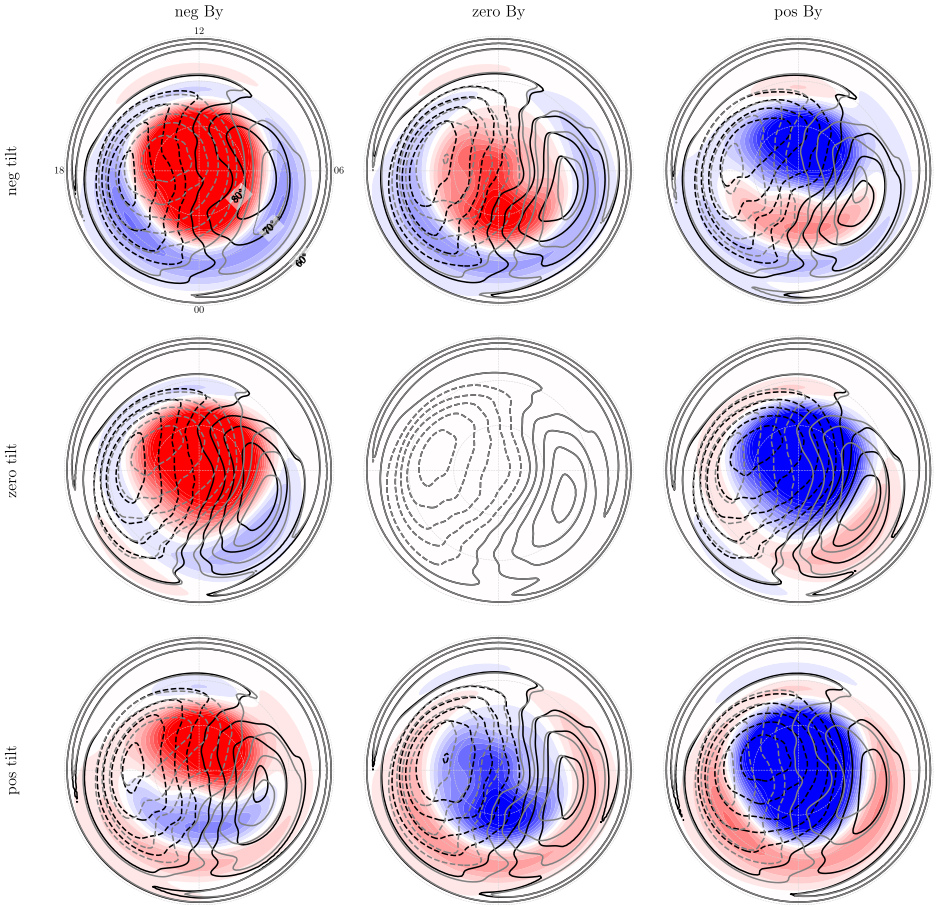

FIGURE 3
Nine different Weimer (2005a),Weimer (2005b) electric potentials from the southern (grey) and northern (black) hemispheres. The color shows the potential mismatch at matching coordinates, using the color scale from Figure 1. For all panels the solar wind velocity is 400 km/s, density 5 cm^{-3}, and $\sqrt{B_y^2 + B_z^2}$ = 5 nT. The three columns correspond to three different combinations of IMF clock angle, arctan2 (B_y, B_z); −225°, − 180°, and 135°. The three rows correspond to three different combinations of dipole tilt angle: ψ = −20°, 0°, and 20°.

is not fully determined: It gives no knowledge about $\boldsymbol{\delta}$ in the direction perpendicular to the electric field, or in regions where the electric field is zero. The rest of Section 2 is basically an effort to maximize the utility of this equation by taking into account expected properties of $\boldsymbol{\delta}$: It can be derived from a scalar potential α that is magnetic field-aligned, and it is relatively smooth. The synthetic test shows that the technique still has limitations, and one should be careful in interpreting the results, especially displacements along equipotentials.

Nevertheless, in this section we apply the technique described above to convection patterns from the statistical model by Weimer (2005a),Weimer (2005b), which is based on measurements from the Dynamics Explorer 2 satellite. The statistical model outputs convection maps as a function of solar wind speed and density, interplanetary magnetic field, and dipole tilt angle. The IMF B_y component and the dipole tilt angle ψ are expected to influence inter-hemispheric asymmetries in both convection and magnetic field line footpoints. In fact, Weimer mixes observations from the two hemispheres by assuming that the potential in the south is the same as the potential in the north for opposite signs of B_y and ψ:

$$\Phi\left(\lambda, B_y, \psi, \dots\right) = \Phi\left(-\lambda, -B_y, -\psi, \dots\right). \tag{22}$$

We have chosen convection maps for solar wind velocity 400 km/s, density 5 cm^{-3}, and $\sqrt{B_y^2 + B_z^2}$ = 5 nT. We investigate three different combinations of IMF clock angle, arctan2(B_y, B_z); −225°, −180°, and 135°; and three different combinations of dipole tilt angle: ψ = −20°, 0°, and 20°. This gives a total of nine combinations. We estimate the interhemispheric displacement field implied by these convection patterns, given the assumptions and caveats discussed in the previous section.

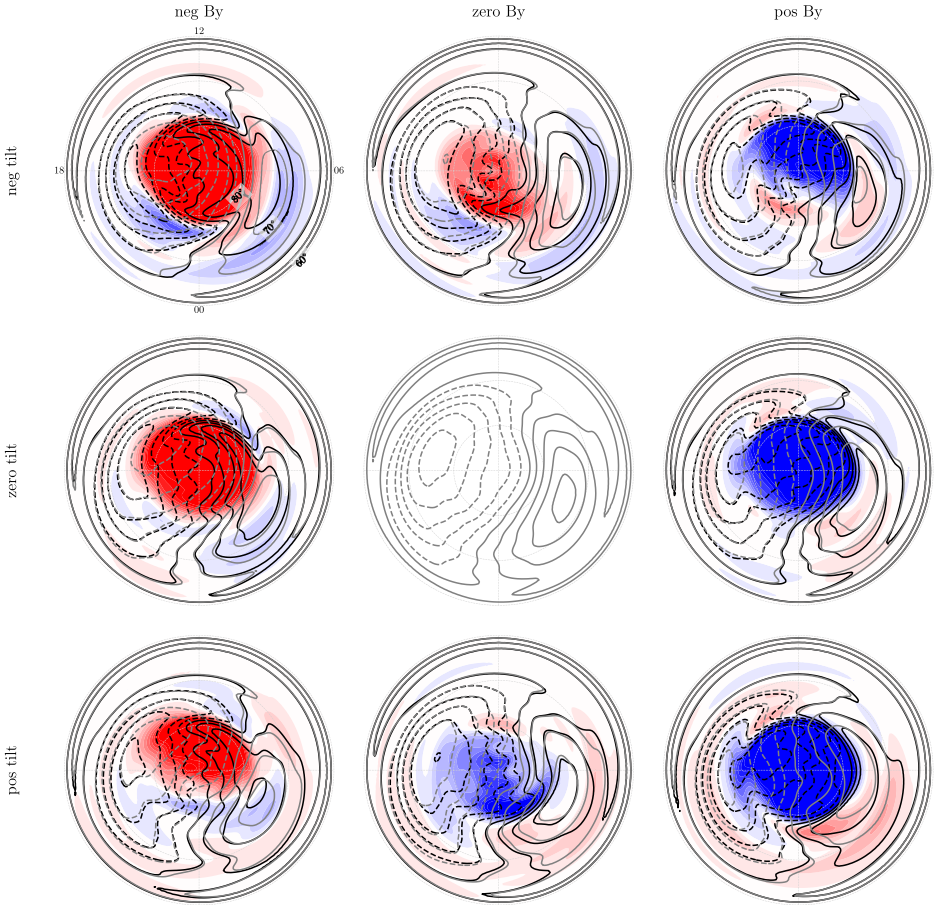

FIGURE 4
Weimer (2005a),Weimer (2005b) electric potentials in the same format as in Figure 3, but with the Northern hemisphere potentials shifted using our estimated displacement field. The red-white-blue color scale is the same as in Figure 1.

The convection potentials from the northern (black) and southern (grey) hemispheres for the nine different combinations are shown in Figure 3. Co-rotation has been added using the equations of Section 2.1. Because of Equation 22, the panels should be symmetric about the center, and the potentials in the center are exactly equal. Deviations from symmetry must be due to numerical effects related to the interpolation of the Weimer (2005a,b) potentials from the original grid to our evaluation points and in later figures also numerical effects related to the inversion.

Figure 3 shows large potential mismatches (the color scale is the same as in Figure 1), especially near the pole. Figure 4 shows the same convection potentials after shifting Φ_N by an amount $\boldsymbol{\delta}$, where the displacement field $\boldsymbol{\delta}$ is estimated as explained in the previous section. We see that the potential mismatches are significantly reduced, except for near the poles. This means that the displacement field that we have derived explains much of the mismatch on closed magnetic field lines.

The actual displacement field ($\boldsymbol{\delta}_h$) is shown in Figure 5. The pins show where magnetic field lines in the northern hemisphere that nominally map to the dot are shifted. We notice the following: 1) The displacement fields are non-uniform, which means that single point observations of field-line footpoint displacement (Østgaard et al., 2004; Østgaard et al., 2011; Ohma et al., 2018) are not enough to describe how the two hemispheres are connected. This point was also well illustrated by Ganushkina et al. (2013), who investigated latitudinal and longitudinal displacements in footpoint location using the Tsyganenko (2002) model. 2) The displacement is typically strongest in the midnight sector, and 3) this displacement appears to depend more strongly on the dipole tilt angle than on the sign of the IMF B_y. It is also interesting to note that the displacement field changes sign along the midnight meridian in all maps. We also see features in the displacement field which are almost certainly artifacts: The westward pins at ~ 65° post-noon in the top row (eastward in the bottom row) are more or less along equipotential contours. Including them in (Eq. 3) would not significantly increase or decrease $\Delta\Phi$, which means that their

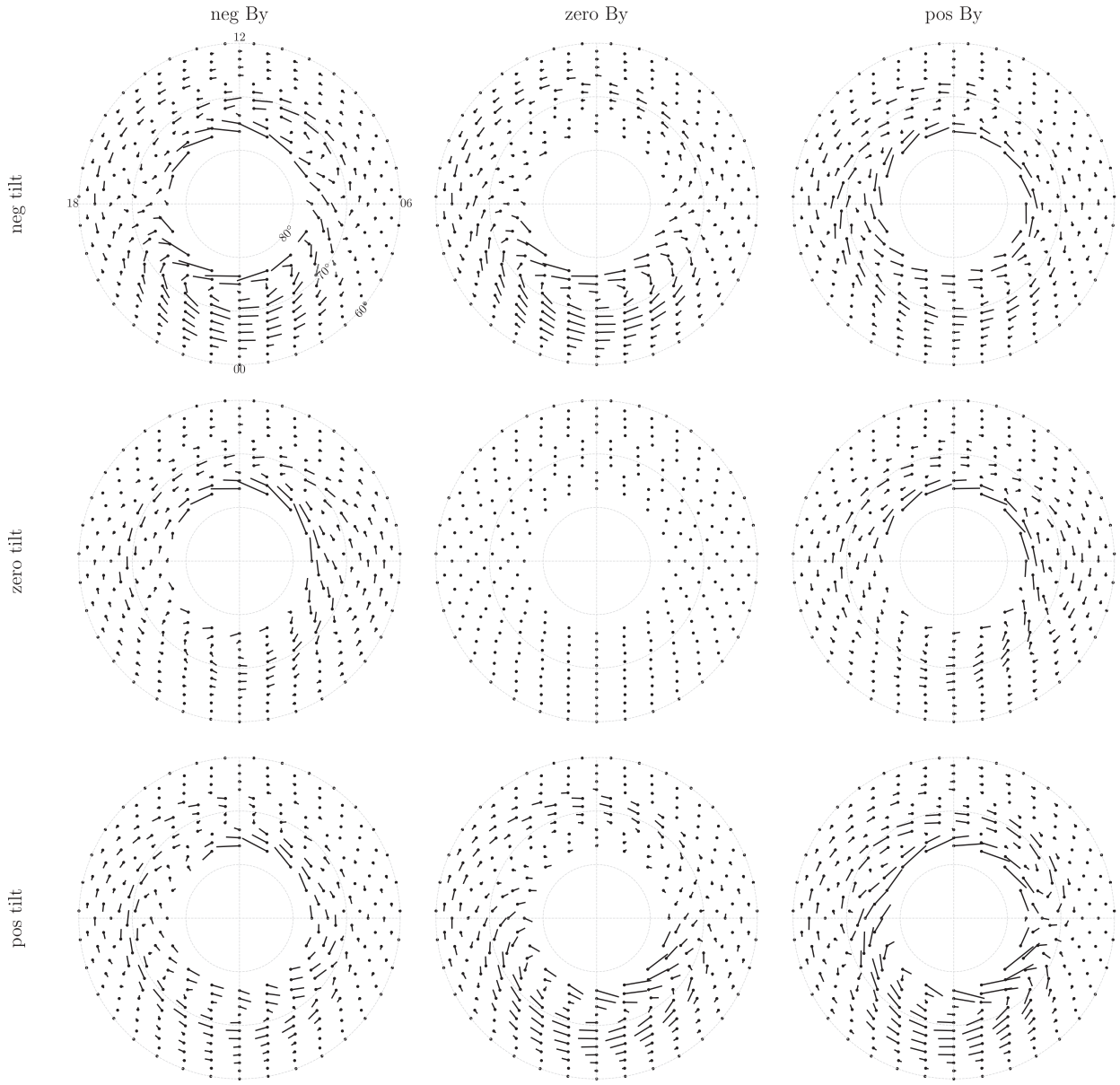

FIGURE 5
The displacement fields estimated from the potentials in Figure 3.

existence (or non-existence) is not substantiated by the observed potentials.

The strong dependence on dipole tilt angle is surprising. Observations of substorm onsets indicate that the effect of dipole tilt angle on magnetic field line footpoint displacement is weak (Elhawary et al., 2022). It is also surprising that the dipole tilt effect is in the same direction across the nightside. When the dipole axis is tilted, the tail is expected to "warp" tailward of the inner dipolar magnetic field lines (Fairfield, 1979; Liou and Newell, 2010). The warping of the tail would imply an additional B_y component with opposite signs at dawn and dusk (Petrukovich, 2011).

The B_y dependence seen in the displacement field is more expected: If we ignore the tilt effect, by looking at middle row, we see that positive B_y tends to give a displacement field that points from dawn to dusk, consistent with a B_y component induced in the magnetosphere as explained by Tenfjord et al. (2015), and observed by Wing et al. (1995); Tenfjord et al. (2017); Tsyganenko (2002). Negative B_y gives displacement fields in the opposite direction. These fields appear to maximize on the

noon-midnight meridian, which is also in line with expectations. The reversal at higher latitudes is however not expected from modeling and observations. One possible explanation is that field lines poleward of the reversal are on average open.

It is also interesting to note that the largest displacements are seen when B_y and tilt have the same sign. This was also observed by Petrukovich (2009) whose observations of B_y in the tail did not behave as one would expect from the warping effect, but instead showed that B_y correlates with dipole tilt angle at midnight and pre-midnight, and no effect post-midnight. This is more in line with the uniform displacement field seen on the nightside Figure 5. The magnitude of the dipole tilt angle effect seen in Figure 5, when compared to the B_y effect, is still surprising. In sum, comparisons with previous studies give good reason to be skeptical to the results presented in Figure 5. We elaborate on this skepticism in the next section.

4 Discussion

In this paper we have introduced the concept of a displacement field, a 2D vector field on a spherical shell that describes how magnetic field line footpoints in the northern hemisphere are displaced relative to their southern counterpart due to perturbations in the magnetic field of the magnetosphere. The concept of a non-uniform displacement vector field goes beyond previous studies that have studied the displacement at single points (Frank and Sigwarth, 2003; Østgaard et al., 2004; Østgaard et al., 2005; Ohma et al., 2018). We have argued that the displacement field must have the same mathematical properties as plasma convection in the F-region, where ideal MHD is assumed to be valid. It can be related to a scalar field (called α in this paper). We showed how the displacement field is related to the ionospheric convection in the two hemispheres in regions of closed magnetic field lines, and used this to estimate displacement fields implied by the Weimer (2005a),Weimer (2005b) empirical model of ionospheric convection.

We see a clear reduction in potential mismatch in the Weimer model with our derived displacement field (Figure 4 compared to Figure 3). This means that the displacement field and Weimer model are consistent to the extent of the remaining mismatch; but we should still be careful in reading too much into the estimated displacement fields. We have discussed some reasons for this above: The lack of information that we get from Eq. 3 where $\mathbf{E}_S \cdot \boldsymbol{\delta} = 0$, and the challenge in determining which regions to consider as covered by closed magnetic field lines. A third reason to be skeptical about the result is that the Weimer (2005a),Weimer (2005b) model was not designed to be consistent with a realistic displacement field. We expect that the uncertainty in electric potential values, which we use in our calculations, may be relatively large. The reason for this is that the model is constrained by measurements of the derivative of the potential and not by the potential itself. For example, regions in the Weimer model where the potential variations are small could lead to large and unrealistic displacements with our method. These regions would be based on measurements of weak plasma velocity, and it should not be expected that the coinciding potential contours are precisely determined. Nevertheless, we used the Weimer (2005a),Weimer (2005b) model in this paper because it is very well established, and we are not aware of any other empirical model that would be better suited for our purposes. The main purpose of estimating the displacement field in this way is to show that it is possible to link the two hemispheres using the assumption of ideal MHD, and that differences in convection electric potentials are related to the integrated effect of magnetic perturbations on the footpoints of closed magnetic field lines.

The displacement field shows how magnetic field line footpoints in the northern hemisphere are displaced relative to the expected position when tracing along a magnetic field model from the southern hemisphere. The Altitude-Adjusted Corrected Geomagnetic Coordinate system (Shepherd, 2014) and the Apex coordinate systems (VanZandt et al., 1972; Richmond, 1995) are constructed so that corresponding coordinates in the two hemispheres belong to the same model magnetic field line. We have used a dipole model, but one could also use more realistic models like the full International Geomagnetic Reference Field (Alken et al., 2021). Papitashvili et al. (1997) presented a coordinate system based on Tsyganenko (1989)'s model of the magnetospheric magnetic field. With such a model, if it is accurate, the ionospheric convection electric potential should be equal on matching coordinates (again assuming ideal MHD). Using this property with a modern magnetospheric model may be the most feasible way to construct an empirical model of ionospheric convection that by design is consistent in the two hemispheres.

A series of papers have explored the coupled hemispheres from an electric circuit perspective: Benkevich et al. (2000); Lyatskaya et al. (2014) suggested that incident magnetic field-aligned currents in one hemisphere can be redistributed in the ionosphere in both hemispheres via horizontal and interhemispheric field-aligned currents. The interhemispheric currents would primarily be located at the sunlight terminator where, from a circuit point of view, it would be easier to close currents in the opposite sunlit hemisphere. Observational tests of these ideas have not found such inter-hemispheric currents to exist (Østgaard et al., 2016). The models predicting inter-hemispheric currents did not take into account any displacement between magnetic field line footpoints. With the approach in the present paper, steady-state electric currents and the displacement field $\boldsymbol{\delta}$ can be related if we also know the ionospheric conductance, by use of the ionospheric Ohm's law. Whether or not the implied currents in the two hemispheres are connected to each other, or connect to other currents along the way in the magnetosphere, is not possible to tell by considering ionospheric observations alone.

Since we lack continuous observations of conjugate auroras, and since convection electric potential estimates are inaccurate, the best way to study the displacement field is probably with simulations. Ohma et al. (2021) showed that the displacement field reduces in step with nightside reconnection. However, they did not link the displacement to ionospheric convection. One reason why this may not be straightforward is that the ionospheric electric field in MHD codes is calculated independently in the two hemispheres, and there is therefore no guarantee that the potential matches on opposite ends of closed magnetic field lines. If it does not match, it means that there is a potential drop along magnetic field lines between hemispheres, in violation of the fundamental assumption of such models: That ideal MHD is valid. The displacement field and its relation to ionospheric electric potentials could be used to remove this possible inconsistency, by requiring that $\Phi_N(\boldsymbol{r}) = \Phi_S(\boldsymbol{r} + \boldsymbol{\delta})$ on closed field lines. $\boldsymbol{\delta}$ can be calculated by magnetic field line tracing, or by keeping track of the differences in ionospheric convection in the two hemispheres over time.

On the observational side, the most direct way of estimating displacement fields is to match features in the aurora. However, this has so far been done only on a point by point basis, when two satellites have happened to observe the two hemispheres simultaneously. A dedicated satellite mission to observe the aurora in both hemispheres (Branduardi-Raymont et al., 2021) would undoubtedly reveal the displacement field in much more detail, and greatly increase our understanding of geospace as a coupled two-hemisphere system.

Data availability statement

Publicly available datasets were analyzed in this study. This data can be found here: https://github.com/klaundal/displacement_field.

Author contributions

KL had the idea for the study, wrote the code and manuscript. MM made critical contributions to the inversion technique. AO helped with field line tracing and testing of the technique. JR and SH helped develop the idea, and supported the work throughout the process. All authors read and commented on the manuscript.

Funding

The work was funded by the Trond Mohn Foundation, and by the Research Council of Norway under contracts 223252/F50 and 300844/F50.

Weimer 2005 convection model output was provided by the Community Coordinated Modeling Center (CCMC) at Goddard Space Flight Center through their publicly available simulation services (https://ccmc.gsfc.nasa.gov). We are grateful to DW, Virginia Tech, for developing the Weimer 2005 model and for making it available *via* CCMC.

Conflict of interest

The authors declare that the research was conducted in the absence of any commercial or financial relationships that could be construed as a potential conflict of interest.

Publisher's note

References

Alken, P., Thébault, E., Beggan, C. D., Amit, H., Aubert, J., Baerenzung, J., et al. (2021). International geomagnetic reference field: The thirteenth generation. *Earth Planets Space* 73, 49. doi:10.1186/s40623-020-01288-x

Aster, R. C., Borchers, B., and Thurber, C. H. (2019). "Chapter two - linear regression," in *Parameter estimation and inverse problems*. Editors R. C. Aster, B. Borchers, and C. H. Thurber. 3rd edition (Netherland: Elsevier), 25–53. doi:10.1016/B978-0-12-804651-7.00007-9

Benkevich, L., Lyatsky, W., and Cogger, L. L. (2000). Field-aligned currents between conjugate hemispheres. *J. Geophys. Res.* 105, 27727–27737. doi:10.1029/2000ja900095

Branduardi-Raymont, G., Berthomier, M., Bogdanova, Y. V., Carter, J. A., Collier, M., Dimmock, A., et al. (2021). Exploring solar-terrestrial interactions via multiple imaging observers. *Exp. Astron. (Dordr).* doi:10.1007/s10686-021-09784-y

Crooker, N. U., and Rich, F. J. (1993). Lobe cell convection as a summer phenomenon. *J. Geophys. Res.* 98, 13403–13407. doi:10.1029/93JA01037

Elhawary, R., Laundal, K. M., Reistad, J. P., and Hatch, S. M. (2022). Possible ionospheric influence on substorm onset location. *Geophys. Res. Lett.* 49, e2021GL096691. doi:10.1029/2021GL096691

Fairfield, D. H. (1979). On the average configuraton of the geomagnetic tail. *J. Geophys. Res.* 84, 1950–1958. doi:10.1029/ja084ia05p01950

Fiori, R. A. D. (2020). "Spherical cap harmonic analysis techniques for mapping high-latitude ionospheric plasma flow—application to the swarm satellite mission," in *Ionospheric multi-spacecraft analysis tools. ISSI scientific report series*. Editors M. Dunlop and H. Lühr (Cham: Springer), 17. doi:10.1007/978-3-030-26732-2_9

Förster, M., and Haaland, S. (2015). Interhemispheric differences in ionospheric convection: Cluster EDI observations revisited. *J. Geophys. Res. Space Phys.* 120, 5805–5823. doi:10.1002/2014JA020774

Frank, L. A., and Sigwarth, J. B. (2003). Simultaneous images of the northern and southern auroras from the Polar spacecraft: An auroral substorm. *J. Geophys. Res.* 108, 8015. doi:10.1029/2002JA009356

Fraser-Smith, A. C. (1987). Centered and eccentric geomagnetic dipoles and their poles, 1600-1985. *Rev. Geophys.* 25, 1–16. doi:10.1029/rg025i001p00001

Ganushkina, N. Y., Kubyshkina, M. V., Partamies, N., and Tanskanen, E. (2013). Interhemispheric magnetic conjugacy. *J. Geophys. Res. Space Phys.* 118, 1049–1061. doi:10.1002/jgra.50137

Grocott, A., Milan, S. E., and Yeoman, T. K. (2008). Interplanetary magnetic field control of fast azimuthal flows in the nightside high-latitude ionosphere. *Geophys. Res. Lett.* 35, L08102. doi:10.1029/2008GL033545

Grocott, A., Yeoman, T. K., Milan, S. E., and Cowley, S. W. H. (2005). Interhemispheric observations of the ionospheric signature of tail reconnection during IMF-northward non-substorm intervals. *Ann. Geophys.* 23, 1763–1770. doi:10.5194/angeo-23-1763-2005

Haines, G. V. (1985). Spherical cap harmonic analysis. *J. Geophys. Res.* 90, 2583–2591. doi:10.1029/JB090iB03p02583

Heppner, J. P., and Maynard, N. C. (1987). Empirical high-latitude electric field models. *J. Geophys. Res.* 92, 4467–4489. doi:10.1029/JA092iA05p04467

Hesse, M., Birn, J., and Hoffman, R. A. (1997). On the mapping of ionospheric convection into the magnetosphere. *J. Geophys. Res.* 102, 9543–9551. doi:10.1029/96JA03999

Laundal, K. M., Finlay, C. C., Olsen, N., and Reistad, J. P. (2018). Solar wind and seasonal influence on ionospheric currents from Swarm and CHAMP measurements. *J. Geophys. Res. Space Phys.* 123, 4402–4429. doi:10.1029/2018JA025387

Laundal, K. M., Østgaard, N., Snekvik, K., and Frey, H. U. (2010). Interhemispheric observations of emerging polar cap asymmetries. *J. Geophys. Res.* 115. doi:10.1029/2009JA015160

Laundal, K. M., and Richmond, A. D. (2017). Magnetic coordinate systems. *Space Sci. Rev.* 206, 27–59. doi:10.1007/s11214-016-0275-y

Liou, K., and Newell, P. T. (2010). On the azimuthal location of auroral breakup: Hemispheric asymmetry. *Geophys. Res. Lett.* 37. doi:10.1029/2010GL045537

Longden, N., Chisham, G., Freeman, M. P., Abel, G. A., and Sotirelis, T. (2010). Estimating the location of the open-closed magnetic field line boundary from auroral images. *Ann. Geophys.* 28, 1659–1678. doi:10.5194/angeo-28-1659-2010

Lyatskaya, S., Khazanov, G. V., and Zesta, E. (2014). Interhemispheric field-aligned currents: Simulation results. *J. Geophys. Res. Space Phys.* 119, 5600–5612. doi:10.1002/2013ja019558

Milan, S. E., Lester, M., Cowley, S. W. H., Oksavik, K., Brittnacher, M., Greenwald, R. A., et al. (2003). Variations in the polar cap area during two substorm cycles. *Ann. Geophys.* 21, 1121–1140. doi:10.5194/angeo-21-1121-2003

Newell, P. T., Ruohoniemi, J. M., and Meng, C.-I. (2004). Maps of precipitation by source region, binned by IMF, with inertial convection streamlines. *J. Geophys. Res.* 109, A10206. doi:10.1029/2004JA010499

Ohma, A., Østgaard, N., Laundal, K. M., Reistad, J. P., Hatch, S. M., Tenfjord, P., et al. (2021). Evolution of IMF B_y induced asymmetries: The role of tail reconnection. *J. Geophys. Res. Space Phys.* 126, e2021ja029577. doi:10.1029/2021JA029577

Ohma, A., Østgaard, N., Reistad, J. P., Tenfjord, P., Laundal, K. M., Snekvik, K., et al. (2018). Evolution of asymmetrically displaced footpoints during substorms. *J. Geophys. Res. Space Phys.* 123, 10,030–10,063. doi:10.1029/2018JA025869

Østgaard, N., Humberset, B. K., and Laundal, K. M. (2011). Evolution of auroral asymmetries in the conjugate hemispheres during two substorms. *Geophys. Res. Lett.* 38. doi:10.1029/2010GL046057

Østgaard, N., Mende, S. B., Frey, H. U., Immel, T. J., Frank, L. A., Sigwarth, J. B., et al. (2004). Interplanetary magnetic field control of the location of substorm onset and auroral features in the conjugate hemispheres. *J. Geophys. Res.* 109, A07204. doi:10.1029/2003JA010370

Østgaard, N., Reistad, J. P., Tenfjord, P., Laundal, K. M., Rexer, T., Haaland, S. E., et al. (2018). The asymmetric geospace as displayed during the geomagnetic storm on 17 August 2001. *Ann. Geophys.* 36, 1577–1596. doi:10.5194/angeo-36-1577-2018

Østgaard, N., Reistad, J. P., Tenfjord, P., Laundal, K. M., Snekvik, K., Milan, S., et al. (2016). "Mechanisms that produce auroral asymmetries in conjugate hemispheres," in *Auroral dynamics and Space weather, geophysical monograph 215* (New York: John Wiley & Sons), 133–144.

Østgaard, N., Tsyganenko, N. A., Mende, S. B., Frey, H. U., Immel, T. J., Fillingim, M., et al. (2005). Observations and model predictions of substorm auroral asymmetries in the conjugate hemispheres. *Geophys. Res. Lett.* 32, L05111. doi:10.1029/2004GL022166

Papitashvili, V. O., Papitashvili, N. E., and King, J. H. (1997). Magnetospheric geomagnetic coordinates for space physics data presentation and visualization. *Adv. Space Res.* 20, 1097–1100. doi:10.1016/s0273-1177(97)00565-6

Petrukovich, A. A. (2009). Dipole tilt effects in plasma sheet b_y : Statistical model and extreme values. *Ann. Geophys.* 27, 1343–1352. doi:10.5194/angeo-27-1343-2009

Petrukovich, A. A. (2011). Origins of plasma sheet b_y. *J. Geophys. Res.* 116. doi:10.1029/2010JA016386

Pettigrew, E. D., Shepherd, S. G., and Ruohoniemi, J. M. (2010). Climatological patterns of high-latitude convection in the Northern and Southern hemispheres: Dipole tilt dependencies and interhemispheric comparisons. *J. Geophys. Res.* 115. doi:10.1029/2009JA014956

Qian, L., Burns, A. G., Emery, B. A., Foster, B., Lu, G., Maute, A., et al. (2014). *The NCAR TIE-GCM*. Washington: American Geophysical Union, 73–83. chap. 7. doi:10.1002/9781118704417.ch7

Reistad, J. P., Laundal, K. M., Østgaard, N., Ohma, A., Burrell, A. G., Hatch, S. M., et al. (2021). Quantifying the lobe reconnection rate during dominant IMF B_y periods and different dipole tilt orientations. *JGR. Space Phys.* 126, e2021JA029742. doi:10.1029/2021JA029742

Reistad, J. P., Laundal, K. M., Østgaard, N., Ohma, A., Thomas, E., Haaland, S., et al. (2019). Separation and quantification of ionospheric convection sources: 1. A new technique. *JGR. Space Phys.* 124, 6343–6357. doi:10.1029/2019JA026634

Reistad, J. P., Østgaard, N., Tenfjord, P., Laundal, K. M., Snekvik, K., Haaland, S., et al. (2016). Dynamic effects of restoring footpoint symmetry on closed magnetic field lines. *J. Geophys. Res. Space Phys.* 121, 3963–3977. doi:10.1002/2015JA022058

Richmond, A. D. (1995). Ionospheric electrodynamics using magnetic apex coordinates. *J. Geomagn. Geoelec.* 47, 191–212. doi:10.5636/jgg.47.191

Shepherd, S. G. (2014). Altitude-adjusted corrected geomagnetic coordinates: Definition and functional approximations. *J. Geophys. Res. Space Phys.* 119, 7501–7521. doi:10.1002/2014JA020264

Siscoe, G. L., Erickson, G. M., Sonnerup, B. U. O., Maynard, N. C., Siebert, K. D., Weimer, D. R., et al. (2001). Global role of $E_{\parallel}$ in magnetopause reconnection: An explicit demonstration. *J. Geophys. Res.* 106, 13015–13022. doi:10.1029/2000JA000062

Tenfjord, P., Østgaard, N., Snekvik, K., Laundal, K. M., Reistad, J. P., Haaland, S., et al. (2015). How the IMF by induces a by component in the closed magnetosphere and how it leads to asymmetric currents and convection patterns in the two hemispheres. *J. Geophys. Res.*, 9368–9384. doi:10.1002/2015JA02157

Tenfjord, P., Østgaard, N., Strangeway, R., Haaland, S., Snekvik, K., Laundal, K. M., et al. (2017). Magnetospheric response and reconfiguration times following IMF B_y reversals. *J. Geophys. Res. Space Phys.* 122, 417–431. doi:10.1002/2016JA023018

Thomas, E. G., and Shepherd, S. G. (2018). Statistical patterns of ionospheric convection derived from mid-latitude, high-latitude, and polar superdarn hf radar observations. *J. Geophys. Res. Space Phys.* 123, 3196–3216. doi:10.1002/2018JA025280

Torta, J. M. (2020). Modelling by spherical cap harmonic analysis: A literature review. *Surv. Geophys.* 41, 201–247. doi:10.1007/s10712-019-09576-2

Tsyganenko, N. A. (1989). A magnetospheric magnetic field model with a warped tail current sheet 37, *Planet. Space Sci.* 37. 5–20.

Tsyganenko, N. A. (2002). A model of the near magnetosphere with a dawn-dusk asymmetry 1. Mathematical structure. *J. Geophys. Res.* 107, SMP 12-1–SMP 12-15. doi:10.1029/2001JA000219

VanZandt, T. E., Clark, W. L., and Warnock, J. W. (1972). Magnetic apex coordinates: A magnetic coordinate system for the ionospheric F2 layer. *J. Geophys. Res.* 77, 2406–2411. doi:10.1029/ja077i013p02406

Weimer, D. (2001). Maps of ionospheric field-aligned currents as a function of the interplanetary magnetic field derived from Dynamics Explorer 2 data. *J. Geophys. Res.* 106, 12889–12902. doi:10.1029/2000ja000295

Weimer, D. R. (2013). An empirical model of ground-level geomagnetic perturbations. *Space weather.* 11, 107–120. doi:10.1002/swe.20030

Weimer, D. R. (2005a). Improved ionospheric electrodynamic models and application to calculating joule heating rates. *J. Geophys. Res.* 110, A05306. doi:10.1029/2004JA010884

Weimer, D. R. (2005b). Predicting surface geomagnetic variations using ionospheric electrodynamic models. *J. Geophys. Res.* 110, A12307. doi:10.1029/2005JA011270

Wing, S., Newell, P. T., Sibeck, D. G., and Baker, K. B. (1995). A large statistical study of the entry of interplanetary magnetic field y-component into the magnetosphere. *Geophys. Res. Lett.* 22, 2083–2086. doi:10.1029/95gl02261

frontiers | Frontiers in Astronomy and Space Sciences

TYPE Original Research
PUBLISHED 16 August 2022
DOI 10.3389/fspas.2022.953954

OPEN ACCESS

EDITED BY
Daniel Okoh,
National Space Research and Development Agency, Nigeria

REVIEWED BY
Vivian Otugo,
Rivers State University, Nigeria
Patrick Essien,
University of Cape Coast, Ghana

*CORRESPONDENCE
Michael Madelaire,
michael.madelaire@uib.no

SPECIALTY SECTION
This article was submitted to Space Physics, a section of the journal Frontiers in Astronomy and Space Sciences

RECEIVED 26 May 2022
ACCEPTED 05 July 2022
PUBLISHED 16 August 2022

CITATION
Madelaire M, Laundal KM, Reistad JP, Hatch SM and Ohma A (2022), Transient high latitude geomagnetic response to rapid increases in solar wind dynamic pressure.
Front. Astron. Space Sci. 9:953954.
doi: 10.3389/fspas.2022.953954

Transient high latitude geomagnetic response to rapid increases in solar wind dynamic pressure

Michael Madelaire*, Karl M. Laundal, Jone P. Reistad, Spencer M. Hatch and Anders Ohma

Birkeland Centre for Space Science, Bergen, Norway

Rapid changes in solar wind dynamic pressure can produce a transient geomagnetic response in the high latitude ionosphere. In this study we carry out a superposed epoch analysis of the geomagnetic response based on 2,058 events. The events are divided into 12 groups based on interplanetary magnetic field clock angle and dipole tilt and the magnetic perturbation field is modeled using spherical harmonics. We find that the high latitude transient current vortices associated with a sudden commencement are most clearly observed when the interplanetary magnetic field is northward during equinox and winter in the northern hemisphere. The high latitude geomagnetic response during northward interplanetary magnetic field is decomposed into a preliminary and main impulse. The preliminary impulse onset is 1–2 min prior to the onset of the low/mid latitude geomagnetic response and its rise time is 4–6 min. The main impulse onset is around 2 min after the low/mid latitude geomagnetic response and has a rise time of 6–11 min. When examining the change relative to pre-onset conditions a coherent transient geomagnetic response emerges for all IMF clock and dipole tilt angles. The current vortex associated with the main impulse on the dawnside appears at (9.3 ± 0.5 mlt, $64.8^\circ \pm 1.5^\circ$ mlat) and moves westward with a velocity of 5 ± 1.4 km/s. The vortex on the duskside appears at (15.3 ± 0.9 mlt, $65.8^\circ \pm 2.5^\circ$ mlat) and does not move significantly. In addition, the models were used to recreate the SMR index showing a significant mlt dependence on the magnetic perturbation above 40° mlat and below 10° mlat. The former is thought to be caused by high latitude ionospheric currents. The latter is potentially a combination of the event occurrence probability being skewed toward certain UT ranges for large dipole tilt angles and a UT dependence of the equatorial electrojet magnitude caused by the south atlantic magnetic anomaly.

KEYWORDS

solar wind dynamic pressure, rapid pressure increase, magnetospheric compression, sudden commencement, high latitude ionosphere, superposed epoch analysis, transient current vortex

1 Introduction

A (Storm) Sudden Commencement (SC) occurs when a rapid increase in solar wind dynamic pressure (P_d) impinges on our magnetosphere. These events are interesting as they allow us to observe a perturbation of the system and the subsequent transient response that unfolds in the following 10 s of minutes. In this study we focus on the geomagnetic response as observed from ground magnetometers and define SC as independent of whether or not it is followed by a geomagnetic storm as suggested by Curto et al. (2007).

SCs were initially thought to be associated with flux transfer events, but their connection to rapid changes in P_d was later shown in two case studies (Friis-Christensen et al., 1988; Glassmeier et al., 1989). In each study ground magnetometers were used to infer the ionospheric equivalent current which revealed transient current vortices.

A few years later Sibeck (1990), Kivelson and Southwood (1991) and Glassmeier and Heppner (1992) published theories on a mechanism that generates transient ionospheric current vortices. They all suggested that a shear flow close to the magnetopause or low-latitude boundary layer would give rise to Field Aligned Currents (FACs) that map to the ionosphere. However, they disagreed on the expected response. Sibeck (1990) and Kivelson and Southwood (1991) argue that the arrival of the solar wind pressure structure will launch a compression wave in the magnetosphere. This wave is faster than the solar wind in the magnetosheath and results in an expansion followed by a contraction of the magnetopause and thus two sets of twin vortices are created. Glassmeier and Heppner (1992) argues that a pressure pulse will create two sets of twin vortices while a single pressure increase/decrease will only result in a single set of twin vortices. Alternatively, it was suggested by Araki (1994), building on Tamao (1964), that the compression wave undergoes a mode conversion to a transverse mode inside the magnetosphere where gradients in Alfvenic speeds are large. Beside the theory of the underlying mechanism Araki (1994) presented a model of the expected response, D_{sc}, which was decomposed into two parts.

$$D_{sc} = DL + DP \tag{1}$$

DL refers to a step-like increase in the horizontal magnetic field component at low/mid latitudes due to an increased magnetopause current. DP refers to the ionospheric response dominant at high latitudes and is itself composed of two parts.

$$DP = DP_{PI} + DP_{MI} \tag{2}$$

The preliminary impulse PI and main impulse MI both refer to two sets of twin transient high latitude ionospheric current vortices generated during the SC (Araki, 1994). The PI is the first set of current vortices that are generated on the dayside i.e. one at pre-noon and another at post-noon. The electric current in the pre-noon vortex flows anti-clockwise while the current in the post-noon vortex is clockwise, i.e., similar to the NBZ current vortices generated during northward IMF due to lobe reconnection (Cowley and Lockwood, 1992). The MI is the second set of vortices, also generated at pre- and post-noon, however, the current flows opposite to that of the PI vortices, i.e., similar to that of the region 1/region 2 (R1/R2) current vortices (Cowley and Lockwood, 1992).

Our goal is to determine the influence of environmental parameters, such as Interplanetary Magnetic Field (IMF) clock angle and dipole tilt, on the development of the high latitude geomagnetic response to rapid increases in P_d. Due to the lack of data (events) in previous studies it has not been possible to carry out statistical studies on more than one environmental parameter without compromising the statistical integrity.

Many case studies of SCs have been conducted, e.g., Lam and Rodger (2001) tested the physical model presented by Araki (1994) against a single event. They found good correspondence between predictions and observations at high latitudes on the dayside while the predictions were less reliable at low latitudes and at night. Moretto et al. (2000) modeled the high latitude ionospheric response and resolved both growth and decay of current vortices, however, their propagation did not agree with Araki (1994), thus questioning the validity of the physical models with respect to real events. They noted that the shock normal was not parallel to the Sun-Earth line and might therefore result in an asymmetric geospace response which Araki (1994) did not take into account.

It is difficult to find instances where sensors are aligned optimally in the solar wind, magnetosheath, magnetosphere and on ground such that a full picture of the geospace response can be observed. Magnetohydrodynamic (MHD) simulations are therefore a very powerful tool as they provide a controlled environment where everything can be observed. Many studies have utilized MHD simulations in attempts to understand both the magnetospheric origin and the ionospheric response during rapid increases of P_d (Slinker et al., 1999; Keller et al., 2002; Fujita et al., 2003a,b, 2005; Ridley et al., 2006; Samsonov et al., 2010; Samsonov and Sibeck, 2013; Shi et al., 2014; Welling et al., 2021). These studies differ in several aspects. The MHD code used varies and in some cases the solar wind parameters uphold the Rankine-Hugoniot jump conditions and other times they do not. Some studies model common pressure changes while others model Carrington-like events. With these variabilities it is understandable that the resulting conclusions as to the magnetospheric origin also vary. Some studies agree with Araki (1994) that the magnetospheric vortices are generated inside the magnetosphere while others conclude that they are generated at the magnetopause. The studies conducted by Samsonov et al. (2010); Samsonov and Sibeck (2013) stand out as they do not agree with any of the preexisting theories. They suggest that the initial compression wave reflects on an inner boundary, probably the ionosphere, resulting in a sunward moving wave which by interacting with the anti-sunward flow creates a shear.

Russell et al. (1994a,b) and Russell and Ginskey (1995) present statistical studies of the geomagnetic response at low/mid latitudes during northward and southward IMF conditions. They found the geomagnetic response to be 18.4 nT/nPa$^{1/2}$ during northward IMF while it is 13.8 nT/nPa$^{1/2}$ (25% less) during southward IMF. Stauning and Troshichev (2008), Huang (2005) and Madelaire et al. (2022) carried out statistical studies of the transient high latitude response using the PCN index (World Data Center For Geomagnetism, Copenhagen, 2019), i.e., the Northern Polar Cap and refers to an index based on a single ground magnetometer station (Thule) close to the northern magnetic pole that attempts to quantify anti-sunward plasma convection in the polar cap. They found that the DP_{PI} and DP_{MI} corresponds to a negative and positive excursion in the PCN index, respectively. Madelaire et al. (2022) showed that the DP_{PI} and DP_{MI} peaked around 3 and 9 min after onset of the DL response. In addition, Stauning and Troshichev (2008) created maps of the equivalent ionospheric current using ground magnetometers showing the creation and decay of ionospheric current vortices, however, no environmental parameters were taken into account.

In this paper we carry out a superposed epoch analysis of the transient high latitude geomagnetic response using the list of rapid pressure increases presented by Madelaire et al. (2022). In Section 2, we describe the list of events and ground magnetometer data utilized to carry out the analysis. In Section 3, we describe the modeling technique employed in our superposed epoch analysis as well as how equivalent ionospheric currents are retrieved. In Section 4, we discuss the modeled transient high latitude geomagnetic response. In Section 5, we discuss the high latitude impact on low/mid latitude geomagnetic perturbations and the differences between our results and the physical models. Section 6 concludes the paper.

2 Data

The statistical analysis presented here is based on a list of 3,867 rapid increases in P_d presented by Madelaire et al. (2022). The Earth arrival time of each event is based on a correlation analysis between P_d and the SYM-H index. The moment P_d and SYM-H begin to increase are both referred to as onset. The onset is the common reference point used to combine data from multiple events. The events are divided into 12 groups based on IMF clock angle and dipole tilt, and are identical to those defined by Madelaire et al. (2022). Dipole tilt, θ_d, is separated into three groups and IMF clock angle, θ_c, into four groups which when combined make 12 groups. Dipole tilt is positive when the northern hemisphere points toward the Sun and the three associated groups are referred to as season. Equation 3 summarize the criteria used,

$$\begin{aligned}
&\text{Summer} && : && (13^\circ < && \theta_d) && && \\
&\text{Equinox} && : && (-13^\circ < && \theta_d && < 13^\circ) \\
&\text{Winter} && : && (\theta_d && && < -13^\circ) \\
&B_Z+ && : && (-55^\circ < && \theta_{c,a} && < 55^\circ) \cap (-55^\circ < && \theta_{c,b} < 55^\circ) \\
&B_Y+ && : && (55^\circ < && \theta_{c,a} && < 125^\circ) \cap (55^\circ < && \theta_{c,b} < 125^\circ) \\
&B_Z- && : && (125^\circ < && \theta_{c,a} && < -125^\circ) \cap (125^\circ < && \theta_{c,b} < -125^\circ) \\
&B_Y- && : && (-125^\circ < && \theta_{c,a} && < -55^\circ) \cap (-125^\circ < && \theta_{c,b} < -55^\circ),
\end{aligned} \tag{3}$$

where $\theta_{c,b}$ and $\theta_{c,a}$ refer to the IMF clock angle before and after the rapid increase in P_d. After imposing these event selection criteria the list of events is reduced to 2058. Supplementary Table S1 in the supplementary materials summarizes the number of events in each group.

The focus of our analysis is the ground magnetic perturbation associated with the identified events. Superposing multiple events allows for global coverage of the geomagnetic response. Measurements of the magnetic perturbation field are provided by the SuperMAG web service (https://supermag.jhuapl.edu/). It is given in a local magnetic coordinate system, assumed to be aligned with the Earth's main field, with a 1-min temporal resolution (Gjerloev, 2012). We further processed the data by rotating it into geocentric coordinates using the CHAOS-7.2 model (Finlay et al., 2020) and then into Quasi-Dipole (QD) coordinates. The QD reference frame is height dependent and maps along field lines; it is therefore useful when studying phenomena at a specific height such as ionospheric currents (Laundal and Richmond, 2017). Only data from the northern hemisphere is used in this study as data coverage in the southern hemisphere is sparse, especially at high latitudes.

3 Methods

The main purpose of the list of rapid P_d increases published in Madelaire et al. (2022) was to facilitate a superposed epoch analysis of SCs. Madelaire et al. (2022) presented such an analysis based on geomagnetic indices, which is difficult at high latitude since the complexity of the polar ionospheric current can hardly be summarized in a single index. In this study we aim to represent ground magnetometer data in terms of a spherical harmonic (SH) expansion and then calculate the equivalent horizontal currents and FACs. This section will provide a summary of SHs, how the inverse problem is solved and finally how equivalent currents are calculated.

3.1 Spherical harmonics

If the divergence and curl of a vector field are zero it can be fully described by a scalar potential field which will satisfy Laplace's equation. It can be argued that this is true for the magnetic field measured on ground. A rigorous presentation of

this is given in Chapman and Bartels (1940). The magnetic potential field can be expanded in terms of spherical harmonic:

$$V(r,\theta,\phi) = a\sum_{n=1}^{\infty}\sum_{m=0}^{n}\left(\left[g_n^m\cos(m\phi) + h_n^m\sin(m\phi)\right]\left(\frac{a}{r}\right)^{n+1} + \left[q_n^m\cos(m\phi) + s_n^m\sin(m\phi)\right]\left(\frac{r}{a}\right)^{n}\right)P_n^m(\cos(\theta)) \tag{4}$$

where a is the reference radius, r is radius, θ co-latitude, ϕ longitude, (g_n^m, h_n^m) are the SH coefficients related to the internal field, (q_n^m, s_n^m) are the SH coefficients related to the external field, $P_n^m(\cos(\theta))$ are Schmidt quasi-normalized Legendre functions, and n and m are the SH-degree and -order, respectively.

3.2 Inverse problem

The magnetic field components are easily retrieved by evaluating the negative derivative of the potential. This presents a linear relationship between magnetic field observations and the SH coefficients that can be expressed in matrix format as

$$\boldsymbol{d} = \boldsymbol{G}\boldsymbol{m} \tag{5}$$

where $\boldsymbol{d}$ and $\boldsymbol{m}$ contain observations and SH coefficients, respectively,

$$\boldsymbol{d} = \left[\boldsymbol{B}_r, \boldsymbol{B}_\theta, \boldsymbol{B}_\phi\right]^T, \quad \boldsymbol{m} = \left[g_1^0, q_1^0, g_1^1, h_1^1, \ldots, q_n^m, s_n^m\right]^T \tag{6}$$

while $\boldsymbol{G}$, the data kernel, describes the linear relation between the two.

The inverse problem, to isolate $\boldsymbol{m}$ in Eq. 5, can conveniently be solved using a least squares approach where the 2-norm of the data misfit is minimized. Depending on the nature of the observations this approach can be prone to overfitting. In this study the inversion method is modified with a combination of iterative reweighting and Tikhonov regularization. The resulting objective function becomes

$$\Phi(\boldsymbol{m}) = (\boldsymbol{d} - \boldsymbol{G}\boldsymbol{m})^T\boldsymbol{W}(\boldsymbol{d} - \boldsymbol{G}\boldsymbol{m}) + \alpha^2\boldsymbol{m}^T\boldsymbol{L}^T\boldsymbol{L}\boldsymbol{m} \tag{7}$$

where $\boldsymbol{W}$ are data weights, α is the regularization parameter determining the trade-off between minimizing data misfit and the model norm, and $\boldsymbol{L}$ describes the nature of the regularization. When minimizing the model 2-norm $\boldsymbol{L}^T\boldsymbol{L}$ is a diagonal matrix and commonly the identity matrix. A minimum in Φ can be found by imposing $\frac{\partial}{\partial \boldsymbol{m}}\Phi(\boldsymbol{m}) = 0$ on Eq. 7 and isolating for $\boldsymbol{m}$.

$$\boldsymbol{m} = \left(\boldsymbol{G}^T\boldsymbol{W}\boldsymbol{G} + \alpha^2\boldsymbol{L}^T\boldsymbol{L}\right)^{-1}\boldsymbol{G}^T\boldsymbol{W}\boldsymbol{d} \tag{8}$$

Here $\boldsymbol{W}$ is decomposed into $\boldsymbol{W} = \boldsymbol{W}_d \circ \boldsymbol{W}_r$ where $\boldsymbol{W}_d$ and $\boldsymbol{W}_r$ refer to weights related to data coverage and iterative reweighting, respectively.

The iterative reweighted scheme used in this study applies Huber weights (Constable, 1988; Huber and Ronchetti, 2009) that are iteratively updated until the maximum percentage change of the model 2-norm between the previous and current iteration is equal to or less than 0.01% (Aster et al., 2013b). The weights based on data coverage are unchanging throughout the iterations and used to reduce spatial bias. They are determined as the inverse of the amount of observations in each cell of an equal area grid.

The Tikhonov regularization scheme applied here assumes $\boldsymbol{R} = \boldsymbol{L}^T\boldsymbol{L}$ to be diagonal. The values that populate the diagonal of $\boldsymbol{R}$ is based on the Lowes-Mauersberger power spectrum (Sabaka et al., 2014) for internal $W_n^i(r)$ and external $W_n^e(r)$ sources, Eq. 9, evaluated at ionospheric heights. Due to a dependence on height relative to the reference height and SH degree, the external field and higher harmonic terms will be dampened more severely than the internal field and lower harmonic terms, respectively.

$$W_n^i(r) = R_i(n)\sum_{m=0}^{n}\left[(g_n^m)^2 + (h_n^m)^2\right], \quad R_i(n) = (n+1)\left(\frac{a}{r}\right)^{2n+4}$$
$$W_n^e(r) = R_e(n)\sum_{m=0}^{n}\left[(q_n^m)^2 + (s_n^m)^2\right], \quad R_e(n) = n\left(\frac{r}{a}\right)^{2n-2} \tag{9}$$

Applying regularization necessitates choosing a value for the regularization parameter. This is done automatically for each epoch using Generalized Cross-Validation (GCV) (Aster et al., 2013a) to ensure reproducibility and reduce human bias. The optimal value for the regularization parameter can be found by solving the inverse problem, Eq. 8, for a series of α-values and evaluate the GCV score, Eq. 10 where N is the number of observations. The optimal value of α is related to the lowest GCV score. As this approach can be computational very heavy, we implemented a simple steepest descent algorithm to minimize unnecessary computations.

$$GCV(\alpha^2) = \frac{N}{\mathrm{Tr}\left[\boldsymbol{I} - \boldsymbol{G}\boldsymbol{G}^{-\alpha}\right]^2}\sum_{k=1}^{N}\left[(\boldsymbol{d} - \boldsymbol{G}\boldsymbol{m})^T\boldsymbol{W}(\boldsymbol{d} - \boldsymbol{G}\boldsymbol{m})\right]_k$$
$$\boldsymbol{G}^{-\alpha} = \left(\boldsymbol{G}^T\boldsymbol{W}\boldsymbol{G} + \alpha^2\boldsymbol{L}^T\boldsymbol{L}\right)^{-1}\boldsymbol{G}^T\boldsymbol{W} \tag{10}$$

In addition to reducing the model 2-norm the inverse problem is constrained by truncating the SH-degree at 40 resulting in 1,680 model parameters. The model is further constrained by 1) using only $n - m$ odd terms which enforces hemispheric symmetry. 2) truncating the SH-order at 3 under the assumption that the east/west gradient is more smooth than the north/south gradient (Laundal et al., 2016). As a result of these two constraints the amount of model parameters is reduced to 272.The combination of iterative reweighting and Tikhonov regularization has been sketched out in Algorithm 1.In order to evaluate the variance in the model solutions a bootstrapping approach was taken. The inverse problem for each group of events was repeated 50 times while resampling the events going into the solution with replacement. Predictions from the various model realizations thus provide a variance estimate.

Algorithm 1. Inversion scheme.

```
generate_required_data();    # G, d, R, W
for all α do
  reset_weights();    # Preparing for a new run.
  while conv ≥ threshold do
    if iteration > 1 then
      calculate_weights();    # Based on the initial inversion.
    end if
    solve_inv_problem();
    if iteration == 1 then
      calculate_sigma();    # Used to calculate Huber weights.
    end if
    if iteration > 1 then
      calculate_convergence();    # Check if the solution has converged
    end if
  end while
  calculate_gcv();    # Done for all α.
end for
find_min_gcv();    # Determine the optimal regularization parameter.
```

3.3 Equivalent currents

The equivalent horizontal ionospheric current (EHIC) can similarly be represented by a scalar potential (Laundal et al., 2016) and therefore expressed in terms of the same SH coefficients as in Eq. 4.

$$\Psi = \frac{a}{\mu_0}\sum_{n,m}\frac{2n+1}{n+1}\left(\frac{a+h}{a}\right)^n P_n^m(cos(\theta))\left[q_n^m cos(m\phi) + s_n^m sin(m\phi)\right] \tag{11}$$

Here h is the height with respect to a where the potential is evaluated. It is important to point out that Eq. 11 is the current potential expressed by the external magnetic field and h is therefore set to 110 km.

Evaluating the horizontal gradient of Ψ gives the EHIC.

$$\boldsymbol{j}_\perp = \hat{\boldsymbol{r}} \times \nabla\Psi \tag{12}$$

Where $\hat{\boldsymbol{r}}$ is a unit vector in the radial direction. The magnetic perturbation as a result of the ionospheric Hall current can be set equal to $\mathbf{j}_\perp$ if the magnetic field lines are assumed to be radial and the conductance uniform (Fukushima, 1969, 1976). Additionally, following Amm et al. (2002) an expression for the FACs can be written as

$$j_\parallel = \beta^{-1}\left[\nabla \times \boldsymbol{j}_\perp\right]_r \tag{13}$$

where β is the Hall and Pedersen conductance ratio and assumed to be constant. Equation 13 can be written in terms of Ψ by applying the relation from equation 34 in Sabaka et al. (2014).

$$j_\parallel = \frac{n(n+1)}{\beta r^2}\Psi \tag{14}$$

β is still unknown and will later be assumed to be 1 resulting in what we will refer to as equivalent field aligned currents (EFACs). Thus providing estimates of the EHIC and EFAC in terms of SH coefficients.

4 Results

A rapid increase in P_d can cause a SC which is commonly decomposed into two main parts; the low/mid and high latitude geomagnetic response, Eq. 1, with varying spatial and temporal scales. Madelaire et al. (2022) carried out a superposed epoch analysis of the SMR and PCN index in order to examine these geomagnetic responses. In this study we carry out a superposed epoch analysis using SH modeling. With this approach we create a continuous model, in space, based on multiple events allowing us to estimate magnetic field perturbations and ionospheric equivalent currents. In this section we 1) present model results prior to onset to illustrate the methods ability to recreate IMF and dipole tilt dependent current patterns and 2) examine incoherent and coherent high latitude ionospheric responses and the dependence on IMF orientation and dipole tilt.

4.1 Prior patterns

This study builds on the premise that a superposed epoch analysis using a spherical harmonic modeling technique is capable of robustly reproducing the underlying pattern common for a majority of events in a group. As an initial assessment Figure 1 shows the mean and standard deviation of the external radial magnetic field perturbation B_r across all 50 model realizations at epoch −5 (5 min prior to onset) for all 12 event groups above 50° mlat (magnetic latitude). The figure is divided into three rows indicating dipole tilt and four columns indicating IMF clock angle. The magnitude of the model predictions vary significantly across groups and the maps have therefore been given individual colorbars. The number in the upper right corner of each map indicate the maximum of their respective colorbars, in units of nT.

Maps of the mean are in good agreement with previous studies on current patterns and their dependency on IMF clock angle and dipole tilt (Cowley and Lockwood, 1992; Pettigrew et al., 2010; Weimer, 2013; Laundal et al., 2018). Predictions during summer are of higher magnitude than equinox and winter mainly as a result of variations in sunlight-induced conductivity and auroral precipitation with decreasing dipole tilt (Moen and Brekke, 1993; Liou et al., 2001). During B_Z+ there are strong NBZ currents and overall stronger currents on the duskside as a result of co-rotation (Förster et al., 2017). During B_Z-region 1 and 2 (R1/R2) currents are strong as a result of reconnection on both day and nightside giving rise to a two-cell current pattern. During B_Y± conditions the dawn and dusk cells become more circular or crescent as a result of the dayside reconnection geometry, giving rise to alternate current paths.

10.3389/fspas.2022.953954

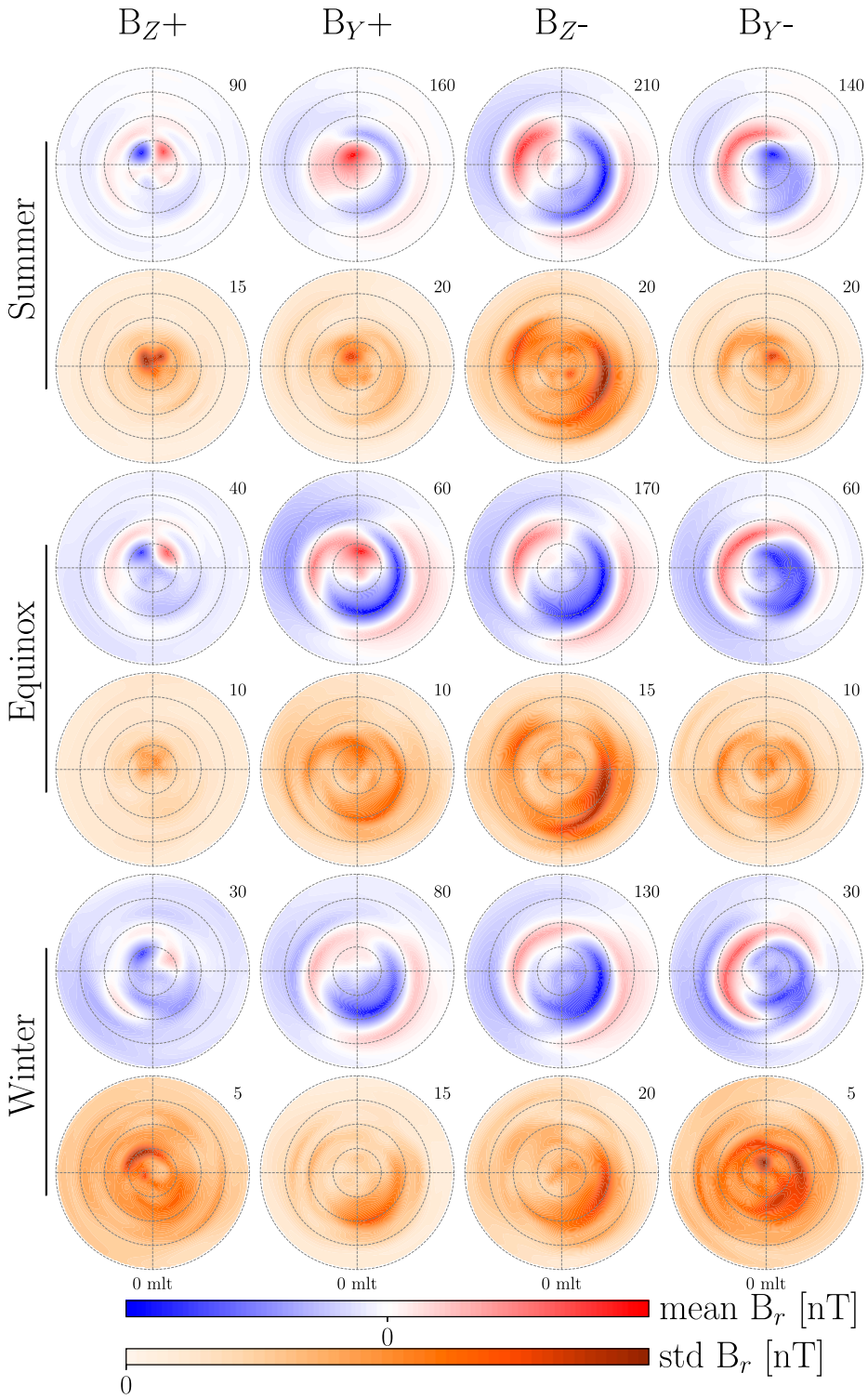

FIGURE 1
Illustration of the average model and its variation 5 min prior to onset. Each map shows either the mean or standard deviation of B_r as predicted by the 50 model realizations. The number in the upper right corner of each map indicates the magnitude of the colorbars for that specific map in units of nT. The columns and rows indicate the IMF clock and dipole tilt angle, respectively.

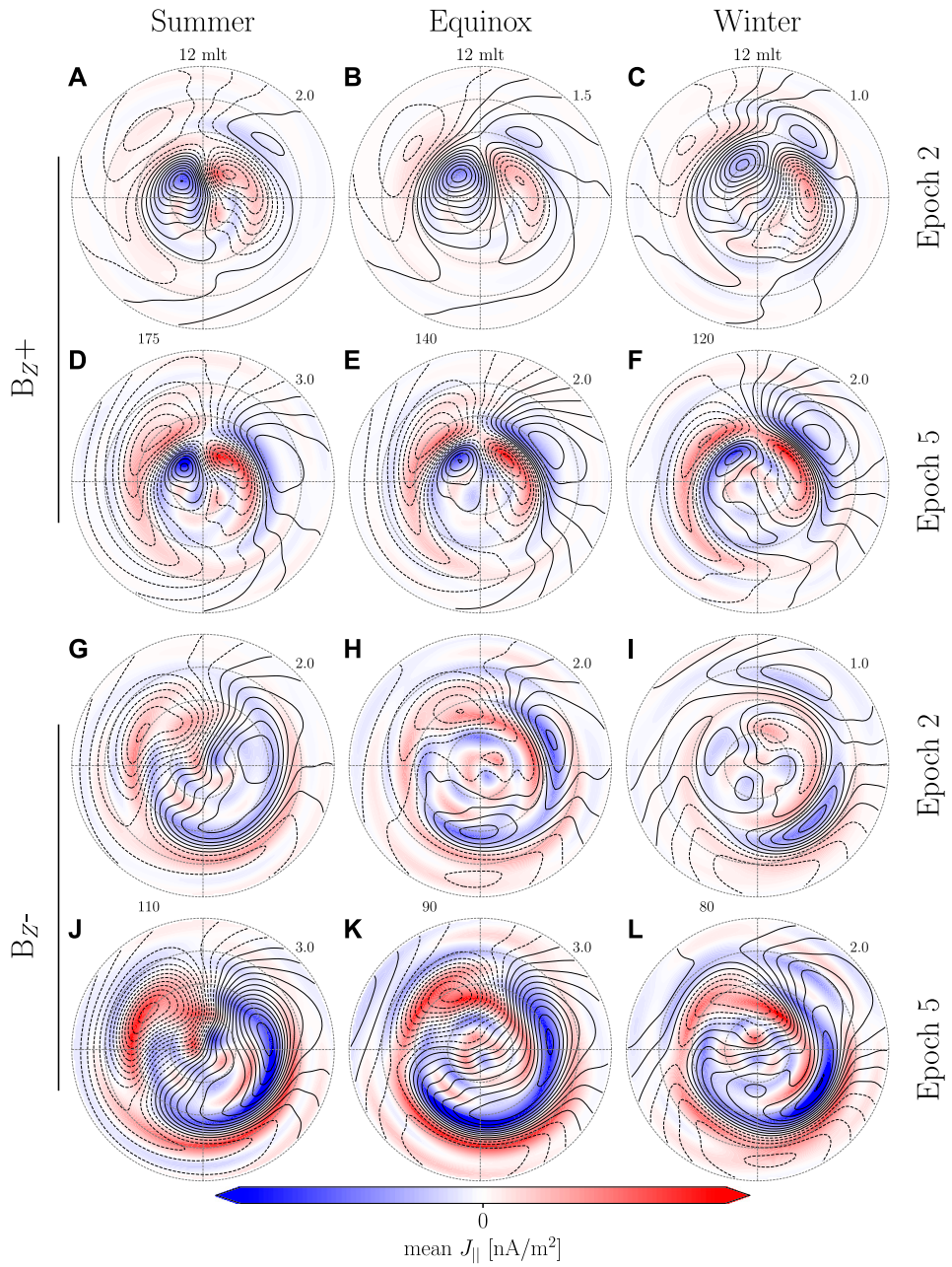

FIGURE 2
Maps of EHIC and EFAC 5 min before and after onset for the B_Z groups. The colored contour indicates EFACs while Ψ is shown by the black equipotential lines. Each set of figures is described by the two numbers written between them. The first indicates the step size of Ψ in kA while the second indicates the maximum of their unique colorbar.

Variation between model realizations is generally low, but can become large near the edges of current cells as a result of a varying latitudinal extent of the cells. The variations might be reduced if the magnitude of the IMF and increase in P_d was taken into account when creating the event groups.

4.2 High latitude geomagnetic response

The geomagnetic response is divided in two, Eq. 1. DP is further divided into PI (preliminary impulse) and MI (main impulse), Eq. 2, representing two sets of transient convection vortices. The resulting magnetic perturbation is superimposed

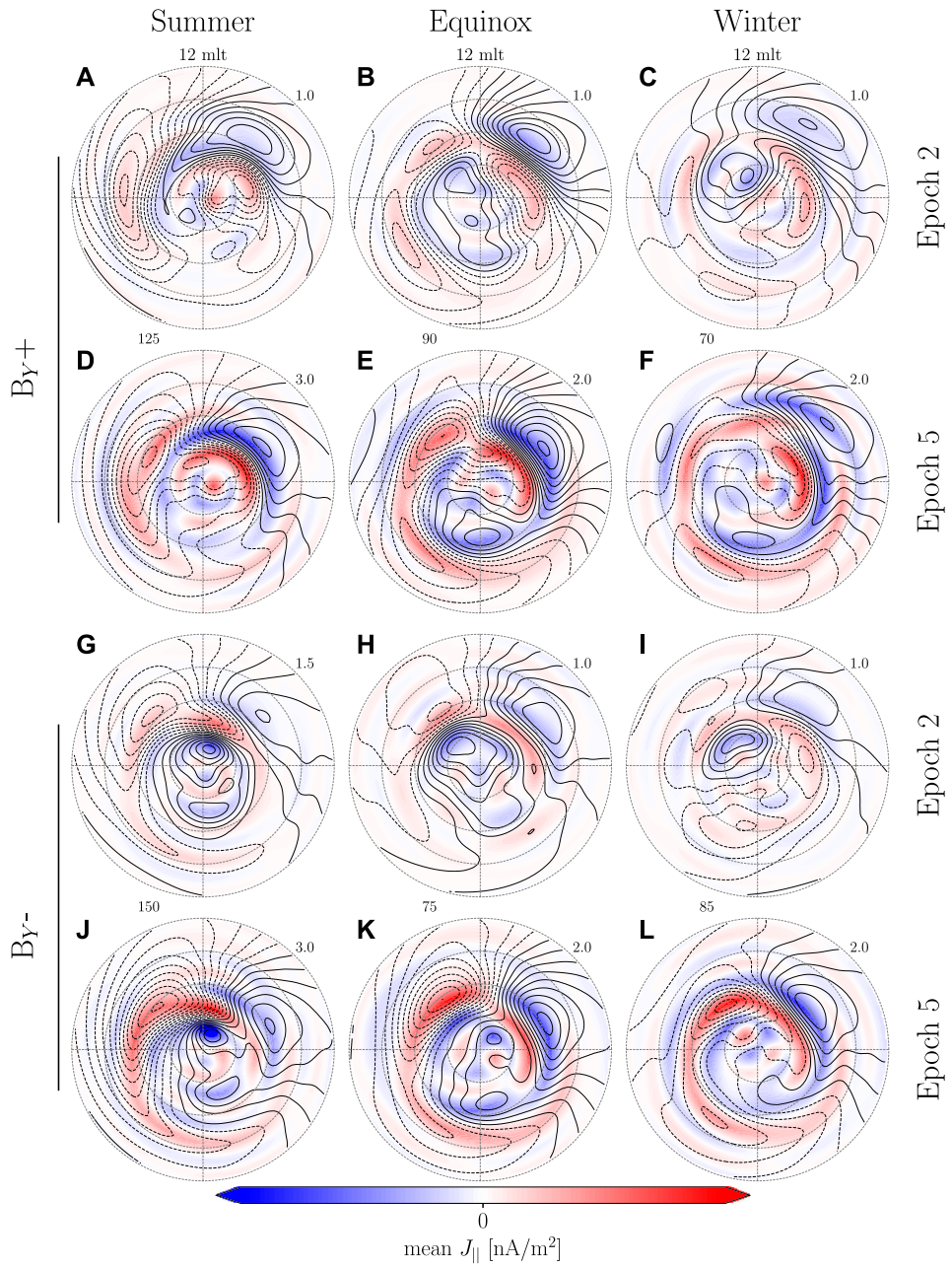

FIGURE 3
Similar to Figure 2, but for B_Y dominated IMF.

on the pre-existing perturbation magnetic field shown in Figure 1. The signal from these transient convection vortices will in most cases be overshadowed by the dominant pre-existing signal. Figures 2, 3 show Ψ, Eq. 11, and EFACs (equivalent field aligned currents), Eq. 14, at epoch −5 and 5 (5 min before and after onset). The colored contours are EFACs, where red (blue) indicate an upward (downward) FAC, and Ψ is illustrated in terms of equipotential lines.

B_Z+ models during equinox (Figures 2B,E) and winter (Figures 2C,F) show clear differences before and after onset. After onset the area around the NBZ currents intensifies and the current vortices extend towards the nightside. These vortices are confined by a second set of current vortices on their equatorward edge that have opposite orientation. The orientation, spatial extent and temporal evolution of these two set of current vortices are in agreement with previous case studies (Friis-Christensen et al., 1988; Moretto et al.,

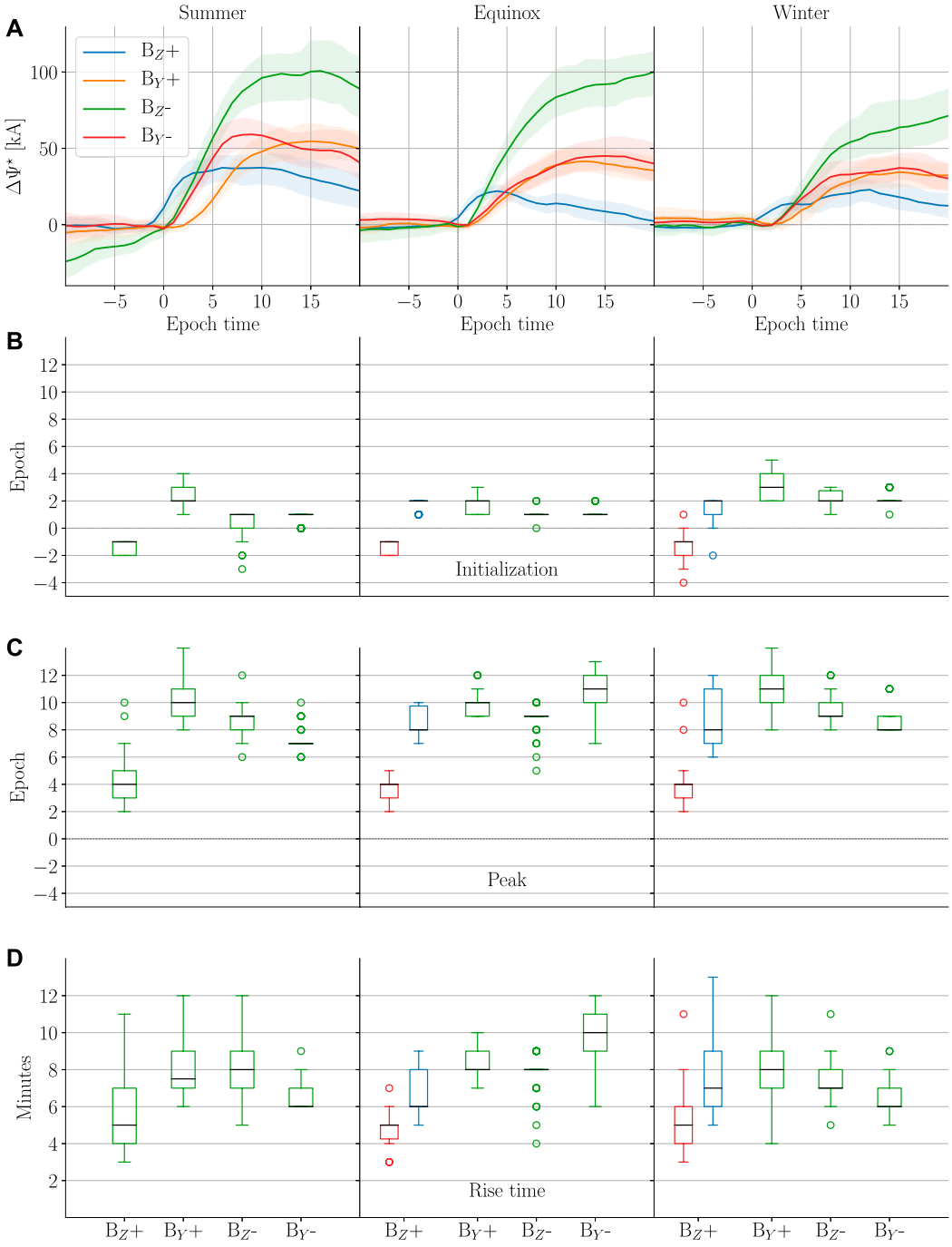

FIGURE 4
(A) Time series of $\Delta\Psi$ for all 12 groups. The mean and 90% confidence interval across all 50 mode realizations is shown as a solid line and a shaded area, respectively. The time series was set to zero with respect to when the response initiates indicated by the asterisk on the *y*-axis. **(B–D)** Summary of statistics related to Figure 4A shown as box plots. **(B)** shows the epoch at which response initiates for the 12 groups. **(C)** shows when the $\Delta\Psi$ time series peaks. **(D)** shows the rise time [difference between **(A** and **B)**]. During equinox and winter B_Z+ is given by two (red and blue) boxplots which are related to a decomposition illustrated in Figure 5.

2000), statistical studies (Stauning and Troshichev, 2008) and MHD simulation studies (Slinker et al., 1999; Keller et al., 2002; Fujita et al., 2003a,b, 2005; Ridley et al., 2006; Samsonov et al., 2010; Samsonov and Sibeck, 2013; Shi et al., 2014; Welling et al., 2021). For all other event groups the general magnitude increases, but no transient response is observed (Figures 2A,D,G–L and

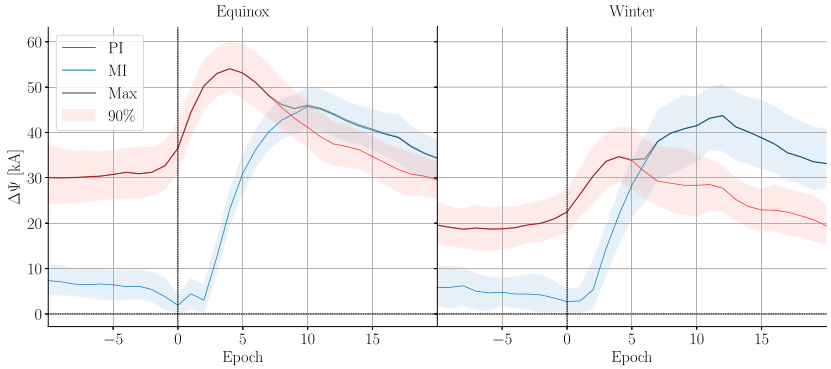

FIGURE 5
Decomposition ΔΨ for B_Z+ during equinox and winter into PI and MI.

Figures 3A–L). One factor that could play a role in the lack of a transient response is the increased dayside reconnection which enhances the preexisting convection pattern. The lack of a visible transient response is likely due to stronger pre-existing convection as a result of dayside reconnection.

4.2.1 Incoherent ionospheric response

In this section we attempt to look past the pre-existing magnetic field in order to examine the temporal evolution of the transient ionospheric response. This is more easily achieved by summarizing it by a single parameter. Here we use ΔΨ, the maximum difference in the current potential given by Eq. 11. Under normal circumstances the potential will be bi-modal with the global min/max coinciding with the current pattern allowing for easy determination of the maximum difference. Changes to the system will often manifest themselves as an increase or decrease in ΔΨ making it convenient for an analysis of the temporal evolution. Figure 4A shows the mean ΔΨ across all model realizations along with the 90% confidence interval. The time series was set to zero with respect to when the response initiates. The time at which the response initiates was determined using the rise time algorithm described by Madelaire et al. (2022). The algorithm also provides the peak (when the time series begins to plateau) allowing for the rise time to be determined.

The shape, size and temporal evolution changes significantly with IMF clock angle and dipole tilt. In the rest of this section we take a closer look at the characteristics of Figure 4A.

4.2.1.1 Initialization

The epoch at which ΔΨ, in Figure 4A, begins to increase is illustrated as box plots in Figure 4B. The red and blue box plots relate to a decomposition done later in this section and the reader should disregard the blue box plot for now. The signal initiates around epoch 1–3 for all event groups except for B_Z+ groups where the initialization occurs around epoch −2 to −1.

Determining ΔΨ is normally easy due to the bi-modal nature of Ψ. However, when multiple cells of similar magnitude grow and decay, as is the case for B_Z+ during equinox and winter, the global min/max will jump around thus making the current method invalid. In these two cases we observed an increase in and around the NBZ cells, consistent with the PI (preliminary impulse), followed by an increase at 65°–75° mlat similar to R1/R2 starting on the dayside, consistent with the MI. We constrained the area within which ΔΨ was computed so as to separate the PI and MI. The PI was isolated by evaluating Ψ above 72° mlat and between 6 and 18 mlt (magnetic local time). The MI was isolated by evaluating Ψ between 65° and 80° mlat. Separate constraints were applied to the dawn and dusk cell due to an asymmetric response which will be further discussed in Section 4.2.2. At dusk Ψ was evaluated between 12 and 18 mlt while dawn was constrained to 6–12 mlt until epoch 5 whereafter it was relaxed to 0–12 mlt. The result of hard-coding where Ψ was evaluated allows for the separation of the two responses as shown in Figure 5. Here the mean PI (MI) is shown in red (blue) with a 90% confidence interval, and the maximum of the two is shown in black. We have labeled the two time series PI and MI as the current vortices observed correspond to the expected orientation and location of the convection vortices associated with PI and MI.

Returning to Figure 4B the PI (MI) is shown with red (blue) box plots. The PI values fit very well with those determined for B_Z+ during summer where the response near the NBZ cells is dominant. The MI initialization fits very well with the initialization of ΔΨ for all other IMF clock angles. One might question why there is no PI for non-B_Z+ groups. This is likely because the PI occurs poleward of the global min/max where ΔΨ is evaluated and its magnitude is not large enough to shift their location.

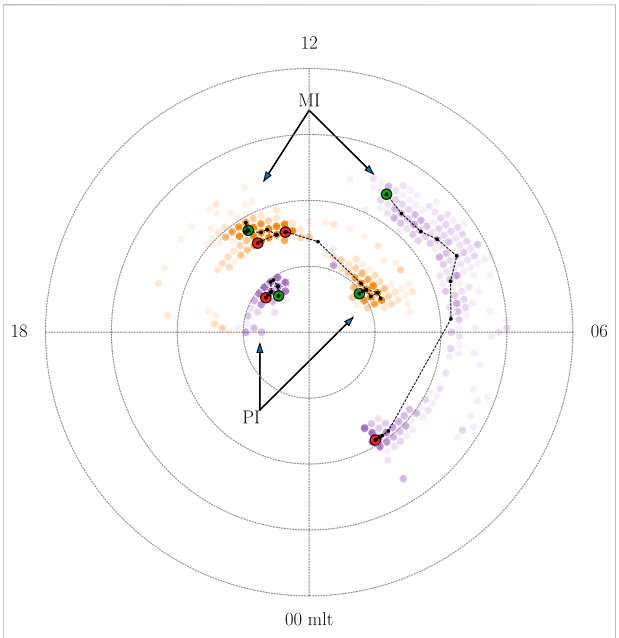

FIGURE 6
Illustration of the PI and MI current vortex centers resulting from the decomposition of ΔΨ during B_Z+ Winter in Figure 5. The poleward (equatorward) purple/orange dots indicate convection cell centers for PI (MI) across all 50 model realizations between epochs −2–8 (0–10). The black lines indicated the average path of the convection cell where the green and red dots indicate the start and end, respectively.

4.2.1.2 Peak and rise time

The peak and rise time of ΔΨ are shown in Figures 4C,D. For B_Z+ the peak occurs around epoch 4 while for all other IMF conditions it occurs around epoch 7–11. The difference is not surprising considering how clearly the PI can be observed during B_Z+. The results are consistent with the superposed epoch analysis of the PCN index conducted by Madelaire et al. (2022). The rise time for the PI is around 5 min while it is 6–10 min for the MI. When comparing Figures 4B–D, the largest source of variation in rise time is from the peak determination. This is consistent with Takeuchi et al. (2002) who studied the rise time of the low/mid latitude geomagnetic response and found it to be around 2–10 min with one event reaching 30 min, presumably due to a highly inclined shock normal.

4.2.1.3 Magnitude and decay

The average increase in P_d across event groups is of similar size, one might therefore assume that the magnitude of the geomagnetic response would be of similar magnitude across all IMF groups in a particular season. Comparing ΔΨ within the individual seasons shows B_Z-to have a magnitude around 2 (3) times larger than B_Y± (B_Z+). The solar wind-magnetosphere coupling efficiency is highly dependent on the IMF clock angle (Newell et al., 2007) and it is therefore no surprise that ΔΨ is significantly larger for B_Z-due to dayside reconnection.

The ΔΨ ratio between summer and winter is ~1.8 for all IMF clock angles. The ratio of the PI for B_Z+ is 2.4 indicating a much higher seasonal dependence. Samsonov et al. (2010) studied the effects of an interplanetary shock using a MHD simulation and concluded that the PI was associated with lobe reconnection. If this finding is true the larger variation in the PI can be controlled partly by dipole tilt as it has a large impact on the lobe coupling efficiency (Reistad et al., 2019).

Similar to the magnitude, the decay is IMF clock angle dependent. The decay during B_Z+ is quicker compared to other event groups. The B_Y± groups plateau or decay slowly while B_Z-plateau or trend upwards. The longer lived response for B_Y± and B_Z-is most probably a consequence of increased dayside reconnection brought on by the new pressure balance.

4.2.2 Northward IMF case

In Section 4.2.1 we examined the ionospheric response to rapid increases in P_d and found dependencies on both IMF clock angle and dipole tilt. Here we examine the temporal evolution using the model during B_Z+ as the transient event is strongest relative to the background for these environmental conditions.

The decomposition of ΔΨ in Figure 5 illustrates the magnitude of PI and MI along with their temporal extent. The decomposition was made by evaluating the local min/max of Ψ. The positions used in that calculation can be visualized to show how the cells move and the variation between model realizations. Figure 6 shows the location of the current potential min/max in orange/purple dots. Superimposed is the average path where the green (red) dots indicate the beginning (end). The PI is shown from epoch −2–10 and the MI is shown from 0 to 15. It is clear that the center of the PI current vortices and the MI vortex at dusk do not move much. However, the MI at dawn moves from around 10 to 6.5 mlt between epoch 2–8 (6 min) at 67° mlat leading to a westward velocity of 6.3 km/s. This is similar in size to the estimates of 3–5 km/s by Friis-Christensen et al. (1988) and 5 km/s by Slinker et al. (1999). After epoch 8 the center jumps from 6 to 2 mlt as the current vortex weakens and becomes indistinguishable from the pre-existing feature on the night side.

Figures 7, 8 show maps of EHIC and EFAC superimposed. Here model predictions are shown with 1–min resolution spanning epoch −1–6 and then with 2–min resolution from epoch 6–14. Before onset there is a set of NBZ cells with centers located around (9 mlt, 80° mlat) and (14 mlt, 82° mlat). There appears to be virtually no westward electrojet, while there is an eastward electrojet, possibly due to co-rotation (Förster et al., 2017). On the nightside there are 2 cells located around (1 mlt, 75° mlat)

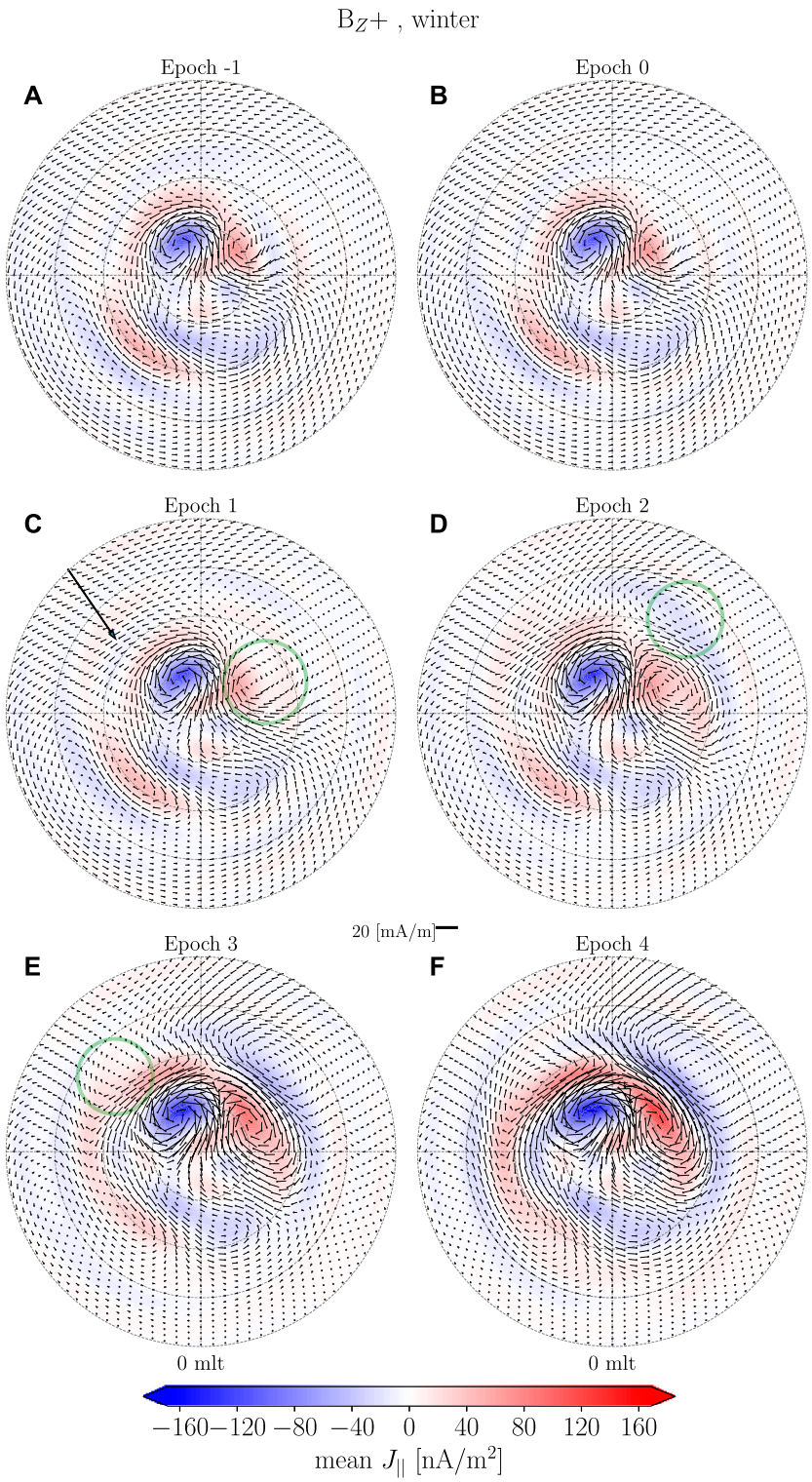

FIGURE 7
Maps of B_Z+ during Winter from epoch –1–4. The contours and arrows indicated EFACs and EHICs, respectively.

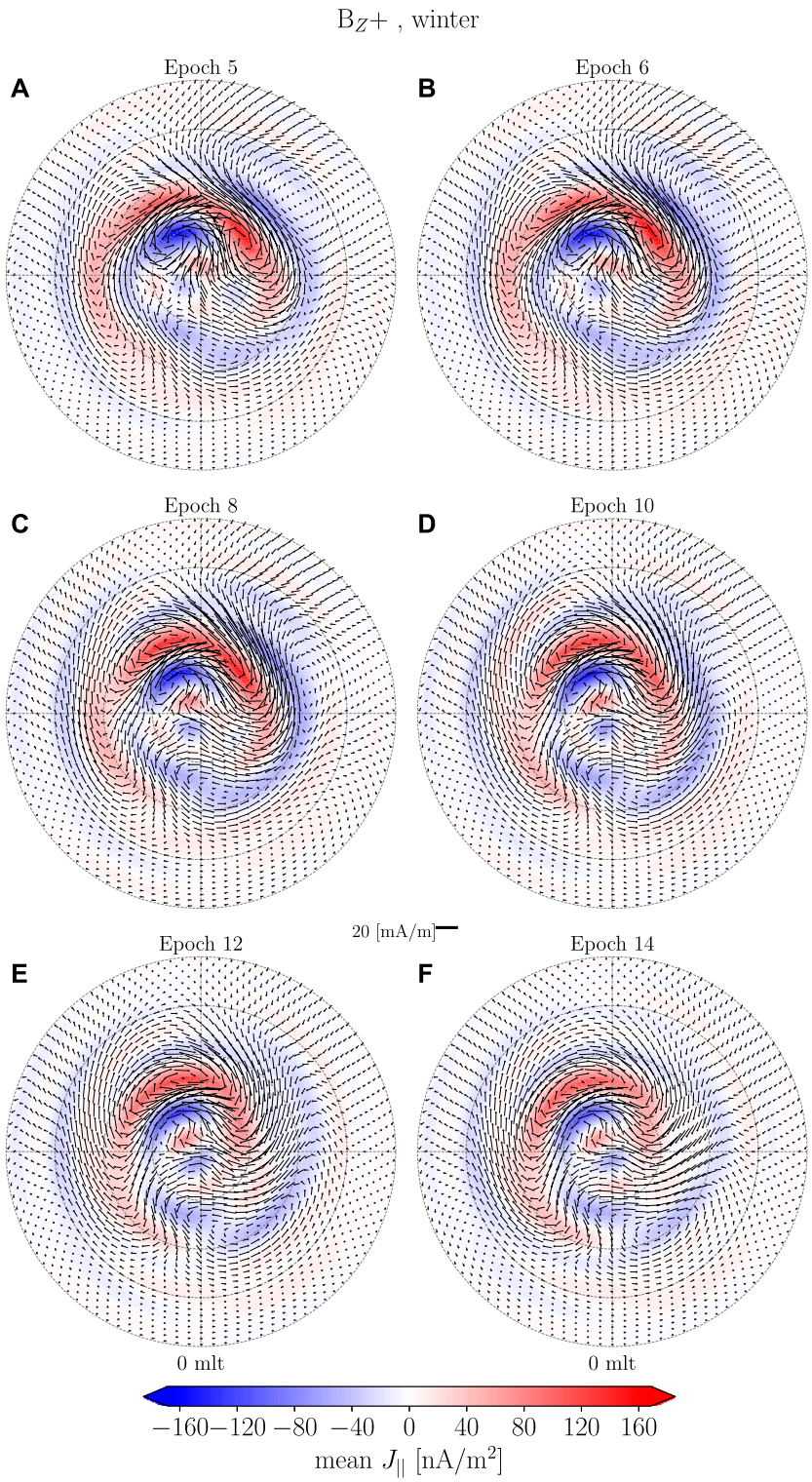

FIGURE 8
Maps of B_Z+ during Winter from epoch 5–14. The contours and arrows indicated EFACs and EHICs, respectively.

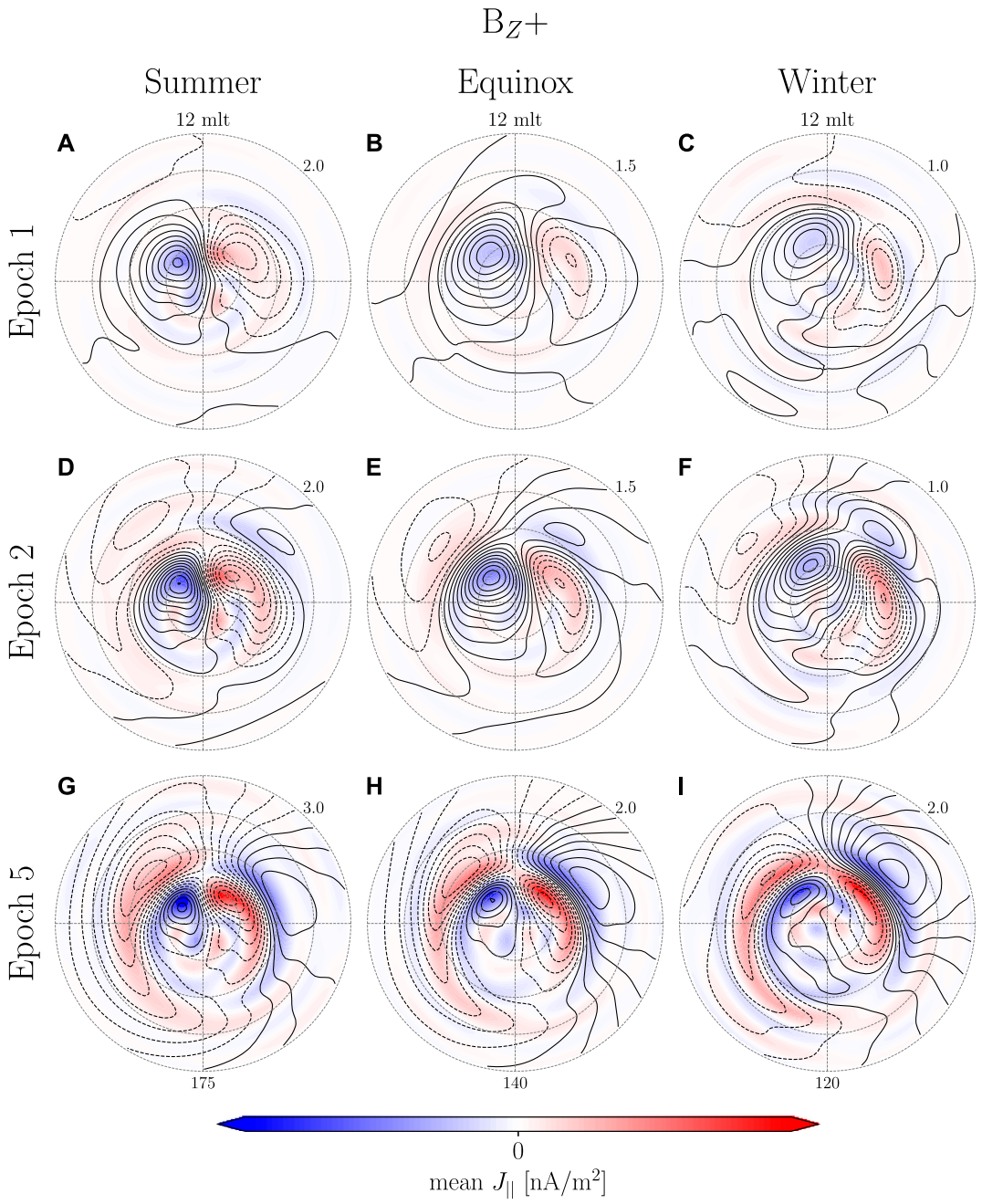

FIGURE 9
Relative change from epoch −2 to epoch 1, 2, and 5 for B_Z+. The blue/red contour illustrates EFAC while the black contour is Ψ. Each column represents a specific dipole tilt range and the number at the bottom of each column is the maximum value of the associated colorbar in units nA/m^2. The number in the top right of each map is the step size of the black contour in kA.

and (21 mlt, 70° mlat) and are likely related to nightside reconnection.

There is no apparent difference when comparing epochs −1 and 0 (Figures 7A,B). One minute after onset, Figures 7A,C small intensification is observed at pre- and post-noon around 65°–80° mlat as indicated by the annotations. Two minutes after onset, Figure 7D, the equatorward boundary of the pre-noon structure has moved poleward to 70° mlat and merged with the pre-existing NBZ cell with its center located around (8 mlt, 78° mlat). Additionally, a current vortex with opposite orientation has appeared at (10 mlt, 65° mlat). At post-noon we see a general intensification of the pre-existing current

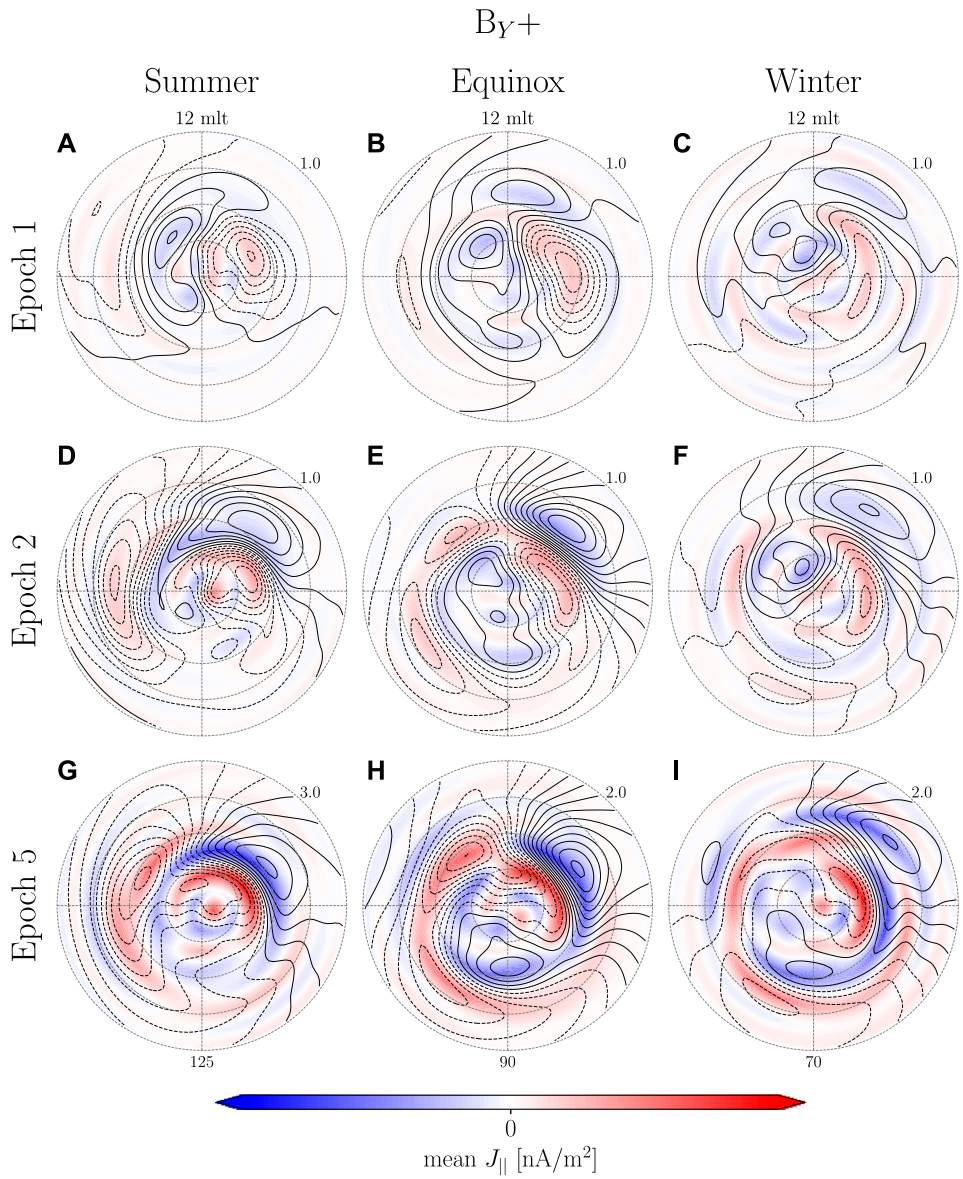

FIGURE 10
Similar to Figure 9, but for B_Y+.

pattern. It is possible that the pre-existing eastward electrojet obscures the PI which therefore is manifested as a general increase of the pre-existing current pattern. Between epoch 3 and 4, Figures 7E,F, the PI current vortices intensify, move poleward and start draping towards the nightside while their centers do not move. At dawn the MI current vortices intensifies, extending toward the night side while its center moves 1–2 MLT westward. At dusk the center of the MI current vortex appears and as it intensifies it moves poleward, from (15 mlt, 65° mlat) to (15 mlt, 70° mlat), and merges with the pre-existing nightside current vortex. Between epoch 5 and 6, Figures 8A,B, the PI cell intensifies while their equatorward extent decrease. At the same time the MI also intensifies and the center of the dawnside vortex moves westward. The duskside MI current vortex becomes more well defined and moves poleward. Between epoch 8 and 10, Figures 8C,D, the PI decreases in intensity and at dawn the PI vortex merges with the MI vortex at dusk. The center of the MI vortex at dawn moves westward and becomes less well defined. At dusk the MI cell intensifies and moves slightly westward towards the noon meridian. Between epoch 12 and 14, Figures

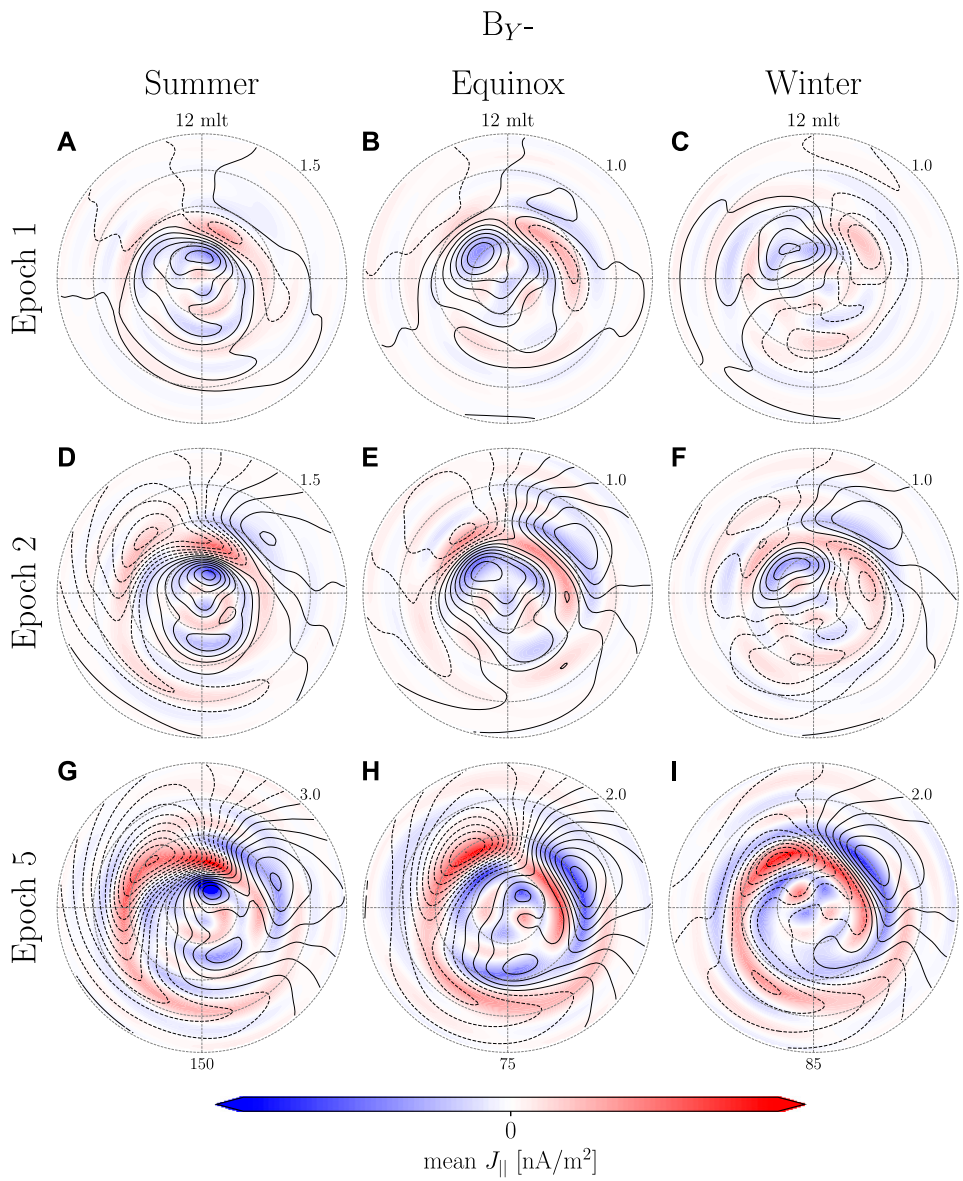

FIGURE 11
Similar to Figure 9, but for B_Y-.

8E,F, the PI response continues to decrease in strength. The MI response slowly disappears at dawn while it remains strong at dusk.

In our examination of the B_Z+ during winter a transient high latitude geomagnetic response was observed and will be discussed further in Section 5.

4.2.3 Coherent ionospheric response

Despite the lack of a visible transient response in a majority of the event groups it might very well still be there, hidden under a more dominant current pattern. A weak transient signal can be examined by evaluating the relative change as long as the contribution from the change of the transient signal is larger than that of the background signal.

In Figures 2E,F the MI-associated current vortices appears to extend far equatorward. This, to some extent, is an artifact caused by how DL geomagnetic response maps into the horizontal magnetic field at subauroral latitudes, mainly the north/south component, resulting in what appears to be large scale east/west aligned ionospheric current. We remove this effect by approximating the magnetic perturbation from magnetospheric sources as an

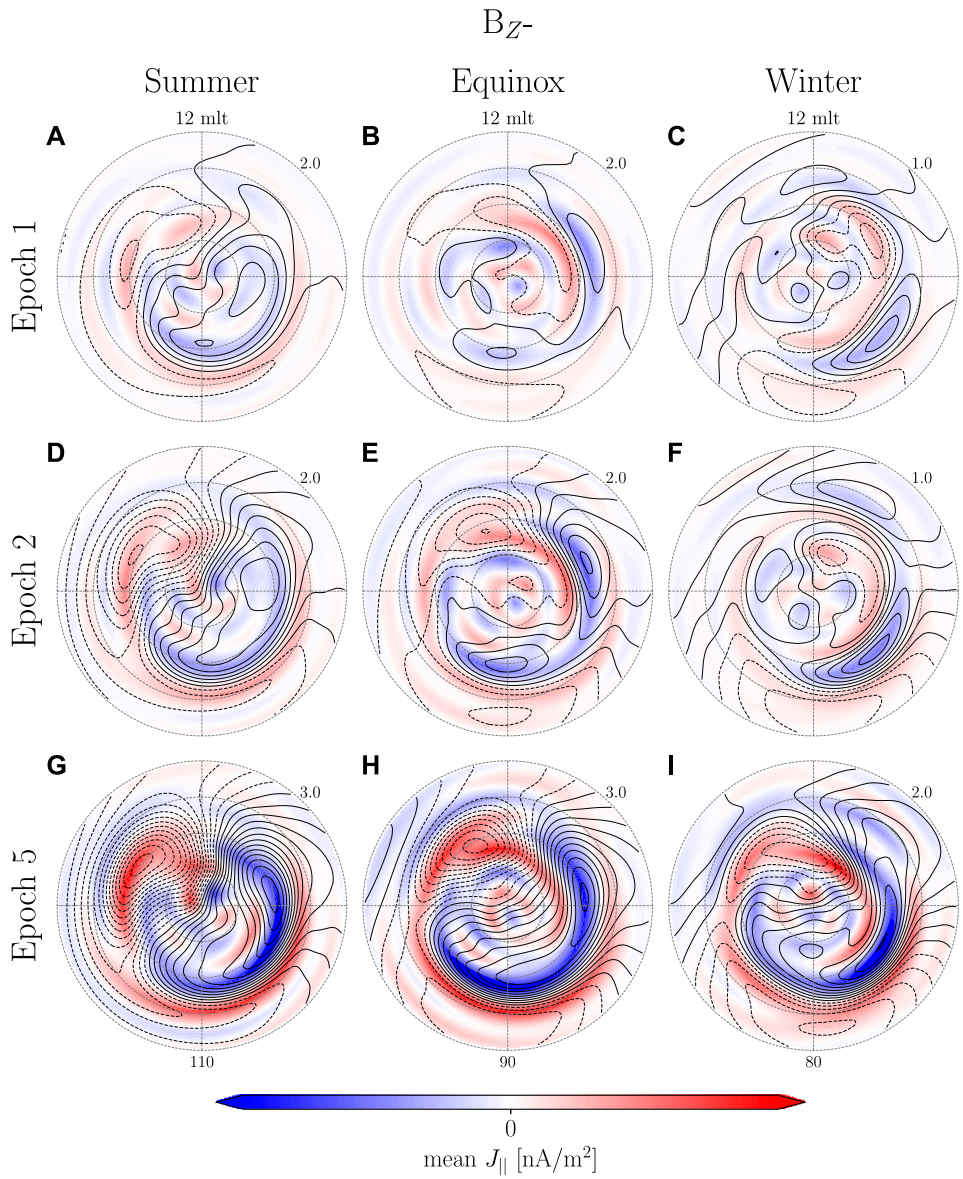

FIGURE 12
Similar to Figure 9, but for B$_Z$-.

external dipole field. The external dipole field can be seen as uniform magnetic field in $\hat{z}$,

$$B_m = B_r \sin(\theta) - B_\theta \cos(\theta), \tag{15}$$

which except for a sign difference is the same as the SH expansion of the external magnetic field to degree 1 and order 0. B_m is determined at each epoch as the average of 1,000 model predictions at 30° mlat that are evenly spaced in mlt. The effect of the magnetospheric compression is then isolated by subtracting a baseline prior to onset. Finally, a corrected SH model is created,

$$q_1^{0*} = q_1^0 + B_m. \tag{16}$$

Figures 9–12 shows the relative change from epoch −2 to epoch 1, 2 and 5 using the corrected model for B$_Z$+, B$_Y$+, B$_Y$- and B$_Z$-, respectively. Each column represents a season and the rows different epochs i.e., each column pertains to one of the 12 groups. The number below the maps in the last rows indicate the maximum value of the colorbar for that group in nA/m^2. The number in the upper right corner of each map is the step size of the black contour in kA.

When comparing B_Z+ between Figure 9 to Figure 2A–F it is clear that the transient high latitude response shows very little dipole tilt dependence. At epoch 1 (Figure 9A–C) only the PI is present. At epoch 2 (Figure 9D–F) the MI starts forming around 60°–65° mlat. At epoch 5 (Figure 9G–I) both PI and MI increase in magnitude and the center of the MI vortex at post-noon has moves poleward by 5° mlat while the vortex at pre-noon moves westward.

The B_Y± groups at epoch 1 (Figures 10A–C and Figure 11A–C) show PI current vortices. They are not as well defined when comparing with B_Z+, but there does not appear to be any favoring of one vortex over the other as might be expected when comparing B_Y+ and B_Y-. At epoch 2 (Figures 10D–F and Figures 11D–F) the PI moves slightly poleward as the MI forms on its equatorward edge. In some cases, Figures 10D, 11D,E, one of the PI vortices disappear or merge with one of the MI vortices. This might be attributed to the model's spatial resolution, the fact that we are looking at a relative change or the combination of northward and southward IMF in B_Y± groups causing higher variation between events close to the pole. At epoch 5 (Figures 10G–I, 11G–I) the PI is almost completely gone and the MI is well defined with the exception of B_Y+ winter where no clear MI current vortex appear on the dusk side. Under these environmental conditions it is also only the MI vortex on the dawnside that moves toward the nightside.

The current potential for B_Z- at epoch 1 (Figures 12A–C) is highly variable, i.e. many local min/max, and it is therefore difficult to associate any of the structures to PI or MI. During summer (Figures 12A,D,G) the current pattern is very similar to the expected current pattern during southward IMF (Laundal et al., 2018). The center of the 2 cells are shifted towards the dayside indicating some similarity to the MI current vortices. During equinox and winter current vortices appear on the night side at epoch 1 and increase in strength at epoch 2 (Figures 12B,C,E,F). At epoch 2 during equinox (Figure 12E) two MI associated vortices appear on the dayside; one on the dawnside and another very close to noon on the duskside. At epoch 5 (Figure 12H) the dawnside MI vortex merges with that on the nightside. The same can be observed during winter, however, the post-noon current vortex first appears at epoch 5 (Figure 12I). Common for all B_Z-groups is a general lack of the PI current vortices and a very strong nightside geomagnetic response possibly associated with dipolarization of the tail magnetic field as observed by Lee and Lyons (2004).

5 Discussion

In our examination of the transient high latitude response we looked closely at the model for northward IMF during winter as these are the conditions under which the transient response is strongest relative to the background. The model shows vortices that evolve on a minute time scale. The spatial extent of the vortices vary with time, however, the center of the vortices tend not to move except for the MI-associated vortex on the dawnside which moves westward with an estimated velocity of 6.3 km/s. The shock impact angle is surprisingly not one of the factors controlling the motion of the MI-associated vortices at dawn and dusk. Our reasoning is as follows. Madelaire et al. (2022) argued that the majority of the events in their list of rapid increases in P_d are not interplanetary shock. It is therefore likely that our results represent an average impact angle that is skewed toward dusk, in agreement with the statistical survey of rapid solar wind pressure changes presented by Dalin et al. (2002). In contrast the case study of Moretto et al. (2000), which used the AMIE technique to model the ionospheric response of an inclined shock arriving first at the dawn side, also found that the MI-associated convection vortex at dusk did not move, while that at dawn did. If the impact angle controlled which vortex convects toward the nightside, the response of the vortices reported by Moretto et al. (2000) would presumably be opposite the observed response; that is, the dusk vortex would have moved toward the nightside while the dawn vortex remained stationary. Existing simulation-based studies of interplanetary shocks unfortunately do not lend much insight (Slinker et al., 1999; Keller et al., 2002; Fujita et al., 2003a,b; Ridley et al., 2006; Samsonov et al., 2010; Welling et al., 2021): while they universally show a symmetric ionospheric response across the noon-midnight meridian with both MI cells moving anti sunward, all have been carried out with an interplanetary shock aligned with the Sun-Earth line.

5.1 Coherent high-latitude response

A coherent transient high latitude geomagnetic response is observed for all groups when examining the relative change with respect to epoch −2 (Figures 9–12). When comparing different groups we find the EFAC magnitude and PI current vortices to be more dominant during B_Z+ likely due to a higher contribution from lobe reconnection. During B_Z-there is a general lack of PI and the MI is poorly resolved due to a significant enhancement of the pre-existing current pattern. The appearance of MI current vortices during B_Z+ and B_Y± is very consistent. We estimate the westward velocity of the dawnside associated MI current vortex based on epoch 2–5 (Figures 9–11) to be between 3.6 and 7.8 km/s with a mean of 5 km/s and a standard deviation of 1.4 km/s. The initial appearance of the MI current vortex on the dawnside occurs at (9.3 ± 0.5 mlt, 64.8° ± 1.5° mlat) while it on the duskside occurs at (15.3 ± 0.9 mlt, 65.8° ± 2.5° mlat) with the majority of the mlt variation caused by Figure 11D.

The SH model is a global representation of the magnetic potential. It is important to understand the benefits and shortcomings of the method such that results can be interpreted in the correct context and improvements or

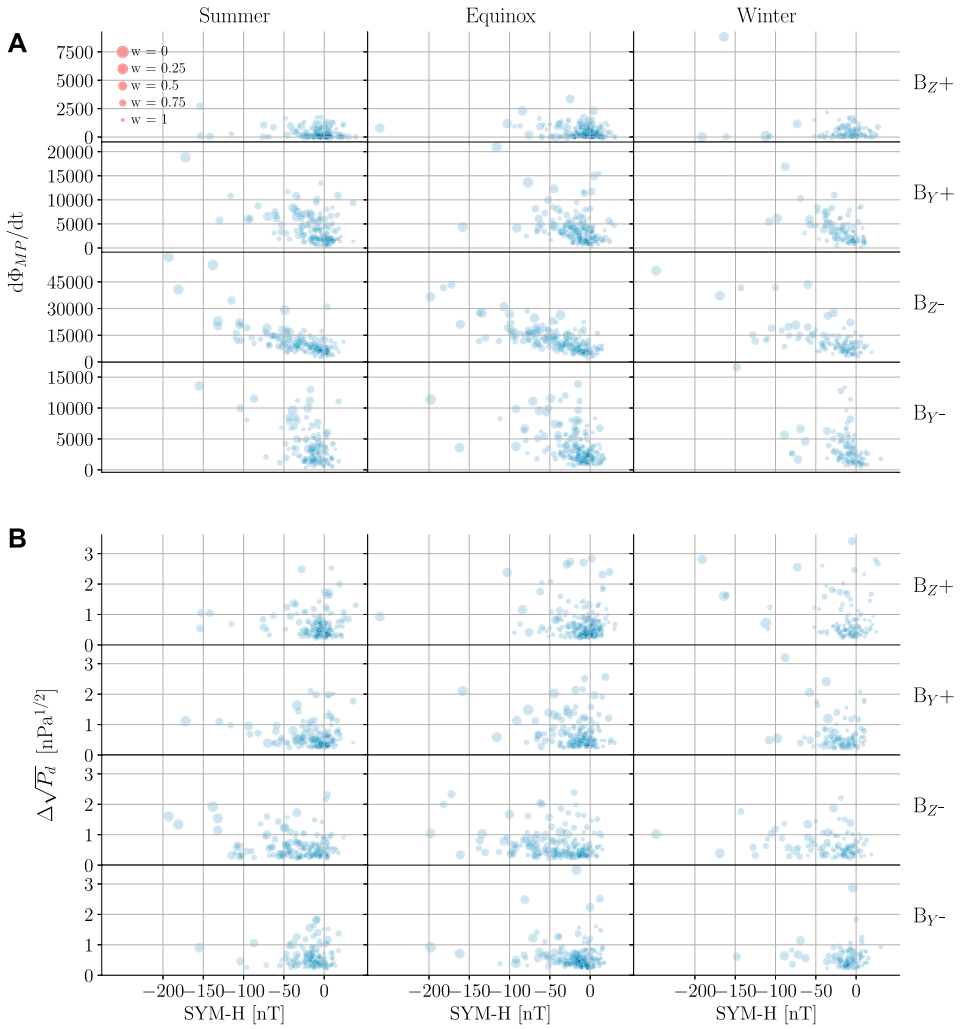

FIGURE 13
Huber weights at epoch 5 for each event. In **(A)** illustrated as function of the Newell coupling function and SYM-H before onset and in **(B)** as function $\Delta\sqrt{P_d}$ and SYM-H before onset. Each dot indicates an event and the size of each dot illustrates the weight of each event. A large (small) dot indicates an event that is weighted low (high).

alternatives might be proposed. The spatial resolution of any modeling method will partly depend on data coverage. When using ground magnetometers the data coverage is seldom uniform and the spatial resolution is highly dependent on the area with the lowest data density. By combining multiple events, as done here, we can achieve much denser data coverage resulting in a better spatial resolution. Combining multiple events generates inconsistencies as observations that are spatially very close can vary significantly. The variation is reduced by only combining events thought to be of similar nature. The model will inevitably be an average highlighting features common for all the events. We have tried to quantify the variation in our model using bootstrapping (Figure 1), but in order to understand how and why events vary from the average they need to be analyzed individually. The spherical elementary current system technique (Amm et al., 2002) is ideal for analyzing single events as it is not globally defined and can take advantage of the regions with dense data coverage. This method is implemented by Laundal et al. (2022); they combine magnetic perturbation and convection measurements from space and ground with conductance measurements via ionospheric Ohm's law to significantly improve data coverage and information retrieved. This will be a very useful tool when the EZIE satellite mission (Laundal et al., 2021) launches in the near future providing measurements of the magnetic field in the mesosphere. In the future we intend to carry out a regional analysis of events to study their variation in more detail.

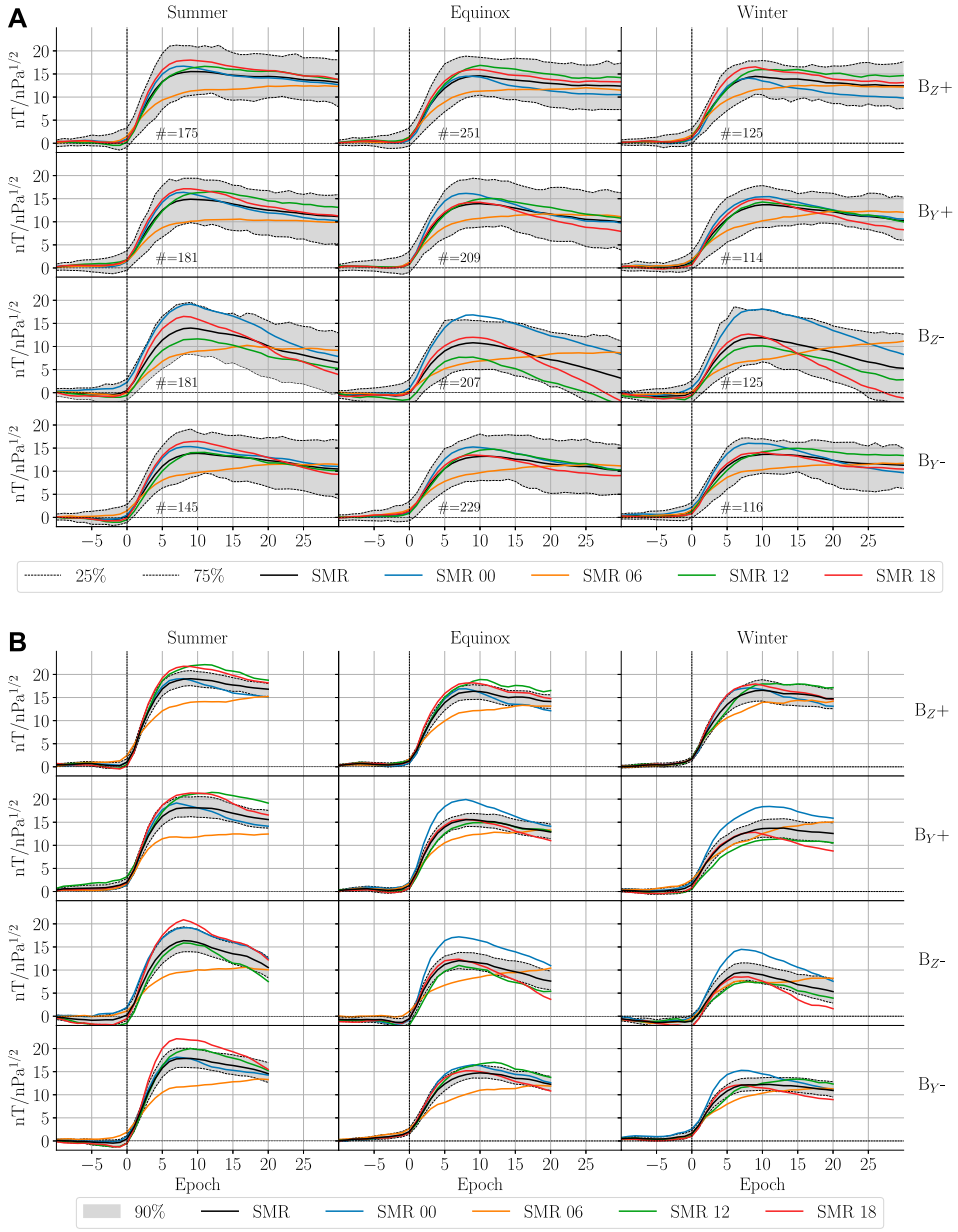

FIGURE 14
Comparison between the superposed epoch analysis of the SMR index by Madelaire et al. (2022) and the recreated SMR index from the SH models. **(A)** Similar to Figure 9 of (Madelaire et al., 2022). **(B)** The recreated SMR index where the solid lines indicate the mean of SMR and its local time components. The gray area indicates a 90% confidence interval of the global SMR. The SMR time series for each model realization has been scaled with respect to the median increase in $\sqrt{P_d}$ and a baseline prior to onset subtracted.

5.2 Huber weights

A superposed epoch analysis assumes a certain level of comparability between events which we in practice achieve by imposing criteria on IMF clock angle and dipole tilt. It is obvious that there will be differences between events and at times so much so that individual events can be considered outliers. When solving the inverse problem the imposed spatial relationship, inherent in SHs, will force the solution toward the typical event and thereby automatically reduce the relative importance of certain data. Adding iterative reweighting allows for a fine tuning of the fit as the influence of outliers are weighed down and the inversion repeated. The term outliers is often used synonymously with measurement errors, but here refer to events behaving differently from the majority. In practice, the outliers are

weighed down using Huber weights which are determined as part of the iterative procedure.

The Huber weights can be used to analyze how consistent the data selection is and if outliers are correlated with certain environmental parameters. Figure 13 visualizes the average Huber weight for each event using data-points above 50° mlat with respect to certain environmental parameters. Each dot represents an event and the size of the dot indicates the weight of that specific event illustrated by the scale of red dots in the upper left corner; a large (small) dot indicates an event that has been weighed low (high) in the inversion. Figures 13A,B show how the weight relates to the Newell coupling function (Newell et al., 2007) before onset, the SYM-H index before onset and $\Delta\sqrt{P_d}$. It is clear that events with a SYM-H value below −50 nT are generally weighed very low. From Figure 13A we find that the Newell coupling function also can be used to separate between events that are weighted high and low in event groups with southward IMF ($B_Y\pm$ and B_Z-). Figure 13B, on the other hand, shows that $\Delta\sqrt{P_d}$ does not play a large role in whether or not an event deviates from the norm.

These figures are not intended to be employed in determining which parameters to use for grouping events, but are rather an illustration of how information about individual events can be extracted from a superposed epoch analysis. Additionally, they serve as an illustration of how data selection occurs prior to and during the modeling process.

5.3 Low/mid latitude geomagnetic response

A benefit of a global model is the possibility of examining the high latitude impact on low/mid latitude perturbations. Changes in $\sqrt{P_d}$ have previously been related linearly to changes in the Dst index (Burton et al., 1975) as a result of magnetospheric compression. This is best observed at low/mid latitudes as equatorial and subauroral/polar latitudes experience additional effects from electrojets (Sugiura, 1964; Sugiura and Kamel, 1991).

Russell et al. (1994a) did a statistical analysis of the linear relationship during interplanetary shocks and found the slope to be 18.4 nT/nPa$^{1/2}$ at Earth's surface which includes a 50% markup due to ground induced currents. This estimate was given for northward IMF and should be reduced by 25% (13.8 nT/nPa$^{1/2}$) during southward IMF (Russell et al., 1994b). The superposed epoch analysis by Madelaire et al. (2022) was based on the SMR index and found the average relationship to be around 15 nT/nPa$^{1/2}$ during northward IMF and around 12 nT/nPa$^{1/2}$ for southward IMF. Additionally, Madelaire et al. (2022) found a dawn-dusk asymmetry in the SMR index as well as a noon-midnight asymmetry for southward IMF.

The SH models are essentially a weighted average of the events in each group expressed in terms of SH surface waves. Their performance can be compared to the results of Madelaire et al. (2022) by testing if they can recreate their results. The results of the superposed epoch analysis of the SMR index by Madelaire et al. (2022) is reproduced in Figure 14A to facilitate comparison later. The SMR index

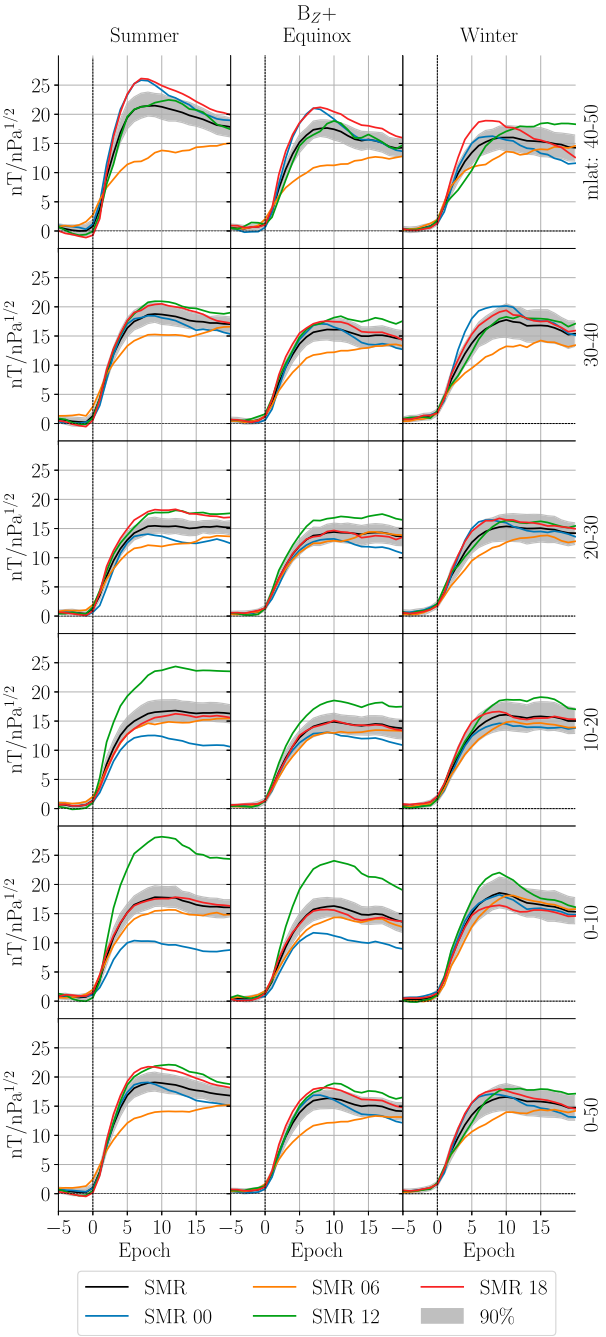

FIGURE 15
A latitudinal profile of the reproduced SMR for B_Z+ during all seasons. The first five rows show contributions from five latitudinal regions between 0° and 50° mlat. The last row shows SMR for the entire latitudinal region which is identical to row 1 of Figure 14B.

was recreated using the SH models; the northward component of the magnetic field perturbations are calculated using the internal and external model for each of the 50 realizations between the equator and 50° mlat. The model predictions are made at the same location as the data that went into the models. A latitudinal correction similar to that of the SMR index was applied (Newell and Gjerloev, 2012). The model predictions from each realization are scaled with the median of $\Delta\sqrt{P_d}$ for the events used in that particular realization. The median is used as there are a few very strong events biasing the mean. A common value for $\Delta\sqrt{P_d}$ is 0.6 $nPa^{1/2}$. The average is then calculated in four local time sectors to replicate SMR 00/06/12/18. Finally, the global SMR index is determined as the average of the four local time indices.

The recreated SMR index is shown in Figure 14B. The expected step-like increase is reproduced. The magnitudes of SMR range from 12 to 19 $nT/nPa^{1/2}$ which is slightly larger than the averages provided in Figure 14A. The dawn-dusk difference is also reproduced which is most pronounced during summer. Comparing Figures 14A,B suggests that the SH models are sufficient to reproduce the expected geomagnetic response observed on ground which is an indication that the modeling scheme performs well.

The latitudinal profile of the recreated SMR for B_Z+ is shown in Figure 15. The first 5 rows show 5 latitude bands between 0° and 50° mlat. The last row is identical to the first row of Figure 14B for more easy comparison. It is clear that the dawn-dusk asymmetry is most pronounced between 40° and 50° mlat. This suggests it is an ionospheric source and not magnetospheric, given its small spatial extent. A recent study (Zhou and Lühr, 2022) investigated SCs with an immediate and strong activation of the westward electrojet. However, they concluded that it required southward IMF preceding the SC. The lower magnitude at dawn between 40° and 50° mlat could reflect the ionospheric vortices generated at high latitude. The seasonal dependence would then be a result of seasonal variations in conductance varying the strength of the high latitude currents and thus the latitudinal extent of their magnetic perturbation.

In the region closest to the equator, 0°–10° mlat, a noon-midnight asymmetry is observed which is present for all IMF clock angles (only B_Z+ shown). The geomagnetic response on the dayside (nightside) tends to be stronger (weaker) than at dawn and dusk. The small latitudinal and longitudinal extent of the dayside/nightside (SMR 12/00) enhancement suggests an ionospheric source. A seasonal dependence is observed as the asymmetry almost disappears during winter. There are several possible explanations for this; Kikuchi (1986); Kikuchi et al. (2001); Kikuchi (2014) proposed that the potential difference at high latitude would be transported toward the equator in an Earth-ionosphere waveguide. In this frame the increased equatorial perturbation is caused by Cowling conductivity. However, Tu and Song (2019) argued against this idea as the waveguide should transport the electric field with the speed of light and the observed delay between high and low latitude is in the order of minutes. Movement of the Sq foci is thought to be responsible for the semiannual variation of the equatorial electrojet (Tarpley, 1973). The seasonal variation is not a modulation of the magnitude, but rather a latitudinal shift along with the Sq foci. Unfortunately, we are not able to test this hypothesis with our model as they are only based on data from the northern hemisphere. It is also possible that there is no hemispheric asymmetry and the seasonal variation is an artifact caused by the event occurrence probability being skewed toward a certain UT range for different dipole tilt angles due to the offset between the geomagnetic and geographic poles. Specifically, events are more likely to occur between 0 and 12 (12–24) UT for positive (negative) dipole tilt. Trivedi et al. (2005) showed that the magnetic perturbation due to SCs measured close to the south atlantic magnetic anomaly are stronger than elsewhere. It is therefore possible that the dipole tilt dependence of the magnetic perturbation at equator latitude simply is due to longitudinal variations in the equatorial electrojet.

It is clear that the geomagnetic response between 10° and 40° mlat is very similar while magnetometer observations between 0°–10° and 40°–50° mlat are under high influence of ionospheric sources. This consideration was taken into account in the development of the Dst index (Sugiura, 1964; Sugiura and Kamel, 1991) and it is therefore curious that it is not taken into account in the SYM-H and SMR index (Iyemori et al., 2010; Newell and Gjerloev, 2012). We do not attempt to understand the origin of the contamination pointed out here as that should be done in a future study using data directly from the magnetometer stations and not our SH models.

6 Conclusion

In this study we carried out a superposed epoch analysis of the transient high latitude geomagnetic response in the northern hemisphere to rapid increases in solar wind dynamic pressure using spherical harmonics. The analysis is based on the list of rapid solar wind pressure increases presented by Madelaire et al. (2022). A total of 2058 events were separated into 12 groups, Supplementary Table S1, based on IMF clock angle and dipole tilt. We found:

1. An incoherent geomagnetic response for a majority of the groups due to a dominant background signal; only during B_Z+ equinox and winter was the transient response visible.
2. A coherent geomagnetic response showing the development of current vortices associated with PI and/or MI of the sudden commencement was observed for all groups when evaluating the relative change with respect to epoch −2.
3. The PI (MI) onset occurs ~2 min before (after) the SYM-H defined onset and the rise time is 4–6 (6–11) min.

4. The pre-noon current vortex associated with the MI initially appears at (9.3 ± 0.5 mlt, 64.8° ± 1.5° mlat) and moves westward with a velocity of 5 ± 1.4 km/s until it reaches ~6 mlt. Here it remains while it slowly decays and a new steady state current pattern emerges.
5. The post-noon current vortex associated with the MI initially appears at (15.3 ± 0.9 mlt, 65.8° ± 2.5° mlat) and does not move towards the nightside which is inconsistent with previously published models and MHD simulations.
6. The high latitude impact on the low/mid latitude perturbation results in significant contamination of the SMR index due to the inclusion of observations from 0° to 10° mlat and 40°–50° mlat.

The purpose of the study was to create a climatological analysis of the transient high latitude geomagnetic response. In the future we intend to examine how individual events in the 12 groups differ from each other and what the controlling environmental factors are.

Data availability statement

Publicly available datasets were analyzed in this study. This data can be found here: Event list (doi. org/10.5281/zenodo.6243103), Ground magnetic perturbation from SuperMAG.

Author contributions

MM is the primary author and carried out the analysis. KML and JPR helped set up the overall structure of the manuscript. All co-authors contributed to the discussions and provided editorial comment thus contributing to the article and approved the submitted version.

Funding

This work was funded by the Research Council of Norway (RCN) under contract 223252/F50. KL and JR were also funded by the RCN under contract 300844/F50. KL and SH were also funded by the Trond Mohn Foundation.

Conflict of interest

The authors declare that the research was conducted in the absence of any commercial or financial relationships that could be construed as a potential conflict of interest.

Publisher's note

Supplementary material

The Supplementary Material for this article can be found online at: https://www.frontiersin.org/articles/10.3389/fspas.2022.953954/full#supplementary-material

References

Amm, O., Engebretson, M. J., Hughes, T., Newitt, L., Viljanen, A., and Watermann, J. (2002). A traveling convection vortex event study: Instantaneous ionospheric equivalent currents, estimation of field-aligned currents, and the role of induced currents. *J. Geophys. Res.* 107, 1334. SIA 1–1–SIA 1–11. doi:10.1029/2002JA009472

Araki, T. (1994). A physical model of the geomagnetic sudden commencement (American geophysical union (AGU)). *Sol. Wind Sources Magnetos. Ultra-Low-Frequency Waves,Geophysical Monogr. Ser.*, 183–200. doi:10.1029/GM081p0183

Aster, R. C., Borchers, B., and Thurber, C. H. (2013a). "Chapter four - tikhonov regularization," in *Parameter estimation and inverse problems*. Editors R. C. Aster, B. Borchers, and C. H. Thurber. Second Edition (Boston: Academic Press), 93–127. Second edition edn. doi:10.1016/B978-0-12-385048-5.00004-5

Aster, R. C., Borchers, B., and Thurber, C. H. (2013b). "Chapter two - linear regression," in *Parameter estimation and inverse problems*. Editors R. C. Aster, B. Borchers, and C. H. Thurber. Second Edition (Boston: Academic Press), 25–54. Second edition edn. doi:10.1016/B978-0-12-385048-5.00004-5

Burton, R. K., McPherron, R. L., and Russell, C. T. (1975). An empirical relationship between interplanetary conditions and dst. *J. Geophys. Res.* 80 (1896-1977), 4204–4214. doi:10.1029/JA080i031p04204

Chapman, S., and Bartels, J. (1940). *Geomagnetism*, 2. Oxford University Press. chap. 17. doi:10.2307/3606494

Constable, C. G. (1988). Parameter estimation in non-Gaussian noise. *Geophys. J. Int.* 94, 131–142. doi:10.1111/j.1365-246X.1988.tb03433.x

Cowley, S. W. H., and Lockwood, M. (1992). Excitation and decay of solar wind-driven flows in the magnetosphere-ionosphere system. *Ann. Geophys.* 10.

Curto, J., Araki, T., and Alberca, L. (2007). Evolution of the concept of sudden storm commencements and their operative identification. *Earth Planets Space* 59–xii. doi:10.1186/BF03352059

Dalin, P. A., Zastenker, G. N., and Richardson, J. D. (2002). Orientation of middle-scale structures in the solar wind plasma. *Cosmic Res.* 40, 319–323. doi:10.1023/a:1019838226629

Finlay, C. C., Kloss, C., Olsen, N., Hammer, M. D., Tøffner-Clausen, L., Grayver, A., et al. (2020). The chaos-7 geomagnetic field model and observed changes in the south atlantic anomaly. *Earth Planets Space* 72, 156. doi:10.1186/s40623-020-01252-9

Förster, M., Doornbos, E., and Haaland, S. (2017). The role of the upper atmosphere for dawn-dusk differences in the coupled magnetosphere-ionosphere-thermosphere system. *Dawn-Dusk Asymmetries Planet. Plasma Environments,Geophysical Monogr. Ser.* 10, 125–141. American Geophysical Union (AGU)), chap. doi:10.1002/9781119216346.ch10

Friis-Christensen, E., McHenry, M. A., Clauer, C. R., and Vennerstrøm, S. (1988). Ionospheric traveling convection vortices observed near the polar cleft: A triggered

response to sudden changes in the solar wind. *Geophys. Res. Lett.* 15, 253–256. doi:10.1029/GL015i003p00253

Fujita, S., Tanaka, T., Kikuchi, T., Fujimoto, K., Hosokawa, K., and Itonaga, M. (2003a). A numerical simulation of the geomagnetic sudden commencement: 1. Generation of the field-aligned current associated with the preliminary impulse. *J. Geophys. Res.* 108, 1416. doi:10.1029/2002JA009407

Fujita, S., Tanaka, T., Kikuchi, T., Fujimoto, K., and Itonaga, M. (2003b). A numerical simulation of the geomagnetic sudden commencement: 2. Plasma processes in the main impulse. *J. Geophys. Res.* 108, 1417. doi:10.1029/2002JA009763

Fujita, S., Tanaka, T., and Motoba, T. (2005). A numerical simulation of the geomagnetic sudden commencement: 3. A sudden commencement in the magnetosphere-ionosphere compound system. *J. Geophys. Res.* 110, A11203. doi:10.1029/2005JA011055

Fukushima, N. (1969). Equivalence in ground geomagnetic effect of chapman-vestine's and birkeland-alfven's electric current systems for polar magnetic storms. *Rep. Ionos. Space Res. Jap.* 23 (1969), 219–227.

Fukushima, N. (1976). Generalized theorem for no ground magnetic effect of vertical currents connected with Pedersen currents in the uniform-conductivity ionosphere. *Rep. Ionos. Space Res. Jpn.* 30, 35–40.

Gjerloev, J. W. (2012). The supermag data processing technique. *J. Geophys. Res.* 117. doi:10.1029/2012JA017683

Glassmeier, K. H., and Heppner, C. (1992). Traveling magnetospheric convection twin vortices: Another case study, global characteristics, and a model. *J. Geophys. Res.* 97, 3977. doi:10.1029/91JA02464

Glassmeier, K. H., Hönisch, M., and Untiedt, J. (1989). Ground-based and satellite observations of traveling magnetospheric convection twin vortices. *J. Geophys. Res.* 94, 2520. doi:10.1029/JA094iA03p02520

Huang, C.-S. (2005). Variations of polar cap index in response to solar wind changes and magnetospheric substorms. *J. Geophys. Res.* 110, A01203. doi:10.1029/2004JA010616

Huber, P., and Ronchetti, E. (2009). *Robust Stat.* 78. doi:10.2307/2287149

Iyemori, T., Takeda, M., Nose, M., and Toh, H. (2010). *Internal report of data analysis center for geomagnetism and space magnetism*. Japan: Kyoto University.Mid-latitude geomagnetic indices asy and sym for 2009 (provisional)

Keller, K. A., Hesse, M., Kuznetsova, M., Rastätter, L., Moretto, T., Gombosi, T. I., et al. (2002). Global mhd modeling of the impact of a solar wind pressure change. *J. Geophys. Res.* 107, 1126. SMP 21–1–SMP 21–8. doi:10.1029/2001JA000060

Kikuchi, T. (1986). Evidence of transmission of polar electric fields to the low latitude at times of geomagnetic sudden commencements. *J. Geophys. Res.* 91, 3101. doi:10.1029/JA091iA03p03101

Kikuchi, T. (2014). Transmission line model for the near-instantaneous transmission of the ionospheric electric field and currents to the equator. *J. Geophys. Res. Space Phys.* 119, 1131–1156. doi:10.1002/2013JA019515

Kikuchi, T., Tsunomura, S., Hashimoto, K., and Nozaki, K. (2001). Field-aligned current effects on midlatitude geomagnetic sudden commencements. *J. Geophys. Res.* 106, 15555–15565. doi:10.1029/2001JA900030

Kivelson, M. G., and Southwood, D. J. (1991). Ionospheric traveling vortex generation by solar wind buffeting of the magnetosphere. *J. Geophys. Res.* 96, 1661–1667. doi:10.1029/90JA01805

Lam, M. M., and Rodger, A. S. (2001). A case study test of araki's physical model of geomagnetic sudden commencement. *J. Geophys. Res.* 106, 13135–13144. doi:10.1029/2000JA900134

Laundal, K. M., Finlay, C. C., Olsen, N., and Reistad, J. P. (2018). Solar wind and seasonal influence on ionospheric currents from swarm and champ measurements. *J. Geophys. Res. Space Phys.* 123, 4402–4429. doi:10.1029/2018JA025387

Laundal, K. M., Gjerloev, J. W., Østgaard, N., Reistad, J. P., Haaland, S., Snekvik, K., et al. (2016). The impact of sunlight on high-latitude equivalent currents. *J. Geophys. Res. Space Phys.* 121, 2715–2726. doi:10.1002/2015JA022236

Laundal, K. M., Reistad, J. P., Hatch, S. M., Madelaire, M., Walker, S., Hovland, A., et al. (2022). Local mapping of polar ionospheric electrodynamics. *JGR. Space Phys.* 127. doi:10.1029/2022JA030356

Laundal, K. M., and Richmond, A. (2017). Magnetic coordinate systems. *Space Sci. Rev.* 206, 27–59. doi:10.1007/s11214-016-0275-y

Laundal, K. M., Yee, J. H., Merkin, V. G., Gjerloev, J. W., Vanhamäki, H., Reistad, J. P., et al. (2021). Electrojet estimates from mesospheric magnetic field measurements. *JGR. Space Phys.* 126, e2020JA028644. doi:10.1029/2020ja028644

Lee, D.-Y., and Lyons, L. R. (2004). Geosynchronous magnetic field response to solar wind dynamic pressure pulse. *J. Geophys. Res.* 109, A04201. doi:10.1029/2003JA010076

Liou, K., Newell, P. T., and Meng, C.-I. (2001). Seasonal effects on auroral particle acceleration and precipitation. *J. Geophys. Res.* 106, 5531–5542. doi:10.1029/1999JA000391

Madelaire, M., Laundal, K. M., Reistad, J. P., Hatch, S. M., Ohma, A., Haaland, S., et al. (2022). Geomagnetic response to rapid increases in solar wind dynamic pressure: Event detection and large scale response. *Front. Astron. Space Sci.* 9. doi:10.3389/fspas.2022.904620

Moen, J., and Brekke, A. (1993). The solar flux influence on quiet time conductances in the auroral ionosphere. *Geophys. Res. Lett.* 20, 971–974. doi:10.1029/92GL02109

Moretto, T., Ridley, A. J., Engebretson, M. J., and Rasmussen, O. (2000). High-latitude ionospheric response to a sudden impulse event during northward imf conditions. *J. Geophys. Res.* 105, 2521–2531. doi:10.1029/1999JA900475

Newell, P. T., and Gjerloev, J. W. (2012). Supermag-based partial ring current indices. *J. Geophys. Res.* 117, n/a. doi:10.1029/2012JA017586

Newell, P. T., Sotirelis, T., Liou, K., Meng, C.-I., and Rich, F. J. (2007). A nearly universal solar wind-magnetosphere coupling function inferred from 10 magnetospheric state variables. *J. Geophys. Res.* 112, n/a. doi:10.1029/2006JA012015

Pettigrew, E. D., Shepherd, S. G., and Ruohoniemi, J. M. (2010). Climatological patterns of high-latitude convection in the northern and southern hemispheres: Dipole tilt dependencies and interhemispheric comparisons. *J. Geophys. Res.* 115. doi:10.1029/2009JA014956

Reistad, J. P., Laundal, K. M., Østgaard, N., Ohma, A., Thomas, E. G., Haaland, S., et al. (2019). Separation and quantification of ionospheric convection sources: 2. The dipole tilt angle influence on reverse convection cells during northward imf. *JGR. Space Phys.* 124, 6182–6194. doi:10.1029/2019JA026641

Ridley, A. J., De Zeeuw, D. L., Manchester, W. B., and Hansen, K. C. (2006). The magnetospheric and ionospheric response to a very strong interplanetary shock and coronal mass ejection. *Adv. Space Res.* 38, 263–272. doi:10.1016/j.asr.2006.06.010

Russell, C. T., Ginskey, M., and Petrinec, S. M. (1994b). Sudden impulses at low latitude stations: Steady state response for southward interplanetary magnetic field. *J. Geophys. Res.* 99, 13403. doi:10.1029/94JA00549

Russell, C. T., Ginskey, M., and Petrinec, S. M. (1994a). Sudden impulses at low-latitude stations: Steady state response for northward interplanetary magnetic field. *J. Geophys. Res.* 99, 253. doi:10.1029/93JA02288

Russell, C. T., and Ginskey, M. (1995). Sudden impulses at subauroral latitudes: Response for northward interplanetary magnetic field. *J. Geophys. Res.* 100, 23695. doi:10.1029/95JA02495

Sabaka, T. J., Hulot, G., and Olsen, N. (2014). Mathematical properties relevant to geomagnetic field modeling. *Handb. Geomathematics*, 1–37. Springer. doi:10.1007/978-3-642-27793-1_17-2

Samsonov, A. A., and Sibeck, D. G. (2013). Large-scale flow vortices following a magnetospheric sudden impulse. *J. Geophys. Res. Space Phys.* 118, 3055–3064. doi:10.1002/jgra.50329

Samsonov, A. A., Sibeck, D. G., and Yu, Y. (2010). Transient changes in magnetospheric-ionospheric currents caused by the passage of an interplanetary shock: Northward interplanetary magnetic field case. *J. Geophys. Res.* 115. doi:10.1029/2009JA014751

Shi, Q. Q., Hartinger, M. D., Angelopoulos, V., Tian, A. M., Fu, S. Y., Zong, Q.-G., et al. (2014). Solar wind pressure pulse-driven magnetospheric vortices and their global consequences. *J. Geophys. Res. Space Phys.* 119, 4274–4280. doi:10.1002/2013JA019551

Sibeck, D. G. (1990). A model for the transient magnetospheric response to sudden solar wind dynamic pressure variations. *J. Geophys. Res.* 95, 3755. doi:10.1029/JA095iA04p03755

Slinker, S. P., Fedder, J. A., Hughes, W. J., and Lyon, J. G. (1999). Response of the ionosphere to a density pulse in the solar wind: Simulation of traveling convection vortices. *Geophys. Res. Lett.* 26, 3549–3552. doi:10.1029/1999GL010688

Stauning, P., and Troshichev, O. A. (2008). Polar cap convection and pc index during sudden changes in solar wind dynamic pressure. *J. Geophys. Res.* 113. doi:10.1029/2007JA012783

Sugiura, M. (1964). Hourly values of equatorial dst for the igy. *Ann. Int. Geophys. Yr.* 35.

Sugiura, M., and Kamel, T. (1991). Equatorial dst index 1957-1986. *IAGA Bull.* 40.

Takeuchi, T., Russell, C. T., and Araki, T. (2002). Effect of the orientation of interplanetary shock on the geomagnetic sudden commencement. *J. Geophys. Res.* 107, SMP 6-1–SMP 6-10. SMP 6–1–SMP 6–10. doi:10.1029/2002JA009597

Tamao, T. (1964). *A hydromagnetic interpretation of geomagnetic ssc**, 18. Japan. Rept. Ionosphere Space Res.

Tarpley, J. D. (1973). Seasonal movement of the sq current foci and related effects in the equatorial electrojet. *J. Atmos. Terr. Phys.* 35, 1063–1071. doi:10.1016/0021-9169(73)90005-6

Trivedi, N. B., Abdu, M. A., Pathan, B. M., Dutra, S. L. G., Schuch, N. J., Santos, J. C., et al. (2005). Amplitude enhancement of events in the South Atlantic anomaly region. *J. Atmos. Sol. Terr. Phys.Space Geophys.* 67, 1751–1760. doi:10.1016/j.jastp.2005.03.010

Tu, J., and Song, P. (2019). On the momentum transfer from polar to equatorial ionosphere. *JGR. Space Phys.* 124, 6064–6073. doi:10.1029/2019JA026760

Weimer, D. R. (2013). An empirical model of ground-level geomagnetic perturbations. *Space weather.* 11, 107–120. doi:10.1002/swe.20030

Welling, D. T., Love, J. J., Rigler, E. J., Oliveira, D. M., Komar, C. M., Morley, S. K., et al. (2021). Numerical simulations of the geospace response to the arrival of an idealized perfect interplanetary coronal mass ejection. *Space weather.* 19, e2020SW002489. doi:10.1029/2020SW002489

World Data Center For Geomagnetism, Copenhagen (2019). The Polar Cap North (PCN) index (definitive). *DTU Space, Geomagnetism.* doi:10.11581/DTU:00000057

Zhou, Y.-L., and Lühr, H. (2022). Initial response of nightside auroral currents to a sudden commencement: Observations of electrojet and substorm onset. *JGR. Space Phys.* 127, e2021JA030050. doi:10.1029/2021ja030050

frontiers | Frontiers in Astronomy and Space Sciences

TYPE Original Research
PUBLISHED 30 August 2022
DOI 10.3389/fspas.2022.932748

OPEN ACCESS

EDITED BY
Jone Peter Reistad,
University of Bergen, Norway

REVIEWED BY
Eelco Doornbos,
Royal Netherlands Meteorological Institute, Netherlands
Fabrizio Sassi,
United States Naval Research Laboratory, United States

*CORRESPONDENCE
Astrid Maute,
maute@ucar.edu

SPECIALTY SECTION
This article was submitted to Space Physics,
a section of the journal
Frontiers in Astronomy and Space Sciences

RECEIVED 30 April 2022
ACCEPTED 25 July 2022
PUBLISHED 30 August 2022

CITATION
Maute A, Lu G, Knipp DJ, Anderson BJ and Vines SK (2022), Importance of lower atmospheric forcing and magnetosphere-ionosphere coupling in simulating neutral density during the February 2016 geomagnetic storm. *Front. Astron. Space Sci.* 9:932748. doi: 10.3389/fspas.2022.932748

Importance of lower atmospheric forcing and magnetosphere-ionosphere coupling in simulating neutral density during the February 2016 geomagnetic storm

Astrid Maute[1]*, Gang Lu[1], Delores J. Knipp[1,2], Brian J. Anderson[3] and Sarah K. Vines[3]

[1]High Altitude Observatory, National Center for Atmospheric Research, Boulder, CO, United States, [2]Ann and H.J. Smead Aerospace Engineering Sciences, University of Colorado, Boulder, CO, United States, [3]John Hopkins University/Applied Physics Laboratory, Laurel, MD, United States

During geomagnetic storms a large amount of energy is transferred into the ionosphere-thermosphere (IT) system, leading to local and global changes in e.g., the dynamics, composition, and neutral density. The more steady energy from the lower atmosphere into the IT system is in general much smaller than the energy input from the magnetosphere, especially during geomagnetic storms, and therefore details of the lower atmosphere forcing are often neglected in storm time simulations. In this study we compare the neutral density observed by Swarm-C during the moderate geomagnetic storm of 31 January to 3 February 2016 with the Thermosphere-Ionosphere-Electrodynamics-GCM (TIEGCM) finding that the model can capture the observed large scale neutral density variations better in the southern than northern hemisphere. The importance of more realistic lower atmospheric (LB) variations as specified by the Whole Atmosphere Community Climate Model eXtended (WACCM-X) with specified dynamics (SD) is demonstrated by improving especially the northern hemisphere neutral density by up to 15% compared to using climatological LB forcing. Further analysis highlights the importance of the background atmospheric condition in facilitating hemispheric different neutral density changes in response to the LB perturbations. In comparison, employing observationally based field-aligned current (FAC) versus using an empirical model to describe magnetosphere-ionosphere (MI) coupling leads to an 7–20% improved northern hemisphere neutral density. The results highlight the importance of the lower atmospheric variations and high latitude forcing in simulating the absolute large scale neutral density especially the hemispheric differences. However, focusing on the storm time variation with respect to the quiescent time, the lower atmospheric influence is reduced to 1–1.5% improvement with respect to the total observed neutral density. The results provide some guidance on the importance of more realistic upper boundary forcing and lower atmospheric

variations when modeling large scale, absolute and relative neutral density variations.

KEYWORDS

neutral density, Swarm-C, TIEGCM model, lower atmosphere, geomagnetic storm, field-aligned current forcing

1 Introduction

Geomagnetic storms are characterized by immense high latitude energy input from the magnetosphere into the upper atmosphere. Joule heating, which is the dominant energy source during large geomagnetic storms, describes the conversion of electromagnetic energy into heat through ohmic current (e.g., Richmond, 2021). The top 5% of geomagnetic storms between 1975–2004 produced on average approximately 331 GW in Joule heating and 73 GW in kinetic energy *via* particle precipitation (Knipp et al., 2004). During very strong storms Joule heating increases significantly to over 1000 GW and dominates over auroral particle precipitation (Lu et al., 2016). This high latitude energy input is approximately 10 times larger than the more continuous wave energy input from the lower atmosphere (around 100–150 GW) (Liu, 2016). The neutral density is affected by all of these energy sources e.g., Joule heating (e.g., Fedrizzi et al., 2012), auroral particle precipitation (e.g., Deng et al., 2013), lower atmosphere (e.g., Liu et al., 2017), direct solar radiation (e.g., Emmert, 2015), and varies spatially and temporally depending on these energy source.

Neutral density is sensitive to changes in geomagnetic activity with its associated energy input into the upper atmosphere (e.g., Müller et al., 2009). There are efforts to quantify the correlation between Joule heating and the neutral density change (e.g., Fedrizzi et al., 2012; Kalafatoglu Eyiguler et al., 2019a). The effect of Joule heating on the neutral density depends on the heating magnitude and on the altitude distribution of the energy deposition. While only 18–34% of the Joule heating is dissipated above 150 km, the energy at these higher altitude is more effective in changing the neutral density on shorter time scales (hours) (e.g., Deng et al., 2011; Huang et al., 2012). For a comprehensive review of neutral density variation during geomagnetic storms we refer to e.g., Prölss (2011).

The neutral density variations are affected by the interplay between heating, atmospheric expansion, neutral wind, and compositional changes. An excellent review about neutral density variations is provided by e.g., Emmert (2015). Thermospheric composition as measured by the ratio of atomic oxygen to molecular nitrogen, O/N_2, plays an important role in understand neutral density variations (e.g., Zhang and Paxton, 2021). In general, heating in the polar region leads to upwelling and a decrease of the O/N_2 ratio by transporting molecular nitrogen from N_2 rich regions into regions with lower N_2 (e.g., Zhang et al., 2004). The modification of the large scale wind system leads to equatorward and downward winds at lower latitudes transporting oxygen rich air from higher to lower altitudes and increases the O/N_2 ratio there (e.g., Forbes, 2007).

The neutral density response to geomagnetic disturbances is spatially and temporally varying. During geomagnetic storms large scale traveling atmospheric disturbances (TADs) are launched with associated neutral density variation propagating away from region of sudden large energy deposition (e.g., Bruinsma and Forbes, 2009; Ritter et al., 2010). Therefore, the equatorial neutral density response lags by approximately 3–5 h with a shorter response time on the dayside than on the nightside e.g., as suggested by Müller et al. (2009); Bruinsma and Forbes (2009); Sutton et al. (2009). In this study we focus on a moderate geomagnetic disturbed period and its large-scale neutral density response, and TADs with their associated neutral density variations are not the focus of this study.

The background atmospheric condition modulates the geomagnetic storm responses in neutral composition and neutral density. For geomagnetic storms during solar minimum compared to solar maximum conditions the magnitude and extend of compositional changes are found to be larger, which is explained by more efficient transport and smaller scale heights during solar minimum conditions (e.g., Emmert, 2015).

The seasonal mean circulation can enhance or reduce the effect of high latitude heating on the composition. During average geomagnetic storm conditions the compositional changes extends more equatorward in the summer hemisphere than in the winter hemisphere (e.g., Zuzic et al., 1997). However, Zhang and Paxton (2021) pointed out that GUVI observed larger O/N_2 depletion extending more equatorward in the northern winter than southern summer hemisphere during the 20–21 November 2003 geomagnetic storm. The authors suggested that this hemispheric asymmetry is associated with interhemispheric differences in the auroral hemispheric power.

Comprehensive overview of solar-cycle, seasonal and diurnal neutral density variation can be found in e.g., Qian and Solomon (2012); Emmert (2015); Liu et al. (2017). The neutral density scales approximately linearly with solar radiation but more strongly during day-time than night-time (e.g., Müller et al., 2009). The neutral density is larger in the summer than in the winter and the latitudinal variation is reduced around the equinox transition. The equinoctial neutral density is larger than the solstice neutral density and larger in March than

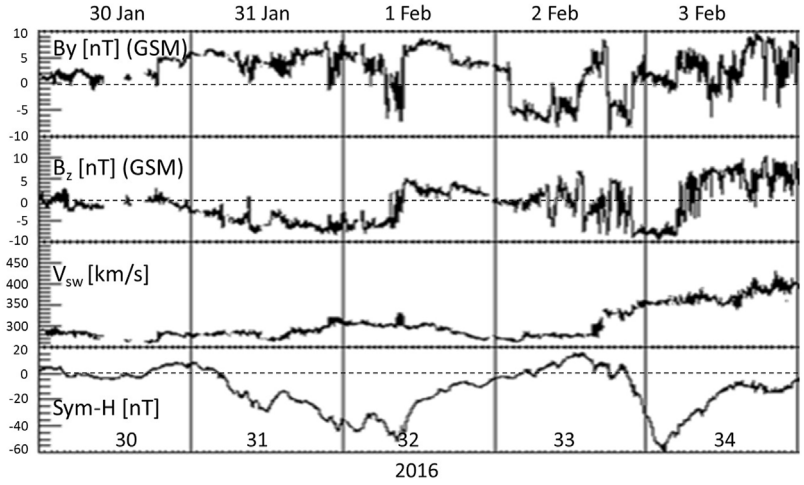

FIGURE 1
Geophysical conditions for 30 January—3 February 2016: IMF B_y (top), B_z [nT] (second from top), solar wind velocity V_{sw} [km/s] (second from bottom), and Sym-H index [nT] (bottom) based on NASA SPDF-OMNIweb data [https://omniweb.gsfc.nasa.gov].

September (e.g., Müller et al., 2009; Qian and Solomon, 2012) due to lower atmospheric forcing and the associated large scale "turbulent eddy" suppressing the maximum density at solstices (e.g., Fuller-Rowell, 1998).

Qian et al. (2009) modified the eddy diffusion in a numerical model to mimic the effect of wave dissipation and improved the agreement with the observed daily averaged neutral density variations, highlighting the importance of lower atmospheric forcing for capturing seasonal variations in daily averaged neutral density. The magnitude of the eddy diffusion coefficient in numerical models depends on the resolved waves as demonstrated by Siskind et al. (2014) who reduced the eddy diffusivity by a factor of five from Qian et al. (2009) when using realistic planetary wave and tidal perturbations. The present study will focus on the influence of the lower atmospheric forcing on the neutral density without changing the default eddy diffusivity in the numerical model, TIEGCM. So far, it is not understood how to adjust eddy diffusivity in the model to account for the changing complexity in the prescribed wave spectra.

In the upper mesosphere and lower thermosphere (MLT) region the atmosphere transitions from a well-mixed fluid to being dominated by molecular diffusion. Increasing the eddy mixing will move this transition to higher altitude and therefore lead to a reduction of atomic oxygen. Another effect of eddy diffusion is an increase in heat conduction from the hotter atmosphere above to the cooler atmosphere below in the MLT region (Roble, 1995). Jones et al. (2014b,a) found an approximate 10% decrease in the low latitude upper thermospheric atomic oxygen at equinox due to including lower atmospheric tides in their simulations. They attributed these depletion to tidal-induced net transport of atomic oxygen. Yamazaki and Richmond (2013) carefully examined the role of migrating tides finding that a major contributor to the atomic oxygen reduction is the modified mean circulation through tidal dissipation. In addition residual circulation in the lower thermosphere was suggested to influence the neutral density by locally modifying the composition which is then transferred to the atmosphere above (Qian and Yue, 2017).

Depending on the focus of a modeling study special attention is often given either to realistic high latitude forcing when examining geomagnetic storm or lower atmospheric forcing when focusing on vertical coupling. Several studies pointed out that neutral density variations of quiescent and storm times can be evaluated separately, assuming linear behavior (e.g., Müller et al., 2009; Kalafatoglu Eyiguler et al., 2019b). The interplay of both forcing on neutral density variations is not well understood and neither is their importance for capturing the absolute and relative neutral density variations.

In this study we focus on a moderate geomagnetic storm and quantify the relative effect of the lower atmosphere forcing and the high latitude forcing on the large scale neutral density variations in different latitudinal regions. As we will show below, there are strong interhemispheric differences in the neutral density variation that cannot be solely explained by the interhemispheric differences in the forcings.

In section 2 we first describe the geophysical conditions associated with the storm, the Swarm neutral density data, and the TIEGCM with its boundary condition. In section 3 the influence of the lower atmosphere on the neutral density is studied. In section 4 we examine the importance of realistic high latitude forcing on the neutral density variation. In section 5 we conclude by comparing the two effects.

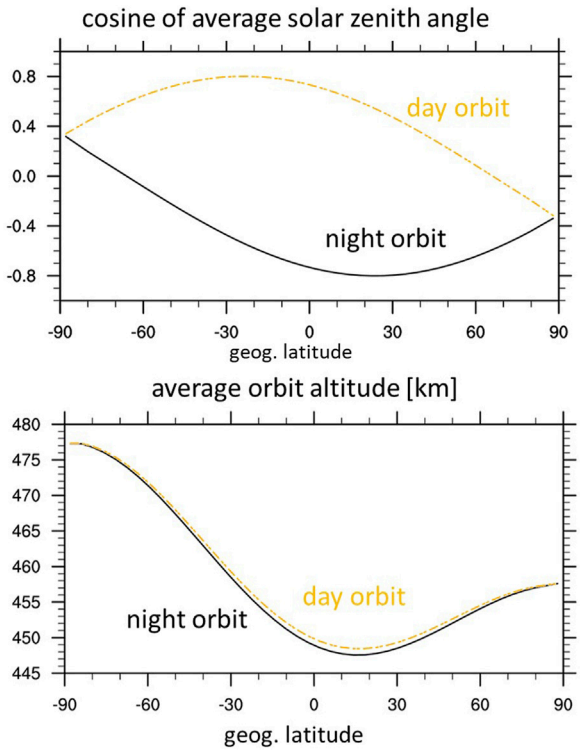

FIGURE 2
Cosine of average solar zenith angle (top) and average orbit altitude (bottom) (averaged between doy 30.0–35.0)

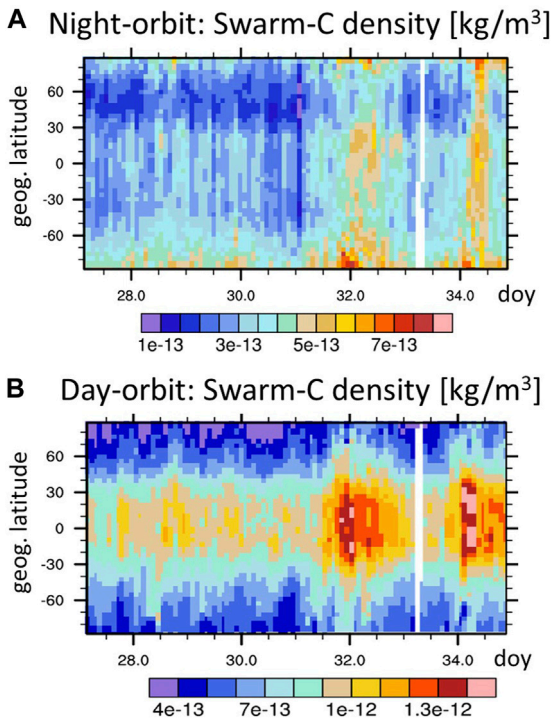

FIGURE 3
Neutral density [kg/m^3] at Swarm-C orbit binned in latitude and time: **(A)**. For the night-time orbit, **(B)**. For day-time orbit.

2 Data and model

In this study we examine the effect of the lower atmospheric and high-latitude forcing on the neutral density during the moderate geomagnetically disturbed period of 31 January to 3 February 2016. We would like to point out that according to Gonzalez et al. (1994) the period is characterized as a moderate geomagnetic storm while using the NOAA Space Weather scale it is a minor geomagnetic storm (G1). This period was a focused study in the project "Next Generation Advances in Ionosphere-Thermosphere Coupling at Multiple Scales for Environmental Specifications and Predictions" mainly due to interesting meso-scale magnetosphere-ionosphere coupling phenomena. Among others, a preliminary data-model comparison revealed significant hemispheric differences in the simulation results for capturing the Swarm neutral mass density measurements, which prompted the current study to further examine the role of the lower atmospheric forcing in addition to the high-latitude forcing from the magnetosphere. In this study we use the Swarm-C neutral density observations and TIEGCM simulations, which are described in the following.

The geophysical conditions for 30 January to 3 February 2016 are summarized in Figure 1. The geomagnetic activity starts late on 30 January (day of year doy 30) with IMF B_y becoming positive (approximately 5nT), followed by IMF B_z turning southward a few hours later and staying southward throughout 31 January (doy 31) till approximately 1 February (doy 32) six UT. While IMF B_y and B_z oscillate frequently on 2 February (doy 33) a more sustained southward IMF B_z period starts late on 2 February lasting a few hours before becoming northward around four UT on 3 February. The Sym-H index, a measure of the symmetric ring current strength, becomes negative on 31 January lasting till 1 February (minima around -50nT), recovers on 2 February, and then is disturbed again on 3 February with a minimum of roughly -60nT. The observed solar radio flux $F_{10.7}$ varies only slightly between 100 and 112 solar flux unit (1 sfu is $10^{-22}\frac{W}{m^2 Hz}$).

2.1 Swarm neutral density

The neutral density are from the Swarm data product (DNSxACC version 0201) derived in a four-stage process as described by Siemes et al. (2016). During this time period Swarm-C orbit altitude is between 450 km and 478 km (see Figure 2). The orbit altitude is approximately 20 km higher in the southern than northern high latitude region. Only considering the altitude

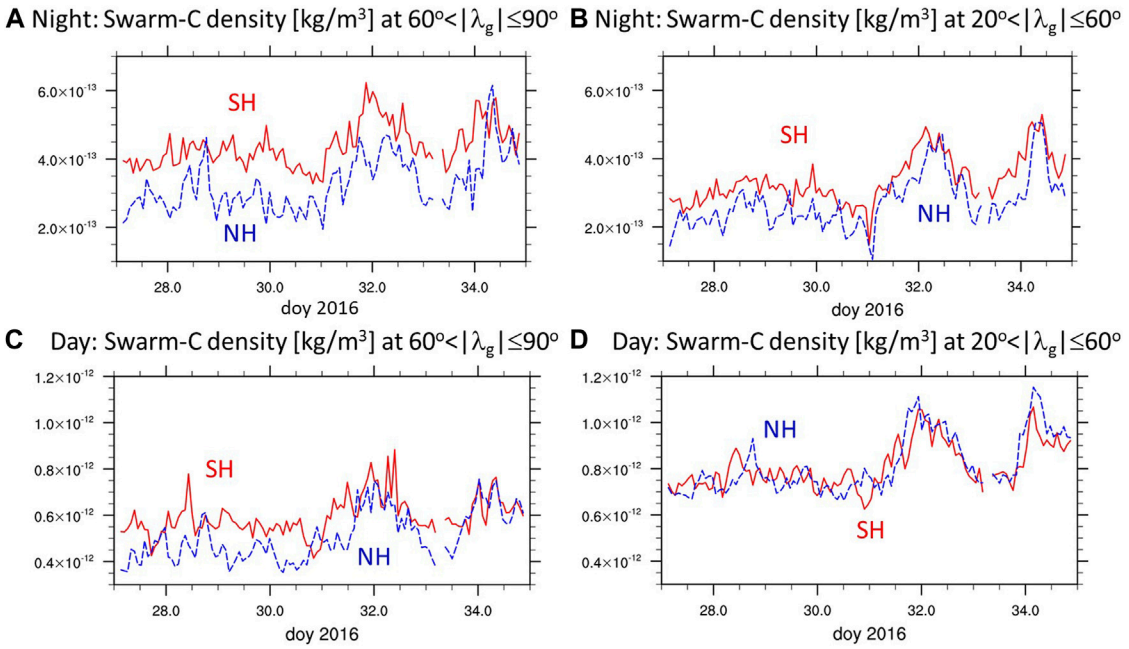

FIGURE 4
Average neutral density [kg/m^3] at Swarm-C orbit in different geographic latitude λ_g bins for the SH (red lines) and NH (blue lines): **(A)**. For night-time orbit at $60° < |\lambda_g| < 90°$, **(B)**. For night-time orbit at $20° < |\lambda_g| < 60°$, **(C)**. For day-time orbit at $60° < |\lambda_g| < 90°$, **(D)**. For day-time orbit at $20° < |\lambda_g| < 60°$.

difference, the neutral density is roughly a factor of 1.4–1.5 larger at lower than higher altitudes based on NRLMSIS2.0 (Emmert et al., 2021). The night-time part of the orbit is around 2.5–3 h solar local time (SLT) at middle and low latitudes and the day-time orbit is around 14–15 h SLT. The average solar zenith angle is given in Figure 2 indicating that the night-time orbits are sunlit in the southern polar region and in darkness in the northern hemisphere.

There are different ways to quantify and compare neutral densities, highlighting specific aspects of the variation. Neutral density can be measured as a global mean (e.g., Solomon et al., 2011), orbit averaged (e.g., Fedrizzi et al., 2012), along orbit tracks (e.g., Shim et al., 2012), absolute (e.g., Yamazaki and Kosch, 2015) and relative, or scaled to a particular altitude (e.g., Kalafatoglu Eyiguler et al., 2019b). In the following we will use the neutral density along the orbit track to avoid any potential biasing due to scaling to a common altitude.

To better compare to the simulated neutral density, the observed neutral density is averaged in 2 h and 4° geographic latitude bins (each bin includes values from no more than two orbits). The geographic latitude and time variation of the binned neutral density is shown in Figures 3A,B for the night- and day-time orbit, respectively. The enhanced neutral density due to the moderate geomagnetic activity is clearly visible around doy 32 and doy 34. In general the observed neutral density is larger in the southern (SH) than northern (NH) hemisphere, however during the daytime at middle and low latitudes this is not the case.

To better quantify the temporal variations of the neutral density we focus on average densities in latitudinal ranges shown in Figure 4. Note that similar to orbit averaged calculation we do not weight by the decreasing area toward the pole. The top and bottom two panels are for the night- and day-time orbit, respectively, for the polar region with $60^o < |\lambda_g| \leq 90^0$ on the left, and middle latitude region $20^o < |\lambda_g| \leq 60^0$ on the right (λ_g is the geographic latitude). In the polar region during the night-time orbit the SH neutral density is on average approximately 30% larger than in the NH, while during the day-time orbit the SH neutral density is on average 18% larger than in the NH with respect to the average density in both hemispheres. During the night-time orbits there is an approximate 22% difference in the middle latitude neutral density between the two hemispheres but during the day-time both hemispheres have similar average neutral density variations.

Several factors can contribute to the interhemispheric differences in the neutral density. The seasonal solar zenith angle change leads to hemispheric differences in neutral dynamics and composition. Counteracting the seasonally higher neutral density in the SH summer than NH winter is the difference in Swarm orbit altitude. In addition, the lower atmospheric forcing, which itself has an inherent seasonal variation, can modify the thermospheric and ionospheric

TABLE 1 Overview of simulation set up: all simulations are done with the TIEGCM; the simulations WacXBP and TIEGCM(FAC) are the same and the former abbreviation is used in section 3 highlighting the lower boundary forcing and the latter in section 4 focused on the high latitude forcing; simulations WacXBP, Climate, WacXP-CB, WacXB-symP are described in section 3 while simulations TIEGCM(FAC) and TIEGCM(Weimer) are described in section 4. We abbreviated in the table WACCMX-SD with WACX-SD and climatology with "Climat"

Abbreviation	WacXBP	Climate	WacXP-CB	WacXB-symP	TIEGCM (FAC)	TIEGCM (Weimer)
LB perturbation P	WACX-SD	Climat	WACX-SD	symmetric WACX-SD	WACX-SD	WACX-SD
LB background B	WACX-SD	Climat	Climat	WACX-SD	WACX-SD	WACX-SD
high latitude forcing	FAC	FAC	FAC	FAC	FAC	Weimer

state, including the neutral density. During geomagnetic storms the enhanced high latitude energy input into the IT system can contribute to hemispheric differences. In the following we will focus on the importance of lower atmospheric and high latitude forcing in simulating the neutral density variations with TIEGCM.

2.2 TIEGCM

The TIEGCM is a self-consistent model which includes atmospheric dynamics, chemistry and energetics of the thermosphere and ionosphere. The ionospheric electrodynamics in the TIEGCM is driven by the wind dynamo, gravity and plasma pressure gradient driven current, and effects due to magnetosphere-ionosphere coupling (Richmond and Maute, 2013). Detailed information about the model can be found in Qian et al. (2014); Maute (2017).

The model spans from approximately 97 km to 450–600 km depending on the solar cycle conditions. We use a horizontal resolution of $2.5^o \times 2.5^o$ in geographic latitude and longitude. At high latitude the magnetosphere-ionosphere coupling is simulated by either prescribing empirical high latitude electric fields based on Weimer (2005) or observed field-aligned current (FAC) based on AMPERE data (Anderson et al., 2000, 2014). The auroral particle precipitation in both simulations is defined *via* an analytical auroral model (Roble and Ridley, 1987; Emery et al., 2012). Modifications of the default TIEGCM auroral parametrization in the Weimer and FAC driven simulations are described in Supporting Information 1. Hereafter, we label the Weimer driven simulation with "Weimer" and the field-aligned current driven simulation with "FAC".

The high latitude FAC patterns are derived in the two hemispheres by processing the AMPERE magnetic field observations from the Iridium satellites using principal component analysis as described by Shi et al. (2020). The limited number of used principal components (PC) results in a smoother FAC distribution compared to the original AMPERE field-aligned current. Therefore, the magnitude of the hemispheric integrated upward and downward FAC is reduced using PC based FAC compared to the original AMPERE FAC. To get hemispheric integrated FAC strength comparable to the original AMPERE data, we increase the FAC magnitude in the simulations by 45% in both hemispheres.

Maute et al. (2021) describe the method of prescribing high latitude FAC in the TIEGCM and the key points are summarized in the following. The electric potential is determined in a three step process. In the first step, the electric potential is calculated due to the global wind dynamo and the hemispherically symmetric, with respect to the geomagnetic field, component of the prescribed FAC. In the second step, the FAC at the top of the ionosphere in each magnetic hemisphere due to the symmetric potential solution from step 1 and the local wind dynamo is calculated. The difference between the original prescribed FAC and the calculated FAC from step 2 in a given hemisphere is used in step 3. In step 3 the FAC determined in step 2 in a given hemisphere is prescribed at the upper boundary at high latitudes with a zero potential constraint at the equatorward edge of the region (here at $|40^o|$ magnetic latitude). The potential from step 1 is hemispherically symmetric and from step 3 is hemispherically asymmetric on a magnetic grid. The total electric potential is the sum of the solutions from step 1 and step 3. In each step we have to ensure that the current into and out of the ionosphere are balanced by adjusting the FAC. We distribute any non-balanced FAC according to the local Pedersen conductance as described in Marsal et al. (2012).

At the TIEGCM lower boundary (LB) (approximately at 97 km) we can specify the background variations as well as perturbations in the horizontal wind, neutral temperature, and geopotential height. To evaluate the importance of the lower atmospheric forcing on the neutral density variation we conduct two simulations. In one simulation we use a climatological LB background and perturbations. We employ the tidal climatology from Global Scale Wave Model (GSWM) (Zhang et al., 2010) and specify the LB background using the mass spectrometer and incoherent scatter radar (MSIS00) model and the horizonal wind model (HWM07) (see Jones et al., 2014b; Maute, 2017). GSWM includes the effect of migrating and nonmigrating, diurnal and semidiurnal tidal components. In the TIEGCM GSWM perturbations are specified hourly for the day in the middle of each month and interpolated temporally. We label this simulation with "Climate".

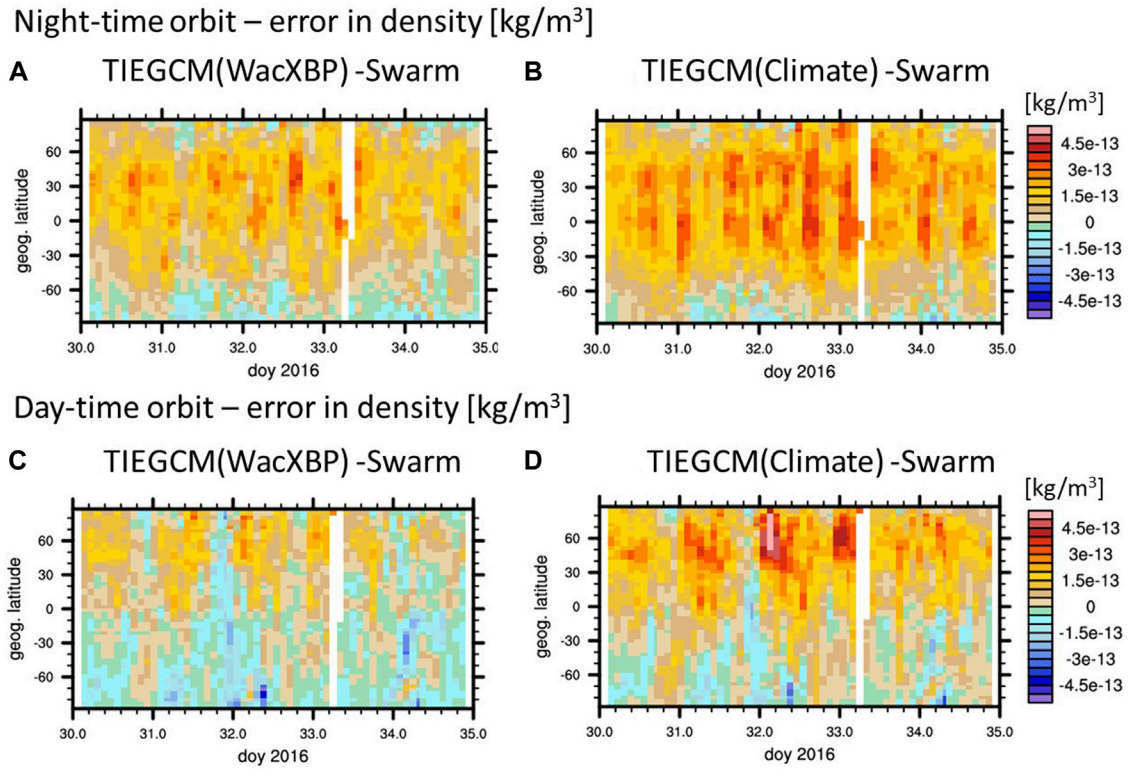

FIGURE 5
Variations for night-time orbit [panel **(A–B)**] and day-time orbit [panel **(C–D)**] of neutral density difference between TIEGCM(WacXBP) and Swarm-C [**(A)**. and **(C)**.] and between TIEGCM(Climate) and Swarm-C [**(B)**. and **(D)**.].

For comparison we conduct a TIEGCM simulation with the LB specified by output from the Whole Atmosphere Community Climate Model- eXtended with Specified Dynamics (WACCMX-SD) (WACCMX-SD, 2019; Gasperini et al., 2020; Pedatella et al., 2021). WACCM-X is a whole atmosphere climate model spanning from the Earth surface to the thermosphere (Liu et al., 2018). To simulate specific time periods the WACCM-X dynamics are nudged up to approximately 50 km towards reanalysis data, here Modern-Era Retrospective analysis for Research and Applications, Version 2 (MERRA-2) (Gelaro et al., 2017). Using the WACCMX-SD results at the TIEGCM LB allows us to prescribe the specific background "B" and perturbations "P", including planetary waves and tides, for this time period. We use WACCMX-SD output at the pressure level closest to the TIEGCM LB pressure level. In this study we also examine the effects of a more realistic background atmosphere versus perturbation at the TIEGCM lower boundary on the simulated neutral density. Therefore, the background is represented by the daily zonal and diurnal mean of the horizontal winds, neutral temperature, and geopotential height. The perturbation fields are the difference between the total fields and the background. We label the simulation with WACCMX-SD at the LB as "WacXBP" (B for background and P for perturbation from WACCMX-SD simulation). In a control case we use only the WACCMX-SD perturbations (WacXP) with the climatological background (CB) from the "Climate" simulation and we will refer to this simulation as "WacXP-CB". We provide an overview of all simulations in Table 1. All simulations are using the TIEGCM but differ by either the lower boundary forcing and/or the high latitude forcing.

We start all simulations at doy 10, 2016 with the respective lower boundary forcing and the high latitude electric potential defined by Heelis et al. (1982) driven by 3-hourly Kp index (Emery et al., 2012). At doy 30 we continued the simulations with the respective high latitude forcing. For comparing with the neutral density from Swarm-C, we determine the TIEGCM simulated neutral density along the Swarm-C orbit and apply the same binning as for Swarm-C data to the synthetic TIEGCM data. Note that for this time period the TIEGCM upper boundary is always above the Swarm-C orbit altitude. To measure the difference between the simulated and observed neutral density we use the sum of the absolute differences (L-1 norm) of the binned data which does not include any weighting by the error magnitude like the root mean square error does. Relative errors

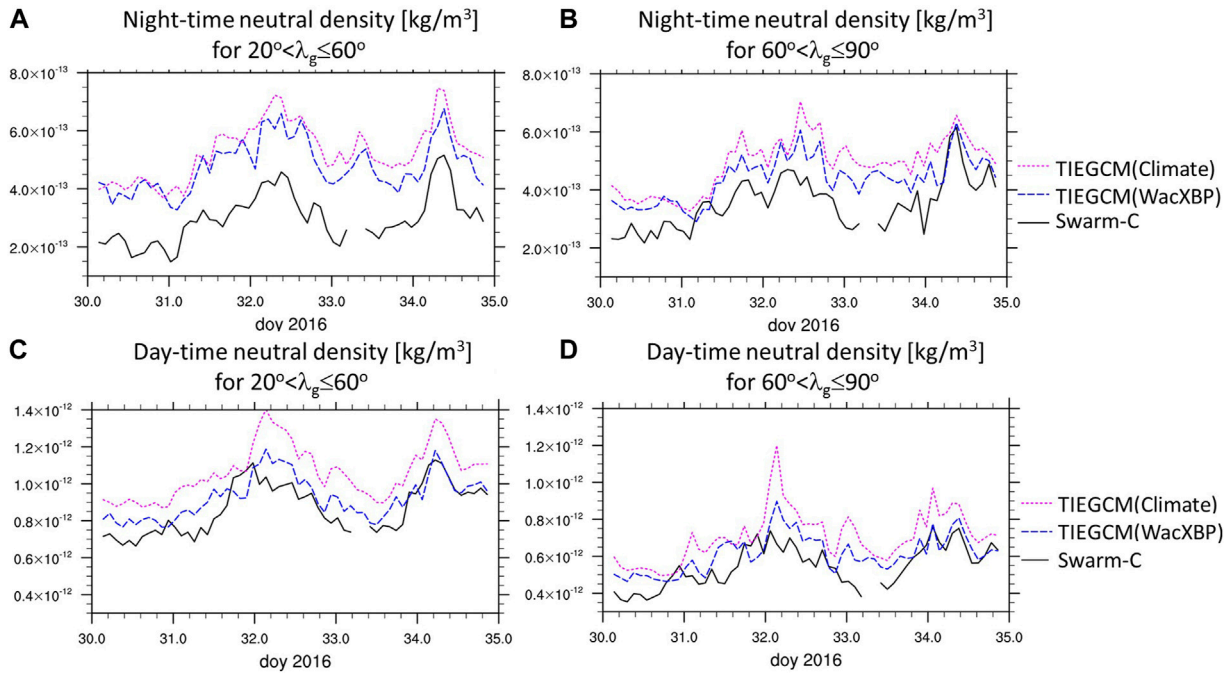

FIGURE 6
Northern hemisphere latitudinal average neutral density variations of Swarm-C (black solid lines), TIEGCM(WacXBP) (dark blue dashed lines), and TIEGCM(Climate) (magenta dotted lines) for night-time orbit **(A–B)** and day-time orbit **(C–D)** for $20^0 < \lambda_g \leq 60^0$ **(A)** and **(C)** and for $60^0 < \lambda_g \leq 90^0$ **(B)** and **(D)**.

TABLE 2 Relative error with respect to the absolute observed neutral density $|\rho_{model} - \rho_{data}|_1/|\rho_{data}|_1$ for the different lower atmospheric forcing over the 5 day period (doy 30–34).

		60-90 S	60-90 S	20-60 S	20-60 S	60–90 N	60–90 N	20–60 N	20–60 N
high latitude	lower boundary	day	night	day	night	day	night	day	night
FAC	WacXBP	11%	**8.4%**	**5.2%**	**20%**	**15%**	**25%**	**9.6%**	**60%**
FAC	Climate	**8.4%**	9.3%	5.7%	37%	30%	39%	23%	77%
FAC	WacXB-symP	8.7%	7.7%	4.9%	28%	20%	30%	16%	68%
FAC	WacXP-CB	11%	9.1%	5.5%	19%	19%	29%	11%	65%

The bold numbers indicate better agreement with observations for the Climate and WacXBP cases.

are calculated with respect to the sum of the observed Swarm-C neutral density variations if not stated otherwise.

3 Effects of lower atmospheric forcing

We first examine the effect of lower atmospheric forcing on the neutral density at Swarm-C altitude by comparing the simulation with climatological forcing at the lower boundary (Climate) to the simulation with WACCMX-SD at the lower boundary (WacXBP). Both simulations use the same high latitude FAC forcing. Figure 5 illustrates the error in the Climate and WacXBP simulations with respect to Swarm-C neutral density for the night-time orbit in the top row and day-time orbit in the bottom row. The absolute simulated neutral density variation is included in the Supplementary Figure S1.

In general, the error in the simulated neutral density is larger during the night-time than day-time orbit. During the day-time the simulated neutral density tends to be larger than the observed one in the northern hemisphere while the simulated neutral density tends to be smaller or equal to the observed one in the southern hemisphere. At night-

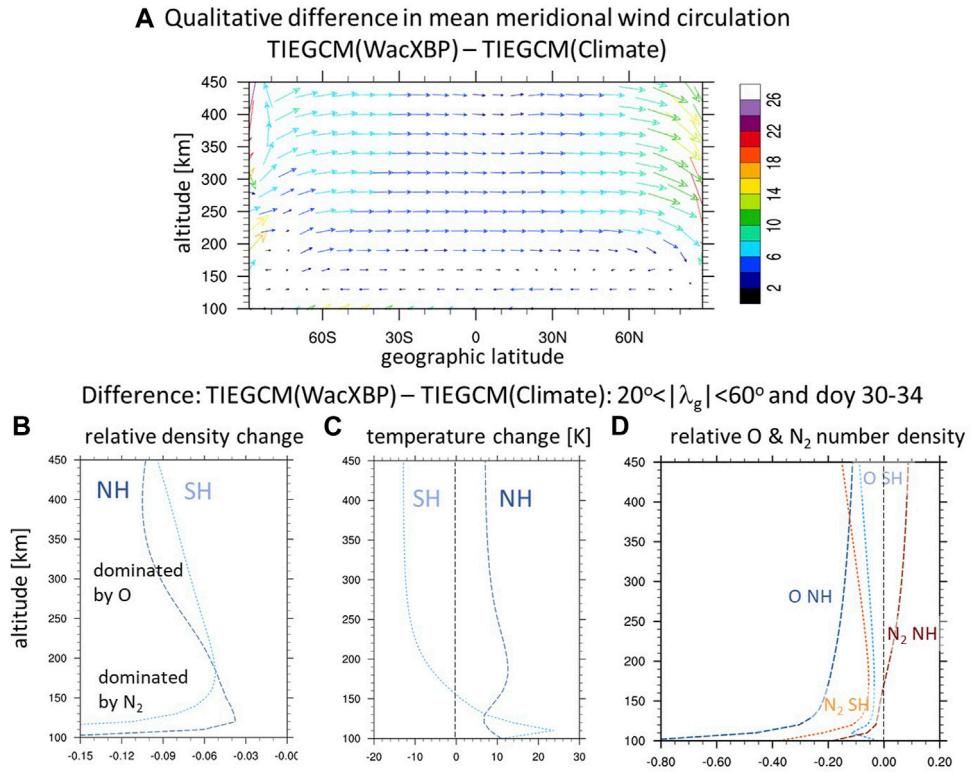

FIGURE 7
(A). Difference between TIEGCM(WacXBP) and TIEGCM(Climate) of doy 30–34 in **(A)**. the diurnal and zonal mean circulation (qualitative, the vertical velocity is increased by a factor of 30 for better illustration); **(B–D)**. average changes over $20° < |\lambda_g| \leq 60°$ and doy 30–34 between TIEGCM(WacXBP) and TIEGCM(Climate) with altitude of **(B)**. neutral density with respect to TIEGCM(WacXBP); **(C)**. temperature [K], **(D)**. O and N_2 number density with respect to TIEGCM(WacXBP).

time the simulated neutral density is overestimated almost everywhere except poleward of 60°S. There is no significant increase in the neutral density error during the disturbed period around doy 32 and 34.

Comparing the error of the Climate simulation (right panels) with the WacXBP simulation (left panels) in Figure 5 illustrates that including more realistic LB variations reduced the error especially in the northern hemisphere. The error is also reduced in the mid- and low-latitude region in the southern hemisphere at night-time but not much at day-time. In the southern polar region there is no large difference between the simulation's ability to capture the neutral density variations.

In Figure 6 we simplify the results by focusing on the average neutral density variation in specific latitudinal ranges. In general, the error is larger during the night-time. In the illustrated northern hemisphere cases the error is reduced in the WacXBP simulation compared to the Climate one, however the reduction tends to be less during the night-time. We summarize in Table 2 the relative error in the different latitudinal regions. The error is reduced by approximately 15% in the northern hemisphere in the WacXBP simulation compared to the Climate one. While the WacXBP simulation with the wave spectrum from the February 2016 period performs better in capturing the neutral density than using the climatology, we cannot rule out that using lower boundary conditions from other years with similar variability would lead to similar results. Examining this is beyond the scope of the current study which focuses on the general importance of the lower atmosphere and the high latitude forcing.

In the following we analyze the simulations to better understand the larger improvement in neutral density in the NH compared to the SH. In the lower thermosphere, approximately below 120 km, the zonal mean wind pattern averaged over 5 days (doy 30–34) is different between the Climate and WacXBP simulations (Figure 7A SI Supplementary Figure S2). In Supplementary Figure S5 we provide a simplified schematic to support the main points of the following discussion. The Climate simulation tends to have a summer to winter circulation throughout the thermosphere with upward velocity in the southern hemisphere (poleward of 20 S), a northward turning, and then downward in the northern hemisphere (equatorward

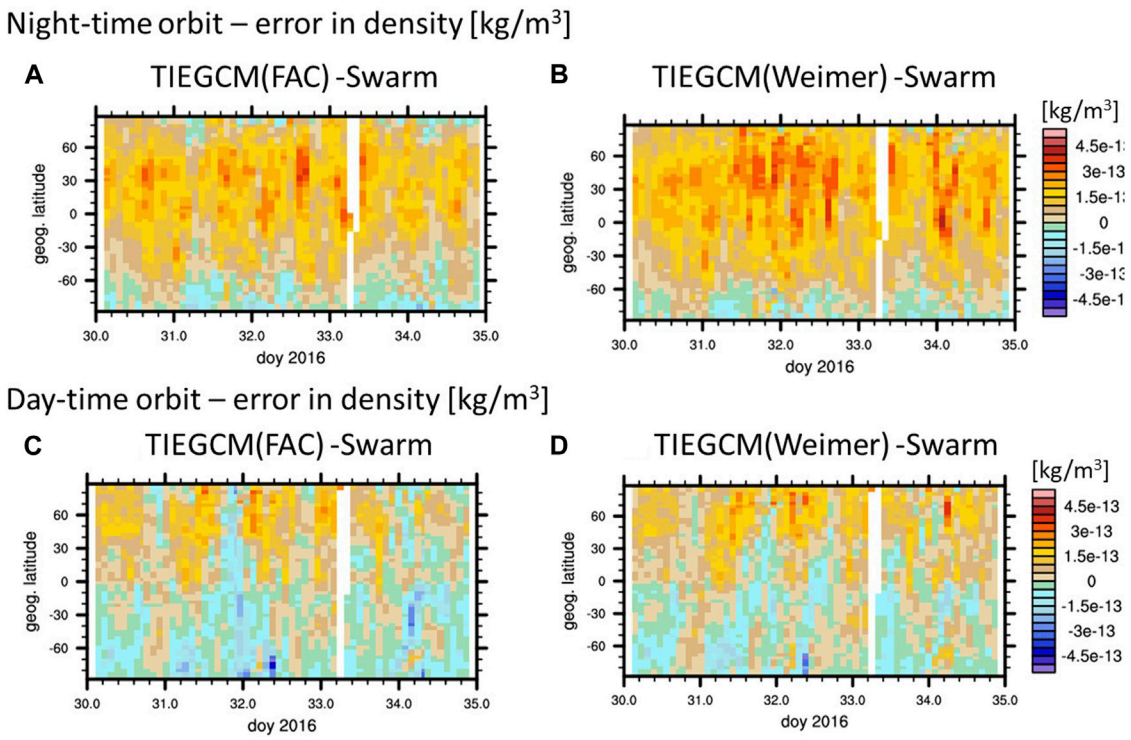

FIGURE 8
Neutral density difference between TIEGCM(FAC) and Swarm-C **(A)** and **(C)** and between TIEGCM(Weimer) and Swarm-C **(B)** and **(D)** for night-time orbit **(A)** and **(B)** and day-time orbit **(C)** and **(D)**.

of 70 N). In the WacXBP simulation the mean velocity tends to be weakly poleward and downward in the southern hemisphere equatorward of 70 S below approximately 120 km (see SI Supplementary Figure S2).

Above approximately 140 km the two simulations have a similar summer to winter circulation. But the WacXBP simulation has a stronger circulation than the Climate simulation, which modifies the temperature and composition (see Figure 7). Figure 7C illustrates the zonal mean neutral temperature changes averaged over 5 days (doy 30–34) between $20^0 < |\lambda_g| \leq 60^o$. Above approximately 150 km the WacXBP simulation is colder than the Climate simulation in the SH associated with increased upwelling and adiabatic cooling in the WacXBP case. In the NH there is increased downwelling in the WacXBP simulation leading to a warmer thermosphere compared to the Climate simulation.

Below approximately 140km the WacXBP simulation is warmer in the southern hemisphere than the Climate simulation probably associated with the tendency of more downward or less upward circulation in the WacXBP simulation compared to the Climate simulation. The mean circulation and the temperature influence the composition and neutral density. Below approximately 180 km the N_2 number density is larger than the O_1 number density and therefore a larger contributor to the neutral density. In the southern hemisphere below approximately 140 km, the N_2 number density is decreased in the WacXBP versus the Climate simulation (Figure 7D) since the Climate simulation's upward velocity transports N_2 from regions of larger number densities to higher altitudes, while the WacXBP simulation has downward or less upward velocity in this region. This decrease in N_2 in the lower thermosphere leads to the reduced neutral density in the southern hemisphere in the WacXBP compared to the Climate case at these altitudes (Figure 7B).

In the northern hemisphere the circulation at the lower altitudes is not significantly different between the simulations. The results suggest that increased tidal variability and associated mixing of the atmosphere leads to smaller N_2 number density in the WacXBP case compared to the Climate simulation which is then reflected in the smaller neutral density at these altitudes in WacXBP compared to the Climate simulation.

At Swarm altitudes around 450km atomic oxygen is expected to be the dominant species. In general, the scale height is larger in the summer than in the winter hemisphere, leading to smaller vertical gradients in the O_1 number density in the southern summer than northern winter hemisphere. Due to larger vertical gradients in the NH the changes in the vertical velocity due to the LB boundary will have increased effects on the number density

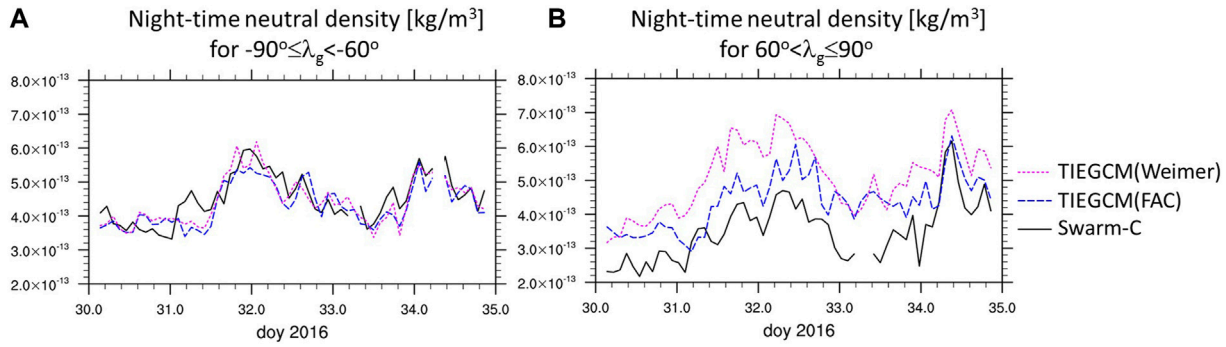

FIGURE 9
Night-orbit high latitudinal average neutral density variations of Swarm-C (black solid lines), TIEGCM(Weimer) (magenta dotted lines), and TIEGCM(FAC) (blue dashed lines) for night-time orbit for $-90^0 \le \lambda_g < -60^0$ **(A)** and for $60^0 < \lambda_g \le 90^0$ **(B)**.

TABLE 3 Relative error with respect to the absolute observed neutral density $|\rho_{model} - \rho_{data}|_1/|\rho_{data}|_1$ averaged over doy 30–34 for different high latitude forcing.

		60-90 S	60-90 S	20-60 S	20-60 S	60–90 N	60–90 N	20–60 N	20–60 N
high latitude	lower boundary	day	night	day	night	day	night	day	night
Weimer	WacXBP	**8.3%**	**8%**	**4.2%**	27%	22%	46%	9.6%	75%
FAC	WacXBP	11%	8.4%	5.2%	**20%**	**15%**	**25%**	9.6%	**60%**

The bold numbers indicate an improvement.

in the northern winter hemisphere than southern summer hemisphere (Qian and Yue, 2017). In the northern hemisphere an increased downwelling in the WacXBP simulation compared to the Climate one (see SI Supplementary Figure S2) transports more efficiently O_1 into regions of higher recombination rates leading to a larger reduction of O_1. Since the scale height in the northern hemisphere tends to be larger in the WacXBP than in the Climate simulation, the absolute difference in O_1 number density between the simulations decreases with altitude (Figure 7D).

In the SH the absolute change in O_1 number density between the simulations are much smaller than in the NH but as in the NH the O_1 number density in the WacXBP simulation is smaller than in the Climate simulation. This might be associated with the competing effects of more atmospheric mixing due to increased tidal variability and vertical winds in the WacXBP simulation. The absolute difference in O_1 number density between the Climate and WacXBP simulations grows slowly with altitude most likely associated with the larger mean temperature and scale height in the Climate than WacXBP simulation in the southern hemisphere. Therefore, the southern hemisphere absolute neutral density changes between Climate and WacXBP simulation increase almost linearly with altitude but are smaller than the absolute difference in the NH between approximately 200–470 km. The simulations suggest that eventually at higher altitudes (above 450 km) the average changes in O_1 number density due to different lower boundary forcings will be similar in both hemispheres (Figure 7D).

The simulations suggest that the magnitude of the interhemispheric difference in the neutral density response to the lower atmospheric forcing depends on altitude and that in the upper thermosphere the maximum interhemispheric difference is around 350 km. Swarm-C is above the maximum differences but still in the altitude region where the NH response to LB changes is stronger than the SH response.

To delineate the effect of LB perturbations and LB background (zonal and diurnal mean) on the IT system, we conduct an additional simulation with WACCMX-SD perturbations (WacXP) by replacing the WacXB background with the climatological LB background from the Climate simulation (CB). The differences between this WacXP-CB simulation and the previously described WacXBP simulation can be attributed to the difference in the LB background forcing. The result is summarize in Table 2 labeled by WacXP-CB. The error is only slightly increased using WacXP-CB compared to WacXBP. This finding aligns with previous studies (e.g., Jones et al., 2014b; Maute, 2017) pointing out that details of the LB background forcing are less important than the LB perturbations.

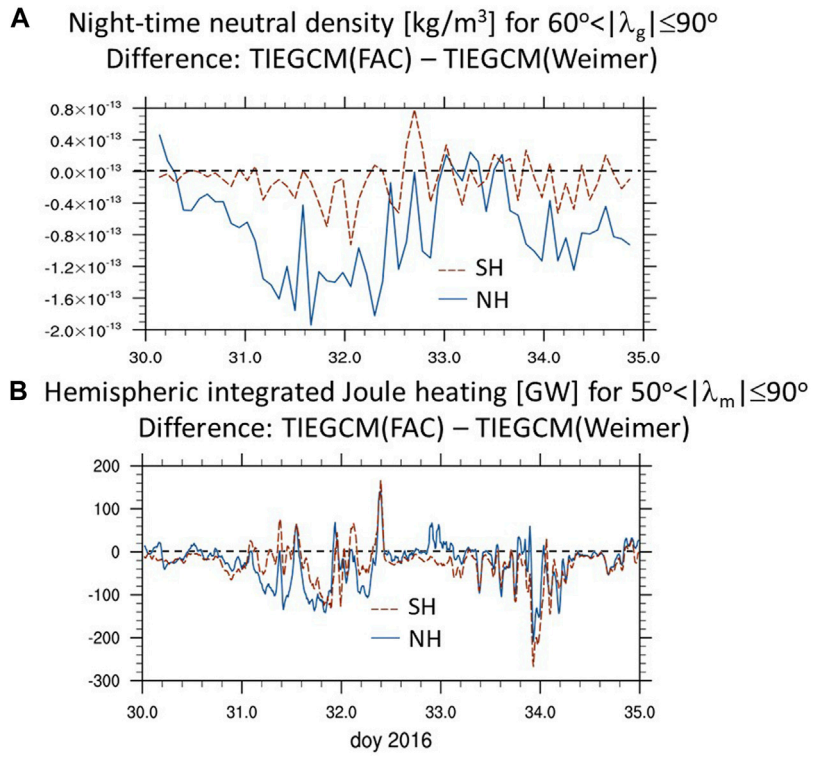

FIGURE 10
Difference of **(A)**. night-orbit high latitudinal averaged ($60^0 < |\lambda_g| \leq 90^0$) neutral density [$kg/m^3$] between TIEGCM(FAC) and TIEGCM(Weimer) and **(B)**. of height and high latitudinal integrated ($50^0 < |\lambda_m| \leq 90^0$) Joule heating rate [GW] between TIEGCM(FAC) and TIEGCM(Weimer) for northern hemisphere (blue solid line) and southern hemisphere (orange dashed line).

While the presented numerical experiments indicate that the LB perturbations are important to capture the large scale neutral density variations in simulations, it is less understood if hemispherically asymmetric component in the WACCMX-SD perturbations contribute especially to the hemispheric difference in the response. We conduct a simplified numerical experiment by including only symmetric LB perturbations based on WACCMX-SD output labeled "WacXB-symP" and the results are summarized in Table 2. For this simulation we include at the LB symmetric zonal wind, temperature and geopotential height, and antisymmetric meridional winds (meridional winds are positive northward) with respect to the geographic equator. Omitting any asymmetric perturbations in the LB leads to an increase in the error difference between southern and northern hemisphere in most latitude regions. Compared to the WacXBP simulation there are systematic changes with up to 2% reduced error in the SH and up to 8% larger error in the NH. More detailed studies are needed to understand the different effect in the two hemispheres. Overall, the simulation results suggest that the asymmetric LB perturbations contributes to the hemispheric differences in the neutral density but it is not the sole driver of such differences.

4 Effects of high latitude forcing

Details of the magnetospheric energy input into the IT system are important especially when examining regional and local effects in the thermosphere and ionosphere, such as the cusp neutral density enhancements (e.g., Lühr et al., 2004; Lu et al., 2016). It is less clear if a more realistic description of high-latitude forcing is also important for the large scale response at middle and low latitudes. Therefore, in the following, we compare the simulation using the empirical Weimer electric field model (labeled Weimer) to the simulation using field-aligned current based on AMPERE observations (labeled FAC). Both simulations use WACCMX-SD forcing at the TIEGCM lower boundary.

Figure 8 illustrates the latitude-time variation of the neutral density error between the simulations and Swarm-C observations. In general TIEGCM(FAC) outperforms the TIEGCM(Weimer) with a smaller neutral density error of up to 7%–20% in the northern hemisphere especially during the night-time. However, the neutral density error of TIEGCM(FAC) and TIEGCM(Weimer) is similar during the day-time at northern middle latitudes. In the southern middle

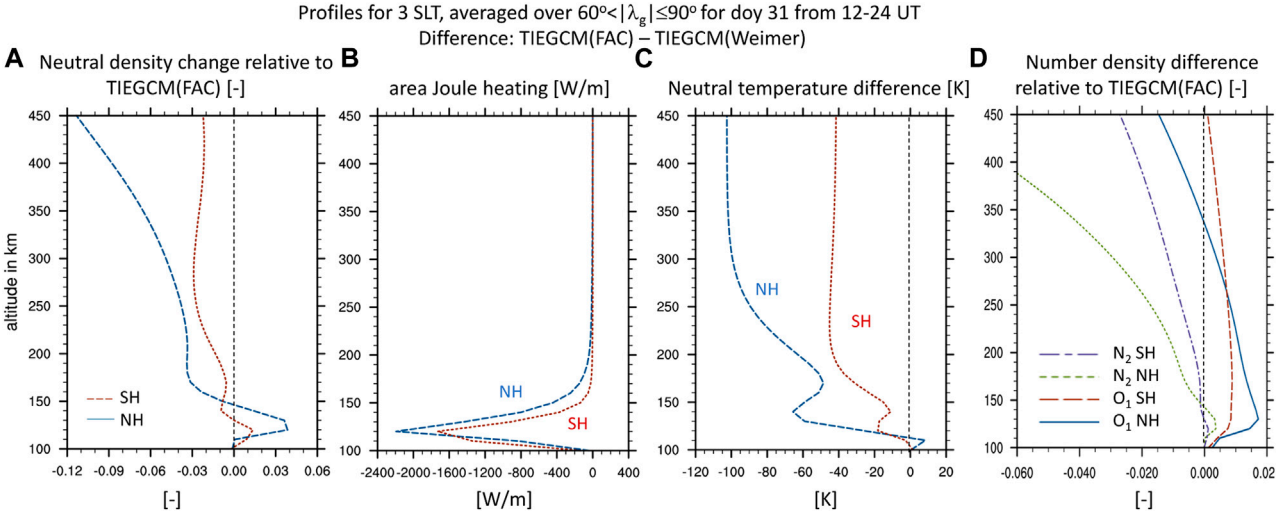

FIGURE 11
Profiles of differences between TIEGCM(FAC) and TIEGCM(Weimer) for northern hemisphere (dark blue dashed lines) and southern hemisphere (dark orange dotted lines)at 3 h SLT averaged between $60^0 < |\lambda_g| \leq 90^0$ and doy 31.5 to 32. **(A)**. relative neutral density change with respect to TIEGCM(FAC), **(B)**. integrated Joule heating difference [W/m], **(C)**. neutral temperature difference [K], and **(D)**. number density difference with respect to TIEGCM(FAC) for N_2 (green short dashed for north, purple long-short dashed for south) and O_1 (blue solid for north and orange long dashed for south).

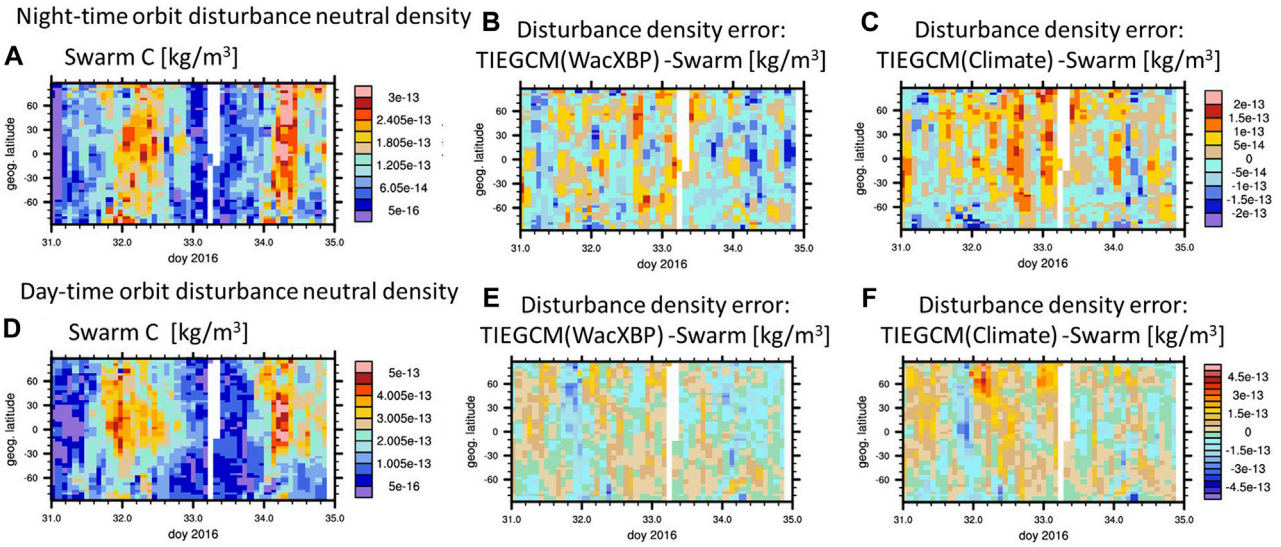

FIGURE 12
Disturbance neutral density variation by removing average of doy 30 UT 0–21 for night-time orbit [panel **(A–C)**] and day-time orbit **(D)** and **(F)** of Swarm C disturbance neutral density **(A)** and **(D)** and difference of disturbance variations between TIEGCM(WacXBP) and Swarm-C **(B)** and **(E)** and between TIEGCM(Climate) and Swarm-C **(C)** and **(F)**.

latitude region the night-time orbit neutral density agreement with Swarm-C is improved using TIEGCM(FAC) but otherwise the TIEGCM(Weimer) simulation has slightly smaller errors by 1–3% in the southern hemisphere compared to TIEGCM(FAC).

The neutral density error is in general larger in the northern than southern hemisphere especially for the night-time orbit as illustrated in Figure 9B by the neutral density variation poleward of |60°| geographic latitude. The average errors are summarized

TABLE 4 Relative error of the disturbance neutral density variation (by removing the average quiescent time variation of doy 30 UT 0–22) for using WacXBP and climatology at the lower boundary with respect to the absolute observed neutral density $|\Delta\rho_{model} - \Delta\rho_{data}|_1/|\rho_{data}|_1$ for doy 30.0 to 35.0.

		60-90 S	60-90 S	20-60 S	20-60 S	60–90 N	60–90 N	20–60 N	20–60 N
high latitude	lower boundary	day	night	day	night	day	night	day	night
FAC	WacXBP	**6.3%**	**8.3%**	**4.7%**	11.4%	**11.4%**	**11.2%**	**6.7%**	13.3%
FAC	Climate	7.3%	9.5%	5.6%	**10.6%**	12.9%	12.1%	7.2%	**14.3%**

The bold numbers indicate an improvement.

in Table 3. Using FAC forcing instead of Weimer leads to larger neutral density changes and improvement at Swarm-C orbit at northern high latitudes, especially during the night-time (Figure 9B blue line), than in southern hemisphere (Figure 9A). This hemispheric difference in the response to the different high latitude forcing cannot be solely explained by the hemispheric difference in Joule heating between the simulations. In Figure 10B we illustrate the difference in hemispheric integrated Joule heating (poleward of 50^o geographic latitude) between the TIEGCM(FAC) and TIEGCM(Weimer) simulations. In general, the northern and southern polar region have similar differences in Joule heating input into the IT system between the two simulations.

There is no simple connection between the neutral density difference of the two simulations in the two hemispheres (Figure 10A) and the Joule heating difference of the two simulations in the two hemispheres (Figure 10B). A simple correlation between the difference in neutral density and hemispheric integrated Joule heating of the two simulations in each hemisphere is very low, even when considering a time lag (northern hemisphere correlation coefficient r = 0.45 and southern hemisphere r = 0.3). Note that a difference of approximately 100 GW in Figure 10B around doy 31.5 to 32.0 represents around 40–50% of the total hemispheric integrated Joule heating from the TIEGCM(Weimer) and almost 100% of the TIEGCM(FAC) (see SI Supplementary Figure S4 for the absolute Joule heating variation).

To better understand why similar amount of Joule heating differences leads to larger neutral density difference in the northern than southern high latitude region we focus on average quantities poleward of 60^o geographic latitude at 3 h SLT for doy 31.5 to 32.0. During this time period there is a similar hemispheric integrated Joule heating difference between the simulations in the two hemispheres (Figure 10B) but the neutral density difference is smaller in the SH than in the NH (Figure 10A).

Figure 11A reiterates that in the upper thermosphere the neutral density difference is much larger in the NH than SH. The effect of Joule heating becomes more pronounce in the dark winter hemisphere, since the same amount of Joule heating difference between the two simulations yields a much larger neutral temperature change in the NH than in the SH (Figure 11C). In addition, Figure 11B shows that the TIEGCM(Weimer) simulation compared to the TIEGCM(FAC) simulation has a slightly larger integrated Joule heating value in the NH than SH and that the energy tends to be dissipated at higher altitudes (above 120 km) in the NH than SH where it can change more efficiently the atmosphere and the neutral density (Deng et al., 2011; Huang et al., 2012). The results are illustrated for 3 h SLT but are similar for 2–4 h SLT.

The relative difference in the composition between these two simulations is shown in Figure 11D. Below approximately 150 km the N_2 number density in TIEGCM(FAC) is larger than in TIEGCM(Weimer) in the NH and this difference is slightly larger than in the SH leading to an associated positive neutral mass density difference (Figure 11A). The difference in atomic oxygen is positive in both hemispheres below approximately 340 km. In the northern hemisphere the smaller scale height in TIEGCM(FAC) compared to TIEGCM(Weimer) eventually leads to negative differences in atomic oxygen above approximately 340 km with values from TIEGCM(FAC) being smaller than from TIEGCM(Weimer). Above approximately 150 km the northern hemisphere N_2 number density in TIEGCM(FAC) becomes smaller with increasing altitude compared to values from TIEGCM(Weimer). Between 180km and 230km the NH neutral density difference is more-or-less constant in altitude which might indicate that the positive atomic oxygen difference tends to compensate for the faster decrease in N_2 number density in the TIEGCM(FAC) compared to TIEGCM(Weimer). However, above 300 km the NH neutral density difference between the two simulations becomes more negative with increasing altitude associated with the temperature and compositional changes.

Compared to the northern hemisphere, the southern hemisphere differences in N_2 and O_1 between the TIEGCM(FAC) and TIEGCM(Weimer) simulations are much smaller, mostly negative for N_2 and positive for O_1, and less changing with altitude than in the northern hemisphere. The smaller SH than NH neutral density difference between the TIEGCM(FAC) and TIEGCM(Weimer) simulations at almost all altitudes might be associated with the increase in O_1 number density at all altitudes and the smaller reduction in N_2 number density together with a smaller temperature change in the SH than NH below 450 km. The southern neutral density difference between the simulations is almost constant between 250 km and 450 km but should become increasingly negative above 450 km.

Even during this moderate geomagnetically disturbed period the dynamical and compositional changes are complex. The

TIEGCM(Weimer) simulation has stronger equatorward thermospheric winds in the NH compared to the TIEGCM(FAC) simulation and the TIEGCM(FAC) exhibits even some poleward winds at subauroral regions in the NH. These neutral wind differences might contribute to the more equatorward movement of the zonal mean atomic oxygen peak in the TIEGCM(Weimer) simulation from 60 N at quiescent time to approximately 35 N while the zonal mean atomic oxygen peak for the TIEGCM(FAC) simulation moves only to 45 N (not depicted). In the TIEGCM(FAC) simulation the atomic oxygen below 350km is larger in the polar region compared to the TIEGCM(Weimer) simulation. Comparing the TIEGCM(Weimer) to TIEGCM(FAC) simulation suggests it might be associated with the increased and steady meridional transport of atomic oxygen away from the polar region.

Many studies focus on the effect of the geomagnetic activity by subtracting a quiescent time variation from the neutral density. In the following we evaluate if the details of the lower atmospheric forcing also influences the neutral density result when removing the average quiescent time variation. For that purpose we will use the Climate and WacXBP simulations and remove an average quiescent time latitudinal variation leading to the "disturbed" neutral density.

Figures 12A,D illustrate the Swarm-C "disturbed" neutral density with the average quiescent time latitudinal variation between doy 30, 0–22 UT removed. As expected, the moderate geomagnetically disturbed period is emphasized around doy 32 and doy 34. The same procedure of removing the quiescent time latitudinal variation is applied to the simulations. The simulation error is determined by subtracting the "disturbed" Swarm-C neutral density. Comparing the error of the TIEGCM(WacXBP) simulation (Figure 12B,E) with the error of the TIEGCM(Climate) simulation (Figure 12C,F) indicates that the error tends to be smaller using WacXBP at the lower boundary.

To provide a more objective measure we determine the relative error which is summarized in Table 4. As before we calculate the relative error with respect to the total Swarm-C neutral density over the whole time period but with the difference that the numerator represents the "disturbed" contribution. Therefore the relative error tends to be lower compared to the previously presented errors but the percentage difference can be better compared to the previous results since the denominator is the same. There is a slight, approximately 1–1.5% average improvement, in the"'disturbance"' neutral density in the northern hemisphere with WacXBP at the lower boundary as compared with the simulation with climatology at the lower boundary, but locally the improvement can be larger (see Figure 12).

5 Conclusion

In this study we focus on large scale neutral density variations between Swarm-C observations and TIEGCM simulations during the moderate geomagnetically disturbed period of 31 January to 3 February 2016. The larger neutral density error between the simulated and observed neutral density in the northern than southern hemisphere motivated us to examine the influence of the lower atmospheric forcing as well as the high latitude forcing on the simulated neutral density variations.

We found that using lower atmospheric forcing based on WACCM-X with specified dynamics compared to using climatological lower atmospheric forcing improves the agreement of the simulation with the observed neutral density, even during the disturbed condition. The improvements are larger in northern (up to 15%) than southern hemisphere during this February period and emphasize the importance of the background atmospheric conditions in facilitating the neutral density change. In general, the winter northern hemisphere is more sensitive to changes associated with LB forcing, leading to larger temperature and compositional changes compared to the southern sunlit hemisphere. While we have seen a larger response at Swarm altitudes to the lower atmospheric forcing in the northern than southern hemisphere, we want to emphasize that the simulation suggest that the magnitude and direction of the change are altitude dependent. The presented simulations suggest that above approximately 470 km (at middle latitudes) the southern hemisphere is more susceptible to the changes in the lower atmospheric forcing. Hemispheric differences in the employed LB forcing contribute to the interhemispheric difference in the neutral density at Swarm-C altitude but do not dominate them. Our study does not address the question of the importance of an accurate wave spectrum versus the importance of generally increased tidal activity at the lower boundary for capturing observed neutral density variation. Future studies should examine the details of the lower atmospheric forcing and their importance for capturing the large scale neutral density and its variability.

While more realistic LB variations compared to climatological LB forcing leads to a neutral density improvement of approximately 15% in the NH, more realistic high latitude forcing improves the neutral density by 7%–15% compared to using empirical high latitude forcing, and again a larger improvement is seen in the northern than southern hemisphere. Further examination indicates that the larger improvement in the northern compared to southern neutral density cannot be solely attributed to the difference in Joule heating input between the simulations. Closer examination of a specific time period indicates that there is a slight difference in Joule heating magnitude in the two hemispheres between the simulations but more importantly more Joule heating is dissipated at higher altitudes in the northern hemisphere in the TIEGCM(Weimer) compared to the TIEGCM(FAC) simulation, where it can more effective change the neutral density aloft (Deng et al., 2011; Huang et al., 2012). In addition, there is a seasonal effect that energy deposited in the winter hemisphere leads in general to larger changes in temperature and composition (Qian and Yue, 2017) compared to the sunlit hemisphere and therefore contributing to the larger neutral density change in the NH than SH. The simulations

indicate that the difference in neutral dynamics due to the different high latitude forcing contribute to the neutral density changes by modifying the transport of constituents.

When focusing on the disturbance neutral density variations by removing the quiescent time variation, more realistic lower atmospheric forcing *via* WacXBP in a simulation still leads to better agreement with the observed disturbances by 1–1.5% on average compared to using tidal climatology at the simulation lower boundary. This average improvement in the "disturbance" density is much smaller than the improvement considering the total neutral density, but the local improvement along the orbit can be larger. We want to note that the presented results depend on how the quiescent variations is defined.

The study highlights the importance of realistic forcing specification at both lower and upper boundary of the IT system even during moderate geomagnetically disturbed period. The background atmospheric conditions are very important to determine the response of the atmosphere to lower atmospheric forcing and to high latitude forcing. Methods correlating Joule heating to neutral density changes (e.g., Kalafatoglu Eyiguler et al., 2019a) need to consider the atmospheric background conditions. The simulations indicate larger night-time than day-time errors in neutral density which can be partially attributed to a bias in ion and viscous drag forces influencing the neutral wind and day-night temperature difference (Hsu et al., 2016). More systematic studies are needed to evaluate the efficiency of realistic concurrent lower atmospheric variations and high latitude forcing on the middle and low latitude thermosphere during different seasons and geophysical conditions.

Data availability statement

The datasets presented in this study can be found in online repositories. The names of the repository/repositories and accession number(s) can be found below: The TIEGCM results associated with this publication are available at the UCAR/NCAR Geoscience Data Exchange (GDEX) https://doi.org/10.5065/22v8-b441. The Iridium derived data products are available at the AMPERE Science Center at http://ampere.jhuapl.edu/dataget/index.html. The Swarm neutral density is available from the European Space Agency at https://swarm-diss.eo.esa.int/\#swarm\%2FLevel2daily\%2FLatest_baselines\%2FDNS\%2FACC\%2FSat_C. The solar wind parameters are available from the NASA/GSFC's Space Physics Data Facility's OMNIWeb service at https://omniweb.gsfc.nasa.gov/form/omni_min.html.

Author contributions

AM conducted the analysis, drafted the manuscript and worked on the interpretation of the analysis. GL contributed to the interpretation of the data and simulations. DK provided the optimal interpolation maps for the field-aligned current used in the TIEGCM. BA and SV provided the magnetic perturbations used in the optimal interpolation maps for the FAC. AM, GL, DK, BA, and SV contributed to the interpretation of data analysis.

Funding

AM, GL, DK, BA and SV are in part supported by NASA Living with a Star grant 80NSSC20K1784. AM and GL are partly funded by AFOSR through award FA9559-17-1–0248. GL is supported in part by the Living With a Star program under NASA grant 80NSSC17K0719 and by the Heliophysics Supporting Research program under NASA grant 80NSSC21K1673. We would like to acknowledge high-performance computing support from Cheyenne (doi:10.5065/D6RX99HX) provided by NCAR's Computational and Information Systems Laboratory, sponsored by the National Science Foundation. This material is based upon work supported by the National Center for Atmospheric Research, which is a major facility sponsored by the National Science Foundation under Cooperative Agreement No. 1852977.

Acknowledgments

AM would like to thank Christian Siemes for helping with the Swarm-C neutral density data and Art Richmond for helpful comments on an earlier draft.

Conflict of interest

The authors declare that the research was conducted in the absence of any commercial or financial relationships that could be construed as a potential conflict of interest.

Publisher's note

Supplementary material

The Supplementary Material for this article can be found online at: https://www.frontiersin.org/articles/10.3389/fspas.2022.932748/full#supplementary-material

References

Anderson, B., Korth, H., Waters, C., Green, D., Merkin, V., Barnes, R., et al. (2014). Development of large-scale birkeland currents determined from the active magnetosphere and planetary electrodynamics response experiment. *Geophys. Res. Lett.* 41, 3017–3025. doi:10.1002/2014GL059941

Anderson, B., Takahashi, K., and Toth, B. A. (2000). Sensing global Birkeland currents with Iridium engineering magnetometer data. *Geophys. Res. Lett.* 27, 4045–4048. doi:10.1029/2000GL000094

Bruinsma, S. L., and Forbes, J. M. (2009). Properties of traveling atmospheric disturbances (TADs) inferred from CHAMP accelerometer observations. *Adv. Space Res.* 43, 369–376. doi:10.1016/j.asr.2008.10.031

[Dataset] WACCMX-SD (2019). *Dataset: SD WACCM-X V2.1*. Climate Data Gateway at NCAR. doi:10.26024/5b58-nc53

Deng, Y., Fuller-Rowell, T. J., Akmaev, R. A., and Ridley, A. J. (2011). Impact of the altitudinal Joule heating distribution on the thermosphere. *J. Geophys. Res.* 116. doi:10.1029/2010ja016019

Deng, Y., Fuller-Rowell, T. J., Ridley, A. J., Knipp, D., and Lopez, R. E. (2013). Theoretical study: Influence of different energy sources on the cusp neutral density enhancement. *JGR. Space Phys.* 118, 2340–2349. doi:10.1002/jgra.50197

Emery, B., Roble, R., Ridley, E., Richmond, A., Knipp, D., Crowley, G., et al. (2012). *Parameterization of the ion convection and the auroral oval in the NCAR thermospheric general circulation models*. Boulder CO, USA: Tech. rep., National Center for Atmospheric Research. doi:10.5065/D6N29TXZ

Emmert, J. T., Drob, D. P., Picone, J. M., Siskind, D. E., Jones, M., Jr., Mlynczak, M. G., et al. (2021). Nrlmsis 2.0: A whole-atmosphere empirical model of temperature and neutral species densities. *Earth Space Sci.* 8, 1. doi:10.1029/2020EA001321

Emmert, J. (2015). Thermospheric mass density: A review. *Adv. Space Res.* 56, 773–824. doi:10.1016/j.asr.2015.05.038

Fedrizzi, M., Fuller-Rowell, T. J., and Codrescu, M. V. (2012). Global Joule heating index derived from thermospheric density physics-based modeling and observations. *Space Weather* 10. doi:10.1029/2011SW000724

Forbes, J. M. (2007). Dynamics of the thermosphere. *J. Meteorological Soc. Jpn.* 85, 193–213. doi:10.2151/jmsj.85b.193

Fuller-Rowell, T. J. (1998). The "thermospheric spoon": A mechanism for the semiannual density variation. *J. Geophys. Res.* 103, 3951–3956. doi:10.1029/97JA03335

Gasperini, F., Liu, H., and McInerney, J. (2020). Preliminary evidence of Madden-Julian oscillation effects on ultrafast tropical waves in the thermosphere. *JGR. Space Phys.* 125, e2019JA027649. doi:10.1029/2019JA027649

Gelaro, R., McCarty, W., Suárez, M. J., Todling, R., Molod, A., Takacs, L., et al. (2017). The modern-era retrospective analysis for research and applications, version 2 (MERRA-2). *J. Clim.* 30, 5419–5454. doi:10.1175/JCLI-D-16-0758.1

Gonzalez, W. D., Joselyn, J. A., Kamide, Y., Kroehl, H. W., Rostoker, G., Tsurutani, B. T., et al. (1994). What is a geomagnetic storm? *J. Geophys. Res.* 99, 5771–5792. doi:10.1029/93JA02867

Heelis, R. A., Lowell, J. K., and Spiro, R. W. (1982). A model of the high-latitude ionospheric convection pattern. *J. Geophys. Res.* 87, 6339–6345. doi:10.1029/JA087iA08p06339

Hsu, V. W., Thayer, J. P., Wang, W., and Burns, A. (2016). New insights into the complex interplay between drag forces and its thermospheric consequences. *JGR. Space Phys.* 121, 10–417. doi:10.1002/2016ja023058

Huang, Y., Richmond, A. D., Deng, Y., and Roble, R. (2012). Height distribution of Joule heating and its influence on the thermosphere. *J. Geophys. Res.* 117. doi:10.1029/2012JA017885

Jones, M., Forbes, J. M., Hagan, M. E., and Maute, A. (2014b). Impacts of vertically propagating tides on the mean state of the ionosphere-thermosphere system. *J. Geophys. Res. Space Phys.* 119, 2197–2213. doi:10.1002/2013JA019744

Jones, M., Forbes, J. M., and Hagan, M. E. (2014a). Tidal-induced net transport effects on the oxygen distribution in the thermosphere. *Geophys. Res. Lett.* 41, 5272–5279. doi:10.1002/2014gl060698

Kalafatoglu Eyiguler, E. C., Kaymaz, Z., Kuznetsova, M. M., Soon Shim, J., and Rastätter, L. (2019a). "Relation between Joule heating and thermospheric neutral density during geomagnetic storms," in 2019 9th international conference on recent Advances in Space technologies (RAST) (IEEE), 663–666. doi:10.1109/RAST.2019.8767867

Kalafatoglu Eyiguler, E. C., Shim, J. S., Kuznetsova, M. M., Kaymaz, Z., Bowman, B. R., Codrescu, M. V., et al. (2019b). Quantifying the storm time thermospheric neutral density variations using model and observations. *Space Weather* 17, 269–284. doi:10.1029/2018SW002033

Knipp, D., Tobiska, W. K., and Emery, B. (2004). Direct and indirect thermospheric heating sources for solar cycles 21–23. *Sol. Phys.* 224, 495–505. doi:10.1007/s11207-005-6393-4

Liu, H.-L., Bardeen, C. G., Foster, B. T., Lauritzen, P., Liu, J., Lu, G., et al. (2018). Development and validation of the whole atmosphere community climate model with thermosphere and ionosphere eXtension (WACCM-X 2.0). *J. Adv. Model. Earth Syst.* 10, 381–402. doi:10.1002/2017ms001232

Liu, H.-L. (2016). Variability and predictability of the space environment as related to lower atmosphere forcing. *Space Weather* 14, 634–658. doi:10.1002/2016sw001450

Liu, H., Thayer, J., Zhang, Y., and Lee, W. K. (2017). The non–storm time corrugated upper thermosphere: What is beyond MSIS? *Space Weather* 15, 746–760. doi:10.1002/2017SW001618

Lu, G., Richmond, A. D., Lühr, H., and Paxton, L. (2016). High-latitude energy input and its impact on the thermosphere. *JGR. Space Phys.* 121, 7108–7124. doi:10.1002/2015JA022294

Lühr, H., Rother, M., Köhler, W., Ritter, P., and Grunwaldt, L. (2004). Thermospheric up-welling in the cusp region: Evidence from CHAMP observations. *Geophys. Res. Lett.* 31. doi:10.1029/2003gl019314

Marsal, S., Richmond, A., Maute, A., and Anderson, B. (2012). Forcing the TIEGCM model with birkeland currents from the active magnetosphere and planetary electrodynamics response experiment. *J. Geophys. Res.* 117. doi:10.1029/2011JA017416

Maute, A., Richmond, A. D., Lu, G., Knipp, D. J., Shi, Y., and Anderson, B. (2021). Magnetosphere-ionosphere coupling via prescribed field-aligned current simulated by the tiegcm. *JGR. Space Phys.* 126. doi:10.1029/2020JA028665

Maute, A. (2017). Thermosphere-ionosphere-electrodynamics general circulation model for the ionospheric connection explorer: TIEGCM-ICON. *Space Sci. Rev.* 212, 523–551. doi:10.1007/s11214-017-0330-3

Müller, S., Lühr, H., and Rentz, S. (2009). Solar and magnetospheric forcing of the low latitude thermospheric mass density as observed by champ. *Ann. Geophys.* 27, 2087–2099. doi:10.5194/angeo-27-2087-2009

Pedatella, N. M., Liu, H.-L., Conte, J. F., Chau, J. L., Hall, C., Jacobi, C., et al. (2021). Migrating semidiurnal tide during the september equinox transition in the northern hemisphere. *Geophys. Res. Atmos.* 126. doi:10.1029/2020JD033822

Prölss, G. W. (2011). Density perturbations in the upper atmosphere caused by the dissipation of solar wind energy. *Surv. Geophys.* 32, 101–195. doi:10.1007/s10712-010-9104-0

Qian, L., Burns, A. G., Emery, B. A., Foster, B., Lu, G., Maute, A., et al. (2014). The NCAR TIE-GCM: A community model of the coupled thermosphere/ionosphere system. *Model. Ionosphere-Thermosphere Syst. Geophys. Monogr. Ser* 201, 73–83.

Qian, L., Solomon, S. C., and Kane, T. J. (2009). Seasonal variation of thermospheric density and composition. *J. Geophys. Res.* 114. doi:10.1029/2008JA013643

Qian, L., and Solomon, S. C. (2012). Thermospheric density: An overview of temporal and spatial variations. *Space Sci. Rev.* 168, 147–173. doi:10.1007/s11214-011-9810-z

Qian, L., and Yue, J. (2017). Impact of the lower thermospheric winter-to-summer residual circulation on thermospheric composition. *Geophys. Res. Lett.* 44, 3971–3979. doi:10.1002/2017GL073361

Richmond, A. D. (2021). "Joule heating in the thermosphere," in *Upper atmosphere dynamics and energetics*. Editors L. P. W. Wang and Y. Zhang (USA: American Geophysical Union), 1–18. doi:10.1002/9781119815631.ch1

Richmond, A., and Maute, A. (2013). *Ionospheric electrodynamics modeling (AGU geophysical monograph series.), vol. 201*. Chichester, UK: John Wiley & Sons. also published online in 2014 by. doi:10.1029/2012GM001331

Ritter, P., Lühr, H., and Doornbos, E. (2010). Substorm-related thermospheric density and wind disturbances derived from champ observations. *Ann. Geophys.* 28, 1207–1220. doi:10.5194/angeo-28-1207-2010

Roble, R. G. (1995). Energetics of the mesosphere and thermosphere. *Up. Mesos. Low. Thermosphere A Rev. Exp. Theory, Geophys. Monogr. Ser* 87, 1–21.

Roble, R., and Ridley, E. (1987). *An auroral model for the NCAR thermospheric general circulation model (TGCM)*. Annales Geophysicae 5A, 369–382.

Shi, Y., Knipp, D., Matsuo, T., Kilcommons, L., and Anderson, B. (2020). Modes of (FACs) variability and their hemispheric asymmetry revealed by inverse and assimilative analysis of Iridium magnetometer data. *J. Geophys. Res. Space Phys.* 125, 1. doi:10.1029/2019JA027265

Shim, J. S., Kuznetsova, M., Rastätter, L., Bilitza, D., Butala, M., Codrescu, M., et al. (2012). Cedar electrodynamics thermosphere ionosphere (eti) challenge for systematic assessment of ionosphere/thermosphere models: Electron density, neutral density, NmF2, and hmF2 using space based observations. *Space Weather* 10. doi:10.1029/2012SW000851

Siemes, C., de Teixeira da Encarnação, J., Doornbos, E., van den IJssel, J., Kraus, J., PereštŸ, R., et al. (2016). Swarm accelerometer data processing from raw accelerations to thermospheric neutral densities. *Earth Planets Space* 68, 92–1186. doi:10.1186/s40623-016-0474-5

Siskind, D. E., Drob, D. P., Dymond, K. F., and McCormack, J. P. (2014). Simulations of the effects of vertical transport on the thermosphere and ionosphere using two coupled models. *J. Geophys. Res. Space Phys.* 119, 1172–1185. doi:10.1002/2013JA019116

Solomon, S. C., Qian, L., Didkovsky, L. V., Viereck, R. A., and Woods, T. N. (2011). Causes of low thermospheric density during the 2007–2009 solar minimum. *J. Geophys. Res.* 116. doi:10.1029/2011JA016508

Sutton, E. K., Forbes, J. M., and Knipp, D. J. (2009). Rapid response of the thermosphere to variations in joule heating. *J. Geophys. Res.* 114. doi:10.1029/2008JA013667

Weimer, D. R. (2005). Improved ionospheric electrodynamic models and application to calculating Joule heating rates. *J. Geophys. Res.* 110, A05306. doi:10.1029/2004JA010884

Yamazaki, Y., and Kosch, M. J. (2015). The equatorial electrojet during geomagnetic storms and substorms. *J. Geophys. Res. Space Phys.* 120, 2276–2287. doi:10.1002/2014JA020773

Yamazaki, Y., and Richmond, A. D. (2013). A theory of ionospheric response to upward-propagating tides: Electrodynamic effects and tidal mixing effects. *J. Geophys. Res. Space Phys.* 118, 5891–5905. doi:10.1002/jgra.50487

Zhang, X., Forbes, J. M., and Hagan, M. E. (2010). Longitudinal variation of tides in the MLT region: 1. Tides driven by tropospheric net radiative heating. *J. Geophys. Res.* 115, 1. doi:10.1029/2009JA014897

Zhang, Y., and Paxton, L. J. (2021). *Storm-time neutral composition changes in the upper atmosphere*. American Geophysical Union, 115–133. chap. 7. doi:10.1002/9781119815631.ch7

Zhang, Y., Paxton, L., Morrison, D., Wolven, B., Kil, H., Meng, C.-I., et al. (2004). O/N2 changes during 1–4 october 2002 storms: IMAGE SI–13 and TIMED/GUVI observations. *J. Geophys. Res.* 109, A10308. doi:10.1029/2004ja010441

Zuzic, M., Scherliess, L., and Prölss, G. (1997). Latitudinal structure of thermospheric composition perturbations. *J. Atmos. Sol. Terr. Phys.* 59, 711–724. doi:10.1016/S1364-6826(96)00098-3

frontiers | Frontiers in Astronomy and Space Sciences

TYPE Original Research
PUBLISHED 06 September 2022
DOI 10.3389/fspas.2022.966164

OPEN ACCESS

EDITED BY
Karl Laundal,
University of Bergen, Norway

REVIEWED BY
Timo Pitkänen,
Umeå University, Sweden
Minna Palmroth,
University of Helsinki, Finland

*CORRESPONDENCE
J. W. B. Eggington,
j.eggington17@imperial.ac.uk

SPECIALTY SECTION
This article was submitted to Space Physics,
a section of the journal
Frontiers in Astronomy and Space Sciences

RECEIVED 10 June 2022
ACCEPTED 10 August 2022
PUBLISHED 06 September 2022

CITATION
Eggington JWB, Coxon JC, Shore RM, Desai RT, Mejnertsen L, Chittenden JP and Eastwood J (2022), Response timescales of the magnetotail current sheet during a geomagnetic storm: Global MHD simulations.
Front. Astron. Space Sci. 9:966164.
doi: 10.3389/fspas.2022.966164

Response timescales of the magnetotail current sheet during a geomagnetic storm: Global MHD simulations

J. W. B. Eggington[1]*, J. C. Coxon[2], R. M. Shore[3], R. T. Desai[1], L. Mejnertsen[1], J. P. Chittenden[4] and J. P. Eastwood[1]

[1]Space and Atmospheric Physics Group, Blackett Laboratory, Imperial College London, London, United Kingdom, [2]Department of Mathematics, Physics, and Electrical Engineering, Northumbria University, Newcastle Upon Tyne, United Kingdom, [3]British Antarctic Survey, Cambridge, United Kingdom, [4]Plasma Physics Group, Blackett Laboratory, Imperial College London, London, United Kingdom

The response of the Earth's magnetotail current sheet to the external solar wind driver is highly time-dependent and asymmetric. For example, the current sheet twists in response to variations in the B_y component of the interplanetary magnetic field (IMF), and is hinged by the dipole tilt. Understanding the timescales over which these asymmetries manifest is of particular importance during geomagnetic storms when the dynamics of the tail control substorm activity. To investigate this, we use the Gorgon MHD model to simulate a geomagnetic storm which commenced on 3 May 2014, and was host to multiple B_y and B_z reversals and a prolonged period of southward IMF driving. We find that the twisting of the current sheet is well-correlated to IMF B_y throughout the event, with the angle of rotation increasing linearly with downtail distance and being more pronounced when the tail contains less open flux. During periods of southward IMF the twisting of the central current sheet responds most strongly at a timelag of ~ 100 min for distances beyond 20 R_E, consistent with the 1–2 h convection timescale identified in the open flux content. Under predominantly northward IMF the response of the twisting is bimodal, with the strongest correlations between 15 and 40 R_E downtail being at a shorter timescale of ~ 30 min consistent with that estimated for induced B_y due to wave propagation, compared to a longer timescale of ~ 3 h further downtail again attributed to convection. This indicates that asymmetries in the magnetotail communicated by IMF B_y are influenced mostly by global convection during strong solar wind driving, but that more prompt induced B_y effects can dominate in the near-Earth tail and during periods of weaker driving. These results provide new insight into the characteristic timescales of solar wind-magnetosphere-ionosphere coupling.

KEYWORDS

magnetotail twisting, current sheet, response timescales, geomagnetic storm, magnetosphere-ionophere coupling, global MHD simulations, space weather

1 Introduction

Geomagnetic storms generate a complex and highly time-dependent response in the solar wind-magnetosphere-ionosphere system. Fundamentally these are driven by enhanced dayside magnetic reconnection due to prolonged periods of southward interplanetary magnetic field (IMF), increasing the amount of open flux in the magnetosphere (Dungey, 1961; Siscoe and Huang, 1985). The advection of open field lines into the nightside eventually triggers tail reconnection, which energises the plasma sheet and injects high-energy particles into the inner magnetosphere, providing a source for ring current and radiation belt populations (Gabrielse et al., 2014; Akasofu, 2018; Sandhu et al., 2018). Tail reconnection during storms is associated with strong substorm activity which is responsible for intense space weather impacts, posing a significant societal risk (Eastwood et al., 2018). Understanding the timescales over which storms evolve is therefore crucial in predicting and mitigating their impact, and is strongly dependent on the global convection process.

The sequence of dayside and nightside reconnection and the ensuing global convection can be described according the expanding/contracting polar cap (ECPC) paradigm (Cowley and Lockwood, 1992). From the ionospheric perspective, the opening of flux on the dayside causes the growth of the open-closed field line boundary around noon, and the resulting flows lead to an expansion of the dayside polar cap. Field lines then advect anti-sunward towards the nightside where they reconnect in the magnetotail, causing ionospheric flows which result in a contraction of the polar cap. Since the dayside and nightside reconnection rates are generally not in balance the polar cap tends to evolve continuously (Milan et al., 2007), with quasi-periodic loading and unloading of nightside open flux associated with substorm activity. The transport of open field lines to the nightside reconnection region occurs over a period of ~ 1 h, depending on driving conditions and the state of the system (Milan et al. (2021) and references therein), and hence changes in solar wind driving are communicated gradually throughout the magnetosphere by convection.

However, changes in the magnetosphere can also be communicated by magnetohydrodynamic (MHD) waves over seconds to minutes; studies have shown that ionospheric convection can fully reconfigure over 10–20 min in response to the onset of magnetopause reconnection (Morley and Lockwood, 2006 and references therein). In this sense there are two different response timescales: firstly, the typical wave transit time for information to be transmitted across field lines from the solar wind to the ionosphere and nightside magnetosphere, and secondly the convection timescale through which flux is circulated from the dayside to the nightside, and then back to the subsolar magnetopause. Ionospheric signatures have been observed almost immediately on both the dayside and nightside in response to southward IMF turnings (e.g., Snekvik et al., 2017), consistent with the first, shorter timescale type of response. The propagation of fast mode waves during strong compression of the magnetosphere can also rapidly reconfigure the magnetotail and trigger sudden commencements on the ground (Desai et al., 2021b; Eggington et al., 2022). It has been found that field-aligned current (FAC) systems start to flow on the dayside ~ 10 min after the onset of dayside reconnection, but after ≳ 1 h on the nightside (consistent with the model proposed by Cowley and Lockwood, 1992) indicative of convection gradually proceeding throughout the system and triggering the onset of substorms and their subsequent evolution (Anderson et al., 2014; Milan et al., 2018; Coxon et al., 2017; Coxon et al., 2019).

The response of the magnetosphere-ionosphere system to changes in the IMF can be decomposed into a separate dynamical dependence on each component, particularly B_y and B_z (in the Geocentric Solar Magnetospheric (GSM) frame), and depends further on the particular configuration of the system at a given time. In a statistical analysis of Active Magnetosphere and Planetary Electrodynamics Response Experiment (AMPERE) data, Coxon et al. (2019) found a 10–20 min dayside FAC response to IMF variation, suggesting a direct driving of the dayside Region 1 FACs, whilst the strongest correlations of the nightside FAC were at timelags of 60–90 min, consistent with the ECPC paradigm as found in similar studies (Anderson et al., 2014; Shore et al., 2019). Even longer timescales of 120–150 min were seen on the nightside, possibly corresponding to the end of the substorm cycle; a > 1 h nightside FAC delay after northward IMF turnings (i.e., negative to positive B_z) was also found by Milan et al. (2018), suggesting gradual contraction of the polar cap due to prolonged nightside reconnection. Whilst these timescales are consistent with global convection, differences in the FAC response can occur between dawn and dusk which cannot be explained purely by the ECPC paradigm. Instead, these can arise to the effect of IMF B_y, which has a well-established asymmetric effect on ionospheric convection (e.g., Grocott et al., 2010; Grocott, 2017). Specifically, Coxon et al. (2019) identified the strongest nightside FAC response to IMF B_y to be between 90 and 150 min, whilst Milan et al. (2018) found that dayside responses to IMF B_y were prompt, but were delayed on the nightside by up to an hour and developed further over up to 4 h.

Asymmetries arise from IMF B_y as a result of unequal loading of magnetic flux into the dawn and dusk tail lobes in the northern and southern hemispheres, such that the IMF exerts a torque on newly-reconnected field lines. This results in a twisting (i.e., rotation in the GSM Y-Z plane) of the magnetotail lobes through an accumulation of B_y in the tail, and hence a rotation of the magnetotail current (neutral) sheet out of the equatorial plane due to asymmetric lobe pressure (e.g., Cowley, 1981; Xiao et al., 2016). The 'penetration' of IMF B_y into the plasma sheet is well-noted in observations (Sergeev, 1987; Borovsky et al., 1998), which also show that an additional B_y component collinear to

IMF B_y is induced on closed tail field lines (e.g., Kaymaz et al., 1994). If driven by global convection this effect should, *via* tail reconnection, result in asymmetries in the ionosphere on the order of hours. This is supported by previous observations showing that timescales of $\gtrsim$ 1 h are required for a B_y to be generated in the tail, with delays as long as ~ 4–5 h seen under northward IMF (Rong et al., 2015; Browett et al., 2017), consistent with Milan et al. (2018).

The twisting of the tail can also occur due to a separate mechanism in which shear flows, set up by MHD waves due to asymmetric lobe pressure, rapidly induce a B_y in the magnetosphere. This has been shown via simulations to proceed onto closed field lines on the order of tens of minutes in response to a step-like increase in IMF B_y, prior to changes in nightside reconnection (Tenfjord et al., 2015). In fact, recent simulations have shown that active nightside reconnection acts to reduce the B_y asymmetry in the tail (Ohma et al., 2021). This can likewise result in ionospheric asymmetries via the displacement of field line footpoints, such as asymmetric aurorae (Motoba et al., 2011). However, the distinction between an initial response to a change in IMF and a full reconfiguration of the system may complicate any deduced timescales; a later study by Tenfjord et al. (2017) using GOES observations during IMF B_y reversals suggested response times of $<$ 15 min and reconfiguration times of $<$ 45 min. Similar delays were seen when investigating northward IMF conditions (Tenfjord et al., 2018).

Observations of IMF B_y reversals have shown a rotation of the current sheet in the (anti-)clockwise direction for a (positive) negative B_y, occurring over timescales of only tens of minutes, and without a dependence on downtail distance (Case et al., 2018). The rotation was more easily observed during northward IMF, and large-scale observations have shown that the twisting effect is stronger on average for northward IMF conditions (Owen et al., 1995; Tsyganenko and Fairfield, 2004; Xiao et al., 2016). A separate study finding a longer twisting timescale of up to ~ 3 h also showed that the delay was longer in the inner magnetosphere, i.e., it propagated inward from the middle magnetotail (Pitkänen et al., 2016). A global MHD simulation using idealised IMF variations showed that the outer portions of the current sheet near the magnetopause respond the most promptly (Walker et al., 1999). At a distance of 20 R_E from the Earth, timescales of ~15 min were found for the outer current sheet compared to a response of up to 1 h in the inner (central) current sheet. The timescale of response was slower further downtail, and the twisting more exaggerated; a similar simulation study associated this downtail delay in plasma sheet twisting with the formation of transpolar arcs (Kullen and Janhunen, 2004). The wide range of response timescales reported by different studies suggests there may be a strong dependence on the particular state of the magnetosphere.

In addition to the mechanisms described above, other sources of plasma sheet B_y exist such as the hinging (i.e., a bending in the GSM X-Z plane) of the current sheet due to the dipole tilt, which introduces some diurnal and seasonal dependence (Petrukovich, 2011). Outside of the MHD description there are various kinetic processes in the magnetotail which affect the current sheet, and which influence the loading-unloading cycle (e.g., Kuznetsova et al., 2007). In particular, observations have shown current sheet flapping motions (perturbations perpendicular to the sheet) which provide an additional mode of energy transport in the tail (e.g., Zhang et al., 2002; Sergeev et al., 2003; Rong et al., 2010). Whilst such disturbances may occur on the MHD scale, their generation has been associated with smaller-scale effects such as instabilities driven by tail reconnection (Zhang et al., 2020 and references therein). However despite these additional complex processes, MHD is still effective at describing the larger scale, more directly-driven response.

Global MHD simulations provide the means to model the global magnetosphere for arbitrary driving conditions, since they can capture the state of the system during a real event by using upstream solar wind data as the model input. Simulating a real geomagnetic storm also provides a meaningful case study to investigate how changes in IMF are propagated through the magnetosphere during non-idealised conditions, which is of particular importance for space weather prediction. During such an event the solar wind conditions are extremely variable, resulting in a magnetospheric response over a variety of timescales. This study will complement previous simulations with synthetic solar wind driving in which timescales are sensitive to the chosen initial conditions, and provide further physical insight into studies based on *in-situ* observations by offering a global perspective. To this end we use the Gorgon MHD code to simulate the first 24 h of a real geomagnetic storm which commenced on 3 May 2014, and analyse the response of the magnetotail to varying strength of driving and changes in IMF orientation. This also provides a foundation for future comparison to observations during the same event, to further elucidate the source of the different timescales.

2 Simulating the storm of 3 May 2014

2.1 Solar wind conditions

In selecting an appropriate event to simulate there is a preference to a storm preceded by steady, quiet solar wind conditions, such that the magnetospheric response is particularly pronounced and its timescales are easily identified. One such candidate occurred between 14:00 UT on 2014/05/03 and 11:00 UT on 2014/05/07, and was identified from the list of geomagnetic storms given in the supporting information of Murphy et al. (2018) (storm number 34 in said list). This event was preceded by several hours of weak, predominantly northward IMF, for which the magnetosphere was relatively closed. We note that there is also good

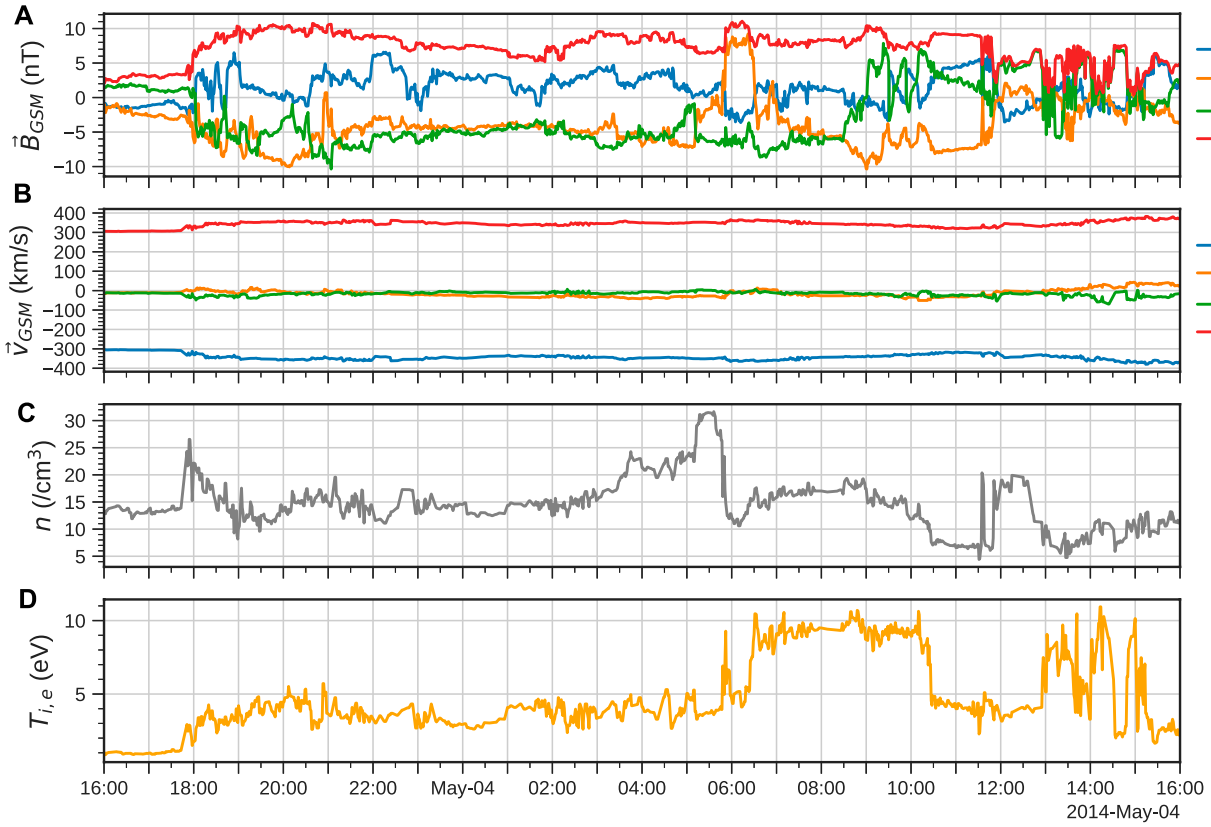

FIGURE 1
Solar wind conditions used to drive the simulation, taken from OMNI. Shown in GSM coordinates **(A)** the IMF **B**, **(B)** the solar wind velocity **v**, **(C)** the number density n and **(D)** the ion (and electron) temperature $T_{i,e}$.

observational coverage of this event in both AMPERE and SuperMAG data, which will be used for comparison in future studies using the simulation results.

Figure 1 shows the (1 min cadence, bow shock-shifted) solar wind conditions from OMNI (Papitashvili and King, 2020) during the first 24 h of the storm, which contained the period of longest continuous southward IMF during the four-day period and hence the most intense geomagnetic activity. The shock front associated with the storm is seen to arrive at around 17:50 UT on 3 May when the density suddenly increases by about a factor of 2. The IMF also grows and turns southward, remaining so for essentially all of the following 15 h and hence presents favourable conditions for steady nightside reconnection. As well as the initial shock, there is a density pile-up followed by a sharp decrease through another shock at around 05:50 UT on 4 May. The temperature is enhanced following both of these shocks, suggesting that the former is a fast forward shock whereas the latter (with an increase in B and v) is consistent with a slow reverse shock (Oliveira, 2017). An additional, smaller dynamic pressure enhancement is then seen around 11:50 UT on 4 May.

The shock around 05:50 UT on 4 May also coincides with a prominent IMF B_y reversal, followed by another at 07:00 UT, which should generate strong asymmetries in the tail and so will be of particular interest in our analysis of the current sheet response. In fact, B_y is negative for almost all of the time for which the IMF is southward, and so there should be a noticeable twisting of the magnetotail throughout. Note the dipole tilt angle ranged from ~ 7° – 25° for this period (shown later in Figure 4C), and hence there should be a noticeable and varying hinging effect in the current sheet as well. The IMF then switches northward at around 09:00 UT on 4 May, and is rarely southward for the remaining 7 h shown here. After the initial shock, the velocity remains relatively constant during the event, meaning that timescales associated with convection should depend primarily on the IMF orientation and can be more easily inferred.

2.2 Simulation setup

The Gorgon MHD code models the terrestrial solar wind-magnetosphere interaction by solving the semi-conservative

resistive MHD equations on a regular, Eulerian, staggered cartesian grid, and is unique amongst magnetospheric MHD codes in solving for the magnetic vector potential (Ciardi et al., 2007; Mejnertsen et al., 2018; Eggington et al., 2020; Desai et al., 2021a). In this study we utilise a grid with uniform resolution of 0.5 R_E, which ensures that the tail is well-resolved at all downtail distances, and a domain spanning X = (−24, 126) R_E, Y = (−60, 60) R_E, Z = (−60, 60) R_E. The time-dependent solar wind parameters are applied at the sunward boundary, with the Earth's dipole (of moment 7.73 × 10^{22} Am^2) at the origin within the inner boundary of radius 3 R_E. Here the FACs are mapped along dipole field lines to a thin-shell ionosphere model where the resulting electrostatic potential is calculated and mapped back out to the magnetosphere to set the plasma flow as an inner boundary condition (Eggington et al., 2018). The ionospheric conductance is calculated from a combination of solar EUV ionization using the empirical formulae of Moen and Brekke, (1993) assuming $F_{10.7}$ = 100 × 10^{-22} $Wm^{-2}Hz^{-1}$, and uniform background polar cap Pedersen and Hall conductances of Σ_P = 7 mho and Σ_H = 12 mho, respectively, as per Coxon et al. (2016).

To capture the geometric effects of the dipole tilt we use a fixed tilt angle of μ = 15° (the contribution due to the seasonal obliquity of the dipole) and impose the diurnal rotation of the dipole onto the solar wind. The coordinate system is thus related to GSM through a rotation by an angle between ~±10° in the X-Z plane, depending on the time of day, except that X and Y are defined in the opposite sense. Hence when we transform into GSM for our analysis, the diurnal variation is imposed back onto the dipole which rotates accordingly. The benefit of using a fixed non-zero tilt angle versus the use of Solar Magnetic (SM) coordinates, in which the dipole is fixed along Z (Hapgood, 1992), is greatly reduced solar wind inflow angles hence allowing for a smaller simulation domain. The solar wind data are taken from OMNI and transformed into simulation coordinates by calculating the mean value of μ during the day in question. We inject solar wind for a total of 24 h starting from 16:00 UT on 3 May, with initialisation performed using the relatively quiet 2 h of conditions prior to this window. Since a varying B_x cannot be injected into the simulation box, we simply set the IMF B_x to zero throughout.

One important point to consider is the dependence of the key timescales in the model (e.g., that of global convection) on the model numerics. In the present study we assume ideal MHD by setting the resistivity in the model to zero, such that the Dungey cycle proceeds due to numerical diffusion as is commonly the case with magnetospheric MHD codes. The resulting dynamics will differ between models due to their use of different solvers, grid resolutions/geometries and model parameters such as ionospheric conductance. For example, models can show disagreement in predictions of magnetospheric topology and ionospheric cross-polar cap potential even when driven with the same solar wind conditions (Honkonen et al., 2013; Gordeev et al., 2015). However whilst key timescales in the simulation may be slightly faster or slower than in reality, the simulation still provides valuable insight into the global phenomena driving the system response and complements observations.

3 Simulation results

3.1 Dayside vs. nightside reconnection rate

To establish the key periods of driving during this event we first investigate the variation in dayside coupling and open flux content in the magnetosphere. The dayside reconnection rate Φ_D can be estimated using the solar wind coupling function of Milan et al. (2012), which has the form:

$$\Phi_D = L_{eff}(v_x) v_x B_{yz} \sin^{9/2}(\theta_{IMF}/2), \quad (1)$$

$$\text{where } L_{eff}(v_x) = 3.8 R_E \left(\frac{v_x}{4 \times 10^5 \text{ms}^{-1}} \right)^{\frac{1}{3}}, \quad (2)$$

for which B_{yz} is the IMF magnitude in the GSM Y-Z plane and θ_{IMF} = arctan (B_y/B_z) is the IMF clock angle. Whilst the strength of coupling in the simulation may differ slightly from this empirical formula, the general trends should be similar. We can establish this based on the growth and decay in the open flux F_{PC}, which we calculate by integrating the magnetic flux through cells at the outer boundary of the simulation domain which contain open field (Eggington et al., 2022). The magnetic connectivity is determined by tracing field lines from each grid cell and finding where they terminate; open field is defined where one end terminates at the Earth (the North pole for our calculation) and the other in the solar wind (see similarly Honkonen et al., 2011; Aikio et al., 2013; Mejnertsen et al., 2021). Figure 2 shows the variation of these quantities during the first 24 h of the storm, with shading indicating periods in the simulation where either the dayside (Φ_D) or nightside (Φ_N) reconnection rate dominate, determined simply by whether dF_{PC}/dt is positive or negative, respectively. The initial switch from northward to southward IMF at 18:00 UT on 3 May is associated with a sudden increase in Φ_D. This remains relatively high for the following 15 h until the switch back to northward IMF at around 09:00 UT, after which Φ_D is generally much lower for the remainder of the event. In that sense the first 24 h of the event can be split into two parts: an extended period of strong, predominantly southward IMF driving, and then a subsequent shorter period of weaker, predominantly northward IMF driving.

The open flux in the simulation gradually increases during the first few hours of the storm, particularly after 18:00 UT on 3 May when the IMF first turns southward. The dayside rate then dominates until around 19:30 UT, with the nightside rate then catching-up and causing a net reduction in F_{PC} over the following hour. Another sudden increase in Φ_D around 20:30 UT causes F_{PC} to climb once more to a peak around 22:00 UT. The open flux content then remains close to this elevated level for the remainder

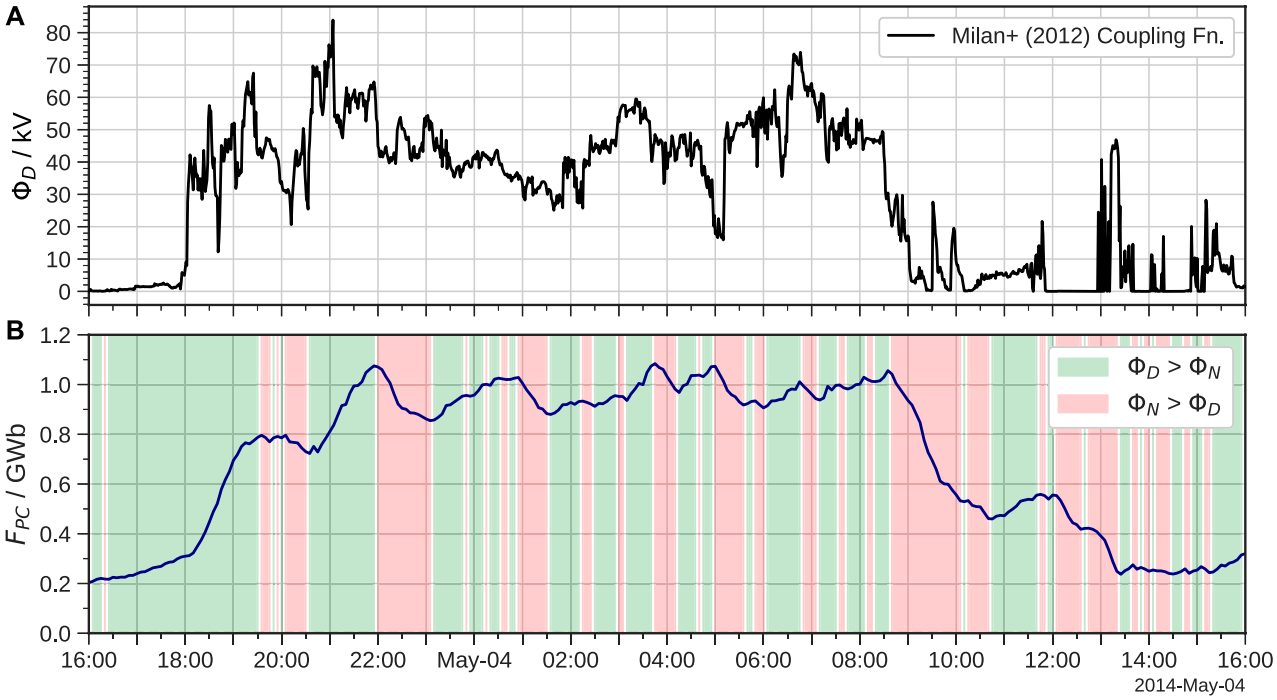

FIGURE 2
Time-series of **(A)** the estimated dayside reconnection rate Φ_D using the coupling function of Milan et al. (2012), and **(B)** the amount of open magnetic flux F_{PC} in the simulation. Green shading indicates where the dayside rate dominates the nightside rate Φ_N, with red indicating the opposite.

of the period of predominantly southward IMF driving, with Φ_D and Φ_N frequently exceeding one-another. Notably, F_{PC} shows very little variation between 01:30–03:00 UT on 4 May and again between 05:30–08:30 UT. This suggests a dynamical state similar to steady magnetospheric convection (SMC), which arises when the dayside and nightside rates are in relative balance such that tail reconnection can proceed in a laminar fashion (DeJong et al., 2009; Walach and Milan, 2015; Milan et al., 2019). Since SMC can persist for several hours (Walach et al., 2017), the magnetotail current sheet may thus be relatively steady during this period and not disturbed by substorm activity.

After the switch to northward IMF at 09:00 UT the nightside rate dominates as expected (since Φ_D becomes very small), closing the majority of the remaining open flux gradually over about 2 h as Φ_N decays. This is slightly longer than the duration for which $\Phi_D > \Phi_N$ after 18:00 UT, indicating a characteristic global convection timescale of around 1–2 h in the simulation. This is broadly consistent with observations of polar cap contractions: a survey of 25 nightside reconnection events found durations up to 150 min with an average of 70 min (Milan et al., 2007). Note that the same study found values of F_{PC} ranging between 0.2 and 0.9 GWb across all events, comparable to those found here which provides further confidence in the simulation. After around 11:00 UT the dayside rate dominates briefly, but the open flux content then remains low for the remainder of the simulation. This confirms that the latter period of the event should be suitable for studying any distinct modes of response that occur under weaker driving unlike that of the preceding stormtime conditions.

3.2 Magnetotail configuration

For our analysis of the magnetotail the simulation data are transformed from Gorgon coordinates into an aberrated GSM (AGSM) frame, which has its X-axis anti-parallel with the average GSM solar wind flow direction. This reduces aberration in the tail due to the v_y and v_z components of the solar wind velocity vector, hence reducing the displacement of the current sheet along the Y- and Z-axes, and has been used in similar studies to account for the 'windsock' effect in the magnetotail (e.g. Fairfield, 1980; Hammond et al., 1994; Xiao et al., 2016). To do this, we calculate the average direction of the flow over the preceding 30 min at all times and rotate the GSM X-axis accordingly; this is a sufficient period of time to capture the displacement at the downtail distances considered in our study. As well as allowing for easier analysis, the use of AGSM facilitates direct comparison to studies such as the above.

To examine the behaviour of the magnetotail in response to changes in the IMF, we take slices in the Y-Z plane at a fixed

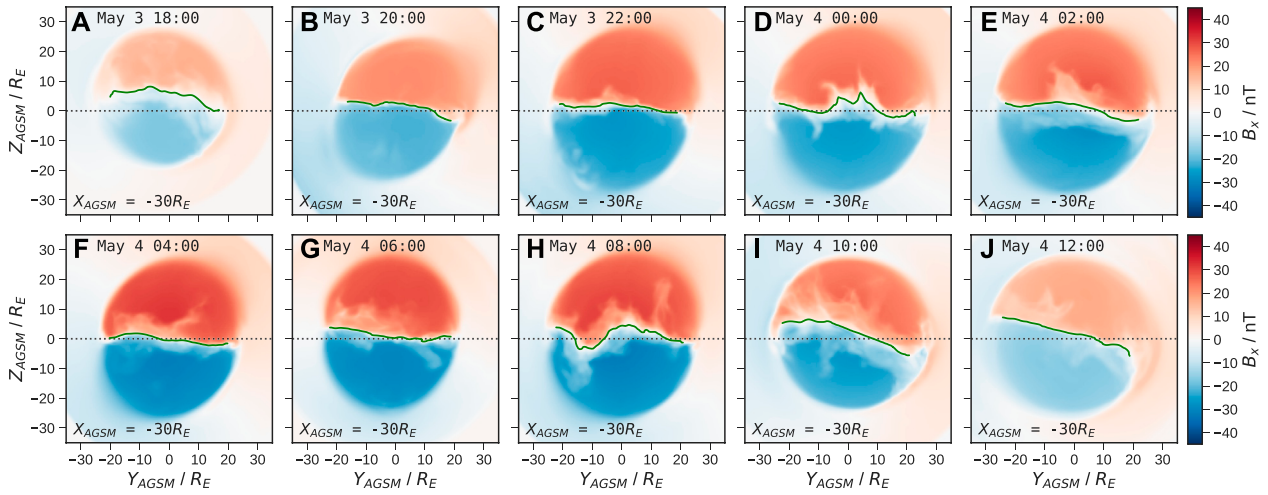

FIGURE 3
Slices **(A–J)** of the magnetotail at $X_{AGSM} = -30\ R_E$ showing the lobe field strength B_x over time in 2 h intervals and averaged over a 10 min sliding window. The location of the magnetotail current sheet is shown by the green lines, with the dotted line indicating the AGSM equator.

downtail distance. We choose $X_{AGSM} = -30\ R_E$ initially since this captures both open and closed field depending on the strength of driving (being tailward of the nightside reconnection line during the peak of the storm), with generally strong lobe field hence an intense current sheet. We take a 10 min sliding mean of the magnetic field in the tail (based on three timesteps each 5 min apart) across the whole simulation, which averages-out smaller disturbances to the current sheet making it easier to identify. Figure 3 shows the resulting B_x in the tail over time, as well as the current sheet indicated by the green line and defined as the $B_x = 0$ contour. Red regions indicate field directed sunward in the northern lobe, and blue indicates anti-sunward field in the southern lobe. The increasing field strength over time demonstrates the loading of open flux in the magnetotail, until the final two panels at 10:00 UT and 12:00 UT which are 1 and 3 h after the IMF has turned northward, respectively. Whilst the reduced flaring in the tail at 10:00 UT demonstrates that the effects of the IMF switch have begun to manifest, the lobe field still remains relatively strong suggesting a delay of >1 h for nightside reconnection to close remaining open flux.

The variation in the orientation of the current sheet clearly demonstrates the twisting of the magnetotail, which at most times is in a clockwise sense. At 08:00 UT the central portion of the current sheet shows anti-clockwise rotation due to the reversal from negative to positive IMF B_y just prior to 06:00 UT (at which time the current sheet does not yet appear to be affected), despite the IMF B_y switching back to negative after 07:00 UT. This suggests a significant delay of $>$ 1 h for the reversal to fully influence the tail. Nonetheless, the outer portions of the current sheet at 08:00 UT do appear to be reconfigured in the sense of negative B_y, suggesting a faster response timescale nearer to the magnetopause and hence an incoherent response between the outer and the inner (central) magnetotail (as shown by Walker et al. (1999)).

The current sheet is notably less twisted for periods when the tail B_x is strongest under southward IMF, suggesting a stronger twisting under northward IMF (visible from 10:00 UT onwards). During the earlier and later timestamps, there is a clear offset and hinging of the current sheet towards positive Z_{AGSM} (above the dotted line), as expected due to the positive dipole tilt angle which is maximal at around 17:00 UT. The hinging is less apparent when the lobe B_x is strongest around 04:00–06:00 UT, though it is difficult to discern whether this is due to enhanced lobe pressure (and tail reconnection) or due to the tilt angle being near its minimum at this time (see Figure 4C).

3.3 Current sheet fitting and IMF cross-correlation

To investigate the twisting of the current sheet in more detail, we first identify its location in 5 min intervals at $X_{AGSM} = -30\ R_E$ over the duration of the event, using the method described above with a 10 min sliding window. The twisting of the current sheet due to changes in B_y is difficult to quantify given its complex time-dependent shape and extent. Therefore, only the portion in the range of $|Y_{AGSM}| < 15\ R_E$ is sampled, so as to accommodate the changing size of the magnetotail and to avoid smearing differing response timescales between the central (small $|Y_{AGSM}|$) and outer (large $|Y_{AGSM}|$) current sheet. This is also motivated by the fact that the central current sheet divides the regions of

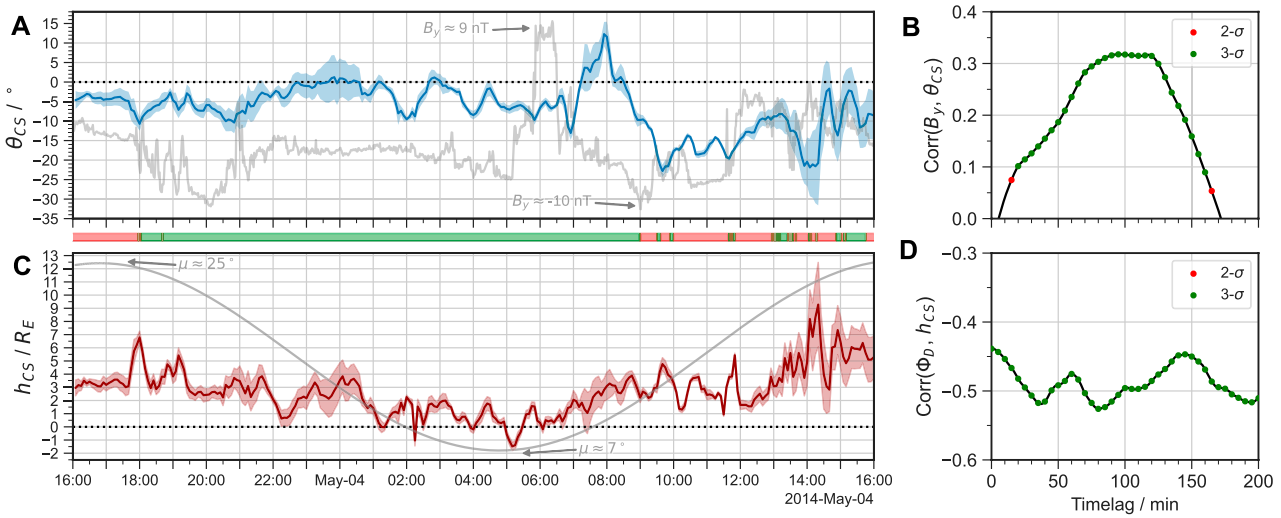

FIGURE 4
Results of the current sheet fitting at $X_{AGSM} = -30\ R_E$, showing **(A)** the rotation angle θ_{CS} (blue line) and **(C)** the hinging parameter h_{CS} (red line) over time, with the shading indicating the uncertainty in the parabolic fit. The variation in **(A)** the IMF B_y and **(C)** the dipole tilt angle μ is indicated by the grey curves to aid with analysis, with extreme values indicated. The colour blocks beneath the time axis of panel **(A)** indicate intervals when the IMF B_z is positive (red) or negative (green). The correlation coefficient is shown **(B,D)** for each timelag of the IMF variables, with statistically significant results indicated in red and green for 2-σ and 3-σ significance, respectively.

strongest lobe field, and represents the region most important for nightside reconnection and the asymmetries which manifest in ionospheric coupling.

As we have established, the morphology of the current sheet can be considered a combination of separate effects: these include the twisting due to the IMF B_y, the hinging due to the dipole tilt, and disturbances due to time-dependent tail reconnection (e.g. at 00:00 UT in Figure 3D), all of which may influence the current sheet incoherently at different Y-positions. In order to extract the first two effects, we fit a second-order polynomial to the current sheet coordinates (Y_{CS}, Z_{CS}) of the form:

$$Z_{CS} = aY_{CS}^2 + \tan(\theta_{CS})Y_{CS} + h_{CS}, \quad (3)$$

for some 'rotation' angle θ_{CS} and 'hinging' parameter h_{CS}. The latter is simply the displacement of the current sheet from the AGSM equator as inferred at $Y_{AGSM} = 0$ (for a given X_{AGSM}), and is distinct from the 'hinging distance' which is defined in specific current sheet models as the distance between the hinging point and the Earth (e.g., Fairfield, 1980; Hammond et al., 1994; Tsyganenko and Fairfield, 2004; Tsyganenko et al., 2015). The uncertainty in the fitting is found from the root-mean squared (RMS) error, which represents the deviation from an idealised, parabolic current sheet, from which we determine the error in both θ_{CS} and h_{CS}. The choice of a simplistic parabolic fit differs from these elliptical models which have performed well at capturing the average current sheet configuration based on large observational datasets (see Xiao et al., 2016 and references therein). However, the time-dependent behaviour of the magnetotail in this case study, combined with the large (and varying) tilt angle, mean a more complex fit is unlikely to provide much benefit and would require more free parameters. Instead, a parabolic fit allows us to effectively deduce the response timescales of the parameters of interest.

The fitting is repeated for each sampled timestep to produce a time-series in the current sheet parameters. We then perform a Pearson cross-correlation of these against time-lagged solar wind parameters to determine the timelag yielding the strongest correlation, representing the characteristic response time. This same approach has been used to deduce equivalent response timescales in the ionospheric FAC and ground magnetic field (Shore et al., 2019; Coxon et al., 2019). We make two assumptions in conducting our cross-correlation analysis: firstly that the rotation depends only on IMF B_y, and secondly that the hinging depends on the amount of magnetic pressure exerted on the current sheet by the lobes, which increases with the dayside reconnection rate Φ_D. For example, Tsyganenko and Fairfield, (2004) found that under southward IMF conditions the current sheet was more rigidly fixed into a tilted configuration than under northward IMF and hence was more deflected in Z_{GSM}. Specifically, this means we cross-correlate θ_{CS} with IMF B_y (in GSM) and h_{CS} with Φ_D, the latter as shown in Figure 2A. Periods where the error in each fitted parameter is greater indicate where the current sheet is actively reconfiguring, e.g., during an IMF B_y reversal. Figure 4 shows these parameters over time, and the results of the cross-correlation.

At the start of the simulation period θ_{CS} is weakly negative, such that the current sheet is rotated slightly clockwise, and then

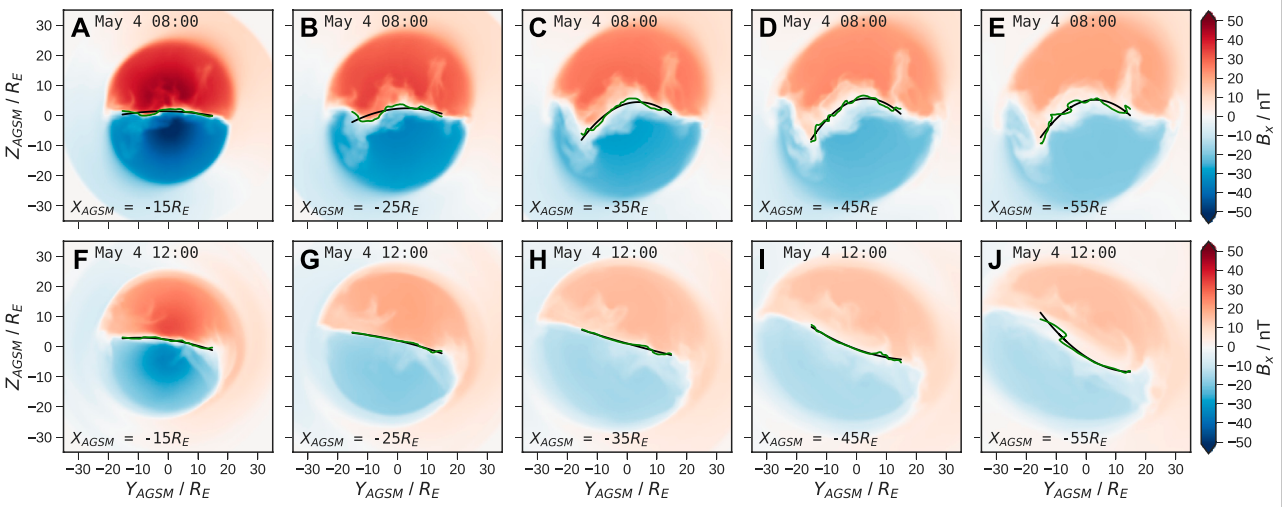

FIGURE 5
Slices of the magnetotail at increasing downtail distances at **(A–E)** 08:00 UT and **(F–J)** 12:00 UT on 4 May, showing the lobe field strength B_x over time in 2 h intervals and averaged over a 10 min sliding window. The location of the magnetotail current sheet is shown by the green lines, with the result of the parabolic fitting via Eq. 3 shown by the black curves.

shows some variability after the shock arrival at 18:00 UT on 3 May. The IMF B_y decreases to a minimum around 20:00 UT, before briefly switching to zero around 21:00 UT but then remaining negative. Meanwhile θ_{CS} reaches a minimum just before 21:00 UT, but then gradually increases over several hours into an untwisted state ($\theta_{CS} \sim 0^{\circ}$) in which there is much higher RMS error. This reflects the fact that the current sheet is more disturbed during this period due to reconnection in the tail, as evident in Figure 3D. This weak rotation despite negative IMF B_y suggests that active nightside reconnection tends to reduce the asymmetry, in agreement with Ohma et al. (2021). For the following several hours until 05:00 UT there is relatively little variability in IMF B_y, which remains negative. Correspondingly, θ_{CS} remains mostly negative but shows more variability than IMF B_y suggesting time-dependent nightside reconnection is important in determining the extent of the twisting in the tail.

The sharp IMF B_y reversal around 06:00 UT results in a strong twisting of the current sheet in the opposite direction, with θ_{CS} showing a pronounced increase. However this effect is not seen until around 07:00 UT, and θ_{CS} only reaches its maximum value of $\sim 12^{\circ}$ at 08:00 UT, more than an hour after the IMF B_y turns negative again. This delay of 1–2 h is indicative of global convection controlling the response. Note that the sharp dynamic pressure decrease which occurs simultaneously to the reversal in IMF B_y (just prior to 06:00 UT, see Figure 1C) results in an expansion of the magnetosphere which will reduce the pressure in the lobes. However this effect occurs over timescales of minutes, communicated by fast mode waves (e.g., Andreeova et al., 2011; Ozturk et al., 2019), and there is relatively little variation in θ_{CS} during the subsequent hour. Therefore whilst the reduced dynamic pressure may affect the extent of the twisting in the tail, which can not easily be separated from direct effects of IMF B_y, the much larger response after 07:00 UT is specific to the B_y reversal.

The switch to predominantly northward IMF at ~ 09:00 UT results in a far stronger twisting in the tail, with θ_{CS} reaching a minimum of $\sim -23^{\circ}$ around 09:30 UT. However, this is only 30 min after the IMF B_y reaches its minimum value at 09:00 UT, suggesting a faster response timescale than under southward IMF conditions. The IMF B_y then becomes less negative and more variable for the remainder of the simulation, which is also reflected in θ_{CS} with the current sheet appearing more disturbed. Another IMF B_y decrease around 13:30 UT also causes a negative twisting around 14:00 UT, again suggesting a 30 min response under these conditions.

Based on these results there appears to be a bimodal response in the twisting of the current sheet, depending on the strength of driving. However, this is not clearly reflected in the results of the Pearson cross-correlation with the strongest response being over a wide range of timelags from 1–2 h, more consistent with the longer convection timescale under southward IMF. The peak timelag is around 100 min, but this has a fairly weak correlation of ~ 0.3. However, since the bimodal behaviour throughout the full simulation period may be smearing the overall correlations (which will be highly sensitive to the response to the B_y reversal), the different periods of driving should be separated to infer the true timescales. This would further reveal if a longer timescale response under northward IMF (as per Browett et al., 2017) is also present, especially further downtail, which we will return to later.

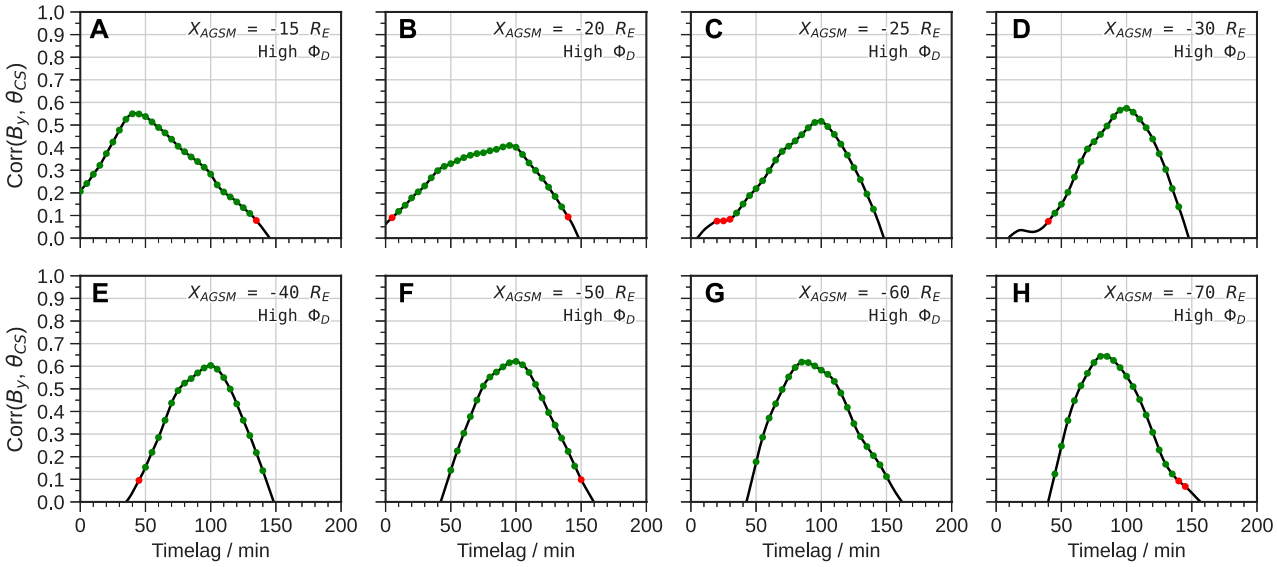

FIGURE 6
Correlations and timelags **(A–H)** of IMF B_y versus current sheet rotation angle θ_{CS} for multiple downtail distances under high Φ_D (predominantly southward IMF) conditions. The scatter points are coloured according to statistical significance as in Figure 4.

Before proceeding we also briefly discuss the behaviour of the hinging parameter h_{CS} during the simulation. This broadly tracks the variation in the dipole tilt angle, being largest at the start and end of the simulation and reaching a minimum value shortly after the tilt angle is minimal around 05:00 UT. Aside from this there is no particularly clear trend in the response during the most strongly driven period, except for a sharp increase at shock arrival near 18:00 UT on 3 May, with the response being relatively flat during the first few hours of 4 May when F_{PC} is fairly steady (see Figure 2B). Towards the end of the simulation when the driving is weaker the hinging is much more variable and h_{CS} reaches much larger values (albeit with large uncertainty). The correlations with Φ_D are consistently negative with 3-σ significance, indicating smaller deflection in Z for southward IMF, which disagrees with the findings of Tsyganenko and Fairfield, (2004). However we note that the 15 h period of strongest dayside coupling also contained most of the 12 h period during which the tilt angle was actively decreasing, which will introduce some bias to the correlations. Regardless, the peak timelag is around 80 min - similar to the 100 min timelag in θ_{CS} - and consistent with the delay for open flux to be accumulated in the tail.

3.4 Response timescales vs. downtail distance

To infer whether this behaviour is sensitive to our choice of downtail distance, we repeat the analysis at a series of slices from $X_{AGSM} = -15\ R_E$ to $-70\ R_E$ in steps of 5 R_E. Note that observations have also shown IMF B_y signatures within the inner magnetosphere at distances of less than 7 R_E (Case et al., 2021), but we limit our analysis only to where the tail field is less dipolar and the current sheet is more twisted. Whilst we also expect twisting further downtail than this range, at such distances the current sheet cannot be as reliably located, in part due to significant aberration of the tail. The result of our current sheet identification is shown for two example timestamps in Figure 5. Note the slices at $X_{AGSM} = -15\ R_E$ lie just Earthward of the main reconnection line at these times, with the remainder being tailward. The black curve represents the result of the polynomial fitting using equation 3, which performs well where the current sheet has a simple geometry (as at 12:00 UT, bottom row), but results in more error during times of reconfiguration when the current sheet is more disturbed (as at 08:00 UT, top row). This error appears greater further downtail where the $B_x = 0$ contour is less smooth and the current sheet is significantly more warped. It is clear that the twisting is much stronger further downtail, in agreement with previous studies (Walker et al., 1999; Tsyganenko and Fairfield, 2004). Nonetheless, the sense of the orientation is well-preserved with distance; this suggests a similar twisting timescale in both the near-Earth and middle magnetotail. At 08:00 UT the current sheet is actively reconfiguring in each slice, with the central current sheet rotated oppositely to the outer current sheet. However, our truncation within $Y_{AGSM} = \pm\ 15\ R_E$ is effective at isolating the timescales of the former. Conversely, the current sheet is more uniform at 12:00 UT, being most strongly twisted at $X_{AGSM} = -55\ R_E$ due to the reduced lobe field strength.

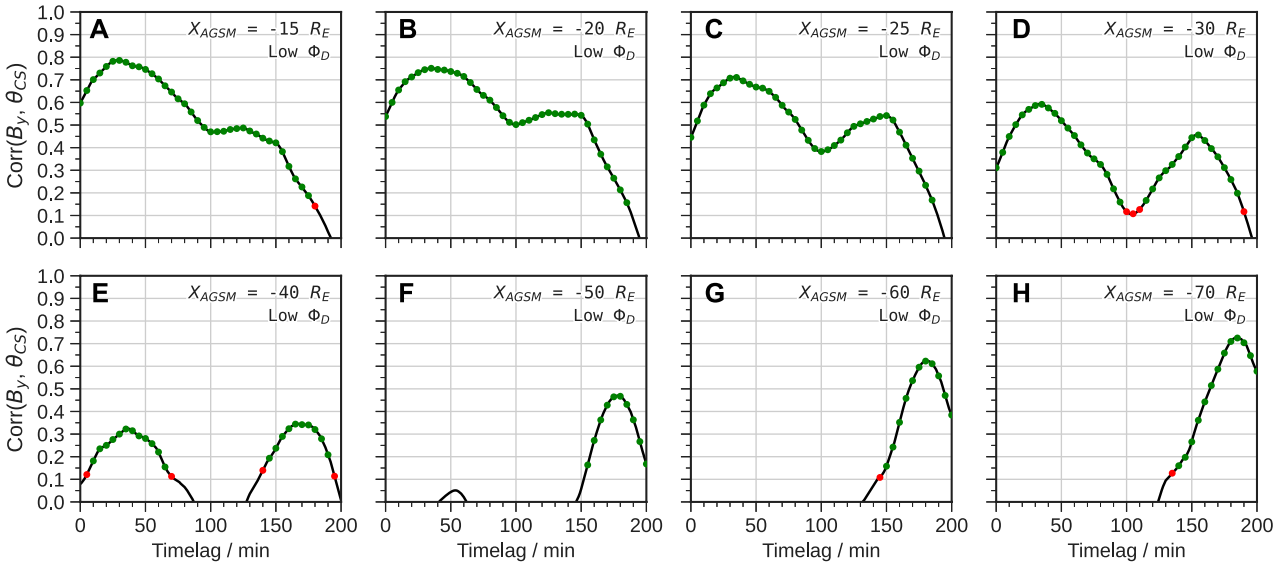

FIGURE 7
Correlations and timelags **(A–H)** of IMF B_y versus current sheet angle θ_{CS} for multiple downtail distances under low Φ_D (predominantly northward IMF) conditions. The scatter points are coloured according to statistical significance as in Figure 4.

To separate the responses under predominantly southward and northward IMF conditions, we now split our analysis into two distinct periods. To focus on conditions during strong solar wind driving, we select a 15 h window spanning from 18:00 UT on 3 May to 09:00 UT on 4 May. During this time Φ_D remains high throughout, resulting in large open flux content and a strong lobe field as evident in Figure 3. For conditions during weaker driving, we select the remaining 7 h time period between 09:00 UT and 16:00 UT for which Φ_D was relatively weak; whilst the IMF did occasionally turn southward during this window, this was only brief and there is unlikely to be sufficient flux opening to contaminate the key timescales. With each time-series we then perform a Pearson cross-correlation as before at every downtail distance.

The result for the predominantly southward IMF period is shown in Figure 6. In all cases there is a clear peak timelag that indicates a dominant twisting timescale. Near to the Earth at $X_{AGSM} = -15\ R_E$ this is relatively short at 40 min, but 20–50 R_E downtail the response is strongest around 100 min. From $X_{AGSM} = -60\ R_E$ to $-70\ R_E$ this shifts towards slightly shorter timescales, suggesting that the far magnetotail may respond more quickly than the middle and near-Earth magnetotail, presumably due to weaker lobe field. The shorter timelag 15 R_E downtail is consistent with the timescales of shear flow-induced B_y due to MHD wave propagation (Tenfjord et al., 2015), whereas the longer timelag at other distances is consistent with the 1–2 h global convection timescale identified in the simulation. This is reflected in the broader correlation distributions in the near-Earth magnetotail suggesting both timescales are present, whereas the distributions become narrow as the shorter timescale drops off rapidly with distance. Note however that the cross-correlation will be most sensitive to the response to the sharp IMF B_y reversals, with convection likely proceeding faster (or slower) than 100 min in the near-Earth and middle magnetotail during some periods.

For the predominantly northward IMF period the results are markedly different, as shown in Figure 7. Between 15 and 40 R_E downtail there is a clear bimodal response: one shorter timescale around 30 min and one much longer response around 2–3 h. The former dominates (with higher correlations) up to 40 R_E beyond which it becomes weakly-correlated and is undetectable in the far magnetotail. Here the longer timescale dominates and becomes slower with distance, but with increasing correlations which even exceed that of the equivalent southward IMF timescale. This strongly supports the notion of MHD wave propagation dominating in the near-Earth magnetotail under northward IMF conditions, whereas in the middle and far magnetotail convection-driven reconfiguration controls the twisting and occurs more slowly than under southward IMF.

The trends described above are summarised for the full range of downtail distances in Figure 8. The mean, minimum and maximum values of θ_{CS} are determined across the entire simulation, as well as the peak correlations and timelags under predominantly southward and northward IMF conditions. We also separate out the timelags for the low Φ_D period to isolate both the shorter and longer timescale response. In the interest of demonstrating the key trends, we do not discard

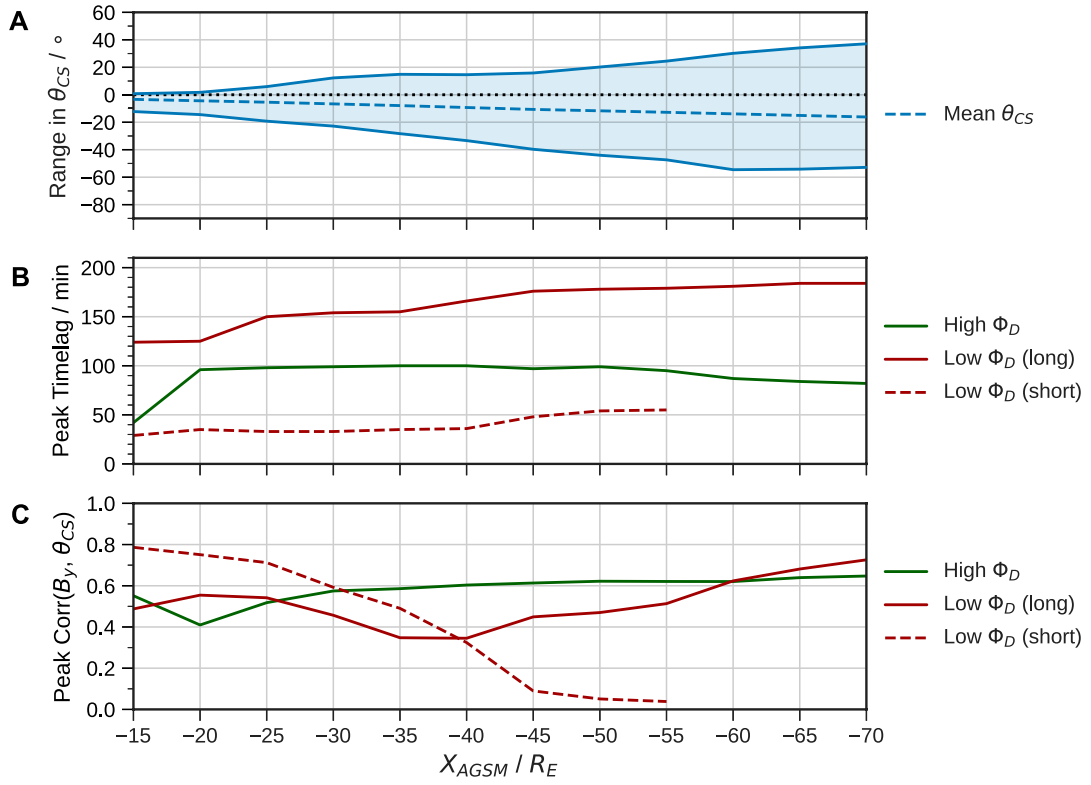

FIGURE 8
Summary of results from the fitting and cross-correlation of θ_{CS}. Shown is **(A)** the range of values over the full simulation, **(B)** the peak timelags and **(C)** the peak correlation coefficients for both high and low Φ_D separated by mode of response. Note the short timescale for low Φ_D is not plotted beyond 55 R_E downtail since it is not detectable here.

TABLE 1 Summary of different response timescales of the magnetotail current sheet twisting to IMF B_y during the simulated storm, separated by region of the magnetotail (with downtail distance indicated) and strength of solar wind coupling Φ_D. These values are inferred from Figure 8.

Region	Induction timescale		Convection timescale	
	High Φ_D	Low Φ_D	High Φ_D	Low Φ_D
Near-Tail (< 30 R_E)	~ 40 min	~ 30 min	~ 100 min	120–150 min
Mid-Tail (30–60 R_E)	None	30–50 min	~ 100 min	150–180 min
Far-Tail (> 60 R_E)	None	None	≲ 90 min	≳ 180 min

the strongest timelag even if has less than 2-σ significance. The extent of the rotation clearly grows linearly with distance, although the minimum θ_{CS} saturates around X_{AGSM} = −60 R_E, which may be a limitation of the parabolic fitting. This trend differs from expectations of magnetotail twisting in induced magnetospheres (for which the draping of field lines should result in a current sheet normal to the IMF, e.g., DiBraccio et al., 2018), demonstrating that the dipole strongly affects the tail configuration even far from the Earth. At all distances the maximum value of θ_{CS} corresponds to the sharp IMF B_y reversal around 06:00 UT on 4 May; near to the Earth this is not sufficient to rotate the current sheet into a strongly positive θ_{CS} orientation, but at X_{AGSM} = −70 R_E this is as large as ~ 40°. The largest twisting angles of ~ -55° at 60–70 R_E downtail are comparable with values of up to 50–60° reported by Owen et al. (1995).

The peak timelag for high Φ_D between 20 and 50 R_E downtail is almost identical at ~ 100 min, and as noted above appears to decrease beyond this (though is still well-correlated at 100 min). In contrast the timescales under northward IMF increase far downtail; this demonstrates that the magnetotail behaves very differently when there is large open flux content versus when it is relatively closed. The trend in the peak correlations also demonstrates that near to the Earth the current sheet is more responsive to IMF B_y under northward IMF than southward IMF. The high Φ_D response is strongest within the mid-tail, with low Φ_D correlations again higher in the far-tail over longer timescales, likely since the twisting is more prominent under these conditions. This indicates that global convection is much more effective at controlling the configuration of the middle-to-far magnetotail, and near to the Earth becomes dominated by shorter timescale effects when the system is not being strongly driven. Note the longer convection timescales found here are similar to the ~ 2–3 h timescale found in observations of tail twisting at distances < 20 R_E during weak driving (Pitkänen et al., 2016), except these are dominated by the shorter timescale in the simulation. The same observations also revealed a trend of increasing response time nearer to the Earth, opposite to that found here, though this included measurements in the inner magnetosphere which is outside the range of our analysis.

4 Discussion and conclusion

In this study we have investigated the response of the magnetotail current sheet to strong, highly variable driving by the solar wind during a geomagnetic storm. The event in question hosted several key features in the IMF, including a switch in B_z from northward to southward and vice-versa, sharp reversals in B_y, and a prolonged ~ 15 h period of predominantly southward IMF. This provides a particularly interesting case study for exploring the response timescales of the system, both in terms of the opening and closing of flux in the magnetosphere and the configuration of the magnetotail current sheet. By investigating the change in open flux content we find that the nightside reconnection response to dayside driving is delayed by 1–2 h when the IMF B_z switches sign, due to the gradual accumulation (or lack thereof) of open flux in the magnetotail by global convection.

The variation in flux content is reflected in the lobe magnetic field 30 R_E downtail, with the event clearly separated into a period of intense lobe B_x which is sustained for several hours, and then a period of weaker lobe field once open flux is closed under northward IMF. Here the orientation of the current sheet matches the polarity of the IMF B_y, and clearly twists in response to an IMF B_y reversal which is more prompt in the outer current sheet than the central portion ($|Y_{AGSM}| < 15\ R_E$), in agreement with previous simulations with idealised driving (Walker et al., 1999). The extent of the twisting is clearly greater under northward IMF when the lobe magnetic pressure is weakest, such that during the period of most active nightside reconnection the rotation is least noticeable, consistent with observations (Owen et al., 1995; Tsyganenko and Fairfield, 2004; Xiao et al., 2016; Case et al., 2018) and simulations (Ohma et al., 2021).

By focussing on the central current sheet and fitting a parabolic profile at each timestep we have calculated a rotation/twisting angle θ_{CS} and hinging parameter h_{CS} of the current sheet over time. We repeated this fitting for a range of downtail distances between 15 and 70 R_E, revealing that θ_{CS} increases linearly with downtail distance, both in a time-averaged sense and for a more sudden response to an IMF B_y reversal, consistent with theoretical expectations and empirical models (e.g., Cowley, 1981; Tsyganenko and Fairfield, 2004), and reaching peak angles of rotation similar to those seen in observations (Owen et al., 1995). Focussing our analysis at 30 R_E downtail, we find that the hinging generally follows the diurnal trend of the dipole tilt angle during the full 24 h period. Cross-correlation between h_{CS} and an empirical solar wind coupling function also indicates that strong driving acts to reduce the hinging due to enhanced lobe B_x, with a peak timelag of ~ 80 min across the entire event due to the accumulation of flux in the tail. Meanwhile, θ_{CS} responds strongly to a sharp reversal in IMF B_y when B_z is southward, such that the tail fully untwists into the opposite direction over a period of 1–2 h, also consistent with the timescales of global convection and the response timescale of nightside ionospheric FACs to IMF B_y identified by Milan et al. (2018) and Coxon et al. (2019). A cross-correlation between θ_{CS} and IMF B_y across the entire event reveals a peak timelag of ~ 100 min; however, the peak correlation is low (~ 0.3) indicating that the relationship is more complex and depends on the strength of driving.

To better understand the different modes of response we separated the cross-correlation into two separate periods: one where Φ_D was greatest (predominantly southward IMF), and one where Φ_D was much lower (predominantly northward IMF). This was repeated for our full range of downtail distances. We find that 20–50 R_E downtail the θ_{CS} global convection timescale of ~ 100 min does indeed dominate when Φ_D is highest, and is more strongly correlated with IMF B_y (~ 0.6 at 30 R_E) than over the entire event. This timelag decreases slightly in the far tail, whereas nearer the Earth at 15 R_E a much shorter timescale of ~ 40 min dominates. For times when Φ_D is lowest, there instead appear two distinct timescales in the twisting: one around 30 min and a much longer timescale of 2–3 h. The former is consistent with the timescales previously associated with induced B_y due to MHD wave propagation (Tenfjord et al.,2015; Tenfjord et al., 2017; Tenfjord et al., 2018), and is dominant between 15 and 40 R_E downtail where it is very strongly correlated to IMF B_y (up to ~

0.8) and shows little dependence on downtail distance, in agreement with observations by Case et al. (2018). Beyond 40 R_E the longer timescale dominates, consistent with Browett et al. (2017) and Rong et al. (2010), and is slower and more strongly correlated (up to ~ 0.7) further downtail.

The characteristic timescales of the current sheet twisting are summarised in Table 1. Note that since we are fitting simultaneously to a wide portion of the current sheet, our best-correlated 'response' will be slower than the initial response of the localised tail B_y which then reconfigures gradually (see Tenfjord et al., 2017). These timescales will also not always be fixed at the peak timelags identified; for example, convection likely proceeds fastest during the peak of the storm. Overall, our results show that whilst shear flow-induced B_y is important in controlling asymmetries in the near-Earth magnetotail, the current sheet response appears to be dominated by global convection effects during stronger driving conditions and in general further downtail, such that its role in nightside ionospheric coupling may be less important. Indeed, longer convection timescales of up to 3–4 h during northward IMF can explain observed delays in the response to IMF B_y in nightside ionospheric FAC (Milan et al., 2018; Coxon et al., 2019) and the formation of auroral arcs (Fear and Milan, 2012; Milan et al., 2005) which have been linked to magnetotail twisting in previous simulations (Kullen and Janhunen, 2004).

Finally, we note some caveats and key points for future work. Whilst our approach isolated the response of the central current sheet for $|Y_{AGSM}| < 15\ R_E$, the faster outer current sheet response was not captured. An extension of this study could be to deduce the difference in timelag as a function of distance from the X-axis, though this is non-trivial given the complex changes in shape and size of the magnetotail. Our methodology could also be applied to multiple different events to determine how timescales differ for more or less extreme solar wind conditions, and for particular configurations of the magnetosphere with different seasonal tilt angle, such as around equinox. As mentioned in the introduction, various non-MHD effects not captured in the simulation can influence the tail configuration and therefore may be important in determining the timescales of response. For example, smaller-scale flapping motions in the current sheet may affect the extent of the twisting, whilst kinetic effects can control the loading-unloading and thus the large-scale tail dynamics (e.g., Zhang et al., 2020; Kuznetsova et al., 2007). In addition, the inclusion of a ring current in the inner magnetosphere might influence the transport of flux returning to the dayside and thus the length of the Dungey cycle. Future simulation studies incorporating these effects can elucidate whether they play a significant role in determining the global response of the current sheet.

As discussed in Section 2.2, it may be that other global MHD models (such as those used by Walker et al., 1999; Kullen and Janhunen, 2004, Tenfjord et al., 2015) would predict slightly different response timescales than the Gorgon model, for example in shear flow-induced B_y due to different transit times of MHD waves dependent on the density and field strength (and thus Alfvén speed) in the magnetosphere. However, whilst we do not expect the timescales identified here to match perfectly with reality, the physical interpretations remain the same. A further question is in relating these timescales to those seen in the ionospheric response. A subsequent study will investigate this within our simulation, and compare to observations of the FAC and ground magnetic field timescales to more directly link the magnetospheric and ionospheric asymmetries.

In summary, by simulating the system during highly variable conditions we have identified multiple different modes of magnetotail response. Whilst previous work has disagreed over whether changes in the IMF can be communicated into the system over tens of minutes or over hours, our results instead suggest that both timescales of response can occur, which resolves this apparent disparity in the literature. Changes in the tail morphology due to loading and anti-sunward transport of open flux during southward IMF arise predominantly over convection timescales, and more exaggerated responses under northward IMF occur at both shorter and longer timescales corresponding to wave propagation and the gradual advection of field lines, respectively. Overall, our results have important implications for the understanding of the characteristic timescales over which asymmetries develop in the magnetosphere-ionosphere system and influence space weather.

Data availability statement

The raw data supporting the conclusions of this article will be made available by the authors, without undue reservation.

Author contributions

JWBE performed the simulation and analysis presented in the paper, and wrote the manuscript. JCC and RS contributed to the conception of the study and the selection of the simulated event. JCC, RS, RD and JPE provided valuable insight into the work and its direction. LM and JPC are authors of the Gorgon simulation code and its post-processing tools and provided technical guidance for the work.

Funding

JWBE was supported by Science and Technology Facilities Council (STFC) Studentship ST/R504816/1. JCC was supported

by STFC Ernest Rutherford Fellowship ST/V004883/1. RS was supported by Natural Environment Research Council (NERC) grants NE/V002716/1 and NE/V002732/1. JWBE, LM, JPC and JPE acknowledge funding by NERC grant NE/P017142/1. JWBE, JPC and JPE acknowledge funding by NERC grant NE/V003070/1. RD, JPC and JPE acknowledge funding by NERC grant NE/P017347/1.

Acknowledgments

This work used the Imperial College High Performance Computing Service (doi: 10.14469/hpc/2232). We acknowledge use of NASA/GSFC's Space Physics Data Facility's OMNIWeb service, and OMNI data.

Conflict of interest

The authors declare that the research was conducted in the absence of any commercial or financial relationships that could be construed as a potential conflict of interest.

Publisher's note

References

Aikio, A. T., Pitkänen, T., Honkonen, I., Palmroth, M., and Amm, O. (2013). IMF effect on the polar cap contraction and expansion during a period of substorms. *Ann. Geophys.* 31, 1021–1034. doi:10.5194/angeo-31-1021-2013

Akasofu, S.-I. (2018). A review of the current understanding in the study of geomagnetic storms. *Int. J. Earth Sci. Geophys.* 4, 1–13. doi:10.35840/2631-5033/1818

Anderson, B. J., Korth, H., Waters, C. L., Green, D. L., Merkin, V. G., Barnes, R. J., et al. (2014). Development of large-scale birkeland currents determined from the active magnetosphere and planetary electrodynamics response experiment. *Geophys. Res. Lett.* 41, 3017–3025. doi:10.1002/2014GL059941

Andreeova, K., Pulkkinen, T. I., Juusola, L., Palmroth, M., and Santolík, O. (2011). Propagation of a shock-related disturbance in the earth's magnetosphere. *J. Geophys. Res.* 116. doi:10.1029/2010JA015908

Borovsky, J. E., Thomsen, M. F., and Elphic, R. C. (1998). The driving of the plasma sheet by the solar wind. *J. Geophys. Res.* 103, 17617–17639. doi:10.1029/97JA02986

Browett, S. D., Fear, R. C., Grocott, A., and Milan, S. E. (2017). Timescales for the penetration of IMF by into the Earth's magnetotail. *J. Geophys. Res. Space Phys.* 122, 579–593. doi:10.1002/2016JA023198

Case, N. A., Grocott, A., Haaland, S., Martin, C. J., and Nagai, T. (2018). Response of earth's neutral sheet to reversals in the IMF by component. *J. Geophys. Res. Space Phys.* 123, 8206–8218. doi:10.1029/2018JA025712

Case, N., Hartley, D., Grocott, A., Miyoshi, Y., Matsuoka, A., Imajo, S., et al. (2021). Inner magnetospheric response to the interplanetary magnetic field by component: Van allen probes and arase observations. *JGR. Space Phys.* 126. doi:10.1029/2020JA028765

Ciardi, A., Lebedev, S. V., Frank, A., Blackman, E. G., Chittenden, J. P., Jennings, C. J., et al. (2007). The evolution of magnetic tower jets in the laboratory. *Phys. Plasmas* 14, 056501. doi:10.1063/1.2436479

Cowley, S. W. H., and Lockwood, M. (1992). Excitation and decay of solar wind-driven flows in the magnetosphere-ionosphere system. *Ann. Geophys.* 10, 103–115.

Cowley, S. W. H. (1981). Magnetospheric asymmetries associated with the y-component of the imf. *Planet. Space Sci.* 29, 79–96. doi:10.1016/0032-0633(81)90141-0

Coxon, J. C., Milan, S. E., Carter, J. A., Clausen, L. B., Anderson, B. J., and Korth, H. (2016). Seasonal and diurnal variations in AMPERE observations of the Birkeland currents compared to modeled results. *J. Geophys. Res. Space Phys.* 121, 4027–4040. doi:10.1002/2015JA022050

Coxon, J. C., Rae, I. J., Forsyth, C., Jackman, C. M., Fear, R. C., and Anderson, B. J. (2017). Birkeland currents during substorms: Statistical evidence for intensification of regions 1 and 2 currents after onset and a localized signature of auroral dimming. *J. Geophys. Res. Space Phys.* 122, 6455–6468. doi:10.1002/2017JA023967

Coxon, J. C., Shore, R. M., Freeman, M. P., Fear, R. C., Browett, S. D., Smith, A. W., et al. (2019). Timescales of birkeland currents driven by the IMF. *Geophys. Res. Lett.* 2018, 7893–7901. doi:10.1029/2018GL081658

[Dataset] Papitashvili, N. E., and King, J. H. (2020). *OMNI 1-min data set [data set]*. NASA Space Physics Data Facility.

DeJong, A. D., Ridley, A. J., Cai, X., and Clauer, C. R. (2009). A statistical study of BRIs (SMCs), isolated substorms, and individual sawtooth injections. *J. Geophys. Res.* 114. doi:10.1029/2008JA013870

Desai, R. T., Eastwood, J. P., Horne, R. B., Allison, H. J., Allanson, O., Watt, C. E. J., et al. (2021a). Drift orbit bifurcations and cross-field transport in the outer radiation belt: Global mhd and integrated test-particle simulations. *JGR. Space Phys.* 126, e2021JA029802. doi:10.1029/2021JA029802

Desai, R. T., Freeman, M. P., Eastwood, J. P., Eggington, J. W. B., Archer, M. O., Shprits, Y. Y., et al. (2021b). Interplanetary shock-induced magnetopause motion: Comparison between theory and global magnetohydrodynamic simulations. *Geophys. Res. Lett.* 48, e2021GL092554. doi:10.1029/2021GL092554

DiBraccio, G. A., Luhmann, J. G., Curry, S. M., Espley, J. R., Xu, S., Mitchell, D. L., et al. (2018). The twisted configuration of the martian magnetotail: Maven observations. *Geophys. Res. Lett.* 45, 4559–4568. doi:10.1029/2018GL077251

Dungey, J. W. (1961). Interplanetary magnetic field and the auroral zones. *Phys. Rev. Lett.* 6, 47–48. doi:10.1103/PhysRevLett.6.47

Eastwood, J. P., Hapgood, M. A., Biffis, E., Benedetti, D., Bisi, M. M., Green, L., et al. (2018). Quantifying the economic value of space weather forecasting for power grids: An exploratory study. *Space weather.* 16, 2052–2067. doi:10.1029/2018SW002003

Eggington, J. W. B., Desai, R. T., Mejnertsen, L., Chittenden, J. P., and Eastwood, J. P. (2022). Time-varying magnetopause reconnection during sudden commencement: Global mhd simulations. *JGR. Space Phys.* 127, e2021JA030006. doi:10.1029/2021JA030006

Eggington, J. W. B., Eastwood, J. P., Mejnertsen, L., Desai, R. T., and Chittenden, J. P. (2020). Dipole tilt effect on magnetopause reconnection and the steady-state magnetosphere-ionosphere system: Global mhd simulations. *J. Geophys. Res. Space Phys.* 125, e2019JA027510. doi:10.1029/2019JA027510

Eggington, J. W. B., Eastwood, J. P., Mejnertsen, L., Desai, R. T., and Chittenden, J. P. (2018). Forging links in Earth's plasma environment. *Astronomy Geophys.* 59, 6. doi:10.1093/astrogeo/aty275

Fairfield, D. (1980). A statistical determination of the shape and position of the geomagnetic neutral sheet. *J. Geophys. Res.* 85, 775–780. doi:10.1029/JA085iA02p00775

Fear, R. C., and Milan, S. E. (2012). The imf dependence of the local time of transpolar arcs: Implications for formation mechanism. *J. Geophys. Res.* 117. doi:10.1029/2011JA017209

Gabrielse, C., Angelopoulos, V., Runov, A., and Turner, D. L. (2014). Statistical characteristics of particle injections throughout the equatorial magnetotail. *JGR. Space Phys.* 119, 2512–2535. doi:10.1002/2013JA019638

Gordeev, E., Sergeev, V., Honkonen, I., Kuznetsova, M., Rastätter, L., Palmroth, M., et al. (2015). Assessing the performance of community-available global mhd models using key system parameters and empirical relationships. *Space weather*. 13, 868–884. doi:10.1002/2015SW001307

Grocott, A., Milan, S., Yeoman, T., Sato, N., Yukimatu, A., and Wild", J. (2010). Superposed epoch analysis of the ionospheric convection evolution during substorms: IMF by dependence. *J. Geophys. Res.* 115. doi:10.1029/2010JA015728

Grocott, A. (2017). *Time-dependence of dawn-dusk asymmetries in the terrestrial ionospheric convection pattern"* (United States: American geophysical union). *Geophys. Monogr.*, 107–123. doi:10.1002/9781119216346.ch9

Hammond, C. M., Kivelson, M. G., and Walker, R. J. (1994). Imaging the effect of dipole tilt on magnetotail boundaries. *J. Geophys. Res.* 99, 6079–6092. doi:10.1029/93JA01924

Hapgood, M. A. (1992). Space physics coordinate transformations: A user guide. *Planet. Space Sci.* 40, 711–717. doi:10.1016/0032-0633(92)90012-D

Honkonen, I., Palmroth, M., Pulkkinen, T. I., Janhunen, P., and Aikio, A. (2011). On large plasmoid formation in a global magnetohydrodynamic simulation. *Ann. Geophys.* 29, 167–179. doi:10.5194/angeo-29-167-2011

Honkonen, I., Rastätter, L., Grocott, A., Pulkkinen, A., Palmroth, M., Raeder, J., et al. (2013). On the performance of global magnetohydrodynamic models in the earth's magnetosphere. *Space weather*. 11, 313–326. doi:10.1002/swe.20055

Kaymaz, Z., Siscoe, G. L., Luhmann, J. G., Lepping, R. P., and Russell, C. T. (1994). Interplanetary magnetic field control of magnetotail magnetic field geometry: Imp 8 observations. *J. Geophys. Res.* 99, 11113–11126. doi:10.1029/94JA00300

Kullen, A., and Janhunen, P. (2004). Relation of polar auroral arcs to magnetotail twisting and imf rotation: A systematic mhd simulation study. *Ann. Geophys.* 22, 951–970. doi:10.5194/angeo-22-951-2004

Kuznetsova, M. M., Hesse, M., Rastätter, L., Taktakishvili, A., Toth, G., De Zeeuw, D. L., et al. (2007). Multiscale modeling of magnetospheric reconnection. *J. Geophys. Res.* 112. doi:10.1029/2007JA012316

Mejnertsen, L., Eastwood, J. P., and Chittenden, J. P. (2021). Control of magnetopause flux rope topology by non-local reconnection. *Front. Astron. Space Sci.* 8. doi:10.3389/fspas.2021.758312

Mejnertsen, L., Eastwood, J. P., Hietala, H., Schwartz, S. J., and Chittenden, J. P. (2018). Global MHD simulations of the earth's bow shock shape and motion under variable solar wind conditions. *JGR. Space Phys.* 123, 259–271. doi:10.1002/2017JA024690

Milan, S. E., Carter, J. A., Sangha, H., Bower, G. E., and Anderson, B. J. (2021). Magnetospheric flux throughput in the dungey cycle: Identification of convection state during 2010. *J. Geophys. Res. Space Phys.* 126, e2020JA028437. doi:10.1029/2020JA028437

Milan, S. E., Carter, J. A., Sangha, H., Laundal, K. M., Østgaard, N., Tenfjord, P., et al. (2018). Timescales of dayside and nightside field-aligned current response to changes in solar wind-magnetosphere coupling. *J. Geophys. Res. Space Phys.* 123, 7307–7319. doi:10.1029/2018JA025645

Milan, S. E., Gosling, J. S., and Hubert, B. (2012). Relationship between interplanetary parameters and the magnetopause reconnection rate quantified from observations of the expanding polar cap. *J. Geophys. Res.* 117. doi:10.1029/2011JA017082

Milan, S. E., Hubert, B., and Grocott, A. (2005). Formation and motion of a transpolar arc in response to dayside and nightside reconnection. *J. Geophys. Res.* 110, A01212. doi:10.1029/2004JA010835

Milan, S. E., Provan, G., and Hubert, B. (2007). Magnetic flux transport in the dungey cycle: A survey of dayside and nightside reconnection rates. *J. Geophys. Res.* 112. doi:10.1029/2006JA011642

Milan, S. E., Walach, M.-T., Carter, J. A., Sangha, H., and Anderson, B. J. (2019). Substorm onset latitude and the steadiness of magnetospheric convection. *J. Geophys. Res. Space Phys.* 124, 1738–1752. doi:10.1029/2018JA025969

Moen, J., and Brekke, A. (1993). The solar flux influence on quiet time conductances in the auroral ionosphere. *Geophys. Res. Lett.* 20, 971–974. doi:10.1029/92GL02109

Morley, S. K., and Lockwood, M. (2006). A numerical model of the ionospheric signatures of time-varying magnetic reconnection: III. Quasi-Instantaneous convection responses in the cowley-lockwood paradigm. *Ann. Geophys.* 24, 961–972. doi:10.5194/angeo-24-961-2006

Motoba, T., Hosokawa, K., Ogawa, Y., Sato, N., Kadokura, A., Buchert, S. C., et al. (2011). *In situ* evidence for interplanetary magnetic field induced tail twisting associated with relative displacement of conjugate auroral features. *J. Geophys. Res.* 116. doi:10.1029/2010JA016206

Murphy, K. R., Watt, C. E. J., Mann, I. R., Jonathan Rae, I., Sibeck, D. G., Boyd, A. J., et al. (2018). The global statistical response of the outer radiation belt during geomagnetic storms. *Geophys. Res. Lett.* 45, 3783–3792. doi:10.1002/2017GL076674

Ohma, A., Østgaard, N., Laundal, K. M., Reistad, J. P., Hatch, S. M., and Tenfjord, P. (2021). Evolution of IMF B_y induced asymmetries: The role of tail reconnection. *J. Geophys. Res. Space Phys.* 126, e2021JA029577. doi:10.1029/2021JA029577

Oliveira, D. M. (2017). Magnetohydrodynamic shocks in the interplanetary space: A theoretical review. *Braz. J. Phys.* 47, 81–95. doi:10.1007/s13538-016-0472-x

Owen, C. J., Slavin, J. A., Richardson, I. G., Murphy, N., and Hynds, R. J. (1995). Average motion, structure and orientation of the distant magnetotail determined from remote sensing of the edge of the plasma sheet boundary layer with$E$> 35 keV ions 35 kev ions. *J. Geophys. Res.* 100, 185–204. doi:10.1029/94JA02417$\gtrbin $

Ozturk, D. S., Zou, S., Slavin, J. A., and Ridley, A. J. (2019). Response of the geospace system to the solar wind dynamic pressure decrease on 11 june 2017: Numerical models and observations. *J. Geophys. Res. Space Phys.* 124, 2613–2627. doi:10.1029/2018JA026315

Petrukovich, A. A. (2011). Origins of plasma sheet by. *J. Geophys. Res.* 116. doi:10.1029/2010JA016386

Pitkänen, T., Hamrin, M., Kullen, A., Maggiolo, R., Karlsson, T., Nilsson, H., et al. (2016). Response of magnetotail twisting to variations in IMF by : A themis case study 1-2 january 2009. *Geophys. Res. Lett.* 43, 7822–7830. doi:10.1002/2016GL070068

Rong, Z. J., Lui, A. T. Y., Wan, W. X., Yang, Y. Y., Shen, C., Petrukovich, A. A., et al. (2015). Time delay of interplanetary magnetic field penetration into earth's magnetotail. *J. Geophys. Res. Space Phys.* 120, 3406–3414. doi:10.1002/2014JA020452

Rong, Z., Shen, C., Petrukovich, A., Wan, W., and Liu, Z. (2010). The analytic properties of the flapping current sheets in the earth magnetotail. *Planet. Space Sci.* 58, 1215–1229. doi:10.1016/j.pss.2010.04.016

Sandhu, J. K., Rae, I. J., Freeman, M. P., Forsyth, C., Gkioulidou, M., Reeves, G. D., et al. (2018). Energization of the ring current by substorms. *JGR. Space Phys.* 123, 8131–8148. doi:10.1029/2018JA025766

Sergeev, V. A. (1987). Penetration of the by component of the IMF into the magnetotail. *Geomagnetism Aeronomy* 27, 612–615.

Sergeev, V., Runov, A., Baumjohann, W., Nakamura, R., Zhang, T. L., Volwerk, M., et al. (2003). Current sheet flapping motion and structure observed by cluster. *Geophys. Res. Lett.* 30, 1327. doi:10.1029/2002GL016500

Shore, R. M., Freeman, M. P., Coxon, J. C., Thomas, E. G., Gjerloev, J. W., and Olsen, N. (2019). Spatial variation in the responses of the surface external and induced magnetic field to the solar wind. *JGR. Space Phys.* 124, 6195–6211. doi:10.1029/2019JA026543

Siscoe, G. L., and Huang, T. S. (1985). Polar cap inflation and deflation. *J. Geophys. Res.* 90, 543–547. doi:10.1029/JA090iA01p00543

Snekvik, K., Østgaard, N., Tenfjord, P., Reistad, J. P., Laundal, K. M., Milan, S. E., et al. (2017). Dayside and nightside magnetic field responses at 780 km altitude to dayside reconnection. *J. Geophys. Res. Space Phys.* 122, 1670–1689. doi:10.1002/2016JA023177

Tenfjord, P., Østgaard, N., Haaland, S., Snekvik, K., Laundal, K. M., Reistad, J. P., et al. (2018). How the IMF by induces a local by component during northward IMF$B_z$and characteristic timescales. *J. Geophys. Res. Space Phys.* 123, 3333–3348. doi:10.1002/2018JA025186

Tenfjord, P., Østgaard, N., Snekvik, K., Laundal, K. M., Reistad, J. P., Haaland, S., et al. (2015). How the IMF by induces a by component in the closed magnetosphere and how it leads to asymmetric currents and convection patterns in the two hemispheres. *J. Geophys. Res. Space Phys.* 120, 9368–9384. doi:10.1002/2015JA021579

Tenfjord, P., Østgaard, N., Strangeway, R., Haaland, S., Snekvik, K., Laundal, K. M., et al. (2017). Magnetospheric response and reconfiguration times following IMF by reversals. *J. Geophys. Res. Space Phys.* 122, 417–431. doi:10.1002/2016JA023018

Tsyganenko, N. A., Andreeva, V. A., and Gordeev, E. I. (2015). Internally and externally induced deformations of the magnetospheric equatorial current as inferred from spacecraft data. *Ann. Geophys.* 33, 1–11. doi:10.5194/angeo-33-1-2015

Tsyganenko, N. A., and Fairfield, D. H. (2004). Global shape of the magnetotail current sheet as derived from geotail and polar data. *J. Geophys. Res.* 109, A03218. doi:10.1029/2003JA010062

Walach, M.-T., and Milan, S. E. (2015). Are steady magnetospheric convection events prolonged substorms? *J. Geophys. Res. Space Phys.* 120, 1751–1758. doi:10.1002/2014JA020631

Walach, M.-T., Milan, S. E., Murphy, K. R., Carter, J. A., Hubert, B. A., and Grocott, A. (2017). Comparative study of large-scale auroral signatures of substorms, steady magnetospheric convection events, and sawtooth events. *J. Geophys. Res. Space Phys.* 122, 6357–6373. doi:10.1002/2017JA023991

Walker, R., Richard, R., Ogino, T., and Ashour-Abdalla, M. (1999). The response of the magnetotail to changes in the imf orientation: The magnetotail's long memory. *Phys. Chem. Earth, Part C Sol. Terr. Planet. Sci.* 24, 221–227. doi:10.1016/S1464-1917(98)00032-4

Xiao, S., Zhang, T., Ge, Y., Wang, G., Baumjohann, W., and Nakamura, R. (2016). A statistical study on the shape and position of the magnetotail neutral sheet. *Ann. Geophys.* 34, 303–311. doi:10.5194/angeo-34-303-2016

Zhang, T. L., Baumjohann, W., Nakamura, R., Balogh, A., and Glassmeier, K.-H. (2002). A wavy twisted neutral sheet observed by cluster. *Geophys. Res. Lett.* 29, 5. doi:10.1029/2002GL015544

Zhang, Y. C., Dai, L., Rong, Z. J., Wang, C., Rème, H., Dandouras, I., et al. (2020). Observation of the large-amplitude and fast-damped plasma sheet flapping triggered by reconnection-induced ballooning instability. *J. Geophys. Res. Space Phys.* 125, e2020JA028218. doi:10.1029/2020JA028218

frontiers | Frontiers in Astronomy and Space Sciences

TYPE Original Research
PUBLISHED 15 September 2022
DOI 10.3389/fspas.2022.958977

OPEN ACCESS

EDITED BY
Larry Lyons,
University of California, Los Angeles, United States

REVIEWED BY
Desheng Han,
Tongji University, China
Anita Aikio,
University of Oulu, Finland

*CORRESPONDENCE
S. M. Hatch,
spencer.hatch@uib.no

SPECIALTY SECTION
This article was submitted to Space Physics, a section of the journal Frontiers in Astronomy and Space Sciences

RECEIVED 01 June 2022
ACCEPTED 22 August 2022
PUBLISHED 15 September 2022

CITATION
Hatch SM, Laundal KM and Reistad JP (2022), Testing the mirror symmetry of Birkeland and ionospheric currents with respect to magnetic latitude, dipole tilt angle, and IMF B_y.
Front. Astron. Space Sci. 9:958977.
doi: 10.3389/fspas.2022.958977

Testing the mirror symmetry of Birkeland and ionospheric currents with respect to magnetic latitude, dipole tilt angle, and IMF B_y

S. M. Hatch*, K. M. Laundal and J. P. Reistad

Birkeland Centre for Space Science, Department of Physics and Technology, University of Bergen, Bergen, Norway

It is often assumed that on average, polar ionospheric electrodynamics in the Northern and Southern Hemispheres are mirror symmetric or antisymmetric with respect to the interplanetary magnetic field B_y component and the dipole tilt angle ψ. For example, one might assume that the average Birkeland current density j at magnetic latitude λ is equal to the current density at magnetic latitude $-\lambda$ if the signs of B_y and ψ are reversed and all other parameters are equal: $j(\lambda, B_y, \psi, \dots) = j(-\lambda, -B_y, -\psi, \dots)$. This is a convenient assumption for empirical models, since it effectively doubles the amount of information that a measurement made in one hemisphere contains. In this study we use the Average Magnetic field and Polar current System (AMPS) model to quantify to what extent the assumption holds for Birkeland and ionospheric currents. The AMPS model is an empirical model based on Swarm and CHAMP magnetic field measurements, with no constraints on hemispheric symmetries, and with differences in main magnetic field geometry as well as biases in data point distributions in magnetic coordinates accounted for. We show that when averaged over IMF clock angle orientation, the total ionospheric divergence-free current in each hemisphere largely satisfies the mirror symmetry assumption. The same is true for the total Birkeland current in each hemisphere except during local winter, during which the Northern Hemisphere tends to dominate. We show that this local winter asymmetry is consistent with the average winter hemispheric asymmetry in total precipitating electron current derived from Fast Auroral SnapshoT (FAST) satellite observations. We attribute this and other more subtle deviations from symmetry to differences in sunlight distribution in magnetic coordinates, as well as magnetic field strength and its influence on ionospheric conductivity. Important departures from mirror symmetry also arise for some IMF clock angle orientations, particularly those for which IMF $B_z > 0$, as suggested by other recent studies.

KEYWORDS

ionosphere, magnetosphere, swarm, hemispheric asymmetry, hemispheric conjugacy, ionospheric currents, magnetosphere-ionosphere coupling, interplanetary magnetic field

1 Introduction

The large-scale polar ionospheric electrodynamics is on average largely mirror symmetric between hemispheres with respect to the interplanetary magnetic field (IMF) B_y component and the dipole tilt angle. This means that the average magnetic field perturbation (or equivalent current), plasma flow velocity (or equivalent electric field), or electric conductivity found in one hemisphere would be approximately equal to the corresponding quantity in the opposite hemisphere, on the same main magnetic field line, if the signs of the IMF B_y and the dipole tilt angle had been reversed. This property has been established through numerous climatological studies of plasma flows (e.g., Heppner and Maynard, 1987; Pettigrew et al., 2010; Förster and Haaland, 2015), magnetic fields (e.g., Mead and Fairfield, 1975), and magnetic field perturbations (e.g., Green et al., 2009; Laundal et al., 2016a; Smith et al., 2017). To our knowledge it has not been systematically addressed in climatological studies of auroras or particle precipitation, yet it has been surmised for decades (Gussenhoven et al., 1983; Hardy et al., 1985; Newell et al., 2009, 2010; Dombeck et al., 2018; Zhu et al., 2021). The nearest to directly addressing hemispheric asymmetries in particle precipitation is perhaps Newell and Meng (1988); Hatch et al. (2018) also address hemispheric asymmetries of precipitation associated with Alfvén waves.

The reasons for the symmetry properties of B_y and tilt are believed to be well understood. The dipole tilt angle describes the orientation of the Earth's magnetic dipole axis with respect to the Sun-Earth line, and it ranges from about − 30° to + 30°. The variation in tilt angle is thought to have two primary effects: a change in the solar wind-magnetosphere coupling, and a change in ionospheric conductivity due to differences in insolation. The former effect is due to a change in the geometry of the coupling between the solar wind and magnetosphere, and includes a change in the prevalence of lobe reconnection (Crooker and Rich, 1993; Reistad et al., 2019). These variations are presumably almost perfectly mirror symmetrical between hemispheres, since the Earth's magnetic field in the outer magnetosphere is symmetric between hemispheres. Some have also suggested that the change in geometry influences the subsolar reconnection location and efficiency (e.g., Russell et al., 2003), although this point is contested (Lockwood et al., 2020). The other dipole tilt angle effect—variable ionospheric conductivity due to variations in insolation—alters magnetosphere-ionosphere interactions, with distinct consequences for current patterns (Laundal et al., 2016b,a; Green et al., 2009; Laundal et al., 2018).

The asymmetries associated with the IMF B_y component are likewise ultimately an effect of different reconnection geometries and configurations on the dayside of the magnetosphere. When B_y is positive, newly opened magnetic flux experiences a force towards dawn in the Northern Hemisphere, creating dawnward plasma flow on the dayside in the polar ionosphere. In the Southern Hemisphere the force is toward dusk and the plasma flow is duskward. When B_y is negative, the senses of these forces and flows in the two hemispheres reverse. These effects collectively give rise to a pattern of magnetic perturbations (and corresponding currents via $\nabla \times \mathbf{B} = \mu_0 \mathbf{J}$) known as the Svalgaard-Mansurov effect (Jørgensen et al., 1972). The lateral motion of newly opened flux creates an asymmetric pressure distribution in the magnetotail lobes, which induces a slight asymmetry in the magnetic field mapping to the high latitudes. This asymmetry manifests as an apparent longitudinal shift between hemispheres of conjugate field lines compared to their nominal configuration (Tenfjord et al., 2015). The asymmetry reverses when B_y changes sign; that is, it exhibits mirror symmetry.

From the standpoint of modeling and statistical studies, the utility of assuming hemispheric mirror symmetry/anti-symmetry is that it effectively doubles the amount of information that a measurement provides. This assumption is therefore useful in dealing with data sets where the number of measurements made in one hemisphere (almost invariably the Southern) are deemed too few for a statistical study, or when measurements made by sun-synchronous satellites (e.g., the Defense Meteorological Satellite Program, or DMSP, satellites), whose orbits cover only a portion of the high-latitude ionosphere in magnetic latitude-magnetic local time (MLat-MLT) coordinates in each hemisphere. In such cases, the only alternative to assuming mirror symmetry is to ignore one hemisphere (Weimer, 2013; Waters et al., 2015; Billett et al., 2018; Thomas and Shepherd, 2018).

Thus the assumption of mirror symmetry has often been what enables a comparison of the two hemispheres to be carried out or an empirical model to be created. Studies and models falling into this category address a broad range of topics, including the ionospheric electric potential (Papitashvili et al., 1994; Weimer, 2005; Zhu et al., 2021), conductance (McGranaghan et al., 2015), field-aligned currents (Weimer, 2001), frictional heating and Poynting flux (Weimer and Edwards, 2021), auroral precipitation (Hardy et al., 1985; Newell et al., 2009, 2010; McGranaghan et al., 2021; Zhu et al., 2021) and even auroral boundaries (Gussenhoven et al., 1983). Other examples include models of the magnetospheric magnetic field, which make use of mirror symmetry with respect

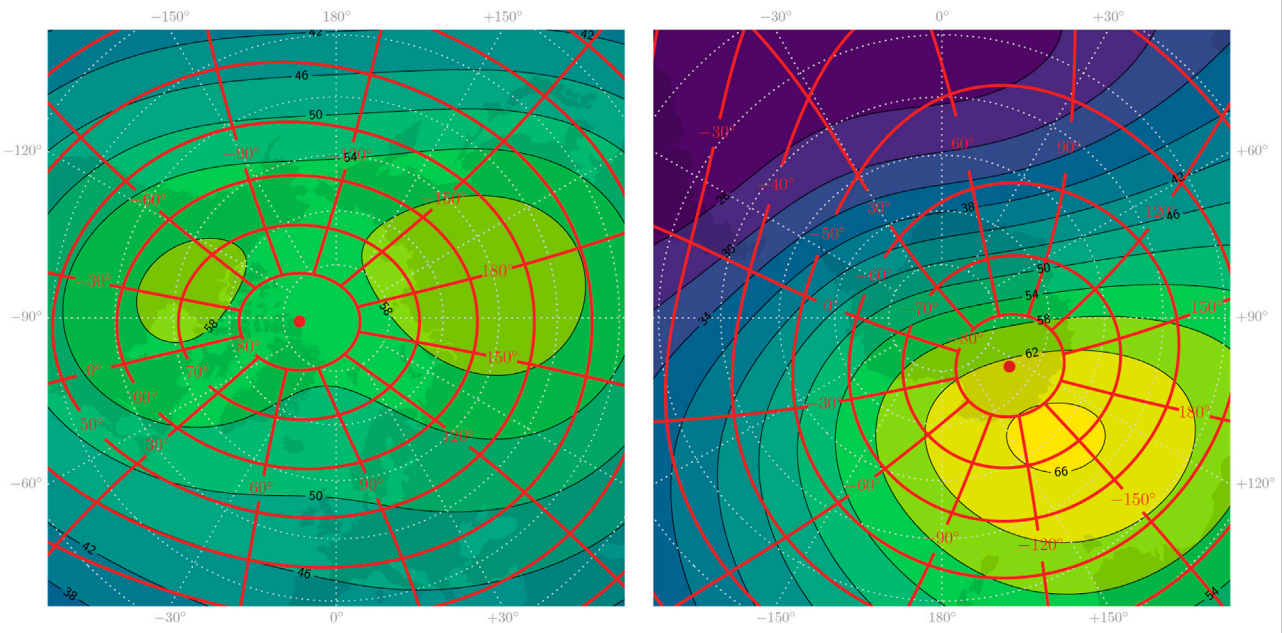

FIGURE 1
Illustration of the differences in Earth's magnetic field in the north (left) and south (right). The colored contours show the IGRF main field magnitude at epoch=2015.0 with contour levels labeled in μT. The red curves represent magnetic apex coordinate grids. Both plots are stereographic projections of an equally large area, centered at the geographic poles. Geographic longitudes are indicated at the edges.

to dipole tilt angle (Mead and Fairfield, 1975; Andreeva and Tsyganenko, 2016).

There are a number of reasons to believe that the mirror symmetry suggested by the effects mentioned above is in fact not exact, first among which are that its inexactness is experimentally established. For example, Pettigrew et al. (2010) report that the cross-polar cap potential is on average several percent larger in the Southern Hemisphere. On the basis of the Iridium® satellites and the Swarm satellites, respectively, Green et al. (2009) and Workayehu et al. (2020) report a hemispheric asymmetry in ratios of total currents flowing into each hemisphere for different seasons and reported that Southern Hemisphere currents are overall weaker. A number of studies have shown (Knipp et al., 2021; Pakhotin et al., 2021; Cosgrove et al., 2022) or suggested (Hatch et al., 2018) that deposition of magnetosphere-origin Poynting flux into the ionosphere is greatest in the Northern Hemisphere. Furthermore, although investigations of the magnetic field near the equatorial plane in the magnetosphere show a large degree of mirror symmetry with respect to IMF By and dipole tilt, there are certainly non-symmetric features present as well (e.g., Cowley and Hughes, 1983; Petrukovich, 2011; Tenfjord et al., 2017). (Additionally, away from the equatorial plane very little investigation of IMF By and dipole tilt dependence has been conducted.)

Beyond this direct experimental evidence, many of the parameters that govern magnetosphere-ionosphere-atmosphere interactions exhibit hemispheric asymmetry. These include hemispheric asymmetries (in coordinate systems organized by Earth's magnetic field) in magnetic field intensity and inclination (Thébault et al., 2015; Laundal et al., 2017), insolation (e.g., Laundal et al., 2017; Hatch et al., 2020), neutral winds (Dhadly et al., 2019), thermospheric composition and temperature (Barlier et al., 1974; Mayr and Trinks, 1977; Qin et al., 2008), and ionospheric densities and temperatures (e.g., Laundal et al., 2019; Hatch et al., 2020; Pignalberi et al., 2021). All of these parameters have some influence on magnetosphere-ionosphere-atmosphere interactions. In terms of quasi-static ionospheric electrodynamics (see, e.g., Richmond, 1995a; Vasyliunas, 2012), their influence is chiefly manifest through the dependence of Pedersen and Hall conductivities in the ionospheric Ohm's law on them, and through the variation of the frame of reference in which this law is typically expressed, which is that of the height-dependent neutral wind (e.g., Strangeway, 2012).

On point of hemispheric differences in insolation, Figure 1 shows quasi-dipole (QD) coordinate (Richmond, 1995a) grids in geographic coordinates in the two hemispheres, and contour plots of magnetic field strength, using the International Geomagnetic Reference Field (IGRF) model (Thébault et al., 2015). Insolation is symmetric with respect to Earth's geographic poles; thus the displacement of the geomagnetic poles as well as the distortion of lines of magnetic latitude and longitude with respect to geographic latitudes clearly indicates that insolation of the magnetic high-latitude regions is asymmetric.

Last, in addition to these parameters that explicitly appear in the governing equations of ionospheric electrodynamics, the possible influence of non-local (with respect to the ionosphere) and kinetic parameters that exhibit hemispheric asymmetries, including magnetospheric plasma density (Haaland et al., 2017), exospheric neutral composition (Keating et al., 1973), and mesosphere/lower-thermosphere dynamics as well as cloud microphysics (Xie et al., 2021), is unknown. In particular, there are significant hemispheric differences in the tidal behavior of mesospheric and lower thermospheric winds (Avery et al., 1989; Vincent, 2015); to our knowledge, how these differences might affect ionospheric dynamics has not been explored.

In this paper, we use a recent empirical model to quantify how much the ionospheric current system in the two hemispheres diverges from mirror symmetry. This model was designed to account for differences in the structure of the earth's magnetic field and for differences in spacecraft sampling. In Section 2 we describe the model. In Section 3 we examine how well the mirror symmetry assumption $j(\lambda, B_y, \psi, \dots) = j(-\lambda, -B_y, -\psi, \dots)$ holds for ionospheric and Birkeland current densities by examining model current densities and integrated currents in each hemisphere, and present a comparison of our results with those of the Iridium®-based Coxon et al. (2016) study. In Section 4 we discuss these results and some additional sources of uncertainty, including the possible variation of ionospheric currents with magnetic longitude, and conclude.

2 Methodology

The tool that we use to test hemispheric mirror symmetry is the Average Magnetic Field and Current System (AMPS) model. This is an empirical model of the three-dimensional current system, presented by Laundal et al. (2018), based on ionospheric magnetic field measurements from the CHAMP and Swarm satellites. The ionospheric perturbation magnetic field is obtained by subtracting the CHAOS model field (Finlay et al., 2020), which models internal and magnetospheric fields, from spacecraft measurements. The ionospheric magnetic perturbation field is represented as a sum of poloidal and toroidal fields, which are in turn represented as functions of scalar potentials expanded in a series of spherical harmonics. See Laundal et al. (2016a) for a full discussion of this technique.

The AMPS model coefficients depend explicitly on IMF clock angle $\theta_c = \arctan 2(B_y, B_z)$, the Newell et al. (2007) coupling function for the rate at which magnetopause flux is opened on the dayside

$$\epsilon = 10^{-3}|v_x|^{4/3} B_T^{2/3} \sin^{8/3}(\theta_c/2) \quad (1)$$

and the related quantity $\tau = \epsilon \cot^{8/3}(\theta_c/2)$, dipole tilt angle ψ, and the $F_{10.7}$ index. Vector components in all of these expressions are in geocentric solar magnetospheric (GSM) coordinates, and the transverse IMF component $B_T = \sqrt{B_y^2 + B_z^2}$. The inputs to the AMPS model that the user is required to provide are therefore the x component of solar wind speed v_x, the y and z components of the IMF B_y and B_z, dipole tilt angle ψ, and the $F_{10.7}$ index.

In this paper we use the publicly available Python implementation of the AMPS model, pyAMPS (Laundal and Toresen, 2018), to calculate associated horizontal and field-aligned current densities, projected on a sphere at 110 km altitude. The most recent update includes Swarm magnetic field measurements through 5 February 2021.

The AMPS model is well suited to test hemispheric symmetries because 1) no constraints on hemispheric symmetry were applied in the derivation of the model, and 2) geometric distortions associated with the Earth's main field were taken into account by use of magnetic apex coordinates (Richmond, 1995b).

3 Results

In this section we present AMPS model current densities from the Northern Hemisphere together with Southern Hemisphere current densities for which the signs of the dipole tilt angle and IMF B_y component have been reversed.

3.1 Birkeland currents

Figures 2–4 show Birkeland currents for negative, zero, and positive dipole tilt angles (respectively winter, equinox, and summer in the Northern Hemisphere), with a transverse IMF component B_T = 4 nT, and solar wind speed v_x = −350 km/s. The current densities in the Northern Hemisphere are shown with filled contours, with magnitudes indicated by the color scale at the bottom of the figure. The current densities in the Southern Hemisphere are shown with black contours, solid for positive (upward) values and dashed for negative. The steps between each contour represents a change of 0.05μA/m^2, the same as for the colored contours. The eight subplots in each figure represent different IMF orientations, indicated by the clock angle diagram in the center. Again, the sign of B_y is reversed for the Southern Hemisphere, so that the left column represents negative B_y for the Northern Hemisphere but positive B_y for the Southern Hemisphere.

Figures 2–4 all show that the current density contours are closely aligned in the two hemispheres. This shows that for the Birkeland current density, $j(\lambda, B_y, \psi, \dots) = j(-\lambda, -B_y, -\psi, \dots)$ is a good approximation for B_T = 4 nT and solar wind speed v_x = −350 km/s. The most promwinent deviation from symmetry is seen during local winter (Figure 2), where current densities are stronger in the Northern Hemisphere than in the Southern Hemisphere for all IMF orientations. On average the integrated total Birkeland current $J = |J_\uparrow| + |J_\downarrow|$ is 18% stronger in the north.

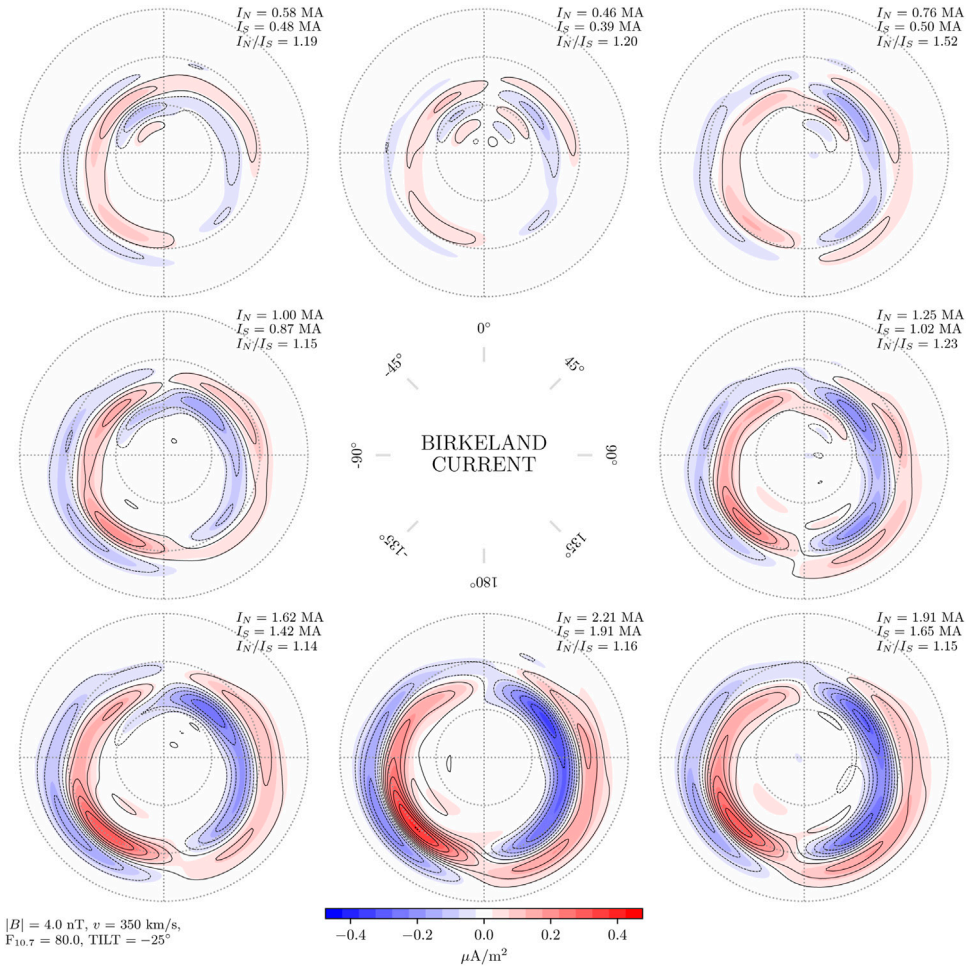

FIGURE 2
Amplitude of Birkeland currents in the Northern Hemisphere (colored contours) and Southern Hemisphere (black contour lines) as a function of IMF clock angle for dipole tilt angle $\psi = -25^{\circ}$, where the signs of B_y and ψ are reversed for the Southern Hemisphere. The spacing between both contours and contour lines is 0.05μA/m^2. In this figure, the mean hemispherically integrated current (top right corner of each panel) in the Northern Hemisphere is 18% stronger than in the Southern Hemisphere.

Examination of the difference of the northern and southern contours for each IMF orientation during local winter (not shown) indicates that the imbalance is primarily on the nightside, where northern Birkeland current densities are stronger. Regarding the other dipole orientations, local summer and equinox, the differences of current densities in the two hemispheres (not shown) appear to be mostly controlled by the orientation of IMF B_y. For example, under positive IMF B_y in the north (negative in the south) the largest hemispheric differences in Birkeland currents are on the dawnside, while for negative IMF B_y in the north (positive in the south) the largest differences are on the duskside.

As described above, Figures 2–4 correspond to a particular set of solar wind and IMF conditions ($B_T = 4$ nT and $v_x = -350$ km/s). Two general questions therefore arise: 1) How does the hemispheric difference in total Birkeland current vary with solar wind and IMF conditions? 2) How does the symmetry between the distributions of Birkeland current densities in each hemisphere vary with solar wind and IMF conditions?

To answer the first question, the top row of Figure 5 shows the north/south ratio of integrated total Birkeland current for dipole tilt angles -25°, 0°, and 25° (panels from left to right), as a function of IMF clock angle θ_c and the product $B_T^{2/3}|v_x|^{4/3}$ that appears in Eq. 1. As with Figures 2–4, the sign of B_y and ψ is reversed for the Southern Hemisphere. The overall trend with IMF clock angle θ_c in these panels is that the integrated total Birkeland current in the Southern Hemisphere tends to be greatest for $\theta_c \in [-180°, 0°]$ (i.e., $B_y < 0$ and weakest for $\theta_c \in [0°, 180°]$ (i.e., $B_y > 0$), and vice versa

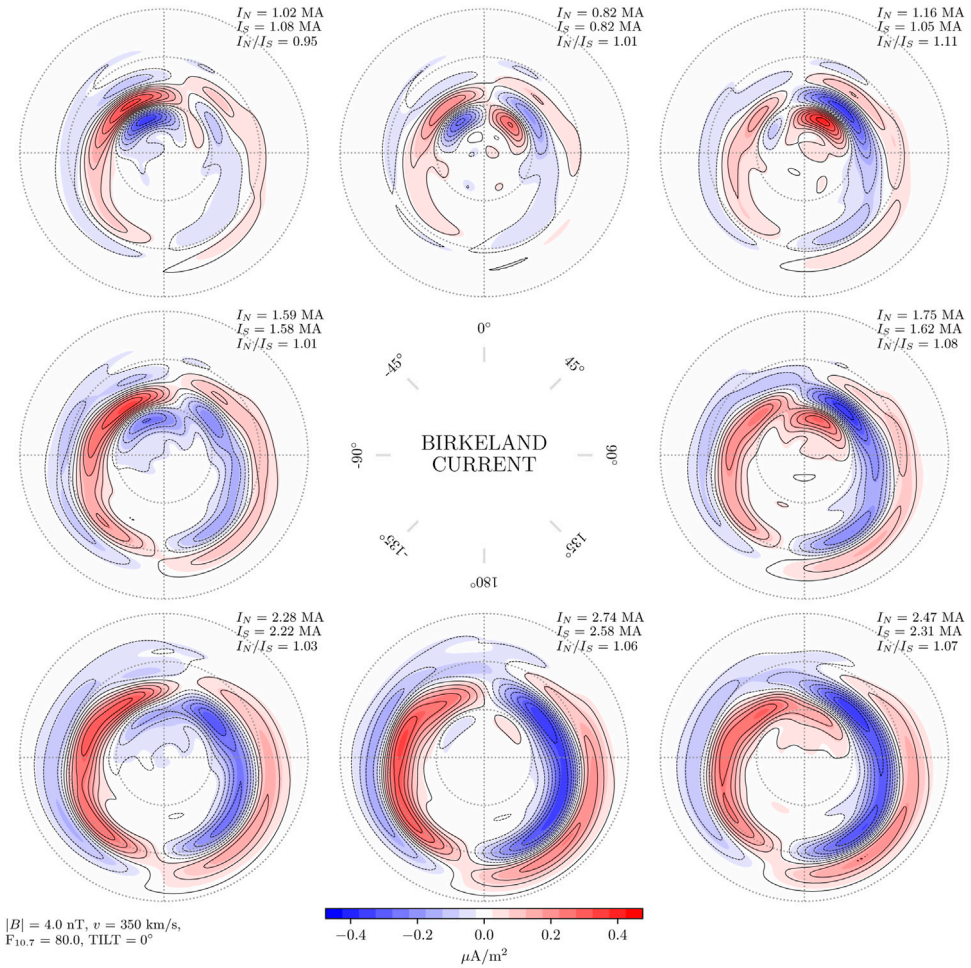

FIGURE 3
Amplitude of Birkeland currents in the Northern Hemisphere (colored contours) and Southern Hemisphere (black contour lines) for dipole tilt angle $\psi = 0^{\circ}$, in the same layout as Figure 2. In this figure the mean hemispherically integrated current in the Northern Hemisphere is 4% stronger than in the Southern Hemisphere.

for the Northern Hemisphere. The left panel additionally indicates that during local winter the integrated total Birkeland current in the Northern Hemisphere is, under virtually every condition at least as great as that in the Southern Hemisphere. The ratio of the two maximizes for $\theta_c \in [0^{\circ}, 90^{\circ}]$ (i.e., $B_z > 0$ and $B_y > 0$).

To answer the second question, we use the Bhattacharyya coefficient *BC* to measure the degree of similarity between pairs of Birkeland current distributions in each hemisphere. This coefficient is a measure of the degree of similarity of two probability distributions. It varies from 0, corresponding to distributions with no overlap, to 1, corresponding to distributions that are identical. The definition of *BC*, as well as our method for calculating it for a given set of northern and southern Birkeland current distributions, is described in the Appendix A.

The bottom row of Figure 5 shows *BC* in the same layout as the top row. In general *BC* is high (> 0.85), indicating an overall high degree of similarity between the northern and southern Birkeland current distributions. There is also a tendency for *BC* to be lower for $B_z > 0$ nT ($\theta_c \in (-90^{\circ}, 90^{\circ})$) and higher for $B_z < 0$ nT. Regarding dipole tilt dependence, the Birkeland current distributions in each hemisphere tend to be least similar for $\psi = -25^{\circ}$, although it should be noted that even for $\psi = -25^{\circ}$ the mean value of *BC* is 0.95.

3.2 Divergence-free equivalent currents

Figures 6–8 show contours that represent the divergence-free current function. The divergence-free current in the AMPS

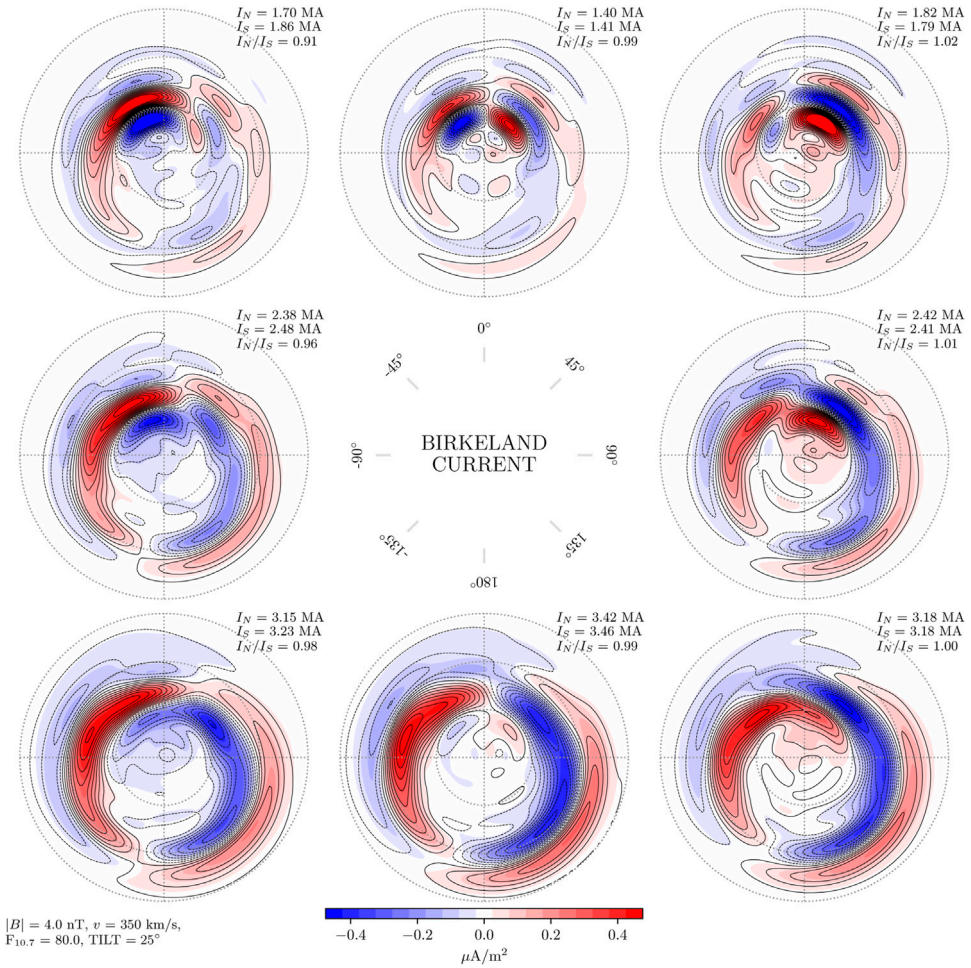

FIGURE 4
Amplitude of Birkeland currents in the Northern Hemisphere (colored contours) and Southern Hemisphere (black contour lines) for dipole tilt angle $\psi = 25^{\circ}$, in the same layout as Figure 2. In this figure, the mean hemispherically integrated current in the Northern Hemisphere is 2% weaker than in the Southern Hemisphere.

model is estimated with magnetic field measurements made from low Earth orbit, but it is similar to the equivalent current that can be estimated from ground magnetometers. A fixed amount of (divergence-free) current, 10 kA, flows between the contours, so that the current density is proportional to the gradient of the current function. The current direction is rotated 90° clockwise to the gradient, and the gradient is positive in the direction from dashed to solid contours.

There are only very subtle differences between the current contours from the two hemispheres in all panels of Figures 6–8. In these three figures the largest mean difference in total current, the current that flows between maximum and minimum of the current function, is only 2%. We conclude that for the average divergence-free current, $j(\lambda, B_y, \psi, \ldots) = j(-\lambda, -B_y, -\psi, \ldots)$ is a good approximation. At the same time it is clear that for individual IMF orientations the difference can be large (e.g., top-left and top-right panels of Figure 6 corresponding to ($B_z > 0$, $B_y < 0$) and ($B_z > 0$, $B_y > 0$), where total current in the two hemispheres differs by factors of 1.19 and 1.14).

Figure 9 summarizes both the variation of the hemispheric difference in total divergence-free current (top row) and the Bhattacharyya coefficients (i.e., overall degree of symmetry) for northern and southern distributions of divergence-free currents (bottom row), in the same layout as Figure 5.

The north-south ratio of total divergence-free current values in each hemisphere (top row of Figure 9) shows a trend similar to that seen for the integrated total Birkeland currents (top row of Figure 5), namely that the southern equivalent current tends to be greatest for $B_y < 0$, and the northern equivalent current tends to be greatest for $B_y > 0$. These general trends are not observed for $\psi = -25^{\circ}$.

Comparing the Bhattacharyya coefficients for the divergence-free current functions in each hemisphere (bottom

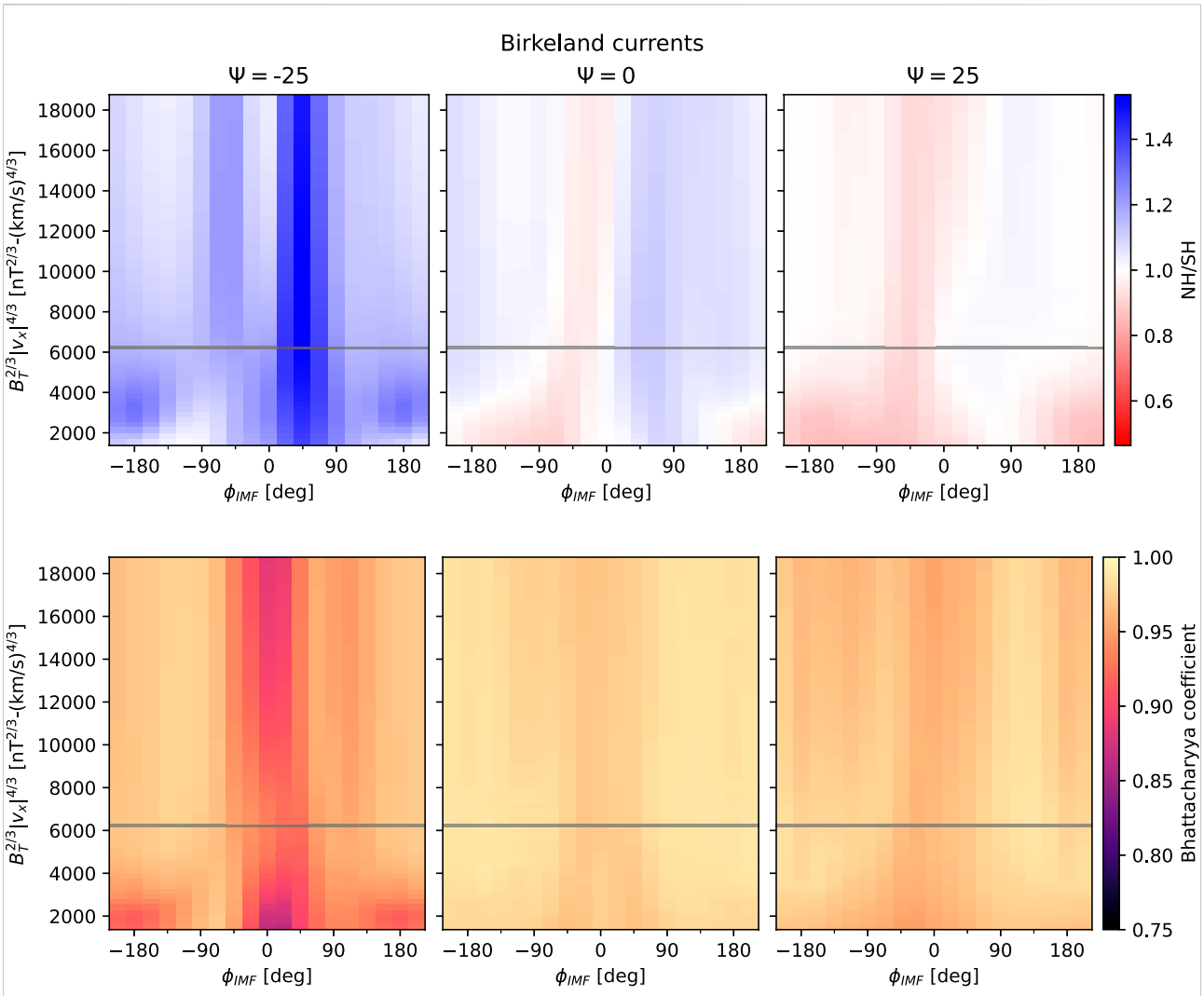

FIGURE 5
Northern and southern total Birkeland current ratio (top row) and Bhattacharyya coefficient (bottom row) as a function of IMF clock angle θ_c and $|v_x|^{4/3}B_T^{2/3}$ (x and y axis, respectively) for dipole tilt angles − 25°, 0°, and 25° (panels from left to right). The sign of B_y (and therefore also θ_c) as well as ψ are reversed for the Southern Hemisphere. The horizontal black line corresponds to the values B_T = 4 nT and v_x = −350 km/s used in Figures 2–4. For fixed v_x = 400 km/s, the minimum and maximum values on the y axis correspond to B_T = 0.375 nT and B_T = 16 nT.

row) with those of the Birkeland current distributions (bottom row of Figure 5) indicates that the degree of similarity of the diverge-free current functions is overall lower than that of the Birkeland current distributions, and is generally lowest for dipole tilt $\psi = -25^{\circ}$. Even so, the minimum and mean values of BC for $\psi = -25^{\circ}$ (0.73 and 0.95) are still relatively high.

3.3 Comparison with Coxon et al. (2016)

The high degree of symmetry found in Figures 2–4 appears to contradict the results of Coxon et al. (2016), who report significantly stronger currents in the Northern Hemisphere than in the Southern, based on the Active Magnetosphere and Planetary Electrodynamics Response Experiment (AMPERE) (Anderson et al., 2000; Waters et al., 2001). AMPERE uses platform magnetometers onboard the fleet of Iridium® satellites to provide estimates of Birkeland currents in both hemispheres in 10-min windows every 2 min. In this section we use an extended AMPERE data set together with the methodology presented by Coxon et al. (2016) for quantifying the overall hemispheric difference in integrated Birkeland current intensity, and compare with corresponding estimates using the AMPS model. Our goal is to determine whether Birkeland currents as represented by the AMPS model evince a clear preference for the Northern Hemisphere, similar to that observed with the AMPERE data set.

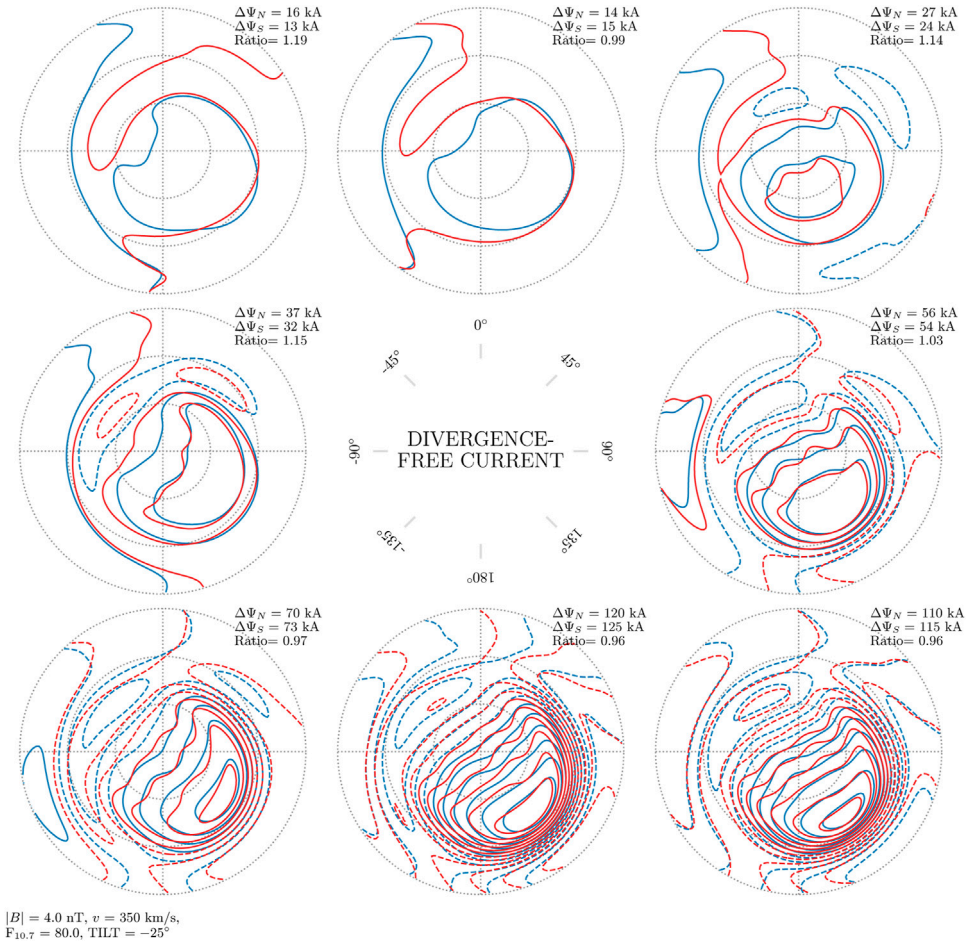

FIGURE 6
Divergence-free current function in the Northern and Southern Hemisphere (blue and red contours, respectively), as a function of IMF clock angle for dipole tilt angle $\psi = -25°$, where the signs of B_y and ψ are reversed for the Southern Hemisphere. The spacing between contours is 10 kA. In this figure, the mean of the total currents in the Northern Hemisphere differs from the mean total current in the Southern Hemisphere by less than 1%.

Coxon et al. (2016) used Iridium®-based estimates of the Birkeland currents to calculate the total current into and out of each hemisphere, and then calculated 27-day (one Bartels rotation) averages for a period of 6 years (2010–2015). To examine the difference in current throughput through each hemisphere, they posited that the Birkeland currents roughly follow a kind of global Ohm's law,

$$J = \Xi \Phi_D, \tag{2}$$

where $J = |J_\uparrow| + |J_\downarrow|$ is the total Birkeland current,

$$\Xi(t) = c_1 + c_2 \sin(t) \tag{3}$$

is a function that plays the role of conductance with $t = 2\pi(d - 79)/365.25$, and d the number of days since 1 January 2010. The coefficients c_1 and c_2 are intended to represent the "background conductance" and "the variation in conductance due to seasonal effects." The Milan et al. (2012) coupling function

$$\Phi_D = \frac{3.8 R_E}{(4 \times 10^5 \mathrm{m/s})^{1/3}} |v_x|^{4/3} B_T \sin^{9/2}(\theta_c/2), \tag{4}$$

estimates the total dayside reconnection rate and has units of kV, or equivalently kWb/s (magnetic flux per time). In this expression the transverse IMF component B_T is given in T and v_x in km/s, and R_E is the radius of Earth in km. Coxon et al. (2016) justify their use of Eq. 2 by pointing to the study of Coxon et al. (2014), who find that J and Φ_D are highly correlated, and observing that the factor relating J and Φ_D (Ξ) has units of conductance.

Following Coxon et al. (2016), we seek to obtain the best-fit values of c_1 and c_2 in Eq. 3 for both the AMPERE and AMPS hemispheric total currents in Figure 10A. To calculate the hemispherically integrated total Birkeland current from the AMPS model in each hemisphere, we first smooth the relevant solar wind and IMF parameters (solar wind speed v_x

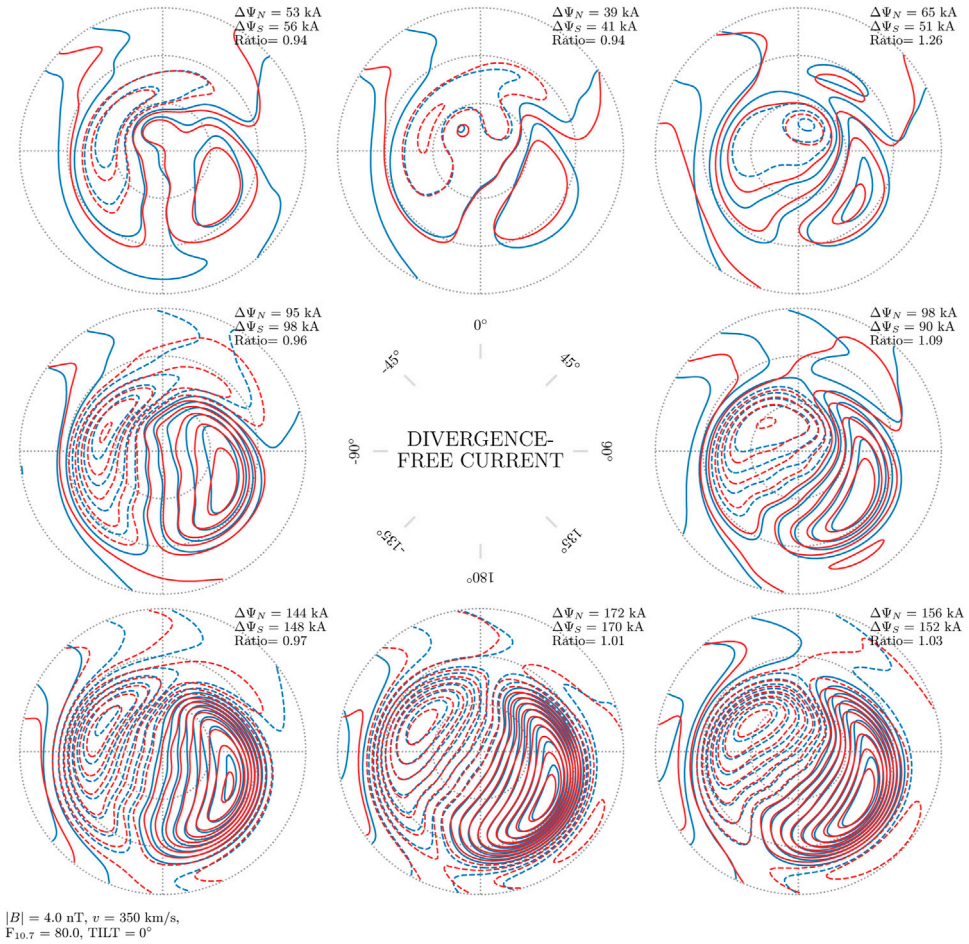

FIGURE 7
Divergence-free current function in the Northern and Southern Hemisphere as a function of IMF clock angle for dipole tilt angle $\psi = 0^{\circ}$, in the same format as Figure 6. In this figure, the mean of the total currents in the Northern Hemisphere is 2% stronger than the mean total current in the Southern Hemisphere.

and IMF B_y and B_z) from the OMNI database (King and Papitashvili, 2005) with a 20-min rolling window and calculate the 27-days average of the F10.7 index, and use these averaged parameters together with dipole tilt as input to AMPS. We then calculate the model Birkeland current for all MLats $\geq 60°$ on an equally-spaced grid, multiply each model current by the area of the corresponding grid cell, and sum the absolute value of the integrated upward or downward current in each bin to obtain the hemispherically integrated total Birkeland current. We also calculate the hemispherically integrated total Birkeland current for all available AMPERE data, from 2010 to 2017, inclusive, and neglect any AMPERE current value with an absolute value of less than 0.2 μAm^{-2} following Coxon et al. (2016) and Clausen et al. (2012).

We then perform a fit to the expression $\Xi(t) = J/\Phi_D$ using J and Φ_D from panels A and B, respectively, in Figure 10, which yields the fit values for c_1 and c_2 shown in Table 1. Coxon et al. (2016) found that $c_{1,N}/c_{1,S}$ = 202.6/154.4 ≈ 1.3, and $c_{2,N}/c_{2,S}$ = 54.0/ −50.6 ≈ −1.1. The ratio of their c_1 coefficients indicates that the baseline of the conductance-like function Σ is greater by ~30% in the Northern Hemisphere, while their ratio of c_2 coefficients indicates 1) slightly greater seasonal variation of Σ in the Northern Hemisphere, and 2) an unsurprising phase difference of approximately half a year in hemispheric variations.

For the slightly extended AMPERE data set that we have used, Table 1 shows that $c_{1,N}/c_{1,S}$ = 174.7/133.4 ≈ 1.3 and $c_{2,N}/c_{2,S}$ = 55.1/ −16 ≈ −3.4. In other words, our extended AMPERE data yields a result very similar to that of Coxon et al. (2016) for the baseline c_1 coefficients. On the other hand we find a substantially weaker seasonal variation (represented by c_2 coefficients) for the Southern Hemisphere.

Turning to AMPS data, $c_{1,N}/c_{1,S}$ = 160/146 ≈ 1.1 and $c_{2,N}/c_{2,S}$ = 56.3/ −29.5 ≈ −1.9. Thus we also find a baseline "global conductance" that is greater in the Northern Hemisphere,

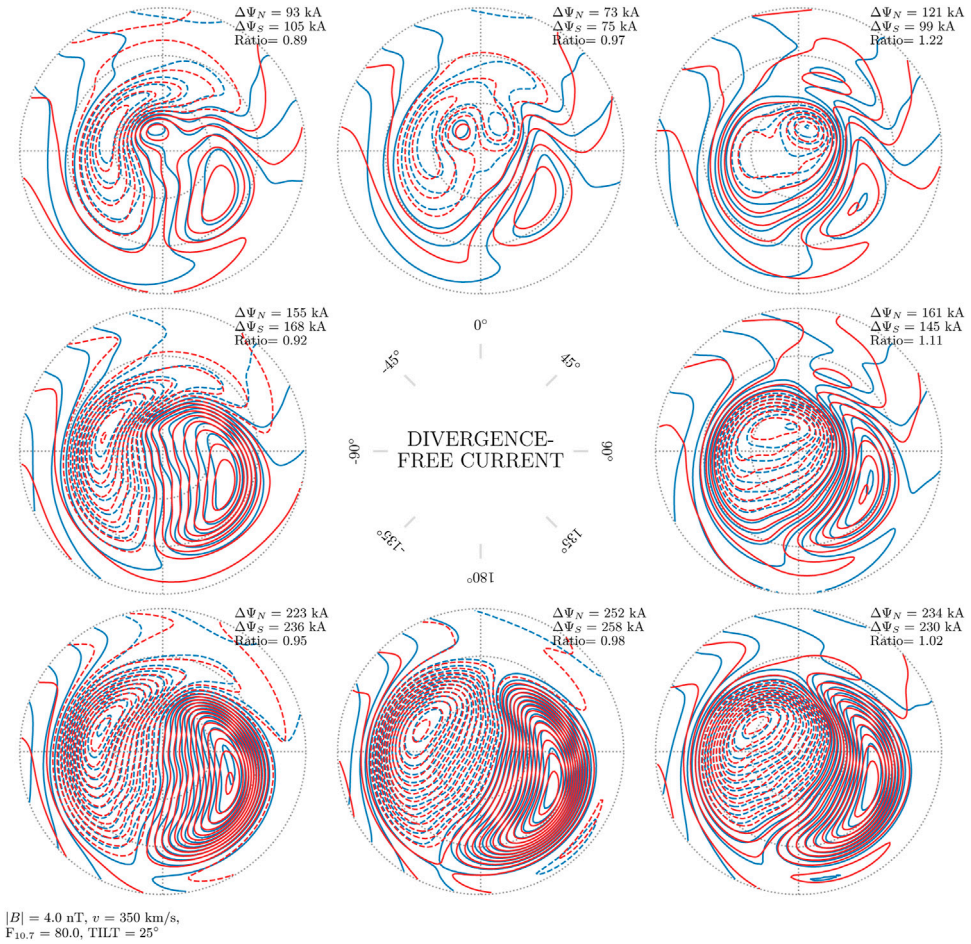

FIGURE 8
Divergence-free current function in the Northern and Southern Hemisphere as a function of IMF clock angle for dipole tilt angle $\psi = 25^{\circ}$, in the same format as Figure 6. In this figure, the mean of the total currents in the Northern Hemisphere differs from the mean total current in the Southern Hemisphere by less than 1%.

although the difference is only 10% instead of 30%. We also find that the seasonal variation is nearly twice as great in the Southern Hemisphere, relative to the extended AMPERE-based c_2 coefficient.

Apart from this fit-based comparison, Figure 10C shows the difference in hemispheric currents in Figure 10A for AMPERE (thick gray line) and the AMPS model (thin black line). Throughout the time series the AMPERE-derived hemispheric current difference tends to have higher peaks than troughs, indicating that according to AMPERE data the Northern Hemisphere total current is greater than that in the Southern. The AMPS-derived hemispheric current difference is generally more centered around zero. To be specific, the averages of the AMPERE and AMPS $J_N - J_S$ time series in Figure 10C are respectively 0.56 and 0.13 MA. The offset of this time series in favor of the Northern Hemisphere as shown in Figure 2 of Coxon et al. (2016) is even more extreme, with the peak and trough typically greater than 2 MA and less than -1 MA, respectively.

4 Discussion

The main conclusions from the preceding analysis of hemispheric differences in Birkeland and divergence-free currents are the following.

1. For both Birkeland and divergence-free horizontal currents, the total currents more or less exhibit mirror symmetry during local equinox and local summer ($\Psi = 0^{\circ}$ and $\Psi = 25^{\circ}$ in the NH, respectively) when averaged over IMF clock angle orientation. During local winter ($\Psi = -25^{\circ}$ in the NH) the two types of currents display different behaviors: For the Birkeland currents, NH total current tends to dominate regardless of IMF clock angle orientation; for the divergence-free currents, NH total current tends to dominate for $B_z > 0$ and $B_T^{2/3}|v_x|^{4/3} \lesssim 4000$ nT$^{2/3}$km/s$^{4/3}$, while SH total current tends to dominate for $B_z < 0$ and $B_T^{2/3}|v_x|^{4/3} \gtrsim 4000$ nT$^{2/3}$km/s$^{4/3}$.

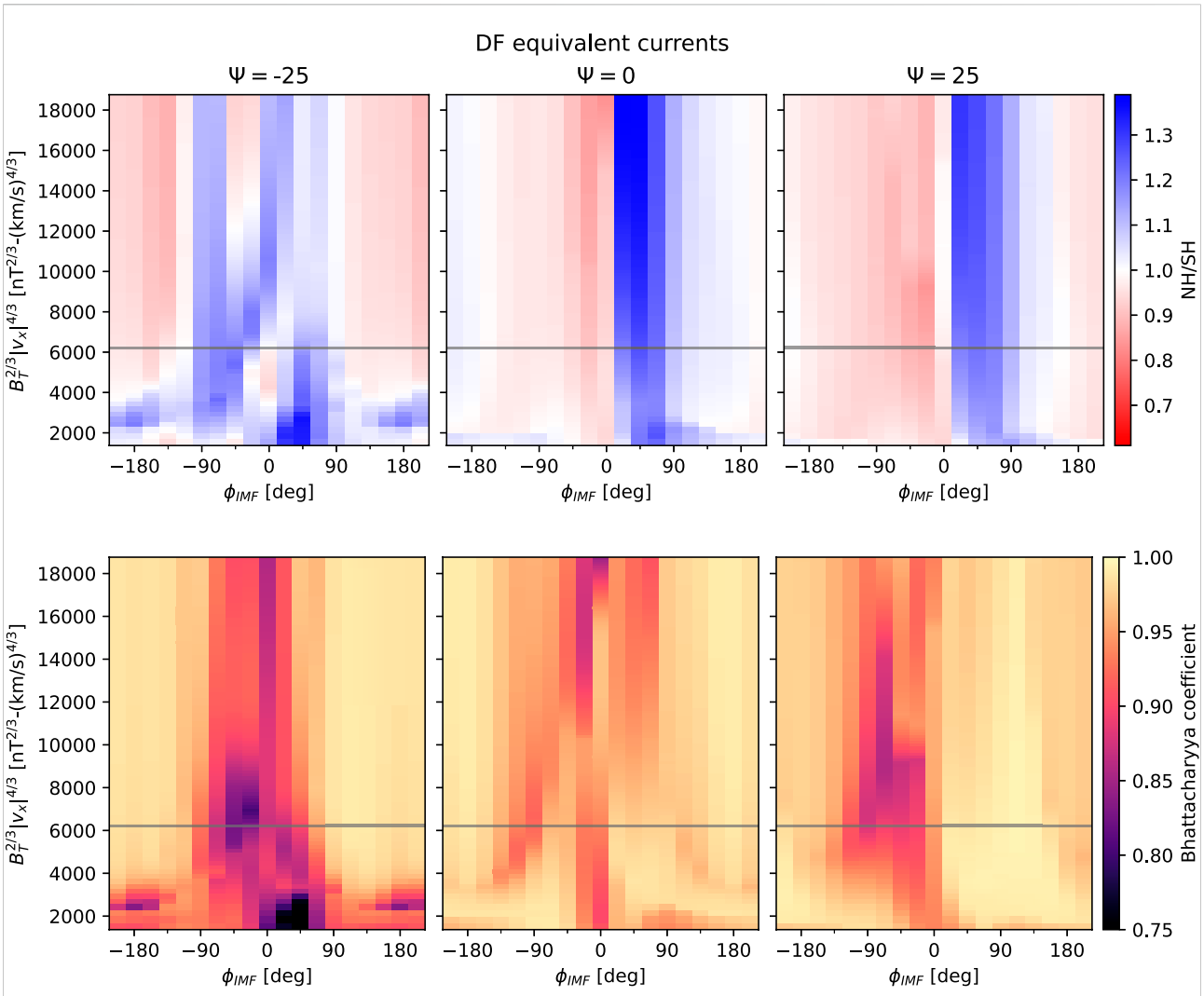

FIGURE 9
Northern and southern total divergence-free current ratio (top row) and Bhattacharyya coefficient of divergence-free current distributions (bottom row) in the same layout as Figure 5.

2. The NH/SH ratio of total Birkeland current exhibits a slight overall dependence on dipole tilt, whereby the NH dominates during local winter (average NH/SH ratio of 1.17 for all values shown in the top left panel of Figure 5), as previously mentioned, and the SH exhibits very slight dominance over the NH during local summer average NH/SH ratio of 0.98 for all values shown in the top right panel of Figure 5).

3. With respect to dependence on IMF orientation, both Birkeland and divergence-free currents display a higher degree of mirror symmetry for $B_z < 0$ than for $B_z > 0$ (Figures 5, 9), regardless of the orientation of B_y. On the other hand, for $B_z > 0$, NH total current tends to be favored for $B_y > 0$ in the NH and $B_y < 0$ in the SH, while SH total current tends to be favored for $B_y < 0$ in the NH and $B_y > 0$ in the SH.

Regarding the overall higher degree of symmetry exhibited by total Birkeland and divergence-free currents in each hemisphere for $B_z < 0$ relative to $B_z > 0$, Workayehu et al. (2021) draw essentially the same conclusion using Swarm satellite measurements, but a rather different methodology based on spherical elementary currents. Regarding the overall variation of the NH/SH ratio of total Birkeland current with season, Workayehu et al. (2020) also find that NH total Birkeland current is greater by about 20% during local winter. Workayehu et al. (2021) also find that NH/SH ratio of total Birkeland current is greatest, 1.2 ± 0.09, for $B_z > 0$ and $B_y > 0$ in the NH ($B_y < 0$ in the SH) during local winter, although we find

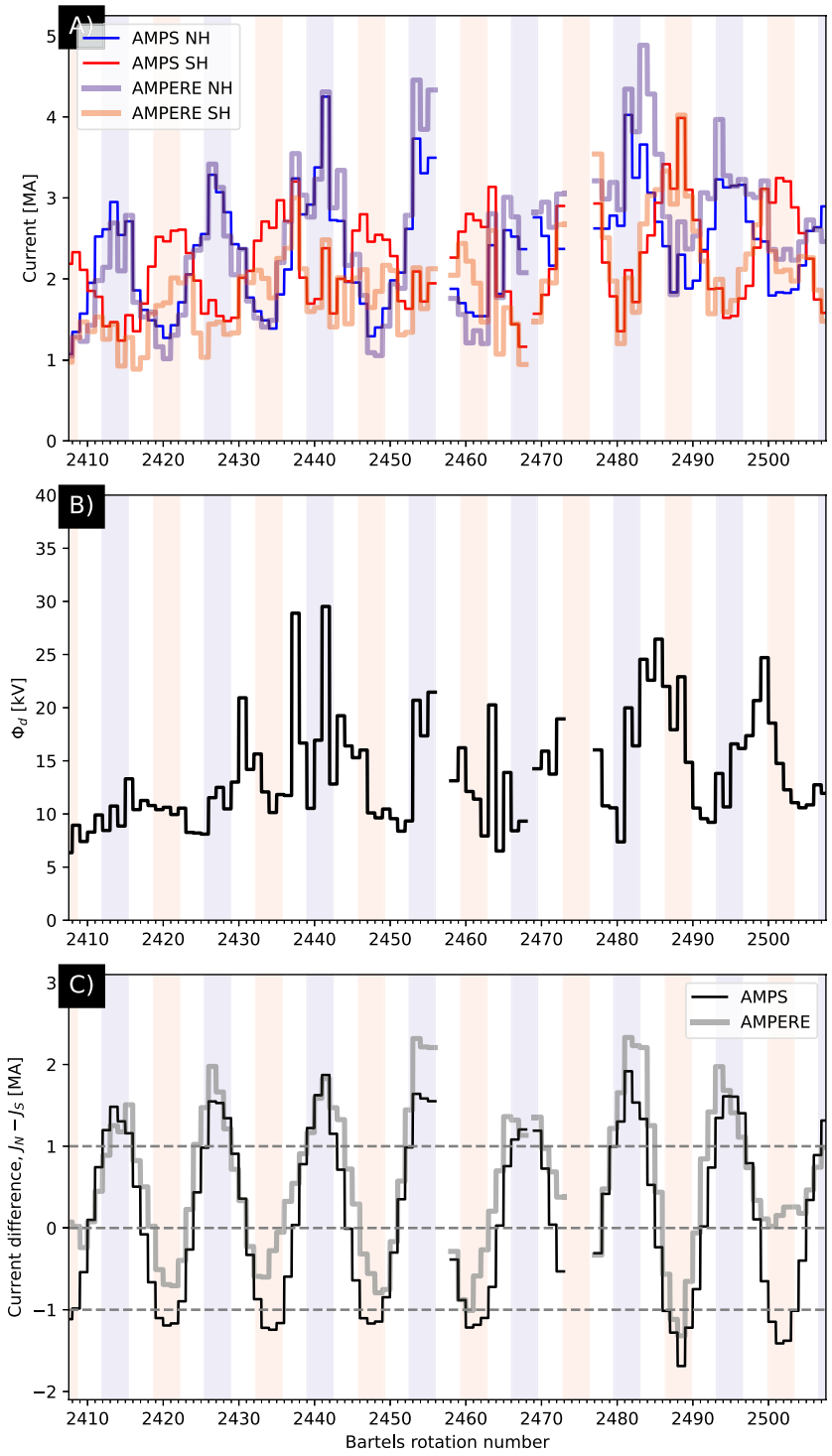

FIGURE 10
Comparison of the total field-aligned current in the two hemispheres and between our model and AMPERE, as a function of Bartels rotation number (number of 27-day periods since 8 February 1832). **(A)** Thick lines indicate AMPERE currents, and thin lines indicate AMPS model currents. Northern and Southern Hemisphere lines are indicated in blue and red, respectively. The red and blue shades in the background indicate the three months around June (blue) and December (red). **(B)** Dayside reconnection rate, in kV, using the (Milan et al., 2012) coupling function. **(C)** The difference in total current between hemispheres. The format of this figure is similar to that of Figure 3a in Coxon et al. (2016).

TABLE 1 Global conductances estimated from Eq. 3.

Source	Hemisphere			$c_1(\pm\Delta c_1)$		$c_2(\pm\Delta c_2)$
AMPERE[a]	North	Σ_N	=	202.6	+	54.0 sin(t)
AMPERE[a]	South	Σ_S	=	154.4	−	50.6 sin(t)
AMPERE[b]	North	Σ_N	=	174.7(±7.9)	+	55.1(±11.3) sin(t)
AMPERE[b]	South	Σ_S	=	133.4(±7.2)	−	16.0(±10.3) sin(t)
AMPS	North	Σ_N	=	160.0(±7.4)	+	56.3(±10.6) sin(t)
AMPS	South	Σ_S	=	146.0(±10.1)	−	29.5(±14.5) sin(t)

[a]Equations 7, 8 in Coxon et al. (2016), based on AMPERE data during 2010–2015 inclusive.
[b]This study, based on AMPERE data during 2010–2017 inclusive.

that the NH/SH ratio is overall greater, between 1.3 and 1.55 for this IMF orientation. Last, Workayehu et al. (2021) also find that the total Birkeland current during local summer is slightly less in the NH than in the SH for all IMF conditions, with an average ratio of 0.94 (their Table 2). On the other hand, while we find very little average difference in divergence-free current between hemispheres during local winter (less than 1%), Workayehu et al. (2020) find that Northern Hemisphere divergence-free currents are about 10% stronger.

We have also carried out a detailed comparison of seasonal variations in Birkeland currents as represented by AMPS and AMPERE data. While we, like Coxon et al. (2016), find that the Northern Hemisphere Birkeland currents are larger than those in the Southern Hemisphere, the difference we find is more modest, and more in line with the differences of order 10–20% that are shown in Figures 2–4. One possible explanation for the overall higher degree of hemispheric symmetry in the Birkeland currents that we find relative to the results of Coxon et al. (2016) is that, for earlier versions of AMPERE data processing, the Southern Hemisphere estimates of the field-aligned current reportedly sometimes include spurious filamentary currents at the high-latitude orbit crossing (Anderson et al., 2017). Additionally, at present, field-aligned currents derived from Iridium®satellite measurements up to and including 2017 sometimes underestimate Birkeland current magnitudes in the Southern Hemisphere. This underestimate is addressed and rectified in an upcoming release of AMPERE data [private communication, C. L. Waters, 2022].

As a result of the high (> 86°) orbital inclination of both the Swarm and Iridium® satellites, the sampling distributions of both satellite constellations prominently peak near the geographic poles at high latitudes; these peaks are clearly visible in column two of Figure 11, which displays the distribution of measurements used to produce the AMPS model on a magnetic latitude-longitude (MLat-MLon) grid in each hemisphere. Incidentally, these distributions indicate that the geographic pole is in the magnetic polar cap in the north, but within the auroral zone in the south. Thus differences in sampling are unlikely to explain the difference between our results and those of Coxon et al. (2016).

On the other hand, methodological differences for deriving statistics from AMPERE and Swarm data could possibly explain how we arrive at somewhat different results. AMPERE statistics are averages of global maps that are each based on 10 min of data, such that the nonuniformity in sampling is included in every such map (e.g., Figure 1 in Waters et al., 2001). AMPS statistics are instead produced by first deriving a model from data on an MLat-MLT grid collected over several years (column one of Figure 11), and then querying the model. While quantifying the effect of these methodological differences would require a dedicated study, our intention here is to point out that it seems reasonable to think that these methodological differences could play a role. Some of these points have been raised by Green et al. (2009), who also report an overall hemispheric difference in Birkeland currents on the basis of AMPERE measurements. They attribute the difference to the satellite orbits, the relatively greater displacement of the magnetic pole from the geographic pole in the Southern Hemisphere, and the unavailability of the along-track component of magnetic field measurements.

Regardless of these possible explanations, we are confident in the AMPS-based results as the AMPS model was designed to account for what we term the “direct effects” of local distortions of the geomagnetic field and the nonorthogonality of coordinate systems based on the geomagnetic field. Hemispheric and longitudinal variations in the main magnetic field, for example, has a direct geometric effect on the current density: For a constant incident current at some absolute magnetic latitude and local time, the observed current density is proportional to the magnetic field strength. This is because as the magnetic field lines converge with decreasing altitude, they focus the same current on a smaller area where the field is strong compared to regions with weaker magnetic field. This geometric effect is taken into account in the AMPS model by virtue of its use of Apex coordinates.

To illustrate this point more concretely we refer to the magnetic field strength shown on MLat-MLon grids in each hemisphere in column three of Figure 11. At 70° MLat and 90° MLon, for example, the magnetic field strengths in the Northern and Southern Hemisphere are approximately 44 and 40 μT, respectively. The difference in magnetic field strengths at these conjugate points therefore imply, for the same total incident current, that the measured current density would be 10% stronger in the Northern hemisphere. Closer to the pole the hemispheric asymmetry in field strength is reversed. But since field-aligned currents tend to be weak in the polar cap, we would expect that for the same total current flowing into each hemisphere, the total current would appear stronger in the north in statistical studies that do not take the geometric effects related to field strength into account. Such effects

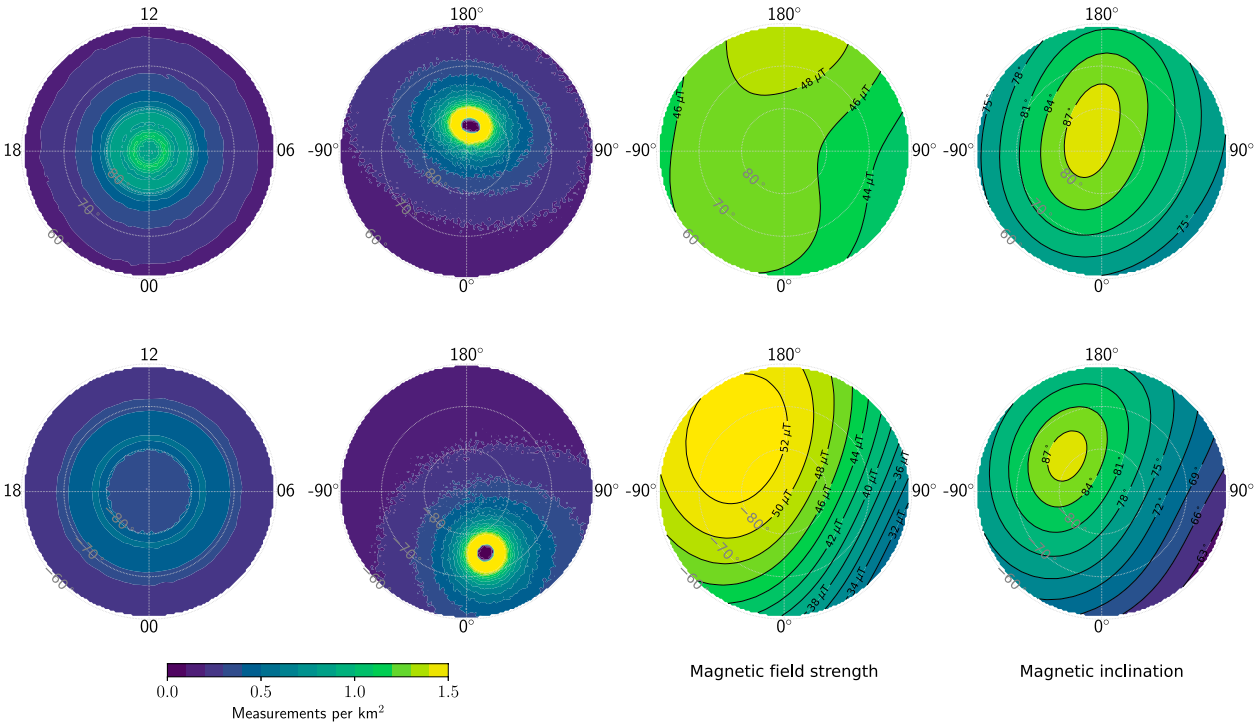

FIGURE 11
Color plots of the distributions of data points used to make the AMPS model in the Northern and Southern Hemisphere (top and bottom row, respectively), shown on a magnetic latitude-local time grid (column one) and magnetic latitude-longitude grid (column two). Also shown are the magnetic field strength (column three) and the inclination angle (column four), evaluated at 450-km altitude using the IGRF model.

could explain some of the difference between statistics based on AMPS and other statistics.

4.1 Possible influence of longitudinal variations in field strength and inclination

Beyond the direct effects of geomagnetic field distortion, there are also indirect effects that are not accounted for in the AMPS model. These include the non-trivial dependence of ionospheric conductance and currents on the geomagnetic field strength and inclination (Gasda and Richmond, 1998). Here we attempt to outline the possible influence of such effects.

To fully understand the differences between ionospheric current systems in each hemisphere, it is not enough to compare features at conjugate magnetic local times, as we have done with Figures 2–8. The reason is that the orientation of the MLat-MLT grid, and the solar zenith angle of points on the grid, varies throughout the day—that is, the geometry of the grid with respect to incident sunlight depends on Universal Time (UT), see Figure 1. The geomagnetic field strength and inclination are, however, functions of MLon rather than MLT (columns three and four, respectively, in Figure 11). Therefore, the nonuniformity of the sampling distribution on the MLat-MLon grid is mapped via UT onto the MLat-MLT grid on which the AMPS model is derived, in such a way that some magnetic field strengths and inclinations are sampled more often than others at a given MLat and MLT.

Short of adding UT as a AMPS model parameter, which would address this issue, we can instead determine the degree of bias toward a particular magnetic field strength and inclination inherent in the distribution of measurements used to construct the AMPS model. We do this by weighting the distributions of magnetic field strength and inclination in each hemisphere (third and fourth columns, respectively, in Figure 11) by the corresponding sampling density distributions (second column in Figure 11), and then integrating these weighted distributions around rings of constant QD latitude to obtain marginal distributions of magnetic field strength and inclination (left and right panels in Figure 12) in the Southern (red) and Northern (blue) Hemispheres. The marginal distributions based on the sampling distributions (solid lines) are shown together with reference marginal distributions (dotted lines) for which all magnetic latitudes and longitudes are weighted equally.

Comparing the sampling and reference Northern Hemisphere marginal distributions, we see that the two match

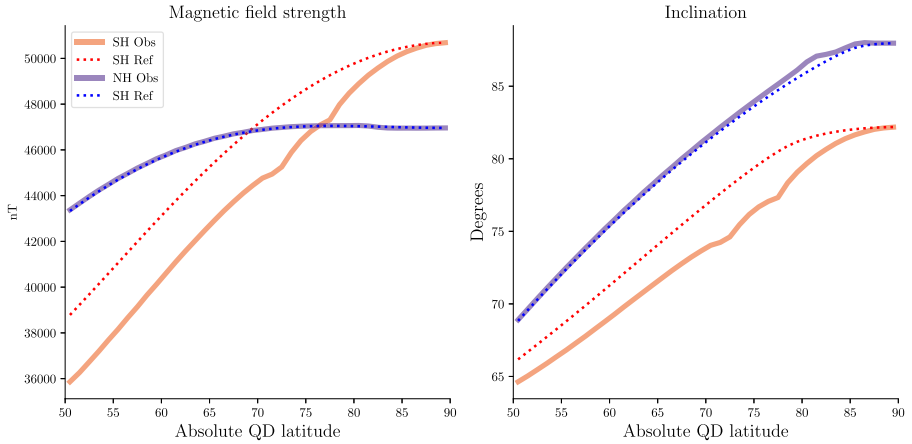

FIGURE 12
Marginal distributions of geomagnetic field strength (left) and field inclination (right) in the Northern (blue) and Southern (red) Hemisphere for the sampling distribution used to create the AMPS model (solid lines, denoted "Obs") and for a reference uniform distribution (dotted lines, denoted "Ref"). Solid lines are obtained by weighting the field strength and inclination in each hemisphere with the corresponding sampling distribution and integrating over longitude, while dotted lines are obtained by instead weighting with a uniform distribution.

closely, indicating that little bias is present in the AMPS model with respect to Northern Hemisphere magnetic field strength and inclination. Making the same comparison with the Southern Hemisphere curves, we see that the field strength of the sample distribution is typically about 8% less than that of the reference distribution except toward the pole, where the two lines must converge. The reason is that at the SH geographic pole, around which the Swarm satellite sampling density is heavily concentrated (second row, bottom panel in Figure 11), the main field strength is weaker than it is at the SH geomagnetic pole (third row, bottom panel in Figure 11). For the same reason, the inclination of the sampling distribution is one or two degrees below that of the reference distribution for all latitudes except near the pole.

To illustrate why these biases in sampled field strength and field inclination could be important, we insert the value of the ratio $B_{0,\mathrm{Obs}}/B_{0,\mathrm{Ref}}$ (= 40 μT /44 μT = 0.93) from the Southern Hemisphere curves at ~ 60° magnetic latitude into Eqs 3, 4 of (Gasda and Richmond, 1998), which express the dependence of Pedersen and Hall conductance on variations in main field strength. A ratio of $B_{0,\mathrm{Obs}}/B_{0,\mathrm{Ref}}$ = 0.93 corresponds to Pedersen and Hall conductances that are 10% higher than they would be if this bias were not present. Beyond observing that such a bias may be important, we do not know what effect this implicit, slight enhancement in conductance that is present in AMPS output for the Southern Hemisphere might have, as the relationship between height-integrated conductances and ionospheric currents is non-trivial and well outside the scope of this study.

4.2 Comparison with particle precipitation

In Section 3 we found that the average integrated Birkeland current during local winter (Figure 2) is 18% stronger in the Northern Hemisphere, primarily on the nightside, with the proviso that the distribution of measurements used to derive the AMPS model is biased in magnetic latitude-longitude. We now examine whether a north-south asymmetry is also observed in particle precipitation statistics, subject to the same bias in magnetic latitude-longitude sampling as AMPS and with the bias removed. We accomplish this using electron precipitation data from the full Fast Auroral SnapshoT mission, covering the period from November 1996 through April 2009. This database is publicly available (Hatch, 2022).

Following a methodology similar to that of Chaston et al. (2007) and Hatch et al. (2016), we calculate the electron current density and energy flux inside the earthward loss cone and above 70 eV up to the 30-keV detector limit. The 70-eV lower limit is used to avoid contamination from spacecraft charging. We then map these measurements along IGRF magnetic field lines from the satellite to a height of 110 km by scaling each measurement by the ratio of the magnetic field strength at these two heights. Since we are interested in local winter, we select measurements from the Northern Hemisphere for which the dipole tilt angle $\psi \leq -20^{\circ}$, and measurements from the Southern Hemisphere for which the dipole tilt angle $\psi \geq 20^{\circ}$. Of a total of 44.4 million total measurements in the FAST precipitation database, for these conditions and for Modified Apex-110 latitudes at or above 60° there are 26.5 million measurements in the Northern Hemisphere and 26.1 million in the Southern. In survey

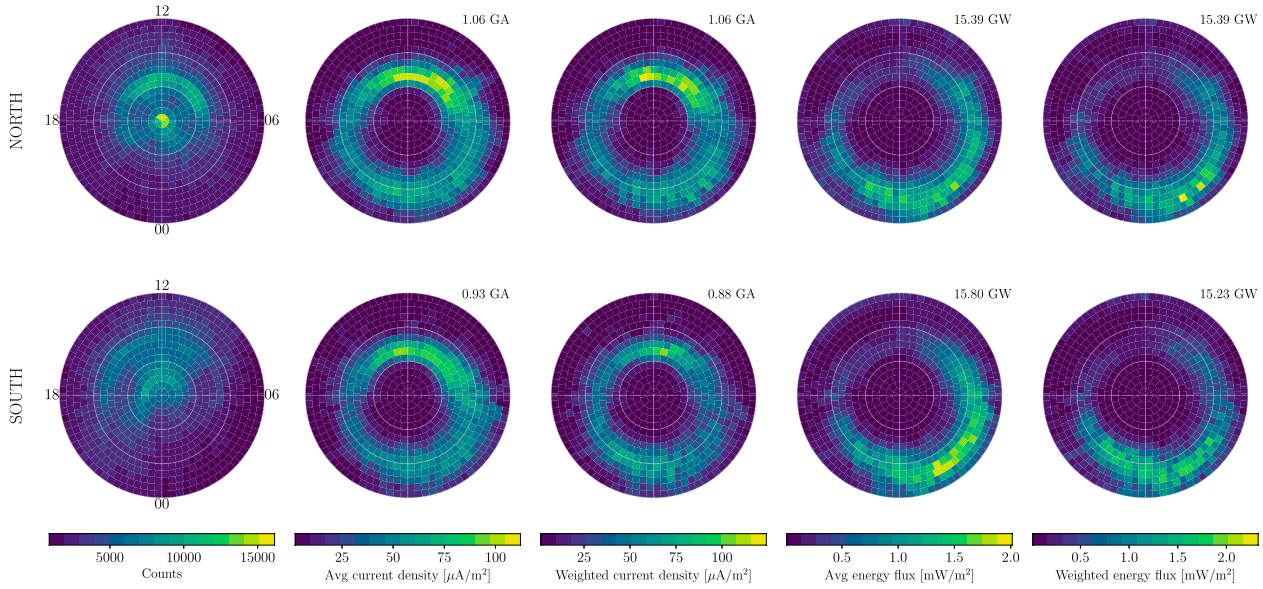

FIGURE 13
FAST electron loss-cone precipitation statistics in the Northern and Southern Hemisphere (top and bottom row, respectively) during local winter. The first column shows the number of measurements in each hemisphere. The second and third columns show the longitude-biased and unbiased average current density, respectively. The fourth and fifth columns show the longitude-biased and unbiased average energy flux. Statistics are calculated on an approximately equal-area MLat-MLT grid.

mode, the typical cadence of the FAST electron electrostatic analyzer (EESA) instrument

The orbit of FAST is, like those of Swarm and AMPERE, polar, and the distribution of measurements on a magnetic latitude-longitude grid (not shown) is very similar to that of the Swarm satellites (column two in Figure 11). Therefore the FAST measurements are biased in longitude in the same way as Swarm measurements. Integrating the distributions of mean current density in column two of Figure 13, we find that the longitude-biased Northern Hemisphere integrated current density is 15% greater than that of the Southern Hemisphere. This is rather comparable to the 18% difference we find with AMPS. Performing the same calculation for the longitude-biased mean energy flux (column four of Figure 13) we find that the longitude-biased Northern Hemisphere integrated energy flux is 3% less than that of the Southern Hemisphere. The only possible explanation for this apparent discrepancy is that the Southern Hemisphere electrons are, on average, more energetic than those in the North during local winter. Incidentally, the reason for the much higher typical current densities seen in columns two and three of Figure 13 relative to those in Figures 2–4 is that the former represent a moment of the observed distribution function that is calculated based on a limited range of pitch angles (i.e., only those within the earthward portion of the loss cone) and energies (0.07–32 keV). This moment excludes any electrons outside these ranges, including all anti-earthward electrons. Distributions of loss-cone current density and energy flux are moreover logarithmic (not shown, but see, e.g., Figure 3 of Hatch et al. (2016)), which means that large current densities greatly influence the mean of any collection of samples of such measurements.

To remove the magnetic longitude sampling bias from these estimates, we calculate a weighted average of the current density and energy flux in each hemisphere (columns three and five of Figure 13), where each measurement is first weighted by the inverse of the number of measurements where that measurement occurs on a magnetic latitude-longitude grid. The effect that this weighting has most clearly seen by comparing the distribution of energy flux in the Southern Hemisphere based on a simple average with that of the weighted average (bottom panel in the fourth and fifth columns, respectively, of Figure 13). Removing the longitude bias visibly reduces the average energy flux between approximately 60° and 70° MLat and 0–6 MLT.

Integrating the distributions of mean number flux in column three of Figure 13, we find that the unbiased Northern Hemisphere integrated number flux is 20% greater than that of the Southern Hemisphere, which is also comparable to the 18% difference we find with AMPS. Performing the same calculation for the unbiased average energy flux (column five of Figure 13) we find that the unbiased Northern Hemisphere integrated energy flux is 1% greater than that of the Southern Hemisphere.

Therefore, removing the longitude bias does not change the conclusion based on the longitude-biased estimates that the Southern Hemisphere electrons observed by FAST must be, on average, more energetic than those observed in the North during local winter over the range of energies measured by the FAST EESA.

AMPS- and FAST-based results therefore appear to corroborate one another. FAST observations additionally indicate that the net electron energy flux into each hemisphere during local winter is approximately equal. We reserve a full investigation of the possible hemispheric differences in current input and energy input for a future study.

5 Conclusion

In summary, we have used the Swarm-based AMPS model of Birkeland and ionospheric divergence-free currents in both hemispheres to quantify how much they depart with the commonly employed mirror symmetry assumption. We have highlighted that the AMPS model is particularly well suited to this test as it is designed to take stock of what we have termed the "direct effects" of the nonorthogonal nature of coordinate systems based on the geomagnetic field. We find that under a reversal of the sign of the dipole tilt angle and IMF B_y in the Southern Hemisphere, the morphology of Birkeland and divergence-free current distributions in each hemisphere are highly similar, with mean Bhattacharyya coefficients of respectively 0.97 and 0.96 for all solar wind driving and IMF clock angle conditions that we have considered. (Without performing this reversal of the sign of dipole tilt angle and IMF B_y the mean Bhattacharyya coefficients are 0.78 and 0.74, respectively.) We also find that on average, the total Birkeland and ionospheric divergence-free currents are similar with mean NH/SH total current ratios of 1.06 and 1.02 for Birkeland and divergence-free currents for all solar wind driving and IMF clock angle conditions considered. In general, differences between total currents in the two hemispheres are strongest during $B_z > 0$, with $B_y > 0$ in the NH ($B_y < 0$ in the SH) tending to favor the NH, and $B_y < 0$ in the NH ($B_y > 0$ in the SH) tending to favor the SH, in accordance with earlier studies (e.g., Workayehu et al., 2021). We have also compared our results with those of Coxon et al. (2016), and find that our results indicate a relatively higher degree of hemispheric symmetry. The largest exception appears to be the Birkeland currents during local winter, when the average difference in integrated currents is approximately 20%, which is in accordance with the results of Workayehu et al. (2020). FAST satellite observations from each hemisphere during local winter corroborate this result, but additionally indicate that the net electron energy input into each hemisphere during local winter is the same within a few percent.

Data availability statement

The original contributions presented in the study are included in the article/Supplementary Material, further inquiries can be directed to the corresponding author.

Author contributions

SH contributed to data analysis and interpretation, study design, and manuscript preparation. KL contributed to data analysis and interpretation, study design, and manuscript preparation. JR contributed to manuscript preparation and data interpretation.

Funding

This work was supported by the Trond Mohn Foundation and by the Research Council of Norway under contracts 223252/F50 and 300844/F50. The study is also funded by ESA through the Swarm Data Innovation and Science Cluster (Swarm DISC) within the reference frame of ESA contract 000109587/13/I-NB. For more information on Swarm DISC, please visit https://earth.esa.int/web/guest/missions/esa-eo-missions/swarm/disc.

Acknowledgments

We thank ESA for providing prompt access to the Swarm L1b data. The support of the CHAMP mission by the German Aerospace Center (DLR) and the Federal Ministry of Education and Research is gratefully acknowledged. The IMF, solar wind and magnetic index data were provided through OMNIWeb by the Space Physics Data Facility(SPDF). We also thank the AMPERE team and the AMPERE Science Center for providing the Iridium®-derived data products.

Conflict of interest

The authors declare that the research was conducted in the absence of any commercial or financial relationships that could be construed as a potential conflict of interest.

Publisher's note

References

Anderson, B. J., Korth, H., Welling, D. T., Merkin, V. G., Wiltberger, M. J., Raeder, J., et al. (2017). Comparison of predictive estimates of high-latitude electrodynamics with observations of global-scale birkeland currents. *Space weather.* 15, 352–373. doi:10.1002/2016SW001529

Anderson, B. J., Takahashi, K., and Toth, B. A. (2000). Sensing global Birkeland currents with Iridium engineering magnetometer data. *Geophys. Res. Lett.* 27, 4045–4048. doi:10.1029/2000gl000094

Andreeva, V. A., and Tsyganenko, N. A. (2016). Reconstructing the magnetosphere from data using radial basis functions. *JGR. Space Phys.* 121, 2249–2263. doi:10.1002/2015JA022242

Avery, S., Vincent, R., Phillips, A., Manson, A., and Fraser, G. (1989). High-latitude tidal behavior in the mesosphere and lower thermosphere. *J. Atmos. Terr. Phys.* 51, 595–608. doi:10.1016/0021-9169(89)90057-3

Barlier, F., Bauer, P., Jaeck, C., Thuillier, G., and Kockarts, G. (1974). North-south asymmetries in the thermosphere during the Last Maximum of the solar cycle. *J. Geophys. Res.* 79, 5273–5285. doi:10.1029/JA079i034p05273

Billett, D. D., Grocott, A., Wild, J. A., Walach, M.-T., and Kosch, M. J. (2018). Diurnal variations in global joule heating morphology and magnitude due to neutral winds. *J. Geophys. Res. Space Phys.* 123, 2398–2411. doi:10.1002/2017JA025141

Chaston, C. C., Carlson, C. W., McFadden, J. P., Ergun, R. E., and Strangeway, R. J. (2007). How important are dispersive Alfvén waves for auroral particle acceleration? *Geophys. Res. Lett.* 34, L07101. doi:10.1029/2006GL029144

Clausen, L. B. N., Baker, J. B. H., Ruohoniemi, J. M., Milan, S. E., and Anderson, B. J. (2012). Dynamics of the region 1 birkeland current oval derived from the active magnetosphere and planetary electrodynamics response experiment (AMPERE). *J. Geophys. Res.* 117. doi:10.1029/2012JA017666

Cosgrove, R. B., Bahcivan, H., Chen, S., Sanchez, E., and Knipp, D. (2022). Violation of hemispheric symmetry in integrated poynting flux via an empirical model. *Geophys. Res. Lett.* 49, e2021GL097329. doi:10.1029/2021GL097329

Cowley, S., and Hughes, W. (1983). Observation of an IMF sector effect in the Y magnetic field component at geostationary orbit. *Planet. Space Sci.* 31, 73–90. doi:10.1016/0032-0633(83)90032-6

Coxon, J. C., Milan, S. E., Carter, J. A., Clausen, L. B. N., Anderson, B. J., and Korth, H. (2016). Seasonal and diurnal variations in AMPERE observations of the Birkeland currents compared to modeled results. *J. Geophys. Res. Space Phys.* 121, 4027–4040. doi:10.1002/2015JA022050

Coxon, J. C., Milan, S. E., Clausen, L. B. N., Anderson, B. J., and Korth, H. (2014). The magnitudes of the regions 1 and 2 Birkeland currents observed by AMPERE and their role in solar wind-magnetosphere-ionosphere coupling. *J. Geophys. Res. Space Phys.* 119, 9804–9815. doi:10.1002/2014JA020138

Crooker, N. U., and Rich, F. J. (1993). Lobe cell convection as a summer phenomenon. *J. Geophys. Res.* 98, 13403–13407. doi:10.1029/93JA01037

Dhadly, M. S., Emmert, J. T., Drob, D. P., Conde, M. G., Aruliah, A., Doornbos, E., et al. (2019). HL-TWiM empirical model of high-latitude upper thermospheric winds. *JGR. Space Phys.* 124, 10592–10618. doi:10.1029/2019JA027188

Dombeck, J., Cattell, C., Prasad, N., Meeker, E., Hanson, E., and McFadden, J. (2018). Identification of auroral electron precipitation mechanism combinations and their relationships to net downgoing energy and number flux. *JGR. Space Phys.* 123 10064–10089. doi:10.1029/2018JA025749

Finlay, C. C., Kloss, C., Olsen, N., Hammer, M. D., Tøffner-Clausen, L., Grayver, A., et al. (2020). The CHAOS-7 geomagnetic field model and observed changes in the South Atlantic Anomaly. *Earth Planets Space* 72, 156. doi:10.1186/s40623-020-01252-9

Förster, M., and Haaland, S. (2015). Interhemispheric differences in ionospheric convection: Cluster EDI observations revisited. *J. Geophys. Res. Space Phys.* 120, 5805–5823. doi:10.1002/2014JA020774

Gasda, S., and Richmond, A. D. (1998). Longitudinal and interhemispheric variations of auroral ionospheric electrodynamics in a realistic geomagnetic field. *J. Geophys. Res.* 103, 4011–4021. doi:10.1029/97JA03243

Green, D. L., Waters, C. L., Anderson, B. J., and Korth, H. (2009). Seasonal and interplanetary magnetic field dependence of the field-aligned currents for both Northern and Southern Hemispheres. *Ann. Geophys.* 27, 1701–1715. doi:10.5194/angeo-27-1701-2009

Gussenhoven, M. S., Hardy, D. A., and Heinemann, N. (1983). Systematics of the equatorward diffuse auroral boundary. *J. Geophys. Res.* 88, 5692. doi:10.1029/JA088iA07p05692

Haaland, S., Lybekk, B., Maes, L., Laundal, K., Pedersen, A., Tenfjord, P., et al. (2017). North-south asymmetries in cold plasma density in the magnetotail lobes: Cluster observations. *J. Geophys. Res. Space Phys.* 122, 136–149. doi:10.1002/2016JA023404

Hardy, D. A., Gussenhoven, M. S., and Holeman, E. (1985). A statistical model of auroral electron precipitation. *J. Geophys. Res.* 90, 4229. doi:10.1029/JA090iA05p04229

Hatch, S. M., Chaston, C. C., and LaBelle, J. (2016). Alfvén wave-driven ionospheric mass outflow and electron precipitation during storms. *J. Geophys. Res. Space Phys.* 121, 7828–7846. doi:10.1002/2016JA022805

Hatch, S. M. (2022). Fast loss-cone electron precipitation database. doi:10.5281/zenodo.6594204

Hatch, S. M., Haaland, S., Laundal, K. M., Moretto, T., Yau, A. W., Bjoland, L., et al. (2020). Seasonal and hemispheric asymmetries of F region polar cap plasma density: Swarm and CHAMP observations. *J. Geophys. Res. Space Phys.* 125. doi:10.1029/2020JA028084

Hatch, S. M., LaBelle, J., and Chaston, C. (2018). Storm phase–partitioned rates and budgets of global Alfvénic energy deposition, electron precipitation, and ion outflow. *J. Atmos. Solar-Terrestrial Phys.* 167, 1–12. doi:10.1016/j.jastp.2017.08.009

Heppner, J. P., and Maynard, N. C. (1987). Empirical high-latitude electric field models. *J. Geophys. Res.* 92, 4467–4489. doi:10.1029/JA092iA05p04467

Jørgensen, T. S., Friis-Christensen, E., and Wilhjelm, J. (1972). Interplanetary magnetic-field direction and high-latitude ionospheric currents. *J. Geophys. Res.* 77, 1976. doi:10.1029/JA077i010p01976

Keating, G. M., Mcdougal, D. S., Prior, E. J., and Levine, J. S. (1973). "North-South asymmetry of the neutral exosphere," in *Space research XIII*. Editors M. J. Rycroft. and S. K. Runcorn (Berlin: Akademie-Verlag), 327.

King, J., and Papitashvili, N. E. (2005). Solar wind spatial scales in and comparisons of hourly Wind and ACE plasma and magnetic field data. *J. Geophys. Res.* 110, A02104. doi:10.1029/2004ja010649

Knipp, D., Kilcommons, L., Hairston, M., and Coley, W. R. (2021). Hemispheric asymmetries in poynting flux derived from DMSP spacecraft. *Geophys. Res. Lett.* 48. doi:10.1029/2021GL094781

Laundal, K. M., Cnossen, I., Milan, S. E., Haaland, S. E., Coxon, J., Pedatella, N. M., et al. (2017). North-South asymmetries in Earth's magnetic field - effects on high-latitude geospace. *Space Sci. Rev.* 206, 225–257. doi:10.1007/s11214-016-0273-0

Laundal, K. M., Finlay, C. C., Olsen, N., and Reistad, J. P. (2018). Solar wind and seasonal influence on ionospheric currents from Swarm and CHAMP measurements. *J. Geophys. Res. Space Phys.* 123, 4402–4429. doi:10.1029/2018JA025387

Laundal, K. M., Finlay, C. C., and Olsen, N. (2016a). Sunlight effects on the 3D polar current system determined from low Earth orbit measurements. *Earth Planets Space* 68, 142. doi:10.1186/s40623-016-0518-x

Laundal, K. M., Gjerloev, J. W., Ostgaard, N., Reistad, J. P., Haaland, S. E., Snekvik, K., et al. (2016b). The impact of sunlight on high-latitude equivalent currents. *J. Geophys. Res. Space Phys.* 121, 2715–2726. doi:10.1002/2015JA022236

Laundal, K. M., Hatch, S. M., and Moretto, T. (2019). Magnetic effects of plasma pressure gradients in the upper F region. *Geophys. Res. Lett.* 46, 2355–2363. doi:10.1029/2019GL081980

Laundal, K. M., and Toresen, M. (2018). *pyAMPS*. Available at: https://github.com/klaundal/pyAMPS. doi:10.5281/zenodo.1182930

Lockwood, M., Owens, M. J., Barnard, L. A., Watt, C. E., Scott, C. J., Coxon, J. C., et al. (2020). Semi-annual, annual and universal time variations in the magnetosphere and in geomagnetic activity: 3. Modelling. *J. Space Weather Space Clim.* 10, 61. doi:10.1051/swsc/2020062

Mayr, H., and Trinks, H. (1977). Spherical asymmetry in thermospheric magnetic storms. *Planet. Space Sci.* 25, 607–613. doi:10.1016/0032-0633(77)90099-X

McGranaghan, R., Knipp, D. J., Matsuo, T., Godinez, H., Redmon, R. J., Solomon, S. C., et al. (2015). Modes of high-latitude auroral conductance variability derived from DMSP energetic electron precipitation observations: Empirical orthogonal function analysis. *JGR. Space Phys.* 120 (11–13), 31. 11. doi:10.1002/2015JA021828

McGranaghan, R. M., Ziegler, J., Bloch, T., Hatch, S., Camporeale, E., Lynch, K., et al. (2021). Toward a next generation particle precipitation model: Mesoscale prediction through machine learning (a case study and framework for progress). *Space weather.* 19. doi:10.1029/2020SW002684

Mead, G. D., and Fairfield, D. H. (1975). A quantitative magnetospheric model derived from spacecraft magnetometer data. *J. Geophys. Res.* 80, 523–534. doi:10.1029/JA080i004p00523

Milan, S. E., Gosling, J. S., and Hubert, B. (2012). Relationship between interplanetary parameters and the magnetopause reconnection rate quantified from observations of the expanding polar cap. *J. Geophys. Res.* 117. doi:10.1029/2011JA017082

Newell, P. T., and Meng, C.-I. (1988). Hemispherical asymmetry in cusp precipitation near solstices. *J. Geophys. Res.* 93, 2643. doi:10.1029/JA093iA04p02643

Newell, P. T., Sotirelis, T., Liou, K., Meng, C. I., and Rich, F. J. (2007). A nearly universal solar wind-magnetosphere coupling function inferred from 10 magnetospheric state variables. *J. Geophys. Res.* 112. doi:10.1029/2006JA012015

Newell, P. T., Sotirelis, T., and Wing, S. (2009). Diffuse, monoenergetic, and broadband aurora: The global precipitation budget. *J. Geophys. Res.* 114. doi:10.1029/2009JA014326

Newell, P. T., Sotirelis, T., and Wing, S. (2010). Seasonal variations in diffuse, monoenergetic, and broadband aurora. *J. Geophys. Res.* 115. doi:10.1029/2009JA014805

Pakhotin, I. P., Mann, I. R., Xie, K., Burchill, J. K., and Knudsen, D. J. (2021). Northern preference for terrestrial electromagnetic energy input from space weather. *Nat. Commun.* 12, 199. doi:10.1038/s41467-020-20450-3

Papitashvili, V. O., Belov, B. A., Faermark, D. S., Feldstein, Y. I., Golyshev, S. A., Gromova, L. I., et al. (1994). Electric potential patterns in the northern and southern polar regions parameterized by the interplanetary magnetic field. *J. Geophys. Res.* 99, 13251. doi:10.1029/94JA00822

Petrukovich, A. A. (2011). Origins of plasma sheetB_y. *J. Geophys. Res.* 116. doi:10.1029/2010JA016386

Pettigrew, E. D., Shepherd, S. G., and Ruohoniemi, J. M. (2010). Climatological patterns of high-latitude convection in the Northern and Southern hemispheres: Dipole tilt dependencies and interhemispheric comparisons. *J. Geophys. Res.* 115. doi:10.1029/2009JA014956

Pignalberi, A., Giannattasio, F., Truhlik, V., Coco, I., Pezzopane, M., Consolini, G., et al. (2021). On the electron temperature in the topside ionosphere as seen by Swarm satellites, incoherent scatter radars, and the international reference ionosphere model. *Remote Sens.* 13, 4077. doi:10.3390/rs13204077

Qin, G., Qiu, S., Ye, H., He, A., Sun, L., Lin, X., et al. (2008). The thermospheric composition different responses to geomagnetic storm in the winter and summer hemisphere measured by "SZ" Atmospheric Composition Detectors. *Adv. Space Res.* 42, 1281–1287. doi:10.1016/j.asr.2007.11.021

Reistad, J. P., Laundal, K. M., Østgaard, N., Ohma, A., Thomas, E., Haaland, S., et al. (2019). Separation and quantification of ionospheric convection sources: 1. A new technique. *JGR. Space Phys.* 124, 6343–6357. doi:10.1029/2019JA026634

Richmond, A. D. (1995a). "Ionospheric electrodynamics," in *Handbook of atmospheric electrodynamics*. Editor H. Volland (Boca Raton, Louisiana: CRC Press), 249–290. Volume II.

Richmond, A. D. (1995b). Ionospheric electrodynamics using magnetic apex coordinates. *J. geomagn. geoelec.* 47, 191–212. doi:10.5636/jgg.47.191

Russell, C. T., Wang, Y. L., and Raeder, J. (2003). Possible dipole tilt dependence of dayside magnetopause reconnection. *Geophys. Res. Lett.* 30. doi:10.1029/2003GL017725

Smith, A. R. A., Beggan, C. D., Macmillan, S., and Whaler, K. A. (2017). Climatology of the auroral electrojets derived from the along-track gradient of magnetic field intensity measured by POGO, magsat, CHAMP, and Swarm. *Space weather.* 15, 1257–1269. doi:10.1002/2017SW001675

Strangeway, R. J. (2012). The equivalence of Joule dissipation and frictional heating in the collisional ionosphere. *J. Geophys. Res.* 117. doi:10.1029/2011JA017302

Tenfjord, P., Østgaard, N., Snekvik, K., Laundal, K. M., Reistad, J. P., Haaland, S., et al. (2015). How the IMF By induces a by component in the closed magnetosphere and how it leads to asymmetric currents and convection patterns in the two hemispheres. *J. Geophys. Res.* 120 (11), 9368–9384. doi:10.1002/2015JA02157

Tenfjord, P., Østgaard, N., Strangeway, R., Haaland, S., Snekvik, K., Laundal, K. M., et al. (2017). Magnetospheric response and reconfiguration times following IMF B_y reversals. *J. Geophys. Res. Space Phys.* 122, 417–431. doi:10.1002/2016JA023018

Thébault, E., Finlay, C., Beggan, C., Alken, P., Aubert, J., Barrois, O., et al. (2015). International geomagnetic reference field: the 12th generation. *Earth Planets Space* 67, 79. doi:10.1186/s40623-015-0228-9

Thomas, E. G., and Shepherd, S. G. (2018). Statistical patterns of ionospheric convection derived from mid-latitude, high-latitude, and polar superdarn hf radar observations. *J. Geophys. Res. Space Phys.* 123, 3196–3216. doi:10.1002/2018JA025280

Vasyliunas, V. M. (2012). The physical basis of ionospheric electrodynamics. *Ann. Geophys.* 30, 357–369. doi:10.5194/angeo-30-357-2012

Vincent, R. A. (2015). The dynamics of the mesosphere and lower thermosphere: a brief review. *Prog. Earth Planet. Sci.* 2, 4. doi:10.1186/s40645-015-0035-8

Waters, C. L., Anderson, B. J., and Liou, K. (2001). Estimation of global field aligned currents using the Iridium system magnetometer data. *Geophys. Res. Lett.* 28, 2165–2168. doi:10.1029/2000gl012725

Waters, C. L., Gjerloev, J. W., Dupont, M., and Barnes, R. J. (2015). Global maps of ground magnetometer data. *J. Geophys. Res. Space Phys.* 120, 9651–9660. doi:10.1002/2015JA021596

Weimer, D., and Edwards, T. (2021). Testing the electrodynamic method to derive height-integrated ionospheric conductances. *Ann. Geophys.* 39, 31–51. doi:10.5194/angeo-39-31-2021

Weimer, D. (2001). Maps of ionospheric field-aligned currents as a function of the interplanetary magnetic field derived from Dynamics Explorer 2 data. *J. Geophys. Res.* 106, 12889–12902. doi:10.1029/2000ja000295

Weimer, D. R. (2013). An empirical model of ground-level geomagnetic perturbations. *Space weather.* 11, 107–120. doi:10.1002/swe.20030

Weimer, D. R. (2005). Improved ionospheric electrodynamic models and application to calculating joule heating rates. *J. Geophys. Res.* 110, A05306. doi:10.1029/2004JA010884

Workayehu, A. B., Vanhamäki, H., and Aikio, A. T. (2020). Seasonal effect on hemispheric asymmetry in ionospheric horizontal and field-aligned currents. *J. Geophys. Res. Space Phys.* 125. doi:10.1029/2020JA028051

Workayehu, A. B., Vanhamäki, H., Aikio, A. T., and Shepherd, S. G. (2021). Effect of interplanetary magnetic field on hemispheric asymmetry in ionospheric horizontal and field-aligned currents during different seasons. *JGR. Space Phys.* 126. doi:10.1029/2021JA029475

Xie, Y., Zhang, R., Zhu, Z., and Zhou, L. (2021). Evaluating the response of global column resistance to a large volcanic eruption by an aerosol-coupled chemistry climate model. *Front. Earth Sci. (Lausanne).* 9. doi:10.3389/feart.2021.673808

Zhu, Q., Deng, Y., Maute, A., Kilcommons, L. M., Knipp, D. J., and Hairston, M. (2021). Ashley: A new empirical model for the high-latitude electron precipitation and electric field. *Space weather.* 19. doi:10.1029/2020SW002671

10.3389/fspas.2022.958977

Appendix A:

To calculate the Bhattacharyya coefficient for a pair of northern and southern Birkeland current distributions (or divergence-free equivalent current distributions), we must first convert each current distribution, which can be positive or negative, to a continuous probability distribution with only positive values. Each distribution $j = j(\lambda, \phi_{MLT})$, with $\lambda \in [45°, 90°]$ and $\phi_{MLT} \in [0, 24]$ magnetic latitude and magnetic local time, respectively, in Apex coordinates. Since j can be positive or negative, we define a new positive distribution $j^* = j^*(\lambda, \phi_{MLT^*})$, where the range of ϕ_{MLT^*} is such that $j > 0$ corresponds to $\phi_{MLT^*} \in [0, 24]$, and $j < 0$ corresponds to $\phi_{MLT^*} \in [24, 48]$. More explicitly,

$$j^*(\lambda, \phi_{MLT}) = \begin{cases} j(\lambda, \phi_{MLT}) & \text{if } j > 0; \\ 0 & \text{otherwise;} \end{cases} \tag{5}$$

and

$$j^*(\lambda, 24 + \phi_{MLT}) = \begin{cases} -j(\lambda, \phi_{MLT}) & \text{if } j < 0; \\ 0 & \text{otherwise.} \end{cases} \tag{6}$$

We then normalize the probability distribution $j*$ such that

$$\int_{45°}^{90°} \cos(\lambda) d\lambda \int_0^{48} d\phi_{MLT^*}\, j^*(\lambda, \phi_{MLT^*}) = 1. \tag{7}$$

After following the above procedure to obtain probability distributions j^*_{NH} and j^*_{SH} for current distributions j_{NH} and j_{SH}, we calculate the Bhattacharyya coefficient

$$BC = \int_{45°}^{90°} \cos(\lambda) d\lambda \int_0^{48} d\phi_{MLT^*} \sqrt{j^*_{NH} j^*_{SH}}. \tag{8}$$

frontiers | Frontiers in Astronomy and Space Sciences

TYPE Original Research
PUBLISHED 20 September 2022
DOI 10.3389/fspas.2022.958749

OPEN ACCESS

EDITED BY
Olga Khabarova,
Institute of Terrestrial Magnetism Ionosphere and Radio Wave Propagation (RAS), Russia

REVIEWED BY
Renata Lukianova,
Space Research Institute, Russia
Vladimir Mishin,
Institute of Solar-Terrestrial Physics (RAS), Russia

*CORRESPONDENCE
Anders Ohma,
Anders.Ohma@uib.no

SPECIALTY SECTION
This article was submitted to Space Physics, a section of the journal Frontiers in Astronomy and Space Sciences

RECEIVED 01 June 2022
ACCEPTED 31 August 2022
PUBLISHED 20 September 2022

CITATION
Ohma A, Laundal KM, Reistad JP and Østgaard N (2022), Evolution of IMF B_y induced asymmetries during substorms: Superposed epoch analysis at geosynchronous orbit. *Front. Astron. Space Sci.* 9:958749. doi: 10.3389/fspas.2022.958749

Evolution of IMF B_y induced asymmetries during substorms: Superposed epoch analysis at geosynchronous orbit

Anders Ohma*, Karl Magnus Laundal, Jone Peter Reistad and Nikolai Østgaard

Birkeland Centre for Space Science, Department of Physics and Technology, University of Bergen, Bergen, Norway

The B_y component of the magnetic field inside the magnetosphere is positively correlated with the B_y component of the Interplanetary Magnetic Field (IMF). This leads to asymmetries in aurora, plasma convection and electric currents between the northern and southern hemispheres It has been demonstrated that magnetic conjugate locations in the northern and southern ionosphere become less displaced during magnetospheric substorms, which are associated with enhanced reconnection in the near-Earth tail. Here we directly address how the average B_y component in the magnetotail evolves relative to substorm onset by performing a superposed epoch analysis of the magnetic field observed at nightside geosynchronous orbit during periods with dominant IMF B_y. The observations demonstrate that the average $|B_y|$ in the magnetotail increases during the loading phase prior to onset. $|B_y|$ maximizes in the expansion phase and is subsequently reduced during the remaining unloading phase. The observed trends become more pronounced using substorm onset lists that on average identify stronger substorms. Since dayside reconnection dominates over tail reconnection during the loading phase, whereas tail reconnection dominates during the unloading phase, the results demonstrate how asymmetries build up during periods with low tail reconnection and are reduced during periods with enhanced tail reconnection in agreement with previous case studies of conjugate auroral substorm features.

KEYWORDS

reduced asymmetry, tail reconnection, substorms, magnetotail reconfiguration, geosynchronous orbit, IMF B_y, magnetotail B_y, north-south asymmetries

1 Introduction

The B_y component of the magnetic field inside the magnetosphere, on both open and closed field lines, is positively correlated with the Interplanetary Magnetic Field (IMF) B_y component (e.g. Fairfield, 1979; Cowley and Hughes, 1983; Lui, 1984; Kaymaz et al., 1994; Wing et al., 1995; Petrukovich et al., 2005; Case et al., 2021). An intrinsic part of having

such an induced B_y component on closed field lines is a relative displacement of magnetic conjugate locations in the two hemispheres. This displacement is seen in auroral observations (Liou et al., 2001; Frank and Sigwarth, 2003; Østgaard et al., 2004, 2011a; Reistad et al., 2013, 2016).

The first physical description of how the IMF B_y component enters the magnetosphere was put forward by Cowley (1981), who proposed that the asymmetries arise through the convection cycle: When a significant B_y component is present in the IMF, the field lines reconnecting at the dayside magnetospause are added asymmetrically to the lobes due to the magnetic tension force acting on these newly opened field lines. The field lines are added more toward dawn in the northern hemisphere and more toward dusk in the southern hemisphere for IMF $B_y > 0$ and more toward dusk in the northern hemisphere and more toward dawn in the southern hemisphere for IMF $B_y < 0$. This asymmetric loading causes asymmetric convection in the lobes; towards dusk in the northern hemisphere and dawn in the southern hemisphere for positive IMF B_y and vice versa for negative IMF B_y. The B_y component subsequently enters the closed magnetosphere as the field lines reconnect in the tail.

Khurana et al. (1996) suggested a different scenario for introducing a B_y component in the closed magnetosphere. They argue that asymmetric loading of magnetic flux in the two lobes for IMF $B_y \neq 0$ affect the closed magnetosphere directly by pressure waves, setting up an asymmetric convection between the two hemispheres and leading to a displacement of the magnetic field lines, introducing the asymmetries more directly. Tenfjord et al. (2015, 2017, 2018) used magnetohydrodynamic (MHD) modeling and magnetometer observations at geosynchronous orbit, and showed a response of the magnetospheric system consistent with this view. Both simulations and observations show that the B_y component inside the closed magnetosphere responds to the IMF B_y component in about 10 min and that the field reconfigures to the IMF B_y component in about 1 hour. Other studies have reported longer time lags between IMF B_y and magnetotail B_y, suggested to be consistent with B_y being introduced into the closed magnetosphere by tail reconnection (Motoba et al., 2011; Rong et al., 2015; Browett et al., 2017). However, these studies do not consider any direct or indirect measurements of the tail reconnection rate. The interpretation that tail reconnection introduces B_y is thus based solely on the inferred time lags, an interpretation that has been challenged (Tenfjord et al., 2017; Ohma et al., 2018).

Reconnection in the near-Earth tail maximizes during magnetospheric substorms, unloading magnetic flux and energy stored in the magnetotail (Hones, 1979; Dmitrieva et al., 2004; Milan et al., 2007). Substorms usually consist of three phases: (1) A growth phase prior to onset (McPherron, 1970), generally associated with southward IMF (Caan et al., 1977; Wild et al., 2009), during which dayside reconnection increases the open flux content in the magnetotail lobes, (2) an expansion phase (Akasofu, 1964), where the polar cap contracts as the aurora expands poleward and the open flux content in the lobes is reduced explosively and (3) a recovery phase, where the magnetosphere-ionosphere system reverts towards its pre-onset configuration. The substorm process represents a loading-unloading cycle of the magnetosphere, with a loading phase prior to onset and an unloading phase after onset. Magnetic pressure builds up in the lobes during the loading phase and decreases during the unloading phase (Caan et al., 1975, 1978; Coxon et al., 2018). Juusola et al. (2011) demonstrated how the occurrence of bursty bulk flows, which can be considered a proxy of tail reconnection, continues to increase throughout the expansion phase, maximizes in the beginning of the recovery phase and remains at an elevated level throughout the recovery phase. The unloading thus continues well into the recovery phase.

During the unloading phase, the magnetotail reconfigures from a stretched, tail-like configuration to a more dipolar configuration (Fairfield and Ness, 1970; Hones, 1979). The stretching of the tail during the loading phase corresponds to a strengthening of the $|B_x|$ component and a weakening of the B_z component, whereas the dipolarization corresponds to a weakening of the $|B_x|$ component and a strengthening of the B_z component. The dipolarization typically commences at radial distances of 7–10 R_E in the midnight region a few minutes before the auroral onset is observed, and subsequently expands in all directions (Miyashita et al., 2009). Near midnight at geosynchronous orbit, the field is dipolarized in about 20 min (Liou et al., 2002).

There is a growing number of studies that observe a reduction of the north-south asymmetries during periods with enhanced near-Earth tail reconnection, opposing the view that the B_y associated asymmetries are introduced by tail reconnection. Østgaard et al. (2011b, 2018) and Ohma et al. (2018) examined the evolution of conjugate auroral features during substorms, and reported that the asymmetries at onset are reduced or even removed during the expansion phase. Grocott et al. (2010) performed a superposed epoch analysis of the ionospheric convection in both hemispheres relative to substorm onset, and showed that the IMF B_y control of the nightside convection on closed field lines disappears during substorms. Using convection data from the northern hemisphere, Reistad et al. (2018) found that the return flow pattern at lower latitudes on the nightside becomes more similar in both location and magnitude as the activity increases. Ohma et al. (2019) investigated the average plasma convection in the lobes, and found more north-south aligned convection during periods with enhanced tail activity. Recently, Ohma et al. (2021b) used MHD simulations with dominant IMF B_y to demonstrate that magnetic conjugate locations in the two hemispheres become less displaced during the unloading phase, associated with a significant increase in the tail reconnection rate. It has been argued by e.g. Østgaard et al. (2018) that the observed

10.3389/fspas.2022.958749

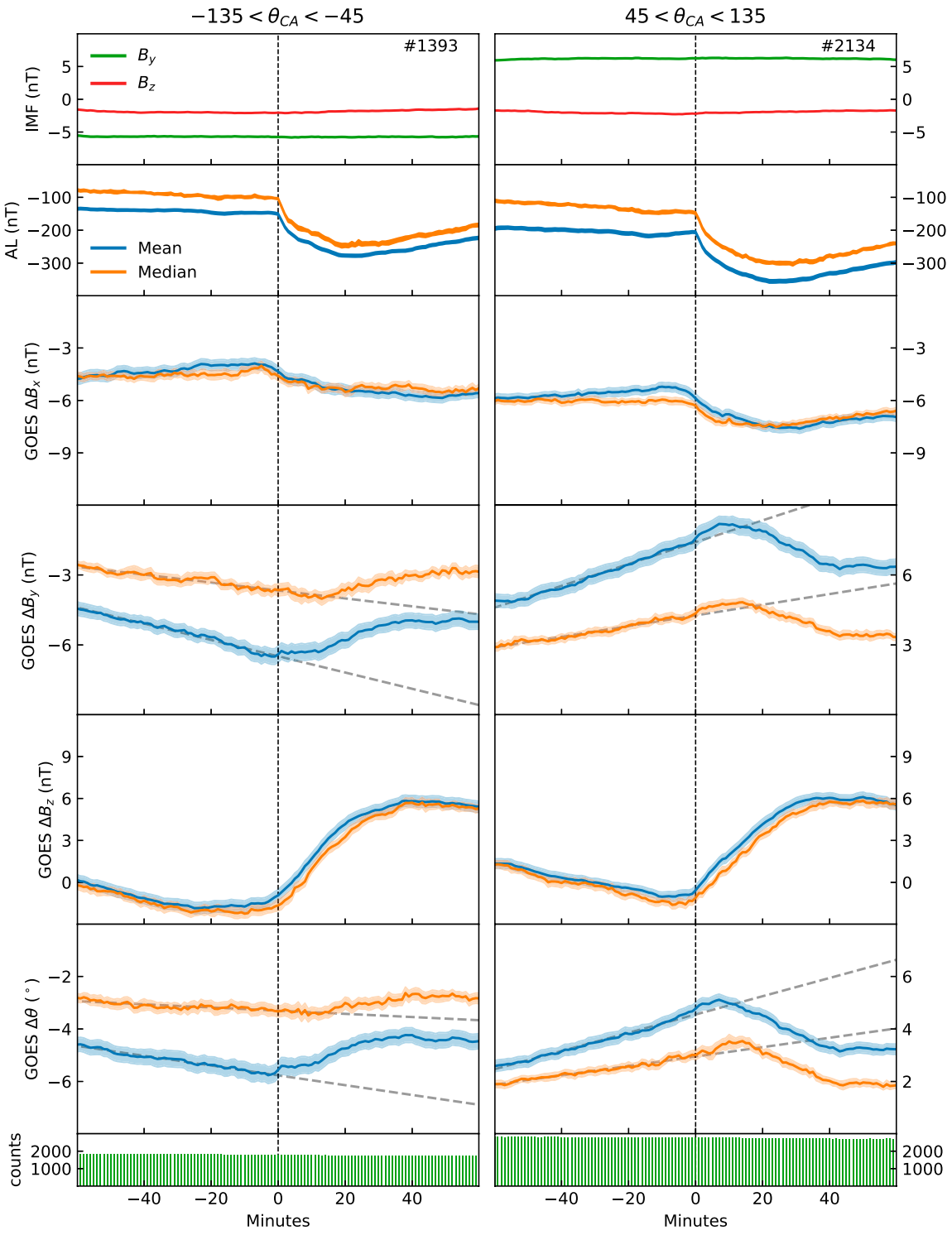

FIGURE 1
Superposed epoch analysis relative to substorm onset as identified by the N&G onset list. The rows display IMF B_y (green) and B_z (red), *AL* index, GOES ΔB_x, ΔB_y, ΔB_z, $\Delta\theta$ and number of observations. Mean is blue, median is orange and curve widths indicate standard error.

reduction is associated with the reduction of lobe pressure occurring in the period following substorm onset.

Few studies directly address how increased tail reconnection affect B_y in the closed magnetosphere. Cowley and Hughes (1983) parametrized their observations based on the *Kp* index–a measure of the general activity level and not specifically tail activity–and found that the average induced B_y decreases as the *Kp* value increases. Using measurements from Cluster neutral sheet crossings, Cao et al. (2014) also considered the *Kp* index, and found increasing B_y as *Kp* increases. However, they excluded neutral sheet crossings with high ion velocity to avoid the local influence of bursty bulk flow on the magnetic field, which could bias their data toward non-substorm intervals. The increased *Kp* thus represents increased dayside reconnection. Saita et al. (2011) used MHD simulations to study substorm-like events for non-zero IMF B_y. Their run with negative IMF B_y shows an enhancement of magnetotail B_y prior to onset and subsequently a reduction after onset, whereas their run with positive IMF B_y is more ambiguous. In three MHD runs presented by Ohma et al. (2021b), the mean B_y induced in the magnetotail consistently increases during the loading phase and decreases during the unloading phase.

In this study, we directly address how the large-scale B_y induced in the magnetotail is influenced by enhanced tail reconnection during periods with strong IMF B_y. We have done this using magnetic field measurements by Geostationary Operational Environmental Satellite (GOES) at geosynchronous orbit, and performed a superposed epoch analysis of the magnetic field observations relative to substorm onset. The data and method used in this study are described in the next section and the results of our analysis are presented in Section 3. We discuss the implications of the observations in Section 4 and conclude the paper in Section 5.

2 Data processing

We use magnetic field measurements obtained by the fluxgate magnetometers on board GOES 8–15, which are all spacecraft operating on geosynchronous orbit above North America (Singer et al., 1996). This constellation of spacecraft is referred to as GOES for the rest of this manuscript. Data are available from December 1995 to December 2019 and are considered in Solar Magnetic (SM) coordinates. After temperature compensation, the accuracy of the instrument is 1 nT. The solar wind data used in this study are the omni 1-min data, which is time shifted to the bow shock (King and Papitashvili, 2005). This data are presented in Geocentric Solar Magnetic (GSM) coordinates. Note that the two coordinate systems have a common *y*-axis.

To identify substorms, we use three different substorm onset lists. The first is the onset list presented by Newell and Gjerloev (2011), which is based on identifying negative bays in the *SML* index (Gjerloev, 2012). This index is based on ~100 magnetometers in the northern hemisphere, mainly at auroral latitudes, and quantifies the strength of the westward electrojet. Due to the large number of observatories in the auroral zone, the *SML* index is sensitive to auroral activations and therefore well suited to get a precise determination of substorm onset. The second onset list we use was presented by McPherron and Chu (2018). This list is based on the Midlatitide Positive Bay (MPB) index (Chu et al., 2015), which is based on 41 magnetometer observatories at mid-latitude in both hemispheres. We use a threshold level on the area of the bays of > 700 nT^{2}min (McPherron and Chu, 2018). This list complements the list based on identifying negative bays at auroral latitudes, as the identification is less sensitive to variations in the auroral zone latitude (Chu et al., 2014). In addition, Ohma et al. (2021a) demonstrated that auroral electrojet based indices are more prone to detect onsets from positive IMF B_y compared to negative IMF B_y, as the average bay signatures are more pronounced for IMF $B_y > 0$ in the northern hemisphere. No significant bias was observed in the McPherron and Chu (2018) list. The third list is presented by Ohtani and Gjerloev (2020). Like the N&G list, this list is based on identifying negative bays in the *SML* index. However, the list is specifically designed to identify isolated substorms. The onsets identified by the three substorm lists are the onsets of the expansion phase (beginning of the auroral substorm), and will be used as zero epoch in the subsequent analysis. In addition to the three onset lists, we have also generated a list of random times used as a control group to compare with the substorm onset lists. These times have been selected at random with similar frequency as the onset frequency from the three real onset lists during the IMF conditions considered in this study.

To identify the average behavior of the large-scale B_y component in the magnetotail (and the orientation of the magnetic field), we perform a superposed epoch analysis of the observed field relative to substorm onset. Only data between 22 and 4 magnetic local time are included in the statistics ($X_{SM} < -3.31\ R_E$). A few clear outliers (spikes) have also been removed from the GOES data. To select periods with dominant IMF B_y, only onsets where the mean IMF clock angle θ_{CA} in a 120-min window centered at onset is between -135° and -45° or between 45° and 135° are included. Intervals with less than 60 IMF vectors are discarded. We also ensure that the IMF orientation is stable in this interval by demanding that the circular variance within the 120-min interval is less than 0.1. This quantity is defined as $\sigma^2 = 1 - R = 1 - \sqrt{\langle \sin\theta_{CA}\rangle^2 + \langle \cos\theta_{CA}\rangle^2}$, where the angular brackets indicate the mean in the considered interval. It has previously been applied to quantify the IMF stability by e.g. Haaland et al. (2007) and Ohma et al. (2019).

We subtract the background magnetic field at the GOES locations using the T01 model (Tsyganenko, 2002a,b) during each substorm event before we calculate the superposed averages. However, instead of using the instantaneous solar wind values, we use the average solar wind values in the 120-min interval

10.3389/fspas.2022.958749

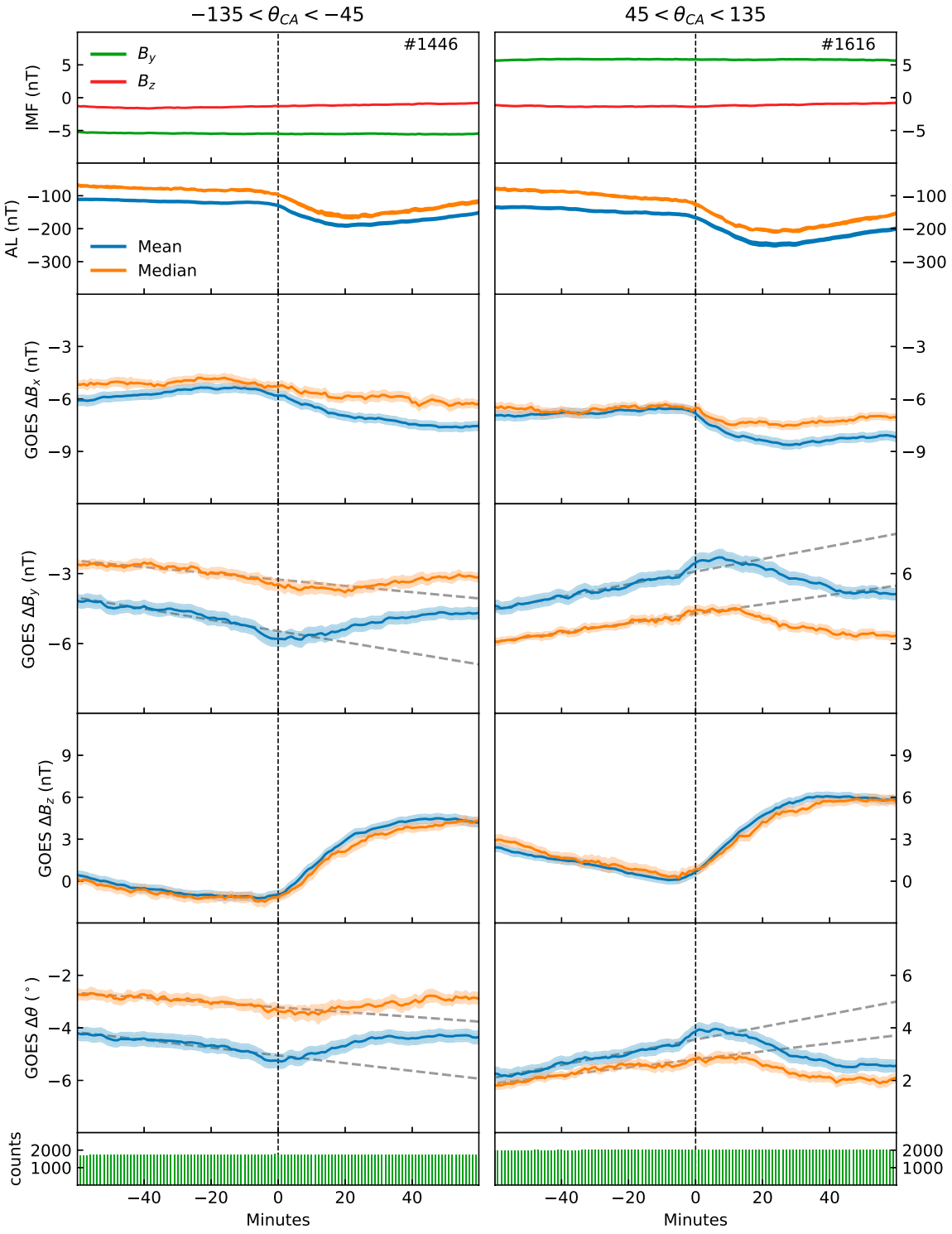

FIGURE 2
Superposed epoch analysis relative to substorm onset as identified by the McP&C onset list, format as Figure 1.

10.3389/fspas.2022.958749

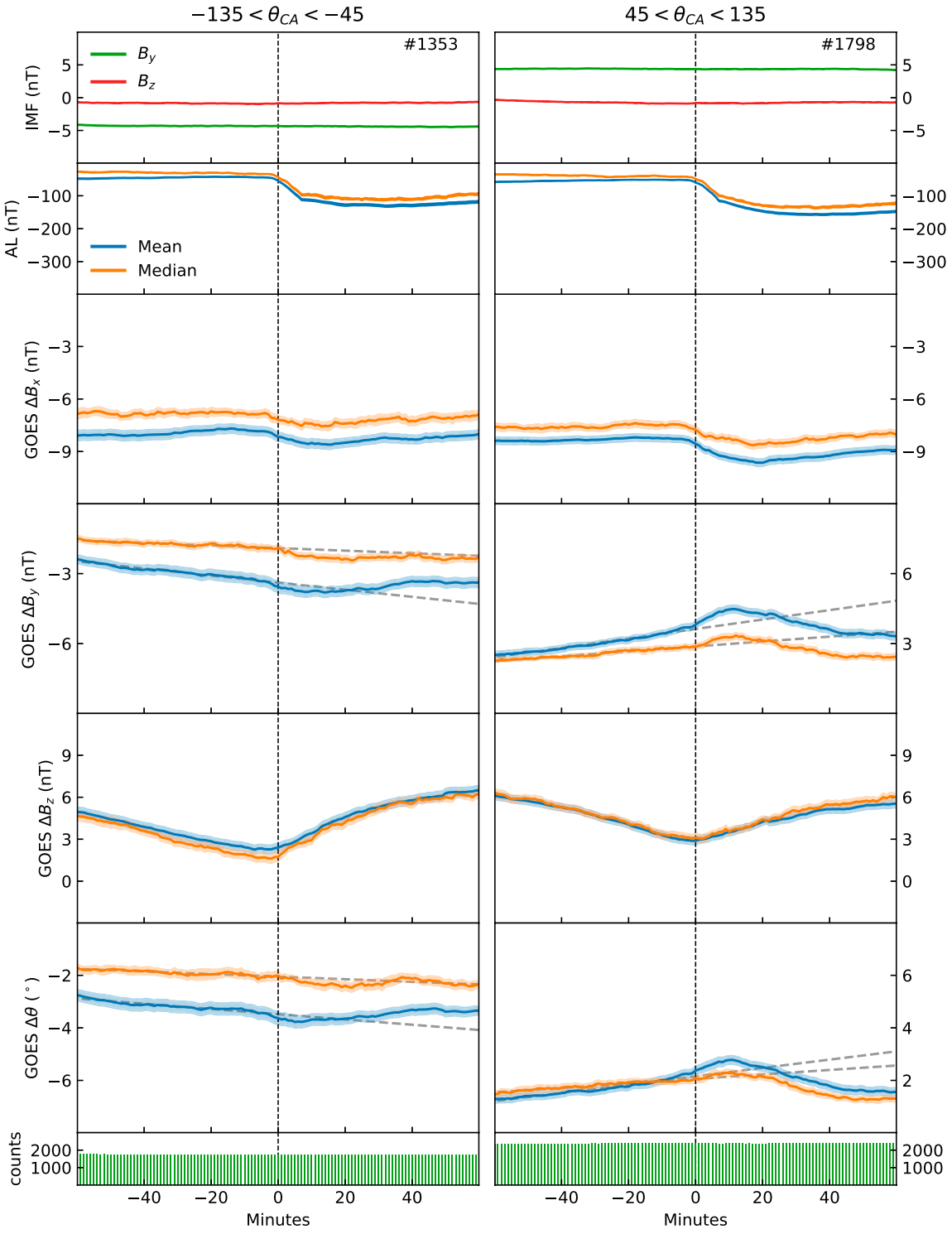

FIGURE 3
Superposed epoch analysis relative to substorm onset as identified by the O&G onset list, format as Figure 1.

10.3389/fspas.2022.958749

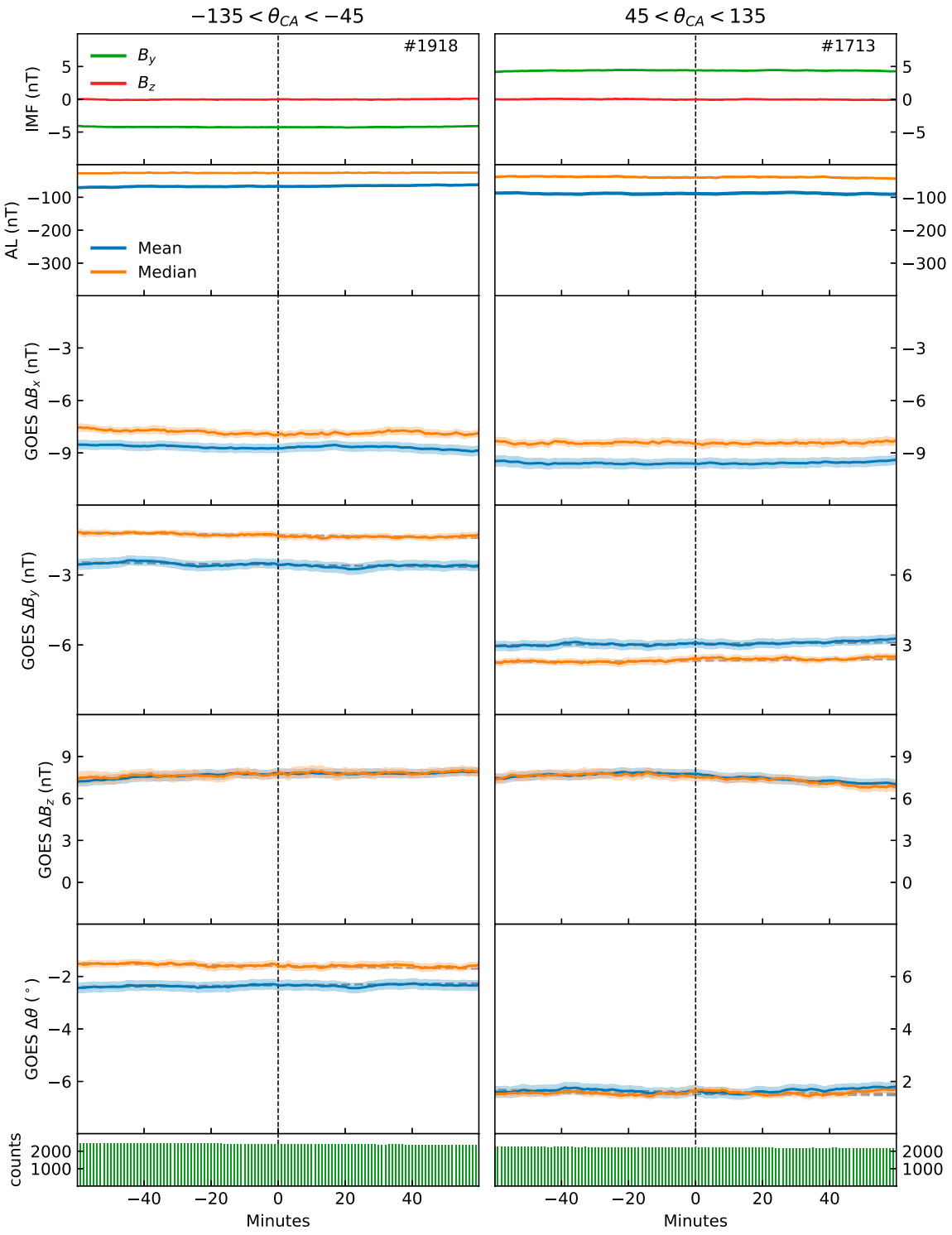

FIGURE 4
Superposed epoch analysis relative to randomly identified control times, format as Figure 1.

centered at onset for each event. We also set IMF B_y = 0. This ensures that the background magnetic field model is static throughout the different substorm events, and that the full induced B_y component is observed. Observed changes are thus only based on measurements and not influenced by potential changes in the background model during the substorms.

After subtracting the background, we calculate the superposed mean and median values. This is done for each component of the magnetic field, in addition to the orientation of the magnetic field in the *yz*-plane as measured in SM coordinates. To estimate the errors we use bootstrapping, which is applicable without assuming that the data are normally distributed. For each time step relative to onset we make a 100 random samples of the data (with replacement). The standard deviation of the mean and median values calculated from these 100 samples represents the error.

3527 onsets in the N&G list, 3062 onsets in the McP&C list and 3151 onsets in the O&G list fulfill all the above criteria. Note that as the three onset lists aim to identify the same phenomena, they are not independent and often identify the same substorms. Regardless, we use several lists as there are significant differences between them. If we consider onsets identified within ±15 min between the three lists to be the same substorm, N&G and McP&C have 1214 shared onsets, N&G and O&G have 1170 shared onsets, and McP&C and O&G have 717 shared onsets. 472 onsets are shared between all three lists. Thus, a major part of the onsets are only present in one list and the observations turn out to be significantly affected by the choice of list. By presenting the result using three lists, similarities and differences between various lists are transparently displayed and directly comparable.

3 Results

The superposed epoch analysis of the GOES magnetic field data relative to substorm onset is displayed in Figures 1–4, showing the mean values from 60 min before onset to 60 min after onset. The left column corresponds to $-135 < \theta_{CA} < -45$ and the right column corresponds to $45 < \theta_{CA} < 135$. Zero epoch indicates substorm onset, as identified by the N&G list (Figure 1), the McP&C list (Figure 2), the O&G list (Figure 3) and the control list (Figure 4). The first row in each figure displays the average IMF B_y (green) and IMF B_z (red), and the numbers in this panel indicate the number of substorms contributing to the statistics. The second row displays the superposed mean (blue) and median (orange) *AL* index. The mean and median B_x, B_y and B_z at geosynchronous orbit are shown in the third, forth and fifth row, respectively. The GOES magnetic field measurements have been labelled with Δ to signify that the observed deviations from the background T01 model are displayed. Note that the IMF is in Geocentric Solar Magnetic (GSM) coordinates, whereas the GOES data are in Solar Magnetic (SM) coordinates. The sixth panel displays how the superposed orientation of the magnetic field relative to the modelled field evolves in the *yz*-plane. For all six panels, the width of the curves indicate the error of the averages estimated using bootstrapping. Finally, the seventh row indicates the number of GOES vectors at each time step.

The trends observed in ΔB_x and ΔB_z in Figures 1–3, combined with the trend in the *AL* index, are consistent with the expected substorm behavior. There is a distinct negative bay in the *AL* index following onset in the three figures, and ΔB_z is clearly weakened prior to onset and dipolarized after onset. The dipolarization occurs in 40 min. This is longer than the 20 min when only the midnight region is considered (Liou et al., 2002), and is a consequence of using data between 22 and 04 magnetic local time. A small increase in ΔB_x before onset, followed by a clear weakening associated with the dipolarization, is observed in all panels. As evident from the figures, the changes in both ΔB_x and ΔB_z commence at or just before zero epoch, which is the expected behavior (Miyashita et al., 2009). The anticipated average evolution of these quantities relative to onset is thus captured by the statistics when considering the three real onset lists. Figure 4, which displays superposed statistics relative to randomly selected time steps, shows no signatures of substorm behaviour, as expected. This figure thus represents the average values for the solar wind conditions selected.

For the N&G list (Figure 1), clear peaks in $|\Delta B_y|$ are observed at or following substorm onset. For negative IMF B_y, the observed ΔB_y becomes increasingly negative prior to onset. Correspondingly, the observed ΔB_y becomes increasingly positive prior to onset for positive IMF B_y. Consistent trends are seen in $\Delta\theta$. As the trend prior to onset is near linear, we have made a linear fit based on the superposed values between -60 and 0 epoch time. These fits are shown as dashed lines, highlighting the changes that occur after onset. $|\Delta B_y|$ and $|\Delta\theta|$ peak at or in the minutes after onset, followed by a decrease during the latter part of the expansion phase and the recovery phase. The peaks in the superposed medians constantly lag the peaks in the superposed means. The absolute value of the superposed means are consistently higher that the superposed medians, and the changes are more extreme. This indicates that the tail of the distributions changes more than its central values.

For the McP&C list (Figure 2), clear peaks are seen in both $|\Delta B_y|$ and $|\Delta\theta|$ in all subset, except for the superposed median values during negative IMF B_y where the change is less pronounced. Again, the increase in $|\Delta B_y|$ and $|\Delta\theta|$ are near linear prior to onset. Peaks occur within 20 epoch followed by a significant decrease. The changes are less pronounced than the corresponding changes when using the N&G list. However, the average onset signatures are also less pronounced ($|\Delta B_z|$ and *AL*), indicating that the identified substorms are, on average, weaker. The differences between the superposed mean and median $|\Delta B_y|$ and $|\Delta\theta|$ using the McP&C list are similar as when using the N&G list.

The superposed mean and median of $|\Delta B_y|$ and $|\Delta\theta|$ using the O&G list are shown in Figure 3. The trends observed here deviate somewhat from that of the other two onset lists. The values increase linearly before onset, and peaks within 20 epoch, except the median for negative IMF B_y which does not have any clear peak. For positive IMF B_y, there is a clear increase following onset, before $|\Delta B_y|$ and $|\Delta\theta|$ decrease significantly. For negative IMF B_y, the superposed means clearly change compared to the linear fit, whereas the superposed medians do not. The trends are thus similar, but even less pronounced than the trends seen in both Figure 1 and Figure 2. This can again be related to weaker average substorms, as indicated by the more vague substorm signatures in ΔB_z and *AL* for the O&G list. As for the other onset lists, mean trends are more pronounced than median trends.

Finally, Figure 4 displays the superposed mean and median relative to randomly identified control times during similar conditions as the real substorm onset. For both positive and negative IMF B_y, $|\Delta B_y|$ and $|\Delta\theta|$ remian at a constant level. The trends seen in Figures 1–3 thus deviate significantly from the trends in the control sample shown in Figure 4, becoming more pronounced as the average substorm strength increases. While the increase in $|\Delta B_y|$ and $|\Delta\theta|$ before onset is gradual and near linear in all subsets, the response after onset is more variable between the lists and IMF B_y polarity. As seen in Figures 1–3, $|\Delta B_y|$ and $|\Delta\theta|$ continue to increase after substorm onset in most subsets. For the superposed mean values, the peaks occur between −1 to 14 min relative to onset, with a mean delay of 7 min. The median values peak between 5 and 22 min after onset, with a mean delay of 14 min. The peaks are directly followed by a significant decrease in nearly all subsets, lasting to about 40 min after onset.

The standard errors of the averages, represented by the width of the curves in Figures 1–4, ranges from 0.1 to 0.4 nT. These rather narrow intervals are a result of the large number of GOES measurements at each epoch time (1500–3000). The standard deviation, however, ranges from 8 to 16 nT. This demonstrates that although the mean and median values are determined with high certainty, individual measurements and events can deviate considerably from these average values. In the above error estimates, we have neglected the 1 nT accuracy of the magnetometers. This seems rather crude, as this accuracy is comparable to the changes observed in Figures 1–3. However, if we assume that the instrumental uncertainty is systematic, it will only affect the magnitude and not the trends seen in Figure 1, on the other hand, the instrumental uncertainty is random, either between subsequent measurements or between events due to different calibration with time or between spacecraft, the error of the averages reduces as $1/\sqrt{\text{number of measurements}}$. This gives an error of 0.02–0.03 nT, or about 10% of the uncertainty caused by the large spread in the data. Also note that the magnitude of the background based on the GOES measurements is about 85 nT. The changes relative to substorm onset are thus small compared to the background, reflected in the small angular changes seen in Figures 1–3. However, even small changes in a field line's orientation cause significant displacement between the hemispheres if a large part of the field line is affected (a dipolar field line at geosynchronous orbit has an arc length of about 103000 km).

4 Discussion

The average GOES $|B_y|$ on the nightside increases gradually and significantly during the growth phase. The mean $|B_y|$ peaks within 20 min of onset, and is followed by a significant decrease during the latter part of the expansion phase and recovery phase. The increase in the induced $|B_y|$ prior to onset clearly signifies that this component is introduced by another mechanism than tail reconnection, which is low during the loading phase (Dmitrieva et al., 2004; Juusola et al., 2011). Furthermore, $|B_y|$ is reduced during the unloading phase, most distinctly between 15 and 40 min after onset, which is the period when the tail reconnection rate maximizes (Juusola et al., 2011). This decrease suggests that the induced B_y component is actually reduced by tail reconnection. These observational trends are consistent with the notion that asymmetries arise directly as a consequence of asymmetric loading of magnetic flux to the lobes (Khurana et al., 1996; Tenfjord et al., 2015) and that near-Earth tail reconnection acts to reduce these interhemispheric asymmetries (Ohma et al., 2018; Reistad et al., 2018; Østgaard et al., 2018).

The statistics indicate an apparent inconsistency with the view that increased tail reconnection removes asymmetries, specifically the clear peak seen after onset for positive IMF B_y in the N&G and O&G lists. This peak implies that tail reconnection enhances B_y at geosynchronous altitudes in the initial part of the expansion phase. However, this does not indicate that the asymmetric configuration of the magnetosphere-ionosphere system in general is caused by tail reconnection as the induced B_y component (1) has already been increasing significantly during the growth phase and (2) increases for some minutes following onset before it decreases significantly, whereas the tail reconnection rate continues to increase throughout the entire expansion phase (Juusola et al., 2011). The observed peak and delay before the induced B_y component is reduced do, however, indicate that the response is on a different time scale that the response in the B_x and B_z component, which both start their substorm related reconfiguration at or a few minutes before the identified onsets. This could imply that the reduction of $|B_y|$ is a consequence of this reconfiguration rather than an integral part of the dipolarization front. There are several physical processes that can contribute to the observed delay between substorm onset and the clear reduction of induced B_y, as outlined in the following paragraphs.

It has been argued that the reduction of asymmetries during the unloading phase is related to the reduction of lobe pressure as open flux is being removed from the lobes by near-Earth tail reconnection (Ohma et al., 2018; Østgaard et al., 2018; Reistad et al., 2018). As pointed out by Ohma et al. (2018), the increased

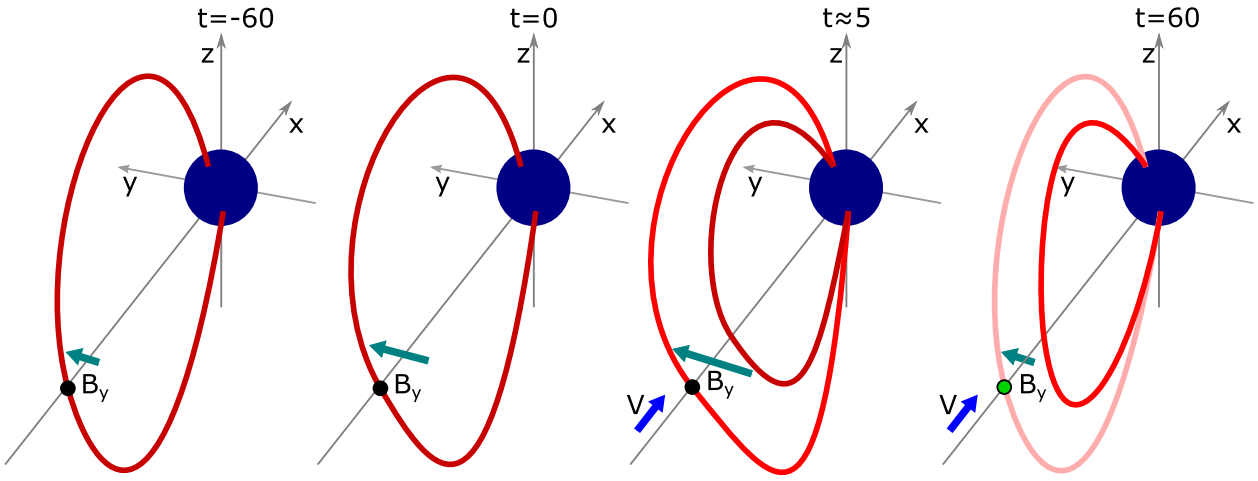

FIGURE 5
Configuration of magnetic field lines in the magnetotail at different stages of the substorm. There is a small positive B_y component at geosynchronous orbit (dark red field line) when the loading phase commences (t = −60 min). This B_y component increases gradually until substorm onset (t = 0 min) due to increased lobe pressure. In the initial unloading phase, B_y increases even more due to pileup of magnetic flux and transport of more asymmetric field lines (pure red) into geosynchronous orbit ($t \approx 5$ min). The induced B_y then decreases, as newly closed field lines (light red) enter geosynchronous orbit and the lobe pressure is reduced (t = 60 min).

magnetic field magnitude associated with the dipolarization also increases the magnetic stiffness of the closed field line region, making it less affected by pressure gradient forces imposed by the lobe pressure. Coxon et al. (2018) used data from the Cluster spacecraft to investigate the evolution of the average lobe pressure relative to substorm onset. They find a 20-min plateau in the lobe pressure after onset before the pressure is reduced. A source of this delay could be that substorm reconnection initially commences on closed field lines (McPherron et al., 1973; Hones, 1979) and that a few minutes elapse before the first open field line reconnects (Hones et al., 1986; Baker et al., 1996). Based on auroral observations, it can take ~10 min before the onset feature expands to the open-closed boundary (e.g. Elphinstone and Hearn, 1993; Milan et al., 2008). Furthermore, Juusola et al. (2011) demonstrated how the presence of fast flows in the tail, which can be considered as a proxy of the reconnection rate, build up during the expansion phase. There could thus be a delay before the nightside reconnection rate significantly surpasses the dayside reconnection rate to reduce the lobe pressure. The 20-min delay reported by Coxon et al. (2018) is in good agreement with the delay observed in this study. However, no clear delay between onset and the reduction of lobe pressure was seen by Caan et al. (1975, 1978) or Yamaguchi et al. (2004). Furthermore, Mende et al. (2003) showed that the polar cap on average contracts directly after onset based on a superposed epoch analysis of global far-ultraviolet auroral images.

In addition to considering the pressure balance between the lobes and the closed magnetotail, the transport and reconfiguration of the field within the tail must be considered. During the unloading phase, magnetic flux is transported Earthward from the reconnection region and the field lines become more dipolar. This leads to a pileup in the inner magnetosphere, increasing the magnetic field strength. If this occurs without changing the orientation of the field lines in the YZ-plane, both B_y and B_z increases. Since the ionospheric footpoint of magnetic field lines cannot move freely–there is a frictional force acting between the ionononized plamsa, trying to follow the magnetic field lines, and the neutral atmosphere–it will likely be a delay before the field lines start to move substantially in the azimuthal direction due to inertia. If this is the case, the induced B_y will increase in the initial unloading phase, whereas the orientation remains about constant. Based on Figures 1–3, this is not completely the case as $\Delta\theta$ increases after onset in some subsets. It is also possible that the field lines that enter geosynchronous orbit during the initial unloading phase are more asymmetric that the field lines they replace, as these field lines where closed also prior to onset, but located farther tailward. As shown by e.g. Ohma et al. (2021b), the asymmetries are largest near the open-closed boundary, which corresponds to the most tailward located field lines of the closed magnetotail. These field lines could thus increase the asymmetry as they enter geosynchronous altitudes.

A sketch of how we envision the large-scale configuration of the magnetotail relative to substorm onset is shown in Figure 5 during positive IMF B_y conditions. Four different time steps relative to substorm onset are shown, where the field lines are red and the green dots indicates the geosynchronous location. The green vectors indicate the magnitude of induced B_y and the blue vectors the presence of Earthward flow.The loading phase typically begins ~60 min before onset (Li et al., 2013). Asymmetric loading of magnetic flux has already been ongoing for some time at the

beginning of the loading phase due to our restrictions on θ_{CA}, which means that the magnetotail is already asymmetric at $t = -60$. Since the dayside reconnection rate is larger than the nightside reconnection rate during this phase, there is a flux pileup in the lobes. The magnetic pressure therefore increases, resulting in increased pressure gradient forces acting on the closed magnetotail. This causes a gradual increase in the induced B_y between -60 and 0 epoch, as the applied force change the field line orientation. The process continues until $t = 0$, where the lobe pressure maximizes. As indicated the sketch, the field line located at geosynchronous orbit (dark red) at $t = -60$ remains at about the same location until $t = 0$, but becomes considerably more twisted.

Reconnection commences in the magnetotail at $t = 0$, which cause the field lines in the inner magnetosphere to convect Earthward and dipolarize. In the first few minutes, reconnection occurs at closed field lines (e.g. Hones et al., 1986). In this initial unloading phase, the field lines keep or increase their orientation as they reconfigure, leading to an increase in B_y at geosynchronous orbit. At $t \approx 5$, the induced B_y peaks. This is indicated in the sketch, where a new field line (clear red) with larger B_y has replaced the field line located there at onset (dark red). Sometime after onset (typically a few minutes), reconnection reaches the open-closed boundary and open lobe field lines starts to reconnect. The lobe pressure then decreases as the open flux is removed, which in turn increases the pressure in the closed flux region. In addition, the field lines that became asymmetric during the loading phase are effectively transported Earthward and replaced by newly closed field lines. Since the B_y component in the lobes is generally lower than the B_y component in the closed magnetosphere (Kaymaz et al., 1994), they are less asymmetric when they reconnect. Furthermore, due to the enhanced convection, they spend less time in the tail before they are transported away. The closed field lines are thus exposed to the asymmetric pressure distribution for a shorter amount of time compared to before onset, and are thus not able to become very asymmetric before they are themselves replaced by new field lines. In response to this combination of the decreased lobe pressure, increased magnetic pressure at closed field lines and stronger convection, the magnetotail reconfigures to a more symmetric state. In the sketch ($t = 60$), a new field line (light red) populates the geosynchronous orbit, with a significantly reduced B_y component due to the above effects.

5 Summary

Performing a superposed epoch analysis of the tail magnetic field at geosynchronous orbit relative to substorm onset during IMF B_y dominated periods, we have shown that the induced $|B_y|$ component increases during the loading phase, peaks in the initial expansion phase and decreases during the remaining expansion and recovery phase. As anticipated, the peaks have the same polarity as the imposed IMF B_y component. The observed trends become more pronounced using substorm onset list that, on average, identify the strongest substorms. The observed evolution is consistent with asymmetric lobe pressure playing the major role in inducing B_y in the closed magnetotail (Khurana et al., 1996; Tenfjord et al., 2015) and that increased tail reconnection act to reduce the IMF B_y associated asymmetries (Ohma et al., 2018, 2021b; Reistad et al., 2018; Østgaard et al., 2018). The delay between substorm onset and the reduction of B_y observed at geosynchronous orbit is proposed to be caused by a combination of inertia, pileup of flux in the inner magnetosphere and a potential delay before lobe pressure decreases.

Data availability statement

Publicly available datasets were analyzed in this study. This data can be found here: The solar wind data including the AL index used in this study can be found at https://cdaweb.gsfc.nasa.gov/sp_phys/data/omni/ and the GOES data at https://satdat.ngdc.noaa.gov/sem/goes/data/. The Newell and Gjerloev (2011) and Ohtani and Gjerloev (2020) substorm lists can be found at https://supermag.jhuapl.edu/substorms/.

Author contributions

AO had the idea for the study, performed the statistical analysis and wrote the manuscript. KL, JR and NØ helped develop the idea and supported the work throughout the process. All authors contributed to manuscript revision, read, and approved the submitted version.

Funding

This project was funded by the Norwegian Research Council under contracts 223252/F50 and 300844/F50, and by the Trond Mohn Foundation.

Acknowledgments

We acknowledge the substorm timing lists identified by Newell and Gjerloev (2011), McPherron and Chu (2018) and Ohtani and Gjerloev (2020), the SMU and SML indices (Newell and Gjerloev, 2011) and the SuperMAG collaboration (Gjerloev, 2012).

Conflict of interest

The authors declare that the research was conducted in the absence of any commercial or financial relationships that could be construed as a potential conflict of interest.

Publisher's note

References

Akasofu, S.-I. (1964). The development of the auroral substorm. *Planet. Space Sci.* 12, 273–282. doi:10.1016/0032-0633(64)90151-5

Baker, D. N., Pulkkinen, T. I., Angelopoulos, V., Baumjohann, W., and McPherron, R. L. (1996). Neutral line model of substorms: Past results and present view. *J. Geophys. Res.* 101, 12975–13010. doi:10.1029/95JA03753

Browett, S. D., Fear, R. C., Grocott, A., and Milan, S. E. (2017). Timescales for the penetration of IMF by into the Earth's magnetotail. *J. Geophys. Res. Space Phys.* 122, 579–593. doi:10.1002/2016JA023198

Caan, M. N., McPherron, R. L., and Russell, C. T. (1977). Characteristics of the association between the interplanetary magnetic field and substorms. *J. Geophys. Res.* 82, 4837–4842. doi:10.1029/JA082i029p04837

Caan, M. N., McPherron, R. L., and Russell, C. T. (1975). Substorm and interplanetary magnetic field effects on the geomagnetic tail lobes. *J. Geophys. Res.* 80, 191–194. doi:10.1029/JA080i001p00191

Caan, M. N., McPherron, R. L., and Russell, C. T. (1978). The statistical magnetic signature of magnetospheric substorms. *Planet. Space Sci.* 26, 269–279. doi:10.1016/0032-0633(78)90092-2

Cao, J., Duan, A., Dunlop, M. W., Wei, X., and Cai, C. (2014). Dependence of IMF by penetration into the neutral sheet on IMF Bz and geomagnetic activity. *J. Geophys. Res. Space Phys.* 119, 5279–5285. doi:10.1002/2014JA019827

Case, N. A., Hartley, D. P., Grocott, A., Miyoshi, Y., Matsuoka, A., Imajo, S., et al. (2021). Inner magnetospheric response to the interplanetary magnetic field by component: Van allen probes and arase observations. *JGR. Space Phys.* 126, e2020JA028765. doi:10.1029/2020JA028765

Chu, X., Hsu, T.-S., McPherron, R. L., Angelopoulos, V., Pu, Z., Weygand, J. J., et al. (2014). Development and validation of inversion technique for substorm current wedge using ground magnetic field data. *JGR. Space Phys.* 119, 1909–1924. doi:10.1002/2013JA019185

Chu, X., McPherron, R. L., Hsu, T.-S., and Angelopoulos, V. (2015). Solar cycle dependence of substorm occurrence and duration: Implications for onset. *JGR. Space Phys.* 120, 2808–2818. doi:10.1002/2015JA021104

Cowley, S. W. H., and Hughes, W. J. (1983). Observation of an IMF sector effect in the Y magnetic field component at geostationary orbit. *Planet. Space Sci.* 31, 73–90. doi:10.1016/0032-0633(83)90032-6

Cowley, S. W. H. (1981). Magnetospheric asymmetries associated with the y-component of the IMF. *Planet. Space Sci.* 29, 79–96. doi:10.1016/0032-0633(81)90141-0

Coxon, J. C., Freeman, M. P., Jackman, C. M., Forsyth, C., Rae, I. J., and Fear, R. C. (2018). Tailward propagation of magnetic energy density variations with respect to substorm onset times. *J. Geophys. Res. Space Phys.* 123, 4741–4754. doi:10.1029/2017JA025147

Dmitrieva, N. P., Sergeev, V. A., and Shukhtina, M. A. (2004). Average characteristics of the midtail plasma sheet in different dynamic regimes of the magnetosphere. *Ann. Geophys.* 22, 2107–2113. doi:10.5194/angeo-22-2107-2004

Elphinstone, R. D., and Hearn, D. J. (1993). The auroral distribution and its relation to magnetospheric processes. *Adv. Space Res.* 13, 17–27. doi:10.1016/0273-1177(93)90306-V

Fairfield, D. H., and Ness, N. F. (1970). Configuration of the geomagnetic tail during substorms. *J. Geophys. Res.* 75, 7032–7047. doi:10.1029/JA075i034p07032

Fairfield, D. H. (1979). On the average configuraton of the geomagnetic tail. *J. Geophys. Res.* 84, 1950–1958. doi:10.1029/JA084iA05p01950

Frank, L. A., and Sigwarth, J. B. (2003). Simultaneous images of the northern and southern auroras from the Polar spacecraft: An auroral substorm. *J. Geophys. Res.* 108, 8015. doi:10.1029/2002JA009356

Gjerloev, J. W. (2012). The SuperMAG data processing technique. *J. Geophys. Res.* 117, A09213. doi:10.1029/2012JA017683

Grocott, A., Milan, S. E., Yeoman, T. K., Sato, N., Yukimatu, A. S., and Wild, J. A. (2010). Superposed epoch analysis of the ionospheric convection evolution during substorms: IMF$B_Y$dependence. *J. Geophys. Res.* 115, A00105. doi:10.1029/2010JA015728

Haaland, S. E., Paschmann, G., Förster, M., Quinn, J. M., Torbert, R. B., McIlwain, C. E., et al. (2007). High-latitude plasma convection from Cluster EDI measurements: Method and IMF-dependence. *Ann. Geophys.* 25, 239–253. doi:10.5194/angeo-25-239-2007

Hones, E. W., Jr., Fritz, T. A., Birn, J., Cooney, J., and Bame, S. J. (1986). Detailed observations of the plasma sheet during a substorm on april 24, 1979. *J. Geophys. Res.* 91, 6845–6859. doi:10.1029/JA091iA06p06845

Hones, E. W., Jr. (1979). Transient phenomena in the magnetotail and their relation to substorms. *Space Sci. Rev.* 23, 393–410. doi:10.1007/BF00172247

Juusola, L., Østgaard, N., and Tanskanen, E. (2011). Statistics of plasma sheet convection. *J. Geophys. Res.* 116, A08201. doi:10.1029/2011JA016479

Kaymaz, Z., Siscoe, G. L., Luhmann, J. G., Lepping, R. P., and Russell, C. T. (1994). Interplanetary magnetic field control of magnetotail magnetic field geometry: IMP 8 observations. *J. Geophys. Res.* 99, 11113–11126. doi:10.1029/94JA00300

Khurana, K. K., Walker, R. J., and Ogino, T. (1996). Magnetospheric convection in the presence of interplanetary magnetic fieldB_y: A conceptual model and simulations. *J. Geophys. Res.* 101, 4907–4916. doi:10.1029/95JA03673

King, J. H., and Papitashvili, N. E. (2005). Solar wind spatial scales in and comparisons of hourly Wind and ACE plasma and magnetic field data. *J. Geophys. Res.* 110, A02104. doi:10.1029/2004JA010649

Li, H., Wang, C., and Peng, Z. (2013). Solar wind impacts on growth phase duration and substorm intensity: A statistical approach. *J. Geophys. Res. Space Phys.* 118, 4270–4278. doi:10.1002/jgra.50399

Liou, K., Meng, C.-I., Lui, A. T. Y., Newell, P. T., and Wing, S. (2002). Magnetic dipolarization with substorm expansion onset. *J. Geophys. Res.* 107, 1131. doi:10.1029/2001JA000179

Liou, K., Newell, P. T., Sibeck, D. G., Meng, C.-I., Brittnacher, M., and Parks, G. (2001). Observation of IMF and seasonal effects in the location of auroral substorm onset. *J. Geophys. Res.* 106, 5799–5810. doi:10.1029/2000JA003001

Lui, A. T. Y. (1984). "Characteristics of the cross-tail current in the Earth's magnetotail," in *Magnetospheric currents*. Editor T. A. Potemra (American Geophysical Union), 28, 158–170. doi:10.1029/GM028p0158

McPherron, R. L., and Chu, X. (2018). The midlatitude positive bay index and the statistics of substorm occurrence. *JGR. Space Phys.* 123, 2831–2850. doi:10.1002/2017JA024766

McPherron, R. L. (1970). Growth phase of magnetospheric substorms. *J. Geophys. Res.* 75, 5592–5599. doi:10.1029/JA075i028p05592

McPherron, R. L., Russell, C. T., Kivelson, M. G., and Coleman, P. J. (1973). Substorms in space: The correlation between ground and satellite observations of the magnetic field. *Radio Sci.* 8, 1059–1076. doi:10.1029/RS008i011p01059

Mende, S. B., Frey, H. U., Morsony, B. J., and Immel, T. J. (2003). Statistical behavior of proton and electron auroras during substorms. *J. Geophys. Res.* 108, 1339. doi:10.1029/2002JA009751

Milan, S. E., Boakes, P. D., and Hubert, B. (2008). Response of the expanding/contracting polar cap to weak and strong solar wind driving: Implications for substorm onset. *J. Geophys. Res.* 113, A09215. doi:10.1029/2008JA013340

Milan, S. E., Provan, G., and Hubert, B. (2007). Magnetic flux transport in the dungey cycle: A survey of dayside and nightside reconnection rates. *J. Geophys. Res.* 112, A01209. doi:10.1029/2006JA011642

Miyashita, Y., Machida, S., Kamide, Y., Nagata, D., Liou, K., Fujimoto, M., et al. (2009). A state-of-the-art picture of substorm-associated evolution of the near-earth magnetotail obtained from superposed epoch analysis. *J. Geophys. Res.* 114, A01211. doi:10.1029/2008JA013225

Motoba, T., Hosokawa, K., Ogawa, Y., Sato, N., Kadokura, A., Buchert, S. C., et al. (2011). *In situ* evidence for interplanetary magnetic field induced tail twisting associated with relative displacement of conjugate auroral features. *J. Geophys. Res.* 116, A04209. doi:10.1029/2010JA016206

Newell, P. T., and Gjerloev, J. W. (2011). Evaluation of SuperMAG auroral electrojet indices as indicators of substorms and auroral power. *J. Geophys. Res.* 116, A12211. doi:10.1029/2011JA016779

Ohma, A., Østgaard, N., Laundal, K. M., Reistad, J. P., Hatch, S. M., and Tenfjord, P. (2021b). Evolution of IMF b_y induced asymmetries: The role of tail reconnection. *JGR. Space Phys.* 126, e2021JA029577. doi:10.1029/2021JA029577

Ohma, A., Østgaard, N., Reistad, J. P., Tenfjord, P., Laundal, K. M., Moretto Jørgensen, T., et al. (2019). Observations of asymmetric lobe convection for weak and strong tail activity. *J. Geophys. Res. Space Phys.* 124, 9999–10017. doi:10.1029/2019JA026773

Ohma, A., Østgaard, N., Reistad, J. P., Tenfjord, P., Laundal, K. M., Snekvik, K., et al. (2018). Evolution of asymmetrically displaced footpoints during substorms. *J. Geophys. Res. Space Phys.* 123. doi:10.1029/2018JA025869

Ohma, A., Reistad, J. P., and Hatch, S. M. (2021a). Modulation of magnetospheric substorm frequency: Dipole tilt and IMF b_y effects. *JGR. Space Phys.* 126, e2020JA028856. doi:10.1029/2020JA028856

Ohtani, S., and Gjerloev, J. W. (2020). Is the substorm current wedge an ensemble of wedgelets?: Revisit to midlatitude positive bays. *JGR. Space Phys.* 125, e2020JA027902. doi:10.1029/2020JA027902

Østgaard, N., Humberset, B. K., and Laundal, K. M. (2011a). Evolution of auroral asymmetries in the conjugate hemispheres during two substorms. *Geophys. Res. Lett.* 38, L03101. doi:10.1029/2010GL046057

Østgaard, N., Laundal, K. M., Juusola, L., Åsnes, A., Haaland, S. E., and Weygand, J. M. (2011b). Interhemispherical asymmetry of substorm onset locations and the interplanetary magnetic field. *Geophys. Res. Lett.* 38, L08104. doi:10.1029/2011GL046767

Østgaard, N., Mende, S. B., Frey, H. U., Immel, T. J., Frank, L. A., Sigwarth, J. B., et al. (2004). Interplanetary magnetic field control of the location of substorm onset and auroral features in the conjugate hemispheres. *J. Geophys. Res.* 109, A07204. doi:10.1029/2003JA010370

Østgaard, N., Reistad, J. P., Tenfjord, P., Laundal, K. M., Rexer, T., Haaland, S. E., et al. (2018). The asymmetric geospace as displayed during the geomagnetic storm on 17 august 2001. *Ann. Geophys.* 36, 1577–1596. doi:10.5194/angeo-36-1577-2018

Petrukovich, A. A., Baumjohann, W., Nakamura, R., Runov, A., and Balogh, A. (2005). Cluster vision of the magnetotail current sheet on a macroscale. *J. Geophys. Res.* 110, A06204. doi:10.1029/2004JA010825

Reistad, J. P., Østgaard, N., Laundal, K. M., Ohma, A., Snekvik, K., Tenfjord, P., et al. (2018). Observations of asymmetries in ionospheric return flow during different levels of geomagnetic activity. *J. Geophys. Res. Space Phys.* 123, 4638–4651. doi:10.1029/2017JA025051

Reistad, J. P., Østgaard, N., Laundal, K. M., and Oksavik, K. (2013). On the non-conjugacy of nightside aurora and their generator mechanisms. *J. Geophys. Res. Space Phys.* 118, 3394–3406. doi:10.1002/jgra.50300

Reistad, J. P., Østgaard, N., Tenfjord, P., Laundal, K. M., Snekvik, K., Haaland, S. E., et al. (2016). Dynamic effects of restoring footpoint symmetry on closed magnetic field lines. *J. Geophys. Res. Space Phys.* 121, 3963–3977. doi:10.1002/2015JA022058

Rong, Z. J., Lui, A. T. Y., Wan, W. X., Yang, Y. Y., Shen, C., Petrukovich, A. A., et al. (2015). Time delay of interplanetary magnetic field penetration into Earth's magnetotail. *J. Geophys. Res. Space Phys.* 120, 3406–3414. doi:10.1002/2014JA020452

Saita, S., Kadokura, A., Sato, N., Fujita, S., Tanaka, T., Ebihara, Y., et al. (2011). Displacement of conjugate points during a substorm in a global magnetohydrodynamic simulation. *J. Geophys. Res.* 116, A06213. doi:10.1029/2010JA016155

Singer, H., Matheson, L., Grubb, R., Newman, A., and Bouwer, D. (1996). "Monitoring space weather with the GOES magnetometers," in *GOES-8 and beyond*. Editor E. R. Washwell (International Society for Optics and Photonics SPIE), 2812, 299–308. doi:10.1117/12.254077

Tenfjord, P., Østgaard, N., Haaland, S. E., Snekvik, K., Laundal, K. M., Reistad, J. P., et al. (2018). How the IMFB_yInduces a LocalB_yComponent during northward IMF$B_z$and characteristic timescales. *J. Geophys. Res. Space Phys.* 123, 3333–3348. doi:10.1002/2018JA025186

Tenfjord, P., Østgaard, N., Snekvik, K., Laundal, K. M., Reistad, J. P., Haaland, S. E., et al. (2015). How the IMF B_y induces a B_y component in the closed magnetosphere and how it leads to asymmetric currents and convection patterns in the two hemispheres. *J. Geophys. Res. Space Phys.* 120, 9368–9384. doi:10.1002/2015JA021579

Tenfjord, P., Østgaard, N., Strangeway, R., Haaland, S. E., Snekvik, K., Laundal, K. M., et al. (2017). Magnetospheric response and reconfiguration times following IMF B_y reversals. *J. Geophys. Res. Space Phys.* 122, 417–431. doi:10.1002/2016JA023018

Tsyganenko, N. A. (2002a). A model of the near magnetosphere with a dawn-dusk asymmetry 1. Mathematical structure. *J. Geophys. Res.* 107, SMP 12-1–SMP 12-15. doi:10.1029/2001JA000219

Tsyganenko, N. A. (2002b). A model of the near magnetosphere with a dawn-dusk asymmetry 2. Parameterization and fitting to observations. *J. Geophys. Res.* 107, SMP 10-11–SMP 10-17. doi:10.1029/2001JA000220

Wild, J. A., Woodfield, E. E., and Morley, S. K. (2009). On the triggering of auroral substorms by northward turnings of the interplanetary magnetic field. *Ann. Geophys.* 27, 3559–3570. doi:10.5194/angeo-27-3559-2009

Wing, S., Newell, P. T., Sibeck, D. G., and Baker, K. B. (1995). A large statistical study of the entry of interplanetary magnetic field Y-component into the magnetosphere. *Geophys. Res. Lett.* 22, 2083–2086. doi:10.1029/95GL02261

Yamaguchi, R., Kawano, H., Ohtani, S., Kokubun, S., and Yumoto, K. (2004). Total pressure variations in the magnetotail as a function of the position and the substorm magnitude. *J. Geophys. Res.* 109, A03206. doi:10.1029/2003JA010196

frontiers | Frontiers in Astronomy and Space Sciences

TYPE Original Research
PUBLISHED 27 February 2023
DOI 10.3389/fspas.2023.1062265

OPEN ACCESS

EDITED BY
Mike Lockwood,
University of Reading, United Kingdom

REVIEWED BY
Jun Liang,
University of Calgary, Canada
Ingrid Cnossen,
British Antarctic Survey (BAS),
United Kingdom

*CORRESPONDENCE
Yue Deng,
yuedeng@uta.edu

SPECIALTY SECTION
This article was submitted to Space Physics, a section of the journal Frontiers in Astronomy and Space Sciences

RECEIVED 05 October 2022
ACCEPTED 03 February 2023
PUBLISHED 27 February 2023

CITATION
Hong Y, Deng Y, Zhu Q, Maute A, Hairston MR, Waters C, Sheng C, Welling D and Lopez RE (2023), Inter-hemispheric asymmetries in high-latitude electrodynamic forcing and the thermosphere during the October 8–9, 2012, geomagnetic storm: An integrated data–Model investigation.
Front. Astron. Space Sci. 10:1062265.
doi: 10.3389/fspas.2023.1062265

Inter-hemispheric asymmetries in high-latitude electrodynamic forcing and the thermosphere during the October 8–9, 2012, geomagnetic storm: An integrated data–Model investigation

Yu Hong[1], Yue Deng[1]*, Qingyu Zhu[2], Astrid Maute[2], Marc R. Hairston[3], Colin Waters[4], Cheng Sheng[1], Daniel Welling[1] and Ramon E. Lopez[1]

[1]Department of Physics, University of Texas at Arlington, Arlington, TX, United States, [2]High Altitude Observatory, National Center for Atmospheric Research, Boulder, CO, United States, [3]Center for Space Sciences, University of Texas at Dallas, Richardson, TX, United States, [4]Centre for Space Physics, University of Newcastle, Newcastle, NSW, Australia

Inter-hemispheric asymmetry (IHA) in Earth's ionosphere–thermosphere (IT) system can be associated with high-latitude forcing that intensifies during storm time, e.g., ion convection, auroral electron precipitation, and energy deposition, but a comprehensive understanding of the pathways that generate IHA in the IT is lacking. Numerical simulations can help address this issue, but accurate specification of high-latitude forcing is needed. In this study, we utilize the Active Magnetosphere and Planetary Electrodynamics Response Experiment-revised fieldaligned currents (FACs) to specify the high-latitude electric potential in the Global Ionosphere and Thermosphere Model (GITM) during the October 8–9, 2012, storm. Our result illustrates the advantages of the FAC-driven technique in capturing high-latitude ion drift, ion convection equatorial boundary, and the storm-time neutral density response observed by satellite. First, it is found that the cross-polar-cap potential, hemispheric power, and ion convection distribution can be highly asymmetric between two hemispheres with a clear B_y dependence in the convection equatorial boundary. Comparison with simulation based on mirror precipitation suggests that the convection distribution is more sensitive to FAC, while its intensity also depends on the ionospheric conductance-related precipitation. Second, the IHA in the neutral density response closely follows the IHA in the total Joule heating dissipation with a time delay. Stronger Joule heating deposited associated with greater high-latitude electric potential in the southern hemisphere during the focus period generates more neutral density as well, which provides some evidences that the high-latitude forcing could become the dominant factor to IHAs in the thermosphere when near the equinox. Our study improves the understanding of storm-time IHA in high-latitude forcing and the IT system.

KEYWORDS

inter-hemispheric asymmetry, ion convection equatorial boundary, ionosphere–thermosphere system, high-latitude electrodynamic forcing, IMF B_y dependence, storm phase response, thermospheric neutral density

1 Introduction

Earth's ionosphere–thermosphere (IT) system can be highly affected by high-latitude forcing, which plays a significant role in the energy and momentum transfer between solar wind and the magnetosphere–ionosphere (MI) system (Richmond, 2011). This forcing strongly intensifies during geomagnetic storms and is often characterized by large-scale anti-sunward convection flows and equatorward expansions of the auroral oval (Cowley and Lockwood, 1992; Fuller-Rowell et al., 1994). As a fundamental element in storm-time magnetospheric energy transport, the field-aligned currents (FACs) are associated with the ion convection patterns (Shi et al., 2020), along with an increase in Joule heating both locally and globally (Deng et al., 2018). As a global phenomenon, storm-time high-latitude forcing and its effects on the IT system can extend from the polar region to lower latitudes, with characteristic responses at different local times (LTs) and hemispheres (Pi et al., 1997; Jakowski et al., 2005; Basu et al., 2008; Astafyeva et al., 2014). One of the principal expansions is that when the interplanetary magnetic field (IMF) B_z suddenly turns negative, the enhanced magnetospheric convection cannot be fully shielded by the ring current in the magnetosphere and the region-2 FAC (Blanc et al., 1983; Goldstein et al., 2005). Different storm-related IT responses have been reported, such as electron density variations including polar patches and total electron content (TEC), traveling ionospheric disturbances (TIDs), and penetration electric fields (Tsurutani et al., 2008; Tulasi Ram et al., 2009; Jin and Xiong, 2020).

Due to Earth's seasonal dipole tilt, the geomagnetic field configuration, and asymmetric high-latitude forcing (Hong et al., 2021), the storm-time IT responses can be significantly different between the Northern and Southern hemispheres, known as the IT system inter-hemispheric asymmetry (IHA). While all the causes are important, this study focuses on high-latitude forcing since the seasonal effect is considered to be reduced due to the data interval being near the equinox. It should be noted that the influence of the geomagnetic field is already included in high-latitude forcing since the forcing used in this study is the ultimate response of Earth's upper atmosphere. We cannot separate the asymmetry of the original magnetosphere sources from the geomagnetic field effects regardless of which season it is (Förster and Cnossen, 2013). Previous studies have shown that high-latitude forcing strongly manifests asymmetries with complex temporal and spatial changes during geomagnetic storms (Burch et al., 1985; Reiff and Burch, 1985; Sandholt and Farrugia, 2007; Cousins and Shepherd, 2010), which could drastically affect the IT system in the two hemispheres. It has been emphasized by previous studies that the general FACs deduced from observations also exhibit hemispheric differences (Anderson et al., 2008; Green et al., 2009; Coxon et al., 2016; Workayehu et al., 2020). The IMF B_y component in the geocentric solar magnetospheric (GSM) coordinate system, i.e., dawn–dusk direction, is thought to be one main cause of a number of asymmetric features in the magnetosphere and IT system (Walsh et al., 2014). Studies also showed that IMF B_y causes obvious IHAs in auroral precipitation (Sandholt and Farrugia, 2007) and high-latitude Joule heating (McHarg et al., 2005). A full understanding of the IT system relies on knowledge of IHA. Despite these extensive studies, the global consequences and causes of the geomagnetic storm-related IHAs remain unknown.

General circulation models (GCMs) are widely used to study the IT system during geomagnetic storms. In order to specify the high-latitude forcing in GCMs, the most common approach is to utilize empirical models, e.g., using Weimer (2005) to specify convection patterns and using Fuller-Rowell and Evans (1987) or Newell et al. (2009) to specify auroral particle precipitation. However, since empirical models mainly describe the average conditions for a given state, they have issues in representing abrupt temporal changes or spatial distributions during a specific storm (Heelis and Maute, 2020). Typically, the two hemispheres are assumed to be mirror images considering a switch in IMF B_y and dipole tilt, and the data from the two hemispheres have been combined without considering differences in data coverage. Certainly, more realistic specifications of external forcing are required to accurately simulate the storm-time global IT responses. For example, magnetohydrodynamic (MHD) models can also be used to specify the high-latitude forcing of GCMs, such as the connection between the Lyon–Fedder–Mobarry (LFM) MHD model and the Thermosphere–Ionosphere-Electrodynamics General Circulation Model (TIEGCM), and the coupled magnetosphere–ionosphere–thermosphere (CMIT) model (Wang et al., 2004; Wiltberger et al., 2004). In addition, the Assimilative Mapping of Ionospheric Electrodynamics (AMIE) technique (Richmond and Kamide, 1988) can provide high-latitude electric potential and electron precipitation patterns used for driving GCMs (Lu et al., 2014; Lu et al., 2020). The Active Magnetosphere and Planetary Electrodynamics Response Experiment (AMPERE) gives another alternative way to calculate the high-latitude electric potential by using the derived FAC and pre-defined electron precipitation or ionospheric conductance patterns (Maute et al., 202l; Robinson et al., 2021; Zhu et al., 2022), which shows improved agreement between simulations and experimental data in driving GCMs for storms (Maute et al., 202l; Maute et al., 2022; Zhu et al., 2022b).

Motivated by the FAC-driven approach and AMIE electron precipitation patterns, the causes and consequences of IHAs of high-latitude forcing and IT responses during the October 8–9, 2012, storm have been investigated systematically with both data and models from over the high, middle, and low latitudes. The remaining part of this paper is organized as follows: Section 2 introduces the methodology of this study. Section 3 overviews the geophysical conditions for the October 8–9, 2012, geomagnetic storm in brief. Section 4 presents the main results of this study through comprehensive data–model and model–model comparisons. Section 5 summarizes the paper.

2 Methodology

The present study utilizes integrated data from multi-instrument observations and models. The satellite observations are given in Section 2.1. Section 2.2 presents the GITM model. The newly developed FAC-driven procedure is given in Section 2.3. Section 2.4 illustrates how we determine the ion convection equatorial boundary according to DMSP observation.

2.1 Data

2.1.1 DMSP ion drift

Data from three Defense Meteorological Satellite Program (DMSP) satellites (i.e., F16, F17, and F18) are used in this study. They flew in sun-synchronous orbits at an altitude of ~840 km with an inclination angle of ~98.8° (Rich and Hairston, 1994) primarily in the dawn–dusk direction during the October 8–9, 2012, geomagnetic storm. The cross-track ion drift (V_y) is measured by using the onboard Special Sensor for Ions, Electrons, and Scintillation (SSIES), which has a temporal resolution of 1 s. In this study, the data with the quality flag of 1 (i.e., most reliable) are used. A linear baseline correction is applied to the original V_y data to remove some co-rotation effects and to ensure V_y is zero at 45° |magnetic latitude| (|MLAT|). Afterward, a 13-point sliding window is applied to the corrected data in order to reduce very-high-frequency fluctuations and extract the large-scale ion convection at high-latitude regions.

2.1.2 GOCE neutral density data

The Gravity Field and Steady-State Ocean Circulation Explorer (GOCE) satellite was launched on 17 March 2009. The satellite was a polar-orbiting satellite (inclination angle: 96.5°) and flew in a near-circular orbit with an altitude from 250 km to 280 km (Bruinsma et al., 2014). The solar local times (SLTs) of the ascending and descending nodes of the GOCE were about 19 and 07 h, respectively. The neutral mass density (hereafter, neutral density for simplicity) was measured by using an onboard accelerometer with a temporal resolution of 10 s (Doornbos et al., 2014). To reduce the variation caused by the satellite orbit altitude change, the neutral density data are normalized to a constant altitude of 270 km using the NRLMSIS 2.0 model (Emmert et al., 2021). More details of the density normalization technique can be found in Bruinsma et al. (2006).

2.1.3 AMPERE FAC data

The AMPERE high-latitude FAC densities are derived from the horizontal magnetic field perturbations measured by 66 Iridium satellites which are distributed along six longitudinally equally spaced orbital planes (Anderson et al., 2002). Each Iridium satellite flies in a near-polar orbit at an altitude of 780 km with an orbital period of 104 min. The radial current components are calculated by fitting the magnetic perturbations measured within a 10-min time window using spherical cap harmonic basis functions (Waters et al., 2001; Green et al., 2006; Waters et al., 2020). Specifically, the patterns are fitted with a longitude order of 5 and latitude order of 20 (i.e., 3°) between colatitude 0° and 60° in the Altitude-Adjusted Corrected Geomagnetic (AACGM) coordinates (Baker and Wing, 1989). The temporal resolution of the FAC data is up to 2 min, and the spatial resolution of the FAC data is 1° in MLAT and 1 h in the magnetic local time (MLT) (Anderson et al., 2014). In this study, AMPERE FAC densities with a magnitude below 0.2 μ A/m^2 mainly distributed in the polar cap region and below 50° |MLAT| are removed, defined by being smaller than the noise level. In addition, due to differences in the geomagnetic field magnitude and the curvature of the magnetic field, the FAC pattern is mapped from 780 km to the APEX reference height of 110 km based on a factor of 1.343. Using a bilinear interpolation, the 10-min resolution AMPERE FAC patterns are spatially interpolated to the electrodynamic solver's grids and then temporally interpolated into a 2 s cadence at which the simulation is performed using linear interpolation.

2.2 GITM

The Global Ionosphere and Thermosphere Model (GITM) is a three-dimensional first-principle general circulation model for Earth's thermosphere and ionosphere system (Ridley et al., 2006). The GITM solves continuity, momentum, and energy equations in a spherical coordinate framework to calculate the density, velocity, and temperature of neutrals, ions, and electrons. The GITM has a flexible grid size and can use a stretchable grid in latitude and altitude. Moreover, the GITM relaxes the hydrostatic assumption in the vertical direction, which allows for the evaluation of non-hydrostatic impacts on the IT system (Lin et al., 2017; Deng et al., 2021). The global ionospheric electrodynamic solver in the GITM is the NCAR-3D electrodynamic model (hereafter NCAR-3D, Maute and Richmond, 2017), which is coupled into the GITM by Zhu et al. (2019). More details about the GITM can be found in Ridley et al. (2006).

In this study, two main GITM simulations were run with different high-latitude electrodynamic forcing: driven by empirical models and by more realistic patterns. A summary of the high-latitude forcing settings of these runs is given in Table 1.

For run 1, the high-latitude electric potential is specified by the Weimer 2005 model (hereafter W05, Weimer, 2005), and electron precipitation is specified by the Auroral energy Spectrum and High-Latitude Electric field variabilitY (ASHLEY) model (Zhu et al., 2021). Both W05 and ASHLEY are driven by IMF and solar wind data. For run 2, the high-latitude electric potential is calculated using AMPERE FAC data and the electron precipitation is specified by the AMIE patterns. The data inputs to AMIE patterns for this storm event include the horizontal magnetic perturbations from 261 ground magnetometers (with 205 in the NH and 56 in the SH) and the electron precipitation measured by the Special Sensor of Ultraviolet Spectrographic Imager (SSUSI) onboard DMSP F16-18 satellites. Details about the AMIE can be found in Lu (2017). More realistic patterns which can resolve additional dynamic and spatial structures than the statistically averaged empirical models are used in run 2 as compared to run 1.

In each simulation, the GITM was run with a spatial resolution of 5° in geographic longitude, 2.5° in geographic latitude, and 1/3 scale height in altitude. The time step of both simulations is 2 s. Realistic IMF B_y and B_z, solar wind, and $F_{10.7}$ data from the CDAWeb OMNI data product are used as model inputs. Specifically, in this study, the GITM simulations run 1 and run 2 are carried out with a 3-day pre-run (00UT (universal time) 10/01-00UT 10/03), a 5-day quiet time (00UT 10/03-00UT 10/08), and a 2-day event time (00UT 10/08 - 00UT 10/10) based on their corresponding high-latitude forcing. The purpose of a pre-run is to ramp up the model from an initial condition to a diurnally reproducible state during the time of interest (Deng and Ridley, 2006), and the outputs during that period typically are not used for scientific study.

TABLE 1 Summary of simulations conducted in this study.

Simulations	Electric ion convection	Auroral electron precipitation
Run 1	Weimer (2005)	ASHLEY-A
Run 2	FAC-driven NCAR-3D	AMIE electron precipitation pattern
Run 3	FAC-driven NCAR-3D	AMIE precipitation (mirror from the NH)

2.3 FAC-driven procedure

This subsection gives a brief overview of the FAC-driven procedure used in this study, and details can be found in Maute et al. (2021) and Zhu et al. (2022). The first step is to calculate the high-latitude electric potential (Φ^R) based on the current continuity equation:

$$\begin{aligned} & p^c \frac{\partial}{\partial \phi_m}\left[\frac{\Sigma_{\phi\phi}^{N/S}}{\cos\lambda_m}\frac{\partial \Phi^{RN/S}}{\partial \phi_m}+\Sigma_{\phi\lambda}^{N/S}\frac{\partial \Phi^{RN/S}}{\partial|\lambda_m|}\right] \\ & +p^c\frac{\partial}{\partial|\lambda_m|}\left[\Sigma_{\lambda\phi}^{N/S}\frac{\partial \Phi^{RN/S}}{\partial \phi_m}+\Sigma_{\lambda\lambda}^{N/S}\cos\lambda_m\frac{\partial \Phi^{RN/S}}{\partial|\lambda_m|}\right] \\ & -(1-p^c)\sigma^R R\cos\lambda_m\Phi^{RN/S} \\ & =p^c\left(R\left[\frac{\partial K_{m\phi}^{DN/S}}{\partial \phi_m}+\frac{\partial\left(K_{m\lambda}^{DN/S}\cos\lambda_m\right)}{\partial|\lambda_m|}\right]+J_{mr}^{N/S}R^2\cos\lambda_m\right), \end{aligned} \quad (1)$$

where

$J_{mr}^{N/S}$ is the FAC input in the Northern (N) and Southern (S) hemispheres.

λ_m, ϕ_m are the magnetic latitude and longitude, respectively, in the modified apex coordinate.

R ($= R_E + h_R$) is the radius to the conducting ionospheric layer with h_R = 110 km.

σ^R, Φ^R are the reference conductivity and high-latitude potential, respectively.

p^c is the ratio factor changing with magnetic latitude.

Σ is the integrated ionospheric conductivities term along a field line.

K^D is the integrated neutral dynamo current term integrated along a field line.

The superscripts N and S represent quantities in the Northern and Southern hemispheres, respectively. The specific definitions of the ionospheric conductivities Σ_{ij} $(i,j = \phi,\lambda)$ and neutral dynamo current K_{mj}^D $(j = \phi,\lambda)$ can be found in Richmond (1995). To specify the boundary of the high-latitude electric potential (Φ^R), a ratio factor p^c varying with magnetic latitude λ_m is used for both hemispheres: p^c is 1 poleward of $|\lambda_m|$ = 45° and is 0 equatorward of $|\lambda_m|$ = 40° and linearly changes between 0 and 1 for the region 40° < $|\lambda_m|$ < 45°. This setting ensures that the high-latitude electric potential (Φ^R) is zero equatorward of $|\lambda_m|$ = 40°.

Once the high-latitude electric potential (Φ^R) in each hemisphere is calculated, the second step is to calculate the global electric potential (Φ) based on Φ^R:

$$\begin{aligned} & p\frac{\partial}{\partial \phi_m}\left[\frac{\Sigma_{\phi\phi}^{T}}{\cos\lambda_m}\frac{\partial \Phi}{\partial \Phi_m}+\Sigma_{\phi\lambda}^{T}\frac{\partial \Phi}{\partial|\lambda_m|}\right] \\ & +p\frac{\partial}{\partial|\lambda_m|}\left[\Sigma_{\lambda\phi}^{T}\frac{\partial \Phi}{\partial \Phi_m}+\Sigma_{\lambda\lambda}^{T}\cos\lambda_m\frac{\partial \Phi}{\partial|\lambda_m|}\right]-(1-p)\sigma^R R\cos\lambda_m\Phi \\ & =pR\left[\frac{\partial K_{m\phi}^{DT}}{\partial \Phi_m}+\frac{\partial\left(K_{m\lambda}^{DT}\cos\lambda_m\right)}{\partial|\lambda_m|}\right]-(1-p)\sigma^R R\cos\lambda_m\Phi^R, \end{aligned} \quad (2)$$

where

Σ^T is the total integrated conductivities of both hemispheres.

K^{DT} is the total neutral dynamo of both hemispheres.

p is the ratio factor changing with magnetic latitude.

Here, the superscript T means the sum of quantities from both hemispheres. p is 1 equatorward of $|\lambda_m|$ = 50° and is 0 poleward of $|\lambda_m|$ = 55° and linearly changes between 1 and 0 for the region 50° < $|\lambda_m|$ < 55°, which means that only the neutral dynamo potential is used equatorward of the lower boundary, e.g., $|\lambda_m|$ = 50° and only the high-latitude potential is used poleward of, e.g., $|\lambda_m|$ = 55° and a combination in between. In this study, similar to the settings in TIEGCM, the NH high-latitude electric potential Φ^R is used to determine Φ in mid- and low latitudes, which is hemispherically symmetric since the field lines are assumed to be equipotential. After that, the high-latitude electric potential in the SH is replaced by (Φ^R) in the SH.

2.4 Identification of the ion convection equatorial boundary

In this study, the latitudinal expansion of the high-latitude ion convection to mid and low latitudes was investigated based on the cross-track ion drift V_y (nearly zonal direction below (|geographic latitude (GLAT)| = 70). The equatorial boundary is identified as the latitude at which the zonal ion drift suddenly gives a threshold. Heelis and Mohapatra (2009) suggested that the DMSP-observed zonal ion drift flow can be used to obtain the convection pattern equatorward expansion and contraction boundary, which is approximately consistent with the equatorward edge of the region-2 FAC. To quantitatively determine the equatorial boundary, a threshold of 15 m/s per degree in the latitudinal gradient of the zonal ion flow is adopted in this study (Heelis and Mohapatra, 2009). In addition, a criterion of 300 m/s greater than the quiet-time background flow is also applied in order to distinguish the enhancement from the quiet-time ion flow background (Hairston et al., 2016).

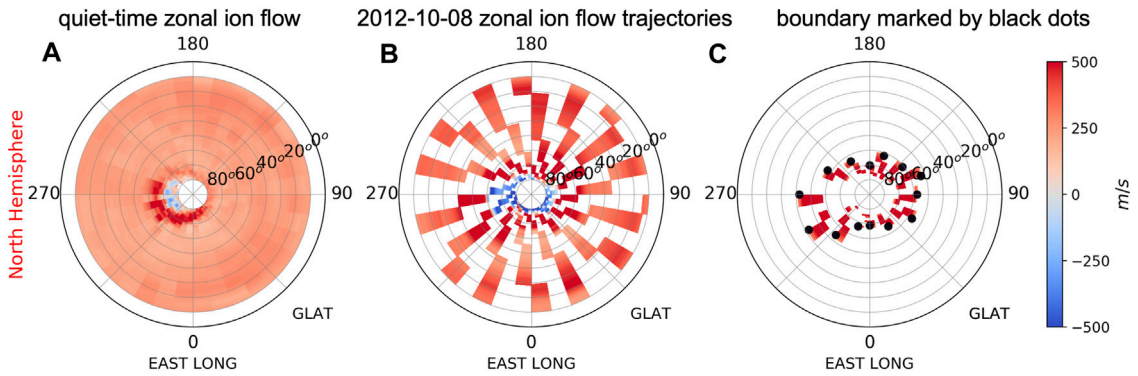

FIGURE 1
Example showing the identification of determining the ion convection equatorial boundaries in the Northern Hemispheric dusk side for DMSP F16. DMSP measured **(A)** quiet-time zonal ion flow background; **(B)** 2012–10–08 storm-time zonal ion flow trajectories; and **(C)** 2012–10–08 storm-time zonal ion flow after the identification. The positive and negative values represent the sunward and anti-sunward flows, respectively. The ion convection equatorial boundaries are marked by black dots in the third column **(C)**. The radius represents the geographic latitude (GLAT), and the polar angle represents geographic longitude (GLON) at a fixed LT, ~18 SLT, or universal time (UT = GLON/15.—18 LT).

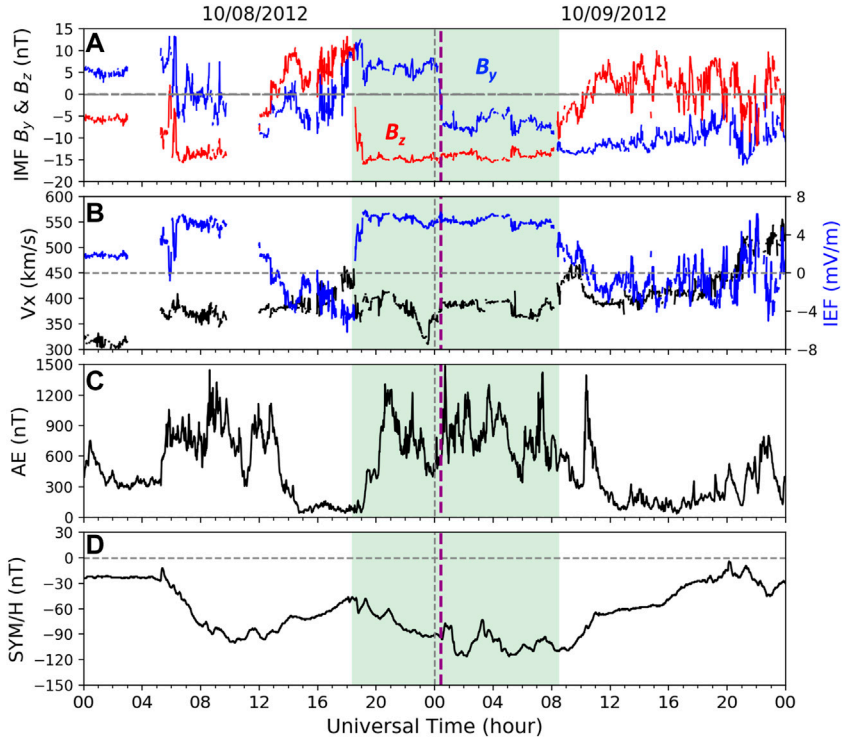

FIGURE 2
(A) Interplanetary magnetic field (IMF) B_y and B_z components, **(B)** solar wind velocity V_x and interplanetary electric field (IEF, $E = -V_x \times B_z$), **(C)** auroral electrojet AE index, and **(D)** SYM/H index during October 8–9, 2012. The green shaded area highlights the period of interest in this study. The vertical purple dashed line marks the IMF B_y reversal time, which is around 00:20 UT on October 9 2012.

Figure 1 shows an example of the NH dusk-side ion convection equatorial boundary determined from the DMSP F16-measured zonal ion flow during the October 8, 2012, storm day. Specifically, the radius represents the GLAT, and the polar angle represents the geographic longitude (GLON) at the DMSP F16 fixed dusk-side LT, ~18 SLT. The zonal ion flows were binned into 1° in GLAT between 10° and 80° GLAT and 2/3 h intervals (i.e., 10° in GLON). Figure 1A shows the quiet-time zonal ion flow background based on 7-day DMSP dusk-side measurements during October 1–7, 2012; Figure 1B shows the storm period zonal flow (around

14 trajectories per day) on October 8. Subtracting the zonal ion flow background 1A from the storm time 1B, the difference is shown in Figure 1C. By combining these two criteria described in the aforementioned paragraph, the ion convection boundary can be determined with black dots consistently for all longitudes, i.e., UT (UT = GLON/15–18 LT). Furthermore, we have also checked that using a larger or smaller threshold such as 400 m/s or 200 m/s only alters the boundary in the GLAT within 2° for this specific storm event.

3 Geophysical conditions

Figure 2 shows the IMF components B_y and B_z, solar wind velocity V_x, interplanetary electric field (IEF, $E_y = -V_x \times B_z$), SYM/H index, and auroral electrojet (AE) index for the moderate geomagnetic storm during October 8–9, 2012. As shown in Figure 2D, the storm sudden commencement (SSC) occurred at 05:16 UT on October 9 2012 and the SYM/H index reached ~ −100 nT around 10:20 UT on October 8 during the first storm main phase (05:30 UT to 10:30 UT on October 8). The second main phase occurred between 18:00 UT on October 8 and 08:30 UT on October 9 during which the SYM/H index decreased to a minimum of ~ −116 nT at 02:07 UT on October 9. During the second main phase, the IMF B_z component (Figure 2A) and IEF (Figure 2B) remained at around −15 nT and 5 mV/m, respectively. Meanwhile, the AE index showed rapid disturbances with basically above 600 nT and can reached up to 1400 nT (Figure 2C). The IMF B_y component stayed at around +8 nT before 01:20 UT and then quickly reversed to ~ −8 nT. This study mainly focuses on the second main phase which offers us a great opportunity to examine the IMF B_y effects on the IHAs of high-latitude electrodynamic forcing and its impacts on the thermosphere.

4 Results and discussion

In Section 4.1, results from the empirical model-based run 1 (W05 and ASHLEY) and realistic pattern-driven run 2 (FAC-driven and AMIE electron precipitation) are compared with DMSP F16-18-observed cross-track ion drift V_y and the ion convection equatorial boundary. Section 4.2 illustrates the IHAs in high-latitude forcing, i.e., ion convection and auroral electron precipitation. The asymmetric storm phase response and B_y dependence of the ion convection equatorial boundary in both hemispheres are also investigated. The storm-time global evolutions of the thermospheric neutral density simulated by the GITM are compared with the GOCE satellite-measured result. The IHA and physical mechanism are examined in Section 4.3.

4.1 Data–model comparisons of the ion convection

4.1.1 Data–model comparison of the ion drift at high latitudes

To determine how well the model output represents the ionospheric ion convection, a data–model comparison of the cross-track ion drift V_y has been conducted along DMSP trajectories during the focus period. As shown in Figure 3, six examples from DMSP F16-18 and the corresponding GITM runs are compared with the top and bottom panels representing the Northern and Southern hemispheres, respectively. For each plot, the black dots show the observed cross-track ion drift, and the blue and red curves represent the empirical model-based run 1 (W05) and realistic pattern-driven run 2 (FAC-driven and AMIE electron precipitation), respectively. In general, the cross-track V_y from both GITM runs is consistent with the DMSP results. When comparing the two sets of runs, the FAC-driven V_y from run 2 can better capture the realistic ion drifts in high latitudes than the W05-based results from run 1, especially inside the auroral zones.

To investigate how GITM simulations capture the high-latitude ion drifts V_y from a statistical perspective, Figure 4 compares the simulated and measured cross-track ion drift at the region poleward of 45° |MLAT| from all DMSP trajectories during the focused period for runs 1 and 2. Linear fitting is performed on the data, and the slope (k) and *y*-intercept (b) are calculated. In addition, the Pearson correlation coefficient (r) and the root mean square error (RMSE) are also calculated. Basically, the cross-track ion drifts V_y from both GITM simulations have smaller magnitudes than the observed cross-track V_y since the slope of the best-fit line of the fitted line is much smaller than 1. This underestimation in the simulation results could be due to the underestimation of high-latitude forcing such as the FAC magnitude. This is a known property of AMPERE FAC data in the dusk-side R2 current. However, the slope of the best-fit line is slightly higher in run 2 than in run 1. Meanwhile, compared with run 1, run 2 shows a greater correlation (e.g., for DMSP F16 run 2 = 0.81 vs. run 1 = 0.68) and a smaller RMSE between the simulated and observed ion drifts (336.20 compared to 426.33) than run 1. Overall, Figure 4 indicates that the FAC-driven GITM simulation can better reproduce the high-latitude ion drift measured by DMSP satellites than the W05.

4.1.2 Data–model comparison of the ion convection equatorial boundary

The data–model comparisons of high-latitude ion convection given in Figure 3 and Figure 4 show a general consistency between the measured and simulated ion drift on the dawn and dusk sides, especially for run 2. Moreover, we would like to see how GITM simulations perform in response to the ion convection equatorial boundary. Figure 5 shows a scatterplot of the ion convection equatorial boundary in the GLAT for both hemispheres measured by DMSP F16 *versus* those from runs 1 and 2 during the focused storm period. In general, the simulations reproduce the DMSP-measured equatorward boundary latitudes well, with a better representation in run 2. Specifically, the correlation coefficients to DMSP F16 are 0.81 in the NH (Figure 5A) and 0.91 in the SH (Figure 5C) for run 1 and 0.92 in the NH (Figure 5B) and 0.95 in the SH (Figure 5D) for run 2. Moreover, as shown in Figures 5A, C, W05 has a clear underestimation of the convection expansion below 60° for the NH and at all the latitudes for the SH. This underestimation of the ion convection equatorial boundary may have some effects on other electrodynamical processes such as the ion-neutral interactions in that region. Overall, both runs show good agreement with the DMSP-observed convection equatorial

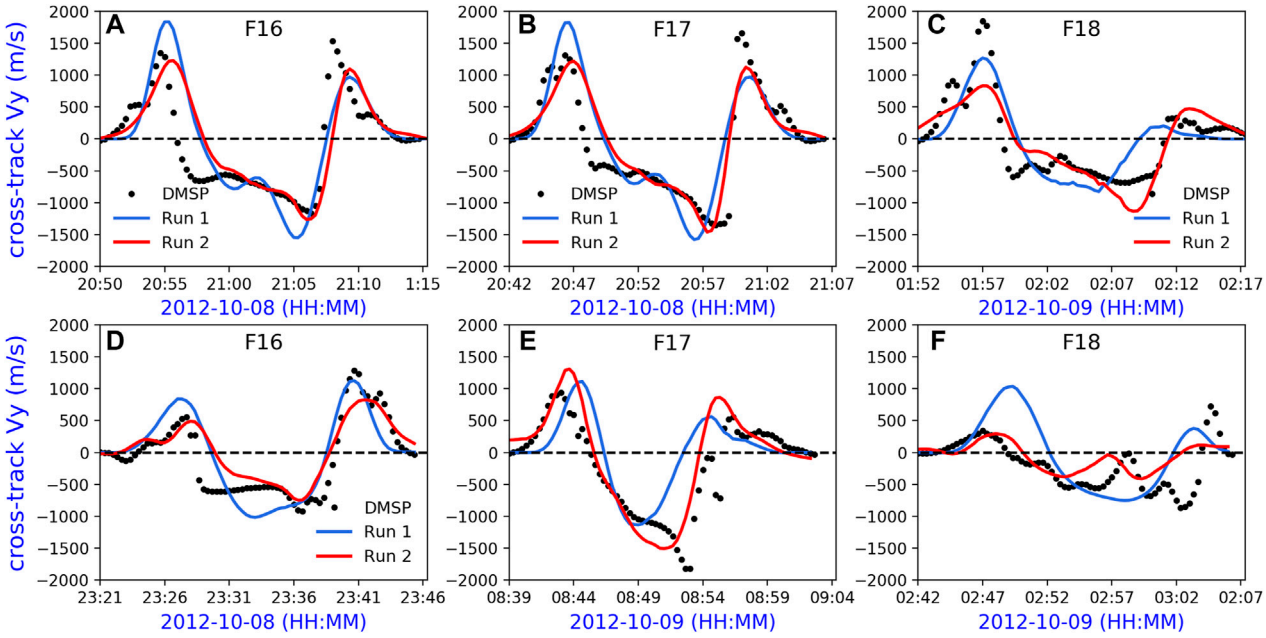

FIGURE 3
Comparison examples of the cross-track ion drift (V_y) along DMSP F16 **(A,D)**, F17 **(B,C)**, and F18 **(C,F)** trajectories. The black dots represent DMSP observations with a 13-point sliding window applied; blue and red lines represent GITM simulation run 1 and run 2, which are driven by empirical models and driven by data-based realistic patterns, respectively.

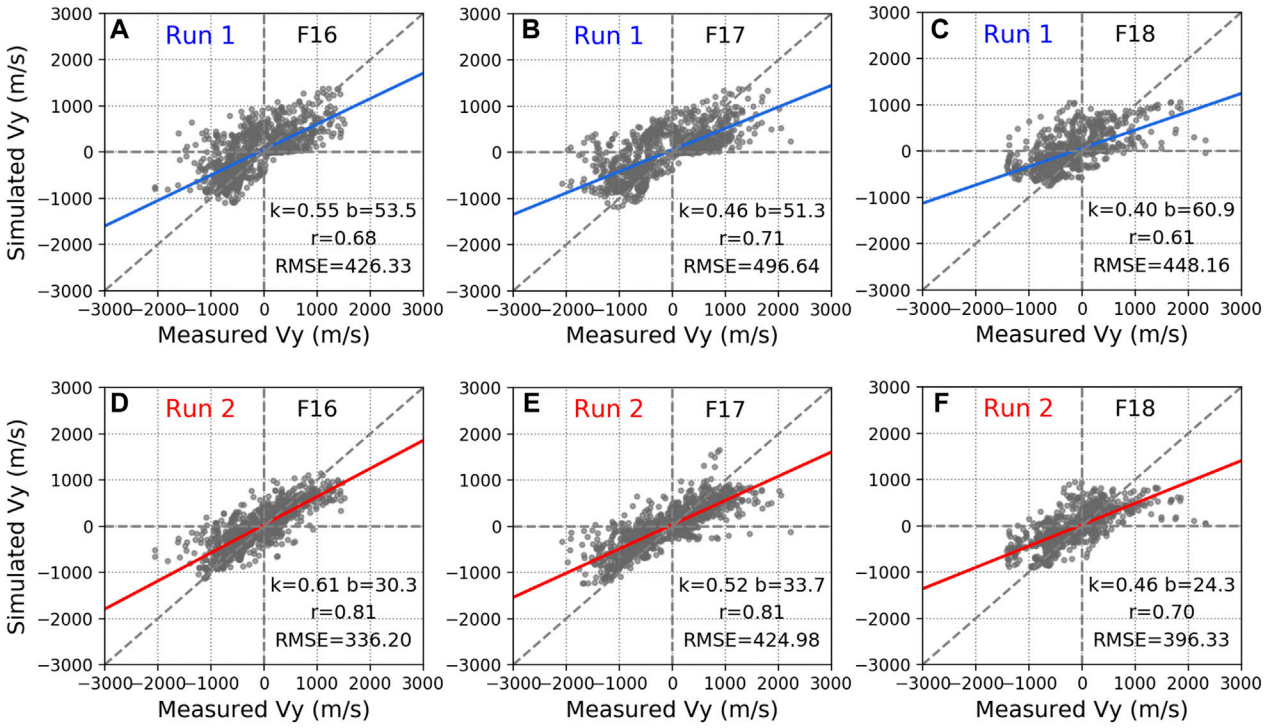

FIGURE 4
Scatter plots of DMSP-measured cross-track ion drift V_y *versus* corresponding GITM run 1 (top, driven by empirical models) and run 2 (bottom, driven by data-based patterns)- simulated V_y for all trajectories of F16 **(A, D)**, F17 **(B, E)**, and F18 **(C, F)** between 18 UT on October 8 and 09 UT on October 9. The straight lines represent the best-fit line. The slope (k), intercept (b), correlation efficient (r), and root mean square error (RMSE) are also shown in each plot.

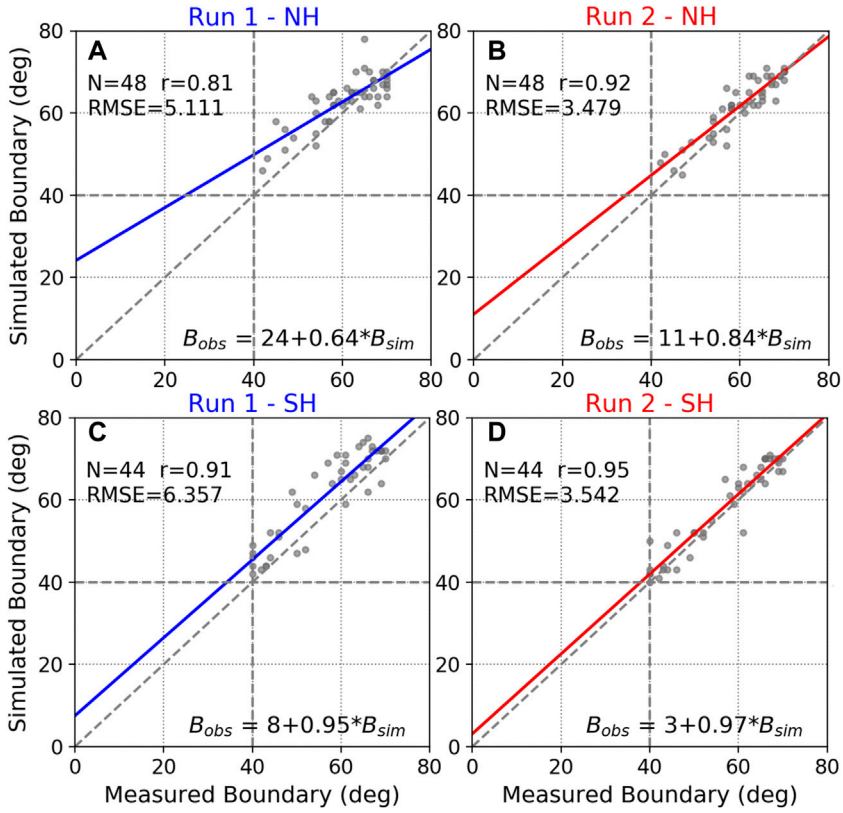

FIGURE 5
Scatter plots of the DMSP F16-measured ion convection equatorial boundary *versus* corresponding results from two GITM simulations run 1 (left, driven by empirical models) and run 2 (right, driven by data-based realistic patterns) during the October 8–9, 2012, geomagnetic storm for the northern **(A, B)** and southern **(C, D)** hemispheres. The straight lines represent the best-fit line. The number of dots (N), correlation coefficient (r), and root mean square errors (RMSE) are shown in the left-up corners, while the linear fitting equation is shown in the lower right corners.

TABLE 2 Summary of data–model comparisons conducted in this paper.

High-latitude ion drift			
Simulations	K, b (F16/17/18)	r (F16/17/18)	RMSE (F16/17/18)
Run 1	0.55, 53.5/0.46, 51.3/0.40, 60.9	0.68/0.71/0.61	426.33/496.64/448.16
Run 2	0.61, 30.3/0.52, 33.7/0.46, 24.3	0.81/0.81/0.70	336.20/424.98/396.33
Ion convection equatorial expansion boundary			
Simulations	k, b (NH/SH)	r (NH/SH)	RMSE (NH/SH)
Run 1	0.64, 24/0.95, 8	0.81/0.91	5.111/6.357
Run 2	0.84, 11/0.97, 3	0.92/0.95	3.479/3.542

boundary. The comparison between runs 1 and 2 is to give the community a rough idea about how well the FAC-driven technique could improve high-latitude electric field specification which is also a justification for using the FAC-driven technique in this study. For later scientific studies in Section 4.2 and Section 4.3, we would like to focus on the GITM run 2 since it has advantages over run 1 as discussed. A summary of the statistical parameters from the data–model comparisons of the two runs can be found in Table 2.

4.2 IHA of high-latitude forcing and the ion convection equatorward expansion

4.2.1 IHA in the high-latitude electrodynamic forcing

Figure 6 shows the temporal variations of the cross-polar-cap potential (CPCP, top panel) and hemispheric power (HP, bottom panel) during October 8–9, 2012, from run 1 (left) and run 2 (right). The vertical dashed line marks the time when IMF B_y is reversed (00:

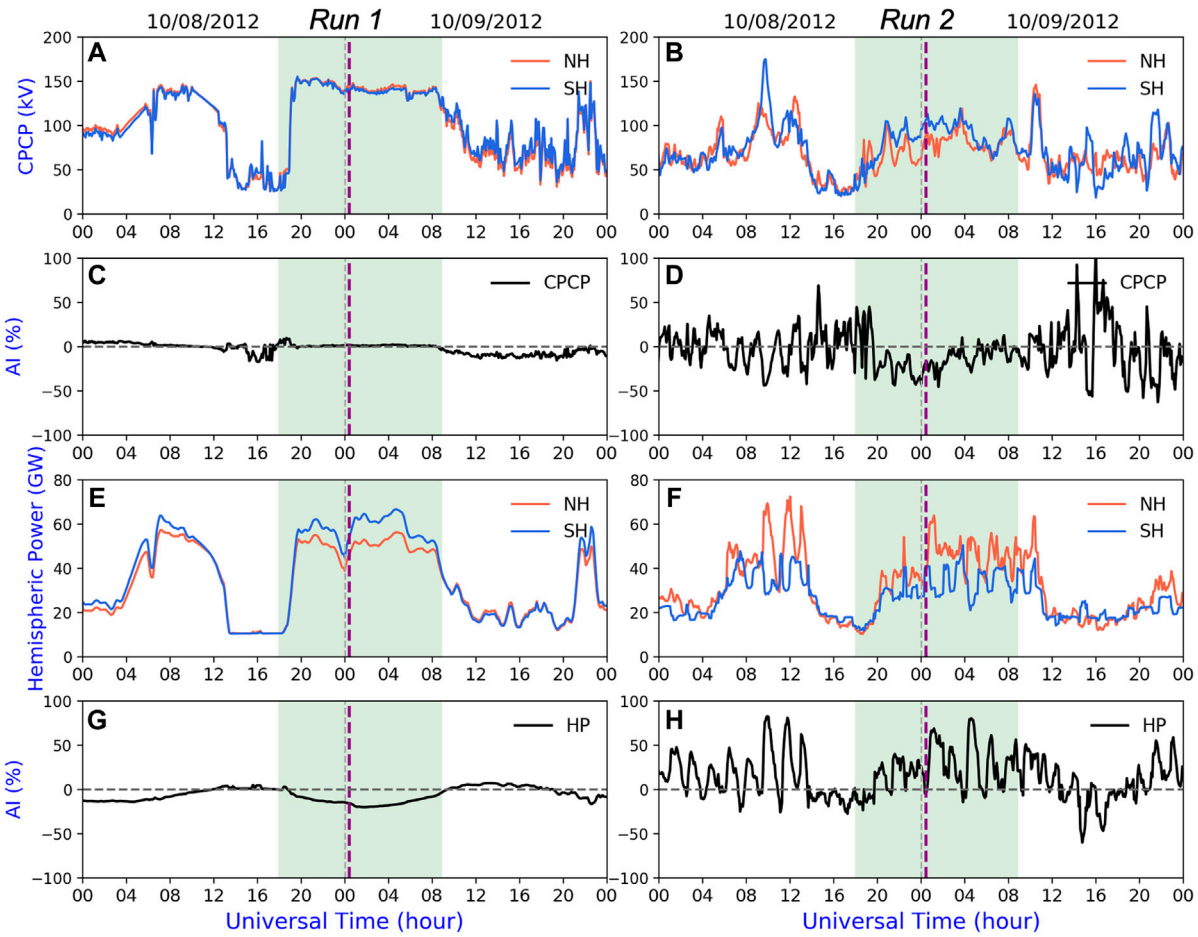

FIGURE 6
Inter-hemispheric comparisons of the **(A, B)** cross-polar-cap potential (CPCP) and **(E, F)** hemispheric power (HP) and their corresponding asymmetry index (AI) during the October 8–9, 2012, geomagnetic storm: **(C, D)** for CPCP and **(G, H)** for HP. The left column is for run 1 (driven by empirical models) and the right is for run 2 (driven by data-based realistic patterns). The vertical purple dashed line marks the IMF B_y reversal time during the storm main phase.

20 UT on October 9) during the storm main phase we focused on in this study. All the red and blue lines correspond to the NH and SH, respectively. Following Hong et al. (2021), the asymmetry index (AI) is used to quantify the temporal changes of IHA for a given quantity:

$$AI = 2 \times (Y_{NH} - Y_{SH}) / (Y_{NH} + Y_{SH}) \times 100\%, \quad (3)$$

where Y_{NH} and Y_{SH} stand for the quantity in the NH and SH, respectively.

As shown in Figure 6A, CPCPs from run 1 are almost the same in the NH and SH during the focused period and the CPCP stays around 145 kV. As for run 2, significant asymmetries between the NH and SH can be seen in Figure 6B even for the recovery phase (e.g., after 12 UT on October 9). An evident asymmetry index (AI up to −50%, see Figures 6C, D) occurs in the CPCP during the focused period, especially before IMF B_y is reversed. In addition, the CPCP also exhibits more pronounced temporal variations than run 1. Similarly, as shown in the bottom two panels of Figures 6E, F, the hemispheric power in run 2 exhibits more dynamic variations and greater IHA than in run 1. The AIs can reach 75% and −22% in run 2 (Figure 6H) and run 1 (Figure 6G), respectively. Different from the CPCP, the HP tends to have greater AI in run 2 when the IMF B_y is negative (after 00: 20 UT on October 9). Additionally, the HP in the NH is generally larger than that in the SH in run 2 while the opposite is true in run 1. This is probably due to the fact that the empirical model is mainly dependent on the given IMF, solar wind, and input seasonal conditions. Another reason is that, as described in Section 2.2, the AMIE patterns have better data coverage from the NH than that in the SH.

To our knowledge, the IHAs in high-latitude forcing could be due to the combined action of the season-related dipole tilt and the non-zero B_y component, which contribute to the asymmetric interaction in the dayside reconnection (Reistad et al., 2021). The well-known Dungey cycle suggests that the distribution of the open magnetic field flux in the two hemispheres should be the same. However, observations showed that the open magnetic flux in the polar cap is often distributed differently between the Northern and Southern hemispheres. Global auroral images from Polar and IMAGE satellites show different polar cap shapes, indicating hemispherically asymmetric distribution of open flux (Laundal and

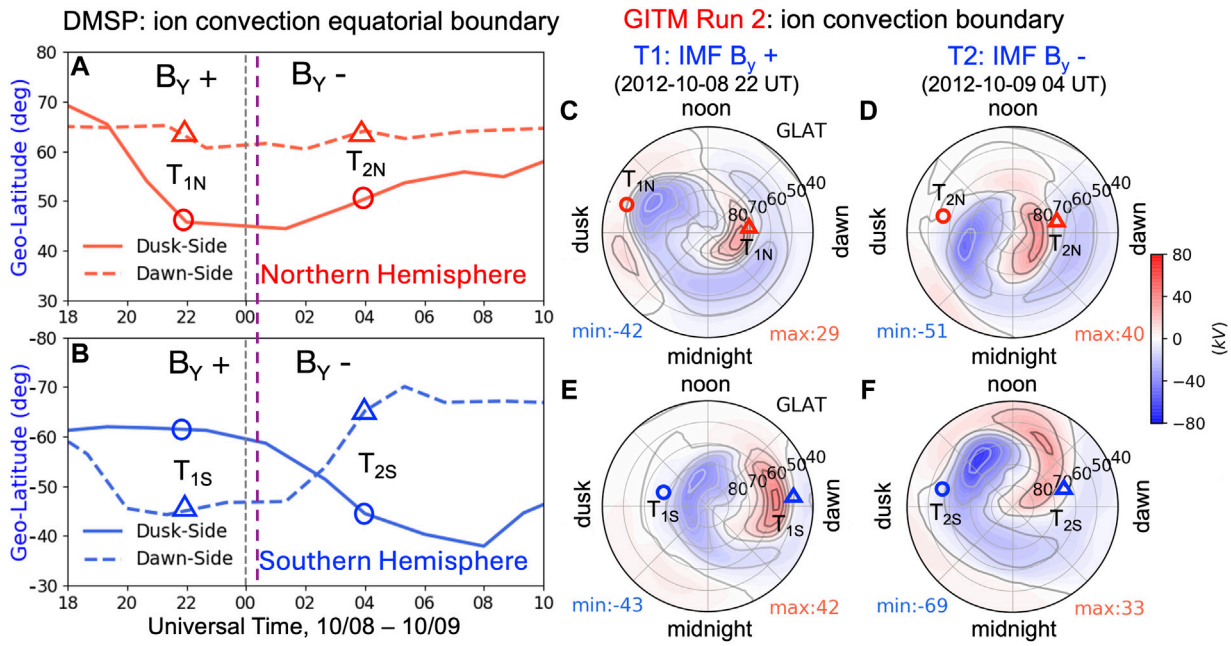

FIGURE 7
The left linear figure shows the temporal variations of the ion convection equatorial boundary along DMSP F16 ascending tracks, i.e., dusk side (solid lines) and descending tracks, i.e., dawn side (dashed lines) for both Northern [**(A)**, red lines] and Southern [**(B)**, blue lines] Hemispheres. The vertical purple dashed line marks the IMF B_y reversal time from positive to negative at around 00:20 UT 9 October 2012. Snapshots of the FAC-driven convection patterns in the Northern (top right) and Southern (bottom right) hemispheres under different IMF conditions: IMF B_y positive **(C, E)**, 22 UT on October 8) and IMF B_y negative [**(D, F)**, 04 UT on October 9]. The circle and triangle symbols refer to the dusk side and dawn side, respectively, under two different IMF B_y conditions.

Østgaard, 2009). This is particularly true when there is an east–west component of the IMF (IMF B_y) (Tenfjord et al., 2015). The lobe reconnection due to IMF B_y causes the magnetic flux to build up asymmetrically (Lu et al., 1994). For example, the responding speed to the solar wind conditions in the two hemispheres can be different, which can result in different temporal variations of the magnetic flux between the two hemispheres (Milan et al., 2020). Therefore, this phase mismatch may result in some instantaneous asymmetry of the CPCP while it should be reduced significantly when the response in both hemispheres is fully developed. In addition to the reconnection for the IMF B_y, the field line potential drops across the hemispheres, and the asymmetries in the current systems produced by differing ionospheric conductivities and neutral dynamos in two polar regions contribute to the possible asymmetry in the CPCP as well. Data–model comparisons are still absolutely crucial to validate the simulation results. While the GITM simulations are able to capture the fundamental features of the ion drifts at high latitudes and the convection boundaries at mid-latitudes, the potential strong asymmetry of the CPCP presented in our simulation has yet to be corroborated with realistic observations. We will make careful comparisons with SuperDARN and other measurements in the follow-on study.

4.2.2 IHA in the ion convection equatorial boundary and its IMF B_y dependence

An enhanced geomagnetic storm can lead to large perturbations in the high-latitude ion convection and then extend to lower latitudes. From Section 4.1.2, we have demonstrated that the ion convection equatorial boundary from DMSP observations and GITM simulations shows a fairly good agreement on both the dawn and dusk sides. To have a detailed picture of the UT variations during this storm, Figures 7A, B directly show the temporal variations of DMSP F16-measured ion convection boundary in GLAT on dawn and dusk sides during the focused IMF B_y reversed period (18 UT on October 8–10 UT on October 9). Over this period, the NH dawn-side convection boundary (red dashed line) only undergoes a small variation (<5°) around 63° N GLAT, while the dusk-side convection boundary can expand to as far as 45° N (red solid line). As for the SH, both the dawn and dusk sides expand to lower GLATs during this interval of time, with the observed lowest boundary at 45° S and 40° S, respectively. One of the most interesting features is that these two sides reach their lowest |GLAT| under opposite IMF B_y conditions: the dawn side first expands under positive B_y and then contracts during negative B_y (blue dashed line), while the dusk side shows the opposite (blue solid line). This result could be explained by the anti-correlated responses between the dawn and dusk sides to B_y (e.g., Cowley, 1981; Reiff and Burch, 1985; Kabin et al., 2003; Tenfjord et al., 2015), the SH dawn-side convection cell is much stronger than the dusk-side cell under positive B_y, while the dusk side is more favorable under negative B_y in the SH.

In terms of the ion convection boundary comparisons between the two hemispheres, the temporal expansion in the NH dusk side (7A) follows a similar tendency to changes in the SH dawn side (7B),

especially under positive IMF B_y. This could be the result of reversed B_y responses in the two hemispheres (Cousins and Shepherd, 2010), a stronger convection cell on average expands to lower latitudes. On the other hand, in contrast to the expansion in the SH dusk side (7b), the NH dawn-side convection expansion (7a) seems to be less important, implying a relatively stable convection cell on the dawn side. Moreover, this response is much stronger in the SH than in the NH, suggesting a stronger B_y dependence of the two cells in the SH (Burch et al., 1985). A possible explanation to the dawn–dusk asymmetry and IHA in the expansion is that the ion convection is subject to asymmetries in FACs and ionospheric conductivities. However, these line plots represent a limited view of ion convection pattern variation at two fixed LTs. The aforementioned hemispheric asymmetries between the NH and SH on both dusk and dawn sides will be further discussed in the following section.

4.2.3 Causes of the IHAs in the high-latitude convection and its equatorial boundary

To better understand the spatiotemporal variations of the ion convection patterns, Figures 7C–F present polar-view snapshots of the 2-D convection patterns from realistic pattern-driven GITM run 2 in both hemispheres under positive B_y at 22 UT October 8 (T1, left) and negative B_y at 04 UT October 9 (T2, right) from run 2. It can be seen in Figures 7E, F that the SH ion convection strengths and their expansions have obvious responses to IMF B_y. From T1 IMF B_y positive to T2 B_y negative, the dawn-side cell decreased from a maxima value of 42 kV (e) to 33 kV (f) associated with the dawn-side boundary contracted from ~45°S (b and e, blue triangle) to 67°S (b and f, blue triangle). Similarly, for the dusk side, the cell with a minimum value −43 kV (e) with respect to −69 kV (f) leads to an expanded dusk-side boundary to much lower at ~ 42°S (b and f, blue circle). However, as shown in Figures 7C, D, a stronger dusk-cell with minima value −51 kV (d) corresponds to a shrinking convection boundary (a and d, red circle). Furthermore, the dawn-cell increased from 29 kV (c) to 40 kV (d) with subtle changes in the boundary location. Again, the NH displays a clear stretch of the dawn-side cell in the noon–midnight direction instead of an equatorward expansion, which could explain the static phenomena along the DMSP F16 trajectory on the NH dawn side as shown in Figure 7A (red dashed line). This result suggests that it might be insufficient to determine the storm period ion convection expansion based on only the dawn and dusk LTs. Overall, the ion convection pattern simulated by the GITM for these two specific periods is in general agreement with the observed convection boundary expansions. Moreover, a stronger convection cell does not necessarily associate with a lower equatorial boundary.

In addition, we also conducted data–model comparisons of the equatorial boundary expansion at specific times. As shown in both the linear and polar plots, the red and blue triangles refer to the dawn side for the NH and SH, respectively. Similarly, the red and blue circles refer to the NH and SH but for the dusk side. The snapshot times T1 and T2 represent the corresponding positive B_y case at ~ 22 UT on October 8 and negative B_y case ~04 UT on October 9, respectively, which are marked in the left line plots. The subscripts N and S refer to the NH and SH, respectively. The boundary expansion features in the 2D contour from FAC-driven GITM run 2 are in a good agreement with the line plots from the DMSP F16 observations. For example, the blue triangle T_{2S} (Figure 7B, dawn side) almost overlaps the expansion of the dawn-side potential cell (Figure 7F, blue color) at around 67°S GLAT.

To identify the possible mechanisms for the observed IHAs in the ion convection patterns, as well as their equatorial boundaries, a separation of the FAC and auroral electron precipitation (associated with the ionospheric conductance) is needed. In reality, the high-latitude FAC and auroral precipitation are connected and respond simultaneously to the changes in geophysical conditions, so it is impossible to completely separate the effects caused by these two variables. However, numerical simulations could help solve this issue by replacing the real forcing with symmetric patterns. We first examine the GITM run 2 (simulation setups in Table 1), which the high-latitude forcing is based on the FAC-driven potential and AMIE electron precipitation patterns. In GITM run 3, the AMIE electron precipitation patterns in the SH are replaced by the mirror precipitation patterns in the magnetic coordinate from the NH accordingly. Therefore, the differences in the SH between run 2 and run 3 illustrate the contributions from the auroral precipitation. Figure 8 shows the Southern hemispheric FAC-driven convection patterns and corresponding auroral energy flux from GITM run 2, run 3, and their differences at 04 UT on October 9 as an example. Specifically, due to the asymmetric electron precipitation, the auroral electron energy flux between the NH and SH is significantly different in both distributions and magnitudes: the SH has a continuous and complete aurora arc structure (Figure 8D) while the NH is more like a discrete aurora (Figure 8E). As shown in Figure 8F, the maxima difference in energy flux can vary from −45% to 55%. This result could be explained by the larger hemispheric power captured at that specific time (see Figure 6F); even the hemispheric power in the NH can be overwhelmingly superior to that in the SH during the focused period. However, the SH and NH electron energy flux-based ion convection (Figures 8A, B) illustrates quite similar distributions, as well as the maxima and minima values for the dawn (33 vs. 34 kV) and dusk (−69 vs. −67 kV) cells. Compared to Figure 8C, the differences caused by the asymmetric auroral precipitation can be ignored at this specific time. Moreover, by comparing the convection contour lines, one can find that the distributions, especially the equatorial boundaries of the convection, are more likely determined by the FAC patterns (R2 FAC edge) while its strength may also depend on the magnitude of the ionospheric conductance-associated precipitation. With this discussion, the effects from the FAC and auroral precipitation can be roughly isolated. It should be noted that this conclusion depends critically on the assumption of the FAC-driven procedure. Similar plots for all the UT times during the focus period indicate the same conclusion as the example time shown in Figure 8.

4.3 IHAs in the storm-time thermosphere: Neutral density response dρ

To investigate the IHAs in the thermosphere during this storm, the neutral density observed by the GOCE satellite was first divided into ascending (dusk side) and descending (dawn side) trajectories. After that, the daily ascending trajectory data are binned into UT

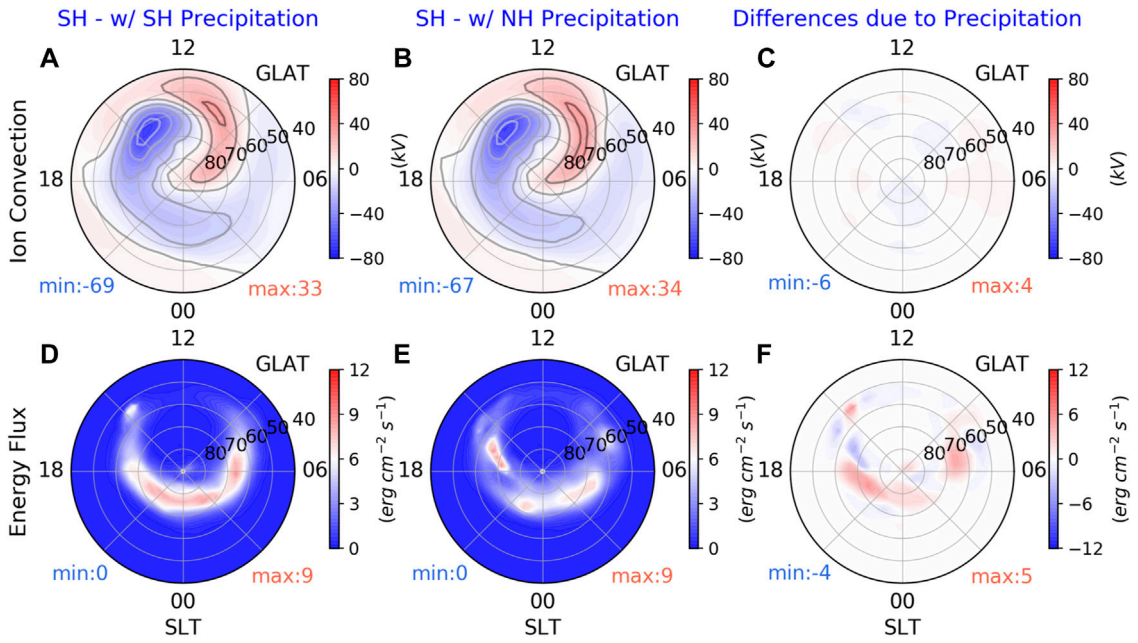

FIGURE 8
Snapshots of the FAC-driven convection patterns (top) for the Southern Hemisphere (SH) driven by different AMIE electron precipitation patterns at 04 UT on October 9 as an example: the SH precipitation itself **(A)**, mirrored precipitation pattern in the geomagnetic field coordinate from the Northern hemisphere (NH, **(B)**, and their difference **(C)**. The corresponding energy flux of the precipitation patterns for the SH **(D)**, NH **(E)**, and their difference **(F)** are shown in the bottom.

and GLAT grids with a bin size of 1 h and 1° in GLAT. We then applied a linear temporal interpolation in UT to project the data into uniformly distributed time series for both quiet-time background days and the storm-time days. Similarly, the approach is also used for GITM run 2-simulated neutral density extracted along the GOCE satellite trajectories for both quiet and storm days.

Figure 9A shows the observed neutral density response, dρ, on the dusk side as a function of UT and GLAT. The quiet-time neutral density background (given by the 2-day average of October 4 and 5) is subtracted from the storm-time observations. During the period of elevated geomagnetic activity, as indicated by the Ap and SYM/H indices shown in Figure 9D, it is clear that the observation generally shows density enhancements which last for several hours, and the neutral density increases after October 9. During the focus period (i.e., green shaded area), the NH shows dρ enhancements between 60° −80° N GLAT between 19:30 UT on October 8 and 00 UT on October 9 while the SH polar region represents stronger enhanced dρ at around 21:45 UT on October 8. The roughly 2-h difference in the responses between the NH and SH might be caused by asymmetric energy deposition such as the Joule heating in the two auroral regions. Another possibility is that the GOCE satellite trajectories are in different LTs in the NH and SH above 70° |GLAT|. Shortly after this period, both the neutral density in the NH and SH undergoes significant large-scale enhancements and the enhancements propagate equatorward and finally arrive at ~30° S at 8 UT on October 9. Basically, the GOCE satellite-observed dusk-side dρ has some properties associated with IHA: the density-enhanced time, the density magnitudes, and the latitudinal propagation.

Figure 9B is similar to Figure 9A but for the dρ from GITM run 2 (FAC-driven potential and AMIE electron precipitation). Specifically, the run 2-simulated neutral density over the same quite-time during October 4 and 5 is used as the quiet-time background subtracting for GITM as done for GOCE data. In general, the simulated dρ is consistent with the GOCE-measured results though some differences exist. For example, the much greater dρ on October 9 than on October 8 can be captured. In agreement with Figure 9A, Figure 9B shows an equatorward propagation of the neutral density enhancement. It is also worth noting that there are some differences in the data–model comparison: neutral density from GITM run 2 is smeared and has less mesoscale structures than those in the GOCE observations (Figure 9A), which may be due to three major reasons: 1) the latitudinal resolution in mid- and low latitudes of the observation (~0.6 deg) is much higher than the simulation (2.5 deg); 2) the mesoscale forces may not be included in the simulations (Deng et al., 2019; Sheng et al., 2021); and 3) large-scale forcing is not perfect.

To quantify the asymmetric density features between the two hemispheres, Figure 9C shows the temporal changes of the AI for the averaged dρ at > 40° |GLAT| on the dusk side for both GOCE (black dot line) and GITM (red dot line). Apparent density asymmetries between the NH and SH can be identified, with the AI varying between −36% and 20% for the observations and between −18% and 20% for GITM results. As expected, the temporal changes of AI show some similarities and differences

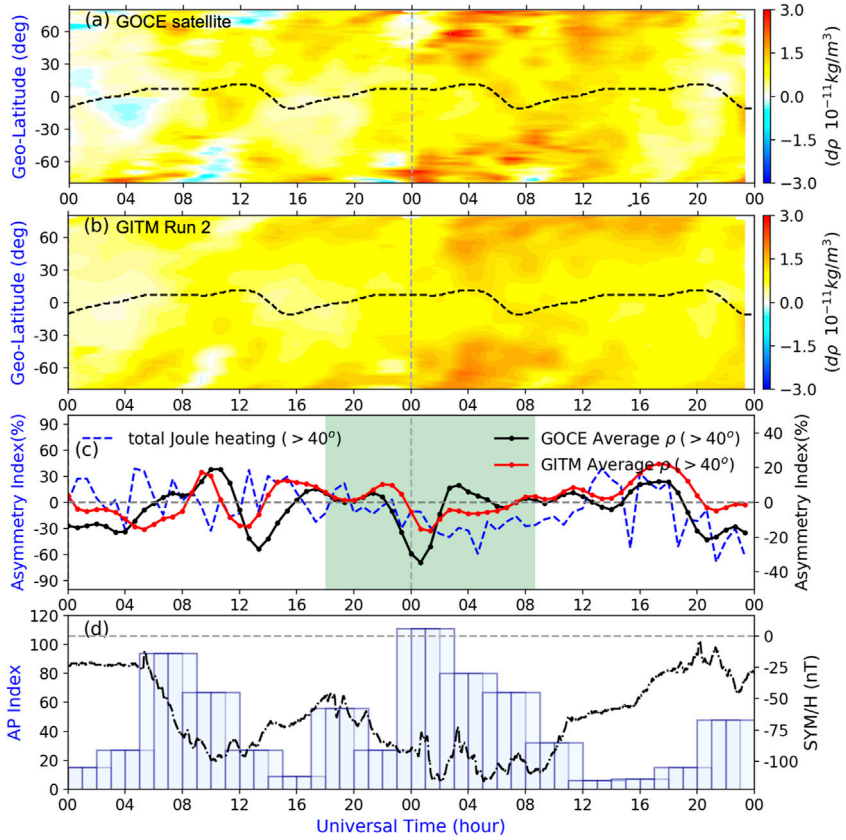

FIGURE 9
(A, B) Neutral density at the dusk side from the GOCE trajectory observation normalized at 270 km and GITM run 2 (driven by data-based realistic patterns)-simulated results sampled along the GOCE trajectory as functions of geographic latitude and universal times during the October 8–9, 2012, geomagnetic storm, respectively. The black dashed line refers to the dip equator. **(C)** Temporal changes of the asymmetry index for total Joule heating (hemispheric-integrated Joule heating, blue dashed line) from GITM run 2 (label on the left *y*-axis); the temporal changes of the asymmetry index for averaged density in the mid- and high-latitudes (>40° |GLAT|) based on the 2-D contour for GOCE (black dot line) and GITM run 2 (red dot line) with the label on the right *y*-axis. To have a general view of the storm-time response of the neutral density, **(D)** gives the geomagnetic activity information: the 3-hourly Ap index (blue) and SYM/H index (black).

between GOCE and GITM results. Both the observational and simulation results show that the AI in dρ reaches its first maxima and minima at around 11 UT and 13 UT on October 8, respectively. During the storm period slightly after B_y is reversed, the asymmetry index reached its minimum value at ~ -36% and −18% for the observational and simulation results, respectively. Moreover, a significant positive peak can be found during the recovery phase for both results but the magnitude in the GITM simulation seems to be much greater. As for the shaded focus period, the AI tends to be positive values (i.e., the NH has more density than the SH) under positive B_y rather than being significantly negative after B_y reversed into negative polarization, especially for the simulated results shown in the red line, implying that dρ might have some IMF B_y dependence associated with high-latitude forcing and energy dissipation.

To help understand the hemispheric difference in neutral density, the asymmetry index of the total (hemispheric-integrated) Joule heating >40° |GLAT| between the two hemispheres from GITM run 2 is also plotted in Figure 9C as a reference for the energy dissipation at high latitudes (blue dashed curves). The most remarkable feature is that negative AI (i.e., the SH has more total Joule heating than the NH) occurs shortly after the focus period and lasts almost to the end of the day, October 9, illustrating that the SH dusk side has more energy input during this period. Moreover, as shown in Figure 9C, between 12–20 UT on October 8, more Joule heating was deposited into the NH (positive AI), resulting in increased density in the NH in density dρ during 16–22 UT on October 8. Immediately after this, greater Joule heating was dissipated into the SH with the minima of AI (~-60%) near 05 UT on October 9 in Joule heating. In general, the total Joule heating can lead to changes in neutral density enhancement, with 2–3 h of delay for the thermosphere to respond to the energy input change during storm times (Wang et al., 2020). On the basis of the aforementioned features, it can be summarized that the variations and IHA in the dρ could be significantly due to the contributions from the Joule heating dissipations.

The storm-time IT system responses are largely controlled by two factors: external high-latitude forcing from the solar wind–magnetosphere–ionosphere interaction and the local conditions in the thermosphere and its embedded ionosphere. Therefore, the IHAs in the thermosphere could also come from

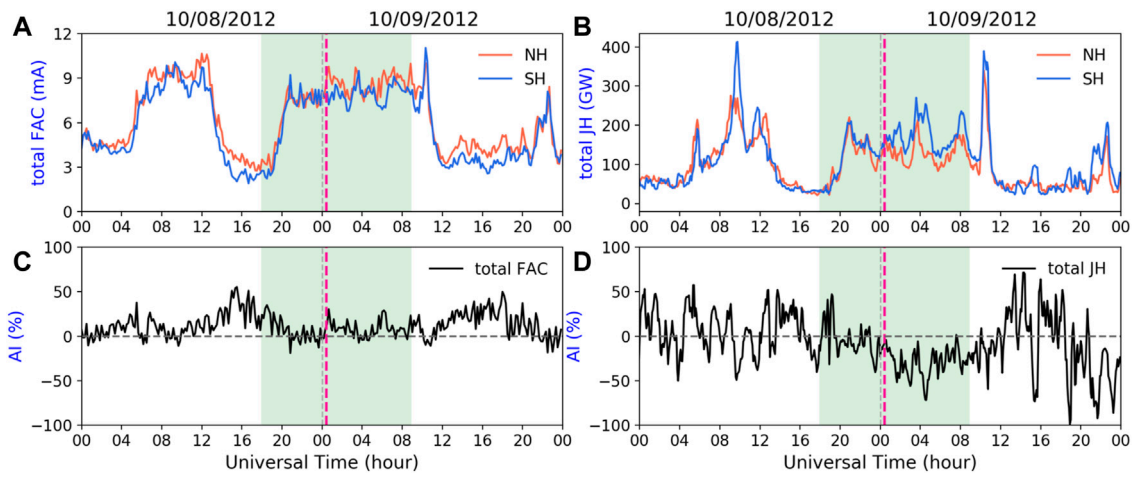

FIGURE 10
Inter-hemispheric comparisons of the total field-aligned current (FAC, **(A)**, total Joule heating **(B)**, and their corresponding asymmetry index (AI, **(C, D)** during the October 8–9, 2012, geomagnetic storm. All the results are from run 2 (driven by data-based realistic patterns) since run 2 has obvious advantages in reproducing the high-latitude forcing. The vertical purple dashed line marks the IMF B_y reversal time during the storm main phase.

several other mechanisms as discussed in the introduction. As described by several previous papers (Laundal and Østgarrd, 2009; Ohtani et al., 2009; Reistad et al., 2015; Laundal et al., 2017), the intrinsic North–South differences in the geomagnetic field could introduce asymmetric interaction of MI coupling in the two hemispheres. It should be pointed out that the IHA due to asymmetric tilt angles and displacements between the two hemispheres is daily UT differences. For example, at any given UT, the two hemispheric auroral zones will be one near nighttime and the other located in the dayside, which implies different solar fluxes would also be concerned during this period. Certainly, the absolute neutral density variation is also subject to the background thermospheric density before the storm, which provides important preconditions (McGranaghan et al., 2014). Previous studies have shown that both the season and geomagnetic field can contribute to the IHAs in the thermospheric neutral density (Emmert, 2015). Further examination shows that no obvious IHAs or enhancements could be found in the neutral density and Joule heating during the quiet-time background, i.e., October 4 and 5 from both GOCE and GITM results; given its proximity to the equinox, the result reveals that the storm-time intensified high-latitude forcing and associated Joule heating could be the dominant factor causing the IHAs to the neutral density dρ in the thermosphere.

So far, we have discussed the storm-time responses in high-latitude forcing, Joule heating dissipation, and the thermosphere, all of which have significant IHAs as illustrated by measured and simulated results. To complete the pathways of IHAs from high-latitude forcing to Joule heating, similar to the inter-hemispheric comparisons in Figure 6, we conducted the same examination for the total FAC and total Joule heating (from run 2). As shown in the left part of Figures 10A, C, the total FAC indicates small positive asymmetry during the focused shaded period between the two hemispheres as expected for the equinox condition, with AI no more than 25%. In terms of the total Joule heating shown on the right, an overall negative AI (up to −75%, Figure 10D) can be found during the same period, indicating that more heating is dissipated into the SH. As a conversion between the electromagnetic energy and mechanical form, Joule heating is conventionally taken in the form $\vec{J} \cdot \vec{E}$ in the neutral frame of reference where $\vec{E}$ is the electric field and $\vec{J}$ is the current density (Vasyliūnas and Song, 2005). Therefore, the negative IHAs in the total Joule heating could be due to the negative IHAs shown in the CPCP (Figure 6B and Figure 10B). Bringing all the results together allows us to generate a global and systematic perspective of the IHA performance during this storm event.

5 Summary

The inter-hemispheric asymmetries in the global IT system have been investigated during the October 8–9, 2012, geomagnetic storm for a focused IMF B_y reversal period. The IHA in the high-latitude convection and auroral precipitation, the convection equatorial boundary, and the thermospheric neutral density have been investigated by combining data analysis and GITM simulations. The major conclusions are summarized as follows:

1) This study demonstrates the advantage of the FAC-driven technique in the global IT system study. Simulations based on realistic, spatial FAC patterns can better capture the high-latitude ion drift and the convection equatorial boundary than the empirical model-driven results. A summary of statistical parameters for the data–model comparisons of the two simulations is given in Table 2.
2) Significant IHAs have been identified in the FAC-driven simulation in both the high-latitude forcing and the IT system, with AI up to −50% in CPCP, 75% in hemispheric power, and −36% in neutral density. The IHAs show a B_y dependence, especially for the convection boundary.
3) By comparing FAC-driven convection patterns based on precipitation from the SH itself or the mirror pattern from

the NH, our results suggest that the distribution of the ion convection, especially the equatorial boundary, is more likely to be determined by the R2 FAC edge while its intensity may also depend on the ionospheric conductance associated with aurora precipitation energy flux.

4) The FAC-driven case well-captures the storm-time thermospheric neutral density response and its IHA on the dusk side. Basically, the density response has some properties associated with IHA: the start time of the enhancement, the relative magnitudes, and the latitudinal propagations between the NH and SH. It is found that the IHA in the neutral density response follows the variations in total Joule heating and has a time delay of ~3 h.
5) Previous studies have shown that both the season and geomagnetic field can determine IHAs in the thermosphere. Our study suggests that Joule heating associated with high-latitude forcing can become the dominant factor even during a moderate storm period when near the equinox.

Data availability statement

We acknowledge the use of NASA/GSFC's Space Physics Data Facility's OMNIWeb (or CDAWeb or ftp) service, and OMNI data. The IMF and solar wind data can be found at (https://omniweb.gsfc.nasa.gov/). The AMPERE FAC data can be found at (https://ampere.jhuapl.edu/). The GOCE neutral density data can be found at (https://earth.esa.int/eogateway/missions/goce/data). The DMSP SSIES ion drift data are available at http://cedar.openmadrigal.org/. The data used in this study along with AMIE outputs and GITM simulation outputs can be found at https://zenodo.org/record/7475704#.Y6UlZhNKhR4.

Author contributions

YH conducted the data analysis and modeling studies. YD guided each step of this work and contributed to individual discussions of results. QZ coupled the NCAR-3D model into the GITM, added the FAC-driven capability to the NCAR-3Dynamo model, and created the AMIE electron precipitation pattern. AM developed the NCAR-3Dynamo module and the FAC-driven procedure. MH developed the identification of determining the equatorial boundary of ion convection. CW processed the Iridium satellite data and provided advice on differences between the hemisphere data fits. CS provided interpretation for the thermospheric neutral density performances. DW and RL assisted in the analysis of the storm event as experts in the research field of IHA and magnetosphere physics. All the co-authors contributed to the discussions, comments, and improvements to the manuscript.

Funding

This research conducted at the University of Texas at Arlington was supported by AFOSR through award FA9559-16-1-0364 and NASA through awards 80NSSC20K0195, 80NSSC20K1786, 80NSSC20K0606, 80GSFC22CA011, and 80NSSC22K0061. YH was also supported by the National Center for Atmospheric Research (NCAR) Advanced Study Program (ASP) Graduate Visitor Program Fellowship. QZ was supported by the NCAR ASP Postdoctoral Fellowship and NASA GOLD ICON Guest Investigators Program under grant 80NSSC22K0061 through the subaward 2021GC1619. YH and QZ were also supported by the NCAR Early Career Scientist Assembly Visitor Fund. AM was supported through AFOSR award FA9559-17-1-0248 and NASA award 80NSSC20K1784. This material is based on the work supported by the National Center for Atmospheric Research, which is a major facility sponsored by the National Science Foundation under Cooperative Agreement No. 1852977.

Acknowledgments

The authors appreciate the two reviewers for their valuable contributions in reviewing and improving this manuscript. They also thank Brian J. Anderson for valuable discussion on AMPERE FAC data. They would like to acknowledge high-performance computing support from Cheyenne (https://doi.org/10.5065/D6RX99HX) provided by the National Center for Atmospheric Research's Computational and Information Systems Laboratory, sponsored by the National Science Foundation. They acknowledge support from the ISSI for the international team on "Multi-Scale Magnetosphere–Ionosphere–Thermosphere Interaction."

Conflict of interest

The authors declare that the research was conducted in the absence of any commercial or financial relationships that could be construed as a potential conflict of interest.

Publisher's note

References

Anderson, B. J., Takahashi, K., Kamei, T., Waters, C. L., and Toth, B. A. (2002). Birkeland current system key parameters derived from Iridium observations: Method and initial validation results. *J. Geophys. Res.* 107 (A6), 1079. doi:10.1029/2001JA000080

Anderson, B. J., Korth, H., Waters, C. L., Green, D. L., and Stauning, P. (2008). Statistical Birkeland current distributions from magnetic field observations by the Iridium constellation. *Ann. Geophys.* 26, 671–687. doi:10.5194/angeo-26-671-2008

Anderson, B. J., Korth, H., Waters, C. L., Green, D. L., Merkin, V. G., Barnes, R. J., et al. (2014). Development of large-scale birkeland currents determined from the active magnetosphere and planetary electrodynamics response experiment. *Geophys. Res. Lett.* 41, 3017–3025. doi:10.1002/2014GL059941

Astafyeva, E., Yasyukevich, Y., Maksikov, A., and Zhivetiev, I. (2014). Geomagnetic storms, super-storms, and their impacts on GPS-based navigation systems. *Space Weather* 12, 508–525. doi:10.1002/2014SW001072

Baker, K. B., and Wing, S. (1989). A new magnetic coordinate system for conjugate studies at high latitudes. *J. Geophys. Res.* 94 (A7), 9139–9143. doi:10.1029/JA094iA07p09139

Basu, Su., Basu, S., Makela, J. J., MacKenzie, E., Doherty, P., Wright, J. W., et al. (2008). Large magnetic storm-induced nighttime ionospheric flows at midlatitudes and their impacts on GPS-based navigation systems. *J. Geophys. Res.* 113, A00A06. doi:10.1029/2008JA013076

Blanc, M., Alcaydé, D., and Kelly, J. D. (1983). Magnetospheric convection effects at mid-latitudes: 2. A coordinated chatanika/saint-santin study of the april 10–14, 1978, magnetic storm. *J. Geophys. Res.* 88 (A1), 224–234. doi:10.1029/JA088iA01p00224

Bruinsma, S., Forbes, J. M., Nerem, R. S., and Zhang, X. (2006). Thermosphere density response to the 20–21 November 2003 solar and geomagnetic storm from CHAMP and GRACE accelerometer data. *J. Geophys. Res.* 111, A06303. doi:10.1029/2005JA011284

Bruinsma, S. L., Doornbos, E., and Bowman, B. R. (2014). Validation of GOCE densities and evaluation of thermosphere models. *Adv. Space Res.* 54, 576–585. doi:10.1016/j.asr.2014.04.008

Burch, J. L., Reiff, P. H., Menietti, J. D., Heelis, R. A., Hanson, W. B., Shawhan, S. D., et al. (1985). IMFB_y-dependent plasma flow and birkeland currents in the dayside magnetosphere: 1. Dynamics explorer observations. *J. Geophys. Res.* 90 (A2), 1577–1593. doi:10.1029/JA090iA02p01577

Cousins, E. D. P., and Shepherd, S. G. (2010). A dynamical model of high-latitude convection derived from SuperDARN plasma drift measurements. *J. Geophys. Res.* 115, A12329. doi:10.1029/2010JA016017

Cowley, S. W. H., and Lockwood, M. (1992). Excitation and decay of solar wind-driven flows in the magnetosphere-ionosphere system. *Ann. Geophys.* 10 (1–2), 103–115.

Cowley, S. (1981). Magnetospheric asymmetries associated with the y-component of the IMF. *Planet Space Sci.* 29 (1), 79–96. doi:10.1016/0032-0633(81)90141-0

Coxon, J. C., Milan, S. E., Carter, J. A., Clausen, L. B. N., Anderson, B. J., and Korth, H. (2016). Seasonal and diurnal variations in AMPERE observations of the Birkeland currents compared to modeled results. *J. Geophys. Res. Space Phys.* 121, 4027–4040. doi:10.1002/2015JA022050

Deng, Y., and Ridley, A. J. (2006). Dependence of neutral winds on convection E-field, solar EUV, and auroral particle precipitation at high latitudes. *J. Geophys. Res.* 111, A09306. doi:10.1029/2005JA011368

Deng, Y., Sheng, C., Tsurutani, B. T., and Mannucci, A. J. (2018). Possible influence of extreme magnetic storms on the thermosphere in the high latitudes. *Space Weather* 16 (7), 802–813. doi:10.1029/2018SW001847

Deng, Y., Heelis, R., Lyons, L. R., Nishimura, Y., and Gabrielse, C. (2019). Impact of flow bursts in the auroral zone on the ionosphere and thermosphere. *J. Geophys. Res. Space Phys.* 124, 10459–10467. doi:10.1029/2019JA026755

Deng, Y., Lin, C. Y., Zhu, Q., and Sheng, C. (2021). "Influence of nonhydrostatic processes on the ionosphere-thermosphere," in *Upper atmosphere dynamics and energetics*. Editors W. Wang, Y. Zhang, and L. J. Paxton doi:10.1002/9781119815631.ch4

Doornbos, E., Bruinsma, S., Fritsche, B., Koppenwallner, G., Visser, P., van den Ijssel, J., et al. (2014). *ESA Contract 4000102847/NL/EL GOCE+ Theme 3: Air density and wind retrieval using GOCE data—final report*. Netherlands: TU Delft.

Emmert, J. T., Drob, D. P., Picone, J. M., Siskind, D. E., Jones, M., Mlynczak, M. G., et al. (2021). NRLMSIS 2.0: A whole-atmosphere empirical model of temperature and neutral species densities. *Earth Space Sci.* 8, e2020EA001321. doi:10.1029/2020EA001321

Emmert, J. T. (2015). Altitude and solar activity dependence of 1967–2005 thermospheric density trends derived from orbital drag. *J. Geophys. Res. Space Phys.* 120, 2940–2950. doi:10.1002/2015JA021047

Förster, M., and Cnossen, I. (2013). Upper atmosphere differences between northern and southern high latitudes: The role of magnetic field asymmetry. *J. Geophys. Res.* 118, 5951–5966. doi:10.1002/jgra.50554

Fuller-Rowell, T. J., and Evans, D. S. (1987). Height-integrated Pedersen and Hall conductivity patterns inferred from the TIROS-NOAA satellite data. *J. Geophys. Res.* 92, 7606–7618. doi:10.1029/JA092iA07p07606

Fuller-Rowell, T. J., Codrescu, M. V., Moffett, R. J., and Quegan, S. (1994). Response of the thermosphere and ionosphere to geomagnetic storms. *J. Geophys. Res.* 99 (A3), 3893–3914. doi:10.1029/93JA02015

Goldstein, J., Sandel, B. R., Forrester, W. T., Thomsen, M. F., and Hairston, M. R. (2005). Global plasmasphere evolution 22–23 April 2001. *J. Geophys. Res.* 110, A12218. doi:10.1029/2005JA011282

Green, D. L., Waters, C. L., Anderson, B. J., Korth, H., and Barnes, R. J. (2006). Comparison of large-scale Birkeland currents determined from Iridium and SuperDARN data. *Ann. Geophys.* 24 (3), 941–959. doi:10.5194/angeo-24-941-2006

Green, D. L., Waters, C. L., Anderson, B. J., and Korth, H. (2009). Seasonal and interplanetary magnetic field dependence of the field-aligned currents for both Northern and Southern Hemispheres. *Ann. Geophys.* 27, 1701–1715. doi:10.5194/angeo-27-1701-2009

Hairston, M., Coley, W. R., and Stoneback, R. (2016). Responses in the polar and equatorial ionosphere to the March 2015 St. Patrick Day storm. *J. Geophys. Res. Space Phys.* 121, 11,213–11,234. doi:10.1002/2016JA023165

Heelis, R. A., and Maute, A. (2020). Challenges to understanding the Earth's ionosphere and thermosphere. *J. Geophys. Res. Space Phys.* 125, e2019JA027497. doi:10.1029/2019JA027497

Heelis, R. A., and Mohapatra, S. (2009). Storm time signatures of the ionospheric zonal ion drift at middle latitudes. *J. Geophys. Res.* 114, A02305. doi:10.1029/2008JA013620

Hong, Y., Deng, Y., Zhu, Q., Maute, A., Sheng, C., Welling, D., et al. (2021). Impacts of different causes on the inter-hemispheric asymmetry of ionosphere-thermosphere system at mid- and high-latitudes: GITM simulations. *Space Weather* 19, e2021SW002856. doi:10.1029/2021SW002856

Jakowski, N., Stankov, S. M., and Klaehn, D. (2005). Operational space weather service for GNSS precise positioning. *Ann. Geophys.* 23, 3071–3079. doi:10.5194/angeo-23-3071-2005

Jin, Y., and Xiong, C. (2020). Interhemispheric asymmetry of large-scale electron density gradients in the polar cap ionosphere: UT and seasonal variations. *J. Geophys. Res. Space Phys.* 125, e2019JA027601. doi:10.1029/2019JA027601

Kabin, K., Rankin, R., Marchand, R., Gombosi, T. I., Clauer, C. R., Ridley, A. J., et al. (2003). Dynamic response of Earth's magnetosphere to $B_y$reversals. *J. Geophys. Res.* 108, 1132. doi:10.1029/2002ja009480

Laundal, K. M., and Østgaard, N. (2009). Asymmetric auroral intensities in the Earth's Northern and Southern hemispheres. *Nature* 460, 491–493. doi:10.1038/nature08154

Laundal, K. M., Cnossen, I., Milan, S. E., Haaland, S. E., Coxon, J., Pedatella, N. M., et al. (2017). North–south asymmetries in Earth's magnetic field. *Space Sci. Rev.* 206, 225–257. doi:10.1007/s11214-016-0273-0

Lin, C. Y., Deng, Y., Sheng, C., and Drob, D. P. (2017). A study of the nonlinear response of the upper atmosphere to episodic and stochastic acoustic-gravity wave forcing. *J. Geophys. Res. Space Phys.* 122, 1178–1198. doi:10.1002/2016JA022930

Lu, G., Richmond, A. D., Emery, B. A., Reiff, P. H., de la Beaujardiere, O., Rich, F. J., et al. (1994). Interhemispheric asymmetry of the high-latitude ionospheric convection pattern. *J. Geophys. Res.* 99 (A4), 6491–6510. doi:10.1029/93JA03441

Lu, G., Hagan, M. E., Häusler, K., Doornbos, E., Bruinsma, S., Anderson, B. J., et al. (2014). Global ionospheric and thermospheric response to the 5 April 2010 geomagnetic storm: An integrated data-model investigation. *J. Geophys. Res. Space Phys.* 119 (12), 10358–10375. doi:10.1002/2014JA020555

Lu, G., Zakharenkova, I., Cherniak, I., and Dang, T. (2020). Large-scale ionospheric disturbances during the 17 March 2015 storm: A model-data comparative study. *J. Geophys. Res. Space Phys.* 125 (5), e2019JA027726. doi:10.1029/2019JA027726

Lu, G. (2017). Large scale high-latitude ionospheric electrodynamic fields and currents. *Space Sci. Rev.* 206 (1–4), 431–450. doi:10.1007/s11214-016-0269-9

Maute, A., and Richmond, A. D. (2017). *F*-region dynamo simulations at low and mid-latitude. *Space Sci. Rev.* 206 (1–4), 471–493. doi:10.1007/s11214-016-0262-3

Maute, A., Richmond, A. D., Lu, G., Knipp, D. J., Shi, Y., and Anderson, B. (2021). Magnetosphere-ionosphere coupling via prescribed field-aligned current simulated by the TIEGCM. *J. Geophys. Res. Space Phys.* 126, e2020JA028665. doi:10.1029/2020JA028665

Maute, A., Lu, G., Knipp, D., Anderson, B., and Vines, S. (2022). Importance of lower atmospheric forcing and magnetosphere-ionosphere coupling in simulating neutral density during the February 2016 geomagnetic storm. *Front. Astron. Space Sci.* 9, 932748. doi:10.3389/fspas.2022.932748

McGranaghan, R., Knipp, D. J., McPherron, R. L., and Hunt, L. A. (2014). Impact of equinoctial high-speed stream structures on thermospheric responses. *Space Weather* 12, 277–297. doi:10.1002/2014SW001045

McHarg, M., Chun, F., Knipp, D., Lu, G., Emery, B., and Ridley, A. (2005). High-latitude Joule heating response to IMF inputs. *J. Geophys. Res.* 110, A08309. doi:10.1029/2004JA010949

Milan, S. E., Carter, J. A., Bower, G. E., Imber, S. M., Paxton, L. J., Anderson, B. J., et al. (2020). Dual-lobe reconnection and horse-collar auroras. *J. Geophys. Res. Space Phys.* 125, e2020JA028567. doi:10.1029/2020JA028567

Newell, P. T., Sotirelis, T., and Wing, S. (2009). Diffuse, monoenergetic, and broadband aurora: The global precipitation budget. *J. Geophys. Res.* 114. doi:10.1029/2009JA014326

Ohtani, S., Wing, S., Ueno, G., and Higuchi, T. (2009). Dependence of premidnight field-aligned currents and particle precipitation on solar illumination. *J. Geophys. Res.* 114, A12205. doi:10.1029/2009JA014115

Pi, X., Mannucci, A., Lindqwister, U., and Ho, C. (1997). Monitoring of global ionospheric irregularities using the worldwide GPS network. *Geophys. Res. Lett.* 24 (18), 2283–2286. doi:10.1029/97GL02273

Reiff, P. H., and Burch, J. L. (1985). IMF by-dependent plasma flow and birkeland currents in the dayside magnetosphere: 2. A global model for northward and southward IMF. *J. Geophys. Res.* 90 (A2), 1595–1609. doi:10.1029/JA090iA02p01595

Reistad, J. P., Østgaard, N., Laundal, K. M., Haaland, S., Tenfjord, P., Snekvik, K., et al. (2015). Intensity asymmetries in the dusk sector of the poleward auroral oval due to IMF B_x. *J. Geophys. Res. Space Phys.* 119, 9497–9507. doi:10.1002/2014JA020216

Reistad, J. P., Laundal, K. M., Østgaard, N., Ohma, A., Burrell, A. G., Hatch, S. M., et al. (2021). Quantifying the lobe reconnection rate during dominant IMF b_y periods and different dipole tilt orientations. *J. Geophys. Res. Space Phys.* 126, e2021JA029742. doi:10.1029/2021JA029742

Rich, F. J., and Hairston, M. (1994). Large-scale convection patterns observed by DMSP. *J. Geophys. Res.* 99 (A3), 3827–3844. doi:10.1029/93JA03296

Richmond, A. D., and Kamide, Y. (1988). Mapping electrodynamic features of the high-latitude ionosphere from localized observations: Technique. *J. Geophys. Res. Space Phys.* 93 (A6), 5741–5759. doi:10.1029/JA093iA06p05741

Richmond, A. D. (1995). Ionospheric electrodynamics using magnetic apex coordinates. *J. Geomagn. Geoelectr.* 47, 191–212. doi:10.5636/jgg.47.191

Richmond, A. D. (2011). "Electrodynamics of ionosphere–thermosphere coupling," in *Aeronomy of the earth's atmosphere and ionosphere. IAGA special sopron book series*. Editors M. Abdu and D. Pancheva (Dordrecht: Springer), Vol. 2. doi:10.1007/978-94-007-0326-1_13

Ridley, A. J., Deng, Y., and Tóth, G. (2006). The global ionosphere thermosphere model. *J. Atmos. Solar-Terrestrial Phys.* 68 (8), 839–864. doi:10.1016/j.jastp.2006.01.008

Robinson, R. M., Zanetti, L., Anderson, B., Vines, S., and Gjerloev, J. (2021). Determination of auroral electrodynamic parameters from AMPERE field-aligned current measurements. *Space Weather* 19 (4), e2020SW002677. doi:10.1029/2020SW002677

Sandholt, P. E., and Farrugia, C. J. (2007). Role of poleward moving auroral forms in the dawn-dusk auroral precipitation asymmetries induced by IMF by. *J. Geophys. Res.* 112, A04203. doi:10.1029/2006JA011952

Sheng, C., Deng, Y., Gabrielse, C., Lyons, L. R., Nishimura, Y., Heelis, R. A., et al. (2021). Sensitivity of upper atmosphere to different characteristics of flow bursts in the auroral zone. *J. Geophys. Res. Space Phys.* 126, e2021JA029253. doi:10.1029/2021JA029253

Shi, Y., Knipp, D. J., Matsuo, T., Kilcommons, L., and Anderson, B. (2020). Modes of (FACs) variability and their hemispheric asymmetry revealed by inverse and assimilative analysis of iridium magnetometer data. *J. Geophys. Res. Space Phys.* 125, e2019JA027265. doi:10.1029/2019JA027265

Tenfjord, P., Østgaard, N., Snekvik, K., Laundal, K. M., Reistad, J. P., Haaland, S., et al. (2015). How the IMF b_y induces a b_y component in the closed magnetosphere and how it leads to asymmetric currents and convection patterns in the two hemispheres. *J. Geophys. Res. Space Phys.* 120, 9368–9384. doi:10.1002/2015JA021579

Tsurutani, B. T., Verkhoglyadova, O. P., Mannucci, A. J., Saito, A., Araki, T., Yumoto, K., et al. (2008). Prompt penetration electric fields (PPEFs) and their ionospheric effects during the great magnetic storm of 30–31 October 2003. *J. Geophys. Res.* 113, A05311. doi:10.1029/2007JA012879

Tulasi Ram, S., Su, S.-Y., and Liu, C. H. (2009). FORMOSAT-3/COSMIC observations of seasonal and longitudinal variations of equatorial ionization anomaly and its interhemispheric asymmetry during the solar minimum period. *J. Geophys. Res.* 114, A06311. doi:10.1029/2008JA013880

Vasyliūnas, V. M., and Song, P. (2005). Meaning of ionospheric Joule heating. *J. Geophys. Res.* 110, A02301. doi:10.1029/2004JA010615

Walsh, A. P., Haaland, S., Forsyth, C., Keesee, A. M., Kissinger, J., Li, K., et al. (2014). Dawn-dusk asymmetries in the coupled solar wind-magnetosphere-ionosphere system: A review. *Ann. Geophys.* 32, 705–737. doi:10.5194/angeo-32-705-2014

Wang, W., Wiltberger, M., Burns, A. G., Solomon, S. C., Killeen, T. L., Maruyama, N., et al. (2004). Initial results from the coupled magnetosphere-ionosphere-thermosphere model: thermosphere-ionosphere responses. *J. Atmos. Solar-Terrest. Phys.* 66, 1425–1441. doi:10.1016/j.jastp.2004.04.008

Wang, X., Miao, J., Aa, E., Ren, T., Wang, Y., Liu, J., et al. (2020). Statistical analysis of Joule heating and thermosphere response during geomagnetic storms of different magnitudes. *J. Geophys. Res. Space Phys.* 125, e2020JA027966. doi:10.1029/2020JA027966

Waters, C. L., Anderson, B. J., and Liou, K. (2001). Estimation of global field aligned currents using the iridium® System magnetometer data. *Geophys. Lett.* 28 (11), 2165–2168. doi:10.1029/2000GL012725

Waters, C. L., Anderson, B. J., Green, D. L., Korth, H., Barnes, R. J., and Vanhamäki, H. (2020). "Science data products for AMPERE," in *Ionospheric multi-spacecraft analysis tools: Approaches for deriving ionospheric parameters*. Editors M. W. Dunlop and H. Lühr (Springer International Publishing), 141–165. doi:10.1007/978-3-030-26732-2_7

Weimer, D. R. (2005). Improved ionospheric electrodynamic models and application to calculating Joule heating rates. *J. Geophys. Res.* 110, A05306. doi:10.1029/2004JA010884

Wiltberger, M., Wang, W., Burns, A. G., Solomon, S. C., Lyon, J. G., and Goodrich, C. C. (2004). Initial results from the coupled magnetosphere ionosphere thermosphere model: magnetospheric and ionospheric responses. *J. Atmos. Solar-Terrestrial Phys.* 66, 1411–1423. doi:10.1016/j.jastp.2004.03.026

Workayehu, A. B., Vanhamäki, H., and Aikio, A. T. (2020). Seasonal effect on hemispheric asymmetry in ionospheric horizontal and field-aligned currents. *J. Geophys. Res. Space Phys.* 125 (10), e2020JA028051. doi:10.1029/2020ja028051

Zhu, Q., Deng, Y., Richmond, A., McGranaghan, R. M., and Maute, A. (2019). Impacts of multiscale FACs on the ionosphere-thermosphere system: GITM simulation. *J. Geophys. Res. Space Phys.* 124 (5), 3532–3542. doi:10.1029/2018JA026082

Zhu, Q., Deng, Y., Maute, A., Kilcommons, L. M., Knipp, D. J., and Hairston, M. (2021). ASHLEY: A new empirical model for the high-latitude electron precipitation and electric field. *Space Weather* 19, e2020SW002671. doi:10.1029/2020SW002671

Zhu, Q., Lu, G., Maute, A., Deng, Y., and Anderson, B. (2022). Assessment of using field-aligned currents to drive the global ionosphere thermosphere model: A case study for the 2013 St patrick's day geomagnetic storm. *Space Weather* 20, e2022SW003170. doi:10.1029/2022SW003170

Zhu, Q., Lu, G., and Deng, Y. (2022b). Low- and mid-latitude ionospheric response to the 2013 St. Patrick's day geomagnetic storm in the American sector: Global ionosphere thermosphere model simulation. *Front. Astron. Space Sci.* 9, 916739. doi:10.3389/fspas.2022.916739

Frontiers in
Astronomy and Space Sciences

Explores planetary science and extragalactic astronomy in all wavelengths

Advances the understanding of our universe - from planetary science to extragalactic astronomy, to high-energy and astroparticle physics.

Discover the latest Research Topics

See more →

Frontiers

Avenue du Tribunal-Fédéral 34
1005 Lausanne, Switzerland
frontiersin.org

Contact us

+41 (0)21 510 17 00
frontiersin.org/about/contact